University of Rochester
Laboratory for Laser Energetics

DOE/NA/3856-1529
April 2020

LLE 2019 Annual Report

October 2018 – September 2019

Cover Photos

Top left: A novel statistical model was used to predict and design multiple cryogenic deuterium–tritium implosions on the OMEGA Laser System, leading to the tripling of the fusion yield to its highest value so far for direct-drive laser fusion. The work was published in the January 2019 issue of the journal Nature with graduate student Varchas Gopalaswamy as the lead author.

Top center: LLE is constructing a new mid-scale ultrashort-pulse laser facility: an all optical parametric amplifier line (OPAL) pumped by the Multi-Terawatt (MTW) laser that will produce 7.5 J in 15 fs. Shown are Jake Bromage and Mike Spilatra working on the integration of MTW-OPAL inside the grating compressor chamber.

Top right: LLE has developed a novel angularly resolved Thomson-scattering (ARTS) diagnostic to measure the plasma electron distribution function. Shown is the installation of the ARTS inside its ten-inch manipulator for an experiment on OMEGA.

Middle left: Two 5-in. × 6-in. optics in a circular containment were coated with a broadband-enhanced metal reflector (BEMR) film inside the Optical Manufacturing's 54-in. coating vacuum chamber. The BEMR coating was developed for use in a short-pulse laser system.

Middle Center: Drs. Millot and Coppari from Lawrence Livermore National Laboratory and Dr. Rygg at LLE led the discovery of superionic water, a new "strange" form of water that is simultaneously solid and liquid, in the laboratory using the OMEGA Laser System. The work was published in the May 2019 issue of the journal Nature.

Middle right: A prototype of a neutron time-of-flight diagnostic designed for the National Ignition Facility using a new type of crystal, known as bibenzyl, was fielded and tested at the Omega Laser Facility.

Bottom left: Katelyn Cook, a recent alumna of LLE's undergraduate student programs, received the 2019 American Physical Society's LeRoy Apker Award for her outstanding research into measuring low-energy nuclear cross sections using inertial confinement fusion while a student at Houghton College in collaboration with LLE and SUNY Geneseo. Shown here is her poster presentation at the 2019 OLUG workshop.

Bottom right: Visible camera image of the first LaserNetUS experiment on OMEGA EP in November 2019 led by Johns Hopkins University to develop Talbot–Lau x-ray deflectometry for the measurement of the electron density profile at the laser ablation front. The LaserNetUS Initiative is funded by the Department of Energy's Office of Fusion Energy Sciences to provide U.S. scientists increased access to unique high-intensity laser facilities at ten institutions.

The work described in this volume includes current research at the Laboratory for Laser Energetics, which is supported by New York State Energy Research and Development Authority, the University of Rochester, the U.S. Department of Energy Office of Inertial Confinement Fusion under Cooperative Agreement No. DE-NA0003856, and other agencies.

For questions or comments, Laboratory for Laser Energetics,
250 East River Road, Rochester, NY 14623-1299, (585) 275-5286.
www.lle.rochester.edu

Prepared for
U.S. Department of Energy
Albuquerque Service Center
DOE/NA/3856-1529

Distribution Category
October 2018–September 2019

Printed in the United States of America
Available from
National Technical Information Services
U.S. Department of Commerce
5285 Port Royal Road
Springfield, VA 22161
www.ntis.gov

University of Rochester
Laboratory for Laser Energetics

DOE/NA/3856-1529
April 2020

LLE 2019 Annual Report

October 2018 – September 2019

Inertial Fusion Program and
National Laser Users' Facility Program

Contents

LLE REVIEW 160 (JULY–SEPTEMBER 2019)

INERTIAL CONFINEMENT FUSION

PLASMA AND ULTRAFAST PHYSICS

DIAGNOSTIC SCIENCE AND DETECTORS

LASER TECHNOLOGY AND DEVELOPMENT

PULSED-POWER SYSTEMS

EDUCATION AND OUTREACH

LASER FACILITY REPORT

NATIONAL LASER USERS' FACILITY AND EXTERNAL USERS' PROGRAMS

YEAR-END REPORTS

PUBLICATIONS AND CONFERENCE PRESENTATIONS

Executive Summary

E. M. Campbell

Director, Laboratory for Laser Energetics

The fiscal year ending September 2019 (FY19) comprised the first year of Laboratory for Laser Energetics work under the renewal U.S. Department of Energy (DOE) National Nuclear Security Administration's (NNSA's) Office of Experimental Sciences Inertial Confinement Fusion Cooperative Agreement No. DE-NA0003856. The Laboratory's work is also sponsored by the New York State Energy Research Development Authority, and other federal agencies. This annual report summarizes work conducted under the Cooperative Agreement at LLE during FY19 including work on the Inertial Confinement Fusion (ICF) and High-Energy-Density (HED) science campaigns; laser, optical materials, and advanced technology development; operation of the Omega Laser Facility for the ICF and HED Campaigns, the National Laser Users' Facility (NLUF), the Laboratory Basic Science (LBS) Program, and other external users; and programs focusing on the education of high school, undergraduate, and graduate students.

Inertial Confinement Fusion Research

One of the principal missions of LLE is to conduct research in ICF with an emphasis on supporting the goal of achieving ignition at the National Ignition Facility (NIF). This program uses the Omega Laser Facility, the NIF, and the full experimental, theoretical, computational, and engineering resources of the Laboratory. During FY19, 2320 target shots were taken at the Omega Laser Facility (comprised of the 60-beam OMEGA UV laser and the four-beam, high-energy petawatt OMEGA EP laser). The ICF and HED Campaigns accounted for approximately 78% of the facility shots. LLE is the lead laboratory worldwide for the laser-direct-drive approach with research focused on cryogenic implosions on the 60-beam OMEGA laser and on laser–plasma interaction physics of importance to all laser-driven concepts at both the Omega and NIF facilities. LLE has also developed, tested, and constructed a number of diagnostics currently being used at both the Omega Laser Facility and on the NIF. During this past year, progress in the Inertial Fusion Research Program continued in three principal areas: ICF experiments and experiments in support of ICF; theoretical analysis and design efforts aimed at improving direct-drive–ignition capsule designs and advanced ignition concepts such as magnetized implosion; and the development of diagnostics for experiments on the NIF, OMEGA, and OMEGA EP Laser Systems. This annual report includes the summaries published in the LLE Review (Quarterly Reports) on the LLE research performed during FY19 in these areas.

Fourteen of the summaries highlighted in the report concern research on ICF including: rarefaction flows and the mitigation of imprint in direct-drive implosions; the use of secondary neutron yields to infer the fuel areal density of magnetized liner inertial fusion; the impact of a non-Maxwellian electron energy distribution function on cross-beam energy transfer (CBET); the inference of electron temperature from x-ray continuum emission for OMEGA direct-drive ICF implosions; the effects of fuel–shell interface instability growth on the performance of room-temperature direct-drive implosions; simulated refraction enhanced x-ray radiography of laser-driven implosions; the effect of CBET on target offset asymmetry in directly driven ICF implosions (see Fig. 1 on p. 128); a wavelength-detuning CBET-mitigation scheme for polar direct drive; the development of a platform for burning-plasma studies using direct-drive double-shell implosions; density measurements of the inner shell release; the role of baroclinicity in the kinetic energy budge; development of an ignition criterion for inertial fusion implosions based on yield amplification from alpha-particle heating; the development of and experiments on a hybrid target design that incorporates both direct- and indirect-drive target designs for mitigating the Rayleigh–Taylor instability; and the development of two modifications to the Guderley solution to the converging shock problem to extend its utility to (1) the addition of an isentropic release wave and (2) fluid partitioning between an electron fluid and an ion fluid.

Plasma and Ultrafast Science

The development of a strong fundamental plasma physics and ultrafast science capability underlies much of ICF and HED science. In this report we present 14 articles that highlight the FY19 laboratory efforts in these areas including: the investigation of the impact of non-Maxwellian electron velocity distribution functions on inferred plasma parameters in collective Thomson scattering; measurements of the heat flux from collective Thomson scattering with non-Maxwellian distribution functions; a review of the laser–plasma interactions enabled by emerging laser and optical technologies; the demonstration of a modified technique for laser-driven magnetic reconnection; the demonstration of a technique to mitigate self-focusing in Thomson-scattering experiments; a report on a numerical study of absolute instability thresholds for stimulated Raman scattering (SRS) and two-plasmon–decay (TPD) instabilities using a broad-bandwidth pump beam; the development of a program that models CBET for the simple case of two intersecting beams; a summary of the investigation of picosecond thermodynamics in a laser-produced plasma using Thomson scattering; efforts to create and control ionization fronts using the flying focus technique; the demonstration that the ionization front produced by a flying focus can upshift the frequency of an ultrashort optical pulse to the extreme ultraviolet over a centimeter of propagation; the measurement of the picosecond evolution of non-Maxwellian electron distribution functions in plasmas generated by the Multi-Terawatt (MTW) laser; a report on the finding that a dynamic instability saturation mechanism allows laser light to be transmitted through coronal plasma even if it surpasses the threshold conditions for SRS (as observed in experiments on the NIF); the development of an experimental platform on the NIF to investigate hot-electron production from laser–plasma instabilities at conditions relevant to direct-drive targets; and the use of 3-D particle-in-cell simulations to investigate the interplay between TPD and SRS at conditions relevant to direct-drive targets.

High-Energy-Density Physics

High-energy-density physics (HEDP) is the study of matter at extreme conditions. The HED condition, often defined by an energy density (in pressure units) in excess of 1 Mbar, not only is foundational for ICF research and national nuclear security, but is also common in the universe, including at the interior of planets such as Earth or Jupiter, stellar interiors, and the atmospheres and the vicinity of compact objects such as white dwarfs, neutron stars, and black holes. HED regimes also enable the study of new realms of quantum mater behavior, properties, and phenomena.

LLE plays a major role in the nation's HEDP Program not only through the numerous users' experiments conducted at the Omega Laser Facility but also by HED physics research (experiments, theory, and modeling) carried out by LLE scientists and graduate researchers. This volume contains summaries of four of these efforts including: a collaborative effort involving LLE and the University of Florida demonstrating the equivalence between the three global representations of the free energy [the Karasiev–Sjostrom–Duffy–Trickey (KSDT) representation]; its descendant, the corrected KSDT; and the Gruth–Dornheim–Bonitz parametrization; a review of work to derive new thermodynamic constraints on internal, thermal, and magnetic states of super-Earth (SE) planets ranging in size from 1 to 10 earth masses; a discussion of exchange-correlation thermal effects in shocked deuterium confirming that the crossover between the quantum and classical statistics occurs below a temperature equal to the Fermi temperature (see Fig. 3 on p. 99); and the presentation of a first-principles construction of a high-pressure–temperature phase diagram of silicon up to multi-TPa pressures that revealed new stable phases.

Diagnostic Science and Detectors

The continued development of state-of-the-art diagnostic instrumentation is required to conduct experiments in support of the national ICF and HED programs. In this volume, we present seven summaries on research and development projects in this area including: a report on the joint development a ten-inch-manipulator–based fast-electron spectrometer with multiple viewing angles for experiments at the Omega Laser Facility led by Osaka University and LLE; a report on the joint study by the University of Rochester, Rochester Institute of Technology, Brookhaven National Laboratory, Savannah National Laboratory, Brimrose Technology Corporation, and the Institute of Electron Technology, Poland, of the ultrafast optical properties of single-crystal cadmium magnesium telluride for use in x-ray detectors; a report on the use of a short-pulse laser and precision triggering system to generate a spatiotemporal flat field for a high-speed gated-optical imager used on the OMEGA UV beamlets; a demonstration of the co-timing of the UV and IR beams of the OMEGA EP Laser System with variations less than 20 ps during routine operations; and a report on the fabrication of aluminum–gallium–nitride photodetectors with micrometer-scale length metal–semiconductor–metal structures.

Laser Technology and Development

In addition to advanced diagnostic development, the ICF and HED experimental programs require continuous laser technology development. This annual report contains six articles on work in this area including: a report on the development of high-efficiency, large-aperture fifth-harmonic generation of 211-nm pulses in ammonium dihydrogen phosphate (ADP) crystals for deep UV Thomson scattering diagnostics performed with LLNL; a study of the interaction of short laser pulses with model contamination microparticles on a high reflector; a review of the current status of chirped-pulse–amplification (CPA) technology and its applications; a summary of heat-flow measurements from surface defects in lithium triborate; an investigation of the role of Urbach tail optical absorption on the subpicosecond laser-induced–damage threshold at 1053 nm in hafnia and silica monolayers; an investigation of mechanisms of laser-induced secondary contamination from metal particles attached on the input surface of optical components; and the demonstration of efficient parametric amplification of broadband spectrally incoherent pulses with applications to the development of a 1% fractional bandwidth laser for improved direct-drive implosions.

Materials Science

A strong materials science effort is required to realize the required laser and instrumentation objectives for ICF and HED research. This report includes the following seven summaries of materials science efforts at LLE: the evaluation of laser-induced–damage threshold in saturated and unsaturated nematic liquid crystals between 600 fs and 1.5 ns at 1053 nm; a report on mechanisms governing laser-induced damage in absorbing glasses under exposure to nanosecond pulses; a review of international efforts to extract tritium from water; measurements of tritium migration in the near surface of stainless-steel 316; a report on the electrochemical synthesis of copper nanoparticles on hydroxyapatite coating for antibacterial implants; a report on silver-hydroxyapatite composite coatings with enhanced antimicrobial activities through heat treatment; a report on a collaborative effort of the University of Rochester, the West Pomeranian University of Technology (Poland), the Institute of Electron Technology (Poland), the University of Iceland, and the Center for Physical Sciences and Technology (Lithuania) to investigate terahertz time-domain spectroscopy of graphene nanoflakes embedded in a polymer matrix; and measurements of the angular dependence of spontaneous Raman scattering in anisotropic crystalline materials using spherical samples.

Laser System Science

Safe, efficient, and effective operation of the Omega Laser Facility at LLE requires a team of scientists and engineers with a high level of expertise in solving the various challenges presented by the operation of ultrahigh-power laser systems at their performance limits. In this volume we present eleven summaries of research and development work carried out at LLE in this area including: the implementation of a wavelength-tunable ultraviolet beam on OMEGA EP (see Fig. 2 on p. 44); the development and construction of a full-beam in-tank (FBIT) diagnostic to characterize the OMEGA focal spots; a comparison of FBIT data with equivalent-target-plane measurements of the OMEGA focal spot; a report on efforts to achieve power imbalance on OMEGA of less than 1% rms; a report on PSOPS, a MATLAB-based semi-analytic model for the OMEGA EP laser to predict system performance; a report on a method for calculating the Raman fluency at the surface of an arbitrary crystal and pump polarization configuration for the purpose of improved understanding of the laser power limitations due to transverse Raman generation and amplification in KDP/DKDP crystals; an investigation of the damage resistance of liquid crystals for OMEGA laser conditions; a study of multilayer glancing-angle deposition on a silica substrate to reduce light scattering on film; the development of a radially nonuniform film-deposition technique to mitigate deformations induced by high-compressive films; the design of a four-mirror image relay for the correction of field-constant coma and field-constant astigmatism; and a description of a process using ellipsometric measurement techniques along with a well-established optical design to create precise index models for improving coating designs.

Target Engineering and Research

The development and microfabrication of precise targets for Omega Laser Facility experiments requires significant effort by LLE including the projects outlined in the following areas: the comparison of shadowgraphy and x-ray phase-contrast methods for the characterization of DT ice layers in ICF fusion targets; a report on the prediction of deuterium–tritium ice-layer uniformity in direct-drive ICF target capsules; a report on measurements of a pressure–composition–temperature (PCT) phase diagram for palladium hydride and palladium deuteride at low temperatures; and a comparison of hydrogen absorption for different samples of stainless-steel with Al_2O_3 coatings.

Omega Laser Facility Operations

Under the facility governance plan implemented in FY08 to formalize the scheduling of the Omega Laser Facility as an NNSA User Facility in support of the science-based Stockpile Stewardship Program, Omega Facility shots are allocated by programs following NNSA guidance.

During FY19, the Omega Laser Facility conducted 1489 target shots on OMEGA and 831 target shots on OMEGA EP for a total of 2320 target shots. OMEGA had an experimental effectiveness of 96.6%, while OMEGA EP recorded an experimental effectiveness of 94.3%. OMEGA EP was operated extensively in FY19 for a variety of user experiments. Per the guidance provided by DOE/NNSA, the facility provided target shots for the ICF, HED, NLUF, and LBS programs (see Fig. 1 below). The ICF and HED programs received 78 % of the facility shots in FY19 conducted by scientists from Lawrence Livermore National Laboratory (LLNL), Los Alamos National Laboratory (LANL), Sandia National Laboratories (SNL), Naval Research Laboratory (NRL), and LLE. The facility also provided a small number of shots (~3% in FY19) for Commissariat à l'énergie atomique et aux energies (CEA), Centre Lasers Intenses et Applications (CELIA)/University of Bordeaux, and Rutherford Appleton Laboratory/York University (RAL/York). Approximately 57% of the facility time was allocated for experiments led by external users.

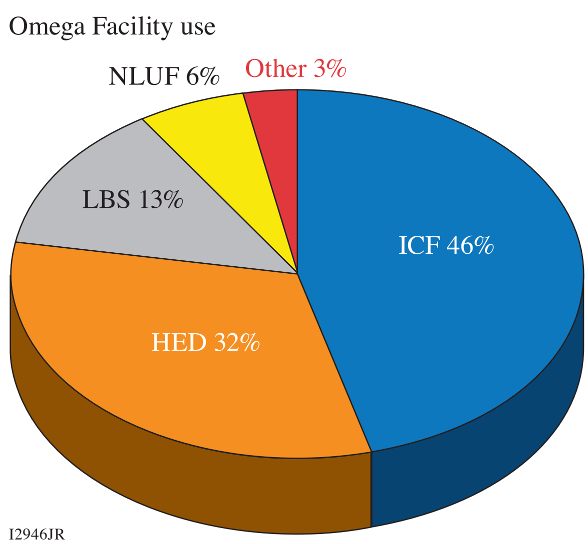

Figure 1
Omega Laser Facility use by program in FY19.

National Laser Users' Facility and External Users' Programs

The Fundamental Science Program at the Omega Laser Facility is also allotted target shots, with projects selected through open-call and peer-reviewed processes. The program has two distinct components: (1) the NLUF Program awarded to individual principal investigators (PI's) on a two-year cycle with the associated Omega Laser Facility time for experiments led by U.S. academia and business; and (2) the LBS Program for basic science experiments conducted by the NNSA ICF laboratories and Office of Science laboratories. In FY19, the Fundamental Science Program obtained a total of 416 target shots (289 for LBS, 127 for NLUF) that accounted for 18% of the 2320 overall Omega Laser Facility shots. The relative lower fraction of the Fundamental Science shots in FY19 is due to the postponed NLUF Solicitation for the 2019 and 2020 period that resulted in no new NLUF projects. Some of the shot time reserved for the NLUF allocation in FY19 was redistributed to LBS, ICF, and HED. Eight collaborative teams participating in the NLUF Program with the Omega Laser Facility shot allocation from the FY17–FY18 awards obtained a total of 127 shots.

During the second and third quarters of FY19, NNSA and the Office of Science jointly completed a funding opportunity announcement, review, and selection process for NLUF experiments to be conducted at the Omega Laser Facility during FY20 and FY21. After the panel review, NNSA selected 11 proposals for funding and Omega shot allocation with a total of 22.5 and 23.5 shot days for experiments in FY20 and FY21, respectively. Following NNSA's guidance, LLE made a one-time additional open-call late in FY19 to receive Omega Laser Facility time proposals for Academic and Industrial Basic Science (AIBS) experiments in order to fulfill the remaining NLUF shot allocation in FY20–FY21. Based on the merit review committee's recommendation, ten new projects were selected with a total of 11 and 10 shot days for AIBS experiments in FY20 and FY21, respectively. Table I (on p. 243) shows the list of NLUF grant projects and AIBS beam-time awards approved for Omega shot allocations in FY20–FY21.

A critical part of the NLUF program is the education and training of graduate students in plasma and HED physics. In addition, graduate students can also access the Omega Laser Facility for shots through their collaborations with national laboratories and LLE. There were more than 60 graduate students from 18 universities involved in the external user-led research programs supported by NLUF/LBS and/or with experiments conducted at the Omega Laser Facility (see Table II on p. 244).

In FY19, a total of 25 LBS projects were allocated a total of 275 shot days for experiments at the Omega Laser Facility, which included five additional projects selected from the FY19 LBS proposals based on their ranking to back-fill some of the NLUF allocations. A total of 289 target shots were conducted for the LBS experiments led by scientists from LLNL, LANL, LLE, SLAC, and Princeton Plasma Physics Laboratory (see Table III, p. 257).

During FY19, LLE issued a solicitation for LBS proposals for beam time in FY20. A total of 36 proposals were submitted, requesting a total of 57.5 shot days, exceeding the LBS allocation by 274%. After review, 22 projects were selected and allocated a total of 21.5 shot days for experiments at the Omega Laser Facility in FY20 as shown in Table IV on p. 258.

In FY19, the Omega Laser Facility was also used for several campaigns (a total of 78 target shots) led by teams from the CEA and CELIA at the University of Bordeaux, France and the joint RAL/University of York of the United Kingdom. These externally funded experiments were conducted at the facility on the basis of special agreements put in place by the UR/LLE and participating institutions with the endorsement of NNSA.

Omega Laser Facility Users Group

The Eleventh Omega Laser Facility Users Group (OLUG) Workshop was held at LLE on 24–26 April 2019. It was attended by 110 researchers, including scientists, postdoctoral fellows (postdocs), and students (Fig. 1, p. 172). The attendees represented institutions from four countries, including the U.S., Canada, U.K., and France. As has been the case for previous workshops, postdocs and students received travel support to attend the workshop from DOE/NNSA. The Workshop program included the presentations of invited science talks from five newly funded NNSA Centers; the NNSA perspective presented by Dr. Sarah Wilk, Deputy Director of NNSA's Office of Experimental Sciences; a facility update and progress on OLUG Recommendations; a summary of the OLUG Executive Committee election results; evening tutorials on "Non-Standard Targets" by LLE scientists and engineers; summaries of the EP-OPAL Workshop and MTW-OPAL; an update on the American Physical Society–Division of Plasma Physics (APS–DPP's) Community Planning Process by Carolyn Kuranz; panel discussions on OLUG Findings and Recommendations; young researcher panel discussions; and three poster sessions comprising a total of 68 posters of which 44 were presented by graduate students, postdocs, and undergraduate students. During the workshop, LLE staff also organized tours of the Omega Laser Facility.

Education and Outreach

As a major university participant in the National ICF Program as part of the NNSA's science-based Stockpile Stewardship Program, education continues to be an important mission for LLE. The Laboratory's education programs cover the range from high school to graduate education. This report provides a summary of LLE's main activities on education in FY19 including:

1. High School Program

LLE holds an annual Summer High School Research Program for Rochester-area high school students who have just completed their junior year. The eight-week program provides an exceptional opportunity for highly motivated students to experience scientific research in a realistic environment. Three hundred and ninety-one students from 55 high schools have participated in the program, among which 137 are female. A total of 39 students, including Simon Narang from the 2019 summer program, have become Scholars in the prestigious Regeneron Science Talent Search for the research projects they carried out at LLE. One hundred and fifty-five students from this program have obtained 190 advanced degrees to date.

2. Undergraduate Student Program

During 2019, LLE employed 54 undergraduate students from the University of Rochester as well as 13 co-op college students from Rochester Institute of Technology, Monroe Community College, and Finger Lakes Community College. Additionally LLE also funded 23 students (and their six faculty advisors) from SUNY Geneseo and Houghton College to conduct research in Physics and Engineering. One of the highlights of LLE's undergraduate student programs in 2019 was the *APS Leroy Apker Award*—an Undergraduate Physics Achievement Award—to *Katelyn Cook*, a recent alumna of LLE's undergraduate student programs, for her outstanding research into measuring low-energy nuclear cross sections using ICF while a student at Houghton College in collaboration with LLE and SUNY Geneseo. Only two awards are made each year, including one to a student from a non-Ph.D. granting institution. After graduating from Houghton in May 2019, Katelyn went on to do nuclear physics research as a Summer Research Assistant at LLNL. She is now a graduate student at Florida State University, pursuing experimental nuclear physics and high-energy-density physics as the focus of her Ph.D. research.

3. Graduate Student Programs

Graduate students are using the Omega Laser Facility as well as other LLE facilities for ICF and HEDP research and technology development activities. These students are making significant contributions to LLE's research program. Twenty-two faculty members with primary appointments with six of the University of Rochester's academic departments collaborate with LLE scientists and engineers. In addition, 14 scientists and engineers at LLE hold secondary faculty appointments with the University at five different academic departments. In FY19, a total of 80 University of Rochester graduate students were involved in research projects at LLE. LLE directly sponsored 51 students pursuing Ph.D. degrees via the NNSA-supported Frank Horton Fellowship Program, among which ten are new Horton fellows (see Table I, p. xv). Their research includes theoretical and experimental plasma physics, HED physics, x-ray and atomic physics, nuclear fusion, material properties under extreme pressure, ultrafast optoelectronics, high-power laser development and applications, nonlinear optics, optical materials and optical fabrication technology, and target fabrication. A total of about 300 UR graduate students have completed their Ph.D. thesis research work supported by LLE since 1970. Many of LLE's alumni now fill responsible positions at the national laboratories, industry, academia, and government.

In FY19, LLE also directly funded research programs that involve graduate students and postdoctoral researchers within the Massachusetts Institute of Technology Plasma Science and Fusion Center, the University of Michigan, the University of Nebraska-Lincoln, the University of Nevada at Reno, Stony Brook University, the University of New Mexico, and Oxford University. These programs involve a total of approximately 18 graduate students, 5 postdoctoral researchers, and 11 faculty members.

In addition, the Omega Laser Facility has significantly facilitated the education and training of more than 200 graduate students and postdoctoral researchers in the HEDP and ICF science areas from other universities through their participation in the NLUF and LBS experiments, or through their collaborations with LLE and national labs. Sixty-one graduate students from 19 universities were involved in these external user-led research programs with the experiments conducted at the Omega Laser Facility in FY19 as described above.

During FY19, 16 Omega graduate students (seven from the University of Rochester and nine from other academic institutions) successfully completed their thesis research and obtained Ph.D. degrees. Table II (p. xviii) lists their name, university, and destination after graduation. Six students (~40% of the total) have joined national laboratories and leading industries for national security, six have stayed in universities, and four work in the private sector. It is expected that a similar number of Ph.D. degrees will be awarded in FY20.

Table I: Recipients of the University of Rochester Frank Horton Fellowship Program at LLE in FY19.

Student Name	Dept.	Faculty Advisor	LLE Advisor	Research Area	Notes
J. Baltazar	ME	S. P. Regan	R. C. Shah	ICF implosion physics	New
Z. Barfield	PA	D. H. Froula		Lateral transport with and without magnetic fields	New
D. Bassler	CH	W. U. Schröder	W. T. Shmayda	Effect of surface chemistry and electronic structure of atomic layer deposition deposits on the tritium inventory of stainless steel	
D. Bishel	PA	G. W. Collins	P. M. Nilson	Mapping the atomic physics of complex ions with detailed nonlocal thermodynamic equilibrium spectroscopy	New
G. Bruhaug	ME	G. W. Collins	H. G. Rinderknecht and M. S. Wei	Advanced x-ray particle sources for HED and ICF diagnostic applications	New
S. Cao	ME	C. Ren		Large-scale fluid and kinetic simulation study of laser–plasma instabilities and hot-electron generation in shock ignition	
D. A. Chin	PA	G. W. Collins	P. M. Nilson and J. R. Rygg	Exploring planetary building blocks through x-ray absorption spectroscopy	NNSA Stewardship Science Graduate Fellow since June 2019
A. R. Christopherson	ME	R. Betti		Theory of alpha heating, burning plasmas, and ignition in inertially confined plasmas	Defending in early 2020
L. Crandall	PA	G. W. Collins	J. R. Rygg	Equation of state of planetary fluids	
A. Davies	PA	D. H. Froula	D. Haberberger	Investigation of collisional electron plasma waves and picosecond thermodynamics in a laser-produced plasma using Thomson-scattering spectroscopy	Defended Ph.D. thesis in Nov. 2019
A. Debrecht	PA	A. Frank		Radiation magnetohydrody-namics of exoplanet winds and evaporation	
M. Evans	PA	P.-A. Gourdain		Experimental studies of ablation in magnetic anvil cells	
C. Fagan	CH	W. U. Schröder	W. Shmayda	The role of surface chemistry and microstructure on the retention of tritium in structural metals	

Table I: Recipients of the University of Rochester Frank Horton Fellowship Program at LLE in FY19 (continued).

Student Name	Dept.	Faculty Advisor	LLE Advisor	Research Area	Notes
P. Franke	PA	D. H. Froula		Measuring the dynamics of electron plasma waves with Thomson scattering	
J. M. Garcia-Figueroa	CHE	D. R. Harding		Controlling the hydrogen content, surface roughness, and other properties of plastic targets using an electron-cyclotron-resonance microwave chemical-vapor–deposition process	
M. Ghosh	CH	P. Huo	S. X. Hu	Understanding the chemistry of hydrocarbons and other materials under high pressure	
M. K. Ginnane	ME	G. W. Collins	J. R. Rygg	Study behavior of materials at high pressure	
X. Gong	ME	G. W. Collins	J. R. Rygg	Structure and electronic properties of sodium and potassium at high pressure	
V. Gopalaswamy	ME	R. Betti		Statistical analysis of OMEGA direct-drive cryogenic DT implosions	
A. Hansen	PA	D. H. Froula		Electron plasma wave dynamics	
R. J. Henchen	ME	D. H. Froula		Hydrodynamic gradients in underdense plasmas	Defended Ph.D. thesis in Dec. 2018 (now a Scientist at Harris Corp.)
B. J. Henderson	PA	G. W. Collins	J. R. Rygg	Broadband reflectivity of shock-compressed materials	
J. Hinz	PA	G. Ghoshal	V. Karasiev	Developing accurate free-energy density functionals via machine learning for warm-dense-matter simulations	
M. Huff	PA	G. W. Collins	J. R. Rygg	Sound-speed measurements on shocked material	
G. W. Jenkins	OPT	J. Bromage		Broadband seed generation and amplification at high average power	
R. Jia	CH	A. Shestopalov	S. G. Demos	Laser damage and chemical passivation of optical surfaces modified with organic molecules	New
A. Kish	PA	A. B. Sefkow		Computational plasma physics, development of hybrid methods	New
L. Leal	PA	R. Betti	A. V. Maximov	Modeling laser-generated plasmas in megagauss external magnetic fields	New

Table I: Recipients of the University of Rochester Frank Horton Fellowship Program at LLE in FY19 (continued).

Student Name	Dept.	Faculty Advisor	LLE Advisor	Research Area	Notes
A. Lees	PA	H. Aluie	R. Betti	Hydrodynamic instability control in a converging geometry	
O. M. Mannion	PA	S. P. Regan	C. J. Forrest	Measurements of the bulk fluid motion in direct-drive experiments	
A. L. Milder	PA	D. H. Froula		Measurement of electron distribution function using collective Thomson scattering	
S. C. Miller	ME	V. N. Goncharov	P. B. Radha	Fine Atwood number effects on deceleration-phase instability in room-temperature direct-drive implosions	
Z. L. Mohamed	PA	D. H. Froula	J. P. Knauer	Gamma emission from fusion reactions	
K. L. Nguyen	PA	D. H. Froula	J. P. Palastro	Application of the flying focus to nonlinear optical and plasma-based applications using a combination of theoretical and computational techniques	
H. Pantell	PA	G. W. Collins	M. Zaghoo	Thermodynamic and mass transport properties of silicate at extreme conditions	New
D. Patel	ME	R. Betti	V. N. Goncharov	Hybrid direct–indirect drive for ICF	
R. Paul	ME	S. X. Hu		*Ab initio* construction of high-pressure phase diagrams of materials	
D. Ramsey	PA	D. H. Froula	J. P. Palastro	Acceleration and radiation from a flying focus	New
J. J. Ruby IV	PA	G. W. Collins	J. R. Rygg	Understanding the thermodynamics of spherically imploding shocks	
E. M. Schiesser	OPT	J. Rolland	S.-W. Bahk	Applying nonsymmetric aberration theory to create scalable, compact beamlines	Defended Ph.D. thesis in Sep. 2019
A. Schwemmlein	PA	W. U. Schröder	J. P. Knauer	Thermonuclear fusion and breakup reaction between light nuclei	
Z. Sprowal	PA	G. W. Collins		Equation of state of hydrogen and hydrogen–helium for planetary interior models	
G. Tabak	PA	G. W. Collins and J. R. Rygg	M. Zaghoo	Study of precompressed materials using shock compression	

Table I: Recipients of the University of Rochester Frank Horton Fellowship Program at LLE in FY19 (continued).

Student Name	Dept.	Faculty Advisor	LLE Advisor	Research Area	Notes
M. Wang	CHE	D. R. Harding		Use of two-photon polymerization to “write” millimeter-size structures with micron resolution	
K. M. Woo	PA	R. Betti		Three-dimensional ablative Rayleigh–Taylor instability	Defended Ph.D. thesis in April 2019
J.-C. Yang	CHE	M. Anthamatten	D. R. Harding	Crystallization in shape-memory polymer networks	
J. Young	PA	P.-A. Gourdain		Laser-triggered X-pinches on MTW	New
D. Zhao	ME	H. Aluie		Multi-scale energy pathways in Rayleigh–Taylor instability flows	
Y. Zhao	MS	W. R. Donaldson		Investigation of the material properties of GaN/AlGaN ultrafast UV photodetectors	Defended Ph.D. thesis in March 2019
H. Zhou	PA	E. Blackman		New developments in mean field electrodynamics and measurable implications for magnetic-field amplification in turbulent, sheared, rotating flows of astrophysical rotators	
Y. Zou	PA	A. Frank		Common envelope evolution: HEDP studies of gravitational wave-merger properties. The role of equation of state and radiation transport	

ME: Mechanical Engineering; PA: Physics and Astronomy; CH: Chemistry; CHE: Chemical Engineering; OPT: Institute of Optics

Table II: Sixteen LLE students who obtained their Ph.D. degrees during FY19.

Name	Institution	Destination after obtaining Ph.D.
E. Schiesser	UR	Synopsys' Optical Solution Group
J. Woo	UR	UR/LLE
Y. Zhao	UR	SLD Laser
R. Henchen	UR	Harris Corp. Space and Intelligence Division
Z. Chen	UR	CITA National Postdoc Fellow at the University of Alberta, Canada
D. N. Polsin	UR	UR/LLE
D. Saulnier	UR	UR Institute of Optics
H. Sio	Massachusetts Institute of Technology	LLNL (2019 Lawrence Fellow finalist)
A. Rasmus	University of Michigan	LANL
L. Elgin	University of Michigan	Sandia National Laboratories
A. Hussein	University of Michigan	University of California, Irvine (UC President Postdoc Fellowship)
P. Kordell	University of Michigan	Northrup Grumman
R. Hua	University of California, San Diego	Canon Medical Research USA
J. Trela	University of Bordeaux, France	CEA, France
A. Bott	Oxford University (UK)	Oxford University (now at Princeton University)
C. Holcomb	Princeton University	The Esteé Lauder Companies

Rarefaction Flows and Mitigation of Imprint in Direct-Drive Implosions

I. V. Igumenshchev,[1] A. L. Velikovich,[2] V. N. Goncharov,[1] R. Betti,[1] E. M. Campbell,[1] J. P. Knauer,[1] S. P. Regan,[1] A. J. Schmitt,[2] R. C. Shah,[1] and A. Shvydky[1]

[1]Laboratory for Laser Energetics, University of Rochester
[2]Plasma Physics Division, Naval Research Laboratory

A 3-D hydrodynamic simulation using the code *ASTER*[1] helped to identify a new mechanism that is responsible for mitigating imprint with a scale length corresponding to Legendre modes down to $\ell \simeq 30$ in direct-drive OMEGA implosions[2] driven by laser pulses with a picket(s). This mechanism involves rarefaction flows developed by unsupported shocks. Rarefaction flows can result in a decay of imprint modulations in implosion shells during their early evolution, consequently improving the stability of these shells with respect to the acceleration Rayleigh–Taylor (RT)[3] growth at a later time.

Figure 1 illustrates the development of imprint modulations in implosion shells compressed by supported and unsupported shocks, which are produced by continuous and picket laser pulses, respectively. The green areas at the ablation front indicate the locations of modulations originating from laser nonuniformities in the beginning of the pulses. These modulations can feed through to the shell (to the left) in the case of a supported shock [Fig. 1(a)] and cannot feed through in the case of a unsupported shock, which develops a post-shock rarefaction flow [Fig. 1(b)]. As a result, imprint is mitigated only in the latter case, in which modulations are localized near the ablation front and moved away (to the right) with the ablating mass.

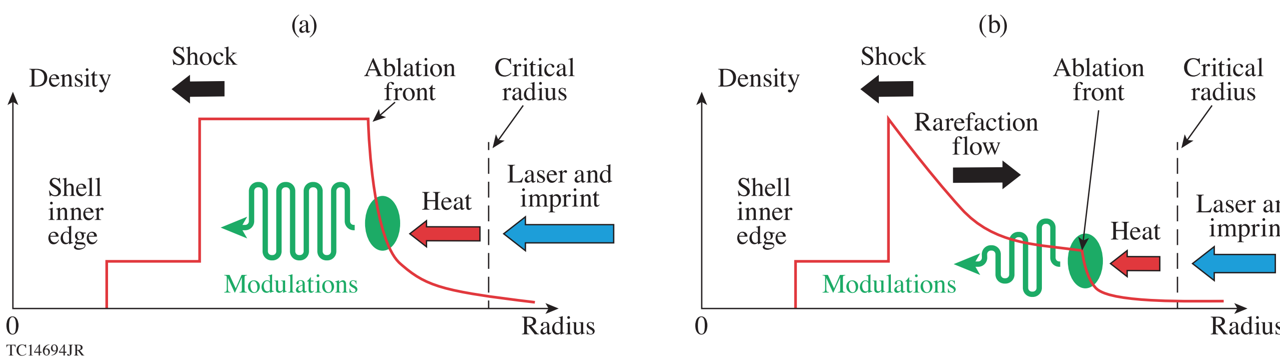

Figure 1
(a) Imprint modulations (the green area) localized at the ablation front can feed through to an implosion shell compressed by a supported shock but (b) cannot feed through in a shell compressed by an unsupported shock.

Three-dimensional *ASTER* simulations were used to demonstrate the new mechanism and employed two OMEGA cryogenic implosion designs having laser pulses with and without a picket. Simulations show that imprint is not mitigated in the no-picket design; therefore, large seeds for RT growth during the target acceleration phase are provided, resulting in a "broken shell" just prior to the target deceleration phase [see Fig. 2(a)]. This implosion shows poor performance, producing only 13% of neutron yield and 37% of neutron-averaged areal mass predicted in 1-D (symmetric) simulations. Contrary to this, simulations of the single-picket design, which develops an after-shock rarefaction flow, show apparent mitigation of the dangerous imprint modes $\ell \sim 100$ to 200. This implosion is characterized by relatively small-amplitude perturbations in the shell with dominant modes $\ell \sim 30$ to 60 [see Fig. 2(b)] and produces 46% of neutron yield and 81% of neutron-averaged areal mass of those in 1-D simulations.

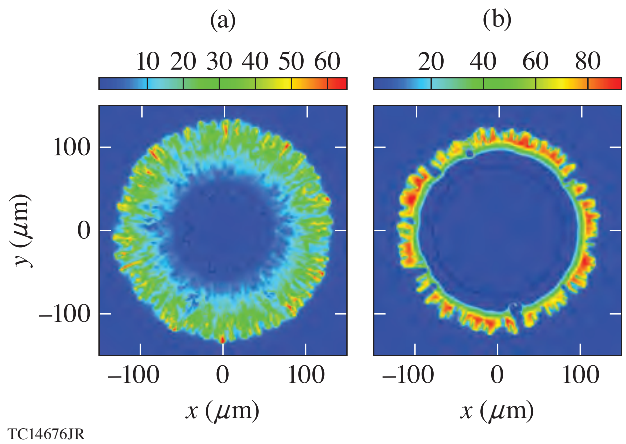

Figure 2
Meridional cross sections of the distribution of density (in g/cm^3) from 3-D simulations of the designs using the (a) no-picket and (b) single-picket laser pulses. The images are shown at times corresponding to moments prior to deceleration of the implosion shells.

This material is based upon work supported by the Department of Energy National Nuclear Security Administration under Award Number DE-NA0003856, the University of Rochester, and the New York State Energy Research and Development Authority.

1. I. V. Igumenshchev *et al*., Phys. Plasmas **23**, 052702 (2016).

2. T. R. Boehly *et al*., Opt. Commun. **133**, 495 (1997).

3. Lord Rayleigh, Proc. London Math Soc. **XIV**, 170 (1883); G. Taylor, Proc. R. Soc. London Ser. A **201**, 192 (1950).

Inferring Fuel Areal Density from Secondary Neutron Yields in Laser-Driven Magnetized Liner Inertial Fusion

J. R. Davies,[1] D. H. Barnak,[1,2] R. Betti,[1] E. M. Campbell,[1] V. Yu. Glebov,[1] E. C. Hansen,[1,3] J. P. Knauer,[1] J. L. Peebles,[1] and A. B. Sefkow[1]

[1]Laboratory for Laser Energetics, University of Rochester
[2]Los Alamos National Laboratory
[3]FLASH Center, University of Chicago

Laser-driven magnetized liner inertial fusion (MagLIF[1]) experiments are being carried out on the OMEGA laser[2–6] to study scaling by providing data from targets ~10× smaller in linear dimensions than those used on the Z pulsed-power machine[7–9] at Sandia National Laboratories. One of the key initial design criteria in the development of MagLIF[1] was to find a means to achieve fusion conditions in a cylindrical implosion at a convergence ratio of less than 30. It is well-known that high-convergence implosions are very sensitive to small departures from symmetry in the drive and targets, making them impractical. By preheating to ~100 eV, temperatures up to 9 keV can be achieved in an adiabatic, cylindrical compression with a convergence ratio <30. In MagLIF an axial magnetic field reduces electron thermal conduction from the fuel into the liner during compression, making it possible to achieve a near-adiabatic compression at a lower implosion velocity. With the compressed axial magnetic field, alpha particles can be confined from deuterium–tritium (D–T) fusion without reaching a radial areal density of $\rho R \sim 0.6$ g/cm^2, if, instead, a radially integrated axial magnetic field $BR \sim 0.6$ T•m is achieved. In experiments on Z, the radially integrated axial magnetic field in the compressed deuterium fuel was inferred to be ~0.4 T•m from the ratio of secondary D–T fusion neutrons to primary D–D fusion neutrons.[9] The D–D fusion reaction has two equally probable branches:

$$\begin{aligned} \mathrm{D}+\mathrm{D} &\longrightarrow \mathrm{T}(1.01\ \mathrm{MeV})+\mathrm{p}(3.02\ \mathrm{MeV}) \\ &\longrightarrow {}^{3}\mathrm{He}(0.82\ \mathrm{MeV})+\mathrm{n}(2.45\ \mathrm{MeV}), \end{aligned} \tag{1}$$

where the kinetic energies given in parentheses are in the center of the momentum frame. The tritium may go on to fuse with the deuterium, producing secondary 14.5-MeV neutrons. The longer the path length of the tritium in the deuterium, and the higher the density of the deuterium, the greater the probability of D–T fusion. Calculations indicated that for the Z experiments, the increase in path length of the tritium resulting from the compressed axial magnetic field was a major contributor to the secondary D–T yield.[9] The BR in MagLIF targets on OMEGA will be at least ~10× lower than on Z because the radius is 10× smaller and the initial axial magnetic field is approximately the same (currently 9 T, but values up to 30 T can be achieved). Therefore, magnetic confinement of charged fusion products cannot be achieved on OMEGA. As a result, the secondary D–T yield from D_2 fuel is determined by the radial areal density ρR of the compressed fuel.[10] While not an important metric for MagLIF, fuel areal density does provide useful information on the convergence ratio of the fuel, which cannot be determined from the x-ray imaging diagnostics available on OMEGA[4] because they do not have sufficient spatial resolution for a compressed fuel that should be <10 μm in radius.

The fuel areal density can be obtained approximately from

$$\rho R = 5.18 \pm 1.04 \frac{Y_{\mathrm{DT}}}{Y_{\mathrm{DD}}}\ \mathrm{g/cm}^2, \tag{2}$$

assuming a point or line source of tritium on the axis, and straight-line propagation of the tritium with no energy loss and no end losses. The result is only weakly dependent on the radial distribution of the tritium production. For the increase in D–T fusion cross section caused by collisional slowing of the tritium to be negligible, and for angular scattering to be negligible, requires

$$\rho R \ll 14.5 T_{\mathrm{keV}}^{3/2}\ \mathrm{mg/cm}^2. \tag{3}$$

For end losses to reduce the mean path length by less than 10% requires

$$\frac{L}{R} > 12, \tag{4}$$

where L is the length of the cylinder. For the magnetic field to cause a negligible increase in path length requires

$$BR \ll 0.25\ \mathrm{T{\cdot}m}. \tag{5}$$

All of these conditions are comfortably satisfied in laser-driven MagLIF experiments on OMEGA.

Successful laser-driven MagLIF shots have been taken with all four combinations of preheat on/off and axial magnetic field on/off for 1.8 mg/cm^3 of deuterium and for compression-only and compression with field for 1.2 mg/cm^3 of deuterium. The inferred areal density by type of shot is given in Table I.

TABLE I: Areal density ρR and the increase in areal density $C_0 = \rho R/(\rho R)_0$ inferred from measured secondary- to primary-yield ratios by shot type and obtained from 1-D *LILAC* and 2-D *HYDRA* simulations for nominal laser and target parameters. For the integrated shot and the compression-only shots at 1.2 mg/cm^3, the upper limit is based on a D–T yield <2 × 10^5.

Type (number of shots)	ρR (mg/cm^2)	$\rho R_{\text{1-D}}$ (mg/cm^2)	$\rho R_{\text{2-D}}$ (mg/cm^2)	C_0	$C_{0,\text{1-D}}$	$C_{0,\text{2-D}}$
Compression only: 1.8 mg/cm^3 (2)	1.2±0.4	3.8	3.3	22±7	77	68
Preheated: 1.8 mg/cm^3 (2)	0.98±0.39	2.2	1.7	19±8	46	35
Magnetized: 1.8 mg/cm^3 (2)	0.67±0.08	1.7	1.9	13±2	34	39
Integrated: 1.8 mg/cm^3 (1)	<0.64	1.6	1.4	<13	32	29
Compression only: 1.2 mg/cm^3 (2)	<2.7	2.2	3.4	<82	70	100
Magnetized: 1.2 mg/cm^3 (2)	1.2±0.3	1.2	1.5	37±8	37	46

The fuel convergence ratio is of more interest in MagLIF than the areal density; both the initial Z point design[1] and the OMEGA point design[3] set out to achieve a convergence ratio of 25. If the fuel density profile remains uniform and there are no end losses, the fuel convergence ratio is $\rho R/(\rho R)_0$, which we will refer to as C_0, our zeroth-order estimate of a neutron-averaged fuel convergence, the values of which are given in Table I. When fuel density peaks at the edge, which is to be expected, C_0 will underestimate the convergence ratio; if fuel density peaks at the center, C_0 will overestimate the convergence ratio. End losses, which are to be expected, will result in C_0 underestimating the convergence ratio. Therefore, we expect C_0 to be somewhat lower than the actual convergence ratio C.

Even if the actual convergence ratio is as high as $2C_0$, the integrated shot has achieved a convergence ratio <26, meeting our initial point design objective, despite the lower fuel density. In any case, the values of C_0 should provide an indication of how the fuel convergence ratio is modified by preheating, magnetization, and fuel density, which are important aspects of MagLIF. The results indicate that preheating, magnetization, and increasing fuel density reduce the fuel convergence ratio, as expected.

The inferred areal densities also provide a useful point of comparison with simulations. Areal densities from 1-D *LILAC*[3,4] and 2-D *HYDRA*[3,4,6] are included in Table I. The simulations overestimate the areal densities for all except the magnetized 1.2-mg/cm^3 shots, where agreement is good, although the 2-D simulations are toward the upper end of the error bar. The simulations give values of C_0 that are 2× to 3× higher than the measurements, excluding the 1.2-mg/cm^3 results. The simulations would be expected to overestimate the areal density because the growth of nonuniformities from the laser beams and targets, which are not considered, will break up the compressed fuel. In 1-D and 2-D the imploding shell must converge on the axis and will stop only once the pressure in the fuel becomes high enough. In 3-D, opposing elements of the shell can miss the axis and not compress the fuel to such a high pressure. The growth of nonuniformities is expected to be greater the higher the convergence, and the discrepancies between the measured and simulated areal densities are greater at higher values, excluding the 1.2-mg/cm^3 results. It is possible that the agreement between measurements and simulations for magnetized 1.2-mg/cm^3 shots is just a matter of chance, with the actual value lying at the lower end indicated by the experimental uncertainty, particularly as the D–T yields in these shots are at the very lowest detectable levels.

The areal density diagnostic described here will be applied to future laser-driven MagLIF shots that will include higher magnetic fields (up to ~30 T), a scan of preheat energies, and higher fuel densities. The simulations will be extended to 3-D, using laser and target parameters as close as possible to the as-shot values, and the effects of cross-beam energy transfer and nonlocal thermal transport will be taken into consideration.

This material is based upon work supported by the Department of Energy Advanced Research Projects Agency-Energy (ARPA-E) under Award Number DE-AR0000568, Department of Energy National Nuclear Security Administration under Award Number DE-NA0003856, the University of Rochester, and the New York State Energy Research and Development Authority.

1. S. A. Slutz *et al*., Phys. Plasmas **17**, 056303 (2010).
2. D. H. Barnak *et al*., Phys. Plasmas **24**, 056310 (2017).
3. J. R. Davies *et al*., Phys. Plasmas **24**, 062701 (2017).
4. E. C. Hansen *et al*., Plasma Phys. Control. Fusion **60**, 054014 (2018).
5. J. R. Davies *et al*., Phys. Plasmas **25**, 062704 (2018).
6. E. C. Hansen *et al*., Phys. Plasma **25**, 122701 (2018).
7. A. B. Sefkow *et al*., Phys. Plasmas **21**, 072711 (2014).
8. M. R. Gomez *et al*., Phys. Rev. Lett. **113**, 155003 (2014).
9. P. F. Schmit *et al*., Phys. Rev. Lett. **113**, 155004 (2014).
10. E. G. Gamaliĭ *et al*., JETP Lett. **21**, 70 (1975); H. Azechi *et al*., Appl. Phys. Lett. **49**, 555 (1986); M. D. Cable and S. P. Hatchett, J. Appl. Phys. **62**, 2233 (1987); S. Kurebayashi *et al*., Phys. Plasmas **12**, 032703 (2005).

Impact of Non-Maxwellian Electron Velocity Distribution Functions on Inferred Plasma Parameters in Collective Thomson Scattering

A. L. Milder,[1,2] S. T. Ivancic,[1] J. P. Palastro,[1] and D. H. Froula[1,2]

[1]Laboratory for Laser Energetics, University of Rochester
[2]Department of Physics and Astronomy, University of Rochester

Optical Thomson scattering is a powerful diagnostic that is widely used to measure plasma conditions in laser-produced plasmas.[1] As large multibeam facilities are constructed to achieve inertial confinement fusion around the world,[2–4] accurate measurements of plasma conditions are becoming increasingly important for understanding the importance of missing physics in the large hydrodynamic simulations. Local and time-resolved measurements of Thomson-scattered spectra have provided valuable insight into a range of studies, including laser–plasma instabilities,[2] thermal transport,[5] and more generally inertial confinement fusion.[6,7]

The high density present in laser-produced plasmas results in scattering optical light from collective plasma-wave fluctuations. The scattering from low-frequency fluctuations generates ion-acoustic spectral features, while scattering from high-frequency fluctuations generates electron plasma wave spectral features. Early collective scattering measurements from high-frequency fluctuations used the theory developed two decades earlier by Salpeter[8] to associate the wavelength of spectral peaks with density, through the Bohm–Gross dispersion relation, and the width of spectral peaks to temperature, through Landau damping, but the small scattering cross section for Thomson scattering has resulted in relatively few experiments where electron temperature and density were measured from the electron plasma wave features.[6,9–11] Recent experiments have used the full Thomson-scattered spectrum to extract plasma conditions, but these studies have been limited to assuming Maxwellian distribution functions. However, variation in the shape of the distribution functions can lead to significant changes to the Thomson-scattering spectrum.[12]

Here, we investigate the sensitivity of electron temperature and density inferred from collective Thomson scattering to non-Maxwellian electron distribution functions. Analyzing synthetic electron plasma wave Thomson-scattering spectra, under the false assumption that the electron distribution function is Maxwellian, can lead to gross errors in the inferred electron density and temperature. Figure 1 shows that the inferred temperature and density can differ from the actual values by 50% and 30%, respectively. These errors stem from changes in the shape of the scattered spectra and can be removed by including the correct shape of the electron distribution function in the analysis. Other changes to the shape of the electron distribution function can result in errors in the inferred parameters, as in the case of heat flux.[7] These errors of 50% in temperature and 30% in density are for extreme changes to the electron distribution function, but even for small changes in the shape of the distribution function, the errors in temperature and density are larger than the statistical uncertainty of ~5% that is typical[10,11] and can be a limiting factor in determining plasma conditions.

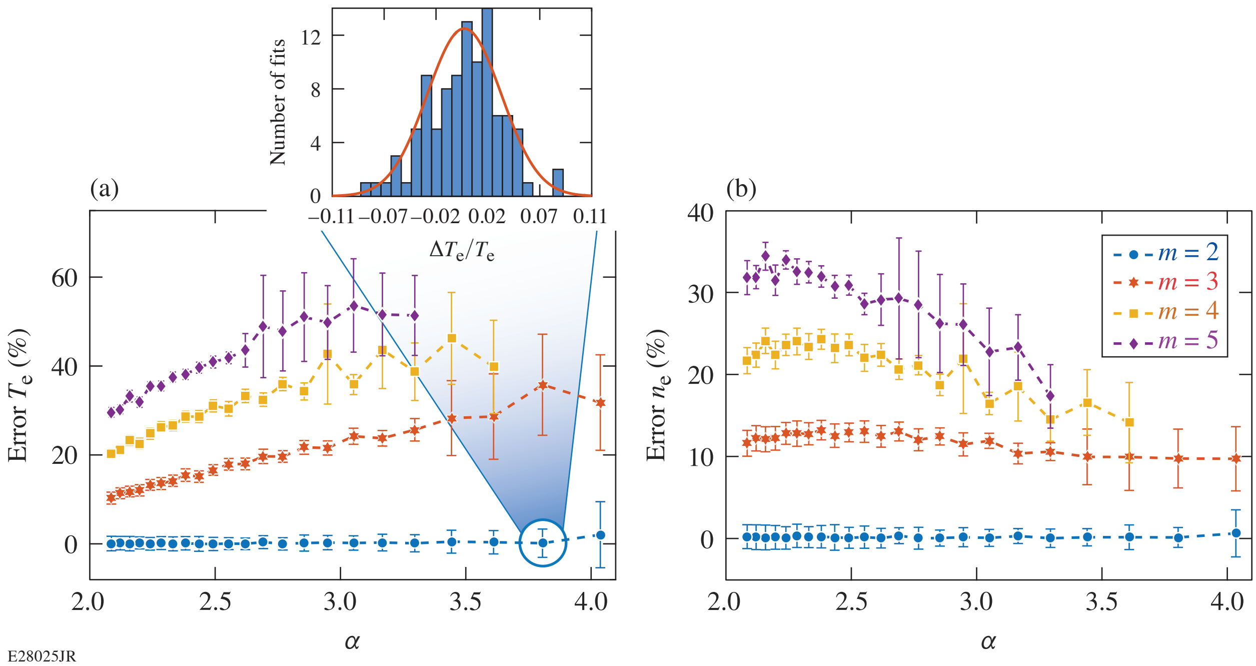

Figure 1
Percent error in (a) temperature and (b) density as a function of the normalized phase velocity $\left(\alpha = v_\phi / v_{\text{th}}\right)$ when the fit model assumes a Maxwellian electron distribution function and the true electron distribution function is super-Gaussian. The absolute difference between the inferred and actual parameter dividend by the actual parameter (percent error) is calculated for a range of phase velocities. The values for four different super-Gaussian orders are plotted in different colors with error bars that represent the standard deviation of 100 fits.

This material is based upon work supported by the Department of Energy National Nuclear Security Administration under Award Number DE-NA0003856, the University of Rochester, and the New York State Energy Research and Development Authority.

1. D. H. Froula *et al.*, *Plasma Scattering of Electromagnetic Radiation: Theory and Measurement Techniques*, 2nd ed. (Academic Press, Amsterdam, 2011).
2. C. A. Haynam *et al.*, Appl. Opt. **46**, 3276 (2007).
3. J. L. Miquel, C. Lion, and P. Vivini, J. Phys.: Conf. Ser. **688**, 012067 (2016).
4. W. Zheng *et al.*, High Power Laser Sci. Eng. **4**, e21 (2016).
5. R. J. Henchen *et al.*, Phys. Rev. Lett. **121**, 125001 (2018).
6. S. H. Glenzer *et al.*, Phys. Plasmas **6**, 2117 (1999).
7. D. H. Froula *et al.*, Phys. Plasmas **13**, 052704 (2006).
8. E. E. Salpeter, Phys. Rev. **120**, 1528 (1960).
9. J. S. Ross *et al.*, Phys. Rev. Lett. **104**, 105001 (2010).
10. J. S. Ross *et al.*, Rev. Sci. Instrum. **81**, 10D523 (2010).
11. S. C. Snyder *et al.*, Phys. Rev. E **50**, 519 (1994).
12. J. Zheng, C. X. Yu, and Z. J. Zheng, Phys. Plasmas **4**, 2736 (1997).

Measuring Heat Flux from Collective Thomson Scattering with Non-Maxwellian Distribution Functions

R. J. Henchen,[1,2] M. Sherlock,[3] W. Rozmus,[4] J. Katz,[1] P. E. Masson-Laborde,[5] D. Cao,[1] J. P. Palastro,[1] and D. H. Froula[1,6]

[1]Laboratory for Laser Energetics, University of Rochester
[2]Department of Mechanical Engineering, University of Rochester
[3]Lawrence Livermore National Laboratory
[4]Department of Physics, University of Alberta, Canada
[5]Commissariat á l'energie atomique et aux énergies, France
[6]Department of Physics and Astronomy, University of Rochester

Thermal transport in plasmas is of particular interest to inertial confinement fusion, where a correct description of heat flux is crucial to modeling the absorption of incident laser beams used to implode fusion targets. Electron thermal transport is a fundamental process in plasma physics that becomes difficult to calculate since even in the most modest conditions, classical theory tends to break down. Extensive work has attempted to determine the nonlocal heat flux that is responsible for transporting thermal energy over large distances but quantitative experiments are required.

In laser-produced plasmas, where energy is primarily deposited locally at the critical density, temperature gradients inherently drive non-Maxwellian electron distribution functions as electrons carry the heat down the temperature gradient and slower electrons carry a return current up the temperature gradient to maintain neutrality. A consequence of heat flux, and the ensuing distortion of the distribution function, is to change the partition of energy between the thermal electrons and the thermal fluctuations. This has a particularly large effect on the amplitude of the fluctuations that have phase velocities near the velocity of the heat-carrying electrons. The heat flux modifies both the number of electrons and the slope of the distribution function, which directly changes the local Landau damping of ion-acoustic and Langmuir waves.

Collective Thomson scattering measures the fluctuation spectrum, and when probing electron plasma fluctuations with phase velocities in the region of heat-carrying electrons, the spectrum can be used to determine the heat flux.[1] The first-order effect of the electron distribution function on the Thomson-scattering spectrum can be observed in the dependence of the peak power scattered into the electron plasma wave feature,

$$P_{\text{peak}} \propto \left.\frac{f_{\text{e}}(v)}{\left[\text{d}f_{\text{e}}(v)/\text{d}v\right]^2}\right|_{v=v_\phi}, \tag{1}$$

where $f_{\text{e}}(v)$ is the electron distribution function and $\text{d}f_{\text{e}}(v)$ is elevated at the phase velocity v_ϕ.

We present the direct measurement of heat flux using collective Thomson scattering from a laser-produced coronal plasma. The heat flux was measured in two ways that were used to experimentally determine the validity of classical thermal transport. The first measurement of heat flux used the classically derived non-Maxwellian electron distribution functions to reproduce the electron plasma wave Thomson-scattering spectra, while the second method used the measured plasma conditions to calculate the classical heat flux. Figure 1(a) shows the experimental setup, where six 351-nm laser beams created a blowoff aluminum plasma. A 526-nm Thomson-scattering probe beam was used to scatter light from five locations in the coronal plasma. At each location the complete collective Thomson-scattering spectrum was measured and used to determine the electron temperature (T_e) and density (n_e) profiles. These plasma conditions were used to calculate the classical heat flux ($q = -\kappa\nabla T_e$), where κ is the classical thermal conductivity that depends only on the local electron temperature and density.

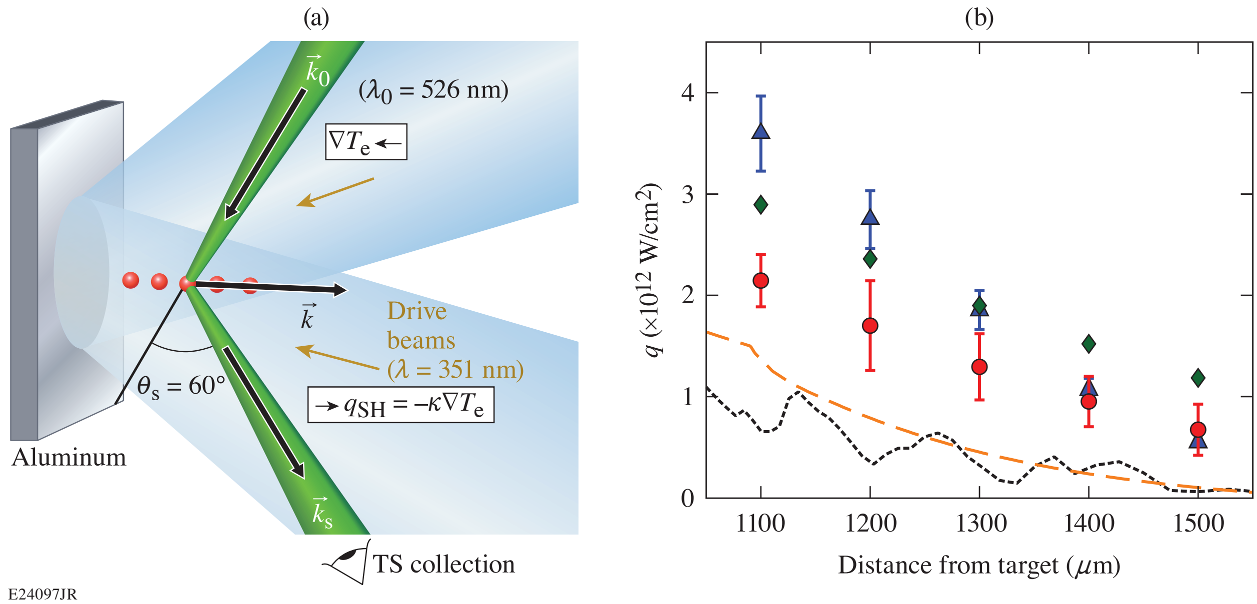

Figure 1
(a) The experimental setup is shown where six beams (blue) produced a blowoff plasma from a planar target (gray). A Thomson-scattering probe beam (green) with wave vector $\vec{k}_0$ was oriented relative to the target to probe plasma waves $(\vec{k})$ along the central axis, where the temperature gradient is the largest. Five Thomson-scattering locations (red) along the target normal provided measurements of plasma parameter profiles (T_e, n_e, ∇T_e). (b) Heat-flux measurements (red circles) are shown at t = 1.5 ns after the start of the $\lambda_{3\omega}$ beams as a function of distance from the initial target surface. Classical heat-flux values determined from the measured plasma parameters (blue triangles) are included along with results from full-scale SNB (black dotted line) and *FLASH* (orange dashed line) simulations in addition to 1-D SNB calculations using the measured plasma profiles (green diamonds).

Figure 1(b) shows that in regions where the electron–ion mean free path is small compared to the temperature gradients $\left(\lambda_{ei}/\left|L_T\right| < 7 \times 10^{-3}\right)$, the two heat-flux measurements agreed (red and blue symbols), which demonstrates the validity of the classical Spitzer–Härm theory. For larger relative temperature gradients (i.e., closer to the intial target surface, <1500 μm), the flux determined from non-Maxwellian electron distribution functions derived from classical theory was not consistent with the heat flux determined from measurements of the plasma conditions. This experimentally demonstrated that in plasmas with steep relative temperature gradients, the classical thermal transport theory is not valid. To determine the flux in this region, non-Maxwellian electron distribution functions consistent with nonlocal thermal transport were used to fit the Thomson-scattering spectra. At the steepest relative temperature gradient (1100 μm), the nonlocal heat-flux measurements were up to 1.5× smaller than the flux determined from classical theory. One-dimensional calculations using the Schurtz–Nicolaï–Busquet (SNB) model (diamonds), initiated with the measured plasma conditions, show a reduced heat flux compared with the classical theory but overestimated the flux at all locations compared with the nonlocal measurements.

This material is based upon work supported by the Department of Energy National Nuclear Security Administration under Award Number DE-NA0003856, the University of Rochester, and the New York State Energy Research and Development Authority.

1. R. J. Henchen *et al*., Phys. Rev. Lett. **121**, 125001 (2018).

Status of Free-Energy Representations for Homogeneous Electron Gas

V. V. Karasiev,[1] S. B. Trickey,[2] and J. W. Dufty[3]

[1]Laboratory for Laser Energetics, University of Rochester
[2]Quantum Theory Project, Departments of Physics and Chemistry, University of Florida
[3]Department of Physics, University of Florida

The homogeneous electron gas (HEG) is a well-studied system at zero temperature as a model for electrons in solids and as a model for fully ionized plasmas at temperatures T well above the Fermi temperature T_F. For a long while far less information was available from either theory or simulation at intermediate temperatures and densities, in large part due to lack of motivation. That has changed recently with growing experimental access to observations on states of matter in this domain. Such access is driving growth in the fields of warm dense matter (WDM) and high-energy-density physics. Accordingly, the first quantum Monte Carlo (QMC) simulations for the HEG in this domain were reported only six years ago.[1] Subsequently Dornheim *et al.*[2] produced improved QMC results for temperatures $0.5 \leq t = T/T_F \leq 8$ over a wide density range (Wigner–Seitz radii $0.1 \leq r_s \leq 10$). They also developed and used significantly improved finite-size corrections. Those data currently seem to be the most-accurate finite-temperature HEG results available.

For practical purposes a representation interpolating such QMC data and extrapolating it via known theoretical limits is needed. The target is an equation of state for the complete thermodynamics of the HEG, provided by the free energy as a function of r_s and t. A rather complete review of the recent simulations and their representations is given in Ref. 3. As noted there, the program for constructing a free energy from theoretical limits and simulation data was originally presented and used in Ref. 4, which presented a representation, "KSDT" (Karasiev–Sjostrom–Dufty–Trickey), based on the original data of Ref. 1 and the $T = 0$ data of Ref. 5. Subsequently, Groth *et al.*[6] used the KSDT approach and protocol to reparametrize the exchange-correlation (XC) contribution to the free energy against the finite-size–corrected QMC results of Ref. 2 along with the Singwi–Tosi–Land–Sjölander (STLS) approximation[7] for low-t ($t < 0.5$) behavior and for connection with the $T = 0$ data of Ref. 5. The resulting representation is denoted as "GDB" (Groth–Dornheim–Bonitz). Essentially simultaneously, a small error in the use of zero-temperature data for KSDT was detected and repaired to yield the corrected KSDT representation "corrKSDT" (see Supplemental Material for Ref. 8).

This work achieved three objectives: The first is based on recent simulation studies of the free energy for the HEG in a domain of the (r_s,t) plane not previously explored. The data combined with thermodynamic consistency and known theoretical limits led to three global representations of the free energy, corrKSDT, its direct antecedent KSDT, and GDB. The equivalence of these for reproducing the simulation data for $f(r_s,t)$ was demonstrated. Furthermore, the equivalence of corrKSDT and GDB for the XC component alone was illustrated, although the original KSDT representation has some inconsequential small errors for $f_{xc}(r_s,t)$ (Ref. 2). Figure 1 demonstrates that the two fits match the available QMC data indistinguishably for $t \geq 0.5$ and are in perfect agreement for $t < 0.5$.

The second objective was to draw attention to the fact that, in spite of these very accurate representations for $f(r_s,t)$, thermodynamic properties obtained by temperature derivatives exhibit striking anomalies. Those occur outside the domain for which simulation data are available and are properties of the extrapolation/interpolation provided by the fitting procedure. This was discussed and it was noted that the entropy per particle (first-order temperature derivative) can become negative for large r_s and small t. For the corrKSDT and GDB representations, this corresponds to state conditions beyond the expected spin polarization

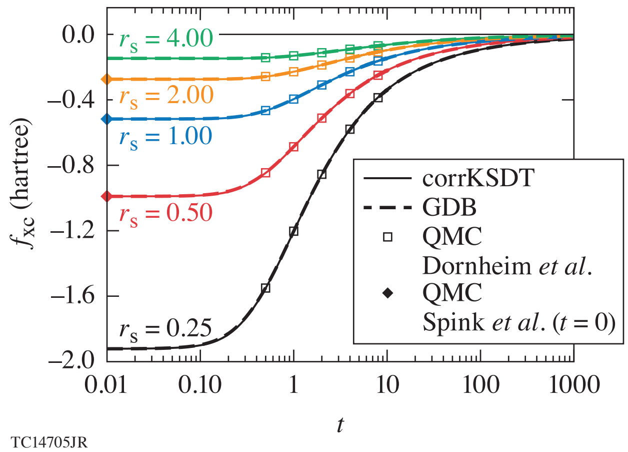

Figure 1
Comparison between f_{xc} values from the corrKSDT and GDB parametrizations and QMC data from Ref. 9 for the unpolarized HEG at $r_s = 0.25$, 0.5, 1, 2, and 4. The ground-state limit ($t = 0$, Ref. 5) QMC values also are shown.

transition and therefore outside the domain of their intended application. A second more-serious anomaly occurs for the specific heat c_V (second derivative with respect to T). In that case, all of the representations predict unusual oscillatory behavior for t between 0.1 and 1 and $r_s \geq 10$. Figure 2 shows c_V calculated for the noninteracting and interacting HEG from the corrKSDT and GDB representations. As anticipated, the specific heat curves from the two parametrizations are practically identical, a consequence of the small procedural differences of parameter fitting in the two. Even though the oscillatory behavior might be an indication of some kind of critical point, it is far more plausible that it is an artifact introduced by the QMC data of Ref. 2 and the way that corrKSDT and GDB represent those data. Without any theoretical or simulation guidance, this must be seen as a possible flaw in the representation function.

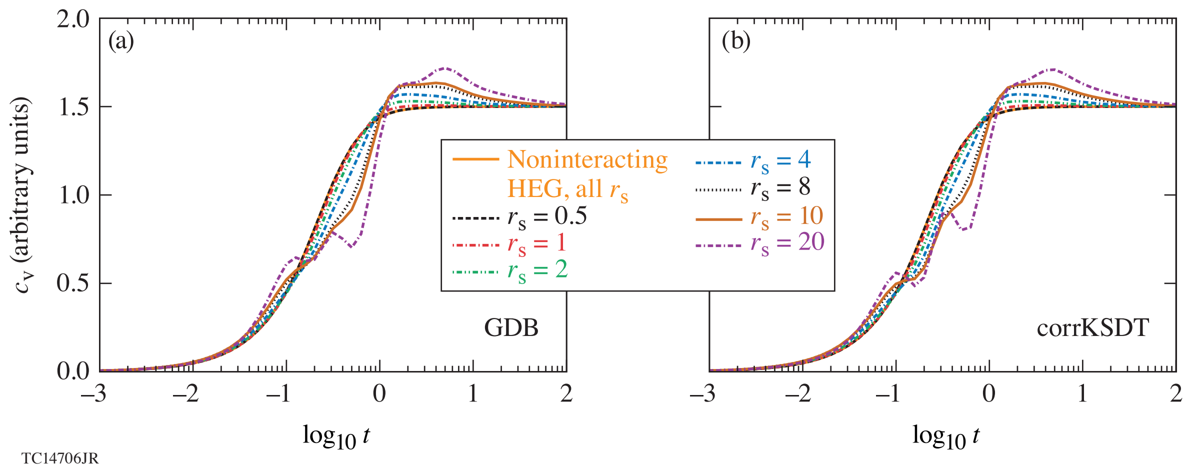

Figure 2
Electron specific heat c_V for the noninteracting and interacting HEG calculated with (a) GDB and (b) corrKSDT parametrizations.

The third objective was to verify the use of the three representations as essentially interchangeable for use as local density approximation (LDA) functionals in free-energy DFT calculations and in more-refined f_{xc} approximations. It is helpful to note the parallel with most $T = 0$ DFT calculations. They are based in a similar way on ground-state HEG simulations. Generalized gradient approximations, for example, have the LDA (consequently the HEG) as a limiting case. Therefore, the extensions discussed here to the entire (r_s,t) plane constitute an essential prerequisite for addressing WDM in an accurate, practical fashion. A first example of a nonempirical semilocal free-energy density functional for matter under extreme conditions, built on the LDA representations here, was noted.[8]

This material is based upon work supported in part by the Department of Energy National Nuclear Security Administration under Award Number DE-NA0003856, U.S. National Science Foundation PHY Grant No. 1802964, the University of Rochester, and the New York State Energy Research and Development Authority. JWD and SBT acknowledge support by U.S. Dept. of Energy grant DE-SC 0002139.

1. E. W. Brown *et al*., Phys. Rev. Lett. **110**, 146405 (2013).
2. T. Dornheim *et al*., Phys. Rev. Lett. **117**, 156403 (2016).
3. T. Dornheim, S. Groth, and M. Bonitz, Phys. Rep. **744**, 1 (2018).
4. V. V. Karasiev *et al*., Phys. Rev. Lett. **112**, 076403 (2014).
5. G. G. Spink, R. J. Needs, and N. D. Drummond, Phys. Rev. B **88**, 085121 (2013).
6. S. Groth *et al*., Phys. Rev. Lett. **119**, 135001 (2017).
7. S. Tanaka and S. Ichimaru, J. Phys. Soc. Jpn. **55**, 2278 (1986).
8. V. V. Karasiev, J. W. Dufty, and S. B. Trickey, Phys. Rev. Lett. **120**, 076401 (2018).
9. T. Schoof *et al*., Phys. Rev. Lett. **115**, 130402 (2015).

A Ten-Inch-Manipulator–Based Fast-Electron Spectrometer with Multiple Viewing Angles

H. Habara,[1] T. Iwawaki,[1] K. A. Tanaka,[1,†] T. Gong,[1,‡] M. S. Wei,[2] S. T. Ivancic,[2] W. Theobald,[2] C. M. Krauland,[3] S. Zhang,[3] and G. Fiksel[4]

[1]Graduate School of Engineering, Osaka University, Japan
[2]Laboratory for Laser Energetics, University of Rochester
[3]Department of Mechanical and Aerospace Engineering, University of California at San Diego
[4]Center for Ultrafast Optical Science, University of Michigan
[†]Currently at Extreme Light Infrastructure: Nuclear Physics, Romania
[‡]Currently at Research Center of Laser Fusion, China Academy of Engineering Physics, People's Republic of China

The measurement of angularly resolved energy distributions of MeV electrons is important for gaining a better understanding of the interaction of ultra-intense laser pulses with plasma, especially for fast-ignition laser-fusion research. It is also crucial when evaluating the production of suprathermal (several tens of keV) electrons through laser–plasma instabilities in conventional hot-spot–ignition and shock-ignition research. For these purposes, we developed a ten-inch-manipulator (TIM)–based multichannel electron spectrometer—the Osaka University electron spectrometer (OU-ESM)—that combines angular resolution with high-energy resolution. The OU-ESM consists of five small electron spectrometers set at every 5°, with an energy range from ~40 keV to ~40 MeV. A low-magnetic-field option provides a higher spectral resolution for an energy range of up to ~5 MeV. This versatile diagnostic with a variable electron energy range can be deployed for experiments on the OMEGA and OMEGA EP Laser Systems.

The spectrometer uses permanent magnets in a Ni-coated yoke to disperse the electrons in energy. Assuming that the magnetic-flux density is constant, the electron motion is determined by the Larmor motion according to the electron's kinetic energy, given by

$$E = mc^2\left[\sqrt{\left(\frac{l^2+h^2}{2h}\right)^2\left(\frac{eB}{mc}\right)^2+1}-1\right], \tag{1}$$

where l is the longitudinal position of the signal on the detector from the magnet entrance, h is the height between the electron incident axis and the detector plane, e is the electric charge, B is the magnetic flux density, m is the electron mass, and c is the speed of light in vacuum, respectively. Because fast electrons created by ultra-intense lasers have considerably large emission angles, a collimator is used to guarantee a parallel electron beam into the magnetic field. Consequently, the number of accelerated electrons, N, per solid angle and per energy is given by

$$\frac{\mathrm{d}N^2}{\mathrm{d}\Omega\mathrm{d}E} = \frac{I_{\mathrm{IP}}}{\Delta l\Delta\Omega}\frac{1}{S(E)\varphi}\frac{h}{ceBl}\sqrt{1+\left(\frac{2h}{l^2+h^2}\right)^2\left(\frac{mc}{eB}\right)^2}, \tag{2}$$

where I_{IP} is the signal intensity on the detector, Δl is the spatial resolution of the detector, $\Delta\Omega$ is the solid angle, $S(E)$ is the detector sensitivity, and φ is the fading rate of the signal.[1]

Although it is very important to observe the energy spectrum in different viewing angles, this usually requires multiple electron spectrometers at different port locations around the target chamber. Given that this option is severely restricted because of port availability and interference issues with other diagnostics and laser beams, we maximized the capability of this diagnostic by combining five mini spectrometers at different viewing angles into a module that fits in a single diagnostic shuttle system—the TIM. Figure 1(a) shows a photograph of the OU-ESM. The diagnostic can be inserted into the TIM's on both the OMEGA and the OMEGA EP target chambers. The pointer pin shown at the bottom of Fig. 1(a) is used to align the diagnostic to a given aiming location. Every spectrometer channel is then automatically pointed correctly to the aiming point within the mechanical tolerance. A 20-mm-thick tungsten heavy metal alloy block on the front face with 700-μm-diam holes in front of each magnet serves as a collimator. A large piece of imaging plate (IP) serves as a detector attached to the cover plate of the detector box. Figure 1(b) shows an example of raw data that were taken in a fast-ignition–relevant experiment when a short IR pulse channeled through a preformed, long-scale-length plasma.[2,3] The pre-plasma was formed by a 1-ns, low-intensity UV pulse. A high-intensity, 10-ps pulse (~1×10^{19} W/cm^2) was injected into the long-scale-length plasma. Figure 1(c) shows the inferred electron spectra. An important feature of the system is that the strength of the magnet in each channel can be changed between 0.45 T (high-field operation) and 0.045 T (low-field operation). The detectable energy range in high-field operation is from ~0.6 to ~40 MeV in the inner channels, whereas energy ranges from ~0.6 to ~25 MeV in the side channels. In the low-field operation, the energy range is from ~40 keV to ~5 MeV in the inner channels and from ~40 keV to ~2.5 MeV in the side channels. The five horizontal lines in Fig. 1(b) correspond to the signals from CH1 (bottom) to CH5 (top). In this experiment, CH3 was located on the laser axis. Channel 2 and CH4 were operated in low-field mode, whereas CH1, CH3, and CH5 were in high-field mode.

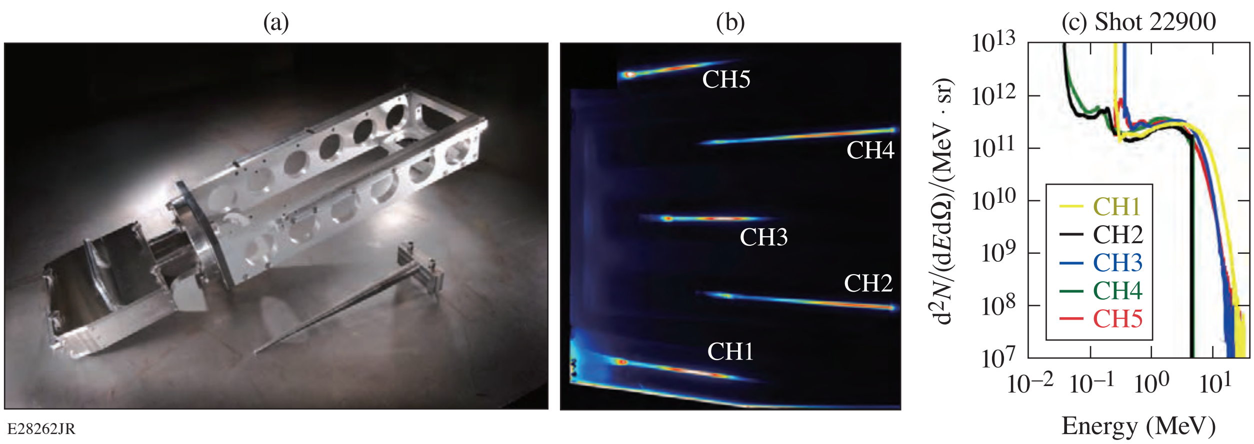

Figure 1
(a) Photograph of the OU-ESM, (b) raw data on an imaging plate, and (c) analyzed fast-electron energy spectra from an OMEGA EP experiment that demonstrated the channeling of an intense 10-ps IR laser pulse through a pre-plasma created by a 2-kJ, 1-ns UV pulse.

This work was fully supported by the Japan/U.S. Cooperation in Fusion Research and Development. Part of this work was also supported by Grant-in-Aid for Scientific Research from the Japanese Society for the Promotion of Science (JSPS) of Japan (Grant No. 15H05751 and 18K03577). This material is also based upon work supported by the Department of Energy National Nuclear Security Administration under Award Number DE-NA0003856, the University of Rochester, and the New York State Energy Research and Development Authority.

1. K. A. Tanaka *et al*., Rev. Sci. Instrum. **76**, 013507 (2005).
2. L. Ceurvorst *et al*., Phys. Rev. E **97**, 043208 (2018).
3. S. Ivancic *et al*., Phys. Rev. E **91**, 051101(R) (2015).

Time-Resolved, Nonequilibrium Carrier and Coherent Acoustic Phonon Dynamics in (Cd,Mg)Te Single Crystals for Radiation Detectors

J. Serafini,[1,2] A. Hossain,[3] R. B. James,[3,4] S. B. Trivedi,[5] and R. Sobolewski[1,6,#]

[1]Department of Physics and Astronomy and Laboratory for Laser Energetics, University of Rochester
[2]Department of Microsystems Engineering, Rochester Institute of Technology
[3]Brookhaven National Laboratory
[4]Savannah River National Laboratory
[5]Brimrose Technology Corporation
[6]Department of Electrical and Computer Engineering, University of Rochester
[#]Also at the Institute of Electron Technology, Poland

Volume-type radiation detectors are devices that collect charged particles, such as electrons, produced by photon interaction with the detector material, typically a single crystal. In the case of highly energetic x-ray radiation photons, they interact with matter through three main mechanisms: the photoelectric effect, the Compton effect, and electron–positron pair production. The photoelectric effect is by far the most dominant effect among them because Compton-scattered photons, as well as high-energy gammas from electron–pair annihilations, typically escape from the detection volume and their energy cannot be collected. Photoconductive devices are, in fact, the most popular solid-state radiation detectors since they can often operate at room temperature, cover the spectral range up to hard x rays and even γ rays, and are easy to design and fabricate.

There is a high demand for solid-state x-ray detectors in applications ranging from medical imaging to homeland security (portable screening units) and astrophysics. Currently, cadmium zinc telluride [(Cd,Zn)Te or CZT] is the accepted material of choice; however, because of its large Zn segregation constant, it has poor crystal-growth yield, making it costly to fabricate in large volumes.[1,2] Proposed alternatives to CZT are cadmium manganese telluride [(Cd,Mn)Te or CMnT] single crystals[3,4] and most recently developed cadmium magnesium telluride [(Cd,Mg)Te or CMgT] (Ref. 5). All of the above materials are ternary alloys that contain tellurium, which ensures their very high stopping power and 100% absorption efficiency for x-ray photons with energies up to above 100 keV (Ref. 4). However, CMgT also possesses all other necessary qualities for an optimal radiation detector, i.e., high density (5.83 g/cm^3), high electron effective mass (49.5), ultrahigh resistivity (~10^{10} Ω-cm), and a good electron mobility lifetime ($\mu\tau_e$) product (>10^{-4} cm^2/V) (Ref. 5). In addition, the CMgT "parent" crystals, CdTe and MgTe, exhibit very similar lattice constants, namely, 6.48 Å and 6.42 Å, respectively,[6] resulting in a high crystallinity yield of the CMgT material.

This summary focuses on the ultrafast optical properties of the latest member of the above-mentioned ternary materials, namely, the CMgT single crystal. We present comprehensive femtosecond pump–probe spectroscopy studies where we measure time-resolved carrier dynamics and, subsequently, analyze the data within a coupled rate-equation model, developed to reveal both the carrier recombination and trapping components of the relaxation process. In addition, we time-resolve long-lived coherent acoustic phonons (CAP's) in a manner similar to a method earlier implemented for CMnT crystals.[7]

In our experiments, we test CMgT crystals with optimal composition and ultrahigh resistivity for x-ray detection applications,[8] namely $Cd_{0.92}Mg_{0.08}Te$, and with two different dopants: indium (CMgT:In) and germanium (CMgT:Ge). In both cases, doping ensures that the resulting crystals exhibit ultrahigh resistivity; however, the used dopants act very differently. Indium doping is intended to simply compensate the native concentration of holes (CdTe-based crystals are naturally *p*-type semiconductors), while

Ge is a deep impurity, introduced to "pin down" the Fermi level at the middle of the band gap. The impurities obviously affect the crystalline quality of the resulting materials, negatively affecting the $\mu\tau_e$ product that needs to be as large as possible for a sensitive detector. Therefore, typically, the single crystals intended for x-ray detectors are annealed after their growth in order to improve their crystalline structure. In our work, we compare time-resolved dynamics of photoexcited carriers in CMgT:In and CMgT:Ge, both as-grown and annealed crystals, in order to determine what material exhibits the best transport properties, i.e., minimal trap concentration and the longest electron lifetime, required for the optimal photoelectric radiation detector.

To understand the physics of the nonequilibrium relaxation dynamics of photoexcited carriers in our CMgT crystals (see Fig. 1 as an example), we fitted our experimental probe-normalized, transient-reflectivity $\Delta R/R$ waveforms, measured in both one- and two-color setups, to the trapping and relaxation model that we developed and presented in Ref. 9. We note that in Fig. 1, as well as all other cases, the numerical total concentration of photoexcited carriers' dependence (solid red line) fit perfectly with the experimental $\Delta R/R$ transient (black circles). The initial fast relaxation time τ_1 is ascribed as the direct trapping of excited electrons, while the subsequent relatively much slower relaxation time τ_2 can be interpreted as the Shockley–Read–Hall recombination. The values of the fitting parameters, in the case of Fig. 1, are τ_1 = 0.21 ps and τ_2 = 4.77 ps. The subpicosecond value of τ_1 indicates that, in this sample, carrier trapping is the dominant mechanism of the photoresponse. The latter also explains the negative dip at the relaxation part of the $\Delta R/R$ signal. The value of τ_2 is also very short, showing that traps are also very effective in nonradiative electron-hole recombination. Therefore, our approach provides a detailed description of the physical processes governing both the carrier excitation and subsequent relaxation dynamics in our as-grown and annealed CMgT:In and CMgT:Ge samples.

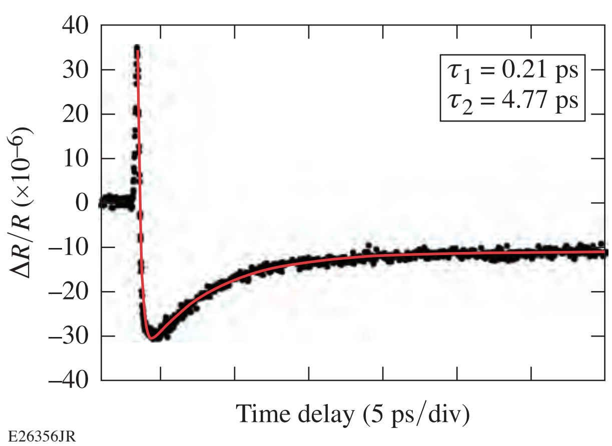

Figure 1
Normalized reflectivity transient change $\Delta R/R$ (black circles) measured in a one-color, pump–probe spectroscopy setup for an as-grown CMgT:In sample. The solid red line is the best fit to the trapping and relaxation model and the corresponding fitting parameters are listed in the inset.

During the course of our two-color pump–probe studies performed on both CMgT:In and CMgT:Ge samples, we consistently observed the presence of weak but very regular oscillations on the relaxation part of $\Delta R/R$ waveforms when traced in a time-delay range of the order of a nanosecond. These oscillations can be satisfactorily interpreted within the propagating strain-pulse model, introduced by Thomsen *et al.*[10] and Wu *et al.*[11] The high-energy and high-fluence femtosecond pump pulses incident on the crystal surface introduce electronic as well as thermal stress and generate a strain transient (lattice discontinuity) that propagates with a velocity of sound v_s into the sample at the direction orthogonal to the surface, locally altering its optical properties; namely, the refractive index of the crystal. The time-delayed probe beam penetrating the crystal is partially reflected from this traveling discontinuity and interferes with the part of the probe light reflected from the crystal surface, resulting in the regular oscillations observed on top of the $\Delta R/R$ photoresponse signal, interpreted as CAP's. CAP propagation was dispersionless with the constant propagation velocity corresponding to the speed of sound in our CMgT, (111) oriented crystal. The intrinsic lifetime of CAP's was estimated to be as long as 10 ns or more.

This material is based upon work supported in part by the Pump Primer II Program at the University of Rochester and in part by the New York State Advanced Technology Center for Innovative and Enabling Technologies (University of Rochester). J. Serafini acknowledges support from the Frank Horton Graduate Fellowship Program at the University of Rochester's Laboratory for Laser Energetics, funded by the U.S. Department of Energy.

1. R. B. James *et al*., in *Semiconductors for Room-Temperature Radiation Detector Applications*, Semiconductors and Semimetals, Vol. 43, edited by T. E. Schlesinger and R. B. James (Academic Press, San Diego, 1995), Chap. 9, pp. 336–383.
2. C. Szeles *et al*., IEEE Trans. Nucl. Sci. **49**, 2535 (2002).
3. A. Mycielski *et al*., J. Alloys Compd. **423**, 163 (2006).
4. A. S. Cross *et al*., Nucl. Instrum. Methods Phys. Res. A **624**, 649 (2010).
5. A. Hossain *et al*., J. Cryst. Growth **379**, 34 (2013).
6. J.-H. Yang *et al*., Phys. Rev. B **79**, 245202 (2009).
7. D. Wang *et al*., Appl. Phys. Lett. **90**, 211905 (2007).
8. J. E. Toney, T. E. Schlesinger, and R. B. James, Nucl. Instrum. Methods Phys. Res. A **428**, 14 (1999).
9. J. Serafini *et al*., Semicond. Sci. Technol. **31**, 045006 (2016).
10. C. Thomsen *et al*., Phys. Rev. B **34**, 4129 (1986).
11. S. Wu *et al*., Phys. Rev. B **76**, 085210 (2007).

High-Efficiency, Large-Aperture Fifth-Harmonic Generation of 211-nm Pulses in Ammonium Dihydrogen Phosphate Crystals for Fusion Diagnostics

I. A. Begishev, M. Romanofsky, S. Carey, R. Chapman, G. Brent, M. J. Shoup III, J. D. Zuegel, and J. Bromage

Laboratory for Laser Energetics, University of Rochester

High-energy ultraviolet (UV) sources are required to probe hot dense plasmas from fusion experiments by using Thomson scattering resulting from the lower self-generated background from the plasma in the 180- to 230-nm spectral region.[1] The fifth-harmonic generation (5HG) of a neodymium laser with a 211-nm wavelength fits that window. Recently[2] we demonstrated 30%-efficient, joule-class fifth-harmonic conversion of 1053-nm pulses using a cesium lithium borate (CLBO) crystal, but larger crystals are necessary for increased UV energy. Also, the extremely hygroscopic property of CLBO crystals requires that they be kept under high (~120°C) temperature. Ammonium dihydrogen phosphate (ADP) crystals, which can be grown to much larger sizes, should be considered as an alternative way of generating a high-energy beam at 211 nm.

For cascade 5HG, however, ADP has a significant limitation: phase-matching conditions for sum–frequency generation are not met at room temperature. Noncritical phase-matching conditions could be reached by cooling ADP crystals to –70°C. This is not trivial, especially for large-aperture crystals, because a definite temperature must be strictly stabilized and maintained across the entire crystal. Any holder that keeps a crystal in the vacuum chamber and maintains a crystal temperature through thermal conductive contact provides some gradient of temperature through a crystal.

The most-effective way to stabilize an entire crystal under low temperature is a two-chamber cryostat, where the internal chamber keeps a crystal almost isolated from a holder but surrounded by 1 atm of helium gas. The internal chamber is held in the high-vacuum external chamber to minimize heating. The cross section of the designed and fabricated two-chamber cryostat is shown in Fig. 1. "Cold flow" travels down from the liquid nitrogen tank through two hollow cylinders to the internal chamber; it then reaches the 65 × 65 × 10-mm ADP crystal through the helium. As soon as the temperature of the crystal (or the internal chamber wall, depending on which temperature sensor is chosen as the control) approaches a chosen set point temperature, the heaters on the wall of the lower cylinder begin working to maintain that temperature through a temperature stabilization loop. A high-performance cryogenic temperature controller is used to monitor and control temperature within the internal chamber to better than 0.01°C resolution. Each of the two heaters mounted on the cryostat is controlled by a proportional-integral-derivative feedback loop. The feedback continually adjusts the output power to the heaters in order to keep the chosen temperature constant. The system has high thermal mass and reaches a target temperature of 200 K in about 36 h.

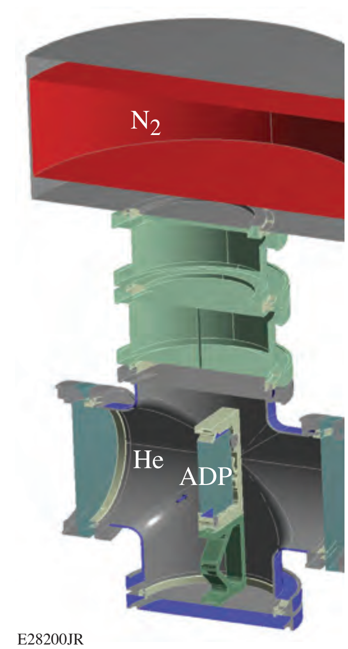

Figure 1
The cross section of the internal chamber, filled with helium (He), with the crystal (ADP) and liquid nitrogen tank (N_2).

This experiment is shown in Fig. 2. Some portion of the energy must be saved at the fundamental frequency (20% in an ideal-case plane wave without any type of absorption and Fresnel reflections), untouched through the first two crystals to mix with the 4ω beam. We have chosen the cascade $o_1e_1 \longrightarrow e_2{:}o_2o_2 \longrightarrow e_4{:}o_1o_4 \longrightarrow e_5$, which allows the energy distribution between o and e waves to be changed by polarization rotation with a half-wave plate (HWP). The first frequency doubler was a Type-II deuterated potassium dihydrogen phosphate (DKDP) crystal (30 × 30 × 27 mm). A second frequency doubler, a Type-I KDP crystal (30 × 30 × 15.5 mm), was used to convert 2$\omega \longrightarrow$ 4ω.

An Nd:YLF laser was optimized to produce square pulses with a flattop, square beam profile (1053 nm, 1 to 2.8 ns, 12 × 12 mm, ≤1.5 J, ≤5 Hz). The fused-silica prism separates the harmonic beams in space. The input and output beam energies were measured using identical cross-calibrated pyroelectric energy meters. All beam profiles were recorded.

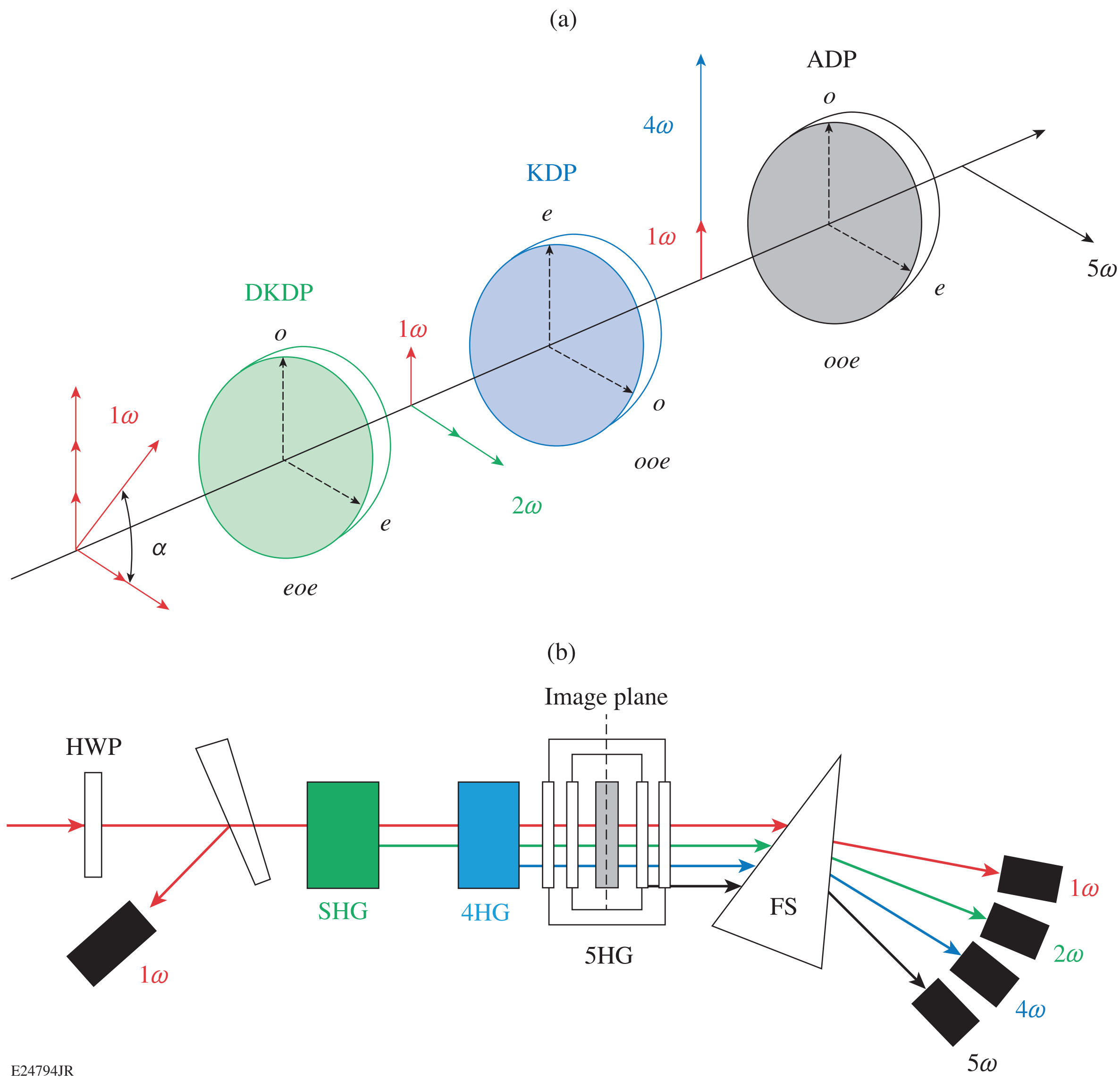

Figure 2
Experiment: (a) The orientation of the crystal axes and polarizations. The angle (α) of the 1ω polarization was set using a half-wave plate for optimal conversion, e: extraordinary, o: ordinary. (b) Setup. HWP: half-wave plate; SHG: second-harmonic generator; 4HG: fourth-harmonic generator; 5HG: fifth-harmonic generator; FS: fused-silica wedge.

Accurate tuning of the experimental parameters allowed for total conversion efficiency from the fundamental to the fifth harmonic, including surface losses and absorption, of 26% (Fig. 3). Temperature acceptance of 5HG is extremely narrow and less than 0.4 K (FWHM). Angular acceptance was measured at 200 K and is 8 mrad external (FWHM).

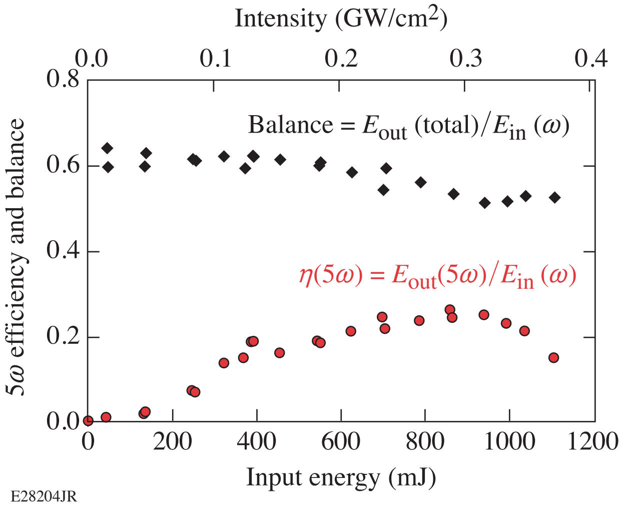

E28204JR

Figure 3
Fifth-harmonic efficiency and energy balance measured as a function of input-pulse energy and intensity.

This material is based upon work supported by the Department of Energy National Nuclear Security Administration under Award Number DE-NA0003856, the University of Rochester, and the New York State Energy Research and Development Authority.

1. J. S. Ross *et al*., Rev. Sci. Instrum. **81**, 10D523 (2010).

2. I. A. Begishev *et al*., Opt. Lett. **43**, 2462 (2018).

Interaction of Short Laser Pulses with Model Contamination Microparticles on a High Reflector

K. R. P. Kafka and S. G. Demos

Laboratory for Laser Energetics, University of Rochester

Contamination in the optical components of large-aperture laser systems is a well-known problem originating from the handling, installation, and operational environment of these large components. The main problems associated with contamination particles are that they can facilitate laser-induced damage (LID) during operation of the system by creating (a) localized absorption and damage of the host optic and (b) intensification (hot spots) of the propagating beam, giving rise to damage in downstream optical components. Previous studies on this issue have focused on identifying the origin of contamination[1] and understanding the interaction of nanosecond laser pulses with the contamination particles.[2,3] These studies have highlighted that contamination can originate from various sources (including ejected debris from LID of adjacent parts, target materials, and the optics themselves) and therefore can involve various types of materials. Depending on the type of contamination particle (metal, transparent, etc.), its interaction with the laser pulse varies and can be characterized by three main effects: (1) particle removal, (2) secondary contamination of the host surface by fragments of the original contamination particle, and (3) LID of the host surface. Particle removal or ejection is often desirable (frequently referred to as "laser cleaning"[4]), but LID and secondary contamination degrade the performance of the optic.

The effectiveness of contamination particles to accelerate LID in optical components in the short-pulse (picosecond to femtosecond) regime has so far remained uninvestigated. Furthermore, direct translation of the knowledge attained for nanosecond-pulse systems is not warranted since short-pulse systems typically employ reflective optical elements and operate at higher laser peak intensities by many orders of magnitude. This work investigates the interaction of 10-ps and 0.6-ps laser pulses with microparticles located on the surface of a multilayer dielectric mirror in order to understand and assess the risk of contamination-induced damage in short-pulse laser systems. Irradiation with one laser pulse caused particles to eject from the surface with an onset fluence in the range 5× to 100× below the particle-free, laser-induced damage threshold (LIDT) of the mirror. Morphological analysis showed, however, that the ejection process always generated ablation craters and/or secondary contamination, both of which can degrade the performance of the optic during subsequent pulses. Ejection and damage mechanisms are discussed for each particle type.

Four different particle materials (one metal, one glass, and two polymers) were used as representative contaminants in this experiment. All four species have similar ≈40-μm diameters, while three are spherical in shape. Although contaminant particles in an actual laser system would have a broad distribution of sizes and irregular shapes, these controlled variables of size and shape enable one to more directly compare and contrast the mechanisms and resulting surface modifications. The particles were used to intentionally contaminate 2-in.-diam commercially available multilayer dielectric mirrors that exhibit high reflection at our 1053-nm laser wavelength at angles of incidence from 0° to 45°.

A dry powder of particles was dispersed onto the mirror sample. The sample was then placed in an experimental setup for short-pulse laser irradiation of individual particles. Laser pulse durations of 0.6 or 10 ps were selected for this work. Beam profile and energy were recorded for each pulse to measure the beam-normal peak fluence of the 300-μm-diam (e^{-2}) Gaussian beam. Isolated contaminant particles were positioned to within 20 μm of the laser peak location and then irradiated by a single pulse. Subsequently, the morphologies of the irradiated sites were analyzed.

The fluences of median (50% probability) ejection (F_E) and median LID (F_{th}), displayed in Fig. 1, are organized by contaminant particle type. Noting the logarithmic scale, these data show that the onset of particle ejection always occurs at fluences significantly lower (in the range 1% to 20%) than F_0, the LIDT of the pristine (noncontaminated) mirror. The ejection fluence of the glass and steel did not vary significantly with pulse duration, whereas each of the two polymers showed a factor of 3 between F_E at the two pulse durations.

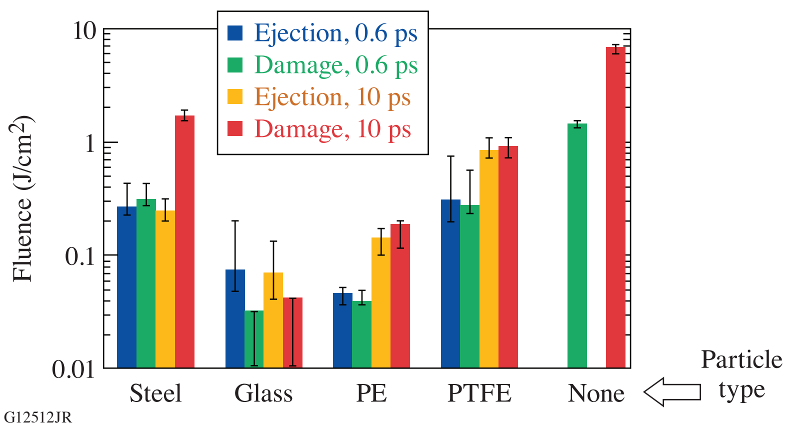

Figure 1
Median ejection and LID fluences. Error bars show the observed range from 0% to 100% probability, except for glass, where all tested fluences caused LID and a large lower bound was artificially added.

The morphological data and analysis for each of the eight tests (two pulse durations, four materials) were subsequently analyzed. Figure 2 displays the subset of this data set that shows the morphologies generated with stainless steel particles. These images show three representative laser fluences: (1) below, (2) just above, and (3) well above the particle ejection fluence. Slightly below the F_E of steel [Figs. 2(a) and 2(d)], a large number of submicrometer particles are observed on the mirror without ejection of the main particle. As fluence is increased to F_E [Figs. 2(b) and 2(e)], the main particle is ejected. This ejection was measured to occur at the same fluence for both pulse durations, consistent with the linear absorption (not dependent on intensity) of metals such as steel. At higher fluences [Figs. 2(c) and 2(f)], in addition to surface contamination by microparticles, LID is observed in sickle shapes on the laser-incident side. This suggests the formation of an interference pattern (from the directly incident beam and the beam reflected from the particle) exceeding the onset of damage initiation, especially exemplified in the 0.6-ps interaction. Under exposure to 10-ps pulses, a film of secondary contamination is observed to form [in Fig. 2(c)]. These observations together may suggest that 0.6-ps interactions bring a greater risk of LID, but 10-ps interactions bring a greater risk of secondary contamination.

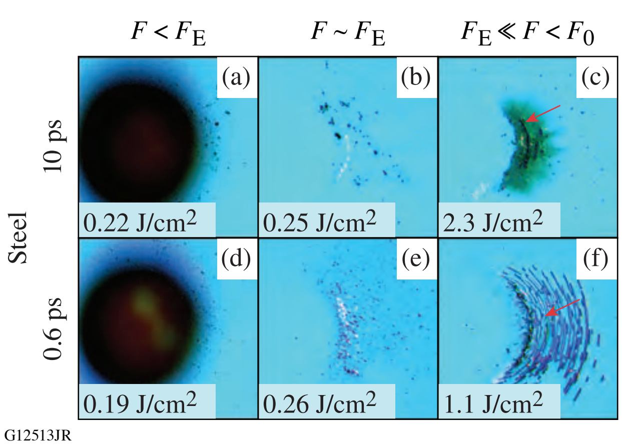

Figure 2
Optical microscopy of one-pulse–irradiated steel particle sites, organized by row (pulse duration) and column (relative fluence). Red arrows indicate ablation of the mirror. The laser is incident from the right at a 45° angle of incidence and *s* polarization.

Although all particle ejections left a residue of particles, films, and/or coating ablation at fluences far below the pristine LIDT, future work seeks to employ this knowledge to develop protocols of laser cleaning for optics in short-pulse, high-powered laser systems and could help devise self-cleaning protocols using the laser itself at lower operating fluences.

This material is based upon work supported by the Department of Energy National Nuclear Security Administration under Award Number DE-NA0003856, the University of Rochester, and the New York State Energy Research and Development Authority.

1. J. Bude *et al*., Opt. Express **25**, 11,414 (2017).

2. M. J. Matthews *et al*., J. Opt. Soc. Am. B **30**, 3233 (2013).

3. S. G. Demos *et al*., Opt. Express **24**, 7792 (2016).

4. W. Zapka, W. Ziemlich, and A. C. Tam, Appl. Phys. Lett. **58**, 2217 (1991).

Evaluation of Laser-Induced–Damage Threshold in Saturated and Unsaturated Nematic Liquid Crystals Between 600 fs and 1.5 ns at 1053 nm

T. Z. Kosc, A. A. Kozlov, S. Papernov, K. R. P. Kafka, S. G. Demos, and K. L. Marshall

Laboratory for Laser Energetics, University of Rochester

A wide-ranging series of liquid crystal (LC) materials, which included compounds with saturated (cyclohexane) and unsaturated (benzene) carbon rings (Table I), were selected to explore the effect of varying degrees of π-electron delocalization and electron density on their laser-induced–damage threshold (LIDT). This work provides baseline measurements on the damage threshold of LC's as a function of their chemical structure, and it extends the currently limited available knowledge at subnanosecond pulse lengths. This information provides insight into the damage-initiation mechanisms in LC's and guidance for the possible implementation of future applications in high-power and/or peak intensity systems. Furthermore, this work can provide insight into the design of new materials such as polymer and glassy LC materials.

Table I: Nematic liquid crystals used in this study.

	Name	Supplier	Absorption Edge
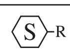	1550C	Dabrowski^	294 nm
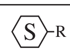	MLC-2037	Merck	306 nm
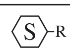 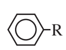	ZLI-1646	Merck	324 nm
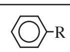	PPMeOB/PPPOB	LLE*	345 nm
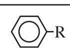	5CB	EMB	377 nm
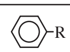	E7	EMB	385 nm

Materials are designated as saturated 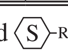 and unsaturated 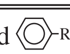 in the first column. Note that ZLI-1646 has a mixture of compound types. Transmission measurements were performed on a Perkin Elmer Lambda-900 spectrophotometer. LC materials were in the isotropic state during measurement. Here, the absorption edge is defined at $T = 98\%$.

^Isothiocyanate compound synthesized by M. Dabrowski, University of Warsaw.

*A 60/40 mixture of two phenyl benzoate ester compounds used on the OMEGA laser and synthesized at LLE.

Both 1-on-1 (single shot per test site) and *N*-on-1 (up to ten shots at 0.1 Hz, with the fluence ramped until damage occurs) damage testing were performed to determine the corresponding LIDT. Because the LC mesophase is fluid, a test site is considered damaged upon any visual change, as observed with an *in-situ* microscope system. The difference between pre-exposure and post-exposure images is used to identify such changes. Damage-induced changes (tiny spot or bubble-like features) were observed as a change in scattered light in a micron-scale area and typically redissolved or migrated on a time scale dependent on laser fluence and fluid viscosity. The number density and size of these features increased with increasing fluence above the damage threshold. Additional details on sample preparation and testing protocol are found in Ref. 1.

Damage-threshold data were acquired at six pulse lengths (τ): 600 fs, 2.5 ps, 10 ps, 50 ps, 100 ps, and 1.5 ns at 1053 nm. Both the 1-on-1 and *N*-on-1 LIDT values are plotted in Fig. 1 as a function of each material's UV-absorption edge. Brackets identify the saturated, unsaturated, and mixed materials. In this study, data for saturated and unsaturated materials are fairly easily differentiated, and the partially saturated material behaves more like a fully saturated material (at least under 1053-nm irradiation). Damage thresholds of three common LC materials (E7, 5CB, and ZLI-1646), which were reported in 1988 (using nanosecond laser pulses at 1053 nm) (Ref. 2), were remeasured and found to be higher. This increase is attributed to significant improvements in the chemical purity of commercial LC compounds. Early measurements of the conjugated compound 5CB and its saturated analog ZLI-S-1185 (Ref. 3) are extended in the present work by exploring additional materials and pulse durations from subpicosecond to nanosecond. Of special significance are the data at 1.5 ns, where the LIDT values of saturated LC's approach those of bare fused silica.[4]

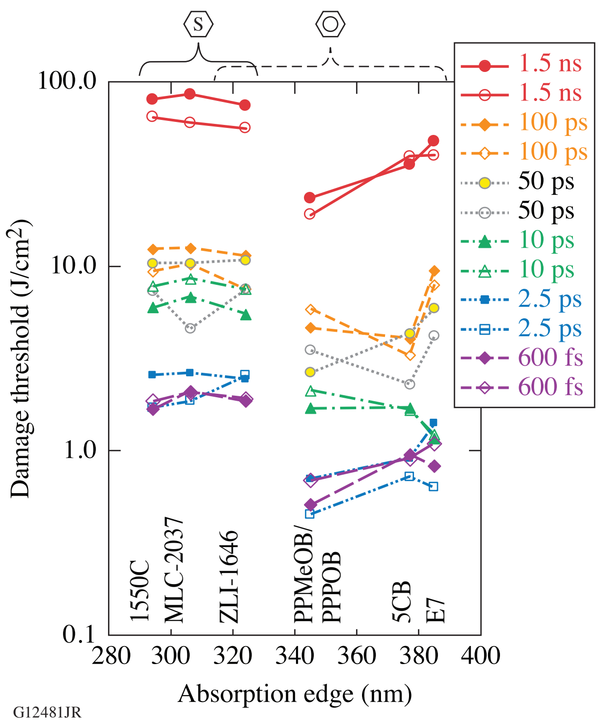

Figure 1
The 1-on-1 (open symbols) and *N*-on-1 (closed symbols) damage thresholds plotted as a function of the UV absorption edge. Materials with completely saturated or mostly saturated carbon rings have absorption edges <330 nm, with correspondingly higher damage thresholds.

The *N*-on-1 LIDT results exhibit a power dependence on the pulse length τ^x where $x \sim 0.5$, as shown in Fig. 2. A similar pulse-length dependence is observed in both dielectrics[4] and biological materials,[5] although in both cases the $\tau^{0.5}$ dependence extends only into the range of tens of picoseconds. This pulse-length dependence is attributed to thermal diffusion effects that govern the damage-initiation process, especially that of defects or defect states, which leads to free electrons and ionization of the material. In the range of tens of picoseconds, multiphoton ionization starts to contribute to electron production, and in the subpicosecond range, multiphoton ionization becomes the dominant process. At this time, we consider the fact that LC damage thresholds at pulse lengths <50 ps still follow the $\tau^{0.5}$ trend reasonably well as coincidental.

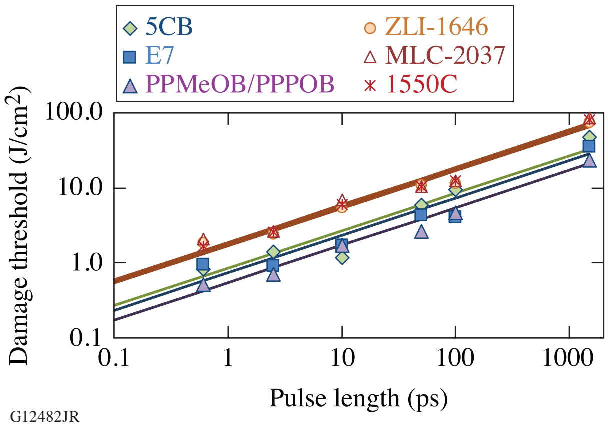

Figure 2
N-on-1 LIDT values for saturated and unsaturated LC materials are shown as a function of pulse length. A fit based on $\tau^{0.5}$ is shown for each material. R^2 values range between 0.91 (E7) and 0.97 (PPMeOB/PPPOB, 1550C, and ZLI-1646).

The absorption mechanisms, which lead to laser-induced damage, are largely dependent on the electronic structure of the material, intrinsic (LC orientation and domain boundaries) and extrinsic (impurities, substrate defects or inclusions) defects, and the laser parameters. The electronic structure in LC materials is generally known, involving a singlet ground state (S0) and excited singlet (S1, S2,…Sn) and triplet states.[6,7] The absorption spectra measurements suggest that, under 1053-nm laser irradiation, the unsaturated materials require three-photon absorption for the S0 ⟶ S1 transition, while the saturated materials require four-photon absorption. This difference in the order of the absorption process required to generate excited-state electrons is clearly captured by the difference in the damage threshold between the two types of materials, where the saturated materials have 2× to 3× higher damage threshold across all pulse lengths tested.

This research has reported damage-threshold fluences for a series of saturated and unsaturated nematic LC materials for pulse lengths between 600 fs and 1.5 ns at 1053 nm. Saturated materials always have higher damage resistance, although the pulse-length–dependent behavior varies somewhat for the two different types of material. Damage mechanisms are still under investigation, but current results point toward the presence of both multiphoton absorption and excited-state absorption.

This material is based upon work supported by the Department of Energy National Nuclear Security Administration under Award Number DE-NA0003856, the University of Rochester, and the New York State Energy Research and Development Authority.

1. T. Z. Kosc *et al*., Proc. SPIE **10447**, 104471G (2017).
2. S. D. Jacobs *et al*., J. Opt. Soc. Am. B **5**, 1962 (1988).
3. M. Guardalben *et al*., in *Laser Induced Damage in Optical Materials: 1988*, Natl. Inst. Stand. Technol. (U.S.), Spec. Publ. 775 (U.S. Government Printing Office, Washington, DC, 1989), pp. 462–469.
4. B. C. Stuart *et al*., Phys. Rev. B **53**, 1749 (1996).
5. A. Oraevsky *et al*., IEEE J. Sel. Top. Quantum Electron. **2**, 801 (1997).
6. R. Sander, V. Herrmann, and R. Menzel, J. Chem. Phys. **104**, 4390 (1996).
7. G. E. O'Keefe *et al*., Liq. Cryst. **21**, 225 (1996).

Mechanisms Governing Laser-Induced Damage in Absorbing Glasses Under Exposure to Nanosecond Pulses

S. G. Demos,[1] B. N. Hoffman,[1] C. W. Carr,[2] D. A. Cross,[2] R. A. Negres,[2] and J. D. Bude[2]

[1]Laboratory for Laser Energetics, University of Rochester
[2]Lawrence Livermore National Laboratory

Significant progress has been made during the past 15 years in understanding the mechanisms of laser-induced damage in transparent optical materials and mirrors. Above a threshold laser fluence, defect structures initiate plasma formation that leads to exposure of the material to high localized pressures followed by an explosive boiling process that involves ejection of superheated material, the launching of a shock wave, and stresses that result in mechanical damage of the surrounding "cold" material.[1] The dynamics and ensuing relaxation pathway are typically manifested as a microscopic crater on the surface or a microscopic void formed in the bulk of the material, depending on the location of damage initiation.

In contrast, laser-induced damage in absorbing dielectric materials under nanosecond laser pulses has received far less attention. Such absorbing materials are typically used as optical filters to attenuate the laser light for various applications including laser safety, sensor protection, and attenuation of stray beams in high-power laser systems such as at the National Ignition Facility. In addition, nominally transparent optical materials (such as glasses) operating in a high-radiation environment can develop color centers, thereby becoming absorbing at the operational wavelength.

Early work suggested that nonlinear absorption plays an important part in laser damage to absorbing optical glasses[2] and that damage occurred at either the surface or internally.[3] Past damage-morphology studies of such glasses under relevant excitation conditions indicated that material modifications are manifested with a typical "melted-surface" morphology[4] but such observations were often observed at fluences where the calculated surface temperature reached during the laser pulse was well below the melting point of the glass. Other reports suggested that the damage morphology changes as a function of the laser beam size and repetition rate.[5] These previous results indicate that key issues regarding laser-induced damage in absorbing glasses remain unclear.

The current study was designed to investigate the dominant mechanisms of laser-induced damage in absorbing optical materials under irradiation with 355-nm pulses having a temporal duration of the order of a nanosecond. A wide array of diagnostics tools was employed to enable one to monitor beam propagation inside the material, quantifying changes in the optical properties of the material, and capturing time-resolved transient material modifications with adequate spatial and temporal resolution. The results suggest that, in addition to linear absorption, excited-state absorption is a key mechanism contributing to enhanced energy deposition. In addition, there are two competing damage-initiation mechanisms: the first through self-focusing activated by a transient, fluence-dependent change of the refractive index; the second through melting of the material as a result of the increase of its temperature.

Figure 1(a) demonstrates a typical example of the first observed damage mechanism, showing the beam intensity profiles along the center of the beam at the exit surface of a 4-mm-thick, Ce^{3+}-doped silica glass sample for four different input laser fluences (0.8 J/cm^2, 6.4 J/cm^2, 8.3 J/cm^2, and 11 J/cm^2, respectively). At a lower peak fluence (<2 J/cm^2), the beam profile remains mostly unchanged. A significant narrowing of the beam is observed, however, at the sample's exit surface at higher fluences. These results clearly demonstrate a self-focusing behavior of the propagating beam into the material that strongly depends on the laser fluence.

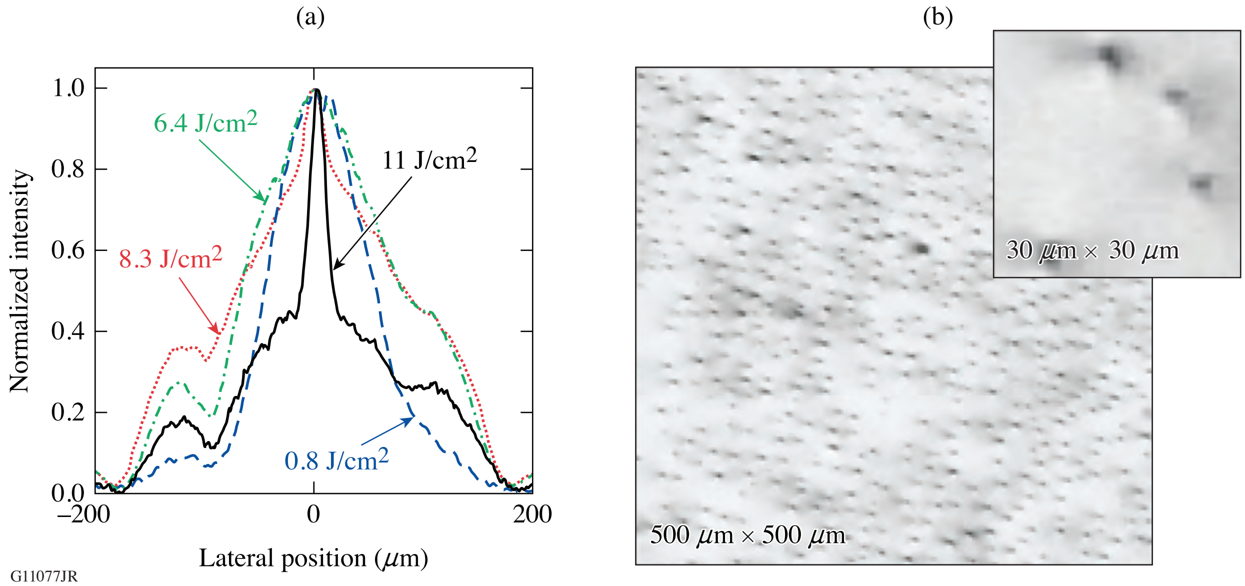

Figure 1
(a) The intensity profile along the middle of the laser beam at the output surface of a 4-mm-thick, Ce^{3+}-doped silica glass sample for different laser (peak) fluences. (b) Images of filamentation-induced damage in Ce^{3+}-doped silica 1.25 mm below the input surface under exposure to ≈20-J/cm^2, 351-nm, 5-ns flat-in-time pulses.

The same material was exposed to single pulses having a beam diameter of the order of 1 cm at various average laser fluences. The entire volume of the sample exposed to the laser beam was subsequently imaged at different depths, starting from the input surface and into the bulk in increments of 250 μm. Figure 1(b) represents a typical image at a depth of 1.25 mm below the surface from a section of the sample that was exposed to a fluence of ≈21 J/cm^2. This image demonstrates the presence of numerous filament damage sites with a diameter of ~2 to 3 μm. This is better demonstrated in the high-magnification inset. The filaments at this fluence are observed to start from a depth of ~500 μm and extend to a depth of ~1750 μm. The highest density of filament damage sites is observed ~1 mm below the surface for all fluences used in these experiments. An examination of individual filaments reveals that their length is ~750 μm.

A detailed investigation of the dynamics of this self-focusing behavior reveals that it arguably originates from a change of the index of refraction following the transition of electrons to a higher excited state. This modulation of the refractive index arises from the difference in the polarizability between the ground and excited states of the impurity ions and even transient defects formed during the excitation process. The relaxation time of this change of the refractive index is the same as the lifetime of the excited state; therefore, it can be much longer than the laser pulse (of the order of 100 ns for Ce^{3+}-doped silica glass). For large beams, the modulation of the refractive index leads to beam breakup and the formation of filaments as shown in Fig. 1(b). The filaments are located over a narrow depth zone (~2 mm) since the self-focusing mechanism is counteracted by the attenuation of the laser beam as it propagates inside the material.

The second damage-initiation mechanism in absorbing glasses is associated with heating of the material near the surface, resulting from the nonradiative relaxation following laser-energy deposition. This can support above-melting temperatures, which introduces nonreversible material modifications (damage). The dominant damage-initiating mechanism for a specific material and irradiation conditions depends on the material's electronic and thermophysical properties.

To understand this dual behavior of laser damage in absorbing glasses, we need to consider that there is a laser-induced damage threshold (LIDT) associated with the material surface reaching above melting temperature ($LIDT_{melt}$), as well as an analogous laser fluence for damage initiation via self-focusing ($LIDT_{focus}$). The experimentally observed damage behavior of a specific material and excitation condition is governed by the mechanism with the lowest threshold. The change in the damage mechanism with beam size can arise from the thermomechanical properties of the material and the fact that the peak surface temperature can be a function of the laser spot size. For small beams, the flow of energy (such as via heat diffusion and/or electron transport) reduces the peak temperature, thereby increasing the effective $LIDT_{melt}$ value. On the other hand, for large beams, there is no (or not significant) energy flow, which leads to the generation of higher local temperatures for the same laser fluence. Consequently, a larger beam size promotes a higher localized temperature in the material for the same laser fluence. In materials with similar $LIDT_{melt}$ and $LIDT_{focus}$, experimentation with different laser beam spot sizes can lead to different observables because of the change in the governing damage-initiation mechanisms. For similar reasons, the local temperature can be a function of the pulse repetition rate.

This material is based upon work supported by the Department of Energy National Nuclear Security Administration under Award Number DE-NA0003856, the University of Rochester, and the New York State Energy Research and Development Authority. This work was performed in part under the auspices of the U.S. Department of Energy by Lawrence Livermore National Laboratory under Contract No. DE-AC52-07NA27344 with support from Laboratory Directed Research and Development grant 16-ERD-016 (LLNL-JRNL-763447).

1. S. G. Demos *et al*., Optica **2**, 765 (2015).
2. Yu. A. Demochko, I. F. Usol'tsev, and V. M. Shaposhnikov, Sov. J. Quantum Electron. **9**, 1556 (1979).
3. R. A. Miller and N. F. Borrelli, Appl. Opt. **6**, 164 (1967).
4. P. K. Whitman *et al*., Proc. SPIE **3578**, 681 (1999).
5. J.-H. Han *et al*., Acta Phys. Sin. **60**, 28106 (2011).

Tritium Extraction from Water

W. T. Shmayda,[1] C. R. Shmayda,[2] and G. Torres[3]

[1]Laboratory for Laser Energetics, University of Rochester
[2]Torion Plasma, Inc.
[3]Nuclear Sources and Services, Inc.

Tritiated water production is ubiquitous in facilities that handle tritium gas. Sources range from decontamination efforts, to the deliberate conversion of elemental tritium, to tritiated water in processes that strive to reduce emissions to the environment, to gaseous effluents, to the environment. At low concentrations, ranging from a few μCi/L to mCi/L, high throughputs are required to process the high-volume, low-activity water. Combined electrolysis and catalytic exchange (CECE) shows promise by offering high throughput, reliability, economic viability, and facile coupling to isotopic separation systems, if necessary. This summary will discuss the features of a CECE facility based on a 7-m^3/h throughput alkaline electrolysis cell.

As of 2018, there are 451 nuclear reactors operating in 31 countries with an additional 59 reactors currently under construction. All of these nuclear power stations have chronic releases of tritium that can be measured in the surrounding groundwater. In the U.S., for example, concentrations between 20 nCi/L and 0.1 μCi/L have been observed. The dose to an individual drinking 4.4 L of 1 μCi/L of water every day for a year is equivalent to only 30% of the annual dose received from natural background radiation. While the scientific community understands that the chronic release of tritium to the groundwater is not dose relevant, the public is far more sensitive to the issue. Even in locations where the ground water activity is below the EPA maximum contaminant level of 4 mrem per year, land owners have successfully sued nuclear power stations over the contamination. Therefore, chronic tritium release to the groundwater remains an imminent concern for any operator of a nuclear power station. Newly constructed fission or fusion plants require robust strategies to mitigate the release of tritium to the environment to help alleviate public backlash and limit legal liabilities.

The CECE technology has been under development for several years in national laboratories[1–6] but has seen limited commercial deployment. The process provides an elegant, compact, and powerful option to concentrate tritium activities in water. The system comprises a liquid phase catalytic column (LPCE) integrated with an electrolysis cell. A schematic of the system is seen in Fig. 1. The electrolysis cell provides a constant supply of elemental tritiated gas to the bottom of the LPCE column. As the gas is directed up the column, a counter flow of clean water is added to the top of the column. The isotopic exchange of the tritium from the rising elemental gas to the descending water has the effect of "washing" the tritium to the bottom of the column. Clean hydrogen gas is emitted from the top of the column, while the majority of the tritium is contained in the water at the bottom. The tritiated feed stock water can be combined with the tritiated water leaving the column to collect in a tank. This water is used to feed the electrolysis cell to create more elemental gas. If the molar feed rate of the clean water at the top of the column and the tritiated feed stock water at the bottom of the column are equal to the molar rate of release of clean hydrogen from the top of the column, the system will remain in balance with all of the tritium concentrating in the water in the bottom tank.

It can be shown that the height of a packed column depends on the isotopic separation factor in the electrolyzer (α_{el}), the isotopic separation factor (α_{col}) in the column, and the concentration at the top of the column (y_{t}); λ is the ratio of the molar gas

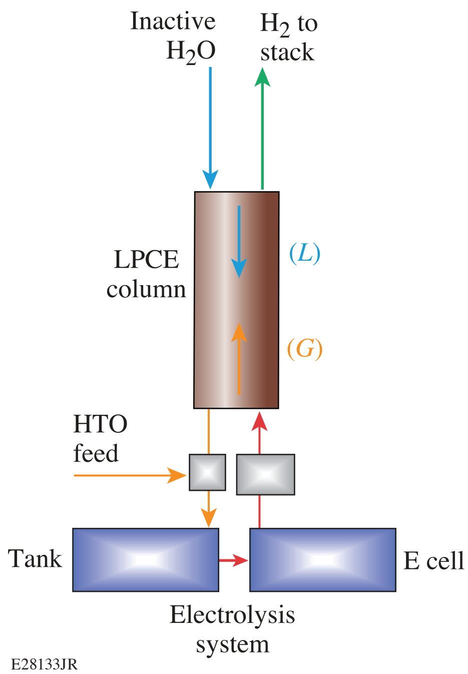

Figure 1
Schematic of the combined electrolysis and catalytic exchange system.

flow up the column (G) to the molar flow rate of water down the column (L) ($\lambda = G/L$); and the height-equivalent theoretical plate (HETP) for the catalyst according to the relation[7]

$$h = \text{HETP} * \frac{\ln\left(\dfrac{x_{\text{el}}}{\alpha_{\text{el}} * y_{\text{t}}} * \dfrac{\alpha_{\text{col}} - \lambda}{\alpha_{\text{col}} - 1}\right)}{\ln\left(\dfrac{\alpha_{\text{col}}}{\lambda}\right)}. \tag{1}$$

The quantities α_{el}, α_{col}, and HETP are fixed when operating at a fixed temperature with a particular catalyst. For a given gas-to-liquid molar ratio, the height of a column is determined by two parameters: the concentration of the electrolyte, x_{el}, and the concentration of the effluent at the top of the column, y_{t}. Both parameters are at the discretion of the end user.

Figure 2 illustrates the column-height dependence on those two parameters for fixed λ. It is more economical to operate at a higher λ because there will be less counter-flowing water that must to be electrolyzed back into elemental gas. For a chosen column height, the trade-off will be to operate at the highest possible λ within a prescribed emission discharge limit at the column top.

If the CECE system is being used to concentrate tritiated water for long-term storage or to reduce volume as the first step in tritium recovery, then the column height is selected for the maximum decontamination factor. Assuming the activity at the top of the column approaches zero, then in steady state, tritium balance requires that the amount of tritium introduced to the system ($L_{\text{f}} * x_{\text{f}}$) must equal the amount drawn as concentrate ($L_{\text{c}} * x_{\text{c}}$), where L_{f} is the molar feed rate into the electrolysis system at a concentration of x_{f} and L_{c} is the rate at which the concentrate is extracted from the system at a concentrate of x_{c}. It follows that the rate of concentrate draw is inversely proportional to the ratio of the feed activity to the concentrate activity:

$$L_{\text{c}} = \frac{x_{\text{f}}}{x_{\text{c}}} * L_{\text{f}}. \tag{2}$$

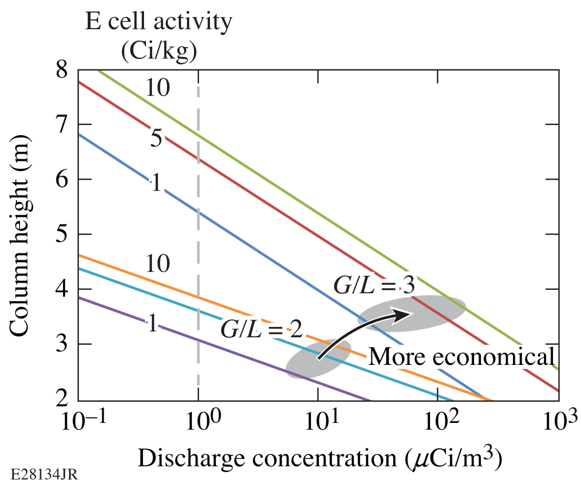

Figure 2
Column-height dependence on the discharge concentration and the gas-to-liquid molar ratio.

As an example, assume a feed concentration of 100 μCi/kg is delivered to the system operating at 90% efficiency, at a gas-to-liquid molar ratio of 2 (λ = 2) and driven by a 21-m^3/h electrolyzer. In steady state, this system will accept 418 U.S. barrels per year (66,480 L) and produce 3.3 L of concentrate at 2 Ci/L for a volume reduction of ~20,000. In this example, a column height of 3.9 m would result in an emission of 0.17 Ci per year and a net activity collection efficiency of 98%. Increasing the column height by an additional 0.7 m would reduce the effluent activity by a factor of 10. At these concentrations, a portion of the electrolyzed gas can be diverted to an isotope separation system for tritium recovery.

The use of nuclear power will continue to grow in the world driven by the need for carbon neutral energy systems. Whether the reactors are fission or fusion based, it will be incumbent on the operators to reduce tritium releases to appease the public perception. CECE systems similar to one described above provide an economical and robust form of tritium concentration and recovery. The experience developed in an industrial environment attests to the simplicity and efficacy of the systems. Options to recover tritium from light water over a broad range of activities and throughputs using the small footprint of the CECE technology indicate that this technology will become an important effluent mitigation tool in the future.

This material is based upon work supported by the Department of Energy National Nuclear Security Administration under Award Number DE-NA0003856, the University of Rochester, and the New York State Energy Research and Development Authority.

1. I. A. Alekseev *et al*., Fusion Sci. Technol. **41**, 1097 (2002).

2. J. P. Butler *et al*., in the *Proceedings of the Sixth International Congress on Catalysis*, edited by G. C. Bond, P. B. Wells, and F. C. Tompkins (Imperial College, London, 1977), Vol. 2, pp. 747–756.

3. J. P. Butler *et al*., U.S. Patent No. 4,228,034 (14 October 1980).

4. I. Cristescu *et al*., Fusion Sci. Technol. **41**, 1087 (2002).

5. L. Geens *et al*., Commission of the European Communities (CEC), Luxembourg, Report EUR-11551 (1988).

6. A. Perevezentsev *et al*., Fusion Sci. Technol. **41**, 1107 (2002).

7. A. Bruggeman *et al*., in *Management of Gaseous Wastes from Nuclear Facilities*, IAEA-SM-245/52 (IAEA, Vienna, Austria, 1980), pp. 157–173.

Distribution of Tritium in the Near Surface of Stainless-Steel 316

M. Sharpe,[1] C. Fagan,[1,2] and W. T. Shmayda[1]

[1]Laboratory for Laser Energetics, University of Rochester
[2]Department of Chemistry, University of Rochester

The interaction and subsequent retention of tritium in stainless steel impacts many activities and procedures at LLE, ranging from protium contamination of the DT fuel supply to decontamination procedures for items fielded in OMEGA. The adsorption of tritium onto the surface of stainless steel represents the first step in the overall retention and permeation of tritium through stainless steel. Understanding the distribution of tritium in the surface region is necessary in determining how tritium responds to an exposure of tritium gas. This knowledge can help determine the effectiveness of barrier materials deposited on stainless-steel surfaces and various surface treatments designed to reduce tritium absorption. Measurement of the near-surface concentrations that develop after storage help quantify the classical observation of tritium migration to steel surfaces after surface decontamination.[1]

There are three regions of interest regarding tritium retention in stainless steel: the surface, the near surface, and the bulk metal. Each region has different chemistry and structures, causing various quantities of tritium to bind in each region. The bulk metal is comprised of a regular lattice of metal atoms, where tritium binds in the interstitial spaces between the metal atoms. The "near surface" represents the transition between the regular metal lattice and the native metal oxide. The surface of stainless steel contains several monolayers of water molecules, which are bound to the metal oxide by a hydroxide layer.

Measuring the tritium concentrations in each region requires three different techniques, each specifically designed to probe the tritium content in that region. Tritium bound to the steel's surface was measured by immersion in a zinc chloride ($ZnCl_2$) solution. This technique has been effective at removing surface-bound tritium without etching into the metal oxide.[2,3] The tritium concentrations in the near surface were measured by dissolving the metal in diluted mixtures of hydrochloric and nitric acid.[4,5] The residual tritium was determined by heating the samples to elevated temperatures.

The migration of tritium from the bulk to the surface was measured by removing surface tritium with an $ZnCl_2$ wash and an acid etched after storing the sample for several days. This removal and storage sequence was repeated several times to monitor how much tritium had migrated to the surface. Such an experiment mimics the effectiveness of decontamination procedures used to clean steel surfaces exposed to tritium gas.

The total tritium contained in the stainless-steel 316 (SS316) samples was 180±20 MBq (4.9±0.5 mCi). The results are shown in Fig. 1 as a function of the storage time for each sample. Six different sets of SS316 samples are included in this figure. Each set was charged with tritium on a different date. These data show negligible, if any, loss of tritium over the 70-day storage period in a dry environment. Two samples contained significantly more tritium than observed on average. This apparent higher activity is most likely a result of cross contamination during sampling.

The combination of the $ZnCl_2$ wash and acid etching provides the distribution of tritium on the surface and in the near surface (<10 μm). The concentration profiles determined from these measurements are shown in Fig. 2. Nine different samples were used. Each sample was stored from 33 to 233 days between charging and measurement. The concentration profiles show that the adsorbed water layers contain large concentrations of tritium. These concentrations decrease by a factor of 10^7 over an ~5-μm

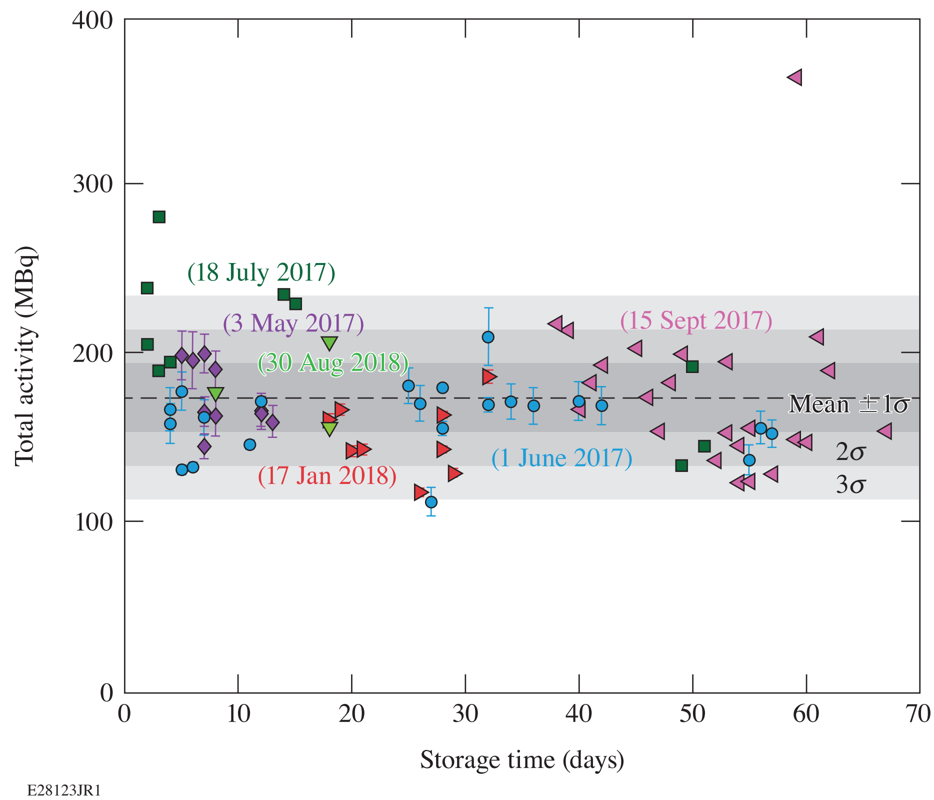

Figure 1
Summary of total tritium inventories from six different sets of samples. Each set was charged with tritium on a different date.

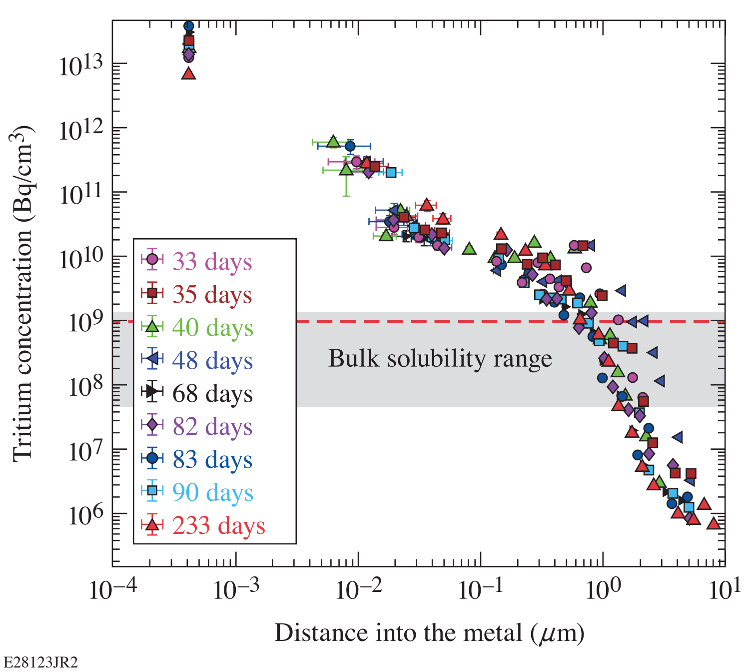

Figure 2
Tritium concentration profiles in the near surface of SS316, as measured using a $ZnCl_2$ wash, followed by acid etching. Shown in the figure are the results of nine different samples, stored from 33 to 233 days prior to measurement.

depth into the metal. Figure 2 also shows the mean and range of hydrogen isotope solubilities in SS316 at 25°C from higher temperature data reported in the literature.[6]

The measured concentration profiles in the near surface of SS316 indicate several things: First, ~30% of the surface is occupied by tritium. Second, the distribution of tritium in the near surface does not change during the 33 to 233 days of storage. This is striking since tritium migration is expected, given the observed concentration gradient and the diffusivity of tritium in SS316 reported in the literature. Tritium appears to be in a quasi-equilibrium state. Finally, comparing the measured concentrations with the reported solubility of tritium in SS316 shows the measured concentrations at depths less than ~1 μm exceed the reported solubilities. These higher concentrations are attributed to the storage capacity of the metal oxide.

Thermal desorption, acid etching, and $ZnCl_2$ wash measurements show the distribution of tritium to be fixed over the measured time period with 40±20% residing in the bulk metal, 42±9% in the near surface, and 21±5% in the adsorbed water.

Tritium migration from the SS316 surface was measured for several samples. Figure 3 presents activity as a function of storage interval, where each interval was between 2 and 4 days. Tritium migrating to the surface decreases after each successive cleaning and storage period, suggesting a depletion of tritium in the near-surface region and an inability to resupply the surface. Perturbing the quasi-equilibrium concentration profiles (shown in Fig. 2) by removing surface tritium concentrations cause some of the tritium to migrate back to the surface from the underlying subsurface in order to re-establish the equilibrium between the surface and the subsurface.

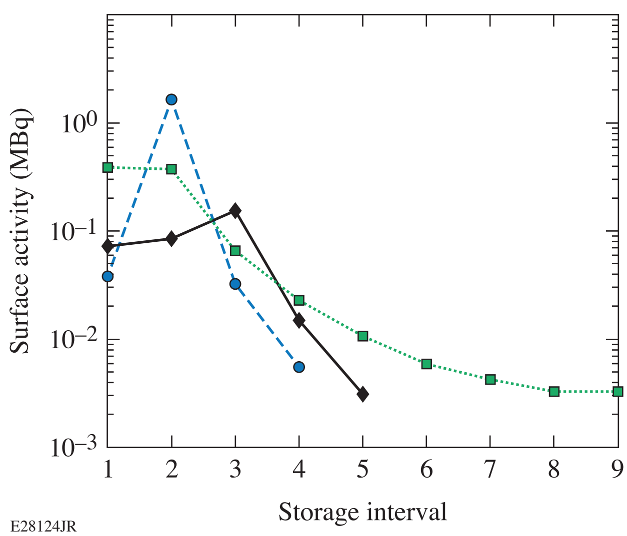

Figure 3
Surface activity for three SS316 samples, measured after the surfaces were cleaned using acid etching and then stored for 2 to 4 days.

This material is based upon work supported by the Department of Energy National Nuclear Security Administration under Award Number DE-NA0003856, the University of Rochester, and the New York State Energy Research and Development Authority.

1. R. A. Surette and R. G. C. McElroy, Fusion Technol. **14**, 1141 (1988).
2. Y. Tanaka *et al*., Mater. Trans. **49**, 805 (2008).
3. M. D. Sharpe *et al*., Fusion Eng. Des. **130**, 76 (2018).
4. T. Hirabayashi and M. Saeki, J. Nucl. Mater. **120**, 309 (1984).
5. R.-D. Penzhorn *et al*., J. Nucl. Mater. **353**, 66 (2006).
6. M. Sharpe, W. T. Shmayda, and W. U. Schröder, Fusion Sci. Technol. **70**, 97 (2016).

Electrochemical Synthesis of Copper Nanoparticles on Hydroxyapatite Coatings for Antibacterial Implants

R. Ghosh,[1] S. Westgate,[1] M. Z. Yates,[1,2] O. Swart,[3] and B. L. Miller[3]

[1]Department of Chemical Engineering, University of Rochester
[2]Laboratory for Laser Energetics, University of Rochester
[3]Department of Dermatology, University of Rochester

The coating of metals with thin ceramic layers is used to reduce the rate of corrosion, add a thermal insulating barrier, or enhance biological activity, among other applications. In this study, coatings of the calcium phosphate ceramic hydroxyapatite (HA) were applied to titanium, and then copper nanoparticles were added to provide antibacterial activity. Synthetic HA has a similar chemical composition to the natural HA found in the mineral component of bone tissue. Coatings of HA on titanium are known to enhance the rate under which an orthopedic or dental implant integrates with surrounding bone. In implant surgery, prophylactic antibiotics are typically used to reduce the potential for post-surgical bone infection. However, the use of antibiotics is undesirable because of the development of resistant strains of bacteria. Metal nanoparticles, such as those reported here, offer a route to provide antibacterial activity without the risk of creating antibiotic-resistant strains of bacteria.

In the present study, a method called cathodic electrolytic deposition was used to synthesize nanoscale HA coatings.[1] Our previous work demonstrated a novel two-stage approach to synthesize silver-hydroxyapatite composite coatings.[2] The cathodic electrolytic process was used in the first stage to synthesize HA on titanium. The HA-coated titanium was then used as the cathode in a second-stage reaction to electrochemically reduce silver ions in solution. The process produced an HA coating decorated with silver nanoparticles, and the silver particles were shown to impart antibacterial activity. While silver is known to be a potent antimicrobial agent, it does pose a risk of toxicity to mammalian cells at high concentrations. In the present study, a similar two-stage synthesis approach was used to create composite copper–hydroxyapatite (Cu–HA) coatings. Copper was chosen because it has the potential for antibacterial activity while being less toxic to other healthy cells.

Figure 1 shows electron microscopy images of Cu–HA coatings produced using varying concentrations of Cu salt in the electrolyte solution used during the second-stage reaction. The HA crystals are visible as nanoscale rods in all images. At the highest Cu salt concentrations, the metallic copper is deposited as a mixture of nanoparticles and larger dendrite structure, as seen in Figs. 1(a) and 1(b). At lower Cu salt concentrations, the number of dendrites declines and, primarily, Cu nanoparticles are synthesized, as seen in Figs. 1(c) and 1(d). The presence of HA was confirmed using x-ray diffraction, and metallic Cu and copper oxide were confirmed on the surface using x-ray photoelectron microscopy.

A series of Cu–HA coatings was made having varying copper content, and the growth of the bacteria *E. coli* and *S. aureus* was measured in the presence of these coatings. It was found that the number of bacteria colony forming units declined with increasing copper content in the coatings. With the highest measured copper content of 6.6 at. %, the number of colony-forming units remaining after 8 h of cell culture declined 78% for *E. coli* and 83% for *S. aureus*.

The results show that the copper nanoparticles are effective at killing a fraction of the bacteria but do not provide a means to completely sterilize an infected surface. Compared to our prior work,[2] copper is less effective than silver in killing bacteria. Copper offers the advantage, however, of less toxicity than silver toward healthy cells. The composite coatings synthesized here

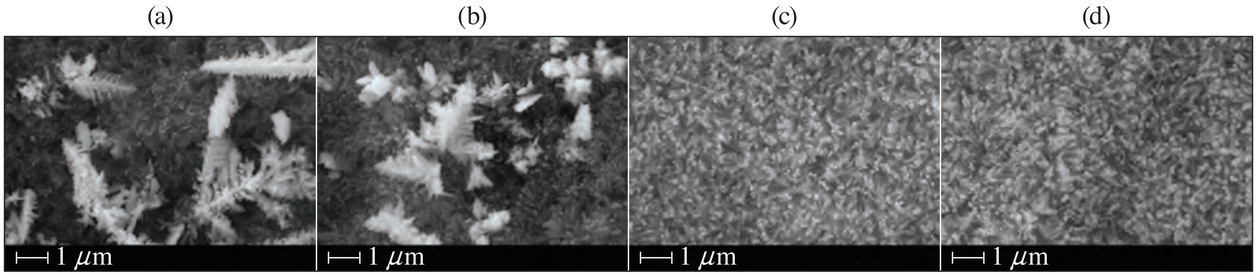

Figure 1
SEM images of Cu–HA composite coatings formed by an electrochemical copper reduction reaction using 12.8-mA/cm^2 current applied for 7 min with a $CuSO_4$ concentration in the electrolyte of (a) 0.625 mM, (b) 0.5 mM, (c) 0.375 mM, and (d) 0.25 mM.

may, therefore, offer a lower-risk route to reducing or eliminating the need for prophylactic antibiotic use in orthopedic implant surgery. In an otherwise sterile surgical environment, the number of bacteria present is expected to be low. Copper on the surface of the implant may reduce the likelihood that any bacteria present develop into a bone infection at the implant surface.

This material is based upon work supported by the Department of Energy National Nuclear Security Administration under Award Number DE-NA0003856, the University of Rochester, and the New York State Energy Research and Development Authority.

1. I. Zhitomirsky, Adv. Colloid Interface Sci. **97**, 279 (2002).

2. C. Fu *et al*., Surf. Coat. Technol. **301**, 13 (2016).

Silver-Hydroxyapatite Composite Coatings with Enhanced Antimicrobial Activities Through Heat Treatment

X. Zhang,[1] W. Chaimayo,[2] C. Yang,[1] J. Yao,[1] B. L. Miller,[2] and M. Z. Yates[1,3]

[1]Department of Chemical Engineering, University of Rochester
[2]Department of Dermatology, University of Rochester
[3]Laboratory for Laser Energetics, University of Rochester

Ceramic coatings find applications in corrosion protection, thermal insulation, altering wetting, electrical insulation, and enhancing chemical or biochemical surface properties. This study focuses on the electrochemical synthesis of nanoscale coatings of the ceramic hydroxyapatite (HA), a calcium phosphate with the stoichiometric formula $Ca_{10}(PO_4)_6(OH)_2$. The HA coating was synthesized from an aqueous electrolyte solution using a process called cathodic electrolytic deposition.[1] After forming the coating on a titanium cathode, a second cathodic electrochemical reaction was used to reduce silver ions from an electrolyte solution and deposit metallic silver nanoparticles onto the HA coating. The resulting silver-hydroxyapatite (Ag-HA) composite coating was investigated for its ability to kill bacteria. Coatings of HA on titanium find commercial application in dental and orthopedic implant applications, where the HA layer is known to enhance the rate of integration of metallic implants with surrounding bone tissue. One of the most serious complications of implant surgery is infection of the bone. The coatings show promise in lowering the chance of infection without the use of antibiotics that create antibiotic-resistant strains of bacteria.

Figure 1 shows electron microscopy images of the HA coating on titanium before and after electrochemical reduction of silver. The HA grows on the surface as nanoscale rod-shaped crystals, as seen in Fig. 1(a). The metallic silver nanoparticles can be seen in Fig. 1(b) as spherical nanoparticles that form preferentially on the tips of the HA nanocrystals. Although HA is known to be an electrically insulating material, our previous results show that HA can conduct electricity if the applied potential is high enough.[2] The fact that metallic silver forms on the tips of the HA indicates that electrons are passing through the HA crystals in

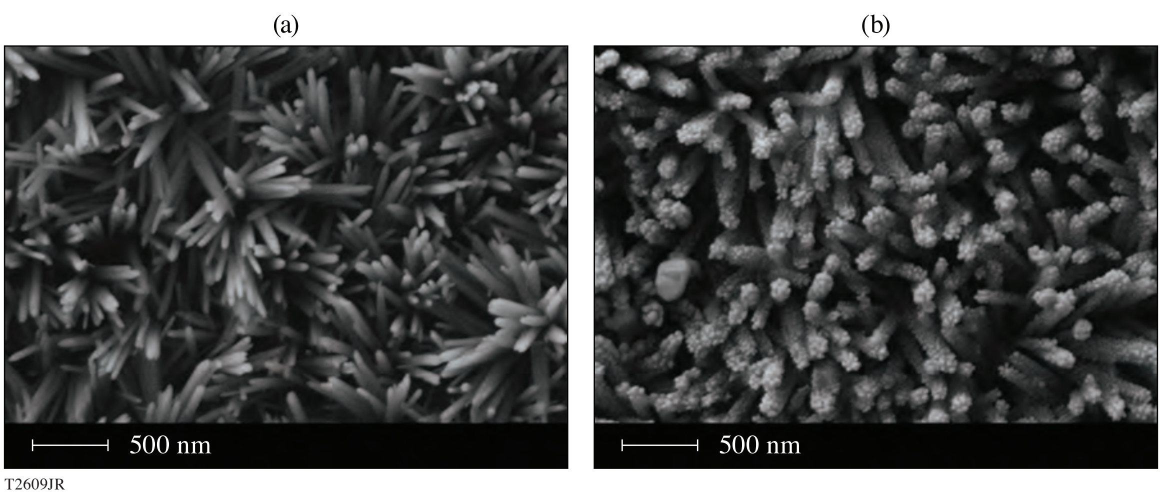

Figure 1
Scanning electron microscope (SEM) images of Ag-HA coating (a) before and (b) after electrochemical deposition of Ag nanoparticles.

order to electrochemically reduce silver cations (Ag^+) in solution to metallic silver (Ag^0). The HA crystal phase was confirmed with x-ray diffraction, and the metallic silver on the surface was confirmed with x-ray photoelectron spectroscopy.

Composite Ag-HA coatings, similar to those shown in Fig. 1, were found by our group to kill bacteria.[3] However, the effectiveness of the coating in killing bacteria varied significantly from sample to sample. The antibacterial activity of silver is related to the dissolution of silver ions into solution. It was postulated that the release of silver ions would be enhanced by the formation of silver oxide, which undergoes the following reactions:

$$Ag_2O + H_2O \longrightarrow 2AgOH \tag{1}$$

$$AgOH \longrightarrow Ag^+ + OH^- \tag{2}$$

To test this hypothesis, the Ag-HA coatings were heated in air at 170°C for 8 h to form an oxide layer. The formation of silver oxide on the surface after heating was confirmed using x-ray photoelectron spectroscopy. Next, the growth of *Escherichia coli* (*E. coli*) was monitored in the presence of HA and Ag-HA coatings before and after the heat treatment.

Light scattering was used to characterize the relative number of bacteria versus time, as shown in Fig. 2. The reported optical density is proportional to the number of bacteria in the sample. The results demonstrate that heat treatment enhances the antibacterial activity and reduces the variation in antibacterial activity from sample to sample. The results demonstrate a simple route to form coatings that may simultaneously enhance integration of implants with surrounding bone tissue while reducing the likelihood of post-surgical bone infection.

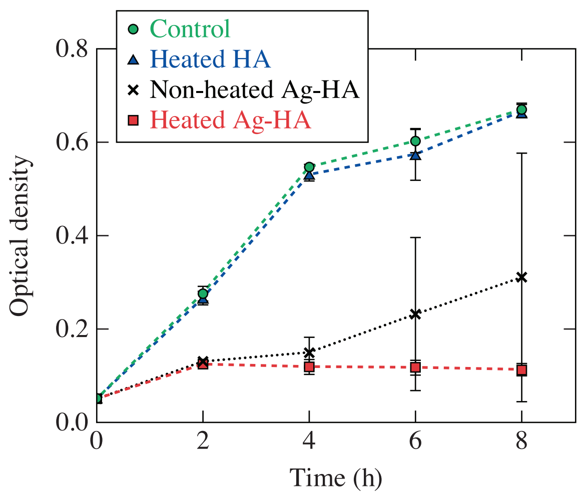

Figure 2
The growth of *E. coli* when exposed to HA and Ag-HA coatings measured by light scattering. Data points indicate the mean value, and error bars indicate standard deviation.

This material is based upon work supported by the Department of Energy National Nuclear Security Administration under Award Number DE-NA0003856, the University of Rochester, and the New York State Energy Research and Development Authority.

1. I. Zhitomirsky, Adv. Colloid Interface Sci. **97**, 279 (2002).
2. C. Fu *et al*., Chem. Mater. **27**, 1164 (2015).
3. C. Fu *et al*., Surf. Coat. Technol. **301**, 13 (2016).

Terahertz Time-Domain Spectroscopy of Graphene Nanoflakes Embedded in a Polymer Matrix

A. Koroliov,[1,#] G. Chen,[1] K. M. Goodfellow,[1] A. N. Vamivakas,[1] Z. Staniszewski,[2] P. Sobolewski,[2] M. El Fray,[2] A. Łaszcz,[3] A. Czerwinski,[3] C. P. Richter,[4] and R. Sobolewski[1,3]

[1]University of Rochester
[2]Polymer Institute, West Pomeranian University of Technology, Poland
[3]Institute of Electron Technology, Poland
[4]University of Iceland, Iceland
[#]Present address: Center for Physical Sciences and Technology, Vilnius, Lithuania

Polymer nanocomposites are prepared by including a nanofiller (carbon, ceramic, metal/metal oxide, and/or others) in a polymer matrix to alter (or improve) its properties, such as mechanical, electrical, and optical properties, barrier properties, flame resistance, etc.[1] Recently, a great deal of interest has been focused on carbon nanofillers and, in particular, graphene. Graphene is a 2-D nanomaterial consisting of sheets of carbon atoms bonded by sp^2 bonds in a hexagonal configuration: its unique mechanical, electrical, thermal, and optical properties have been extensively studied.[2] These properties have been leveraged in the development of a wide range of different graphene–polymer nanocomposites,[3] using a variety of fabrication methods and polymer types, for numerous structural and functional applications,[4] including, e.g., biomedical devices,[5] biosensing,[6] and gas barrier membranes.[7]

Here we report the use of a THz time-domain spectroscopy (THz-TDS) to characterize graphene nanofiller dispersion within multiblock copolyester nanocomposite materials. Both the copolymer matrix and the nanocomposites were developed to serve as construction materials for extracorporeal heart-assist devices in the context of the Polish Artificial Heart Program.[8] The test samples used were processed using the same compression molding process as the prototype pneumatic membrane. To our knowledge, this is the first time that the dispersion of graphene nanoplatelets within a nanocomposite—prepared at an industrially relevant scale and using an economically viable process—has been studied by the THz-TDS method. Consequently, this work serves as an important proof of concept of THz-TDS of nanocomposites within the product development chain.

Two different neat copolymers were prepared, with different hard to soft segment ratios, resulting in a more elastic material with 40 wt% of hard segments (PET-DLA 4060) and a stiffer copolyester with 60 wt% of hard segments (PET-DLA 6040). Additionally, nanocomposites with the same hard to soft segment ratios but with 1 wt% of a commercial graphite nanoplatelet nanofiller (Graphene Supermarket, Grade A0-3) were prepared via *in-situ* polymerization.[9,10]

The THz-TDS system, used to measure the THz-range transmission spectra of both the neat copolymers and graphene nanocomposite samples, was based on a commercial, low-temperature–grown GaAs (LT-GaAs) photoconductive antenna emitter and detector from TeraVil Ltd, Vilnius, Lithuania.[11] The emitter and detector were excited and probed, respectively, by 100-fs-wide pulses, with an 800-nm wavelength and a 76-MHz repetition rate, generated by a femtosecond Ti:sapphire laser. The spectral range of the spectrometer was ~4 THz, with maximum amplitude at ~0.5 THz. The sample was placed directly between the emitter and detector, and measurements were taken at room temperature. To reduce the influence of water absorption, the THz emitter, detector, and sample holder were placed inside a Plexiglas® box that was purged with dry nitrogen, ensuring that the humidity during the measurement was below 5%.

For each sample, we first performed a reference run with no sample inside the spectrometer to confirm the performance of the system. Next, we took two measurements: one of a graphene nanocomposite and the other of a corresponding neat copolymer specimen. To get better results and reduce noise, each set of measurements consisted of at least ten averages. Our measurements were focused on two different sample types: nominally a 0.3-mm-thick, elastic PET-DLA 4060 copolymer ("thin sample") and a 0.9-mm-thick, stiffer PET-DLA 6040 copolymer ("thick sample"). For both sample types, the nanofiller content was the same, i.e., 1 wt%. Since our further analysis crucially depends on the sample thickness, all measurements were repeated several times at different spots of the test sample.

Figure 1(a) presents time-domain signals transmitted through dry nitrogen (the reference measurement), the thin and thick neat copolymer, and the corresponding 1-wt% graphene–polymer nanocomposite samples, respectively, while Fig. 1(b) presents the corresponding power spectra of our time-domain signals obtained by means of fast Fourier transformation. We note that while both copolymers absorb THz radiation, as compared to the dry-nitrogen reference signal, adding graphene flakes to the polymer matrix substantially reduces the bandwidth of the power spectrum, obviously because of the extra absorption of THz radiation by nanoflakes. The cutoff frequencies for the thin copolymer sample and the corresponding 1-wt% graphene-polymer nanocomposite are ~3.1 THz and 2.9 THz, respectively, while for the thick copolymer and the 1-wt% graphene–polymer nanocomposite, they are 2.25 THz and 1.75 THz, respectively.

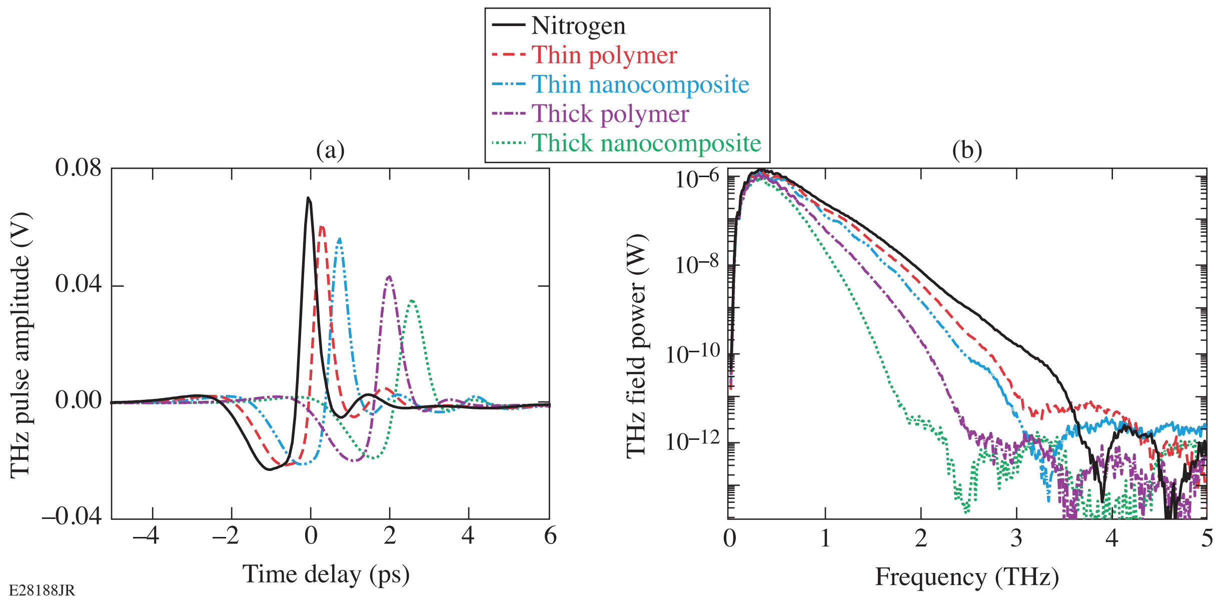

Figure 1
(a) Time-resolved transient signals for the tested thin and thick polymers and 1-wt% graphene nanocomposite samples and the empty spectrometer (nitrogen). (b) The corresponding power spectra showing absorption of the samples. Note: The thin samples consist of the PET-DLA 4060 copolymer, while the thick ones consist of PET-DLA 6040.

Using Fresnel equations, the THz-TDS approach allowed us to find the complex index of refraction $\hat{n}(\omega) = n(\omega) + i\kappa(\omega)$ and the dielectric function $\hat{\varepsilon}(\omega) = \varepsilon_1(\omega) + i\varepsilon_2(\omega)$, as well as the complex $\hat{\sigma}(\omega)$ of our graphene nanocomposite samples. The $\hat{\sigma}(\omega)$ spectrum was, subsequently, fitted using the Drude–Smith model.[12] The excellent fit confirmed applicability of the Drude–Smith approach to modeling the carrier transport in our graphene–polymer nanocomposites, indicating that our nanofiller flakes were fully isolated in the polymer matrix. The high quality and uniformity of the dispersion were implied by the high value of the conductivity and moderate effective dielectric constant retained by the graphene nanoflakes.

In summary, the THz-TDS method probes the dielectric properties of the sample in an almost cm^2 cross-section beam path, thereby providing "global" information regarding the dispersion of graphene and its *in-situ* electronic quality. Because it is a nondestructive testing method, it holds great potential for monitoring any nanofiller dispersion in a polymer matrix throughout the product-development chain: after polymer nanocomposite synthesis, following processing into a given prototype, and even after product testing.

This material is based upon work supported in part by the PumpPrimerII Program at the University of Rochester. A. N. Vamivakas acknowledges support from the Air Force Office of Scientific Research (FA9550-16-1-0020). M. El Fray acknowledges support from the Polish National Centre for Research and Development (PBS1/A5/2/2012).

1. D. R. Paul and L. M. Robeson, Polymer **49**, 3187 (2008).
2. Y. Zhu *et al*., Adv. Mater. **22**, 3906 (2010).
3. J. R. Potts *et al*., Polymer **52**, 5 (2011).
4. K. Hu *et al*., Prog. Polym. Sci. **39**, 1934 (2014).
5. M. Silva, N. M. Alves, and M. C. Paiva, Polym. Adv. Technol. **29**, 687 (2018).
6. P. Sobolewski, M. Piwowarczyk, and M. E. Fray, Macromol. Biosci. **16**, 944 (2016).
7. Y. Cui, S. I. Kundalwal, and S. Kumar, Carbon **98**, 313 (2016).
8. M. El Fray and M. Czugala, WIREs Nanomed. Nanobi. **4**, 322 (2012).
9. Z. Staniszewski and M. El Fray, Polimery **61**, 482 (2016).
10. Z. Staniszewski *et al*., Eur. Polym. J. **107**, 189 (2018).
11. A. Geižutis *et al*., Opt. Mater. **30**, 786 (2008).
12. N. V. Smith, Phys. Rev. B **64**, 155106 (2001).

Tunable UV Upgrade on OMEGA EP

B. E. Kruschwitz, J. Kwiatkowski, C. Dorrer, M. Barczys, A. Consentino, D. H. Froula, M. J. Guardalben, E. M. Hill, D. Nelson, M. J. Shoup III, D. Turnbull, L. J. Waxer, and D. Weiner

Laboratory for Laser Energetics, University of Rochester

Controlled experiments are necessary to test and refine simulation tools for the mitigation of cross-beam energy transfer (CBET) in direct-drive laser-driven inertial confinement fusion using wavelength detuning.[1–3] To this end, experiments have been proposed at the Omega Laser Facility that feature a wavelength-tunable UV beam coupled into the target chamber of the 60-beam OMEGA laser (via the P9 port). The new capability is referred to as the tunable OMEGA P9 (TOP9) beam. These experiments will characterize the interaction of the tunable beam with one or more fixed-wavelength beams from the 60-beam OMEGA Laser System as a function of wavelength detuning, polarization, and interaction angle. The top-level requirements for the tunable UV beam are dictated by the experimental needs and are listed in Table I.

Table I: Top-level system requirements for the tunable UV beam for CBET mitigation experiments.

Parameter	Minimum requirement	Goal
Wavelength-tuning range	350.2 to 353.4 nm	
Wavelength step size	≤0.1 nm	
UV power on target	0.1 TW (351 nm to 352.6 nm) 0.01 TW (350.2 nm to 353.4 nm)	0.5 TW for pulses ≤1 ns 0.1 TW for pulses ≤2.5 ns (full tuning range)
Polarization	(1) linear, direction rotatable over 2π (2) random (distributed polarization rotator)	

An OMEGA EP beamline[4] was chosen in order to leverage both the short- and long-pulse capabilities of the OMEGA EP beamline, as illustrated in Fig. 1. The TOP9 system utilizes the short-pulse optical parametric chirped-pulse–amplification (OPCPA) front end to take advantage of the spectrally broad gain in the optical parametric amplification (OPA) process. For the TOP9 system, the OPCPA front end is converted into a tunable OPA system by replacing the chirped broadband seed laser with a tunable narrowband laser.[5] The pulses are then injected into the OMEGA EP beamline for amplification to the >100-J level. The TOP9 system also takes advantage of the existing long-pulse UV infrastructure of the OMEGA EP beamline, with the frequency-conversion crystals (FCC's) providing frequency tripling, and suites of laser diagnostics characterizing the laser performance at each stage.

A beam transport system (see Fig. 2) was designed and built to transport the UV beam through the shield wall between the OMEGA EP and OMEGA Laser Bays, where it is directed into the P9 port of the OMEGA target chamber and focused to target. The OMEGA EP periscope features a retractable lower mirror to intercept the TOP9 beam after the FCC. A vacuum image relay limits beam degradation caused by diffraction and reduces the UV beam path in air. A new platform was built onto the north-end mirror structure in the OMEGA Target Bay to support the image relay and other associated optics, including an insertable distributed polarization rotator or a rotatable half-wave plate, the combination satisfying the system's polarization control requirements.

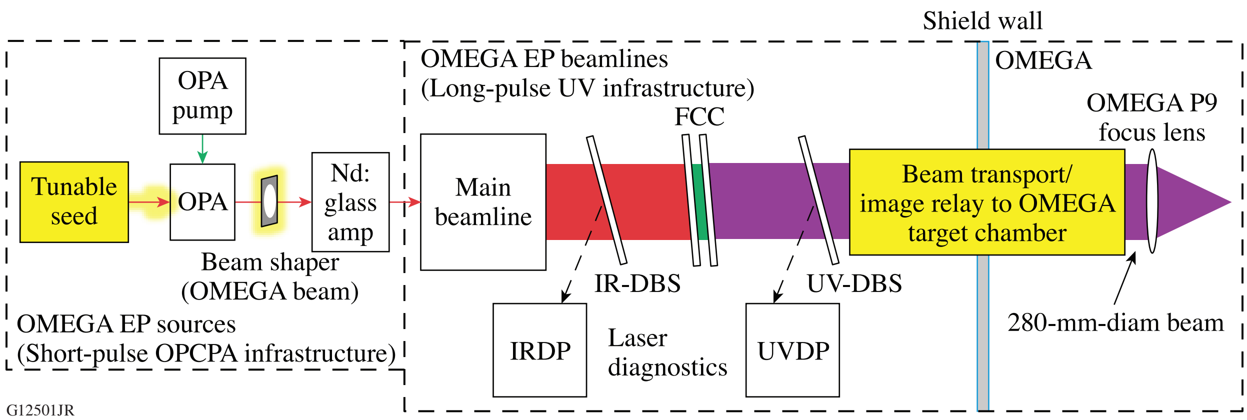

Figure 1
High-level diagram of the TOP9 OMEGA EP beam with upgraded elements highlighted in yellow. (OPA: optical parametric amplification; OPCPA: optical parametric chirped-pulse amplification; IR-DBS: infrared diagnostic beam splitter; IRDP: infrared diagnostics package; FCC: frequency-conversion crystals; UV-DBS: ultraviolet diagnostic beam splitter; UVDP: ultraviolet diagnostics package).

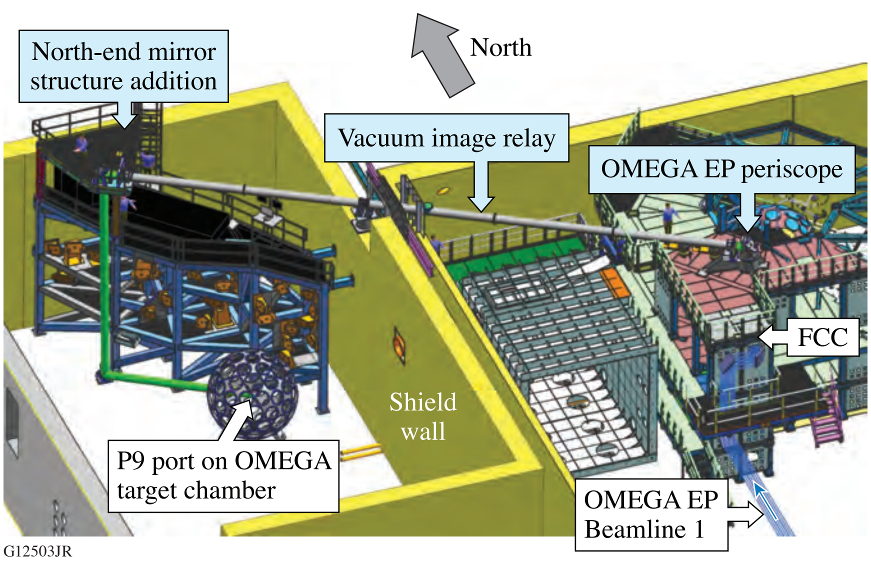

Figure 2
Solid-model drawing of the TOP9 transport system with key features indicated.

The performance envelope (plotted in Fig. 3) defines the range of pulse durations and energies that can be delivered with the tunable UV beam; it was developed based on consideration of a number of limiting effects. For short-duration pulses, the UV power is limited by concerns over small-scale self-focusing caused by the nonlinear Kerr effect in the transmissive optical materials (ΣB), comprising the TOP9 transport system and final optics.[6] For longer-duration pulses, the performance is limited by the development of transverse stimulated Brillouin scattering (SBS) in the optics.[7] Shots to the OMEGA EP target chamber allow for higher energies as a result of a larger beam size available, fewer transmissive optics in the transport path, and proximity to the target chamber.

The TOP9 beam has been commissioned to the OMEGA target chamber. The full-beam small-signal net gain as a function of wavelength was measured using a series of shots to a full-aperture calorimeter at the output of the transport spatial filter. The laser system produces the required 1ω energy at the extreme wavelengths by pumping up to 9 of the 11 main amplifier disks that are available in the OMEGA EP beamline. Longitudinal chromatic aberration in the beamline was measured and found to be corrected to <λ/20 by OMEGA EP's diffractive color-correcting injection lens. Near-field beam quality has been measured to be consistent with standard OMEGA EP performance.

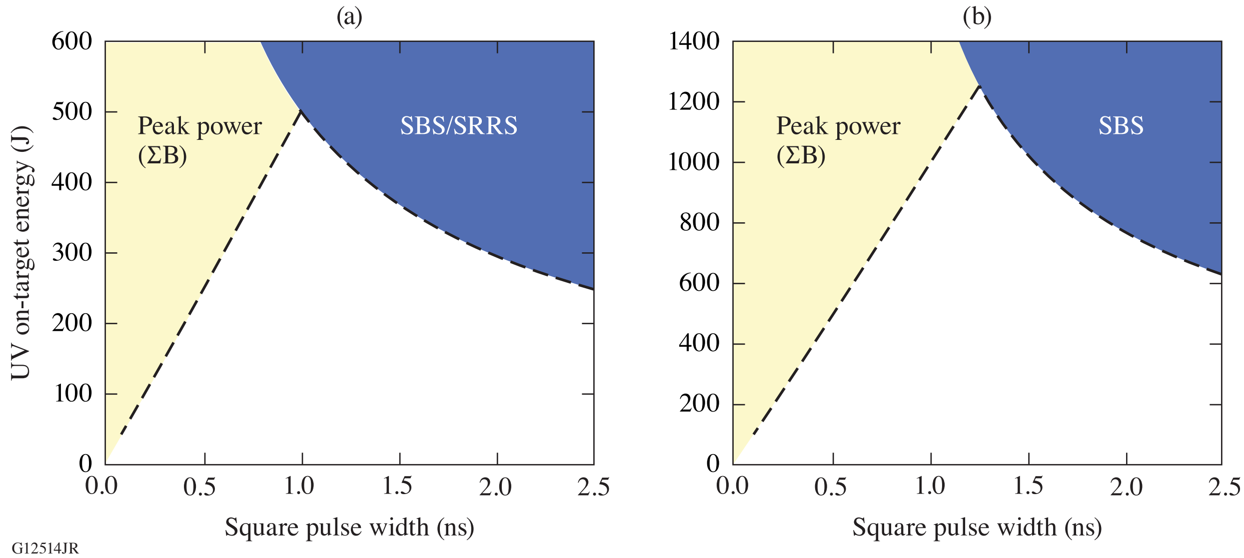

Figure 3
Performance envelope (maximum on-target energy versus square-pulse duration) for tunable UV shots to (a) the OMEGA target chamber (28-cm-diam round beam) and (b) the OMEGA EP target chamber (36-cm-sq beam). SRRS: stimulated rotational Raman scattering.

Pulse shaping is yet another active area of development. To maintain stability, the OPA is operated in saturation, which renders the creation of arbitrary pulse shapes difficult. Current pulse shapes are square at the output of the front-end OPA stages and tend to be distorted because of gain saturation in the downstream Nd:glass amplifiers and nonlinear frequency conversion. Nevertheless, arbitrary pulse shaping has been demonstrated in a laboratory prototype,[5] and it is a goal to provide arbitrarily shaped pulses with tailored ramps, steps, and other features that are currently available with the standard front ends of both OMEGA and OMEGA EP.

Construction of the tunable UV system was completed in May 2018, and commissioning of the system to the OMEGA target chamber was completed in June 2018. To date, the system has performed well in four experimental campaigns that studied CBET and other laser–plasma interactions, and it will enable future experiments that will advance the effort to mitigate CBET.

This material is based upon work supported by the Department of Energy National Nuclear Security Administration under Award Number DE-NA0003856, the University of Rochester, and the New York State Energy Research and Development Authority.

1. I. V. Igumenshchev *et al*., Phys. Plasmas **19**, 056314 (2012).
2. J. A. Marozas *et al*., Phys. Plasmas **25**, 056314 (2018).
3. D. Turnbull *et al*., Plasma Phys. Control. Fusion **60**, 054017 (2018).
4. J. H. Kelly *et al*., J. Phys. IV France **133**, 75 (2006).
5. C. Dorrer *et al*., Opt. Express **25**, 26,802 (2017).
6. A. E. Siegman, Lasers (University Science Books, Mill Valley, CA, 1986), pp. 385–386.
7. J. R. Murray *et al*., J. Opt. Soc. Am. B **6**, 2402 (1989).

In-Tank, On-Shot Characterization of the OMEGA Laser System Focal Spot

L. J. Waxer, K. A. Bauer, E. C. Cost, M. Heimbueger, J. H. Kelly, V. Kobilansky, S. F. B Morse, D. Nelson, R. Peck, R. Rinefierd, S. Sampat, M. J. Shoup III, D. Weiner, G. Weselak, and J. Zou

Laboratory for Laser Energetics, University of Rochester

The success of inertial confinement fusion experiments conducted on LLE's OMEGA 60-beam laser depends on the uniform illumination of the target. For these experiments, not only is the focal-spot intensity (i.e., power/unit area) of each beam tightly controlled, but the overall on-target, beam-to-beam intensities must be carefully balanced. Simulations indicate that the root-mean-square (rms) intensity balance on target should be <1% (Ref. 1). Depending on the amount of overlap between the beams, this requirement implies that the focal-spot intensities of each of OMEGA's 60 beams must achieve an rms balance of 2% to 3%.

To meet this specification, much attention has been paid to the power balancing (i.e., energy/unit time) of each of OMEGA's 60 beams at the laser output.[2] Through a balancing of gains, losses, and frequency conversion, OMEGA now consistently delivers an rms power balance that meets the 2% to 3% specification. As stated above, however, the quantity of importance to experiments is the *on-target intensity* balance. To characterize the intensity balance, one must also measure the on-shot focal spot of each beam at the target. Up until now, OMEGA has had the ability to characterize the on-shot focal spot of four beams (one at a time) at an equivalent target plane (ETP) located upstream of the target chamber. The ETP provides a detailed analysis of a single-beam focal spot, but it cannot provide an assessment of intensity balance on target. In addition, since the ETP pickoff is upstream of the target chamber, any effects caused by nonlinearities in the final focusing optics (located on the target chamber) are not characterized.

To characterize actual on-shot conditions, LLE has built a full-beam-in-tank (FBIT) diagnostic that measures the OMEGA focal spot at the center of the target chamber (TCC). The FBIT diagnostic picks off a full-aperture, low-energy sample of the beam after it has been transmitted through most of the final optics assembly. Specifically [see Fig. 1(a)], the standard plane-parallel, antireflective (AR)-coated vacuum window is replaced with an uncoated window with a small wedge (7.5 arcmin). The 3.7% reflection from the back surface of this wedge provides a low-energy sample of the main beam. This sample beam creates a sequence of forward-going replica beams, each having an intensity that is $(0.037)^2$ times that of the previous replica.

As shown in Fig. 1(b), each of the replicas comes to a focus at a different location in the target chamber. This provides a region near the TCC, where one of the replicas can be intercepted and delivered to a camera. The OMEGA target chamber contains several ports for instruments that are used to diagnose a particular experiment. Six of these ports contain ten-inch–manipulator (TIM) platforms that provide a flexible means to insert different diagnostics into the target chamber while maintaining vacuum conditions. The FBIT diagnostic uses TIM's to insert a pickoff optic, imaging optics, and a charge-coupled–device (CCD) camera into the target chamber to capture one of the beam replicas from the wedged vacuum window.

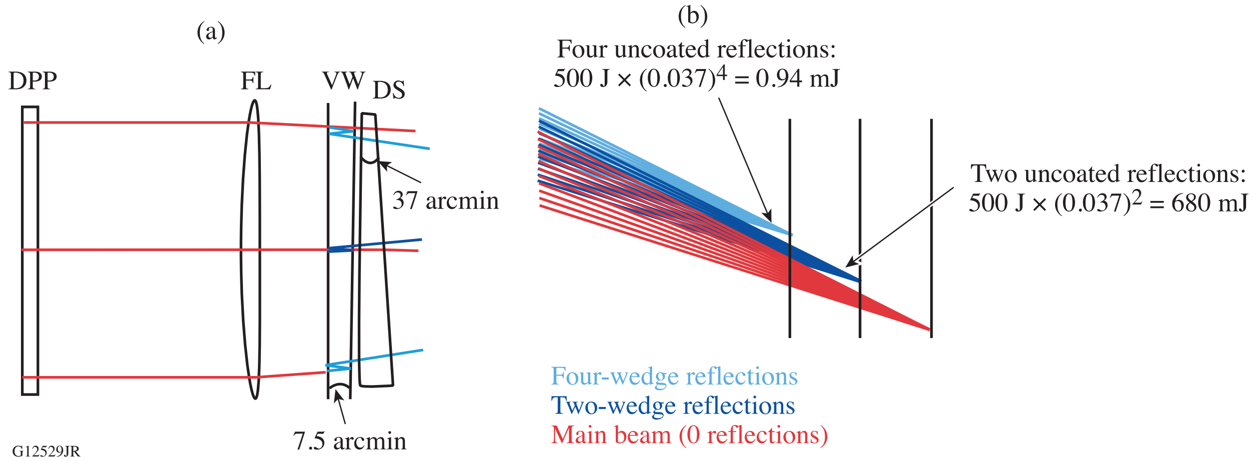

Figure 1
(a) Diagram of the final optics assembly used for the full-beam-in-tank (FBIT) diagnostic. For clarity, wedges are exaggerated and some of the reflections have been omitted. (b) The uncoated wedged vacuum window creates a series of replicas of the main beam. Each is reduced in intensity by 0.037^n, where n is the number of reflections in the wedge. Each replica focuses at a different location in the target chamber. DPP: distributive phase plate, FL: focus lens, VW: vacuum window, DS: debris shield.

One of the key requirements for any focal-spot diagnostic is that it does not introduce significant optical distortions so that the measured focal spot is an accurate representation of the actual spot. The wedged vacuum window provides an excellent method for sampling the beam near the target, but a focusing beam that makes multiple passes through a wedged optic is significantly aberrated. To mitigate this, the aberrations from the wedge are compensated by introducing an opposing wedge (37 arcmin) in the debris shield [see Fig. 1(a)]. In addition to the wavefront introduced by four passes through the wedged vacuum window, there are also manufacturing errors that will further degrade the focal-spot quality. With four reflections from the vacuum window surfaces, a high-quality reflected and transmitted wavefront is required. The achieved reflected and transmitted wavefront for the vacuum window was of the order of 0.06 waves (λ = 632.8 nm), which results in minimal additional distortion of the focal spot from manufacturing. Figure 2(a) shows a simulated focal spot for a diffraction-limited input. Included in this simulation are the measured reflected and transmitted wavefront of a manufactured wedged vacuum window and the measured transmitted wavefront of a manufactured compensating debris shield, showing that the system can be built with minimal distortion to the incoming beam (the yellow circle represents 12× the diffraction limit, which roughly corresponds to the OMEGA focal-spot size). Figure 2(b) shows an on-shot measurement of the OMEGA focal spot made by the FBIT diagnostic. The measured focal spot is significantly more aberrated than the spot predicted from just the aberrations of the FBIT itself. To ensure that the FBIT diagnostic will provide an accurate measurement of the focal spot, we have characterized each of the wedged vacuum window/debris-shield combinations. Figure 2(c) shows the predicted focal spot for a diffraction-limited input to the combination with the largest measured aberrations. While this predicts significantly more degradation to the focal-spot quality, this effect is still overwhelmed by the system aberrations [see Fig. 2(d)].

We have presented the design and implementation of an on-shot, on-target focal-spot diagnostic for the OMEGA Laser System. To our knowledge, this is the first diagnostic capable of measuring the on-shot focal spot of a large laser system inside the target chamber. The diagnostic makes use of an uncoated, wedged vacuum window to create reduced energy replicas of the main beam. One of these replicas is captured by a TIM-based instrument and relay imaged to a CCD camera. We have measured on-shot far fields and near fields and are working to characterize at least 30 beams during this fiscal year. These data will provide an estimate of the on-shot laser uniformity on target.

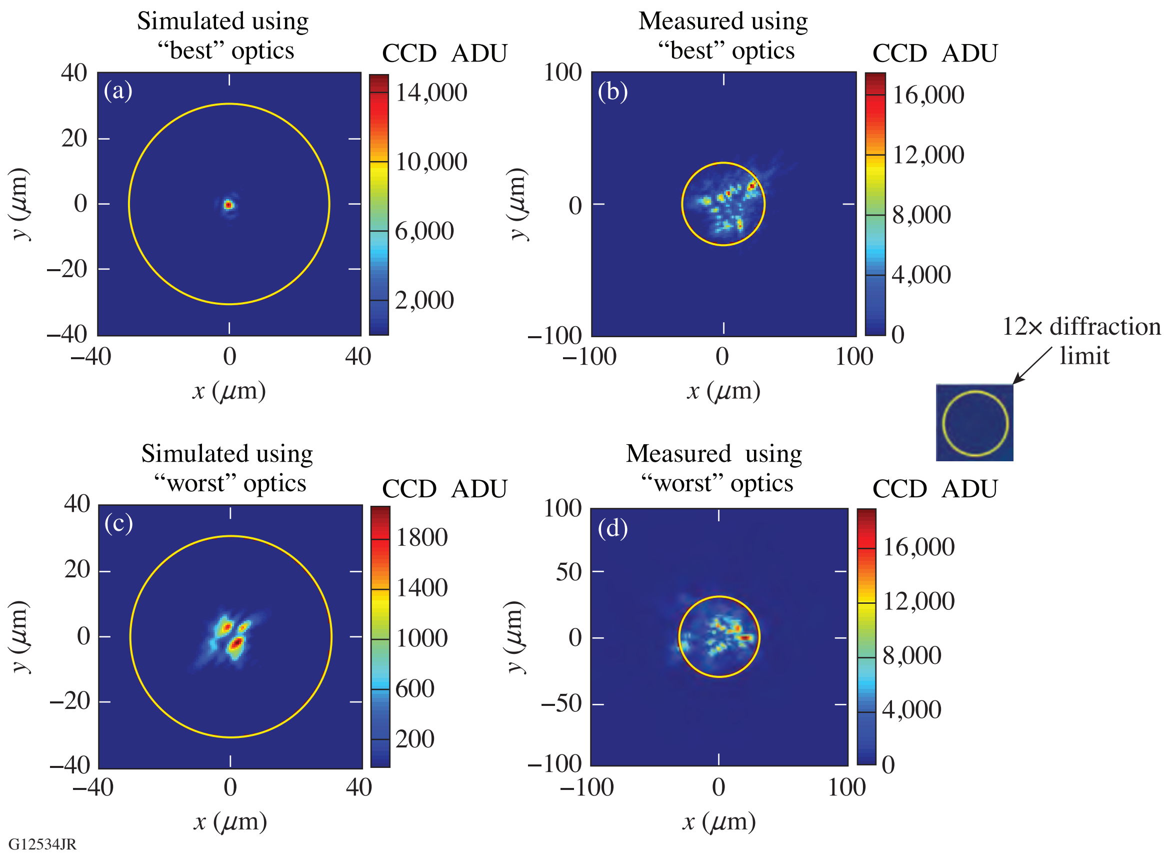

Figure 2
(a) Predicted FBIT-measured focal spot using the wedged vacuum window/wedged debris-shield combination with the "best" optical quality (using a diffraction-limited input to the final optics assembly). (b) FBIT measurement of the on-shot OMEGA focal spot using this combination of optics to generate the replica beam. (c) Predicted FBIT-measured focal spot using the wedged vacuum window/wedged debris-shield combination with the "worst" optical quality (using a diffraction-limited input to the FBIT). (d) FBIT measurement of the on-shot OMEGA focal spot using this "worst" combination of optics to generate the replica beam. The yellow circle represents a 12× diffraction-limited focal-spot size. ADU: Analog-to-digital units.

This material is based upon work supported by the Department of Energy National Nuclear Security Administration under Award Number DE-NA0003856, the University of Rochester, and the New York State Energy Research and Development Authority.

1. V. N. Goncharov *et al*., Plasma Phys. Control. Fusion **59**, 014008 (2017).

2. S. Sampat *et al*., Appl. Opt. **57**, 9571 (2018).

Comparison of On-Shot, In-Tank, and Equivalent-Target-Plane Measurements of the OMEGA Laser System Focal Spot

K. A. Bauer, M. Heimbueger, S. Sampat, L. J. Waxer, E. C. Cost, J. H. Kelly, V. Kobilansky, J. Kwiatkowski, S. F. B. Morse, D. Nelson, D. Weiner, G. Weselak, and J. Zou

Laboratory for Laser Energetics, University of Rochester

Target-physics simulations indicate that on-target uniformity of the OMEGA Laser System[1] of the order of 1% rms is required for each 100-ps interval of a cryogenic target implosion pulse shape.[2] Current laser diagnostic systems on OMEGA, located upstream of the target chamber, characterize the on-shot energy and temporal profile of all 60 beams at the output of the laser. In addition, there is the capability to characterize both the UV near field and the equivalent-target-plane (ETP) focal spot of a single beam. These two diagnostics use a 4% pickoff beam, located upstream of the final optics assembly, near the output of the frequency-conversion crystals. Combining the data from all of these diagnostics suggests that the beam-to-beam uniformity is sufficient to nearly meet this requirement.[3] Conversely, the results from implosion experiments suggest that the on-target uniformity is worse than the diagnostics measure. To resolve this discrepancy, we have recently developed the full-beam-in-tank (FBIT) diagnostic, which is capable of measuring the on-shot, on-target focal spot of multiple beams inside the OMEGA target chamber.[4] FBIT has the ability to directly characterize the on-shot near field and far field of multiple beams in the target chamber. FBIT uses a small sample of the full-energy beam inside the target chamber to analyze the beam separately from the light that hits the target. The main portion of the beam crosses target chamber center (TCC) and is terminated at a calorimeter in the opposing port so the on-target fluence (J/cm^2) of the beam can be calculated. Since FBIT directly measures the focal spot in the target chamber, we can analyze the fluence of each beam, which can be used in combination with data from OMEGA temporal diagnostics to investigate intensity (power per unit area) balance.

To meet the uniformity requirements for target implosion experiments, a smoothed far-field focal spot, with a size comparable to that of the target, is necessary. A distributed phase plate (DPP),[5] a distributed polarization rotator (DPR),[6] and smoothing by spectral dispersion (SSD)[7,8] all contribute to meeting the uniformity specifications. Using FBIT, we can study the individual effects on the focal spot of each of these in turn.

Figure 1 shows the evolution of the OMEGA focal spot as the single-beam uniformity improves. First we show the raw OMEGA far-field spot [Fig. 1(a)]; then a DPP is inserted at the input to the focus lens [Fig. 1(b)], which redistributes the spatial phase of the beam, effectively reducing the coherence across the beam. Next, SSD modulation is applied in one dimension [Fig. 1(c)], followed by both dimensions [Fig. 1(d)]. Finally, the DPR is added to the system [Fig. 1(e)] to increase the smoothing on target.

These images show the on-shot effect of each optic on the focal spot in the target chamber, measurements that were previously unavailable prior to FBIT. Images of multiple beamlines that include 2-D SSD and a DPR show similar results (Fig. 1 data were taken in Beamline 56). We can fit the azimuthal average of the beam profiles of each beamline to estimate the width of the profile, an example of which is shown in Fig. 2. The fit shows 1/e R_0 values of approximately 360 μm, which is very close to the designed spot size of the DPP's.

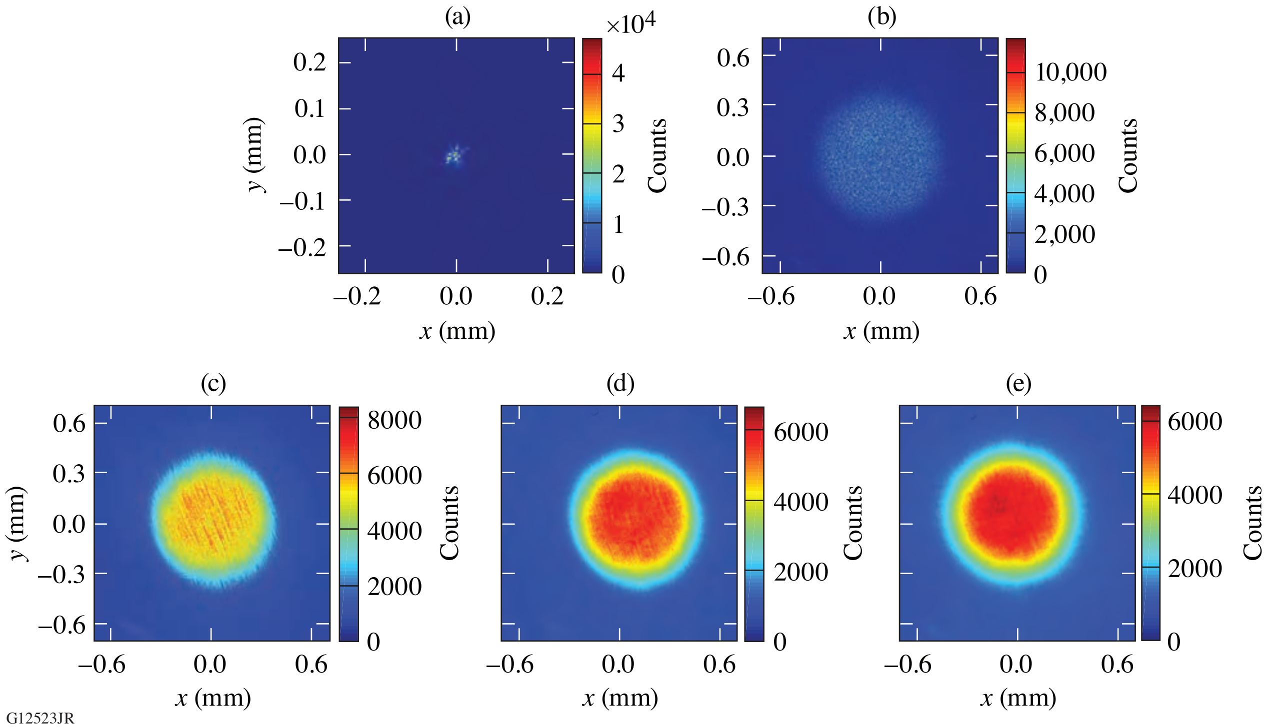

Figure 1
Evolution of the SSD focal spot, as seen from FBIT: (a) raw OMEGA far-field focal spot; (b) OMEGA far-field focal spot with a DPP; (c) focal spot with a DPP and 1-D SSD modulation; (d) focal spot with a DPP and 2-D SSD modulation; (e) focal spot with a DPP, 2-D SSD, and a DPR. Note that (a) is plotted on a different spatial scale to better show the far-field spot.

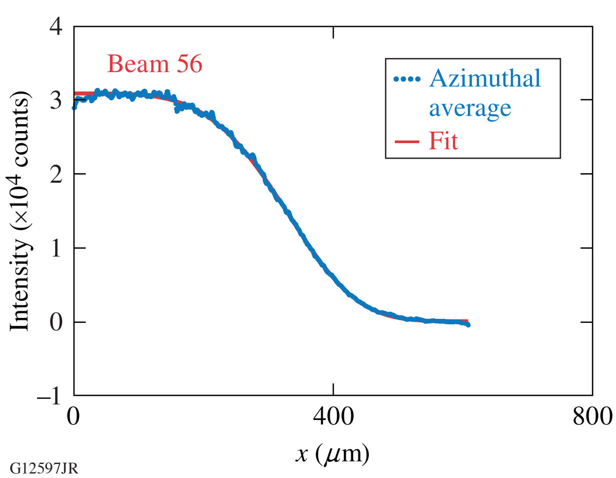

Figure 2
A super-Gaussian fit is used on the azimuthal average of the DPP far-field focal spot with 2-D SSD and a DPR.

We demonstrate the wide array of data that the new FBIT diagnostic is able to obtain. We can compare the focal spot from multiple beamlines easily within a shot cycle, analyze the SSD kernel, and characterize the effect of polarization smoothing on the focal spot. Using this data, we can more effectively understand the limitations of other diagnostics in the OMEGA Laser System and improve existing simulations of the laser performance on target. The preliminary data shown in Ref. 9 suggest that the upstream diagnostics compare closely with results found by using the FBIT diagnostic.

This material is based upon work supported by the Department of Energy National Nuclear Security Administration under Award Number DE-NA0003856, the University of Rochester, and the New York State Energy Research and Development Authority.

1. T. R. Boehly *et al*., Opt. Commun. **133**, 495 (1997).
2. S. Skupsky and R. S. Craxton, Phys. Plasmas **6**, 2157 (1999).
3. S. Sampat *et al*., Appl. Opt. **57**, 9571 (2018).
4. L. J. Waxer *et al*., Proc. SPIE **10898**, 108980F (2019).
5. *LLE Review Quarterly Report* **33**, 1, Laboratory for Laser Energetics, University of Rochester, Rochester, NY, LLE Document No. DOE/DP/40200-65 (1987).
6. *LLE Review Quarterly Report* **45**, 1, Laboratory for Laser Energetics, University of Rochester, Rochester, NY, LLE Document No. DOE/DP40200-149 (1990).
7. S. P. Regan *et al*., J. Opt. Soc. Am. B **17**, 1483 (2000).
8. S. P. Regan *et al*., J. Opt. Soc. Am. B **22**, 998 (2005).
9. K. A. Bauer *et al*., Proc. SPIE **10898**, 108980G (2019).

Power Balance on the OMEGA 60-Beam Laser

S. Sampat, T. Z. Kosc, K. A. Bauer, M. H. Romanofsky, A. L. Rigatti, J. Kwiatkowski, R. D. Dean, W. R. Donaldson, L. J. Waxer, R. Moshier, and J. H. Kelly

Laboratory for Laser Energetics, University of Rochester

Lasers that have multiple output beams can generate those beams by one of several methods: aperture division, amplitude division, and temporal division (multiplexing). The generated beams are often further amplified, frequency converted, and/or conditioned depending on the ultimate application. Inequalities in amplification, frequency conversion, or conditioning can lead to differences in the outputs of each of the beams, for which it can be difficult to compensate. This issue is termed "beam imbalance." For a multibeam laser, however, the quantification of the balance of the output beams is often the parameter used to assess laser performance. Balancing is performed by measuring the output properties such as energy, power, and/or intensity.

Energy balance requires that each beam's output have the same total energy without regard to either the spatial distribution or the temporal shape. Power balance requires that, in addition to energy balance, the instantaneous spatially integrated temporal shapes of the output beams match over some averaging time. A typical pulse shape used for cryogenic target implosion experiments on OMEGA is shown in Fig. 1(a). Typical beam-to-beam variations of the output pulse shape are shown in Fig. 1(b).

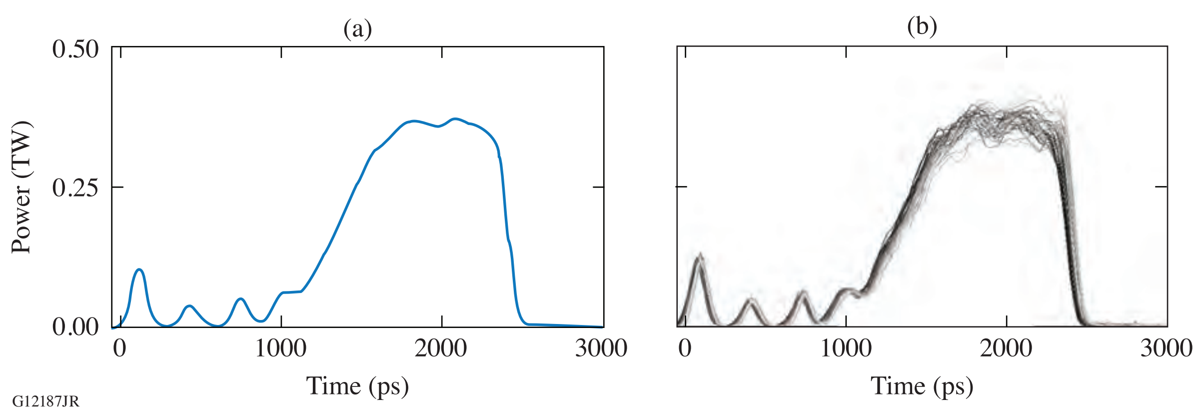

Figure 1
(a) Typical pulse shape used for cryogenic target implosion experiments on OMEGA containing three pickets followed by a drive. (b) The depicted pulse shape has an energy imbalance of 3.5% across 60 beams; the picket and drive have a power imbalance of 2.5% and 3.5% rms, respectively.

The power-balance requirement on OMEGA, as defined by an rms energy computation across 60 beams, is predicated on inertial confinement fusion target-physics simulations that indicate that a less than 1% rms power imbalance is required over any 100-ps interval of the pulse.[1] The near-term goal is to improve the first picket power balance to 1% rms imbalance while simultaneously reducing the drive imbalance. Power balance is sensitive to several factors that are less significant when assessing system energy balance. Given OMEGA's architecture that uses a single "seed" beam to generate 60 beams via splitting and subsequent amplification, choosing the appropriate amplifiers to compensate for any incidental losses on the system is paramount.

Since OMEGA's beamlines consist of amplifiers with varying degrees of saturation, a particular beam's square pulse distortion (SPD) can be significantly impacted by improper management of a saturating amplifier's gain.

A graphic with a simulation of this phenomenon is shown in Fig. 2. In Figs. 2(a) and 2(b), the black curve represents an IR pulse at the input of a different saturating amplifier. The blue and green curves are the pulse at the output of that amplifier. In both cases, a positive voltage offset has been applied to the amplifier's nominal voltage, thereby increasing its linear gain. Figure 2(a) shows the effect of increasing linear gain on the pulse shape in an amplifier where $F_{\text{out}}/F_{\text{sat}}$ is low and, therefore, the pulse shape is not significantly affected. On OMEGA, disk amplifier stages E and F operate under this regime. Figure 2(b) shows the effect of increasing linear gain in a heavily saturated amplifier. Here, the effect of a voltage change is expected to have a stronger impact on pulse shape. On OMEGA, the stage-D amplifiers operate under this heavily saturated regime.

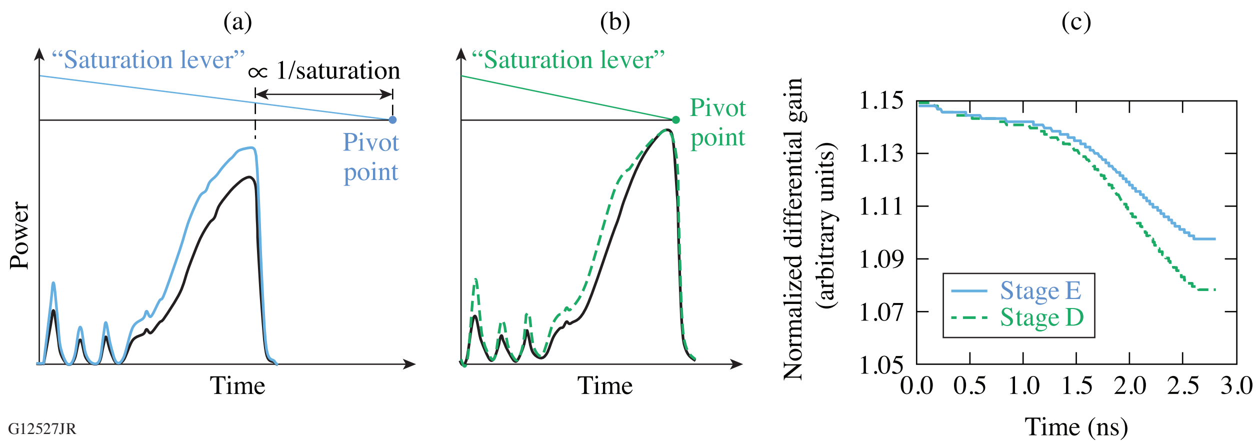

Figure 2
[(a),(b)] The black curve shows the same pulse simulated at the output of the stage-E disk and stage-D rod amplifiers, respectively. The blue and green curves show the change in the pulse shape resulting from a positive offset applied to the amplifier's operating voltage. (a) A uniform decrease in pulse power. (b) The effect of saturation results in a pronounced change in pulse power at the beginning of the pulse and almost no change at the back end of the pulse that experiences saturated gain. (c) A direct measure of the change in pulse shape showing the ratio of the nominal pulse to the gain-reduced pulse.

The "saturation lever" is a visual depiction of the aforementioned effect of operating in different saturation regimes and how gain manipulation of different saturating amplifiers can result in a more-pronounced effect on SPD and, thereby, power balance on the system. The location of the saturation lever pivot point with respect to the back of the pulse is dependent exclusively on the ratio of the output fluence to the saturation fluence of any given amplifier. In Fig. 2, vertical displacement of the end opposing the pivot point of the saturation lever represents a positive change in the amplifier's flash-lamp capacitor bank voltage.

Recent target-physics simulations have suggested that temporal simultaneity in the arrival of the ramp on the drive portion of the pulse shape [$t \sim 1400$ ps in Fig. 1(b)] governs implosion dynamics to a large degree. This region of the pulse can be manipulated by systematically adjusting the gain of the stage-D rod amplifiers, which affects the SPD more than the stage-E and -F amplifiers. This effort is currently being simulated in Miró and is planned for experimental testing in the near future.

This material is based upon work supported by the Department of Energy National Nuclear Security Administration under Award Number DE-NA0003856, the University of Rochester, and the New York State Energy Research and Development Authority.

1. V. N. Goncharov *et al*., Plasma Phys. Control. Fusion **59**, 014008 (2017).

FY19 Q1 Laser Facility Report

J. Puth, M. Labuzeta, D. Canning, and B. E. Kruschwitz

Laboratory for Laser Energetics, University of Rochester

During the first quarter (Q1) of FY19, the Omega Laser Facility conducted 331 target shots on OMEGA and 204 target shots on OMEGA EP for a total of 535 target shots (see Tables I and II). OMEGA averaged 11 target shots per operating day, averaging 94.4% Availability and 98.0% Experimental Effectiveness.

OMEGA EP was operated extensively during Q1 of FY19 for a variety of user experiments. OMEGA EP averaged 8.5 target shots per operating day, averaging 93.8% Availability and 92.9% Experimental Effectiveness.

Table I: OMEGA Laser System target shot summary for Q1 FY19.

Laboratory/ Program	Planned Number of Target Shots	Actual Number of Target Shots	ICF	Shots in Support of ICF	Non-ICF
CEA	16.5	18	—	—	18
HED	99	112	—	—	112
LBS	5.5	7	—	—	7
LLE	82.5	75	—	75	—
LLNL	5.5	8	8	—	—
NLUF	38.5	46	—	—	46
Calibration	0	65	—	65	—
Total	247.5	331	8	140	183

Table II: OMEGA EP Laser System target shot summary for Q1 FY19.

Laboratory/ Program	Planned Number of Target Shots	Actual Number of Target Shots	ICF	Shots in Support of ICF	Non-ICF
HED	63	86	—	—	86
LBS	7	8	—	—	8
LLE	21	23	—	23	—
LLNL	7	15	15	—	—
NLUF	49	56	—	—	56
NRL	7	10	10	—	—
Calibration	0	6	—	6	—
Total	154	204	25	29	150

Sub-aperture short-pulse beam operation has been activated on OMEGA EP. This modifies the nominally *f*/2 square beam (measured along the diagonal) to an *f* number that suits a given experimental objective. Circular *f*/6, *f*/8, and *f*/10 profiles are currently available and additional profiles could be realized with modest effort. Kinematic nesting of the apodizers enables rapid shot-to-shot configuration from one *f* number to another. Energy limits are naturally decreased proportional to beam area. This capability has been successfully employed to investigate wakefield electron acceleration and plasma lens concepts.

Experimental Validation of Low-*Z* Ion-Stopping Formalisms Around the Bragg Peak in High-Energy-Density Plasmas

J. A. Frenje,[1] R. Florido,[2] R. C. Mancini,[3] T. Nagayama,[4] P. E. Grabowski,[5] H. G. Rinderknecht,[6] H. Sio,[1] A. Zylstra,[7] M. Gatu Johnson,[1] C. K. Li,[1] F. H. Séguin,[1] R. D. Petrasso,[1] V. Yu. Glebov,[6] and S. P. Regan[6]

[1]Plasma Science and Fusion Center, Massachusetts Institute of Technology
[2]iUNAT– Departamento de Física, Universidad de Las Palmas de Gran Canaria, Spain
[3]Physics Department, University of Nevada, Reno
[4]Sandia National Laboratories
[5]Lawrence Livermore National Laboratory
[6]Laboratory for Laser Energetics, University of Rochester
[7]Los Alamos National Laboratory

An understanding of the DT-α energy deposition and heating of a high-energy-density (HED) plasma is critical for determining the ignition threshold in hot-spot–ignition experiments. This requires a fundamental understanding of the DT-α stopping around the Bragg peak, where the ion velocity (v_i) is similar to the average velocity (v_{th}) of the thermal plasma electrons for a wide range of electron (T_e) and ion temperatures (T_i), and electron number densities (n_e). Ion stopping in HED plasmas has, therefore, been subject to extensive analytical and numerical studies for decades,[1–3] but a theoretical treatment of ion stopping especially around the Bragg peak remains a difficult problem. The consensus is that the ion stopping at $v_i \gg v_{th}$ is treated well by the Born approximation because the interaction between the fast ions and plasma electrons is small, resulting in small energy transfers compared to the kinetic energy of the ions. At $v_i < v_{th}$, the ion stopping is harder to characterize but generally described by collisional theories that treat two-body collisions and large-angle scattering between the ions and plasma electrons. At ion velocities near v_{th}, the Born approximation breaks down because scattering is no longer weak and collisional theories make it difficult to provide a complete, self-consistent picture of the ion stopping because of the dynamic dielectric response of the plasma electrons. Rigorous quantum mechanical treatments based on convergent kinetic theories[1] attempt to rectify these challenges by utilizing the strengths of the different approaches applied to the different regimes; however, it is not clear how best to combine them and quantify their errors. Precise measurements of the ion stopping around the Bragg peak are therefore essential to guide the theoretical efforts.

Although numerous efforts have been made to theoretically describe the behavior of ion stopping in HED plasmas, only a limited set of experimental data exists to test these theories. In addition, most of these experiments used only one particle with a distinct velocity in the high-velocity ion-stopping regime ($v_i > v_{th}$) and, therefore, did not simultaneously probe the detailed characteristics of the Bragg peak below and above v_{th}. To the best of our knowledge, only two experiments have attempted to simultaneously probe the low- and high-velocity side of the Bragg peak,[4,5] but the limitation of these experiments was that the HED plasma conditions could not be characterized to the level required for experimental validation of various ion-stopping formalisms. The work described here significantly advances previous efforts by providing the first accurate experimental validation of ion-stopping formalisms around the Bragg peak.

The experiments reported herein were carried out on OMEGA, where eight D^3He gas-filled, thin-glass capsules were symmetrically imploded with 60 laser beams, delivering up to 12.0 kJ to the capsule in a 1-ns square pulse. These capsules were also filled with a small amount of argon for a time- and space-resolved measurement of the electron-temperature and electron-number-density profiles.[6]

For accurate experimental validation of the ion stopping around the Bragg peak, the energy loss ($-\Delta E_i$) of DD tritons (DD-t), DD protons (DD-p), D^{3}He-α (D^{3}He-α), and D^{3}He protons (D^{3}He-p), while traversing the well-characterized HED-plasma conditions, were simultaneously measured. Examples of measured spectra of DD-t, DD-p, D^{3}He-α, and D^{3}He-p are shown in Fig. 1 for shot 75699. The vertical arrows in Fig. 1 indicate the median energy for each measured spectrum, and by contrasting these energies to the average-birth energies (vertical dashed lines), $-\Delta E_i$ was determined to an accuracy of ~10% and used to assess the ion stopping in the HED plasma. (See Ref. 7 for more details about these measurements.)

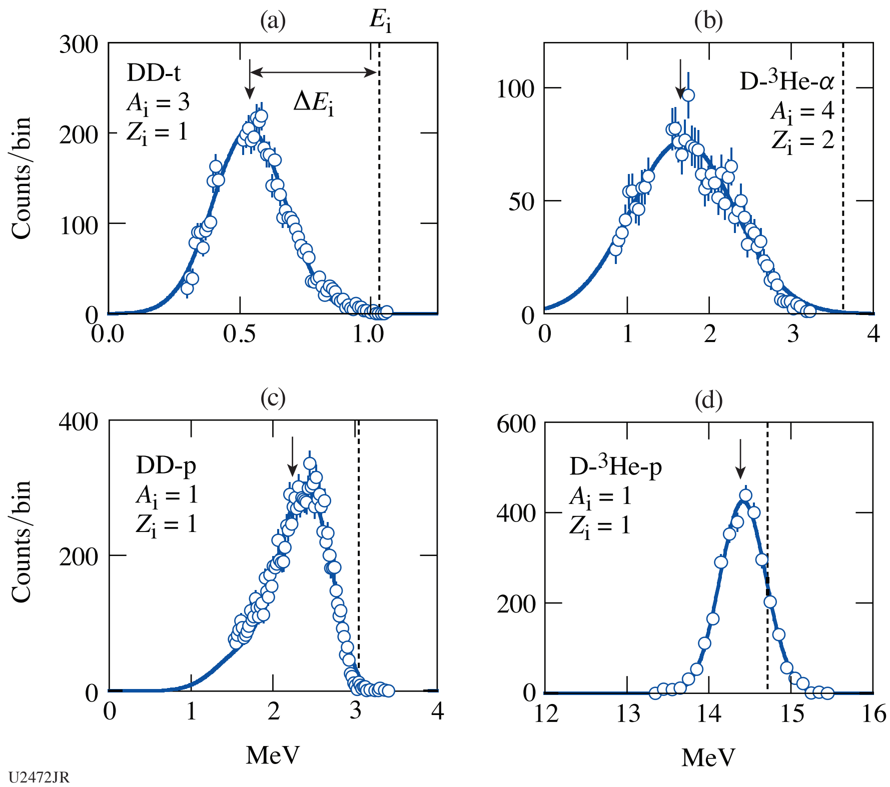

Figure 1
Measured spectra of DD-t, D^{3}He-α, DD-p, and D^{3}He-p for shot 75699. These fusion products are produced by the reactions: D + D $\longrightarrow$ t (1.01 MeV) + p (3.02 MeV) and D + ^{3}He $\longrightarrow$ ^{4}He (3.71 MeV) + p (14.63 MeV), where the energies in the parentheses are the fusion-product birth energies (at zero ion temperature).

To illustrate the measured energy loss of fusion products with different initial energy (E_i), charge (Z_i), and mass (A_i) passing through an HED plasma, the energy-loss data must be presented in the form of $-\Delta E_i/Z_i^2$ versus E_i/A_i. Figure 2 shows the $-\Delta E_i/Z_i^2$ versus E_i/A_i for shots conducted in this study. The solid curves in Fig. 2 were obtained by integrating the Brown–Preston–Singleton (BPS) plasma stopping-power function, describing only the ion–electron Coulomb interaction. Clearly, the data demonstrate that the BPS formalism is providing a good description of the ion stopping for these HED plasma conditions, except for the stopping of DD-t at $v_i \sim 0.3v_{th}$. At this velocity, the BPS formalism systematically underpredicts DD-t energy loss for all shots. This observation cannot be explained by the inclusion of ion–ion Coulomb scattering in the modeling because ion-stopping theories based on multi-ion component response predict that the contribution of the ion–ion Coulomb scattering to the total DD-t plasma-stopping power is ~10% at $v_i \sim 0.3v_{th}$. This points to the idea that the contribution from the ion–ion component to the total ion stopping at this velocity could, in fact, be larger than predicted by theories. This is certainly plausible since all theories ignore the ion–ion nuclear elastic scattering, which is more strongly weighted toward large-angle scattering than Coulomb scattering. To explain the data at $v_i \sim 0.3 v_{th}$, the total ion stopping must be increased by ~20%, possibly a result of ion–ion nuclear elastic scattering. This postulation, if correct, would have an impact on our understanding of DT-α heating of the fuel ions in an ignition experiment.

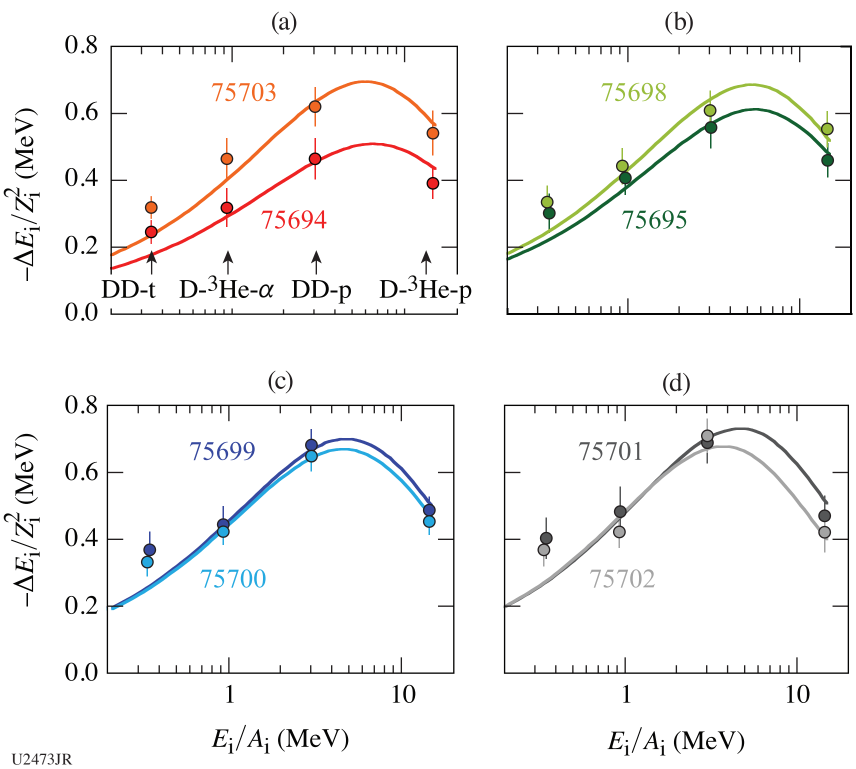

Figure 2
The measured and predicted ion stopping $\left(-\Delta E_i / Z_i^2\right)$ as a function of E_i / A_i for all shots. The data set is contrasted to BPS predictions (considering only ion–electron Coulomb interactions).

The work described herein was performed in part at the LLE National Laser User's Facility (Grant No. DE-NA0003539), and was supported in part by U.S. DOE (Grant No. DE-NA0002949) and LLE (subcontract Grant No. 416107-G). In addition, R.F. was supported by Grant No. ENE2015-67581-R (MINECO/FEDER-UE) from the Spanish Ministry of Economy and Competitiveness.

1. L. S. Brown, D. L. Preston, and R. L. Singleton, Jr., Phys. Rep. **410**, 237 (2005).
2. C.-K. Li and R. D. Petrasso, Phys. Rev. Lett. **70** 3059 (1993); **114**, 199901(E) (2015).
3. G. Maynard and C. Deutsch, J. Phys. France **46**, 1113 (1985).
4. D. G. Hicks *et al*., Phys. Plasmas **7**, 5106 (2000).
5. J. A. Frenje *et al*., Phys. Rev. Lett. **115**, 205001 (2015).
6. T. Nagayama *et al*., Phys. Plasmas **21**, 050702 (2014).
7. J. A. Frenje *et al*., Phys. Rev. Lett. **122**, 015002 (2019).

Probing Fuel-Ion Species Dynamics in Shock-Driven Inertial Confinement Fusion Implosions Using Multiple Reaction Histories

H. Sio,[1] J. A. Frenje,[1] A. Le,[2] S. Atzeni,[3] T. J. T. Kwan,[2] M. Gatu Johnson,[1] G. Kagan,[2] C. Stoeckl,[4] C. K. Li,[1] C. E. Parker,[1] C. J. Forrest,[4] V. Yu. Glebov,[4] N. V. Kabadi,[1] A. Bose,[1] H. G. Rinderknecht,[4] P. A. Amendt,[5] D. T. Casey,[5] R. C. Mancini,[6] W. T. Taitano,[2] B. Keenan,[2] A. N. Simakov,[2] L. Chacón,[2] S. P. Regan,[4] T. C. Sangster,[4] E. M. Campbell,[4] F. H. Séguin,[1] and R. D. Petrasso[1]

[1]Plasma Science and Fusion Center, Massachusetts Institute of Technology
[2]Los Alamos National Laboratory
[3]Dipartimento SBAI, Università degli Studi di Roma "La Sapienza," Italy
[4]Laboratory for Laser Energetics, University of Rochester
[5]Lawrence Livermore National Laboratory
[6]Physics Department, University of Nevada, Reno

Strong shocks are ubiquitous in inertial confinement fusion (ICF) and many astrophysical plasmas,[1] and the experimental results described in this work may provide new insights into phenomena in these fields. ICF produces thermonuclear fusion in the laboratory by imploding a spherical target filled with light-ion fuel, and capsule compression begins with launching strong shock(s) into the central gas during the shock phase. During this time, sharp gradients at the shock front are expected to drive temperature and density differences between the different fuel-ion (D, T, and ^{3}He) populations. These multi-ion effects that may impact and modify plasma conditions are not modeled in average-ion-fluid codes but are simulated in kinetic-ion simulations.

In contrast with previous studies that relied on time-integrated measurements, this work[2] presents time-resolved observation of fuel-ion species dynamics in ICF implosions using DT and D^{3}He reaction histories (Fig. 1). These reaction histories were measured with a particle x-ray temporal diagnostic (PXTD),[3] which captures the relative timing between these reaction histories with unprecedented precision (~10 ps). These time-resolved measurements are contrasted with average-ion-fluid *DUED* and multi-ion *LSP* simulations. The difference between the measured fusion reaction histories during the shock phase is consistent with rapidly changing fuel-ion composition caused by a strong shock in the central gas of an ICF target.

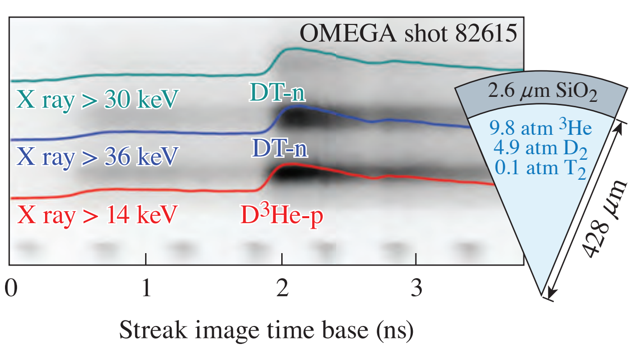

Figure 1
PXTD streak image on OMEGA shot 82615. The target is a thin-glass capsule filled with D^{3}He and a trace of T$_2$. PXTD measured both the x-ray emissions as well as the D^{3}He and DT reaction histories from the implosion.

This experiment uses an exploding-pusher platform,[4] which is simple and ideal for studying the multi-ion dynamics during the shock phase in an ICF implosion. The reason for this is that shock-phase plasma conditions (temperature, density, ion mean-free-path, shock strength) are similar in all these implosions. These exploding-pusher targets are 860 μm in diameter with a 2.7-μm-thick SiO_2 shell. The gas-fill density is 2.2 mg/cm^3, with an atomic fuel composition of 49.6% D, 49.7% ^{3}He, and 0.7% T. These targets are driven symmetrically by 60 laser beams on the OMEGA Laser System with a total energy of 14.4 kJ using a 0.6-ns-sq pulse shape. These implosions are hydrodynamic-like, with $\lambda_{ii}/R_{burn} \sim 3$, where λ_{ii} is the ion mean free path and R_{burn} is the fuel radius at peak burn.

The primary measurements in this experiment are the absolute DT and D^{3}He reaction histories, which are simultaneously measured with the PXTD (Fig. 1). This is done by measuring the time-arrival histories of the monoenergetic 14.1-MeV DT-n and 14.7-MeV D^{3}He-p as they escape the implosion. Since all measurements are made with the same diagnostic, the relative timing uncertainty between the DT and D^{3}He reaction histories is ~10 ps (versus ~40 to 50 ps, with the standard method of cross-timing between two stand-alone diagnostics). This innovation is crucial to capturing the relative timing between different nuclear burns with sufficiently high precision to enable meaningful comparison between measurements and simulations. In comparison with the average-ion-fluid *DUED*[5] simulation (Fig. 2), a significantly higher D^{3}He reaction rate is observed relative to DT at the onset of the shock burn. This is observed on all four shots, and higher-than-expected ion temperature alone early in time in the fuel cannot explain this observation.

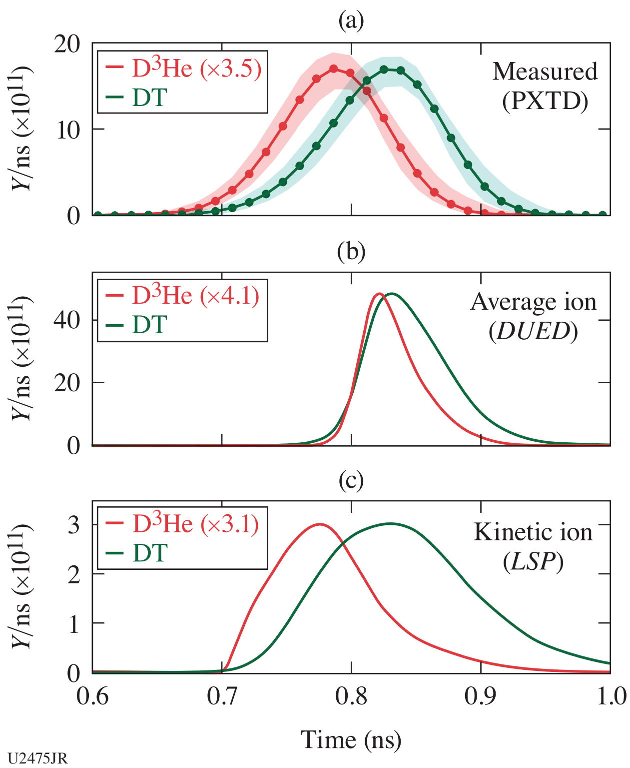

Figure 2
Absolute D^{3}He (red) and DT (blue) reaction histories measured by PXTD and simulated by *DUED* and *LSP*, for OMEGA shot 82615. The magnitudes of the D^{3}He histories are scaled to match the DT histories for clarity in each case. Uncertainties in the PXTD data are indicated by the shaded regions.

The measured timing difference is consistent, however, with ion-species separation driven by sharp pressure gradients at the shock front in the implosion. The dominant terms driving the D and ^{3}He ions forward relative to the T ions are from the ion pressure gradient (barodiffusion,[6] which accelerates the lighter D ions ahead) and the electron pressure gradient (electrodiffusion,[7] which accelerates the higher-charge ^{3}He ions ahead).

Fuel-ion–species separation is also observed in a kinetic-ion *LSP*[8] simulation, which, unlike the average-ion-fluid code *DUED*, treats the D, T, and ^{3}He ion population separately. During shock convergence, fuel-ion–species separation has already developed between the D, T, and ^{3}He ions, with the T ions lagging behind the shock front. This led to a depletion of T ions on the central fuel region when the shock rebounds, delaying the DT burn relative to the D^{3}He burn. Qualitatively, *LSP* simulations clearly demonstrate how fuel-ion–species separation that developed during shock propagation and rebound manifest as a timing differential between reaction histories (Fig. 2).

In summary, the time-resolved DT and D^{3}He reaction rates in hydrodynamic-like shock-driven implosions cannot be explained by average-ion simulations and is attributed to ion-species separation between the D, T, and ^{3}He ions during shock convergence and rebound. At the onset of the shock burn, the ^{3}He/T fuel ratio in the burn region inferred from the measured reaction histories is much higher as compared to the initial ^{3}He/T gas-fill ratio. Since T and ^{3}He have the same mass but a different charge, these results indicate that the charge-to-mass ratio plays an important role in driving fuel-ion–species separation during strong shock propagation. It is unclear how these multi-ion effects affect implosion performance during the deceleration and compression phase since existing experimental results have been mixed. A planned upgrade to the PXTD diagnostic (the cryoPXTD) will provide improved nuclear and x-ray data for these implosion experiments, as well as time-resolved electron temperature measurement for the OMEGA cryogenic program. Future work includes quantifying these effects in very hydrodynamic shock-driven implosions; in very kinetic implosions; in the ablative phase of compressive implosions; and in astrophysical settings such as SN 1987a (Ref. 1), where nonequilibrium kinetic effects and signatures (such as temperature differences between ion species) could be present.

This material is based upon work supported by the Department of Energy, National Nuclear Security Administration under Award Numbers DE-NA0001857, DE-NA0002949, and DENA0002905. The work was also supported in part by NLUF (DE-NA0002035). HS was supported by a DOE NNSA SSGF fellowship (DE-FC52-08NA28752) during this work.

1. S. Q. Park *et al*., Astrophys. J. **610**, 378 (2004).
2. H. Sio *et al*., Phys. Rev. Lett. **122**, 035001 (2019).
3. H. Sio *et al*., Rev. Sci. Instrum. **87**, 11D701 (2016).
4. M. J. Rosenberg *et al*., Phys. Rev. Lett. **112**, 185001 (2014).
5. S. Atzeni *et al*., Comput. Phys. Commun. **169**, 15 (2005).
6. P. Amendt *et al*., Phys. Rev. Lett. **105**, 115005 (2010).
7. G. Kagan and X.-Z. Tang, Phys. Plasmas **19**, 082709 (2012).
8. D. R. Welch *et al*., Comput. Phys. Commun. **164**, 183 (2004).

Impact of the Langdon Effect on Cross-Beam Energy Transfer

D. Turnbull,[1] A. Colaïtis,[1,2] A. M. Hansen,[1] A. L. Milder,[1,2] J. P. Palastro,[1] J. Katz,[1] C. Dorrer,[1] B. E. Kruschwitz,[1]
D. J. Strozzi,[3] and D. H. Froula[1]

[1]Laboratory for Laser Energetics, University of Rochester
[2]Centre National da la Recherche Scientifique
[3]Lawrence Livermore National Laboratory

The prediction that laser-plasma heating distorts the electron distribution function (EDF) away from Maxwellian dates back four decades.[1] In conditions relevant to laser-based fusion, however, no direct evidence of this so-called "Langdon effect" has previously been observed. Here, measurements of the complete Thomson-scattering spectrum indicate the presence of super-Gaussian EDF's that are consistent with Langdon theory. In such plasmas, ion-acoustic wave (IAW) frequencies increase monotonically with super-Gaussian exponent.[2] To match experiments that measured power transfer between crossed laser beams mediated by IAW's, a model that accounts for the non-Maxwellian EDF is required, whereas the standard Maxwellian calculations overpredict power transfer over a wide region of parameter space. Including this effect is expected to improve the predictive capability of cross-beam energy transfer (CBET) modeling at the National Ignition Facility (NIF) and may restore a larger operable design space for inertial confinement fusion experiments. This is also expected to motivate further inquiry in other areas impacted by non-Maxwellian EDF's, such as laser absorption, heat transport, and x-ray spectroscopy.

Laser fusion experiments require many overlapping laser beams to propagate through long, underdense plasmas in order to precisely deposit their energy at desired locations, but laser–plasma interactions can complicate the intended result. Cross-beam energy transfer is one example, whereby a frequency difference between two lasers in the plasma rest frame resonantly drives an ion-acoustic wave that scatters light from one beam to the other. The ability to manipulate this process in indirect-drive hohlraum targets via laser frequency detuning was initially seen as beneficial, providing control over implosion symmetry while operating the NIF at its maximum energy. However, when integrated observables indicated that there was less CBET than calculated, a tunable saturation clamp on IAW amplitudes was added to models, although the level ($\delta n/n = 10^{-3}$ to 10^{-4}) was too small to be explained by known saturation mechanisms.[3] Moreover, it varied between platforms—undermining the predictive capability of simulations and limiting fusion performance.

This motivated the development of a CBET platform at LLE, where a wavelength-tunable laser (TOP9) was built to study CBET in a well-characterized quasi-stationary plasma. Initial experiments reported here suggest that the Langdon effect may be responsible for overpredicting power transfer in indirect-drive–relevant conditions. The term comes from a 1980 Letter in which A. B. Langdon explained that inverse bremsstrahlung absorption of electromagnetic radiation in plasma preferentially heats low-energy electrons, distorting the electron distribution function away from Maxwellian and toward a super-Gaussian of the order of $m = 5$ (Ref. 1). He defined the scaling parameter $\alpha = Z_{\text{eff}} v_{\text{osc}}^2 \big/ v_{\text{th}}^2$, where Z_{eff} is the effective ion charge state, v_{osc} is the velocity of electrons oscillating in the laser field, and v_{th} is the electron thermal velocity. Subsequent Fokker–Planck simulations under a wide range of laser heating conditions demonstrated that intermediate super-Gaussian EDF's are produced in the form $f_m(v) = C_m \exp[-(v/v_m)^m]$, where $v_m^2 = \left(3k_\text{B}T_\text{e} \big/ M_\text{e}\right)\left[\Gamma(3/m)\big/\Gamma(5/m)\right]$, $C_m = \left(N_\text{e}\big/4\pi\right)\left\{m\Big/\left[\Gamma(3/m)v_m^3\right]\right\}$, Γ is the gamma function, and $m(\alpha) = 2 + 3\big/\left(1 + 1.66\big/\alpha^{0.724}\right)$ is only a function of α (Ref. 4).

Although it is often assumed that the Langdon effect only impacts absorption in high-Z plasmas, such non-Maxwellian distribution functions are known to affect the ion-acoustic wave dispersion relation $\omega = kc_\text{s}[3\Gamma^2(3/m)/\Gamma(1/m)/\Gamma(5/m)]^{1/2}$, which would directly impact CBET by shifting the ion-acoustic resonance.[2] The square root term modifies the usual dispersion relation and leads to a monotonic increase of IAW frequency with super-Gaussian order, which results from the smaller number of low-energy electrons [$f(v \approx 0)$] available to shield the ion oscillations.

In the CBET experiments, TOP9 was crossed with a single nearly co-propagating pump beam in a plasma that was preformed from a mixture of hydrogen and nitrogen gas; its power was then diagnosed using a transmitted beam diagnostic. Results will be shown with and without nearly counter-propagating heater beams, which (when present) enhanced the Langdon effect without contributing significantly to the CBET gain. Both spatially and temporally resolved Thomson scattering were used to characterize the plasma conditions (including m) in order to constrain the CBET modeling. A heater-only intensity (I) scan was performed by varying the number of beams from 1 to 4. In addition to electron temperature increasing with I to the ≈0.2 power, the non-Maxwellian super-Gaussian exponent m was observed to increase from 2.4 up to 2.85 in excellent agreement with theory.

On the CBET experiments with three heaters plus one pump, m was determined to be 2.82 from the Thomson-scattering spectrum, whereas it was only 2.4 for the case of the pump only. In the former case, accounting for the non-Maxwellian EDF (again, using the modified electron susceptibility) was required to match the data, whereas the standard Maxwellian model currently used in inertial fusion calculations overpredicted the energy transfer [shown in Fig. 1(a)]. Without heater beams, the effect is smaller and the data cannot easily distinguish between the Maxwellian and non-Maxwellian models [Fig. 1(b)]. Calculations for NIF-like plasma conditions yield $\alpha = 0.7$ and $m = 2.96$—even further from Maxwellian than the conditions produced in the TOP9 experiments because of the large number of overlapping beams. Since the Langdon effect suppresses gain on the rising edge of the ion-acoustic resonance and most resonances are outside the NIF's available wavelength tuning range in an indirect-drive fusion experiment, calculations suggest the Langdon effect uniformly reduces CBET gain on the NIF by 27.7% on average. This level of CBET reduction would significantly impact implosion symmetry. Accounting for the Langdon effect might therefore remove the need for an artificial saturation clamp and should improve the predictive capability of integrated modeling.

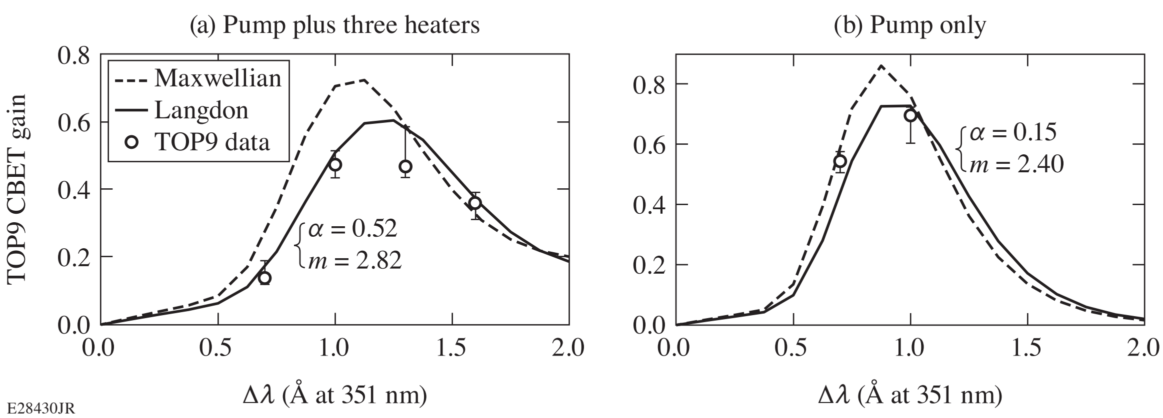

Figure 1
TOP9 CBET results. (a) TOP9 data are shown for the case in which three heater beams coexisted temporally with the pump and wavelength-tunable beam. A calculation that accounts for the non-Maxwellian EDF measured by Thomson scattering agrees with the data, but the Maxwellian calculation is discrepant. (b) Without the heater beams, the EDF was closer to Maxwellian and the data cannot easily distinguish between the two models.

This material is based upon work supported by the Department of Energy National Nuclear Security Administration under Award Number DE-NA0003856, the University of Rochester, and the New York State Energy Research and Development Authority.

1. A. B. Langdon, Phys. Rev. Lett. **44**, 575 (1980).
2. B. B. Afeyan *et al*., Phys. Rev. Lett. **80**, 2322 (1998).
3. P. Michel *et al*., Phys. Rev. Lett. **109**, 195004 (2012).
4. J. P. Matte *et al*., Plasma Phys. Control. Fusion **30**, 1665 (1988).

Interpreting the Electron Temperature Inferred from X-Ray Continuum Emission for Direct-Drive Inertial Confinement Fusion Implosions on OMEGA

D. Cao, R. C. Shah, S. P. Regan, R. Epstein, I. V. Igumenshchev, V. Gopalaswamy, A. R. Christopherson, W. Theobald, P. B. Radha, and V. N. Goncharov

Laboratory for Laser Energetics, University of Rochester

We present findings on which the x-ray–inferred electron temperature T_e will be interpreted for direct-drive ICF implosions on OMEGA: (1) an analytic description of the electron temperature as the emission-weighted, harmonic mean temperature; (2) an optimal x-ray energy that gives emission weighting closest to neutron weighting; (3) simulation results showing disparity between hot-spot electron temperature and ion temperature, even without fluid motion biasing for OMEGA-scale implosions; and (4) simulation results showing correlation of the implosion degradation with the hot-spot electron temperature and x-ray yield.

It can be shown that the inferred T_e from x-ray continuum emission represents an emission-weighted, harmonic average temperature of the emitting body. From an x-ray spectrum that can be both time and spatially integrated, the emitting body's temperature can be obtained by applying a linear fit in log space and calculating that fit's negative inverse slope, as shown in Fig. 1 for an example profile. This inferred temperature is found to follow the harmonic average relation

$$\frac{1}{kT_{\mathrm{fit}}} = \frac{1}{I_\nu}\iint \varepsilon_\nu^{\mathrm{FF}}\left[\frac{1}{kT_e(\mathbf{r})}\right]\mathrm{d}V\mathrm{d}t = \left\langle \frac{1}{kT_e(\mathbf{r})}\right\rangle, \tag{1}$$

where T_{fit} is the inferred electron temperature, k is the Boltzmann constant, I_ν is the total x-ray yield at photon energy $h\nu$, V is the volume, t is time, T_e is the true electron temperature, and $\varepsilon_\nu^{\mathrm{FF}}$ is the free–free bremsstrahlung emissivity assuming full ionization.

As shown in Fig. 1(c) for the example profile, results from applying Eq. (1) give the same value as performing the linear fit exercise in Fig. 1(b). Since the inferred electron temperature will be a harmonic average, it will be generally lower than an emission-weighted, arithmetic average by ~100 eV as shown in Fig. 1(c).

With a physical understanding of the inferred temperature and its weighting on photon energy, it is next important to know the photon energy most optimal for inferring the hot-spot electron temperature. Given that complementary ion temperature measurements are neutron weighted, it would be most meaningful for the electron temperature to be weighted by the same spatial distribution as the neutron emission for the purpose of assessing implosion performance. By using a power law approximation $\varepsilon_\nu^{\mathrm{FF}} \propto T^\eta$ for the emissivity, where the exponent η is given by

$$\eta = \frac{h\nu_0}{kT_0}, \tag{2}$$

it is found that photons with energies near $4kT_0$, where T_0 is the characteristic hot-spot temperature (e.g., has a neutron-weighted temperature of ~3.75 keV for OMEGA), are produced with a T^4 dependence (i.e., the same temperature dependence as neutron

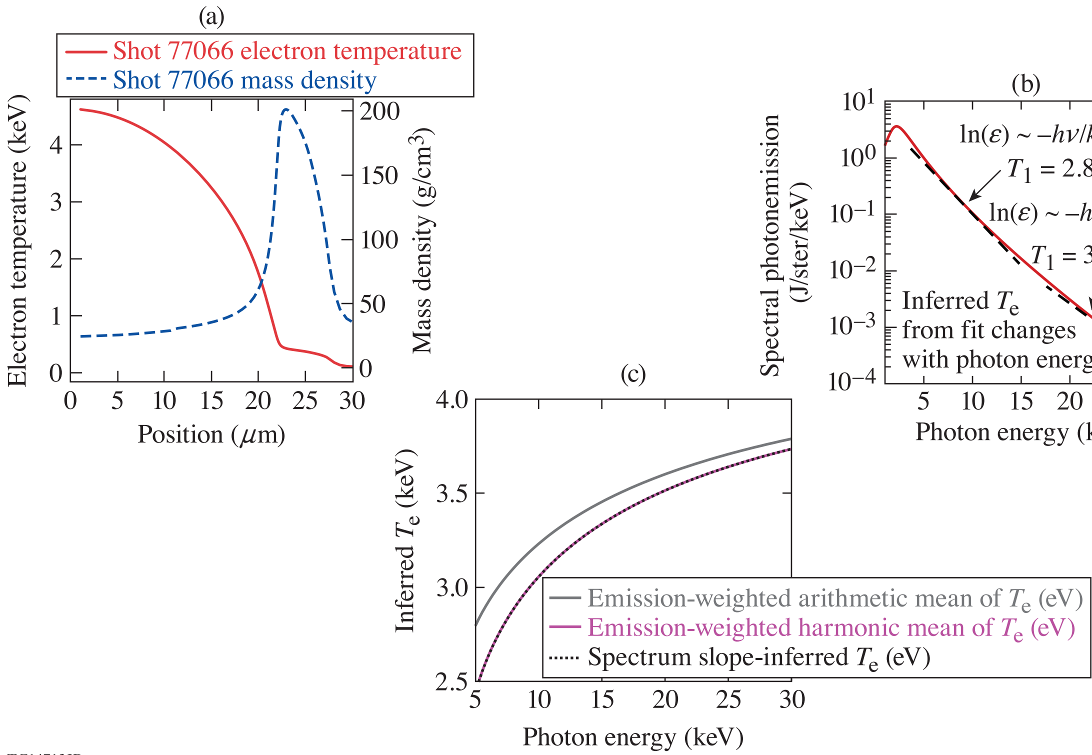

TC14713JR

Figure 1
The process used to extract instantaneous, spatially averaged hot-spot temperature from hard x-ray emission. From a hot spot represented by the profiles in (a), the escaping photons create the x-ray spectrum[1] in (b). The electron temperature is inferred from the log slope of the spectrum in (b) and changes with photon energy caused by the distribution of temperatures within the hot spot. This in turn creates an array of slope-inferred temperatures as shown in (c). This inferred electron temperature is equivalent to the emission-weighted harmonic mean electron temperature from the hot spot and is generally lower than the emission-weighted, arithmetic mean electron temperature. A time-integrated T_e can be inferred using the same process from a time-integrated x-ray spectrum.

production from deuterium–tritium fusion). At this photon energy, the inferred electron temperature can be said to have an emission weighting that closely, but not equally, resembles neutron weighting. This can be seen in Fig. 2(a), which compares the normalized x-ray emission and neutron production for an isobaric temperature and density profile.[2]

For OMEGA-scale implosions, simulations show that the neutron-weighted ion temperature is not well approximated by the electron temperature, regardless of the photon energy used. This is shown in Fig. 2(b) using *LILAC*[3] post-shot simulations of all past DT cryogenic shots performed on OMEGA that are stored in the simulation database.[4] At all photon energies, the functional mapping between the electron temperature and the neutron-weighted ion temperature does not follow a clear $y = x$ trend. Moreover, the consequent mapping uncertainty in ion temperature can be as large as ~400 eV according to scatter in Fig. 2(b), compared to the precision error of ~130 eV from current neutron time-of-flight diagnostics on OMEGA.

This imprecise surrogacy between the ion and electron temperatures is caused by the hot spot's thermal nonequilibrium state for the simulated OMEGA implosions. The persistence of this thermal nonequilibrium can be surprising, considering that the equilibration time, which scales[5] as $\tau_{ei} \sim T^{3/2}\rho^{-1}$, is typically of the order of 10 ps or only about 10% of the burnwidth FWHM. It was found, however, that electron thermal conduction was responsible for inhibiting thermal equilibration from dominating. It is expected that hot spots will be more equilibrated for higher convergence ratio implosions at a larger scale.

Despite the non-surrogacy between the electron and ion temperatures, 3-D simulations suggest the difference of the electron temperature from the 1-D prediction $\left(\Delta T_e = T_e^{\text{inferred}} - T_e^{\text{1-D}}\right)$ can be useful as an implosion diagnostic. Figure 3 shows a comparison of the inferred electron temperature and x-ray yield between the two cases. One simulation represented an ideal case where the implosion was perfectly 1-D and another included perturbations typically observed on OMEGA from target offset ($\Delta r = 5.4\ \mu$m), beam imbalance ($\sigma_{rms} = 3.5\%$), and beam port geometry as well as laser imprint modulations ($\ell_{max} = 200$). Both simulations use target parameters from OMEGA shot 89224, an $\alpha \sim 5$ implosion with an in-flight aspect ratio $\left(\mathrm{IFAR} = R_{shell}/\Delta R_{shell}\right)$ of ~40 and peak implosion velocity of 480 km/s.

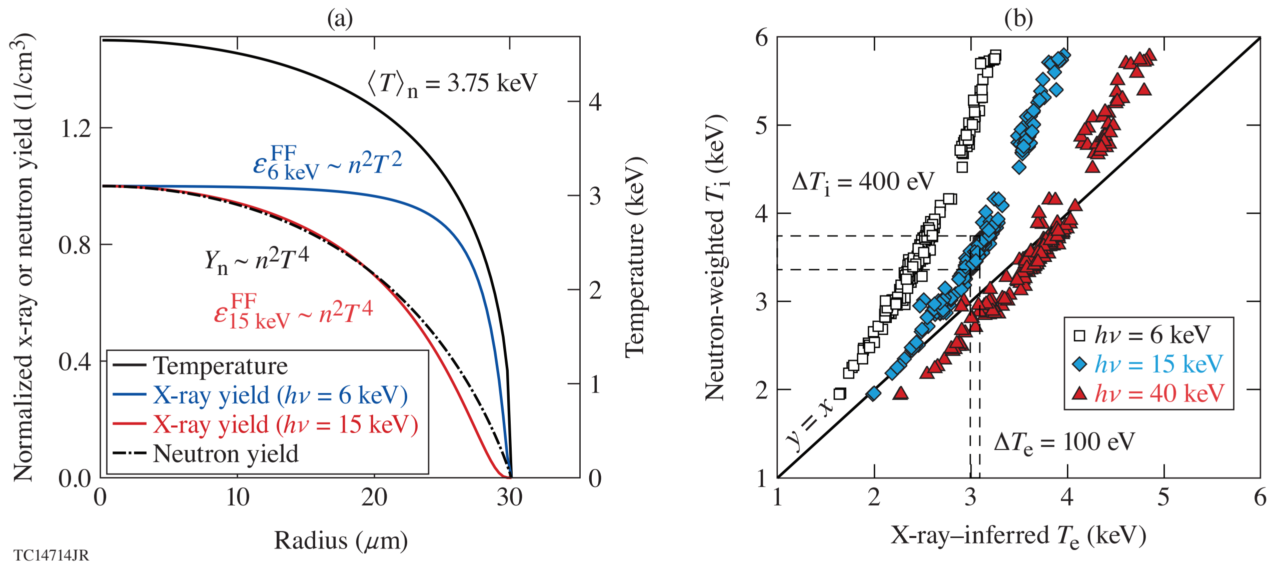

Figure 2
(a) Normalized x-ray and neutron yields comparison for a representative, isobaric hot-spot profile,[2] where $T_e = T_i$. At photon energy near 4× the neutron-weighted temperature, the emission approximately follows the neutron production. (b) The neutron-weighted ion temperature to the x-ray inferred electron temperature for all OMEGA DT cryogenic post-shot simulations in the simulation database.[4] The scatter in both plots suggests that direct surrogacy between the inferred electron temperature and the neutron-weighted ion temperature is not robust.

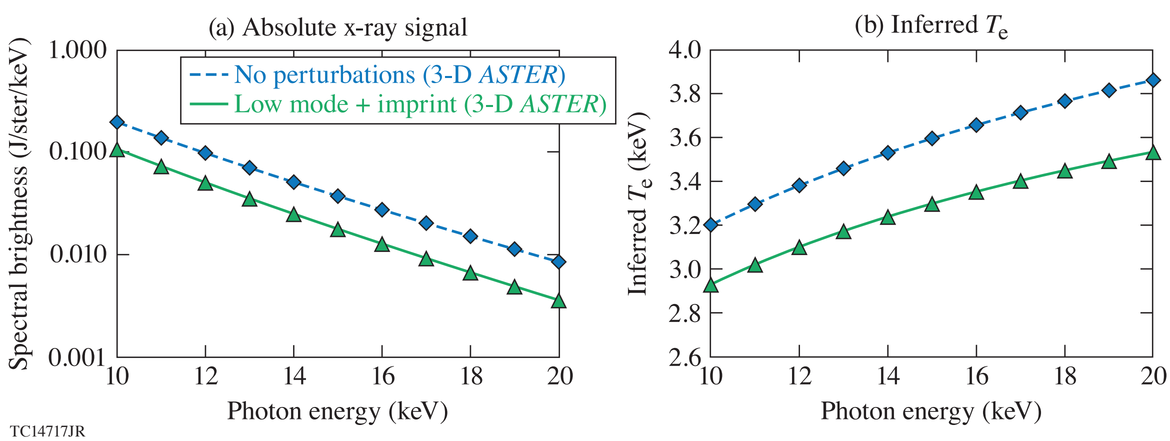

Figure 3
(a) Comparison of the electron temperature inferred from x-ray continuum emission as a function of photon energy between two *ASTER*[6] simulations with different levels of implosion perturbations. (b) Comparison of the x-ray emission as a function of photon energy for the same two *ASTER* simulations. The inferred electron temperature and the x-ray yield are not only sensitive to implosion degradation but are also sensitive enough to be measurable in experiments. The additional information these observables provide not only gives more opportunities for validating simulations, but also expands the capability of diagnosing fuel assembly during stagnation.

Between the 1-D and perturbed simulations, the neutron-weighted ion temperature dropped from 4.67 keV to 4.35 keV, and the neutron yield dropped from 4 to 2×10^{14}, a result stemming from decreased hot-spot compression. Similar to the neutron-weighted ion temperature, the electron temperature dropped by almost the same amount (~300 eV) throughout the 10- to 20-keV emission energy range. These changes being similar is not a coincidence; the 10- to 20-keV emission energy range is centered on the optimal energy range at which emission weighting is closest to neutron weighting. The drop being almost consistent across the entire range suggests the weighting is robust across a wide energy space. Most importantly, these changes in the electron temperature and absolute x-ray emission are larger than the expected detector uncertainty of ~5% and, therefore, expected to be observable. Measuring the electron temperature for a variety of cryogenic implosions on OMEGA should reveal trends more reliable than those depending on the neutron-weighted ion temperature. In addition, methods published by R. Epstein *et al.*[7] and T. Ma *et al.*[8] can be used for estimating hot-spot mix amounts with the absolute x-ray emission measurements. With the existence of a T_e measurement, the thermal-equilibrium assumption can also be removed and thereby improve the estimate's accuracy for implosions on OMEGA.

Interpretation and sensitivity analysis of the hot-spot electron temperature inferred from hard x rays have been performed. The electron temperature inferred from hard x-ray continuum emission was shown to be an emission-weighted, harmonic mean electron temperature. As this value varies with photon energy, it was shown both analytically and with simulations that the optimal photon energy for approximate neutron weighting is near 15 keV or more generally near 4× the neutron-weighted hot-spot temperature. Simulations also suggest, however, that one should not expect the hot-spot electron and ion temperatures to be equal in value for OMEGA-scale implosions caused by thermal nonequilibrium. For perturbed implosions, the deviation of the inferred electron temperature from 1-D is predicted to be sensitive to implosion performance. The drop in electron temperature is of the same order as the drop in the ion temperature, and the x-ray yield-over-clean ratio should similarly track the neutron yield-over-clean ratio. This sensitivity is expected to be significant enough to be observed in experiments and will be exploited for evaluating and optimizing future OMEGA DT cryogenic implosions.

This material is based upon work supported by the Department of Energy National Nuclear Security Administration under Award Number DE-NA0003856, the University of Rochester, and the New York State Energy Research and Development Authority.

1. J. J. MacFarlane *et al.*, High Energy Density Phys. **3**, 181 (2007).
2. R. Betti *et al.*, Phys. Plasmas **8**, 5257 (2001).
3. J. Delettrez *et al.*, Phys. Rev. A **36**, 3926 (1987).
4. V. Gopalaswamy *et al.*, Nature **565**, 581 (2019).
5. S. Atzeni and J. Meyer-ter-Vehn, *The Physics of Inertial Fusion: Beam Plasma Interaction, Hydrodynamics, Hot Dense Matter*, 1st ed., International Series of Monographs on Physics, Vol. 125 (Oxford University Press, Oxford, 2004).
6. I. V. Igumenshchev *et al.*, Phys. Plasmas **23**, 052702 (2016).
7. R. Epstein *et al.*, Phys. Plasmas **22**, 022707 (2015).
8. T. Ma *et al.*, Phys. Rev. Lett. **111**, 085004 (2013).

Fuel–Shell Interface Instability Growth Effects on the Performance of Room-Temperature Direct-Drive Implosions

S. C. Miller,[1,2] J. P. Knauer,[1] C. J. Forrest,[1] V. Yu. Glebov,[1] P. B. Radha,[1] and V. N. Goncharov[1,2]

[1]Laboratory for Laser Energetics, University of Rochester
[2]Department of Mechanical Engineering, University of Rochester

Performance degradation in direct-drive inertial confinement fusion implosions is caused by several effects, one of which is Rayleigh–Taylor (RT) instability growth during the deceleration phase. In room-temperature plastic target implosions, deceleration-phase RT growth is enhanced by the density discontinuity and finite Atwood number at the fuel–shell interface (see Fig. 1). The Atwood number $\left[A_\mathrm{T}=\left(\rho_\mathrm{shell}-\rho_\mathrm{fuel}\right)/\left(\rho_\mathrm{shell}+\rho_\mathrm{fuel}\right)\right]$ of the interface is systematically varied by altering the ratio of deuterium to tritium (D:T) within the DT gas fill. The stability of the interface is best characterized by the effective Atwood number, which is primarily determined by radiation heating of the shell. Both simulation and experimental data show that yield performance scales with the fraction of D and T present in the fuel and that the observed inferred ion-temperature asymmetry $\left(\Delta T_\mathrm{i}=T_\mathrm{i}^\mathrm{max}-T_\mathrm{i}^\mathrm{min}\right)$, which indicates the presence of long-wavelength modes, has a small sensitivity to the different D:T ratios. Three D:T ratios (10:90, 25:75, and 50:50) were chosen based on the material interface A_T to create *stable*, *neutrally stable*, and *unstable* conditions, respectively, during the deceleration phase.

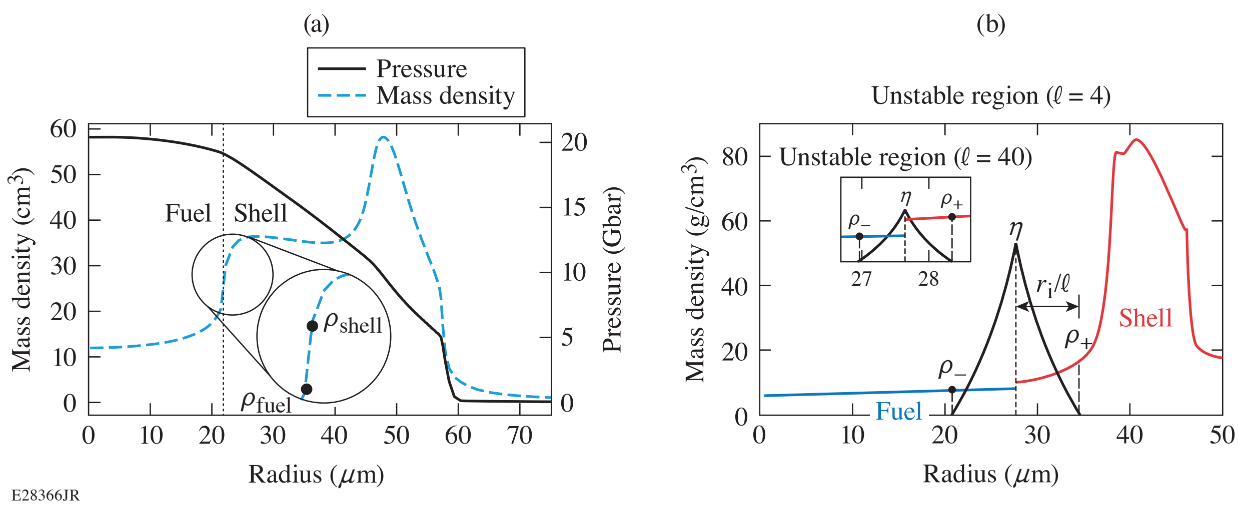

Figure 1
(a) The fuel–shell interface of room-temperature targets during the deceleration phase is classically unstable because of the jump in density. (b) Any ℓ-mode perturbations (η) present at the interface (r_i) will grow if $A_\mathrm{T}>0$. The size of the unstable region is proportional to the wavelength of the perturbation.

The fuel–shell interface Atwood number ($A_\mathrm{T,i}$) is found to be *stable* for 10:90 ($A_\mathrm{T,i}=-0.03$), *neutrally stable* for 25:75 ($A_\mathrm{T,i}\approx 0.0$), and *unstable* for 50:50 ($A_\mathrm{T,i}=0.05$) using the ideal-gas equation of state and continuity conditions for pressure and temperature across the interface:

$$\frac{\rho_{\text{shell}}}{\rho_{\text{fuel}}} = \frac{m_{\text{i}}^{\text{shell}}}{m_{\text{i}}^{\text{fuel}}} \frac{1 + Z_{\text{fuel}}}{1 + Z_{\text{shell}}}.$$

Unstable modes present at the material interface grow during the deceleration phase of the implosion. Linear stability analysis of RT instability growth in semi-infinite density profiles has shown that these unstable modes are local to the interface, and that within the linear growth regime, the size of the unstable region is proportional to the perturbation wavelength.[1] The amplitude of the perturbation is highest on the interface itself and decays exponentially as the distance from the interface increases. In spherical geometry, the velocity perturbations decay as $\left(r_{\text{i}}/r\right)^{\ell+2}$ for $r > r_{\text{i}}$ and $(r/r_{\text{i}})^{\ell-1}$ for $r < r_{\text{i}}$, according to the radial distance (r) from the material interface (r_{i}) and mode number (ℓ). The effective Atwood number,[2] defined as $A_{\text{T}} = \left(\rho^{+} - \rho^{-}\right)/\left(\rho^{+} + \rho^{-}\right)$, uses the mass density averaged over the perturbation region $\left(\pm r_{\text{i}}/\ell\right)$ rather than the fuel and shell densities at the material interface (c.f., $A_{\text{T,i}}$). Figure 1(b) illustrates mass-density profiles with unstable regions for $\ell = 4$ and $\ell = 40$ perturbations. During the deceleration phase, these unstable regions are influenced by x-ray radiation that is released in the DT fuel of the hot spot. This x-ray radiation is absorbed into the colder CH shell, causing the material to heat up and expand inward, and results in a thicker shell with increased density and A_{T} near the material interface. This radiation preheat effect is present in both D:T 10:90 and 50:50 targets and causes their respective effective Atwood numbers to be comparable across a range of unstable modes.

Small-amplitude ($k\eta < 1$), single-mode perturbations grow exponentially in time, and since the Atwood number affects the exponential growth rates, 10:90 experiences significantly smaller growth factors (by a factor of ~5) compared to 50:50. As perturbation amplitudes become nonlinear ($k\eta > 1$), the growth changes from exponential to linear in time[2,3] and the difference in the growth factors between 10:90 and 50:50 becomes much smaller (only ~20%). Perturbations must grow to significant levels and become nonlinear in order for target performance to be affected. This explains why target performance should have small sensitivity to the Atwood number variations used in the experiment described below.

Multiple targets were fabricated to meet the design specification based on the classical material interface $A_{\text{T,i}}$. Each target was designed to be 860 μm in diameter with 27-μm-thick CH shells and a DT fuel fill pressure of 10 atm. Additional targets were created and opened up to measure the actual fuel D:T ratios after fabrication. Significant levels of protium (^{1}H) were found and were much higher than the initial D:T fill ratios. The yield-over-clean ratios $\left(Y_{\text{exp}}/Y_{\text{1-D}}\right)$, which used post-shot 1-D simulations that included the measured fuel levels, were consistent across all D:T ratios (see Fig. 2). This suggests that each shot experienced

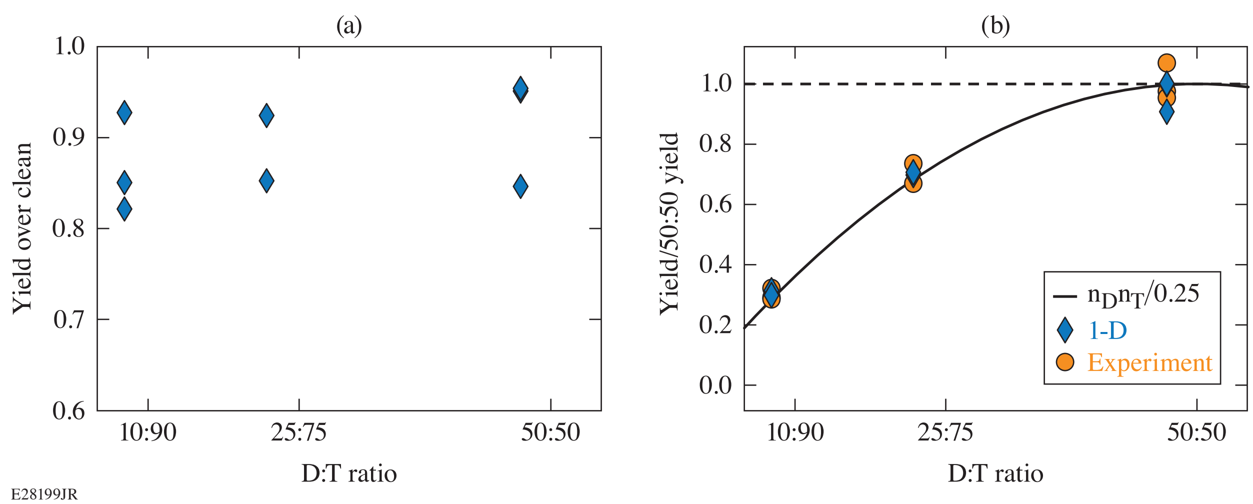

Figure 2
(a) Yield over clean $\left(Y_{\text{exp}}/Y_{\text{1-D}}\right)$ and (b) yield scaling. In (b), D:T 50:50 data points that lie above the dashed line at $y = 1.0$ indicate a higher than average yield. The solid black curve represents a simple yield scaling relation based on the DT number densities in the fuel.

the same level of asymmetry and instability growth. Additionally, the yield of each target, for both measured and simulated, scaled according to the fraction of deuterium and tritium in the fuel. Figure 2(b) illustrates the DT yield of each shot normalized to the respective (simulated or experimental) average 50:50 yield. Close clustering of the data points around the solid black curve indicates that the yield scaled according to the fuel composition.

Performance of the implosion is also assessed through inferred ion temperatures (T_i). These observations are taken from different lines of sight within the OMEGA target chamber. Ion temperature asymmetry $\left(\Delta T_i = T_i^{max} - T_i^{min}\right)$, currently taken from the set of six different neutron time-of-flight (nTOF) measurements, is used to identify significant differences in T_i caused by velocity broadening. Large ΔT_i indicates that there are significant nonradial components of velocity in the hot spot near peak neutron-production time, most likely caused by instability growth and highly directional flow variance. Figure 3 shows ΔT_i for each D:T ratio for both simulated and experimental results. Both simulated and experimentally inferred T_i indicate a comparable level of asymmetry across all D:T ratios. The experimental error bars (±100 eV) arise from the noise level in the detector signal, uncertainty in the numerical fit analysis,[4] and instrument response function of each detector.

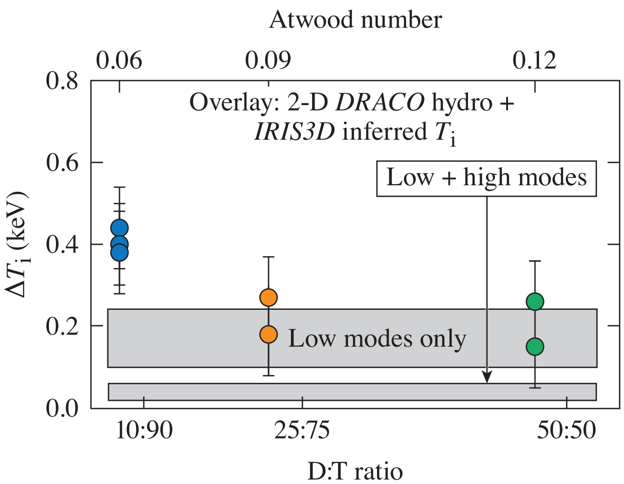

E28193JR

Figure 3
Inferred DT T_i asymmetry $\left(\Delta T_i = T_i^{max} - T_i^{min}\right)$, as a function of the D:T ratio and estimated Atwood number. The 2-D *DRACO* simulations provided the hydrodynamics and *IRIS3D*[5] provided the synthetic neutron diagnostics.

Simulations indicate that radiation preheat in all D:T ratios cause the interface to have comparable density profiles near the fuel–shell interface, and therefore similar A_T and instability growth factors. While 10:90 and 50:50 experience different linear instability growth factors for small-amplitude perturbations, nonlinear perturbations that impact target performance grow at comparable rates in either D:T configuration. In both experiments and simulations, the yield of all target configurations scales according to the composition of the fuel. Significant ΔT_i outside measurement uncertainty requires highly directional flow variance in order for detectors to observe differences from various lines of sight. Because both 10:90 and 50:50 had similar effective Atwood numbers, the simulated deceleration RT instability growth was nearly identical for nonlinear RT growth, and there was little influence on the inferred T_i and ΔT_i by altering the D:T ratio. Measurement uncertainty and noise levels make behavior trends inconclusive, and it is likely that the hot spot is relatively insensitive to changing the D:T ratio, as simulations suggest.

This material is based upon work supported by the Department of Energy National Nuclear Security Administration under Award Number DE-NA0003856, the University of Rochester, and the New York State Energy Research and Development Authority.

1. V. N. Goncharov, Phys. Rev. Lett. **88**, 134502 (2002).
2. V. N. Goncharov, "Self-Consistent Stability Analysis of Ablations Fronts in Inertial Confinement Fusion," Ph.D. thesis, University of Rochester, 1998.
3. U. Alon *et al*., Phys. Rev. Lett. **74**, 534 (1995).
4. R. Hatarik *et al*., J. Appl. Phys. **118**, 184502 (2015).
5. F. Weilacher, P. B. Radha, and C. J. Forrest, Phys. Plasmas **25**, 042704 (2018).

Simulated Refraction-Enhanced X-Ray Radiography of Laser-Driven Shocks

A. Kar, T. R. Boehly, P. B. Radha, D. H. Edgell, S. X. Hu, P. M. Nilson, A. Shvydky, W. Theobald, D. Cao, K. S. Anderson, V. N. Goncharov, and S. P. Regan

Laboratory for Laser Energetics, University of Rochester

X-ray radiography is a useful diagnostic in inertial confinement fusion (ICF) implosions to obtain shock positions by imaging shock waves. Specifically, it has been demonstrated that refraction-enhanced x-ray radiography[1] (REXR) can infer shock-wave positions of more than one shock wave, launched by a multiple-picket pulse in a planar plastic foil. REXR relies on the density gradient across a shock front that deflects x rays from their trajectory through refraction. It also accounts for the attenuation of the x rays as they travel through a denser medium with lower transmission by tracking their intensities. The benefit of this technique over existing x-ray postprocessors such as *Spect3D*[2] is that it includes x-ray refraction.

REXR is successful in overcoming some of the limitations of a velocity interferometer system for any reflector (VISAR) by locating shock waves before shocks merge and during the early time and the main drive of the laser pulse. VISAR does not provide any information about the shock wave early in time because of a time lag associated with the critical surface formation for the diagnostic to work. During the main drive, the high intensity of the laser leads to x-ray photoionization of the target ahead of the shock front. This blanks out the VISAR signal, preventing it from determining the shock wave's location.[3]

A point-projection radiography system was used to image a shock wave in a planar plastic foil on OMEGA [Fig. 1(a)]. The laser drive was comprised of a square pulse with ~350 J of energy that generated the shock wave in the foil. For the x-ray radiography, x rays of 5.2-keV energy corresponding to the He_α emissions of vanadium were projected from a 10-μm pinhole to image the shock wave onto an x-ray framing camera. The framing camera started to acquire the image at 8.63$\pm$0.1 ns after the start of the laser pulse that generated the shock. The target was placed in the middle, 14 mm away from the pinhole and 533 mm away from the x-ray framing camera. This setup was simulated using the hydrodynamic code *DRACO* and the density profiles obtained from it were used to generate the simulated radiograph in Fig. 1(b). Figure 1(c) shows that the relative degree of transmission in the unshocked plastic, shocked plastic, and shocked aluminum with respect to the vacuum was in good agreement between the experiment and REXR. REXR showed that it is necessary to incorporate refraction and attenuation of x rays along with the appropriate opacity and refractive-index tables to interpret experimental images.

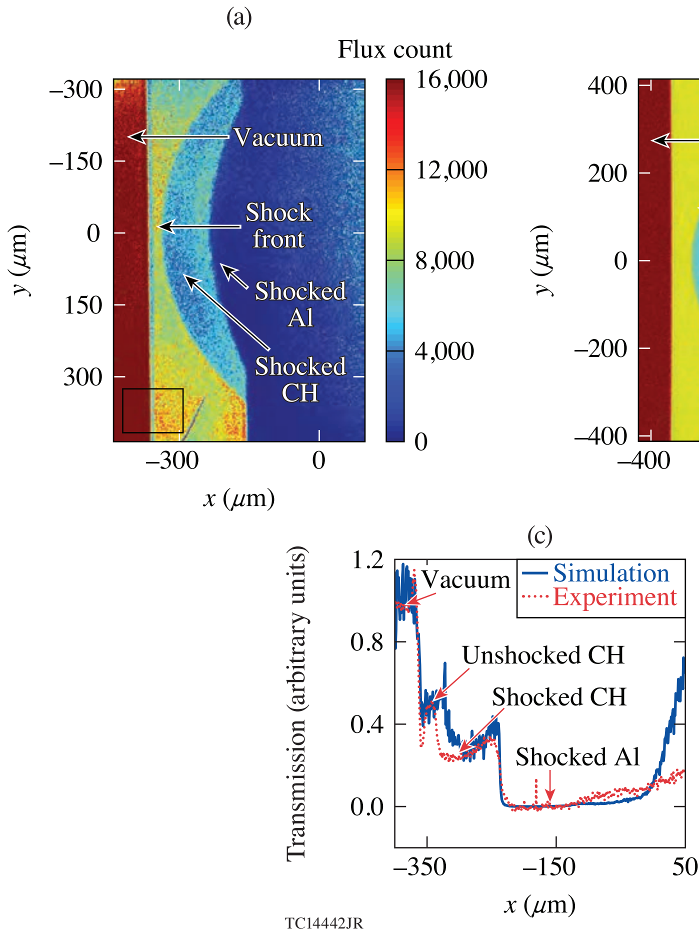

Figure 1
(a) Image obtained from an x-ray framing camera on OMEGA showing the bowing effect of the shock wave in plastic with the main features labeled. (b) Simulated radiograph for the same OMEGA experiment shows the shock profile in a plastic ablator. The x-ray flux is representative of the degree of transmission of the x rays through the different areas: vacuum (in red), unshocked plastic (in yellow), shocked plastic (in cyan), and shocked aluminum (in blue). (c) The transmission curves along the center of the beam axis obtained from the simulated radiograph and the experimental image showed good agreement between them for plastic and aluminum. For reference, the transmission in the vacuum region is set to 1 since there is no attenuation.

An experimental design to image multiple shock waves with REXR was proposed for the laser pulse in Fig. 2(a). Figure 2(b) shows the shock positions early in time and during main drive pulse that can be inferred from REXR when experimental diagnostics such as VISAR fail to locate the shock positions. REXR can be applied to design multiple-picket pulses with a better understanding of the shock locations. This will be beneficial to obtain the required adiabats for ICF implosions.

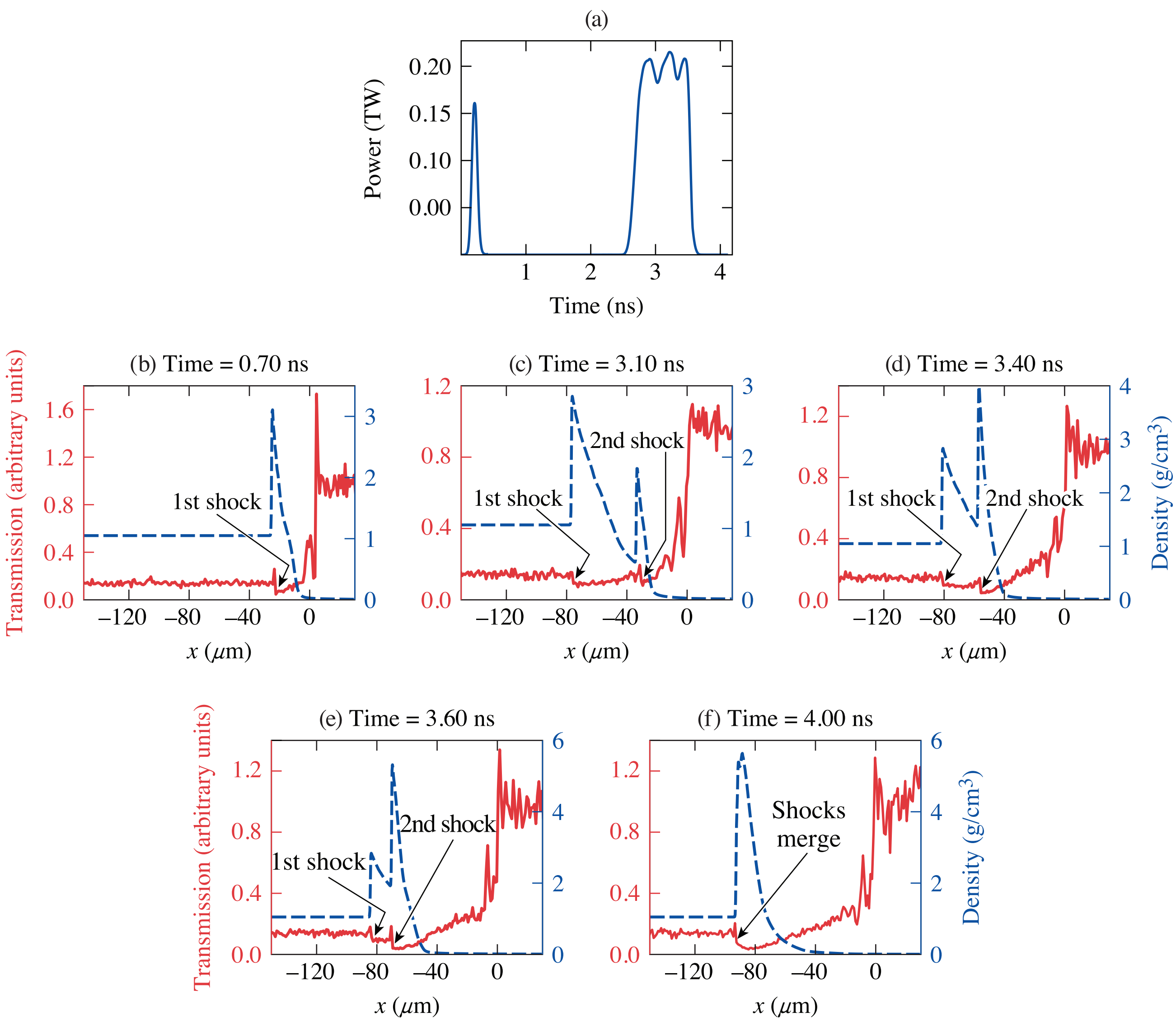

TC14448JR

Figure 2
(a) A single-picket pulse with a main drive pulse of 190-J energy that launches two shock waves whose positions were inferred. [(b)–(f)] The transmission (red) and density profiles (blue) across the center of the beam axis obtained for the pulse shape in (a). The transmission has been scaled so that the intensity in the vacuum region is 1. The spikes followed by the dip (local minimum) in the transmission curve correspond to the shock fronts as labeled. The density profile also spikes at those points to illustrate this fact.

This material is based upon work supported by the Department of Energy National Nuclear Security Administration under Award Number DE-NA0003856, the University of Rochester, and the New York State Energy Research and Development Authority.

1. J. A. Koch *et al*., J. Appl. Phys. **105**, 113112 (2009).

2. J. J. MacFarlane *et al*., High Energy Density Phys. **3**, 181 (2007).; Prism Computational Sciences Inc., Madison, WI, Report PCS-R-041, Ver. 3.0 (2002).

3. T. R. Boehly *et al*., Phys. Plasmas **13**, 056303 (2006).

Laser–Plasma Interactions Enabled by Emerging Technologies

J. P. Palastro,[1] F. Albert,[2] B. Albright,[3] T. Antonsen Jr.,[4] A. Arefiev,[5] J. W. Bates,[6] R. L. Berger,[2] J. Bromage,[1] E. M. Campbell,[1] T. Chapman,[2] E. Chowdhury,[7] A. Colaïtis,[8] C. Dorrer,[1] E. Esarey,[9] F. Fiúza,[10] N. Fisch,[11] R. K. Follett,[1] D. H. Froula,[1] S. H. Glenzer,[10] D. Gordon,[6] D. Haberberger,[1] B. M. Hegelich,[12,13] T. Jones,[6] D. Kaganovich,[6] K. Krushelnick,[14] P. Michel,[2] H. Milchberg,[4] J. Moloney,[15] W. Mori,[16] J. F. Myatt,[17] P. M. Nilson,[1] S. P. Obenschain,[6] J. L. Peebles,[1] J. Peñano,[6] M. Richardson,[18] H. G. Rinderknecht,[1] J. Rocca,[19] A. J. Schmitt,[6] C. Schroeder,[9] J. L. Shaw,[1] L. O. Silva,[20] D. Strozzi,[2] S. Suckewer,[11] A. Thomas,[14] F. Tsung,[16] D. Turnbull,[1] D. Umstadter,[21] J. Vieira,[20] J. Weaver,[6] M. S. Wei,[1] S. C. Wilks,[2] L. Willingale,[14] L. Yin,[3] and J. D. Zuegel[1]

[1]Laboratory for Laser Energetics, University of Rochester
[2]Lawrence Livermore National Laboratory
[3]Los Alamos National Laboratory
[4]University of Maryland, College Park
[5]University of California, San Diego
[6]Naval Research Laboratory
[7]Ohio State University
[8]Université de Bordeaux, Centre Lasers Intenses et Applications, France
[9]Lawrence Berkeley National Laboratory
[10]SLAC National Accelerator Laboratory
[11]Princeton University
[12]Gwangju Institute of Science and Technology, Center for Relativistic Laser Science
[13]University of Texas, Austin
[14]University of Michigan
[15]University of Arizona
[16]University of California, Los Angeles
[17]University of Alberta
[18]University of Central Florida
[19]Colorado State University
[20]Instituto Superior Técnico, Portugal
[21]University of Nebraska, Lincoln

Introduction

The recent awarding of the Nobel Prize to Donna Strickland, Ph.D., and Gerard Mourou, Ph.D., for chirped-pulse amplification (CPA) has highlighted the impact that broadband laser systems have had throughout science.[1] Plasma physics, in particular, has developed a unique synergy with CPA's: plasma has provided the only medium that can withstand the increases in intensity delivered by CPA's over the last 30 years. CPA is not, however, the only breakthrough in optics technology that has or promises to expand the frontier of laser–plasma interactions. Over the past ten years, creative optical solutions have produced unprecedented intensities, contrast, repetition rates, and gain bandwidths; renewed interest in long-wavelength drivers; and provided novel methods for spatiotemporal pulse shaping. Over the next ten years, these emerging technologies will advance diverse fields of plasma physics, including

- direct drive, indirect drive, and magnetized inertial confinement fusion
- nonperturbative nonlinear propagation and material interactions
- advanced accelerators
- plasma-based radiation sources
- ultrahigh-magnetic-field generation
- high-field and electron–positron plasmas
- structured light–plasma interactions

One such field—*plasma optics*—promises to overcome fundamental limitations of solid-state optical technology and will usher in the next frontier of plasma research. Progress and science discovery in pursuit of this frontier will require a community approach to experiments, simulations, and theory, together with investments in an ecosystem of laser facilities and simulation software.

Inertial Confinement Fusion

With the global population rising to over 9 billion by the end of the 21st century and the rising tide of climate change, the pursuit of environmentally acceptable energy sources has become more critical than ever. While still in the research stage, controlled fusion could deliver an almost endless supply of power with relatively low environmental impact. The inertial confinement fusion (ICF) approach, in particular, was one of the earliest applications to harness high-power lasers and has, on several occasions, implemented innovative optical techniques to effect step changes in performance: efficient frequency tripling, spatial coherence control (phase plates), induced spatial incoherence, and smoothing by spectral dispersion.[2–6] While these successes have allowed ICF to push the intensity ever higher, designs must still navigate around laser–plasma instabilities and laser imprint.[7,8] Laser–plasma instabilities inhibit the deposition of energy in the ablator and put the laser at risk for damage by scattering light into unwanted directions. Moreover, these instabilities can generate superthermal electrons that preheat the fusion fuel, reducing its compressibility. Laser imprint, i.e., density nonuniformities on the capsule surface imparted by speckles, seeds the Rayleigh–Taylor instability and can cause the capsule to break up during compression.

Creative uses of the bandwidth available on current laser systems may inhibit low-frequency laser–plasma instabilities like stimulated Brillouin scattering by detuning the interaction between multiple laser beams or by moving speckles before the instability can grow.[9] *Modern broad-bandwidth lasers, on the other hand, could revolutionize ICF by providing unprecedented spatiotemporal control over laser–plasma interactions.* These lasers can deliver pulses with the temporal incoherence necessary to suppress high-frequency instabilities like two-plasmon decay and stimulated Raman scattering, while also providing smoothing sufficient to eliminate imprint.[10–12] Generally speaking, the broad bandwidth mitigates laser–plasma instabilities by detuning the interaction between multiple waves or incoherently drives many small instabilities instead of a single coherent instability. To this end, optical parametric amplifiers (OPA's) offer an excellent candidate for the next-generation ICF driver. OPA's create high-power, broad-bandwidth light that can be seeded with a variety of temporal formats, including the random intensity fluctuations of parametric fluorescence, spike trains of uneven duration and delay, or chirplets.[13] The bandwidth of the resulting pulses, or those from an existing wideband architecture, could be further increased by stimulated rotational Raman scattering during propagation to the final focusing optics. Preliminary experiments have demonstrated that this technique can broaden the spectrum of frequency-multiplied Nd:glass and KrF pulses to multiterahertz bandwidths.[14]

Nonperturbative Nonlinear Propagation and Material Interactions

The field of nonperturbative nonlinear propagation and material interactions spans the boundary of nonlinear optics and plasma physics with relevant dynamics occurring over a trillion orders of magnitude in time: starting with the attosecond dynamics of bound electrons that determine the nonlinear optical response, evolving into the femto- and picosecond formation and evolution of plasma, and concluding with the micro- and millisecond hydrodynamic evolution of the neutral medium. *The emergence of high-power, high-repetition-rate (>kHz) ultrashort-pulse lasers enables novel regimes of nonlinear propagation and material interactions governed by a combination of nonthermal and thermal modifications to matter*—regimes with scientific, industrial, and security applications such as understanding new states of warm dense matter, femtosecond micromachining, laser eye surgery, electromagnetic pulse generation, and long-range propagation through atmosphere for remote sensing.

For a single high-power pulse propagating in transparent media, plasma formation counteracts the nonlinear collapse during self-focusing, leading to high-intensity propagation over distances much longer than a Rayleigh range.[15–18] At high repetition rates, each laser pulse experiences a nonlinear environment modified by its predecessors, which combines traditional effects such as thermal blooming[19] with ultrafast nonthermal effects, including ionization and impulsive (molecular) Raman excitation.[20] Already, experiments have demonstrated that a train of laser pulses can heat air through these processes, leaving behind a long-lasting neutral density channel that can guide subsequent laser pulses[21] and enhance the collection efficiency in remote detection.[22]

For high-repetition-rate material interactions, a laser pulse will interact with matter that has been strongly modified by the nonthermal heating of previous pulses. This heating can create periodic surface structures, change the reflectivity and absorption, or alter the molecular composition altogether. The interaction involves multiple physics phenomena, including the time-dependent dielectric response, stimulated scattering mechanisms, phase changes, electronic band-gap structure, and combined optical–collisional photoionization. In many of the solid and liquid media relevant to applications, the material properties governing these phenomena are not well characterized or even measured. Expanded use of spectral interferometry measurements,[23,24] as well as the pursuit of new techniques, could greatly improve understanding and facilitate the development of applications.

Plasma Accelerators

Particle accelerators provide a looking glass into a subatomic world inhabited by the fundamental building blocks of the universe. Conventional accelerators, based on vacuum technology, continue to make impressive strides, routinely improving beam quality and achieving unprecedented energies. With each advance, however, conventional accelerators grow in size or cost. Laser-plasma accelerators promise to break this trend by taking advantage of the extremely large fields either inherent to or driven by ultrashort laser pulses and a medium—plasma—that can sustain them. Armed with a vision of smaller-scale, cheaper accelerators and empowered by advances in laser technology, these "advanced accelerators" have achieved rapid breakthroughs in both electron and ion acceleration.

Early laser-wakefield acceleration (LWFA) experiments made steady progress by trapping and accelerating electrons in plasma waves excited by unmatched laser pulses—pulses with durations exceeding the plasma period.[25,26] Such pulses confined LWFA to suboptimal regimes in which plasma waves were driven either by laser pulse self-modulation or beat waves. With the advent of high-power, broadband multipass amplifiers, progress exploded—to this day, the maximum electron energy continues to climb with laser power.[27–30] These amplifiers deliver ultrashort pulses with durations less than the plasma period, allowing experiments to access the forced, quasi-linear, and bubble regimes.[31–33] Aside from increasing the maximum energy of the electron beams, the ultrashort pulses enable transformative injection techniques, through self-trapping or controlled ionization, that greatly reduced the electron beam emittance and energy spread.[34–36] *The emergence of amplifiers that can operate at both high peak and high average power provide a technological path toward a LWFA-based electron–positron collider.* While many physics and technology challenges must still be overcome, the high repetition rates of these systems could deliver the luminosity needed to achieve a number of events comparable to traditional colliders.[37]

While the large inertia of ions precludes their efficient acceleration through LWFA, a high-intensity pulse incident on a solid or shocked target can drive several mechanisms that accelerate ultrashort, high-flux ion beams from rest.[38–45] These mechanisms can be broadly separated into a few categories: ions accelerated by the sheath field of hot electrons escaping the back side of a solid target or target-normal sheath acceleration;[38,39] ions gaining energy by reflecting off a moving electrostatic potential, caused by either radiation pressure (hole boring)[40] or thermal pressure (shock acceleration);[41,42] beam-plasma modes excited during relativistic transparency;[43] solitary wave generation;[44] or hybrid schemes that combine elements of these with other mechanisms. Developments in high-power, broadband amplifiers have made sources based on these mechanisms widely accessible for a range of applications, producing ion beams with energies comparable to longer, higher-energy pulses. Proton sources, for instance, are now routinely used to radiograph high-energy-density matter, providing an invaluable probe for resolving plasma dynamics on picosecond time scales.[38,46] *Advances in laser contrast and amplifiers that operate at both high peak and high average power would represent a transformative step toward the realization of laser-driven proton/ion beams as injectors for high-brilliance accelerators and medical therapy.* When integrated with recent developments in high-repetition-rate cryogenic targets, high-repetition-rate lasers offer significantly greater control over the acceleration process and enable high-quality beams with tens to hundreds MeV and high particle flux. This integration would also provide an ideal platform for understanding the origin and evolution of magnetic instabilities in proton beams.[45]

Radiation Sources

The strong accelerations experienced by electrons in intense laser–plasma interactions unleashes a torrent of secondary radiation that spans the electromagnetic spectrum. *Leveraging increases in laser repetition rate and intensity with creative interaction configurations and plasma structuring could spark the development of plasma-based radiation sources that excel in throughput, brightness, coherence, power, or efficiency.* These plasma-based sources offer compact, low-cost alternatives to sources based on conventional accelerators that, if harnessed, could be widely accessible for applications.

The development of sources in two frequency bands in particular, x-ray and terahertz (THz), would have far-reaching benefits in medicine, defense, and basic science.[47] Laser–plasma interactions generate x rays through a number of diverse mechanisms: betatron radiation from electrons oscillating in wakefields,[48,49] bremsstrahlung emission from energetic electrons crashing into high-density matter,[50] laser photons double Doppler-upshifted by a counter-traveling, relativistic electron beam, i.e., Compton scattering,[51,52] stimulated emission of photons from relativistic electrons wiggling in a free-electron laser,[53] x-ray lasing through transient collisional excitation,[54,55] or high harmonic generation from electrons accelerated in and out of a surface by an intense laser field.[56] This diversity provides the flexibility to choose a mechanism that best meets the requirements of applications such as phase-contrast imaging, radiosurgery, lithography, and nuclear resonance fluorescence for standoff detection of radioactive or other threatening materials. On the opposite end of the spectrum, the interaction of intense laser pulses with structured plasmas can efficiently drive THz radiation. The ponderomotive force of a laser pulse excites a time-dependent current. In a nonuniform plasma, this current radiates into the far field, emitting frequencies within a band determined by the pulse duration.[57,58] This radiation could bridge the "terahertz gap"—the scarcity of sources between the frequency ranges accessible by electronics and lasers—and do so with high-power, ultrashort THz pulses. In contrast to x rays, THz radiation is non-ionizing and can be safely used for noninvasive biomedical imaging and medical tomography. Further, the energy separation of rotational–vibrational eigenstates makes THz radiation ideal for time domain spectroscopy and standoff detection of chemical and biological molecules.[59,60] In terms of discovery science, THz radiation can directly excite matter to highly excited phonon states, unlocking new regimes of high-energy-density physics.[61]

Magnetized Plasmas

Like plasmas, magnetic fields occur ubiquitously throughout the universe and play a critical role in shaping astrophysical environments. Emulating these environments in the laboratory with well-diagnosed experiments can provide a valuable complement to conventional astrophysical observations. High-power lasers facilitate these experiments by creating scale-equivalent plasma conditions with self-generated or external magnetic fields, or by directly driving up magnetic fields through laser–plasma interactions. Either way, the magnetic fields fundamentally alter the laser–plasma interaction. The presence of ultrastrong, quasistatic magnetic fields modifies the microscopic kinetics by diverting, confining, or undulating electrons; the collective behavior by bringing the cyclotron resonance within reach of optical excitation; and laser propagation through peculiar dispersive effects such as polarization rotation, slow light, and induced transparency.

The capability to perform controlled, focused experiments by generating strong magnetic fields with lasers has only recently emerged. The current approach, based on existing laser technology, uses a long, high-energy pulse to drive a current through induction coils. Aside from basic laboratory astrophysics, these platforms allow one to investigate magnetized high-energy-density physics related to the transport of high-energy particles and high-gain ICF schemes like fast ignition.[62] *The projected intensities delivered by next-generation laser systems could directly drive volumetric magnetic fields rivaling those occurring on the surface of neutron stars (~MT).* These extreme fields, created by the highly nonlinear currents driven by an intense laser pulse propagating through a relativistically transparent, high-density plasma, would result in a number of immediate breakthroughs:[63–65] they would significantly enhance the transfer of energy from a laser pulse to electrons and facilitate the emission of gamma rays from relativistic electrons by providing a powerful undulator.[64,66] The development of such a gamma-ray source would be critical for the development of nuclear and radiological detection systems. Furthermore, the gamma-ray source would enable discoveries linked to our understanding of the early universe and high-energy astrophysics, including the direct creation of matter and antimatter from light[67] and allow the direct control and study of nuclear excitation and structure.[68]

High Field and Electron–Positron Plasmas

Nonperturbative quantum electrodynamics (QED) represents the current frontier of laser–plasma interactions—a frontier in which ripping electron–positron pairs from the Dirac sea may make targets a thing of the past[69]—a frontier in which vacuum exhibits magnetization, polarization and birefringence[67]—a frontier in which the analogy of Hawking radiation in electric fields, Unruh radiation, could provide insight into the life-cycle of black holes.[70] Compared to any other physical theory, perturbative QED predictions have been experimentally confirmed to unprecedented accuracy. While electric fields strong enough to accelerate an electron to its rest mass over a Compton wavelength, i.e., at the Schwinger limit, are sufficient to test nonperturbative QED models, creative laser-plasma configurations can create highly nonlinear environments at much lower field strengths. This strategy has already proven successful in experimental demonstrations of nonlinear Compton scattering,[71] positron production,[72,73] and radiation reaction.[74] Nevertheless, the exotic theoretical and computational predictions of nonperturbative QED models have rapidly outpaced the experimental capabilities to test them. *By providing flexible laser-plasma configurations and extremely high intensities, a next-generation laser could access unexplored regimes of nonperturbative, collective QED effects in plasmas and test the exotic predictions of the models.* Such a facility could bring the mysteries of astrophysical objects, including black holes, pulsars, and magnetars, down to earth and uncover the dynamic interaction of inner shell electrons with highly ionized, heavy nuclei.[75,76]

Structured Light–Plasma Interactions

Beyond simply adjusting parameters like intensity and frequency, the spatiotemporal structure of light offers additional degrees of freedom for controlling the interaction of intense laser pulses with plasma. Structured light fields emerge spontaneously when two or more electromagnetic plane waves interfere. The interference of three waves, for instance, can produce phase singularities, which give rise to one of the most fascinating features of structured light—orbital angular momentum (OAM). OAM pulses can impart angular momentum to the plasma, modifying the topology and dispersion of driven waves and the phase space of the charged particles they accelerate.[77,78] As an example, a laser pulse with a helical intensity profile, or "light spring," can ponderomotively excite a wakefield that traps and accelerates a vortex electron beam, i.e., a beam that rotates around the optical axis.[78] OAM can also modify the nonlinear propagation and interaction of high-power pulses with transparent media, resulting in helical plasma filaments or high harmonic radiation with vortex phase structure.[79,80]

More-complex interference patterns exhibit striking properties that appear to violate special relativity: the peak intensity of a self-accelerating light beam follows a curved trajectory in space,[81] while the peak intensity of a "flying focus" pulse can travel at an arbitrary velocity, surpassing even the vacuum speed of light.[82] These arbitrary velocity intensity peaks result from the chromatic focusing of a chirped laser pulse. The chromatic aberration and chirp determine the location and time at which each frequency component within the pulse comes to focus, i.e., reaches its peak intensity, respectively. By adjusting the chirp, the velocity of the intensity peak can be tuned to any value, either co- or counter-propagating along the laser axis. This, in turn, grants control over the velocity of an ionization front or ponderomotive force—a control with the potential to advance several plasma-based applications, including Raman amplification, photon acceleration, wakefield acceleration, and THz generation.[83,84] While these unexpected features of structured light bring about new and rich laser–plasma interactions, they have remained relatively unexplored because of the technological challenges of creating such pulses. *The further development of ultrafast pulse-shaping techniques to manipulate the spatiotemporal degrees of freedom would provide a virtual forge for creating pulses to optimize or bring about novel laser–plasma interactions.* In doing so, these techniques would enrich all of the subfields discussed above.

Plasma Optics

Ultimately, advances in plasma physics will require repetition rates or intensities that exceed the damage limitations of solid-state optical components. Even with improvements in high-damage optical coatings, the size of solid-state optical components must increase to maintain tolerable fluences. Aside from the prohibitive cost of such large optics, this approach will eventually become counteractive: larger optics can withstand higher powers, but their fabrication introduces surface aberrations that reduce focusability and, as a result, the peak intensity. *Plasma-based optical components could provide the disruptive technology* *needed to usher in the next frontier of plasma research*. Plasma optics, being already ionized, have substantially higher damage thresholds than solid-state components and can be inexpensively and rapidly replaced, for instance, at the repetition rate of a gas jet or capillary or the flow rate of a water jet.[85–89]

Similar to conventional optics, a laser pulse propagating in plasma acquires a spatiotemporal phase determined by the refractive index. By controlling the spatial variation, evolution, or nonlinearity of the plasma density, the plasma can provide dispersion, refraction, or frequency conversion, respectively, and, in principle, be made to mimic any solid-state optical component. Already, several such components routinely improve experimental performance: plasma gratings successfully tune the implosion symmetry of ICF capsules at the National Ignition Facility;[90] plasma waveguides combat diffraction, extending the interaction length in LWFA's;[91] and plasma mirrors (1) enhance intensity contrast by orders of magnitude, allowing for impulsive laser–matter interactions free of premature heating[92] and (2) redirect laser pulses in multistage LWFA's without degrading electron-beam emittance.[93] Several other plasma components, while still in the nascent stages of development, have been successfully demonstrated in experiments: lenses,[94,95] wave plates,[96] q-plates,[97] beam combiners,[98] compressors, and amplifiers.[99] Plasma amplifiers, in particular, could eventually replace CPA's in the final power-amplification stage of a laser, eliminating the need for large, expensive gratings.[100] In principle, these amplifiers can achieve intensities $10^3\times$ larger than CPA's in the infrared or operate in wavelength regimes inaccessible to CPA's altogether, e.g., the ultraviolet or x-ray range.[101] A next-generation high-power laser that implemented plasma components could deliver extremely high intensity pulses—pulses that would transform the landscape of laser–plasma interactions.

This material is based upon work supported by the Department of Energy National Nuclear Security Administration under Award Number DE-NA0003856, the University of Rochester, and the New York State Energy Research and Development Authority.

1. D. Strickland and G. Mourou, Opt. Commun. **55**, 447 (1985).
2. R. S. Craxton, IEEE J. Quantum Electron. **QE-17**, 1771 (1981).
3. J. Nuckolls *et al*., Nature **239**, 139 (1972).
4. Y. Kato and K. Mima, Appl. Phys. B **29**, 186 (1982).
5. R. H. Lehmberg, A. J. Schmitt, and S. E. Bodner, J. Appl. Phys. **62**, 2680 (1987).
6. S. Skupsky *et al*., J. Appl. Phys. **66**, 3456 (1989).
7. W. L. Kruer, *The Physics of Laser Plasma Interactions*, Frontiers in Physics, Vol. 73, edited by D. Pines (Addison-Wesley, Redwood City, CA, 1988).
8. S. E. Bodner, Phys. Rev. Lett. **33**, 761 (1974).
9. L. Divol, Phys. Rev. Lett. **99**, 155003 (2007).
10. J. W. Bates *et al*., Phys. Rev. E **97**, 061202 (2018).
11. R. K. Follett *et al*., Phys. Rev. Lett. **120**, 135005 (2018).
12. J. P. Palastro *et al*., Phys. Plasma **25**, 123104 (2018).
13. G. Cerullo and S. De Silvestri, Rev. Sci. Instrum. **74**, 1 (2003).
14. J. Weaver *et al*., Appl. Opt. **56**, 8618 (2017).
15. A. Couairon and A. Mysyrowicz, Phys. Rep. **441**, 47 (2007).
16. H. M. Milchberg *et al*., Phys. Plasma **21**, 100901 (2014).
17. P. Panagiotopoulos *et al*., Nat. Photonics **9**, 543 (2015).
18. S. Tochitsky *et al*., Nat. Photonics **13**, 41 (2019).

19. K. A. Brueckner and S. Jorna, Phys. Rev. **164**, 182 (1967).

20. J. P. Palastro, T. M. Antonsen, and H. M. Milchberg, Phys. Rev. A **86**, 033834 (2012); **90**, 069902(E) (2014).

21. N. Jhajj *et al*., Phys. Rev. X **4**, 011027 (2014).

22. E. W. Rosenthal *et al*., Optica **1**, 5 (2014).

23. Z. W. Wilkes *et al*., Appl. Phys. Lett. **94**, 211102 (2009).

24. T. Winkler *et al*., Appl. Surf. Sci. **374**, 235 (2016).

25. A. Modena *et al*., Nature **377**, 606 (1995).

26. E. Esarey, C. B. Schroeder, and W. P. Leemans, Rev. Mod. Phys. **81**, 1229 (2009).

27. T. Katsouleas, Nature **431**, 515 (2004).

28. X. Wang *et al*., Nat. Commun. **4**, 1988 (2012).

29. H. T. Kim *et al*., Phys. Rev. Lett. **111**, 165002 (2013).

30. W. P. Leemans *et al*., Phys. Rev. Lett. **113**, 245002 (2014).

31. V. Malka *et al*., Science **298**, 1596 (2002).

32. W. Lu *et al*., Phys. Rev. Lett. **96**, 165002 (2006).

33. W. Lu *et al*., Phys. Rev. ST Accel. Beams **10**, 061301 (2007).

34. D. H. Froula *et al*., Phys. Rev. Lett. **103**, 215006 (2009).

35. A. Pak *et al*., Phys. Rev. Lett. **104**, 025003 (2010).

36. C. McGuffey *et al*., Phys. Rev. Lett. **104**, 025004 (2010).

37. C. B. Schroeder *et al*., AIP Conf. Proc. **1086**, 208 (2009).

38. M. Roth *et al*., Phys. Rev. Spec. Top., Accel. Beams **5**, 061301 (2002).

39. L. Willingale *et al*., Phys. Rev. Lett. **96**, 245002 (2006).

40. A. Henig *et al*., Phys. Rev. Lett. **103**, 245003 (2009).

41. D. Haberberger *et al*., Nat. Phys. **8**, 95 (2012).

42. F. Fiuza *et al*., Phys. Rev. Lett. **109**, 215001 (2012).

43. L. Yin *et al*., Phys. Plasma **18**, 063103 (2011).

44. D. Jung *et al*., Phys. Rev. Lett. **107**, 115002 (2011).

45. S. Göde *et al*., Phys. Rev. Lett. **118**, 194801 (2017).

46. L. Willingale *et al*., Phys. Plasmas **17**, 043104 (2010).

47. F. Albert and A. G. R. Thomas, Plasma Phys. Control. Fusion **58**, 103001 (2016).

48. F. Albert *et al*., Phys. Rev. Lett. **111**, 235004 (2013).

49. J. P. Palastro, D. Kaganovich, and D. Gordon, Phys. Plasma **22**, 063111 (2015).

50. N. Lemos *et al*., Plasma Phys. Control. Fusion **60**, 054008 (2018).

51. S. Chen *et al*., Phys. Rev. Lett. **110**, 155003 (2013).

52. N. D. Powers *et al*., Nat. Photonics **8**, 28 (2014).

53. A. R. Maier *et al*., Phys. Rev. X **2**, 031019 (2012).

54. B. R. Benware *et al*., Phys. Rev. Lett. **81**, 5804 (1998).

55. Y. Wang *et al*., Nat. Photonics **2**, 94 (2008).

57. J. M. Mikhailova *et al*., Phys. Rev. Lett. **109**, 245005 (2012).

57. C. Miao, J. P. Palastro, and T. M. Antonsen, Phys. Plasma **23**, 063103 (2016).

58. C. Miao, J. P. Palastro, and T. M. Antonsen, Phys. Plasma **24**, 043109 (2017).

59. J. F. Federici *et al*., Semicond. Sci. Technol. **20**, S266 (2005).

60. H. Liu *et al*., Proc. IEEE **95**, 1514 (2007).

61. M. Kozina *et al*., Nat. Phys. **15**, 387 (2019).

62. G. Fiksel *et al*., Rev. Sci. Instrum. **86**, 016105 (2015).

63. J. Peebles *et al*., Phys. Rev. E **98**, 053202 (2018).

64. O. Jansen *et al*., Plasma Phys. Control. Fusion **60**, 054006 (2018).

65. T. Wang *et al*., Phys. Plasma **26**, 013105 (2019).

66. D. J. Stark, T. Toncian, and A. V. Arefiev, Phys. Rev. Lett. **116**, 185003 (2016).

67. M. Marklund and P. K. Shukla, Rev. Mod. Phys. **78**, 591 (2006).

68. D. Habs *et al*., Eur. Phys. J. D **55**, 279 (2009).

69. N. B. Narozhny and A. M. Fedotov, Eur. Phys. J. Spec. Top. **223**, 1083 (2014).

70. P. Chen and G. Mourou, Phys. Rev. Lett. **118**, 045001 (2017).

71. C. Bula *et al*., Phys. Rev. Lett. **76**, 3116 (1996).

72. H. Chen *et al*., Phys. Rev. Lett. **102**, 105001 (2009).

73. G. Sarri *et al*., Nat. Commun. **6**, 6747 (2015).

74. J.M. Cole *et al*., Phys. Rev. X **8**, 011020 (2018).

75. G. Brodin *et al*., Phys. Rev. Lett. **98**, 125001 (2007).

76. B. Hafizi, D. F Gordon, and J. P Palastro, Phys. Rev. Lett. **118**, 133201 (2017).

77. J. Vieira *et al*., Nat. Commun. **7**, 10371 (2016).

78. J. Vieira, J. T Mendonça, and F. Quéré, Phys. Rev. Lett. **121**, 054801 (2018).

79. N. Barbieri *et al*., Appl. Phys. Lett. **104**, 261109 (2014).

80. F. Sanson *et al*., Opt. Lett. **43**, 2780 (2018).

81. G. A. Siviloglou *et al*., Phys. Rev. Lett. **99**, 213901 (2007).

82. D. H. Froula *et al*., Nat. Photonics **12**, 262 (2018).

83. J. P. Palastro *et al*., Phys. Rev. A **97**, 033835 (2018).

84. D. Turnbull *et al*., Phys. Rev. Lett. **120**, 024801 (2018).

85. H. Sheng *et al*., Phys. Rev. E **72**, 036411 (2005).

86. D. Kaganovich *et al*., Phys. Rev. E **59**, R4769 (1999).

87. D. Panasenko *et al*., J. Appl. Phys. **108**, 044913 (2010).

88. D. F. Gordon *et al*., Phys. Plasmas **25**, 063101 (2018).

89. D. Kaganovich *et al*., Appl. Opt. **57**, 9392 (2018); **58**, 368(E) (2019).

90. P. Michel *et al*., Phys. Plasmas **17**, 056305 (2010).

91. C. G. Durfee and H. M. Milchberg, Phys. Rev. Lett. **71**, 2409 (1993).

92. A. Lévy *et al*., Opt. Lett. **32**, 310 (2007).

93. S. Steinke *et al*., Nature **530**, 190 (2016).

94. Y. Katzir *et al*., Appl. Phys. Lett. **95**, 031101 (2009).

95. J. P. Palastro *et al*., Phys. Plasmas **22**, 123101 (2015).

96. D. Turnbull *et al*., Phys. Rev. Lett. **116**, 205001 (2016).

97. K. Qu, Q. Jia, and N. J. Fisch, Phys. Rev. E **96**, 053207 (2017).

98. R. K. Kirkwood *et al*., Nat. Phys. **14**, 80 (2018).

99. Y. Ping *et al*., Phys. Rev. E **62**, R4532 (2000).

100. V. M. Malkin, G. Shvets, and N. J. Fisch, Phys. Rev. Lett. **82**, 4448 (1999).

101. V. M. Malkin, N. J. Fisch, and J. S. Wurtele, Phys. Rev. E **75**, 026404 (2007).

A Modified Technique for Laser-Driven Magnetic Reconnection

P. M. Nilson,[1] W. Fox,[2,3] J. Matteucci,[3] and D. H. Froula[1,4]

[1]Laboratory for Laser Energetics, University of Rochester
[2]Princeton Plasma Physics Laboratory
[3]Department of Astrophysical Sciences, Princeton University
[4]Department of Physics & Astronomy, University of Rochester

For over a decade, numerous experimental and computational studies have investigated magnetic reconnection in high-energy-density plasmas.[1–3] An improved understanding of the reconnection theory and its application to extreme astrophysical environments and controlled fusion motivates these studies. One method for driving reconnection uses the collision between two laser-produced plasmas at the surface of a solid target. As the plasmas expand, the oppositely oriented Biermann fields are forced together and reconnect. In all previous studies, the plasmas were generated up to several laser-spot diameters apart, allowing time for the plasmas to expand and the Biermann fields to grow before colliding and forcing reconnection at their outermost edges.

In this work, a modified technique for driving reconnection is proposed and demonstrated. Two high-energy laser pulses were focused to 2×10^{14} W/cm^2 and pointed one laser-spot diameter apart on the surface of a thick plastic foil. The closer spot separation minimizes the time for plasma expansion before the interaction occurs and allows the largest magnetic fields at the edge of each laser spot to interact and reconnect. Proton radiography was used to demonstrate the technique by mapping the changes in magnetic connectivity at the target surface. The data show where the magnetic fields are located, where they are transported to, how they merge and reconnect, and where they reside post reconnection.

Figure 1 shows the experimental setup carried out on the OMEGA EP Laser System. Two long-pulse beams with a 351-nm wavelength were focused on the surface of a 5×5-mm^2, 50-μm-thick plastic foil. Each beam delivered 2 kJ of energy in a 2.5-ns square pulse focused to an 820-μm-diam focal spot. The laser intensity was 2×10^{14} W/cm^2 and each laser beam included distributed phase plates. The main target interaction was probed with an ultrafast proton beam. The protons were accelerated from a 20-μm-thick Cu foil mounted inside a plastic tube facing the main target. The Cu foil was irradiated at normal incidence with

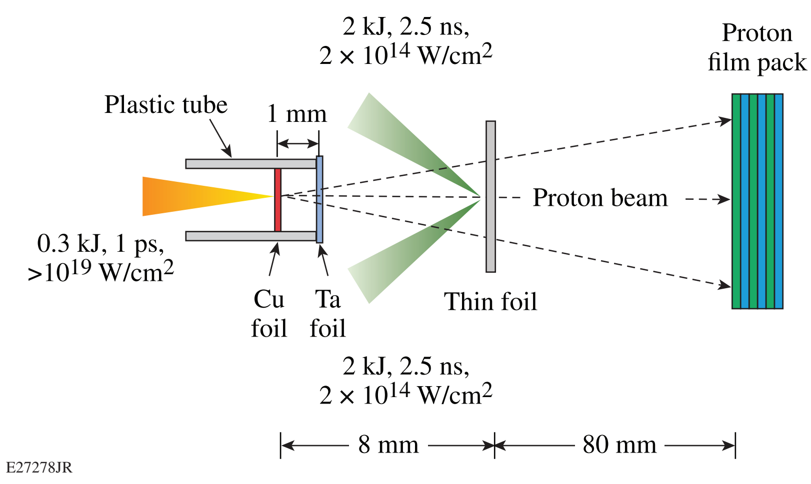

Figure 1
Experimental setup.

a 0.3-kJ, 1-ps pulse of 1.053-μm light at focused intensities above 10^{19} W/cm^2. A proton beam with energies up to several tens of MeV was accelerated by target normal sheath acceleration. To protect the rear surface of the Cu foil from the coronal plasma and x-ray preheat generated by the long-pulse interaction, a 5-μm-thick Ta foil was used to cap the end of the plastic tube. A filtered radiochromic film detector stack was used to measure the proton beam after it traversed the main target interaction.

Figure 2 shows proton radiographs of a series of two-beam interactions with a laser-spot separation of one focal-spot diameter (~820 μm). The laser pulses were co-timed. Data are shown at eight different times between $t = t_0 + 0.17$ ns and $t = t_0 + 1.97$ ns. Each time interval was measured on a different shot. The images were generated with 29-MeV protons. At $t = t_0 + 0.17$ ns [Fig. 2(a)], the radiograph shows a pair of dark rings consistent with two distinct Biermann fields at the edge of each laser focal region.[4] These dark rings remain continuous and physically separate at $t = t_0 + 0.27$ ns [Fig. 2(b)]. The plasmas have begun to merge at $t = t_0 + 0.37$ ns [Fig. 2(c)], and the detected proton flux at the intersection point is diminished. Over the next 800 ps, the inner dark rings progressively transform into a continuous oval-like pattern [Figs. 2(c)–2(f)]. This changing pattern is consistent with a transition from two isolated Biermann fields into a single global magnetic field that surrounds the laser focal regions. Post reconnection, the change in magnetic connectivity is sustained and the dark oval pattern is measured at $t = t_0 + 1.47$ ns [Fig. 2(g)] and $t = t_0 + 1.97$ ns [Fig. 2(h)].

The work described here uses a simple but crucial modification to the conventional laser-driven reconnection geometry that has significant physical implications. Compared to the original laser-driven reconnection technique, the geometry modifies where, when, and how magnetic reconnection occurs. The interaction between the neighboring plumes occurs earlier in time, the distance the largest magnetic fields must be transported before the reconnection layer forms is reduced, and the driven-reconnection process is less perturbed by plasma accumulation at the midplane. Most notably, the geometry allows for field-line reconnection

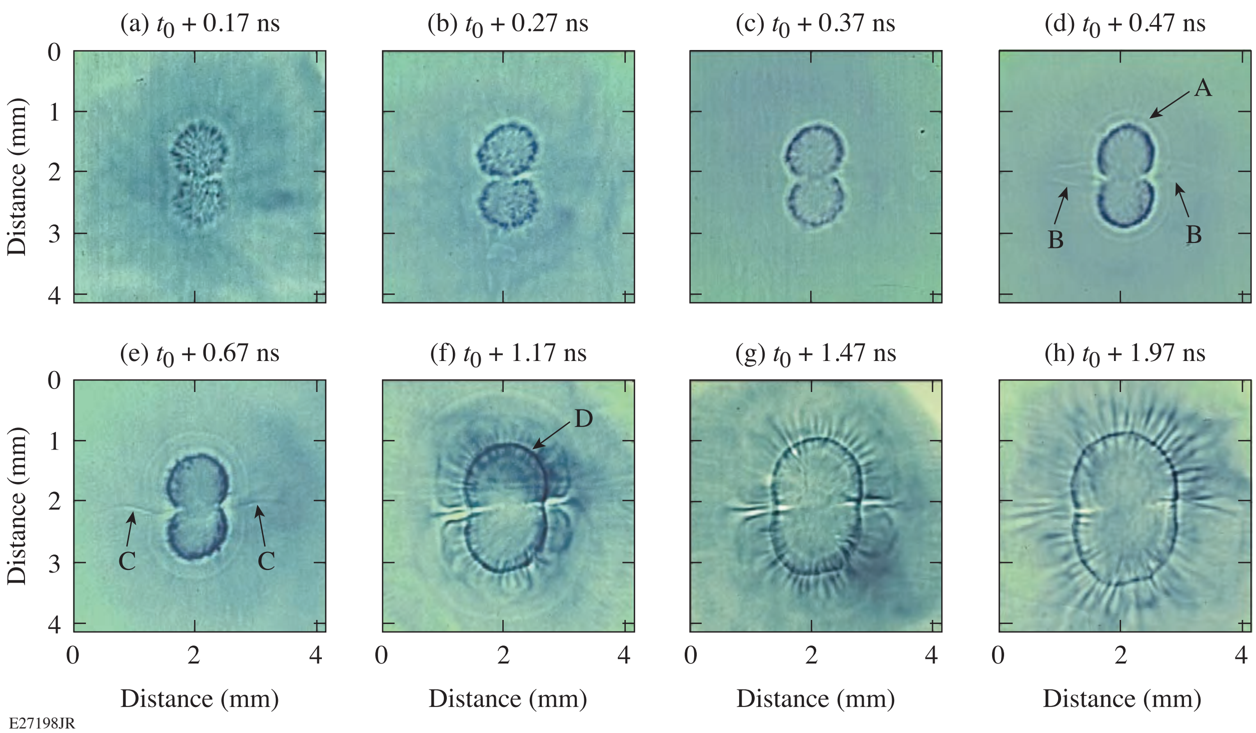

Figure 2
Proton radiographs of two-beam interactions with 50-μm-thick plastic foils taken at eight different times. Diagnostic signatures of the plasma–vacuum boundary (A), outflowing plasma (B and C), and magnetic fields (D) close to the laser focal regions are highlighted.

of the largest-magnitude magnetic fields that are generated at the edge of each laser spot, unhindered by stagnating plasma flows. It is important to note that no previous studies have identified this possibility or attempted to drive reconnection at such close laser-spot separation.

This material is based upon work supported by the Department of Energy National Nuclear Security Administration under Award Number DE-NA0003856, the University of Rochester, and the New York State Energy Research and Development Authority.

1. P. M. Nilson *et al*., Phys. Rev. Lett. **97**, 255001 (2006).
2. C. K. Li *et al*., Phys. Rev. Lett. **99**, 055001 (2007).
3. W. Fox, A. Bhattacharjee, and K. Germaschewski, Phys. Rev. Lett. **106**, 215003 (2011).
4. L. Gao *et al*., Phys. Rev. Lett. **114**, 215003 (2015).

Mitigation of Self-Focusing in Thomson-Scattering Experiments

A. M. Hansen, D. Turnbull, J. Katz, and D. H. Froula

Laboratory for Laser Energetics, University of Rochester

Accurately diagnosing plasma conditions is vital to the success of a wide variety of high-energy-density physics experiments. Optical Thomson scattering from collective ion-acoustic and electron wave features offers a method of measuring plasma parameters with spatial and temporal resolution. Analysis of Thomson-scattered spectra reveals an abundance of useful data including electron density, electron temperature, ion temperature, ionization state, ion species composition, bulk flow velocity, and heat flux.

A challenge associated with Thomson-scattering measurements arises from the small scattering cross section. To overcome this challenge, a high-energy probe laser beam is required to measure single-shot Thomson-scattering spectra with acceptable signal-to-noise ratio (SNR), but in order for the laser beam to propagate through the plasma, its power must remain below the self-focusing threshold,

$$P_{\mathrm{c}}(W) = 3 \times 10^7 \frac{T_{\mathrm{e}}(\mathrm{keV})}{n_{\mathrm{e}}/n_{\mathrm{c}}}, \tag{1}$$

where T_{e} is the electron temperature and $n_{\mathrm{e}}/n_{\mathrm{c}}$ is the electron density normalized to the critical plasma density for the wavelength of the Thomson-scattering laser.

Figure 1 shows the limitations of the Thomson-scattering SNR introduced by limiting the incident probe laser power to the threshold for self-focusing. The region below the curves has a reduced SNR because of the lower-than-optimum incident laser power. Increasing the laser power to raise the SNR above the curves results in self-focusing. The small SNR demonstrates the challenges

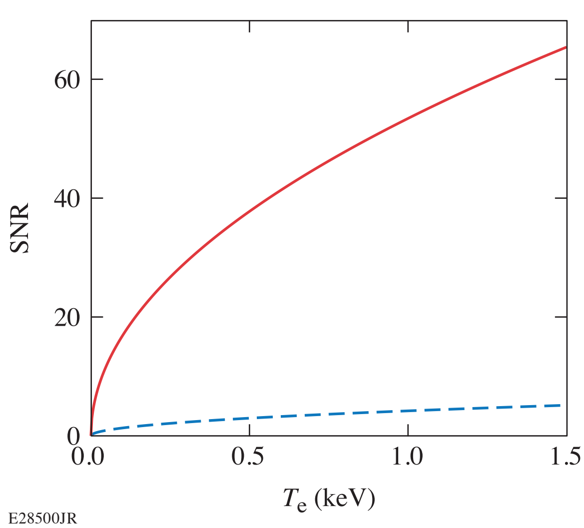

Figure 1
The curves represent the maximum measurable signal-to-noise ratio achievable in a Thomson-scattering experiment as a function of electron temperature assuming a Thomson-scattering probe beam with a power equal to the critical power for self-focusing for a beam with (dashed) and without (solid) a phase plate.

of obtaining high-fidelity Thomson-scattering spectra. The SNR can be improved by a factor of 10 by using a distributed phase plate (DPP). A DPP increases the filamentation threshold by distributing the laser's power across many lower power speckles.

Two-dimensional Thomson-scattering measurements (Fig. 2) show the limits of probe-beam propagation that are consistent with the limitations of self-focusing [Eq. (1)]. For experiments above the self-focusing threshold [Fig. 2(a)], the Thomson-scattering beam was observed to self-focus and no Thomson-scattering signals were observed from the Thomson-scattering volume located at the center (0, 0). By introducing a phase plate to the Thomson-scattering beam [Fig. 2(c)], excellent laser beam propagation was observed along with high-SNR Thomson-scattering spectra. The electron plasma and ion-acoustic wave features were measured, and these spectra were used to determine the electron density, temperature, and flow velocity as a function of time and space in a gas-jet plasma heated by a total of 1.8 kJ of laser energy on the OMEGA laser. The results show very uniform 1.5-mm density and temperature plateaus, which are ideally suited for future laser–plasma interaction experiments.

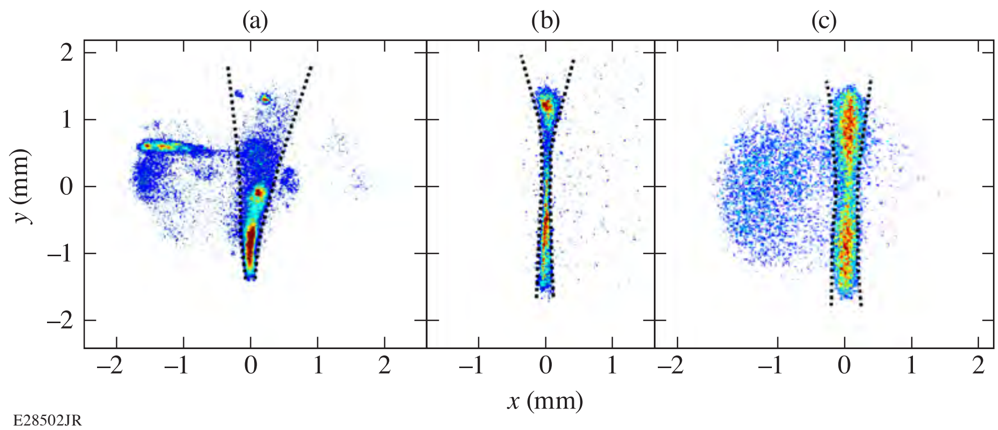

Figure 2
Two-dimensional images of Thomson-scattered light from a 2ω probe beam propagating through a gas-jet plasma (propagates from bottom to top). (a) No DPP, $P/P_c = 100$, $n_e = 4 \times 10^{20}$ cm^{-3}, $P = 45$ GW; (b) no DPP, $P/P_c = 4$, $n_e = 4 \times 10^{19}$ cm^{-3}, $P = 15$ GW; and (c) with DPP, $P/P_{c;DPP} = 0.1$, $n_e = 2 \times 10^{20}$ cm^{-3}, $P = 40$ GW.

This material is based upon work supported by the Department of Energy National Nuclear Security Administration under Award Number DE-NA0003856, the University of Rochester, and the New York State Energy Research and Development Authority.

Thresholds of Absolute Instabilities Driven by a Broadband Laser

R. K. Follett,[1] J. G. Shaw,[1] J. F. Myatt,[2] C. Dorrer,[1] D. H. Froula,[1] and J. P. Palastro[1]

[1]Laboratory for Laser Energetics, University of Rochester
[2]Department of Electrical and Computer Engineering, University of Alberta, Canada

In direct-drive inertial confinement fusion (ICF), a millimeter-scale spherical capsule is uniformly illuminated by symmetrically oriented laser beams.[1] The lasers ablate the outer layer of the capsule, which generates pressure to implode the fuel. The primary mechanism by which laser energy is converted into thermal energy in the ablator is through electron–ion collisional absorption, but a number of parametric instabilities can also occur when the lasers interact with the plasma corona of the imploding capsule, many of which can adversely affect the quality of the implosion.

Of particular importance are the stimulated Raman scattering (SRS) and two-plasmon–decay (TPD) instabilities, which correspond to the decay of an incident electromagnetic wave into an electromagnetic wave and an electron plasma wave (EPW) or into two EPW's, respectively.[2] The resulting high-phase-velocity EPW's can accelerate electrons to high energies. These energetic electrons can deposit their energy in the cold fuel, reducing the compressibility of the capsule.

It has long been known that introducing bandwidth into the drive lasers reduces the homogeneous growth rate for these instabilities,[3] and it has been shown analytically that bandwidth can increase the thresholds for absolute SRS and TPD.[4] There are no existing lasers, however, with sufficient energy and bandwidth to demonstrate instability suppression in ICF experiments. Optical parametric amplification of a broadband seed beam using a high-energy monochromatic pump beam provides a potential path toward high-energy broadband lasers. As an alternative, recent experiments have successfully demonstrated that stimulated rotational Raman scattering can increase the bandwidth of high-energy lasers.[5]

This summary presents a numerical study of absolute instability thresholds for SRS and TPD using a broadband pump beam. The calculations suggest that the absolute thresholds can be increased significantly with ~1% bandwidth at ICF-relevant conditions. Several different field spectra are considered, and it is found that the coherence time of the laser is the predominant factor in determining the effectiveness of a given pump spectrum.

Figure 1 shows absolute instability thresholds for SRS and TPD as a function of the laser period over the laser coherence time for Gaussian, Lorentzian, flat, and Kubo–Anderson process (KAP) power spectra (KAP bandwidth corresponds to a laser field that has a constant intensity but undergoes random Poisson-distributed phase jumps). The thresholds were calculated using the laser–plasma simulation environment (*LPSE*). The coherence time was defined as $\tau_c = \int_{-\infty}^{\infty} |g(\tau)|^2 \mathrm{d}\tau$, where $g(\tau) \equiv \left\langle E_0^*(t) E_0(t+\tau) \right\rangle \big/ \left\langle |E_0(t)|^2 \right\rangle$ and E_0 is the electric field of the pump beam. The thresholds are normalized to the analytic thresholds for a monochromatic pump[6,7]

$$I_{\mathrm{thr,SRS}}\left(10^{14}\ \mathrm{W/cm}^2\right) = \frac{858}{\left[L_\mathrm{n}(\mu\mathrm{m})\right]^{4/3}\left[\lambda_0(\mu\mathrm{m})\right]^{2/3}}, \tag{1}$$

where L_n is the density scale length and λ_0 is the pump central wavelength.

As a function of coherence time, the thresholds for the various power spectra shown in Fig. 1 exhibit a universal scaling. This demonstrates that the pump coherence time is the predominant factor in determining how effective a laser with a given power spectrum will be for instability suppression. Despite being the only field spectrum that does not have amplitude modulation in the time domain, KAP bandwidth results in nearly the same thresholds as the other spectra, which indicates that amplitude modulation does not significantly impact the absolute threshold.

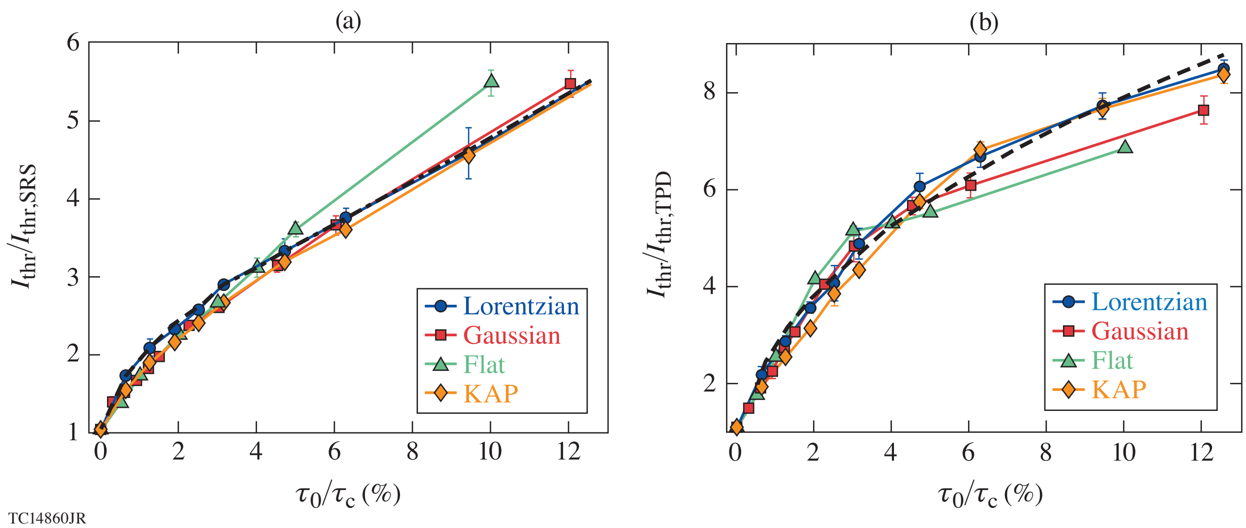

Figure 1
Absolute (a) SRS and (b) TPD thresholds from *LPSE* simulations plotted in terms of the laser period over the coherence time for an $L_n = 208$-μm scale length plasma with an electron temperature of $T_e = 2$ keV. The various field spectra are represented by blue circles (Lorentzian), red squares (Gaussian), green triangles (flat), and yellow diamonds (KAP). The error bars correspond to the standard deviation from four-run ensembles varying the random-number–generator seed for the pump spectra. τ_0 is the laser period.

Approximate scaling laws for the absolute instability thresholds were obtained by systematically varying the laser bandwidth, density scale length, central wavelength, and electron temperature:

$$I^{\tau}_{\mathrm{thr,SRS}}\left(10^{14}\ \mathrm{W/cm^2}\right) \approx \frac{798}{L_n(\mu\mathrm{m})\,\lambda_0(\mu\mathrm{m})}\left(\frac{\tau_0}{\tau_c}\right)^{1/3}, \tag{2}$$

$$I^{\tau}_{\mathrm{thr,TPD}}\left(10^{14}\ \mathrm{W/cm^2}\right) \approx \frac{232\left[T_e(\mathrm{keV})\right]^{3/4}}{\left[L_n(\mu\mathrm{m})\right]^{2/3}\left[\lambda_0(\mu\mathrm{m})\right]^{4/3}}\left(\frac{\tau_0}{\tau_c}\right)^{1/2}, \tag{3}$$

where T_e is the electron temperature. In addition to the bandwidth dependence in Eqs. (2) and (3), the threshold scalings with L_n, λ_0, and T_e have changed relative to the monochromatic result. Equations (2) and (3) predict that a laser with $\tau_0/\tau_c \approx 1.5\%$ would allow a doubling of the drive intensity in direct-drive implosions.

This material is based upon work supported by the Department of Energy National Nuclear Security Administration under Award Number DE-NA0003856, the University of Rochester, and the New York State Energy Research and Development Authority.

1. R. S. Craxton *et al*., Phys. Plasmas **22**, 110501 (2015).
2. W. L. Kruer, *The Physics of Laser Plasma Interactions*, Frontiers in Physics, Vol. 73 (Addison-Wesley, Redwood City, CA, 1988).
3. J. J. Thomson and J. I. Karush, Phys. Fluids **17**, 1608 (1974).
4. L. Lu, Phys. Fluids B **1**, 1605 (1989).
5. J . Weaver *et al*., Appl. Opt. **56**, 8618 (2017).
6. B. B. Afeyan and E. A. Williams, Phys. Fluids **28**, 3397 (1985).
7. A. Simon *et al*., Phys. Fluids **26**, 3107 (1983).

Complex Ray Tracing and Cross-Beam Energy Transfer for Laser-Plasma Simulations

A. J. Tu, R. K. Follett, and A. B. Sefkow

Laboratory for Laser Energetics, University of Rochester

Cross-beam energy transfer (CBET), which occurs when laser beams overlap in a plasma and drive ion-acoustic waves, may be responsible for a 50% decrease in hydrodynamic efficiency in OMEGA implosions.[1] A program was developed that models CBET for the simple case of two intersecting beams. The algorithms in this code followed a five-step process, which involved mapping ray trajectories to a grid, finding ray interactions, calculating gain coefficients for the interactions, and solving for final values through iteration.

A ray-tracing code was developed that propagates laser beams by representing them as bundles of rays and then evolving the rays in time according to the following set of differential equations:[2]

$$\frac{\mathrm{d}\mathbf{x}}{\mathrm{d}t} = v_{\mathrm{g}}, \tag{1}$$

$$\frac{\mathrm{d}\mathbf{v}_{\mathrm{g}}}{\mathrm{d}t} = -\frac{c^2 \nabla n_{\mathrm{e}}}{2n_{\mathrm{c}}}, \tag{2}$$

where $\mathbf{x}$ is the position vector, t is time, and $\mathbf{v_g}$ is the group velocity vector, defined by

$$\mathbf{v_g} = \frac{\partial \omega}{\partial \mathbf{k}} = \frac{c^2 \mathbf{k}}{\omega}, \tag{3}$$

where ω is the angular frequency, $\mathbf{k}$ is the wave-number vector, and n_{c} is the critical density, defined by

$$n_{\mathrm{c}} = \frac{\omega^2 m_{\mathrm{e}} \varepsilon_0}{e_{\mathrm{c}}^2}. \tag{4}$$

These equations take into account the dispersion relation and the density profile of the background plasma. The energy deposited by the beams, as well as the beam intensities and electric fields, can be calculated and plotted onto a grid using the first-order linear interpolation method.

To map ray trajectories and find interactions, we store an array of each ray's coordinates along its trajectory. We also keep track of the gridlines it crosses and the cells through which it passes. Two rays are said to intersect if they are from different beams and they both pass through the same grid cell.

For each interaction, we calculate the gain coefficient from the following formula:[3]

$$\left(L_s^{ijkl}\right)^{-1} = \frac{e^2 \left| E_{k0} \right|^2}{4 m_\mathrm{e} c \omega_{ij} k_\mathrm{B} T_\mathrm{e} \left(1 + 3T_\mathrm{i} / Z T_\mathrm{e}\right)} \frac{n_\mathrm{e}}{n_\mathrm{c}} \frac{\omega_s}{\nu_\mathrm{ia}} P\left(\eta_{ijkl}\right), \tag{5}$$

$$P(\eta) = \frac{\left(\nu_\mathrm{ia} / \omega_s\right)^2 \eta}{\left(\eta^2 - 1\right)^2 + \left(\nu_\mathrm{ia} / \omega_s\right)^2 \eta^2}, \tag{6}$$

$$\eta_{ijkl} = \frac{\omega_{kl} - \omega_{ij} - \left(\mathbf{k}_{kl} - \mathbf{k}_{ij}\right) \cdot \mathbf{u}}{\omega_s}, \tag{7}$$

where L_s^{ijkl} is the laser absorption length; e is the elementary charge; E_{k0} is the initial electric field of the pump ray; m_e is the electron mass; c is the speed of light; ω_{ij} and ω_{kl} are the frequencies of the seed beam and the pump beam, respectively; k_B is the Boltzmann constant; T_e is the electron temperature; T_i is the ion temperature; Z is the ionization state; n_e is the electron density; n_c is the critical density; ν_ia is the ion-acoustic wave energy damping rate; $\mathbf{k}_{ij}$ and $\mathbf{k}_{kl}$ are the seed and pump ray vectors, respectively; $\mathbf{u}$ is the plasma flow velocity; and ω_s is the acoustic frequency.

Once we determine the energy transfer for a single intersection, we must propagate the energy change to all downstream cells (see Fig. 1). After doing this for all possible ray intersections, we iterate the process, if necessary. This new program matches the results of Follett's CBET program,[3] which uses the same equations but different numerical algorithms; it also performs the calculations 10× faster.

Furthermore, a new ray-tracing method was investigated, namely complex ray tracing, which represents a laser beam with only five rays: a chief ray (a.k.a., base ray), two waist rays, and two divergence rays. The electric field or intensity at any point can be calculated by finding the distance between the point and three of the rays along a line perpendicular to the chief ray.[4]

We tried two different approaches to implement this technique: In the first approach (cell by cell), we traced all five rays at the beginning and then went cell by cell to calculate the intensity for each cell. While this method was very accurate, it was very slow when the number of cells became large. The second method (update outward along the chief ray) started by tracing the waist and divergence rays; then, while the chief ray was traced, we updated the intensities outward from the chief ray. This method worked quickly and accurately: it ran 4× faster than the standard ray-tracing method and produced a smoother plot.

With this program, we reproduced a basic version of Young's double-slit experiment, showing that complex ray tracing can model additional effects such as diffraction and interference. In the future, this work will be implemented into the 3-D hybrid fluid-kinetic code *CHIMERA*.

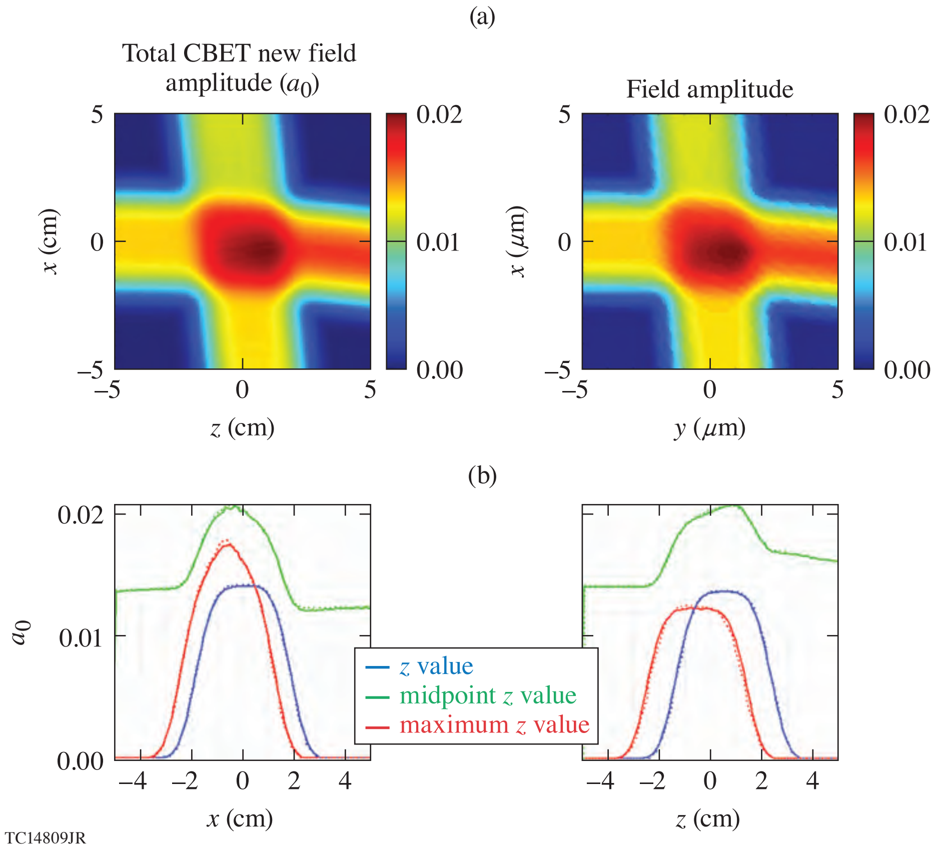

Figure 1
Comparison of Follett's CBET code[3] with the developed code. (a) Our results are on the left and Follett's results are on the right. Energy from the upward-traveling beam has been transferred to the rightward-traveling beam. (b) Our results are shown as solid lines and Follett's results are shown as dotted lines. The blue, green, and red lines show the electric-field profiles taken at the minimum z, midpoint z, and maximum z values, respectively.

This material is based upon work supported by the Department of Energy National Nuclear Security Administration under Award Number DE-NA0003856, the University of Rochester, and the New York State Energy Research and Development Authority.

1. J. F. Myatt *et al*., Phys. Plasmas **24**, 056308 (2017).
2. T. B. Kaiser, Phys. Rev. E **61**, 895 (2000).
3. R. K. Follett *et al*., Phys. Rev. E **98**, 043202 (2018).
4. H. Yu *et al*., Appl. Opt. **55**, 6530 (2016).

New Thermodynamic Constraints on Internal, Thermal, and Magnetic States of Super-Earths

M. Zaghoo

Laboratory for Laser Energetics, University of Rochester

The discovery of exoplanetary systems orbiting host stars has revolutionized planetary astronomy. As we begin to understand the diversity of these planets' architectures across a wide range of planet–star separation, we rely on transit-based methods to characterize their masses, radii, albedo, and soon, atmospheres. Ascertaining planetary structure, evolution, and habitability require, however, a better understanding of key internal geophysical and geochemical processes that drive the planetary geochemical differentiation, internal composition, core sizes, and heat budgets, all of which depend on the behavior of planetary constituent materials, particularly silicates and iron, at extreme conditions.

In the past few years, advances in high-pressure physics experiments, particularly those employing ramp-dynamic compression tools, have addressed this challenge.[1] The experiments provided precise data on the compressibility of iron, its Grüneisen parameter,[2,3] and the solidus line of $MgSiO_3$ (Ref. 4) as well as its conductive behavior at conditions comparable to 4 to 5 M_E (Ref. 5). Additionally, recent static high-pressure experiments revealed that liquid iron's thermal conductivity at conditions corresponding to Earth's core mantle boundary (CMB) is substantially higher than values previously used in the geophysics literature.[6,7]

In this work, we derive new thermodynamic data using recent experimental results on both iron and silicates to better model the internal states for super-Earth (SE) planets ranging from 1 to 10 M_E (see Fig. 1). We combine the state-of-the-art equation of state and melting experimental data with parametric thermal evolution models to obtain new pressure, density, and temperature radial profiles of these planets. We reveal that for planets more massive than 3 M_E, a thick layer of deep magma oceans surrounding solid iron cores will develop. We present new theoretical data on the thermal conductivity of SE's iron cores at extreme conditions, based on the revised estimates for Earth's values, and carefully assess the power requirements required to maintain the convective state of these cores. We show that the drastic rise in the conductive losses along the CMB will dominate the heat

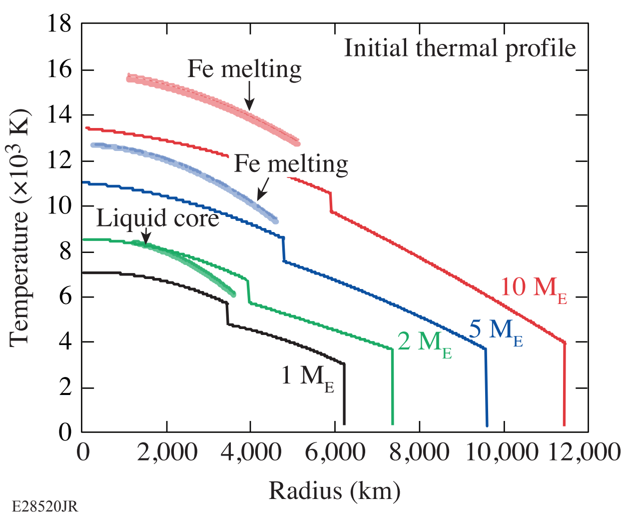

Figure 1
Radial thermal structure profiles of rocky SE planets ranging from 1 to 10 M_E calculated within the thermal boundary layer model. Also shown are the pure-Fe liquidus lines. The shaded area represents the reduction in the melting line caused by added impurities. The intersection of the thermal profile with the liquidus denotes the onset of iron crystallization, the inner core boundary. For planets 4 to 10 M_E, the liquidus does not cross the planetary thermal profile, meaning that these planets will likely lack an iron fluid core.

flux in the more-massive planets, driving their cores into a sub-adiabatic and non-convective state. Absent substantial intrinsic heat sources, the cessation of convection will consequently shut down the dynamo action in their cores. Our results lend support to the recently proposed concept of "super habitability," employed to describe terrestrial-like planets with enhanced characteristics amenable to their habitability.[8] We have shown that it most likely extends up to only ~4 M_E; beyond which, a new paradigm that describes the suitability of carbon-based life forms on more-massive rocky planets might be needed.

This material is based upon work supported by the Department of Energy National Nuclear Security Administration under Award Number DE-NA0003856, the University of Rochester, and the New York State Energy Research and Development Authority.

1. T. Duffy, N. Madhusudhan, and K. K. M. Lee, in *Treatise on Geophysics*, 2nd ed., edited by C. Schubert (Elsevier, Oxford, 2015), Vol. 2.
2. R. F. Smith *et al*., Nat. Astron. **2**, 452 (2018).
3. J. K. Wicks *et al*., Sci. Adv. **4**, eaao5864 (2018).
4. D. E. Fratanduono *et al*., Phys. Rev. B **97**, 214105 (2018).
5. R. M. Bolis *et al*., Geophys. Res. Lett. **43**, 9475 (2016).
6. H. Gomi *et al*., Phys. Earth Planet. Inter. **224**, 88 (2013).
7. K. Ohta *et al*., Nature **534**, 95 (2016).
8. R. Heller and J. A. Armstrong, Astrobiology **14**, 50 (2014).

Exchange-Correlation Thermal Effects in Shocked Deuterium: Softening the Principal Hugoniot and Thermophysical Properties

V. V. Karasiev, S. X. Hu, M. Zaghoo, and T. R. Boehly

Laboratory for Laser Energetics, University of Rochester

Reliably predicting the properties of hydrogen and its isotopes under extreme conditions remains a problem of great importance and broad scientific interest. Accurate knowledge of the equation of state (EOS) and transport properties over a wide range of thermodynamic conditions of this simplest and most-abundant element in the universe is used as input for planetary astrophysics models to describe interiors of planets[1] as well as the inertial confinement fusion (ICF) simulations to design targets.[2–4] The most-advanced theoretical and computational methods are used to interpret experimental results and to predict properties at thermodynamic conditions that are difficult to access experimentally.

On the other hand, new experimental measurements with improved accuracy[5,6] serve as an important benchmark to assess the accuracy of theoretical predictions. It was found[6] that recent shock-compression data for deuterium are well described by finite-temperature density functional theory (DFT) methods.[7–9] Standard generalized gradient approximation (GGA) exchange-correlation (XC) functionals such as Perdew–Burke–Ernzerhof (PBE)[10] describe the peak compression reasonably well, but at pressures above 250 GPa along the Hugoniot, the DFT calculations with the PBE functional predict a stiffer behavior than recent experimental data.[5]

All current DFT calculations of the Hugoniot data and transport coefficients are performed with temperature-independent XC functionals developed for ground state;[4,6,11–14] therefore, XC thermal effects, which play an important role in warm-dense-matter (WDM) conditions,[15] are not taken into account. Figure 1 shows the (r_s,t) domain where the temperature dependence of XC might be important for accurate predictions. The relative importance of XC thermal effects is shown as a function of the Wigner–Seitz radius $r_s = (3/4\pi n)^{1/3}$ and reduced temperature $t = T/T_F$, where $T_F = \left(3\pi^2 n\right)^{2/3} \big/ 2k_B$ is the Fermi temperature and n is the electron number density. XC thermal effects might become important for t values around a few tenths and above. Here we

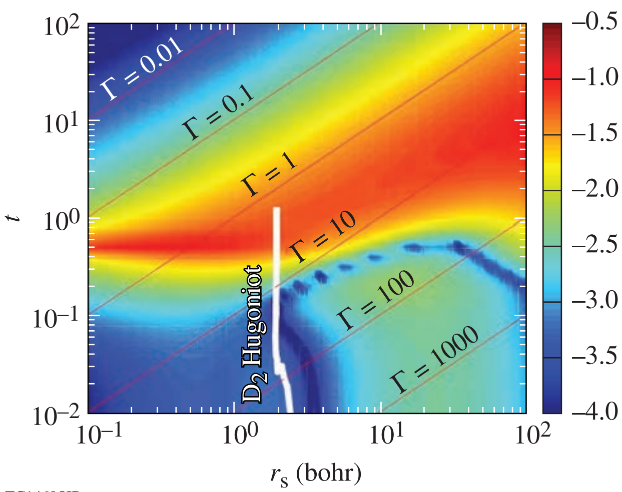

TC14695JR

Figure 1
The relative importance of explicit temperature dependence in the XC free-energy functional for the homogeneous electron gas measured as $\log_{10}\left\{\left|f_{xc}\left(r_s,t\right)-e_{xc}\left(r_s\right)\right| \big/ \left[\left|f_s\left(r_s,t\right)\right|+\left|e_{xc}\left(r_s\right)\right|\right]\right\}$, where f_{xc} is the XC free-energy per particle given by the corrKSDT parameterization,[16,17] e_{xc} is the zero-temperature XC energy per particle,[18] and f_s is the noninteracting free energy per particle.[19] $\Gamma = 2\lambda^2 r_s \big/ t$ with $\lambda = (4/9\pi)^{1/3}$ is the classical coupling parameter. The solid white line corresponds to the liquid deuterium principal Hugoniot path; the end point corresponds to $P = 1$ TPa.

focus on the study of the optical and transport properties along the principal Hugoniot of deuterium with a temperature-dependent Karasiev–Dufty–Trickey (KDT16) generalized gradient approximation XC functional.[16]

Figure 2 compares our theoretical predictions and experimental results across the molecular-to-atomic (MA) transition (low-pressure range $P < 150$ GPa) (Ref. 6). Both functionals, KDT16 and PBE, are in good agreement with experimental measurements in the range of pressure up to 200 GPa. At higher pressures, however, the PBE curve becomes noticeably stiffer as compared to the recent experimental data;[5] the disagreement reaches about 4% at $P = 550$ GPa. The KDT16 predicts a curve that is softer by slightly more than 1% beyond 250 GPa as compared to PBE. Increasing the simulation cell size from 64 to 128 atoms in this range of pressure leads to further softening of the Hugoniot. The KDT16 compressibility is within the experimental uncertainty in the entire pressure range (including high pressures $P > 250$ GPa). Therefore, the inclusion of XC thermal effects in calculations makes the deuterium Hugoniot softer at $P > 250$ GPa and improves agreement with the experimental data; the KDT16 XC functional is able to describe the principal Hugoniot of liquid deuterium consistently over the entire pressure range.

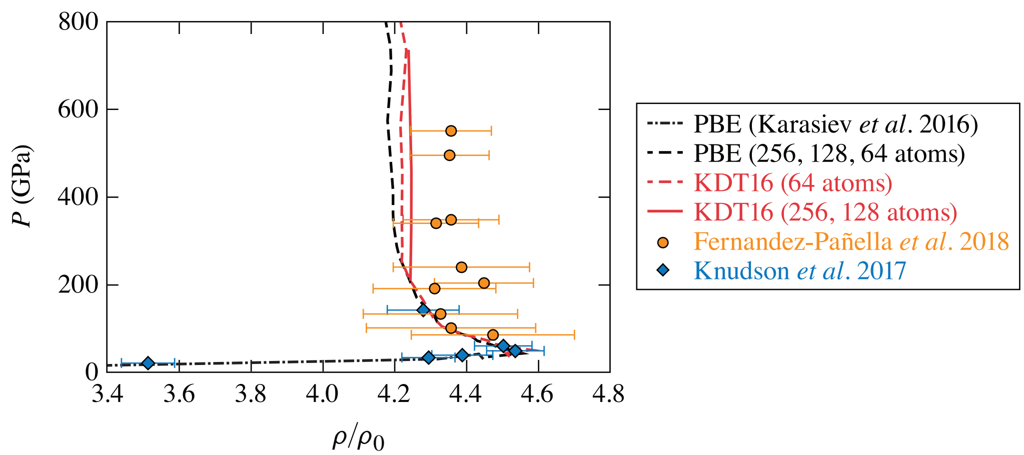

Figure 2
Deuterium principal Hugoniot derived from the initial state $\rho_0 = 0.172$ g/cm^3 and $T_0 = 20$ K. The PBE (dashed black) and KDT16 (dashed red) curves are obtained by combining results from simulations with 256 atoms ($6 \le T \le 20$ kK, pressure range between 34 and 86 GPa for both functionals), 128 atoms ($25 \le T \le 50$ kK, pressure range between 104 and 208 GPa for KDT16), 64 atoms ($60 \le T \le 150$ kK, pressure range between 253 and 736 GPa for KDT16), and 32 atoms for $T = 200$ kK. The solid red curve corresponds to the KDT16 results from simulations with 256 atoms ($6 \le T \le 20$ kK) and 128 atoms ($25 \le T \le 150$ kK).

The reflectivity along the deuterium Hugoniot was calculated at 532 and 808 nm with the KDT16 XC functional and our predicted value of the refractive index. Results of recent experiments[20] on OMEGA and previous measurements[21] are shown in Fig. 3. There is excellent agreement between the KDT16 values and experimental data at 808-nm wavelength for the range of shock speeds considered in calculations, even though the experimental data have relatively large error bars. The KDT16 results at 532 nm are in very good agreement with recent OMEGA experimental data for shock speeds below 50 km/s. The reflectivity is underestimated by the DFT calculations at high shock speeds $U_s > 50$ km/s as compared to the experiment. Experimental reflectance as a function of shock speed changes the slope at U_s near 45 km/s ($T \approx 0.4\ T_F = 60$ kK); this change in the slope is related to lifting of the Fermi degeneracy. The system starts to behave as a classical one at a significantly lower temperature as compared to T_F (see details in Ref. 20). Calculated KDT16 reflectivity at the same 532-nm wavelength rises very quickly from 0.29 at 16 km/s ($T \approx 6$ kK) to 0.39 at 20 km/s ($T \approx 12$ kK), which roughly corresponds to maximum compression near molecular-to-atomic transition; it slowly continues to increase and near 43 km/s the slope also increases.

The deuterium system along the Hugoniot experiences transformations from an insulating molecular liquid to atomic poor metallic liquid and finally to nondegenerate classical plasma. The signature of the molecular-to-atomic transition is found in a sharp increase of electrical dc conductivity and reflectivity at shock speeds in the range between 16 and 20 km/s (a range of temperature

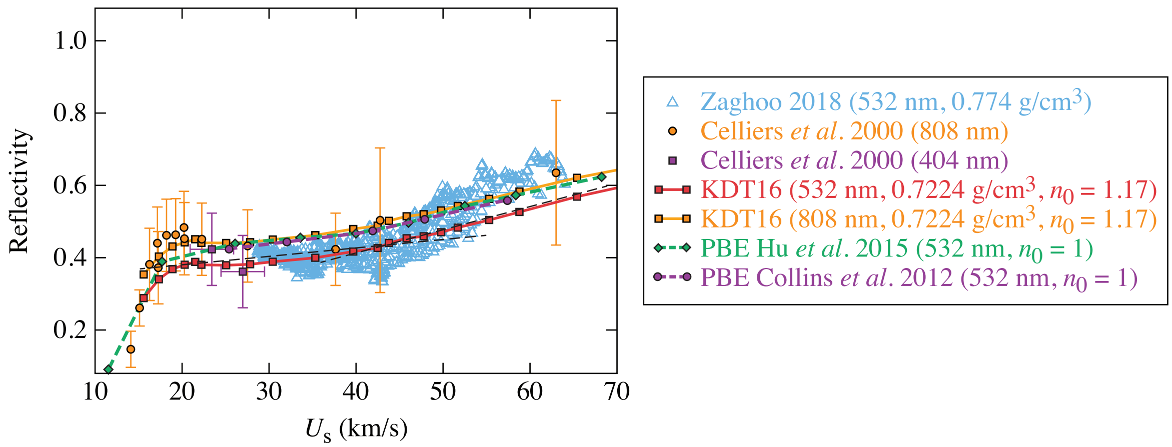

TC14635JR

Figure 3
Reflectivity of shocked deuterium. Theoretical DFT predictions and experimental data are compared.

between 6 and 12 kK). An increase in the slope of calculated reflectivity at $U_s \approx 43$ km/s ($T \approx 0.4\ T_F = 60$ kK), related to the breakdown of the electrons' degeneracy and emergence of classical statistics,[20] is in agreement with experimental measurements.

Our results confirm that the crossover between the quantum and classical statistics occurs below the $T = T_F$ limit. This is apparent in the observed change in the transport and the thermodynamic properties of the deuterium fluid in the region of 0.4 to 0.65 T_F. Future work should investigate the dependence of the onset of this crossover on density.

This material is based upon work supported by the Department of Energy National Nuclear Security Administration under Award Number DE-NA0003856 and U.S. National Science Foundation PHY Grant No. 1802964.

1. J. J. Fortney and N. Nettelmann, Space Sci. Rev. **152**, 423 (2010).
2. S. X. Hu *et al*., Phys. Rev. B **84**, 224109 (2011).
3. S. X. Hu *et al*., Phys. Rev. E **90**, 033111 (2014).
4. S. X. Hu *et al*., Phys. Plasmas **22**, 056304 (2015).
5. A. Fernandez-Pañella *et al*., "Shock Compression of Liquid Deuterium up to 1 TPa," to be published in Physical Review Letters.
6. M. D. Knudson and M. P. Desjarlais, Phys. Rev. Lett. **118**, 035501 (2017).
7. N. D. Mermin, Phys. Rev. **137**, A1441 (1965).
8. M. V. Stoitsov and I. Zh. Petkov, Ann. Phys. **184**, 121 (1988).
9. R. M. Dreizler, in *The Nuclear Equation of State. Part A: Discovery of Nuclear Shock Waves and the EOS*, edited by W. Greiner and H. Stöcker, Nato Science Series B (1989), pp. 521–532.
10. J. P. Perdew, K. Burke, and M. Ernzerhof, Phys. Rev. Lett. **77**, 3865 (1996); **78**, 1396(E) (1997).
11. B. Holst, R. Redmer, and M. P. Desjarlais, Phys. Rev. B **77**, 184201 (2008).
12. L. Caillabet, S. Mazevet, and P. Loubeyre, Phys. Rev. B **83**, 094101 (2011).
13. L. A. Collins *et al*., Phys. Rev. B **63**, 184110 (2001).
14. L. A. Collins, J. D. Kress, and D. E. Hanson, Phys. Rev. B **85**, 233101 (2012).

15. V. V. Karasiev, L. Calderín, and S. B. Trickey, Phys. Rev. E **93**, 063207 (2016).

16. V. V. Karasiev, J. W. Dufty, and S. B. Trickey, Phys. Rev. Lett. **120**, 076401 (2018).

17. V. V. Karasiev *et al*., Phys. Rev. Lett. **112**, 076403 (2014).

18. J. P. Perdew and A Zunger, Phys. Rev. B **23**, 5048 (1981).

19. R. P. Feynman, N. Metropolis, and E. Teller, Phys. Rev. **75**, 1561 (1949).

20. M. Zaghoo *et al*., Phys. Rev. Lett. **122**, 085001 (2019).

21. P. M. Celliers *et al*., Phys. Rev. Lett. **84**, 5564 (2000).

Spatiotemporal Flat Field of the Gated Optical Imager Used on the 3ω Beamlets Diagnostic

J. Katz, N. Whiting, and S. T. Ivancic

Laboratory for Laser Energetics, University of Rochester

Introduction

Gated optical imagers (GOI's) use microchannel-plate (MCP)–type intensifier tubes to electronically control the exposure duration of a 2-D image. Short exposure durations can be used to reduce motion blur in a dynamic scene or reject late-time sources of background noise such as ghost reflections or persistent thermal emission. The current state-of-the-art high-speed GOI's that use 18-mm-diam image tubes can achieve gate times of the order of 100 ps (Refs. 1 and 2). In the gated-off state, the entrance face of the MCP is negatively biased relative to the photocathode, preventing the flow of electrons to the MCP. The tube is gated on by applying a positive voltage pulse to a photocathode that temporarily overcomes a preimposed bias. Photoelectrons can then pass through the MCP amplification stage and are imaged on a phosphor screen. The MCP tube geometry and electrical capacitance of the photocathode influence the speed at which a transient voltage can be applied to the tube surface. In the fastest regimes the gating process is both spatially and temporally dynamic. Different regions of the image see different on/off times and exposure durations as the gate pulse propagates across the photocathode. Quantitative knowledge of the overall detector sensitivity as a function of position and time is required to accurately compare data recorded at different image positions. This type of calibration is critical to the 3ω beamlets diagnostic on OMEGA, which simultaneously records a four-frame image on a single exposure.[3] The beamlet energy, polarization state, and temporal evolution are determined by comparing the individual beamlet signals in each subimage.

Calibration Apparatus

A short-pulse laser was used to map out the optical gate profile over a series of image acquisitions by triggering the GOI at different times with respect to the incoming pulse (Fig. 1). A frequency-doubled Ti:sapphire (λ = 395-nm) laser with 1-ps pulse duration was up-collimated to ~20-mm diameter and free-space propagated to the GOI photocathode. The up-collimator produced a relatively flattop beam profile by selecting only the central 1/10th of the original Gaussian laser near field. A sample of the laser pulse was split and fiber coupled for use as an energy and timing reference. Once fiber coupled, the pulse was split again with one leg sent to a time-integrated energy meter and the second leg sent to a high-speed (90-ps) photodiode. The photodiode output and an electrical monitor pulse produced from the GOI pulser were recorded on separate channels of an 8-GHz oscilloscope

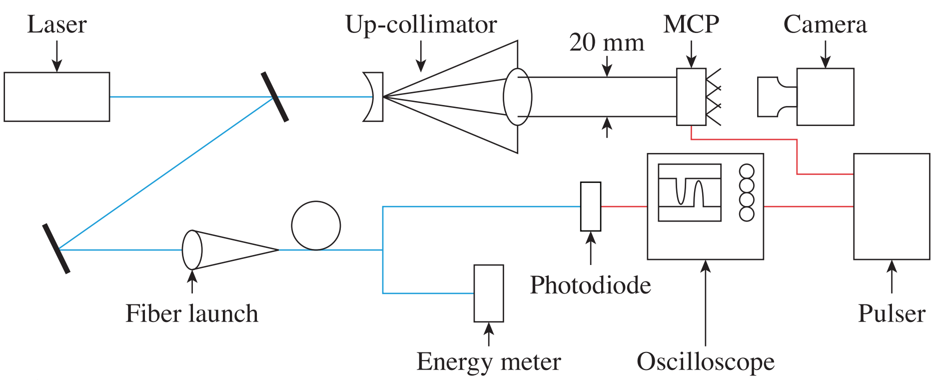

Figure 1
A laser with 1-ps pulse duration is used to characterize the GOI gate as a function of time and image position. The arrival time of the laser pulse relative to the GOI trigger is varied over a series of image acquisitions to map out the gate profile. An oscilloscope measures the laser timing relative to a monitor of the GOI gating pulse. The energy of each incident pulse is quantified using an energy meter.

sampling at 40 Gs/s. The relative trigger time for each image frame was measured by comparing the reference pickoff timing to the monitor pulse and was determined with 5-ps accuracy. The pulse energy was also measured by integrating the photodiode oscilloscope trace. Agreement between the two pulse energy measurements was 2.5% rms, allowing fluctuations in laser pulse energy to be corrected for in each image frame.

Generation of a Flat-Field Calibration

To establish the baseline spatial uniformity of the illumination beam, a series of images were collected with the GOI in slow gate exposure mode. The slow gate setting provides millisecond exposure durations using separate gating circuitry. The flat-field images are used to quantify intensity nonuniformities introduced by the laser near field, diffraction from the up-collimator, and dust particles on the transport optics. The scan of the fast gate included ~85 shots. A system jitter of ±50 ps prevents the scan from being generated with equal spacing time steps but timing information can be recovered to ±5 ps by fitting the monitor and diode traces in post-processing. By sorting the acquisitions by trigger time, a gain history with approximately 5-ps sample intervals is generated. As shown in Fig. 2(a), the 3ω beamlets' GOI has an exposure duration of approximately 250 ps. A sensitivity figure of merit $G(x,y)$ is calculated by integrating the gate history as a function of time on a pixel-by-pixel basis, given by Eq. (1).

$$G(x,y) = \frac{1}{\mathrm{FF}(x,y)} \sum_{i}^{n} \frac{I_{i+1}(x,y) + I_i(x,y)}{2E_i} \left(t_{i+1} - t_i\right), \tag{1}$$

where $I(x,y)$ is the signal intensity of a given image pixel on the ith image in the set, t_i is the relative time that the image was acquired, E_i is the corresponding pulse energy, and FF is the normalized image from the slow-gate flat field. Equation (1) generates a composite image that contains the time-integrated gain sensitivity as a function of image position [Fig. 2(b)].

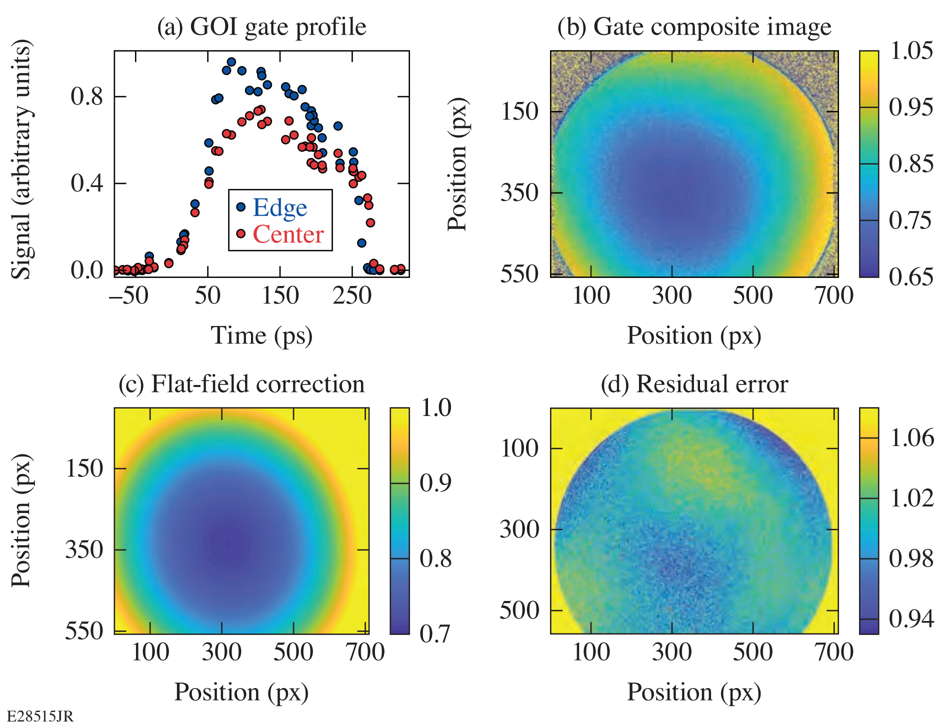

Figure 2
(a) The gain as a function of time is shown at two different pixel locations on the GOI image. (b) A composite image is generated by integrating the gain history at each point in the image. (c) The flat-field calibration function is generated by fitting the composite image fit with a 2-D second-order polynomial. (d) Dividing the composite image by the flat-field function corrects the spatial variations in gain to 2.2% rms.

Figure 2(b) shows the measured sensitivity as a function of image position. The edges of the MCP tube are more sensitive than the center. The magnitude of sensitivity variation is a function of bias voltage. In general, faster gate times can be achieved for a given electrical gate pulse by increasing the MCP to photocathode bias. In this case, electrons flow only during the peak portion of the gate pulse. However, this also results in a lower electron extraction field, making the gating process more sensitive to variations in extraction field uniformity. Excessive bias produces fast gate profiles but can result in a complete lack of sensitivity in the image center. Ultimately the bias setting is a compromise between spatial sensitivity uniformity and gate speed. Recording the spatiotemporal flat field at different settings allows the bias voltage to be optimized. In the case of the standard beamlets configuration, the 250-ps gate duration is accompanied by a 40% peak-to-valley (p–v) variation in sensitivity from the image center to the edge.

A smooth and continuous calibration function was generated from the composite gate image by fitting it to a 2-D second-order polynomial [Fig. 2(c)]. The fitting process averages out pixel-to-pixel statistical noise and smooths residual features from diffraction and dust that persisted after flat fielding. Figure 2(d) shows the residual sensitivity variation of the original composite image after the flat-field correction. Dividing the composite image by the correction function results in a 2.2% rms variation in measured signal intensity with a p–v of ~6%.

Conclusions

A short-pulse laser and precision trigger monitor system were used to generate a spatiotemporal flat field for a high-speed GOI used in the 3ω beamlets. Measuring the detector sensitivity as a function of time and image position makes it possible to optimize the GOI operating voltages. A method for averaging calibration data into a single scalar correction function is described. Implementation of the correction function reduces spatial gain variations from ~40% p–v and 9.3% rms to 6% p–v and 2.2% rms.

This material is based upon work supported by the Department of Energy National Nuclear Security Administration under Award Number DE-NA0003856, the University of Rochester, and the New York State Energy Research and Development Authority.

1. P. E. Young *et al*., Rev. Sci. Instrum. **59**, 1457 (1988).
2. B. Little, Rev. Sci. Instrum. **89**, 10E117 (2018).
3. D. H. Edgell *et al*., Rev. Sci. Instrum. **89**, 10E101 (2018).

Co-Timing UV and IR Laser Pulses on the OMEGA EP Laser System

W. R. Donaldson and A. Consentino

Laboratory for Laser Energetics, University of Rochester

Independently managing the timing of individual beams so they all arrive at the target at the time specified by the principal investigator is crucial to the success of experiments on the OMEGA EP Laser System. A streak camera is used to observe the x rays emitted when the laser beams strike a gold target, while an optical streak camera is used to measure the UV pulses. Correlating the signal on the two instruments gives a timing accuracy of 10 ps for the short-pulse IR beams and 20 ps for the long-pulse UV beams.

OMEGA EP is a four-beam, kilojoule-class laser system.[1] The four beams can be configured to produce different pulse shapes with durations ranging from 100 ps to 10 ns and energies up to 10 kJ with a wavelength of 351 nm, or up to two of the beams may propagate to the target chamber without being converted to the UV. Instead, the IR light passes through a grating compressor[2] and is delivered to the target as a 1- to 10-ps Gaussian pulse with up to 1 kJ of optical energy. The users of this facility can perform experiments where the beams arrive at the target with adjustable relative delays.

If two pulse shapes are identical, an overlap can be used for alignment as in shown in Fig. 1(a). For non-identical pulse shapes, the timing criteria become more complicated as shown in Figs. 1(b) and 1(c).

OMEGA EP has adopted the following conventions for co-timing the various beam configurations: UV pulses are considered to be co-timed when the points on the rising edge, corresponding to the 2% level of the peak, reach the target simultaneously. For the IR beams, co-timing means that the peak of the Gaussian pulse shape arrives at the target simultaneously, regardless of the width of the pulses. When both IR and UV pulses are co-timed, the peak of the IR Gaussian is aligned with the 2% point on the rising edge of the UV pulse. Of course, any of the beams can be mistimed to produce the arrival times desired by the principal investigator, but the mistimings are always specified relative to the timed definitions.

The co-timing system begins by recording the UV pulse shapes on an optical streak camera[3] as shown in Fig. 2. The signals arrive at the streak camera arbitrarily but at deterministic and reproducible times resulting from the optical-path differences from the pickoff. The arrival times at target chamber center are determined by x rays generated by the optical pulses and measured on an x-ray streak camera. Also recorded on the optical streak camera is an eight-pulse, 1.8-GHz comb pulse tied to the master clock of OMEGA EP. This fiducial links the measured optical pulse to the outputs of the other diagnostics on the system, thereby enabling one to convert the relative timings measured on the streak camera into absolute system times. The PJX x-ray streak camera, developed at LLE,[4] allows one to measure an x-ray pulse with picosecond time resolution and can be mounted in a ten-inch manipulator directly on the OMEGA EP target chamber. Figure 3 shows the output image of the PJX streak camera for the two different timing configurations.

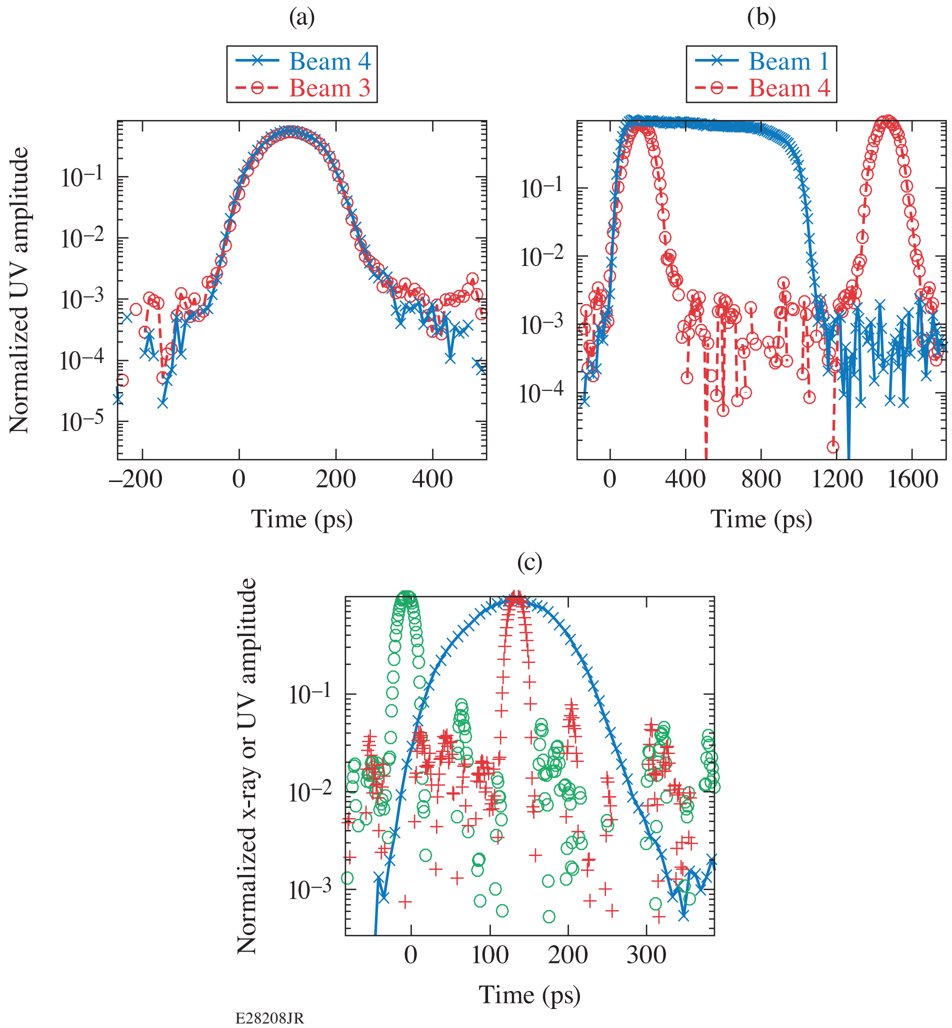

Figure 1
(a) The temporal alignment of two UV pulses with identical shapes. Any point can be used for the alignment. (b) Two dissimilar UV pulse shapes must be aligned by matching equal normalized amplitude points on the rising edge. (c) The UV (blue ×'s) and IR (green circles) are timed such that the peak of the IR pulse coincides with the 2% point of the UV pulse. An alternative timing where the peaks coincide is shown by the red crosses. This timing is not applicable with all UV shapes.

If the system is properly co-timed, the leading x-ray image of each of the four UV beams, shown in Fig. 3(a), should align in the temporal (vertical) direction. In the short-pulse to long-pulse configuration, shown in Fig. 3(b), the peaks of the two short-pulse beams should align with the 2% point on the leading edge of the long-pulse UV beam. Exact timing at the picosecond level requires a quantitative analysis of these images.

The target consists of a 25-μm-thick, 3-mm × 3-mm sheet of polyimide coated with 0.5 μm of gold. The total energy in each UV beam is ~170 J, giving ~85 J in each of the two 100-ps Gaussians; therefore, the peak intensity is ~5×10^{15} W/cm^2. At this intensity, at 351 nm, the temporal profile of the x-ray pulse matches that of the UV pulse as seen in Fig. 4. The x-ray temporal

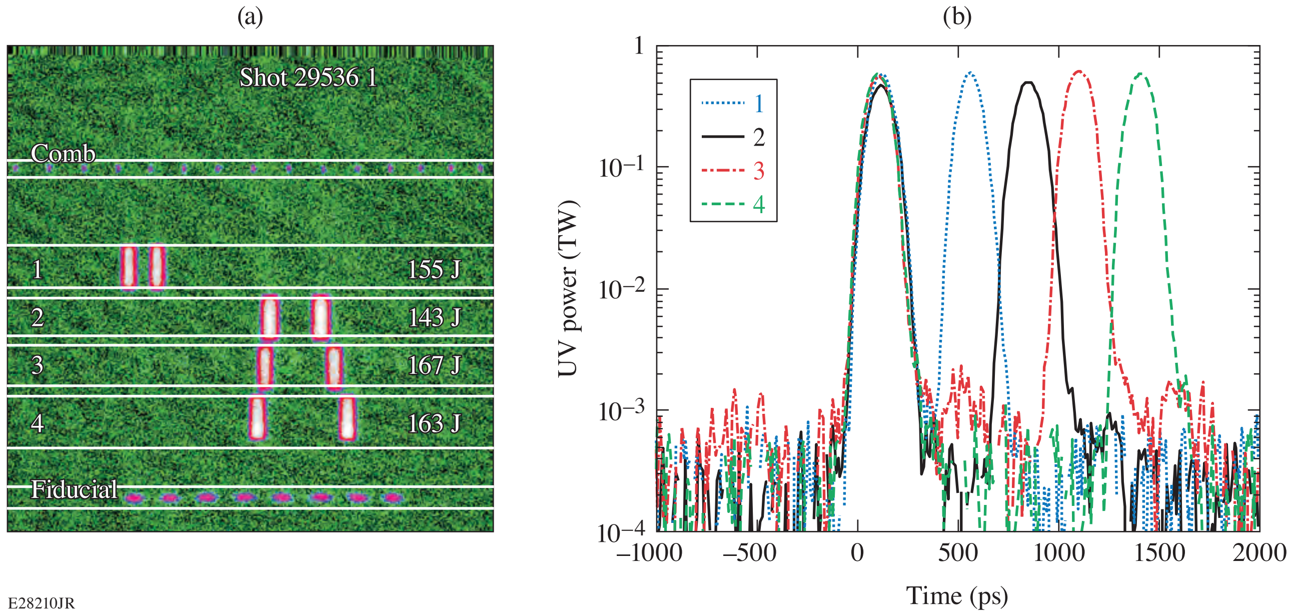

Figure 2
(a) The raw image from the UV streak cameras showing the four double-Gaussian pulse shapes and the two timing comb pulses; (b) the integrated lineouts from the UV ROSS camera of the four beams with the calibrated temporal alignment applied.

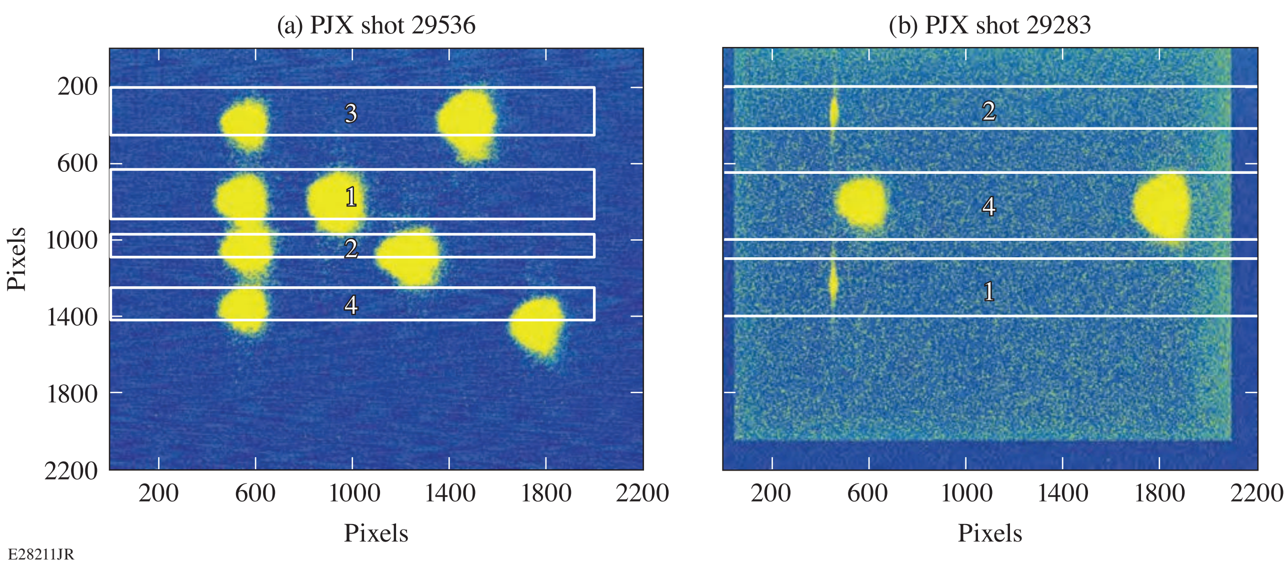

Figure 3
(a) The x-ray streak-camera image of a four-beam, long-pulse shot showing eight pulses from the four beams. (b) Two short-pulse IR beams and one UV beam strike the target. The temporal calibration is ~1 ps per pixel.

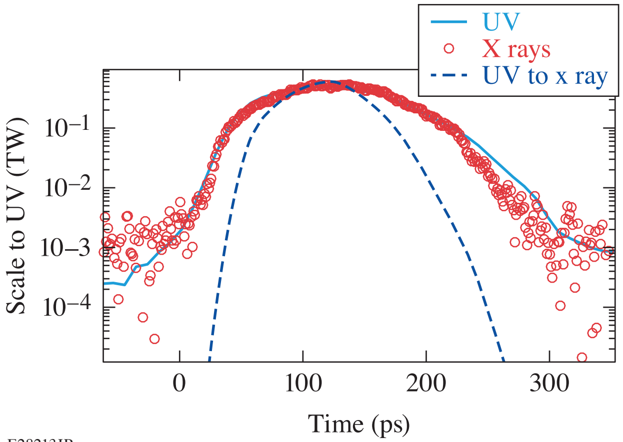

Figure 4
The x-ray temporal pulse shape (red circles) matches the measured UV pulse shape (solid blue line). The dashed blue line is the UV optical power raised to the 3.4 power, which is typical of UV to x-ray conversion at lower powers and obviously does not match the x ray at these intensities.

pulse shape matches the measured UV pulse shape. At intensities below 10^{14} W/cm^2, the emitted x rays typically follow the UV power to the 3.4 power.[5] When the UV optical power is raised to 3.4 power, the power-law conversion obviously does not match the x-ray temporal profile. This is advantageous in processing the data because when the x-ray and UV peaks are aligned, the 2% points on the leading edge, which are the actual timing points, are also aligned.

This is particularly important when timing the short-pulse beams. The IR pulses are treated differently. The shortest pulse duration, 1 ps, is at or below the resolution limit of the PJX streak camera, so the timing campaigns operate with IR pulse durations of 10 ps at best focus of the laser system. No substructure can be discerned in the x rays generated by the IR pulses. The IR x-ray data are fitted with a Gaussian to find the peak. It is worthwhile to note that the 2% point on the IR-generated x ray is at or below the noise floor, making that point inaccessible.

The UV-to-UV and UV-to-IR timing campaigns are run every three months, typically with a three-month separation between the two types of campaigns. The typical variations are less than the 20 ps, which is actually better than the current OMEGA EP timing specification of 25 ps for all beams. Therefore, OMEGA EP maintains a beam-to-beam timing of 20 ps by simultaneously measuring the optical pulse and the x rays generated when that optical pulse strikes a gold target. By operating in a high-intensity regime, the x ray's pulse shape closely tracks the optical pulse, which facilitates the timing.

This material is based upon work supported by the Department of Energy National Nuclear Security Administration under Award Number DE-NA0003856, the University of Rochester, and the New York State Energy Research and Development Authority.

1. J. H. Kelly *et al*., J. Phys. IV France **133**, 75 (2006).

2. J. Qiao *et al*., in *The International Conference on Ultrahigh Intensity Lasers: Development, Science and Emerging Applications (ICUIL 2008)* (ICUIL, Tongli, China, 2008), p. 107.

3. W. R. Donaldson *et al*., Rev. Sci. Instrum. **73**, 2606 (2002).

4. P. A. Jaanimagi *et al*., Proc. SPIE **5580**, 408 (2005).

5. F. J. Marshall *et al*., Phys. Plasmas **11**, 251 (2004).

Current Status of Chirped-Pulse–Amplification Technology and Its Applications

S.-W. Bahk

Laboratory for Laser Energetics, University of Rochester

Chirped-pulse amplification (CPA) is a technology that has become the basis of high-peak-power lasers.[1] The intensity of the electromagnetic field has been dramatically increased since its invention. CPA is an amplification scheme that allows safe amplification of a pulse to high energy. A short low-energy pulse is stretched in time and is injected into an amplifier. After amplification to high energy, the pulse is compressed back to the original short pulse. We discuss key components of CPA in this summary.

We will first discuss the optical pulse compressor and stretcher. The compressor is made up of two parallel gratings in double pass or four gratings in single pass.[2] The accumulated holographic phase through the grating pair is a quadratic function of the frequency, which introduces chirp in time. Large-scale tiled compressors for petawatt facilities have been demonstrated at OMEGA EP[3] and PETAL.[4] A stretcher is a compressor with an imaging system.[5] The imaging system renders the effective optical distance between the two gratings negative as the image of the first grating is formed behind the second grating. The original lens-based imaging system in the stretcher has been replaced with a reflective Offner imaging system.[6]

Amplifiers are based on either optical pumping and stimulated emission or parametric amplification. Laser-diode pumping is most efficient but flash lamps or secondary pump lasers are commonly used for optical pumping. The most widely used femtosecond amplification medium is titanium sapphire, which can amplify a wide range of frequencies, is not easily saturated even at high-energy pulses, and has high amplification efficiency. It is pumped mainly by the second-harmonic pulse of the neodymium lasers. The internal self-lasing problem is a disadvantage but it can be prevented by adding a black coating around the crystal. In the parametric amplification process, the energy in the pump beam is instantaneously transferred to the injection seed beam. Since there is no energy remaining in the crystal, there is no thermal lensing problem. On the other hand, since the temporal and spatial nonuniformity of the pump pulse is directly transferred to the input pulse, a complicated and expensive hardware system is required to manage the pulse. In addition, the limited temporal and spatial overlap reduces the amplification efficiency because the group velocity and direction of the input and pump pulses in the crystal are different. The angle of the pump and the input must be precisely adjusted to meet the phase-matching requirements of the broad frequency band. Lithium triborate, beta-barium borate, and potassium dihydrogen phosphate (KDP) crystals are often used. Stimulated-emission amplifiers and parametric amplifiers may be mixed in some cases.[7] Since deuterated KDP has already been developed for use as a frequency-conversion medium in laser fusion facilities, efforts are being made to utilize it for amplifying large-scale, high-energy broadband pulses.[8]

The spatial and temporal control of a pulse are important to provide the necessary experimental conditions. The focused beam intensity can be greatly increased by an adaptive optic system,[9] which consists of a deformable mirror and a feedback system connected to a wavefront sensor. The deformable mirror has a number of piezoelectric or mechanical actuators attached to the back side of the mirror substrate. The mechanical type has the advantage of maintaining the state even after the power is off. The quality of pulse compression can be similarly improved by controlling the spectral phase of the pulse. It is possible to remove the third-order dispersion by slightly adjusting the angle of the compressor, but the fourth- or higher-order terms can be removed by an acousto-optic programmable dispersion filter.[10] When the dispersion of the pulse is not spatially uniform, spatiotemporal coupling occurs at focus. The radial group delay in refractive image relays disperses the focus in the longitudinal direction and significantly reduces the intensity of the light. A diffractive lens has the opposite angular dispersion than a refractive lens and, therefore, can eliminate radial group delay.[4] Another application of the diffractive lens is "flying focus." The longitudinal chromatic aberration of the diffractive lens and the chirp of the pulse are combined to create the effect of longitudinal focal spot sweeping in time.[11] The efficiency of laser wakefield acceleration might be improved by this scheme. Another example of spatiotemporal effects is "wavefront rotation." This effect was used to isolate low-energy x-ray attosecond pulses.[12]

High-power lasers can generate secondary light sources/particles that can be used in medical, industrial, security, and pure scientific research, but they are less efficient than other alternatives because of their low repetition rate. To increase the repetition rate, the heat accumulation problem of the main amplifiers and the pump laser amplifiers must be solved (not for parametric amplifiers). For thin-disk Yb:YAG crystals used in pump lasers, a laser beam can be shined on one side of the disk and a cooling system can be attached to the other side to remove heat. Since the thickness is much thinner than the width, thermal gradients are formed only in the direction perpendicular to the surface, so that the lens effect of heat and polarization mixing is minimized. The thin-disk laser is used as a pump laser for the L1 optical parametric chirped-pulse–amplification laser at the ELI Beamlines Facility; it is aimed to supply pulses of 20 fs, 100 mJ at 1 kHz (Ref. 13). In large-scale petawatt lasers, the amplifier is stacked with several slabs and then cooled between the slabs by using room-temperature or low-temperature helium gas or water. The team at Lawrence Livermore National Laboratory has successfully constructed a 3.3-Hz petawatt laser based on this scheme [High-Repetition-Rate Advanced Petawatt Laser System (HAPLS)].[14]

Damage risk in the compressor remains the biggest concern for CPA. This risk is highest at the fourth grating, where the pulse is the shortest, because the damage threshold is lowered as the pulse becomes shorter. A multilayer dielectric grating was introduced to improve the damage threshold.[15] The uppermost layer is an etched dielectric grating, and a dielectric layer of high and low refractive indexes is repeatedly stacked under it for high reflectance. The damage threshold is improved by a factor of 10 (1 J/cm^2) compared to gold gratings, but the available bandwidth is narrow. To increase the bandwidth, a metal–dielectric grating has been considered with a dielectric top layer structure and metal layer at the bottom.[16] The thermal loading on gratings at a high repetition is another challenge.

We discuss applications in laser eye surgery and electron acceleration. Femotosecond lasers have been successfully used to cut out cornea flap in refractive surgery.[17] Femotosecond pulses provide better-controlled damage threshold. In electron acceleration, when a strong laser pulse focus passes through a plasma, the electrons are pushed out from focus by ponderomotive forces and a wakefield is formed in the ion density. When the electron is injected into the low potential of the ion wakefield, it moves with the wake as the pulse continues. Since this process occurs very quickly, the electrons accelerate to high energy. Lawrence Berkeley National Laboratory demonstrated 4.2 GeV using a microdischarge tube on the BELLA laser.[18]

CPA has revolutionized laser technology but it is also important to keep inventing new methods. For example, to overcome energy limitations, research is underway to amplify pulses using the Raman amplification phenomenon in a medium of plasma state.[19] In addition, efforts are being made to improve the system using new optical fibers and metamaterials. CPA opened the way for studying exciting advanced science in small laboratories. More commercialized petawatt lasers are becoming available in large laboratories and medical/industrial facilities.

This material is based upon work supported by the Department of Energy National Nuclear Security Administration under Award Number DE-NA0003856, the University of Rochester, and the New York State Energy Research and Development Authority.

1. D. Strickland and G. Mourou, Opt. Commun. **56**, 219 (1985).
2. E. B. Treacy, IEEE J. Quantum Electron. **QE-5**, 454 (1969).
3. J. Qiao *et al*., Opt. Express **15**, 9562 (2007).
4. J. Néauport *et al*., Appl. Opt. **46**, 1568 (2007).
5. O. E. Martinez, IEEE J. Quantum Electron. **QE-23**, 59 (1987).
6. G. Chériaux *et al*., Opt. Lett. **21**, 414 (1996).
7. L. Xu *et al*., Opt. Lett. **38**, 4837 (2013).
8. K. Ogawa *et al*., Opt. Express **17**, 7744 (2009).
9. N. Lefaudeux *et al*., Proc. SPIE **8600**, 86000W (2013).
10. P. Tournois, Opt. Commun. **140**, 245 (1997).
11. J. P. Palastro *et al*., Phys. Rev. A **97**, 033835 (2018).
12. F. Silva *et al*., Nat. Commun. **6**, 6611 (2015).
13. P. Bakule *et al*., Proc. SPIE **10241**, 102410U (2017).
14. T. M. Spinka and C. Haefner, Opt. Photonics News **28**, 26 (2017).
15. M. D. Perry *et al*., Opt. Lett. **20**, 940 (1995).
16. F. Canova *et al*., Opt. Express **15**, 15324 (2007).
17. T. Juhasz *et al*., Proc. SPIE **4633**, 1 (2002).
18. W. Leemans, Phys. Today **62**, 44 (2009).
19. V. M. Malkin, G. Shvets, and N. J. Fisch, Phys. Rev. Lett. **82**, 4448 (1999).

Measurements of Heat Flow from Surface Defects in Lithium Triborate

D. Broege and J. Bromage

Laboratory for Laser Energetics, University of Rochester

With laser sources being pushed to larger bandwidths and higher average powers every day, the importance of thermal effects in nonlinear optics has become an increasingly important area of study. It has been shown that absorption in the bulk of crystals, as well as their coatings, can lead to significant changes in temperature that can have a negative impact on nonlinear processes. One common but often overlooked source of heat in optics exposed to high average powers is the more-localized type, which can be the result of crystal defects, contamination, or damage spots. We have performed what is to our knowledge the first interferometric measurements of temperature distributions in a nonlinear optic resulting from absorption in a localized defect. A supporting analytical model is shown to elucidate features of the resulting temperature distribution and assist in estimating the total absorbed power at the site, with a sensitivity of one part in 10^5. This technique also provides a method of measuring absorption from a defect without the need for collection and measurement of a transmitted beam.

The setup used to perform these measurements consisted of a Mach–Zehnder interferometer with the sample in one arm. A 1064-nm kilowatt beam with a diameter of 2 mm was passed through the sample at a slight angle to induce heating. Changes in optical path length were measured across the face of the crystal, and a differential measurement was made between path lengths under ambient conditions and when the heated crystal reached equilibrium. These values were then used to calculate the corresponding longitudinally integrated temperature change with published material parameters.

The materials used in this study were all uncoated low-bulk-absorption lithium triborate (LBO) crystals, principally cut into 1-cm cubes and polished on four sides. This allowed for pump and probe beams to sample single crystallographic axes. This was used to qualify the measurements, in that a particular heat distribution could be probed with two separate polarizations, yielding two similar signals, but with different amplitudes. The ratio of these amplitudes could be calculated from material parameters and were shown to agree with measured values to within ~10%. The localized absorbers—the focus of our study—were single unintentionally produced damage spots on the crystal surfaces.

The 2-D changes in optical path length that were measured from these crystals showed a distinctive shape. It consisted of a sharp central peak, no larger than 100 μm, with rapidly decaying amplitude moving outward from the source. This stands in stark contrast to the more Gaussian-like distributions seen when heating is the result of absorption in the bulk or in a coating. Thermal imaging measurements showed that the heating occurred on only one face of the crystal, indicating that it was solely the result of localized absorption. Also observable was an asymmetry in the vertical direction, but not the horizontal, indicating that the crystal was warmer at the top surface than at the bottom, which was the result of heat loss into the mount.

With access to finite element analysis tools, calculations of heat flow can be made, but the higher resolutions required to accurately model such a small source require significant memory. We instead employed an analytical model that can be easily derived by relating the total absorbed power to heat flow through a spherical surface at distance r from the absorber through Fourier's law. This results in a temperature distribution of the following form for all points outside the absorber:

$$T(r) = \frac{P}{4\pi\kappa r} \tag{1}$$

and can be shown to be

$$T(r) = \frac{-Pr^2}{8\pi\kappa R^3} + \frac{3P}{8\pi\kappa R} \tag{2}$$

for all points inside the absorber, where r is the observation radius, κ is the thermal conductivity, R is the radius of the absorber, and P is the total absorbed power. For this model to be valid, the source must be small compared to the length of the crystal, and the heat flow through the crystal must be large compared to convective cooling at the surface.

What is immediately evident from the functional form of this distribution is that outside the absorber, its amplitude is proportional to the absorbed power, but completely insensitive to the size of the absorber. Calculations show that a 20-fold decrease in the size of the heat source results in only a factor-of-2 increase in the resulting peak temperature. *This implies that without detailed knowledge of the morphology of the absorber, a decent estimate can be made of the total power absorbed*. Figure 1 shows an overlay of measured changes in optical path length and a simulated data set using the simple model, with an absorbed power of 15.5 mW. The matching between the two is sensitive to the mW level, allowing for a very sensitive estimation of absorbed power at a localized defect. With this knowledge, one can use microscopy to determine the maximum spatial extent of the defect and determine a range of possible absorbances and sizes. In the case of our test spot, with a maximum possible size of 100 μm, assuming absorption is uniform across its face results in an average absorbance of 5%. If, on the other hand, absorbance is 100%, the size of the spot can be no smaller than 22 μm.

This material is based upon work supported by the Department of Energy National Nuclear Security Administration under Award Number DE-NA0003856, the University of Rochester, and the New York State Energy Research and Development Authority.

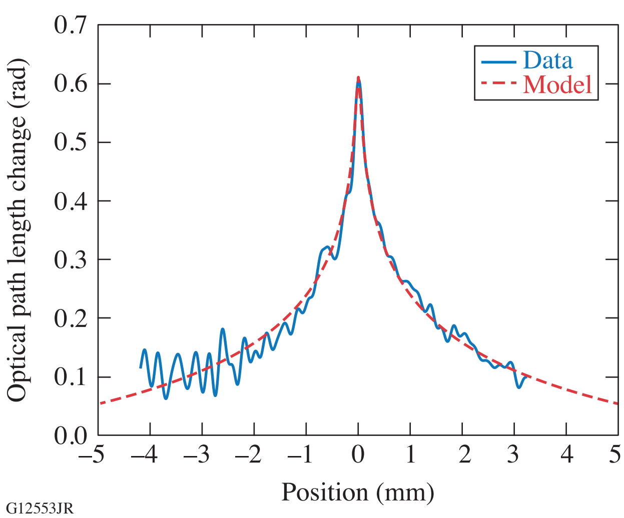

Figure 1
Comparison of measured optical path length change in LBO with an analytical model for 15.5 mW. This model was used along with interferometric measurements of temperature to estimate power absorbed at a localized spot with a sensitivity of one part in 10^5.

The Role of Urbach-Tail Optical Absorption on Subpicosecond Laser-Induced Damage Threshold at 1053 nm in Hafnia and Silica Monolayers

M. Chorel,[1] T. Lanternier,[1] É. Lavastre,[1] L. Lamaignère,[1] N. Roquin,[1] J. Néauport,[1] S. Papernov,[2] A. A. Kozlov,[2] B. N. Hoffman,[2] J. B. Oliver,[2] and S. G. Demos[2]

[1]Commissariat à l'Energie Atomique et aux Energies Alternatives, Centre d'Etudes Scientifiques et Techniques d'Aquitaine, France
[2]Laboratory for Laser Energetics, University of Rochester

Hafnia and silica are widely used as the principal materials in multilayer dielectric (MLD) mirrors for petawatt-class laser facilities such as the OMEGA EP Laser System at LLE. Damage initiation in such dielectric coatings under excitation with pulses shorter than about 2.5 ps is associated with the formation of plasma that facilitates, via a complex energy deposition process, superheating of the affected volume.[1] Assuming a crystalline material, the buildup of the electron density in the conduction band originates with multiphoton excitation between the ground state and conduction band. However, the layers in MLD coatings are generally amorphous with a structure that varies based on the deposition method. Consequently, the optical absorption edge properties can be characterized by an optical gap that most often is analyzed using two methods. At photon energies above the optical gap, the absorption (α) behaves according to the Tauc formula, i.e., $\alpha \hbar\omega \propto (\hbar\omega - E_T)^2$, where E_T is known as the *Tauc gap*. Below the optical gap, the absorption is described by the Urbach tail[2] that arises from localized states in the band gap. In addition, defect states can further extend the absorption edge toward lower energies. As a result, transitions from the ground state to the conduction band are not limited to intraband transitions but include additional pathways through intermediate states at the Urbach tail and defects. It has been previously discussed that red shifting of the Urbach tail can lead to a reduced damage threshold in silica.[3] The role of defects in decreasing the damage threshold has also been documented in various materials including hafnia monolayers.[4]

The optical gap and Urbach tail are in the 200- to 350-nm spectral region for both silica and hafnia layers. Based on the above considerations, this work explores the relationship of the laser-induced–damage threshold (LIDT) (using 1053-nm, 800-fs laser pulses) of silica and hafnia layers obtained by different vendors, using different deposition methods, to the characteristics of the Urbach tail in each material. The damage threshold is estimated following normalization for the electric-field distribution within each layer and is typically referred to as the "intrinsic" LIDT.[5] The damage thresholds are investigated as a function of the estimated optical gap (Tauc gap) of each material and further evaluated as a function of the red-shifted Urbach tail absorption. Analysis of the absorption-edge characteristics is performed via (a) spectroscopic analysis in the UV spectral region and (b) photothermal absorption imaging using 355-nm excitation.

The results suggest that although the fabrication process has a large influence on the intrinsic LIDT, it only marginally affects the estimated optical gap energy. The samples (both silica and hafnia) that exhibit the highest intrinsic LIDT also exhibit the lowest absorption in the three- to five-photon absorption spectral range (≈200 to 350 nm), while the lowest LIDT samples exhibit the highest absorption. This trend was quantified in Figs. 1(a) and 1(b) by plotting the absorption coefficient as a function of the intrinsic LIDT for monolayers of hafnia at 351 nm and silica at 266 nm. The choice of the wavelength is based on using a threshold absorption coefficient value of the order of 10^3 cm^{-1}. These results suggest the presence of a correlation between the absorption at the Urbach tail to the intrinsic LIDT at 1053 nm using 800-fs pulses.

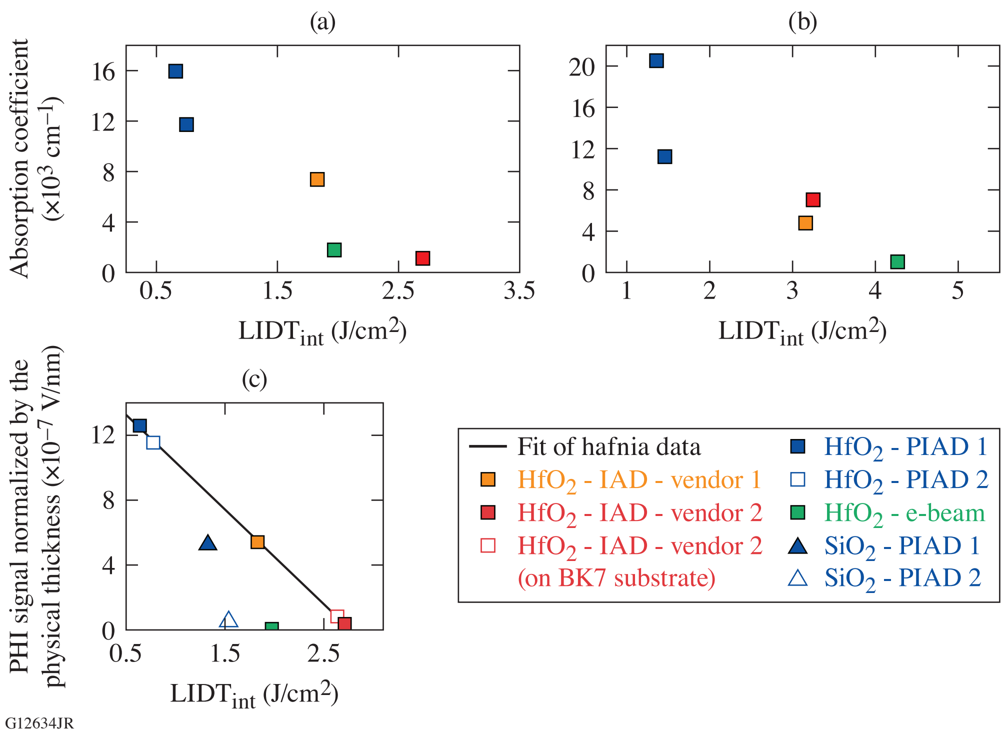

Figure 1
The absorption coefficient of (a) hafnia monolayers at 351 nm and (b) silica monolayers at 266 nm as a function of their intrinsic LIDT. (c) Photothermal heterodyne imaging (PHI) signal at 355 nm normalized by the physical thickness as a function of the intrinsic LIDT for hafnia (squares) and silica (triangles) samples.

The absorption in the UV spectral range was also probed using a photothermal heterodyne imaging system. This technique is based on a pump–probe approach and utilized a 355-nm pump beam to probe the local absorption with spatial resolution of the order of 500 nm. For each sample, several intensity maps were acquired by raster scanning, and an average value of every map for each sample was calculated. The photothermal absorption was normalized by the physical thickness of the layer. The results displayed in Fig. 1(c) demonstrate a direct relationship of the LIDT to the strength of the photothermal absorption signal.

This material is based upon work supported by the Department of Energy National Nuclear Security Administration under Award Number DE-NA0003856, the University of Rochester, and the New York State Energy Research and Development Authority.

1. A. A. Kozlov *et al*., Sci. Rep. **9**, 607 (2019).
2. F. Urbach, Phys. Rev. **92**, 1324 (1953).
3. B. Sadigh *et al*., Phys. Rev. Lett. **106**, 027401 (2011).
4. S. Papernov *et al*., Opt. Express **26**, 17,608 (2018)
5. A. Hervy *et al*., Opt. Eng. **56**, 011001 (2016).

Measurement of the Angular Dependence of Spontaneous Raman Scattering in Anisotropic Crystalline Materials Using Spherical Samples: Potassium Dihydrogen Phosphate as a Case Example

T. Z. Kosc, A. Maltsev, and S. G. Demos

Laboratory for Laser Energetics, University of Rochester

A new and flexible experimental configuration has been developed and tested to measure the spontaneous Raman scattering for samples with any crystal cut, probed with any specific pump polarization, and for which the scatter signal in any direction and with any polarization can be measured. This experimental requirement stems from the challenges, arising from the complexity of light propagation, in obtaining accurate measurements of the angular dependence of the Raman scattering cross section in birefringent materials. The nonlinear optical material KH_2PO_4 (KDP) is used as the model medium. This study is motivated by the need to improve our understanding and management of transverse stimulated Raman scattering (TSRS) in KDP crystals typically used for frequency conversion and polarization control in large-aperture laser systems. Key to this experimental platform is the use of high-quality spherical samples that enable one to measure the Raman scattering cross section in a wide range of geometries using a single sample. The system demonstrated in this work is designed to enable experiments to (1) develop a better understanding of the Raman polarizability tensor and (2) directly measure the angular dependence of the spontaneous Raman scattering in a crystal cut suitable for polarization control.

The spontaneous Raman scattering is an experimentally measureable quantity from which the Raman polarizability tensor of vibrational modes of interest can be established using the theoretically expected formulation based on symmetry as a guide.[1] Given this tensor, the Raman-scattering cross section can be estimated at any orientation and the corresponding TSRS gain coefficient can be calculated. Efforts to develop an empirical description of the Raman tensor has provided an approximation for the off-diagonal elements, but its precise form remains incomplete,[2] while measurements for the Raman scattering cross section are limited.[3] An accurate Raman polarizability tensor would enable (1) the modeling of TSRS for multiple crystal-cut configurations to guide the design of KDP-based optical elements that provide minimum SRS gain, (2) the estimation of material limits in inertial confinement fusion laser designs, and (3) the optimization of hardware designs and operational conditions.

Based on the consideration discussed above, we developed an experimental Raman scattering spectroscopy system (Fig. 1) that uses spherical crystal (KDP) samples and facilitates the measurement of the angular dependence of the spontaneous Raman scattering cross section in directions orthogonal to beam propagation for any specific crystal orientation of interest. The optic axis of the sample sphere is oriented by two programmable rotation stages. Custom vacuum chucks, installed in the open aperture of the rotation stages, are used to "hold" the sphere and rotate it. Any position on the sphere (4π steradians) can be reached with a combination of, at most, three stage moves. Linear stages provide additional vertical and horizontal alignment capabilities in the x–y plane to overlap the sphere center and the excitation laser beam focus with the focal point of the signal collection optics.

The Raman scattering intensity of the totally symmetric mode (914 cm^{-1}) integrated over 100 cm^{-1} about the peak (860 to 960 cm^{-1}) as a function of the azimuthal angle ϕ is shown in the results presented in Fig. 2. The optic axis (OA) was aligned in the azimuthal (horizontal) plane, and for $\phi = 0°$, the OA was oriented along the laboratory z axis (beam propagation direction). Four combinations of polarization of the excitation laser and the analyzer were used, with the excitation polarization parallel to the laboratory x or y axis and the analyzer parallel to the laboratory z or y axis. Accordingly, the inset in Fig. 2 describes the ini-

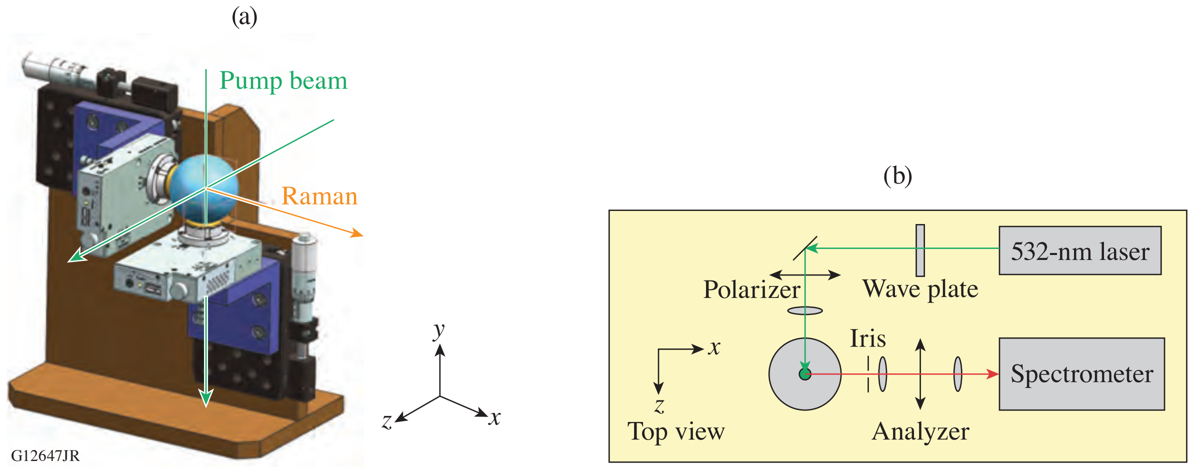

Figure 1
Schematic depiction of (a) the sample holder and (b) the Raman scattering spectroscopy system utilizing high-quality spherical samples to measure the Raman scattering signal orthogonal to the laser excitation beam. The excitation beam propagates along the horizontal laboratory z axis, while the Raman signal was measured at an orthogonal direction along the horizontal laboratory x axis.

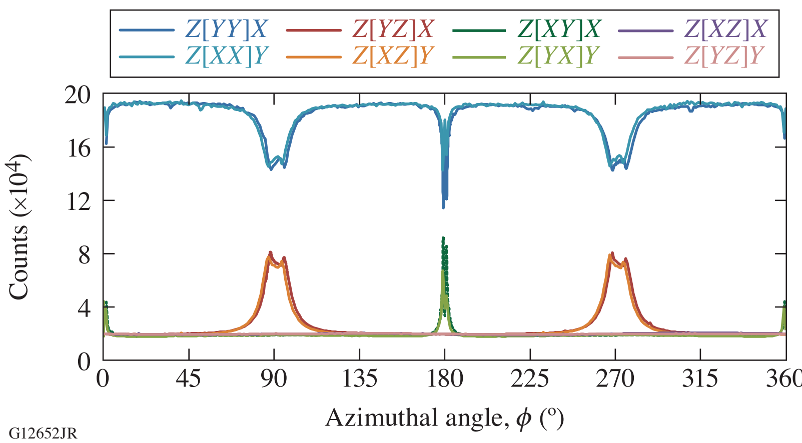

Polarization (with respect to plane of propagation)	
Pump laser	Signal
Perpendicular	Perpendicular
Perpendicular	Parallel
Parallel	Perpendicular
Parallel	Parallel

Figure 2
The integrated spontaneous Raman scattering signal of the totally symmetric internal PO_4 mode is measured as a function of the azimuthal angle for four different initial configurations, which are given in the legend and follow Porto notation. The letters to the left and right of the brackets define the propagation direction of the incident and scattered light; the letters inside the brackets, left to right, are the polarization of the incident and scattered light. Additional information on measurement geometry is provided in the table.

tial setting of the Raman scattering measurement in the Porto notation.[4] The notation in the legend of Fig. 2 refers to the crystal axes (X, Y, Z) at the initial position $\phi = 0°$. Measurements were performed with the Raman signal initially measured along the X crystal axis and then after rotating the sample by 90° about the Z crystal axis to measure the Raman signal along the Y crystal axis (X or Y directions are indistinguishable during measurement and therefore arbitrarily assigned). Consequently, eight different measurements were performed with the above-described initial alignment conditions.

The blue traces in Fig. 2 represent data acquired when both the excitation and signal polarizations were perpendicular to the (horizontal) plane of propagation. Wide double valleys are found at $\phi = 90°$ and 270°, while narrow double valleys are found at $\phi = 0°$ and 180°. An inverse set (red trace) of wide (only) double peaks is seen when the excitation laser is perpendicularly polarized. The presence of narrow double peaks (green trace) requires a parallel polarized excitation laser, but perpendicularly polarized Raman signal. The Raman signal is very low when both the excitation and the signal polarizations are parallel to the plane of propagation. Data sets were nearly indistinguishable when the sphere was rotated 90° about the optics axis to interchange to crystal *X* and *Y* axes.

The data acquired using a 30-mm polished KDP crystal in this new experimental configuration demonstrate that a more-precise measure of the Raman tensor can now be performed. This system was designed to help improve predictive capabilities in order to minimize TSRS-induced effects in large-aperture laser systems by enabling direct measurement to obtain information regarding the optimal crystal cut and crystal mounting configuration.

This material is based upon work supported by the Department of Energy National Nuclear Security Administration under Award Number DE-NA0003856, the University of Rochester, and the New York State Energy Research and Development Authority.

1. R. Loudon, Adv. Phys. **13**, 423 (1964).
2. W. L. Smith, M. A. Henesian, and F. P. Milanovich, "Spontaneous and Stimulated Raman Scattering in KDP and Index-Matching Fluids," 1983 Laser Program Annual Report, pp. 6-61– 6-69, Lawrence Livermore National Laboratory, Livermore, CA, UCRL-500.21-83 (1984).
3. S. G. Demos *et al*., Opt. Exp. **19**, 21050 (2011).
4. T. C. Damen, S. P. S. Porto, and B. Tell, Phys. Rev. **142**, 570 (1966).

Comparison of Shadowgraphy and X-Ray Phase-Contrast Methods for Characterizing a DT Ice Layer in an Inertial Confinement Fusion Target

D. R. Harding, M. D. Wittman, N. Redden, D. H. Edgell, and J. Ulreich

Laboratory for Laser Energetics, University of Rochester

Shadowgraphy and x-ray phase-contrast (XPC) imaging are two techniques that are used to characterize the deuterium–tritium (DT) ice layer in inertial confinement fusion targets. Each technique has limitations that affect how accurately they can characterize small crystalline defects and measure ice-thickness nonuniformities that may be only a few micrometers in height. The purpose of this study is to determine if shadowgraphy is overly sensitive to the size of defects at the ice surface and insufficiently sensitive to the shape of longer-wavelength roughness, and if XPC is too insensitive to defects at the ice's inner surface.

Multiple ice layers with different thicknesses (40 to 63 μm), thickness uniformities (peak-to-valley variations that range from <2 to 12 μm), and crystal defects were analyzed using shadowgraphy and XPC techniques. The inability to rotate the target so that the same region of the ice layer was imaged by each method limited how extensively the two techniques could be compared; however, the relative accuracy of each technique for measuring the size of the perturbation to the ice near the fill tube could be compared because the thermal profile (and therefore the low-mode ice thickness distribution) around the target is axisymmetric around the fill-tube axis: crystal defects that intersected the fields of view of both techniques could also be compared. Results from each technique agreed when the ice layer was uniformly thick and the crystal lacked defects. That agreement worsened as the number of defects at the surface of the ice layer increased or as the perturbation to the ice layer at the fill tube increased. Shadowgraphy is very sensitive to identifying defects in the crystal, and the size of those defects was consistently larger than the size reported by XPC and unlikely to be physically possible since β-heating is expected to smoothen them. Large defects, such as features that typically occur at each end of the *c* axis of the DT crystal, were measured using both techniques.

The dimensions of the ice layer near the fill tube that was thicker (or thinner) than elsewhere were reported by shadowgraphy to be smaller in height and area than by XPC. This is shown in the ice-thickness measurement of a 2-D slice through the target (Fig. 1). XPC analysis reported the ice layer to have a shape with the majority of the spectral power in low modes, which is expected for a thermal nonuniformity induced by the fill tube; shadowgraphic analysis of the ice layer showed the profile at the fill tube to be smaller in height and width. Two separate shadowgraphic analyses that use caustics to trace different paths through the target and, in theory, image the same ice/vapor surface, did not consistently report the ice perturbations to have the same size or shape. The XPC method, in theory and from the consistency of the experimental results, provided the best assessment of low-mode ($\ell < 7$) roughness in ice layers, and the shadowgraphy method using the brightest caustic provided the best method for detecting the presence of grooves in the ice, although not for quantifying the size of them. Caution: If multiple grooves are present, the analysis can be ambiguous and it is best to melt and reform the ice layer.

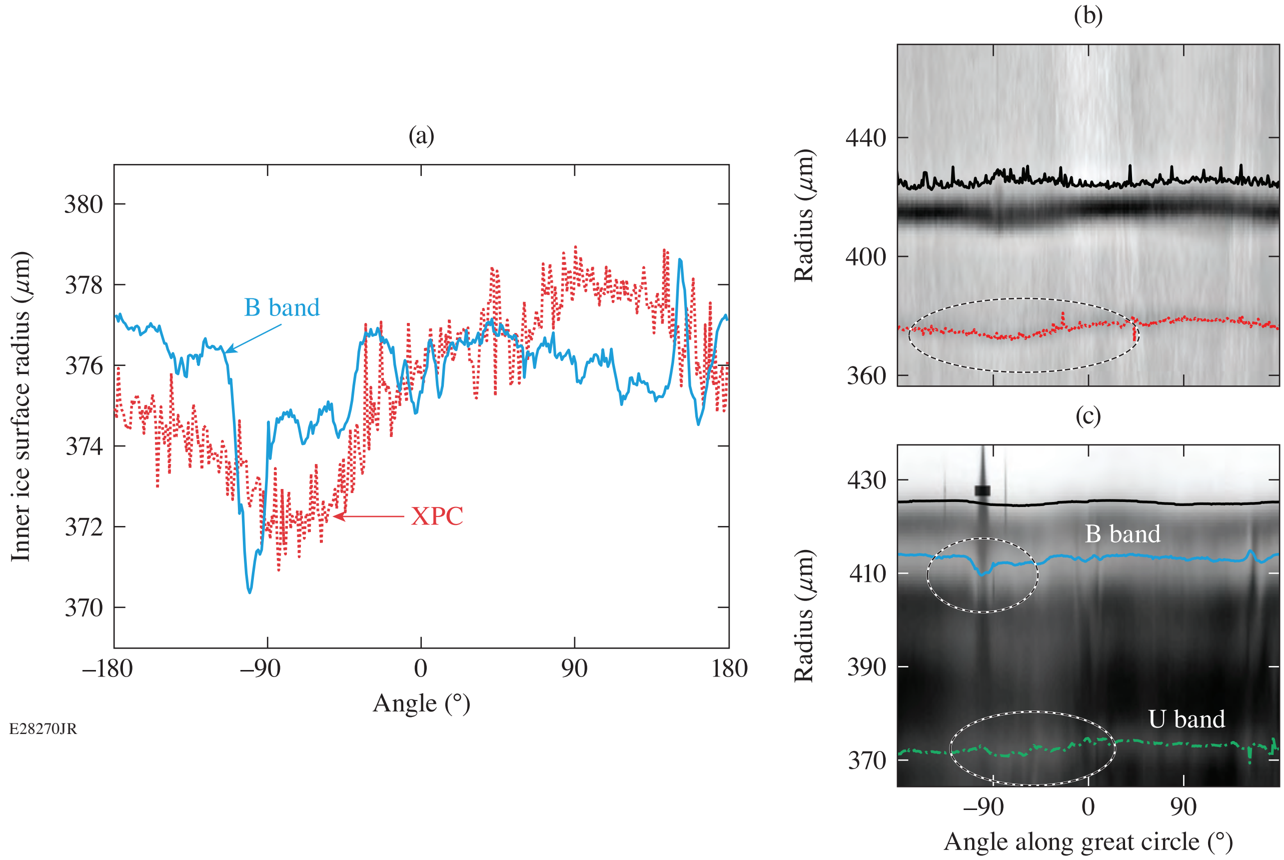

Figure 1
(a) Unwrapped ice/vapor interfaces characterized by shadowgraphy (B band) and XPC analysis are superimposed over each other to demonstrate the effect of the fill tube on the thickness uniformity of the ice layer. The 41-μm-thick ice layer is reported to have a larger and wider perturbed region (circled) in (b) the XPC image and analysis than in (c) either of the (circled) B- and U-band analyses (solid blue line and dashed green line, respectively). The fill tube is located at –90°.

This material is based upon work supported by the Department of Energy National Nuclear Security Administration under Award Number DE-NA0003856, the University of Rochester, and the New York State Energy Research and Development Authority.

Prediction of Deuterium–Tritium Ice-Layer Uniformity in Direct-Drive Inertial Confinement Fusion Target Capsules

B. S. Rice,[1] J. Ulreich,[2] and M. J. Shoup III[2]

[1]Rochester Institute of Technology
[2]Laboratory for Laser Energetics, University of Rochester

High-yield inertial confinement fusion targets require that the uniformity of the DT ice layer be less than 1-μm rms (Ref. 1). The uniformity of the ice layer (i.e., the solid/gas phase boundary) is affected by the surrounding helium environment and the structure that supports the target. To aid the designer of target support structures, the sensitivity of ice-layer uniformity to support structure thermal conductivity and a 3-mW heat source in the surrounding helium are studied using computational fluid dynamic simulations.

Figure 1 shows the detailed geometry used for the multiphase conjugate heat-transfer numerical model. The environment around the target and target support consists of low-pressure (2-Torr) helium gas that carries the heat produced by tritium beta decay to a surrounding copper shroud, which is connected to the cryocooler.

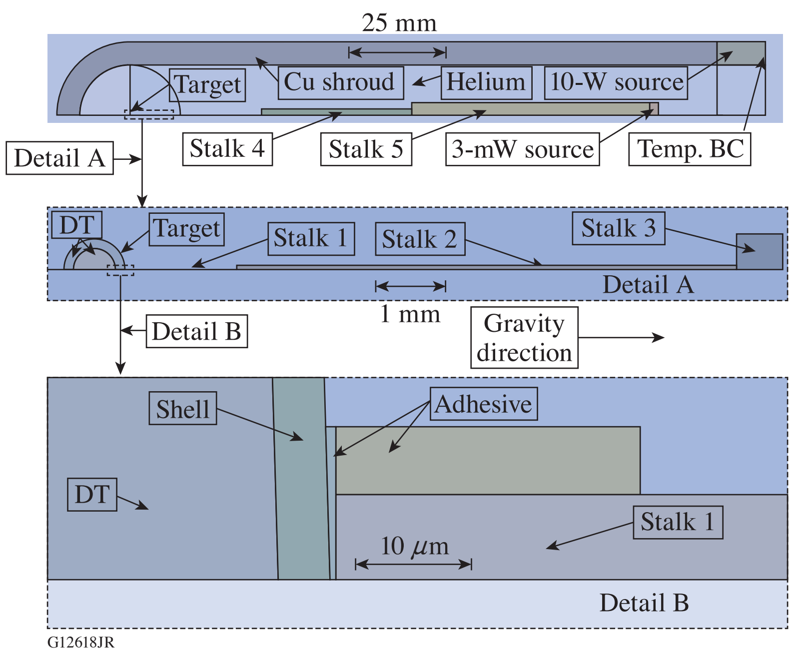

Figure 1
Model geometry detail. Temp. BC: temperature boundary condition.

Figure 2 shows one of the meshes used. The outer portion of DT closest to the target capsule uses an element size of ~5×5 μm to resolve the gas/ice phase boundary. Elements representing the 17-μm SiC support, target capsule shell, and adhesive are also ~5×5 μm in size. Other areas of the model use a coarser mesh for a more-efficient solution. Based on a mesh refinement study, the results presented are mesh independent. Sensitivities to various parameters were studied with this model.

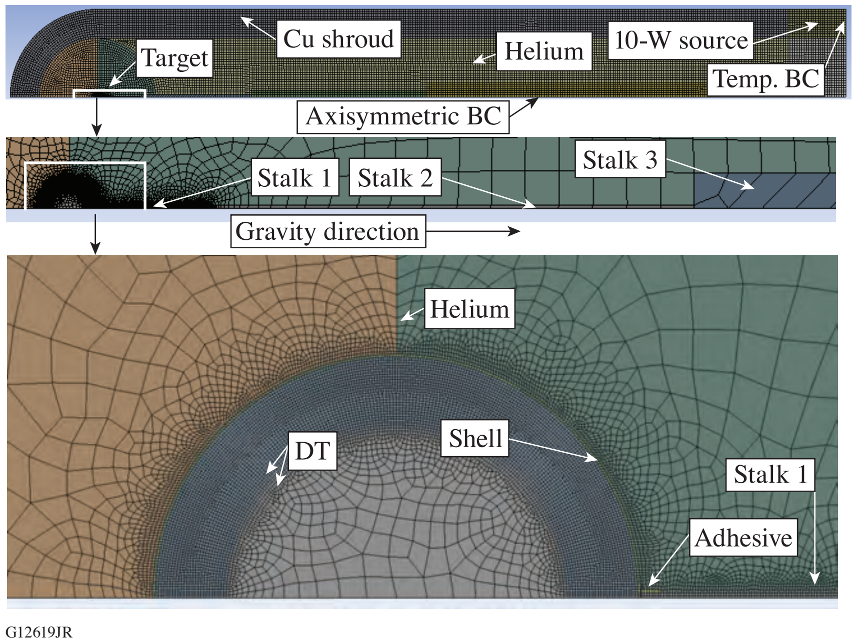

Figure 2
Model of mesh detail.

Experimental data of DT ice-layer uniformity were used to validate several of the multiphase conjugate heat-transfer numerical simulations. Based on experiment results and/or numerical simulations, the following conclusions were made:

- When heat sources are present in the helium environment, it is advantageous for the lower portion of the support structure to have a thermal conductivity of less than ~2 W/m/K.
- For the temperature variations and helium pressures studied, multiphase conjugate heat-transfer ice-layer models yield the same results as multiphase conduction-only models.
- The thermal conductivity of the fiber directly touching the target capsule must be a close match to helium thermal conductivity (0.026 W/m/K) to produce uniform ice layers.
- High target-shell thermal conductivity (~27 W/m/K) mitigates locally thick ice near a highly conductive (~1.5-W/m/K) support stalk.

This material is based upon work supported by the Department of Energy National Nuclear Security Administration under Award Number DE-NA0003856, the University of Rochester, and the New York State Energy Research and Development Authority.

1. S. X. Hu *et al.*, Phys. Plasmas **17**, 102706 (2010).

Developing a Curriculum for the Translation of Microscopy with Ultraviolet Surface Excitation (MUSE) into a High School Science Classroom

K. Kopp and S. G. Demos

Laboratory for Laser Energetics, University of Rochester

The translation of microscopy with ultraviolet surface excitation (MUSE) into a high school science classroom is investigated with the goal of providing a suitable new modality to enhance life science education. A key part of this effort is the development of laboratory exercises that can integrate the advanced capabilities of MUSE into a classroom setting. We consider that MUSE in education can eliminate the need for premade microscope slides and provide a far more engaging and rewarding experience for students.

MUSE is a new microscope technology originally developed to locate defects in optical materials that were responsible for introducing laser-induced damage in optical materials for large-aperture laser systems such as OMEGA. This method is based on the salient property of UV light at wavelengths between 250 and 285 nm to propagate into only the top 10 μm of a tissue specimen, illuminating only the top cell layer.[1–3] The resulting fluorescence images, arising from either the native tissue fluorophores or extrinsic contrast agents, are also localized within this narrow range. This enables one, with proper selection of imaging optics, to acquire high-quality images without implementing any additional optical sectioning method (such as confocal imaging) or physical sectioning of the specimen into very thin layers. In addition, UV light can photoexcite a wide range of common fluorescing stains, which subsequently emit light typically in the visible spectrum.[2,3]

Tissues produce autofluorescence when exposed to any form of photoexcitation, but UV light causes a relatively larger amount of autofluorescence, typically dominated by the emission by tryptophan.[1] MUSE imaging relies on the visible structural differentiation caused by either the nonuniform cellular distribution of naturally occurring biomolecules or the use of fluorescing stains to highlight different cellular compartments. This allows one to image the cellular organization and microstructure without laborious effort (fix, dehydrate, embed in wax, cut, and stain) to produce a thin stained section. In this work, tissue samples were stained using Hoechst 33342 and Eosin Y, which stain the nuclei and cytoplasm, respectively, and are safe for classroom handling and use.[4] Premixed powders in a gelatin capsule have been made with 20 g of Eosin Y and 5 g of Hoechst 33342, and the capsule is readily soluble in 100 mL of de-ionized water, resulting in a stain solution that is plenty for a single class. The goal of this work was to develop a curriculum involving MUSE that can be adapted to life science education. To do this, laboratory exercises for a high school science class were created to enhance student interest with a personalized learning approach.

A MUSE imaging setup was configured similar to that described in Ref. 4. In short, the UV LED illumination is at an oblique angle and focused on the sample directly under the 10× objective. This system was used to view plant and animal microanatomy with a quick, simple, and inexpensive process. This system was also used to image tissues without any preparation, as well as stained tissue samples. Imaging experiments of various objects, plants, and animal tissues were performed toward (a) exploring the spectrum of MUSE imaging suitable for an education setting and (b) developing laboratory experiments relevant to the high school science classroom. Laboratory procedures, background, and examples were written for each experiment. These exercises utilize MUSE technology while complementing the current life science curriculum standards. The labs bring a personalized learning approach to obtaining high-quality images of tissue microstructure that reinforce material learned through classwork. The developed MUSE curriculum focuses on exposing high school students to scientific practices that reinforce their knowledge about life science. Each practice learned through the laboratory exercises is relevant to the public high school life science standards, and the coordinating Next Generation science standard is referenced.[5]

The first practice that this curriculum emphasizes is the identification of major structures in plant samples. Students can view organisms such as leaves (see Fig. 1), grass, and flowers under the microscope and use the resulting images to find certain microstructures, such as leaf veins. By looking at various cells and structures within one organism, students are learning about cellular specialization and organization. This practice reinforces Next Generation standards HS-LS1-1 and HS-LS1-2.

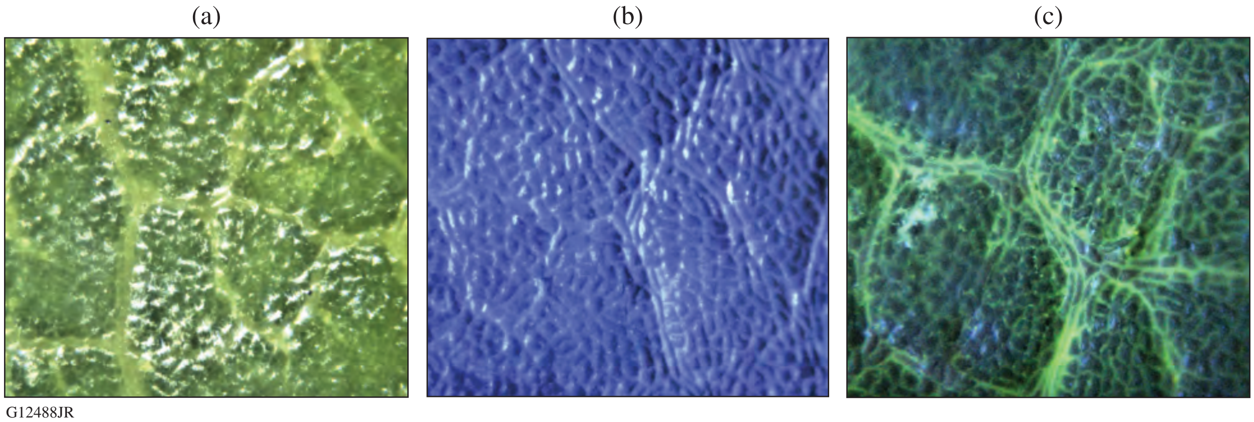

Figure 1
Images from the surface of a maple leaf: (a) conventional white-light illumination, (b) autofluorescent image, and (c) staining with Hoechst 33342 and Eosin Y.

The next scientific practice with which students are involved is the dissection of an organism to view gross anatomy as well as tissue microstructure. When students dissect an organism, they work to understand the hierarchical levels of organization within a multicellular organism. This corresponds to Next Generation standard HS-LS1-2. Students can identify organs and organ systems in an organism and then take a tissue sample to view the same organism's microanatomy at the cellular level.

The last emphasized practice is the comprehension of the structure and function of plant and animal cells. This practice works on a microscopic scale and focuses on life processes at the cellular level. Plant and animal cells have different organelles to perform different functions, and each organelle and cell has specific structures that relate to its function. The various cells work together to perform life processes to maintain homeostasis within an organism. This is shown in Next Generation standard HS-LS1-2.

Additional laboratory exercises can be developed to offer distinctive experiences to students such as experiments that enable one to monitor the dynamic response of cells and tissues to an external stimulus.

This material is based upon work supported by the Department of Energy National Nuclear Security Administration under Award Number DE-NA0003856, the University of Rochester, and the New York State Energy Research and Development Authority.

1. B. Lin *et al.*, Opt. Express **18**, 21,074 (2010).

2. R. M. Levenson *et al.*, Proc. SPIE **9703**, 97030J (2016).

3. F. Fereidouni *et al.*, Nat. Biomed. Eng. **1**, 957 (2017).

4. C. Z. R. Huang, R. W. Wood, and S. G. Demos, J. Biomed. Opt. **23**, 12,1603 (2018).

5. *Next Generation Science Standards: For States, by States*, The National Academies Press, Washington, DC (2013).

FY19 Q2 Laser Facility Report

J. Puth, M. Labuzeta, D. Canning, and L. J. Waxer

Laboratory for Laser Energetics, University of Rochester

During the second quarter (Q2) of FY19, the Omega Laser Facility conducted 380 target shots on OMEGA and 196 target shots on OMEGA EP for a total of 576 target shots (see Tables I and II). OMEGA averaged 12.2 target shots per operating day averaging 95.0% Availability and 96.2% Experimental Effectiveness.

Table I: OMEGA Laser System target shot summary for Q2 FY19.

Program	Laboratory	Planned Number of Target Shots	Actual Number of Target Shots
ICF	LLE	99	106
	LANL	11	8
	LLNL	33	35
ICF subtotal		143	149
HED	LLE	22	21
	LANL	44	46
	LLNL	27.5	30
HED subtotal		93.5	97
LBS		33	33
NLUF		22	25
LLE calibration	LLE	0	76
Grand total		291.5	380

Table II: OMEGA EP Laser System target shot summary for Q2 FY19.

Program	Laboratory	Planned Number of Target Shots	Actual Number of Target Shots
ICF	LLE	52.5	73
	LLNL	14	12
ICF subtotal		66.5	85
HED	LLE	21	29
	LLNL	28	38
	SNL	7	7
HED subtotal		56	74
LBS		21	26
LLE calibration	LLE	0	11
Grand total		143.5	196

OMEGA EP was operated extensively in Q2 FY19 for a variety of user experiments. OMEGA EP averaged 8.2 target shots per operating day averaging 93.6% Availability and 98.4% Experimental Effectiveness.

In Q2 FY19, the full-beam in-tank (FBIT) diagnostic was used to characterize the on-shot, on-target focal spot of five additional OMEGA beams, bringing the total to 11 beams characterized. Measurements included near fields and far fields. The far fields have been measured with and without distributed phase plates, smoothing by spectral dispersion, and distributed polarization rotators. The far-field data represent on-shot conditions during OMEGA cryogenic experiments. An additional 20 beams will be characterized during the remainder of FY19 and early FY20, providing a more-complete characterization of on-target laser uniformity.

The Effect of Cross-Beam Energy Transfer on Target Offset Asymmetry in Directly Driven Inertial Confinement Fusion Implosions

K. S. Anderson,[1] C. J. Forrest,[1] O. M. Mannion,[1] F. J. Marshall,[1] R. C. Shah,[1] D. T. Michel,[1,2] J. A. Marozas,[1] P. B. Radha,[1] D. H. Edgell,[1] R. Epstein,[1] V. N. Goncharov,[1] J. P. Knauer,[1] and M. Gatu Johnson[3]

[1]Laboratory for Laser Energetics, University of Rochester
[2]Applied and Theoretical Optics Department, ONERA, Palaiseau, France
[3]Plasma Science and Fusion Center, Massachusetts Institute of Technology

It is well known that at typical inertial confinement fusion (ICF) laser intensities, cross-beam energy transfer (CBET)[1] can cause significant laser energy losses to directly driven inertial confinement implosions. When CBET occurs, incoming laser light from one beam interacts with refracted, outgoing light from other beams, stealing some energy from the incoming light and scattering that energy away from the target along the path of the outgoing light rays. The result is a decrease in the ablation pressure, implosion velocity, and compression of the capsule, leading to lower fusion yield. One-dimensional simulations of direct-drive implosions at LLE have for years included CBET physics to better model implosions. However, because of the computational expense of including CBET physics in multidimensional simulations, these have often used a simpler, flux-limited Spitzer–Härm thermal transport method, where the flux limiter is variable in time and chosen to match the observables of more-detailed 1-D simulations, which include the nonlocal thermal transport (NLTT) and CBET physics. Because of this, few studies have been performed that include the effects of CBET on the symmetry of direct-drive ICF implosions.

One major source of laser nonuniformity is target mispositioning or offset. When the target is mispositioned with respect to the center of convergence of the laser beams, a perturbation with a dominant $\ell = 1$ mode is present in the illumination pattern on target, with the "hot side" (the side with higher illumination) being opposite the direction of the offset. Previous simulations without CBET have indicated that this $\ell = 1$ offset perturbation persists in time at high amplitude, resulting in highly degraded yields and distorted hot spots, even when target offsets are small, of the order of 10 μm or about 2% of the radius of a typical capsule imploded on the 60-beam OMEGA Laser System. In contrast, fusion yields from cryogenic implosions on OMEGA show relatively low sensitivity to target offsets of this magnitude. This discrepancy between simulation and experiment has not been previously understood.

To study the effect of target offset in a more-controlled environment, experiments with room-temperature capsules were performed on OMEGA with prescribed offsets. These room-temperature experiments are simpler to field on OMEGA and require no cryogenic target handling or shroud, allowing more precise control of target positioning. Furthermore, these capsules have no cryogenic fuel layer, which typically represents a large and variable source of implosion nonuniformity and further complicates analysis. Results from these experiments were compared with 2-D *DRACO* simulations including the effects of CBET[2] plus a modified[3] Schurtz–Nicolaï–Busquet nonlocal thermal transport model (CBET–NLTT) as well as no-CBET *DRACO* simulations using a variable flux limiter (VFL). These comparisons illustrate the effect of CBET on the $\ell = 1$ laser drive uniformity, hot-spot x-ray core symmetry, and fusion yields. Note: the hydrodynamics and transport in *DRACO* are 2-D, but the laser ray-trace package is fully 3-D; this is sufficient to model target offset with CBET.

The normalized fusion yields from both the experiment and simulations are plotted in Fig. 1. The curves in Fig. 1 plot yields for *DRACO* simulations with varying offsets for a single shot (88575) with the CBET–NLTT model (solid red curve) and the VFL model (dashed blue curve). The simulations with the as-measured target offsets are shown with the red diamonds (CBET–NLTT)

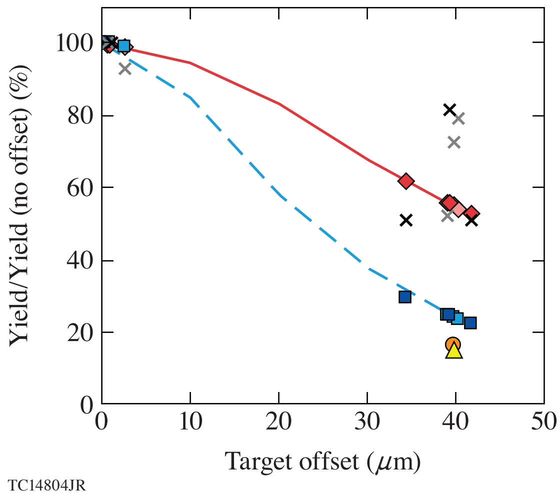

Figure 1
Normalized neutron yields for *DRACO* simulations (CBET–NLTT: red diamonds; VFL: blue squares) and experiment (×'s). D_2 shots are shown in the lighter shades. Normalized yield trend lines are shown for shot 88575 varying the target offset in simulations (CBET–NLTT: solid red curve; VFL: dashed blue curve). For comparison, two simulations with a power-imbalance–induced $\ell = 1$ asymmetry equivalent to that of a 40-μm target offset at $t = 0$ were modeled (CBET–NLTT: orange circle; VFL: yellow triangle).

and blue squares (VFL). Experimental data are shown with the ×'s. Normalized yields are shown for both the D_2 shots (lighter shades) and DT shots (darker shades). The simulation data show that the fusion yields are less sensitive to target offset when the CBET–NLTT model is used versus the VFL model, and that this difference occurs even for small target offsets. The variation in experimental yields in the offset shots is assumed to result from directional interactions with the target-mounting stalk and other systematic and/or random variations between shots, which are not modeled in the simulations.

For the D_2 shots, four x-ray framing cameras were deployed to collect time-resolved images of the coronal x-ray emission during the acceleration phase of the implosion from four different views. These images were then used to infer the centroid of the capsule as a function of time using the methodology of Ref. 4. Simulated time-resolved images were generated by post-processing *DRACO* data with *Spect3D*.[5] The results from both experiment and simulation show that the center of the capsule experiences a linear spatial drift away from its initial position that is approximately linear when plotted versus the distance traveled by the shell. When the capsule radius had shrunk to $\simeq$150 μm, the distance traveled by the capsule center from the $t = 0$ position in the offset shots was measured experimentally to be between 9.2 to 10.0 μm along the offset direction with a 1.1- to 1.5-μm movement orthogonal to the offset direction (the measurement uncertainty was ±1.0 μm). The orthogonal movement is attributed to nonuniformity sources other than target offset. Reasonable agreement with experiment is seen in simulations with the CBET–NLTT model, which indicates the center drift along the offset direction is 12.0 μm. By contrast, the VFL model predicts 16.6-μm center drift, well outside the error bars.

On all shots, time-integrated x-ray images of the hot-spot core emission were obtained from the gated monochromatic x-ray imager (GMXI). The centroid of the core x-ray image was then calculated with respect to that of the target chamber center (TCC) reference shot for each series (D_2 and DT) to quantify the distance of the core in each offset shot relative to the reference target, following the methodology of Ref. 6. Time-integrated simulated images of the core x-ray emission were also generated from *DRACO* using *Spect3D* to compare with the GMXI images. The data are shown in Fig. 2. Figures 2(a) and 2(c) are the density contour of the target at peak compression and the time-integrated x-ray image from the VFL *DRACO* and *Spect3D* of shot 88581, respectively, whereas Figs. 2(b) and 2(d) are the same, respectively, for the CBET–NLTT model. Figure 2(e) is the experimental image. In each image, the position of TCC is shown with an ×. The same analysis was done for the TCC reference shot 88578. Analysis shows that the distances between the centroid of x-ray emission of shots 88581 and 88578 are 61±2 μm for the experiment and 63 μm and 71 μm for the simulated CBET–NLTT and VFL, respectively. Only the CBET–NLTT result fits within the experimental error bars.

This mitigation of offset-induced nonuniformity by CBET effects can be understood geometrically. The shift of the target away from the center of beam convergence means that more laser light refracts past the target to interact with the incoming beams on the hot side, relative to those on the cold side. This stimulates more CBET losses on the hot side than on the cold side, effectively reducing the $\ell = 1$ illumination nonuniformity. This effect is also observed in simulations and experiments of polar-drive experi-

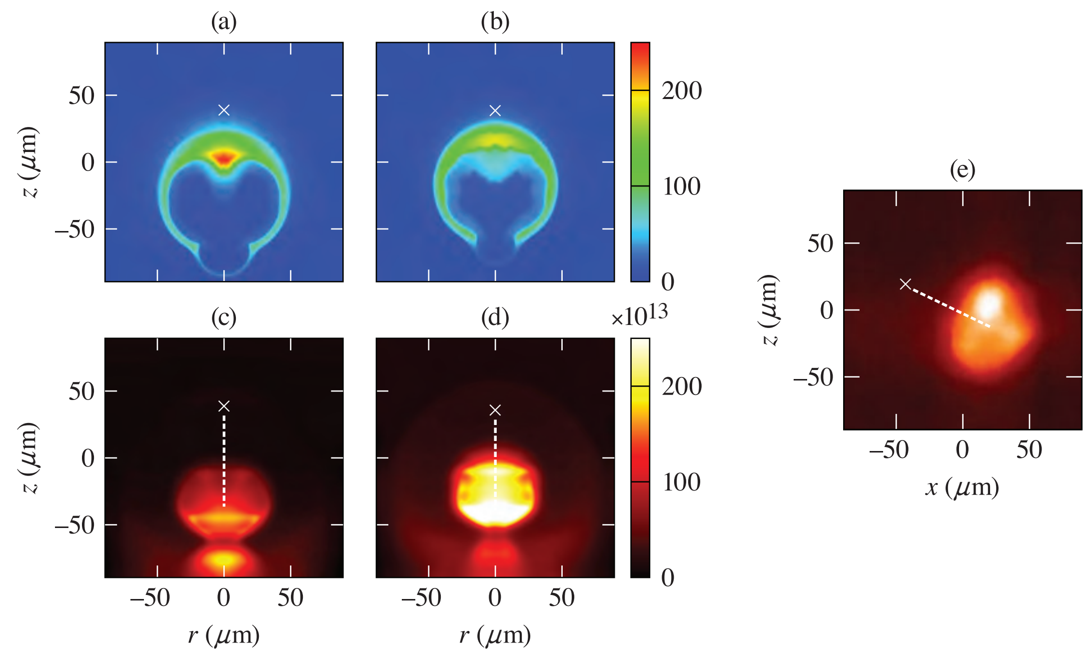

Figure 2
Density plot (g/cm^3) at stagnation from *DRACO* simulations of shot 88581 with (a) VFL and (b) CBET–NLTT. Simulated time-integrated x-ray images generated by *Spect3D* from these simulations are shown in (c) VFL and (d) CBET–NLTT. (e) The experimental image from GMXIc. In all images, the location of TCC is shown by the × and the distance between TCC and centroid of emission indicated by the dashed white line.

ments[2] that show CBET is higher at the equator where beams are pointed away from the target center to improve illumination uniformity, and in experiments where the beam-to-target ratio is reduced[7] to mitigate CBET. *DRACO*'s in-line scattered-light diagnostics support this conclusion, showing enhanced CBET-scattered light from the hot side of the target. To illustrate that this is a geometric effect arising from target offset, both CBET–NLTT and VFL *DRACO* simulations were performed, inducing an $\ell = 1$ using a prescribed laser power imbalance with the same initial mode amplitude as with the target offset of 40 μm. The resulting normalized yields, shown in Fig. 1 by the orange circle (CBET–NLTT) and yellow triangle (VFL), are very close to each other and similar to the yield of the VFL offset simulation, indicating no mitigation of the power-imbalance–induced $\ell = 1$ by CBET.

In conclusion, CBET in direct-drive inertial confinement mitigates the implosion asymmetry caused by target offset. Simulations modeling target offset require a 3-D laser ray-trace model including CBET to accurately capture this asymmetry mitigation and to give better agreement with experimental observables.

This material is based upon work supported by the Department of Energy National Nuclear Security Administration under Award Number DE-NA0003856, the University of Rochester, and the New York State Energy Research and Development Authority.

1. I. V. Igumenshchev *et al*., Phys. Plasmas **17**, 122708 (2010).
2. J. A. Marozas *et al*., Phys. Rev. Lett. **120**, 085001 (2018).
3. D. Cao, G. Moses, and J. Delettrez, Phys. Plasmas **22**, 082308 (2015).
4. D. T. Michel *et al*., Phys. Rev. Lett. **120**, 125001 (2018).
5. J. J. MacFarlane *et al*., High Energy Density Phys. **3**, 181 (2007).
6. W. Grimble, F. J. Marshall, and E. Lambrides, Phys. Plasmas **25**, 072702 (2018).
7. D. H. Froula *et al*., Phys. Rev. Lett. **108**, 125003 (2012).

Wavelength-Detuning Cross-Beam Energy Transfer Mitigation Scheme for Polar Direct Drive on SG-III

J. A. Marozas and E. M. Campbell

Laboratory for Laser Energetics, University of Rochester

Introduction

In direct-drive inertial confinement fusion (ICF), laser beams irradiate a plastic-coated shell of frozen deuterium–tritium (DT) and ablatively drive an implosion. The ultimate goal of ICF is ignition and energy gain; the minimum shell kinetic energy required for ignition (defined as when the energy from DT fusion reactions exceeds the laser energy incident on the target) is given by $E_{\text{min}} \sim \alpha^{1.88} P_{\text{abl}}^{-0.77} v_{\text{imp}}^{-5.89}$ (Ref. 1), where the three parameters of the implosion—α, v_{imp}, and P_{abl} [adiabat (the ratio of the fuel pressure to the Fermi-degenerate pressure at peak implosion velocity), implosion velocity, and ablation pressure, respectively]—are determined primarily by the deposition of the laser energy into the coronal plasma of the target and heat conduction to the ablation surface. Cross-beam energy transfer (CBET)[2] has been identified in direct-drive experiments on the OMEGA[3] and National Ignition Facility (NIF)[4] lasers to reduce absorption, ablation pressure, and implosion velocity. The presence of CBET on the SG-III facility[5] is anticipated to cause similar issues by reducing target absorption and the resulting reduction in ablation pressure and implosion velocity.

CBET laser–plasma interaction results from two-beam energy exchange via stimulated Brillouin scattering,[2] which reduces absorbed light and consequently reduces ablation pressure and implosion velocity. The dominant CBET loss mechanism in direct drive occurs when rays counter-propagate (backscatter mode), increasing scattered light, as illustrated in Fig 1. For the ignition-relevant overlapped beam intensities of ~8×10^{14} W/cm^2 for NIF experiments, CBET is calculated to reduce laser absorption by 22%, the average implosion speed

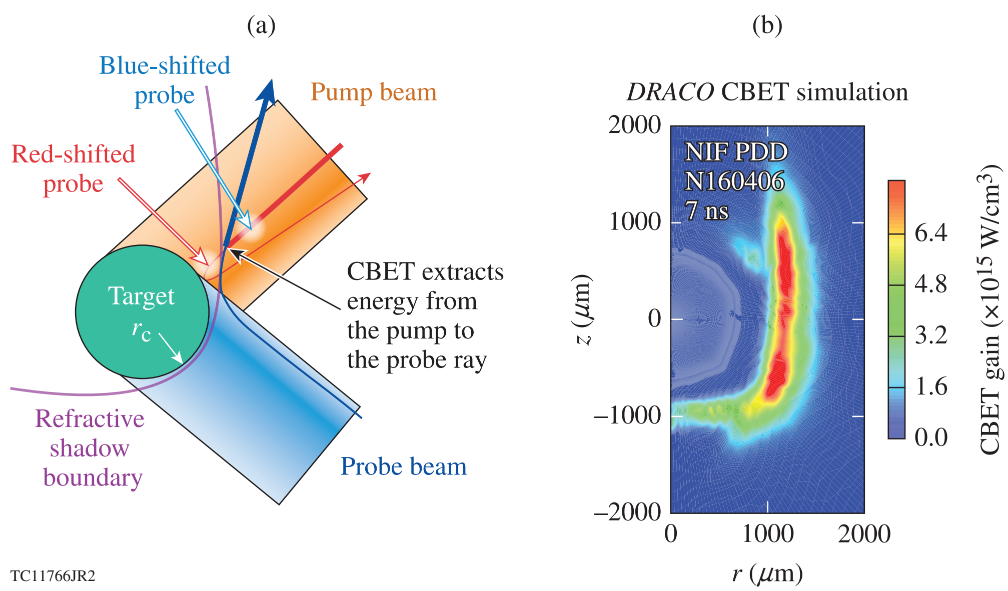

Figure 1
(a) The effect of cross-beam energy transfer (CBET) (backscatter mode) in polar direct drive (PDD) predominantly affects the equatorial region where rays interact. (b) The CBET effect dominates the equatorial region, as shown where successful CBET mitigation benefits the same region.

by ~9%, and the average ablation pressure by 35% (Ref. 6). These drive-related results are consistent with other ongoing OMEGA-[7] and NIF-scale[8] experiments. Reducing the target mass compensates for CBET losses, but the thinner shells become compromised as a result of hydrodynamic instability growth.[9] As shown by the above equation for E_{min}, efficient laser–energy coupling and hydrodynamic stability are essential aspects of direct-drive ICF, making CBET mitigation vital. Mitigation strategies of the deleterious CBET effects invoke combinations of spatial, temporal, and wavelength domains. Wavelength detuning works by altering the resonance condition between interacting beams.[2] Wavelength detuning was first examined for indirect drive[10] and subsequently for direct drive, but it was prematurely dismissed as a viable option.[11] Wavelength detuning was shown to mitigate CBET on the NIF in direct-drive experiments and to increase the drive relative to a no-detuning case;[6] *DRACO* simulations predict similar expectations on the SG-III facility.

Laser Facility and CBET Mitigation

The SG-III facility (see Fig. 2) has a similar indirect-drive configuration as the NIF, albeit with a single beam in each port as compared to NIF's quad architecture.[6,12] The SG-III facility provides a potential collaboration between LLE and SG-III. The indirect-drive beam geometry distributes the beam ports toward the poles of the target interaction chamber, forming cones of beams with a common polar angle.[13] This configuration must be altered to perform direct-drive experiments with a reasonably uniform drive. Repointing higher-intensity beams from lower latitudes toward the equator partially compensates for the indirect-drive port geometry and higher incident angles when illuminating direct-drive targets. In this modified configuration, referred to as polar direct drive (PDD),[14,15] CBET predictably dominates in the equatorial region,[6,12] where most of the cross-beam interactions occur, as shown in Fig. 1(b). As a result, PDD implosions tend to become oblate because CBET reduces the laser drive preferentially in the equatorial region. With this motivation, a basic wavelength-detuning strategy exploits the PDD configuration, where each hemisphere has a different wavelength or color. However, the nominal symmetric wavelength mapping on the NIF developed for indirect-drive targets precludes achieving hemispheric wavelength detuning using typical PDD repointing configurations.[15] A beam repointing method, called cone swapping,[12] was utilized on the NIF; it permits a partial hemispheric wavelength difference about the equator. The SG-III facility is assumed here to provide a more flexible color-to-beam mapping than available on the NIF. Cone swapping could still be applied to the SG-III facility if required but would produce nonoptimal results. For the purposes of this summary, the SG-III facility is assumed to provide three separate initial colors or wavelength shifts $\Delta\lambda_0 = \{\lambda_1,\lambda_2,\lambda_3\}$ detuned from a central wavelength $\lambda_0 \sim 351$ nm. The colors would be used to establish a bi- or tricolor distribution about the northern and southern hemispheres and yield the primary CBET mitigation strategy in any ICF direct-drive laser system.

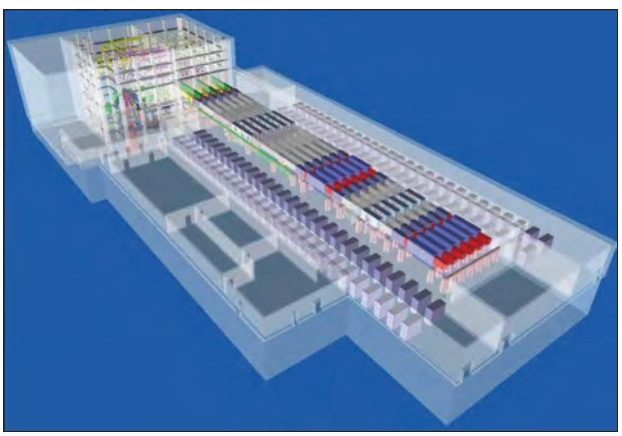

TC14723JR

Figure 2
The SG-III facility has a similar indirect-drive configuration as the NIF, albeit with single beams in each port as compared to NIF's quad architecture. The SG-III facility provides a potential collaboration between LLE and SG-III.

The far-field spot envelope [induced from distributed phase plates (DPP's)[16] and small-divergence smoothing] determines the overlapped nonuniformity on any direct-drive ICF laser system. For the PDD configuration, care is taken to design the spot shapes to account for necessary repointing of the beams toward the equator. An ideal PDD spot shape minimizes any energy that would otherwise be projected over the target horizon when repointed, while maintaining the best underlying beam profile using a method referred to as spot-masking apodization (SMA); this provides a substantial energy savings of ~15% to 20% (Ref. 17). In addition to the consideration of over-the-horizon energy loss, SMA can be employed as a CBET mitigation method by reducing the outer perimeter of the spot shape to a value that slightly underfills the full target diameter without severely effecting overlap nonuniformity like smaller spots.[12] Current SG-III spot shapes could be used in the interim (similar to experiments on the NIF[6]) before optimized DPP's are designed and manufactured.

Simulations Predictions

The initial proposed target designs for SG-III are an energy-scaled version of the first wavelength-detuning experiments performed on the NIF.[6] The warm plastic (CH) target is 640 μm in radius and has a 55-μm-thick CH shell filled with 20 atm of D_2 fuel at room temperature (see Fig. 3). A 100-kJ energy reference pulse provides the drive for the PDD target. This average pulse is a composite of different scaled energies for each ring of beams, where the different energies provide a nearly uniform drive that compensates for angular hydroefficiencies: the intensity on target near the equatorial region is larger than that near the polar region. The nonuniform delivered on-target intensity compensates for higher refraction suffered by equatorial rays as well as the lower hydrodynamic efficiency in that region. The pulse shape shown here would drive the target slowly (~300 μm/ns) to avoid large hydrodynamic instability growth seeded by laser imprint. Initial experiments would focus on the CBET mitigation properties and not initially on the fusion performance.

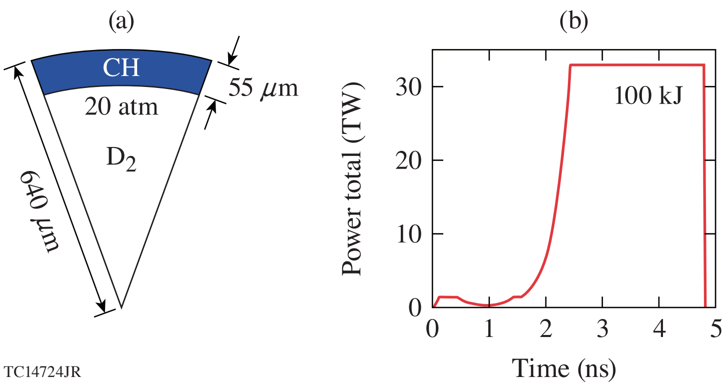

Figure 3
(a) The SG-III warm plastic (CH) target is 640 μm in radius and has a 55-μm-thick CH shell filled with 20 atm of D_2 fuel at room temperature. (b) The 100-kJ pulse provides a modest drive that could be enhanced after initial experiments.

The PDD repointing configuration suggested for the SG-III facility closely resembles what was recently shot on the NIF, where four rings of beams are distributed about the target surface (see Fig. 4). The PDD repointing configuration provides reasonable control of shock and shell uniformity during the implosion for the SG-III facility. The exact locations of the repointed spots can vary slightly for different target designs to optimize nonuniformity.

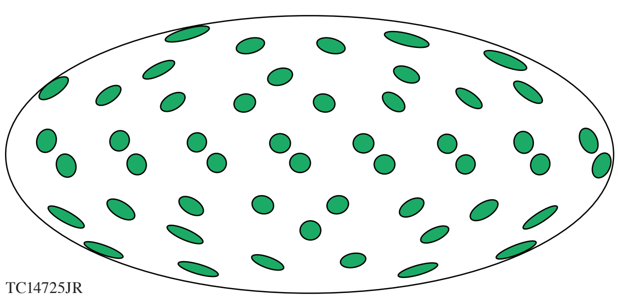

Figure 4
The suggested PDD repointing configuration provides reasonable control of shock and shell uniformity during the implosion for the SG-III facility, where four rings of beams are distributed about the target surface. Each green spot represents a beam port that has been repointed onto the initial target surface. The Hammer projection mapping is used.

Preliminary *DRACO*[12] simulations for the proposed PDD CBET mitigation experiments for the SG-III facility indicate promising results (see Fig. 5). These simulations show that reasonable uniformity can be achieved, assuming nonideal spot shapes that conform to those currently employed on the NIF. Simulations performed in the NIF's configuration using optimal DPP's have shown significant improvement in uniformity, which has boosted neutron yields by 2× to 3× in exploding-pusher configurations when compared to nonideal spot shapes.

Conclusion

The SG-III facility could provide a valuable platform to explore CBET mitigation in the PDD configuration in the 200-kJ energy range. CBET mitigation experiments would require some laser modifications to measure the mitigation efficacy such as

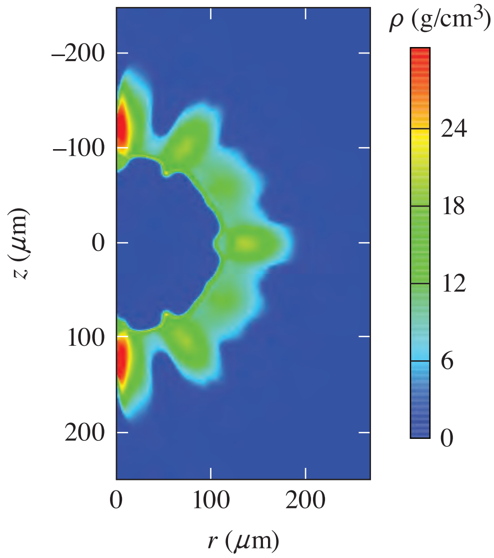

Figure 5
Initial *DRACO*[12] simulation results for PDD CBET mitigation experiments for the SG-III facility indicate promising results.

multiple tunable laser wavelengths, customized DPP's, and direct-drive target filling and manipulators. Higher shot repletion is expected, together with the ability to test a wide range of wavelength separation. The data that SG-III could provide would be valuable for future progress in direct-drive ICF.

This material is based upon work supported by the Department of Energy National Nuclear Security Administration under Award Number DE-NA0003856, the University of Rochester, and the New York State Energy Research and Development Authority.

1. M. C. Herrmann, M. Tabak, and J. D. Lindl, Nucl. Fusion **41**, 99 (2001).
2. C. J. Randall, J. R. Albritton, and J. J. Thomson, Phys. Fluids **24**, 1474 (1981).
3. T. R. Boehly *et al*., Opt. Commun. **133**, 495 (1997).
4. E. M. Campbell and W. J. Hogan, Plasma Phys. Control. Fusion **41**, B39 (1999).
5. W. Zheng *et al*., High Power Laser Sci. Eng. **4**, e21 (2016).)
6. J. A. Marozas *et al*., Phys. Rev. Lett. **120**, 085001 (2018).
7. P. B. Radha *et al*., J. Phys.: Conf. Ser. **688**, 012006 (2016).
8. M. Hohenberger *et al*., Phys. Plasmas **22**, 056308 (2015).
9. V. N. Goncharov *et al*., Phys. Plasmas **21**, 056315 (2014).
10. P. Michel *et al*., Phys. Plasmas **17**, 056305 (2010).
11. I. V. Igumenshchev *et al*., Phys. Plasmas **19**, 056314 (2012).
12. J. A. Marozas *et al*., Phys. Plasmas **25**, 056314 (2018).
13. M. L. Spaeth *et al*., Fusion Sci. Technol. **69**, 25 (2016).
14. S. Skupsky *et al*., Phys. Plasmas **11**, 2763 (2004).
15. J. A. Marozas *et al*., Phys. Plasmas **13**, 056311 (2006).
16. J. A. Marozas, J. Opt. Soc. Am. A **24**, 74 (2007).
17. J. A. Marozas *et al*., J. Phys.: Conf. Ser. **717**, 012107 (2016).

Direct-Drive Double-Shell Implosion: A Platform for Burning-Plasma Physics Studies

S. X. Hu,[1] R. Epstein,[1] W. Theobald,[1] H. Xu,[2] H. Huang,[2] V. N. Goncharov,[1] S. P. Regan,[1] P. W. McKenty,[1] R. Betti,[1] E. M. Campbell,[1] and D. S. Montgomery[3]

[1]Laboratory for Laser Energetics, University of Rochester
[2]General Atomics
[3]Los Alamos National Laboratory

Laser-driven inertial confinement fusion[1] (ICF) has been actively pursued in the laboratory for decades. The current efforts have focused mainly on the so-called "hot-spot" ignition scheme, in which a single shell containing a solid-DT (deuterium–tritium) fuel layer covered by ablator materials is driven to implode by high-energy laser beams in either an *indirect* or *direct* way. In indirect-drive ICF, the high-energy laser beams irradiate inside a hohlraum and convert the laser energy into thermal x-ray emissions that ablatively drive the capsule (placed inside the hohlraum) to implode;[2,3] while for the other scheme, the laser beams *directly* irradiate the ICF target.[4,5] For hot-spot ignition in both schemes, the single shell acts not only as the "piston" but also provides the major DT fuel for the final hot-spot formation. For the piston to have enough energy and still be compressible at stagnation, one needs to drive the single shell for a long distance (for enough acceleration) and to maintain it at a relatively low entropy state (low adiabat). Roughly speaking, for such single-shell hot-spot ignition to work at laser energies in the MJ range, the imploding DT-containing shell must have a velocity of $V_{\text{imp}} > 350$ km/s and a high convergence ratio of CR > 30 (CR = R_0/R_{hs}, with R_0 being the initial shell radius and R_{hs} the final hot-spot radius). These requirements impose formidable challenges for the central-spot–ignition scheme to reach the so-called *burning-plasma stage*,[6] in which the self-heating of plasmas by the DT-fusion–produced α particles exceeds the radiative and conduction loss.

To reach the burning-plasma stage, the single-shell hot-spot ignition in both direct-drive and indirect-drive schemes must overcome daunting challenges, especially for the current low-margin designs due to the limited laser energy. First of all, the large CR, low adiabat, and high implosion velocity demand stringent requirements on target and driver perturbations. For example, 3-D simulations of indirect-drive ICF implosions[7,8] show that the driver asymmetry and target engineering features such as fill tube and interface mixing can gradually "eat" away the design margin for burning plasma to happen. The situation is also similar for direct-drive, high-convergence ICF implosions, in which the perturbations from target imperfection and long-/short-wavelength laser nonuniformities can also significantly degrade the target performance,[9–12] due to the fact that these high-convergence, low-adiabat single-shell implosions are highly susceptible to violent Rayleigh–Taylor (RT) instability growth.[13–17] In addition, the DT layer being part or the whole of the piston requires tremendous effort to maintain its low entropy. Precisely timing several shocks[18–20] is necessary to set the shell in a designed low adiabat. Still, excessive radiation and/or superthermal electrons produced by laser–plasma instabilities, such as two-plasmon decay[21] and stimulated Raman scattering,[22] could possibly preheat the in-flight, low-temperature DT shell and render it less compressible at stagnation. All of these challenges are currently faced by the laser-drive ICF community.

Different from the above-mentioned central-spot ignition, alternative laser-fusion schemes seek to separate the hot-spot formation from the shell (piston) acceleration. Over the past two decades, some efforts in the laser-fusion community have been put into studies of these alternative schemes, including fast ignition,[23] shock ignition,[24,25] double-shell implosions,[26–31] and a triple-shell *Revolver* design,[32] just to name a few. Although these schemes have their own challenges, the separation of hot-spot formation from accelerating the piston generally relaxes the stringent requirements for the single-shell, hot-spot–ignition scheme.

Taking a double-shell implosion as an example, the outer shell (piston) can be set at a much higher adiabat so that RT instability and radiation/fast-electron preheat do not significantly affect the shell integrity as it accelerates, while an inner shell composed of high-density metal layer(s) and filled with DT gas or liquid can be volumetrically shocked/compressed and heated by an ~Gbar pressure reservoir that is created through the spherical stagnation (impact) of the outer shell upon the inner one. Given the electron-rich nature of a high-density inner shell, only a significantly low convergence ratio (CR $\le$ 10) is needed to reach a pressure of ~400 Gbar required for DT plasma burning.[31] The double-shell scheme generally trades some of the physics challenges of high-convergence (CR $\ge$ 30) single-shell implosions for the complexity of double-shell target fabrication and diagnoses.

For the past two decades, the study of double-shell implosions in both experiments and simulations has focused mainly on the indirect-drive scheme.[26–31] With a drive laser at the National Ignition Facility[33] (at an ~MJ energy level), recent 1-D simulations showed that a maximum energy of only ~10 to 15 kJ can be coupled to the kinetic motion of the inner shell,[31] even with a high-density inner-shell material like Au. The limited margin for an energetic inner shell is caused by the lower hydroefficiency in the indirect-drive scheme, in which a much thicker and massive outer shell is needed for x-ray drive. Motivated by the higher overall hydroefficiency of direct drive,[5,10] we have performed a thorough investigation on whether or not a direct-drive double-shell (D^3S) platform has its own merit to create a burning plasma in the laboratory at MJ laser energy. We found that even with the currently reduced hydrocoupling caused by cross-beam energy-transfer (CBET),[34–37] direct-drive double-shell implosions can give at least twice the kinetic energy (~30 kJ) as the indirect-drive case; such a more-energetic inner shell could provide more margin to reach the DT-plasma burning stage. In addition, we propose to use the newly invented technology of magnetron sputtering[38] to make a density-gradient inner shell of a tungsten/beryllium mixture. By varying the tungsten-to-beryllium concentration ratio, one may be able to construct an inner shell with density dropping from $\rho_0 \sim 19$ g/cm^3 (97% W + 3% Be) to $\rho_0 \sim 2.2$ g/cm^3 (1% W + 99% Be) along both inward and outward directions. The idea of using gradient-density layers, proposed earlier for single-shell ICF,[16] can help to mitigate the classical RT problem during the outer-shell collision.[39] It not only reduces the Atwood number but also increases the density scale length at the collisional surface. It can be thought of as multiple "tamper" layers used for indirect-drive double-shell designs[28,29,31] but with a gradual density variation.

In the radiation-hydrodynamic studies of direct-drive double-shell implosions presented here, we have used both the 1-D code *LILAC*[40] and the 2-D code *DRACO*[41] developed at LLE. State-of-the-art physics models, including the nonlocal thermal-transport model,[42,43] the 3-D ray tracing with CBET model,[34–37] accurate material properties such as first-principles equation of state,[44–47] first-principles opacity tables,[48,49] and the average-ion model[50] for the opacity and emissivity of the W/Be mixture, have been employed in our radiation-hydrodynamic simulations. In our D^3S designs, a 70-μm-thick beryllium outer shell is driven symmetrically by a high-adiabat ($\alpha \ge 10$), 1.9-MJ laser pulse to a peak velocity of ~240 km/s. Upon spherical impact, the outer shell transfers ~30 to 40 kJ of kinetic energy to the inner shell filled with DT gas or liquid, giving neutron-yield energies of ~6 MJ in 1-D simulations. Two-dimensional, high-mode *DRACO* simulations indicated that such high-adiabat D^3S implosions are not susceptible to laser imprint, but the long-wavelength perturbations from the laser port configuration along with CBET can be detrimental to the target performance. Nevertheless, neutron yields of ~0.3- to 1.0-MJ energies can still be obtained from our high-mode *DRACO* simulations. One example is shown in Fig. 1, where the robust α-particle bootstrap is readily reached, which could provide a viable platform for burning-plasma physics studies. Once CBET mitigation and/or more laser energy becomes available, we anticipate that breakeven or moderate energy gain might be feasible with the proposed D^3S scheme.

This material is based upon work supported by the Department of Energy National Nuclear Security Administration under Award Number DE-NA0003856, the University of Rochester, and the New York State Energy Research and Development Authority.

1. J. Nuckolls *et al*., Nature **239**, 139 (1972).

2. J. D. Lindl, Phys. Plasmas **2**, 3933 (1995).

3. M. J. Edwards *et al*., Phys. Plasmas **18**, 051003 (2011).

4. D. D. Meyerhofer *et al*., Nucl. Fusion **51**, 053010 (2011).

5. R. S. Craxton *et al*., Phys. Plasmas **22**, 110501 (2015).

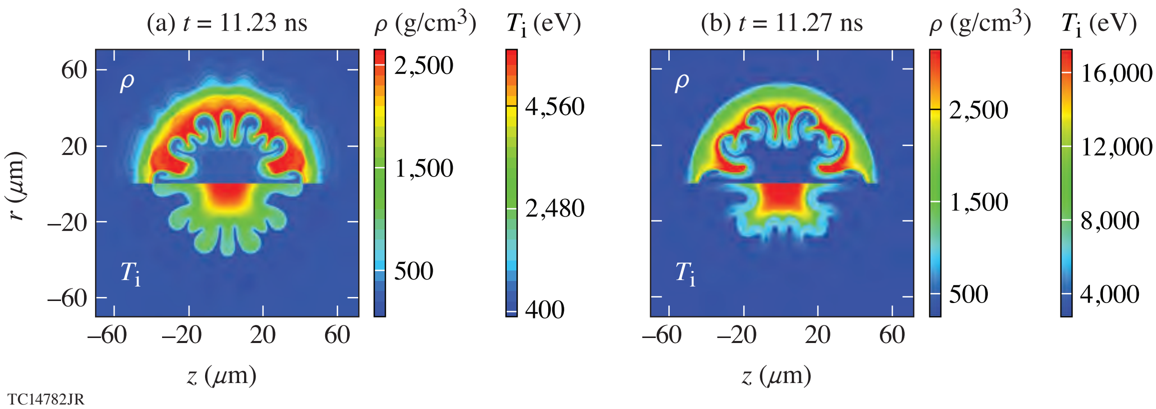

Figure 1
The density (ρ) and ion temperature (T_i) contour plots on the r,z plane during the inner-shell stagnation: (a) at the beginning of bootstrap heating (t = 11.23 ns) and (b) at the peak neutron production (t = 11.27 ns) when the burning-plasma stage is reached.

6. R. Betti and O. A. Hurricane, Nat. Phys. **12**, 435 (2016).
7. D. S. Clark *et al*., Phys. Plasma **25**, 032703 (2018).
8. D. S. Clark *et al*., Nucl. Fusion **59**, 032008 (2018).
9. I. V. Igumenshchev *et al*., Phys. Plasmas **20**, 082703 (2013).
10. V. N. Goncharov *et al*., Phys. Plasmas **21**, 056315 (2014).
11. S. X. Hu *et al*., Phys. Plasmas **23**, 102701 (2016).
12. D. T. Michel *et al*., Phys. Rev. E **95**, 051202(R) (2017).
13. S. E. Bodner, Phys. Rev. Lett. **33**, 761 (1974).
14. H. Takabe *et al*., Phys. Fluids **28**, 3676 (1985).
15. R. Betti *et al*., Phys. Plasmas **5**, 1446 (1998).
16. N. Metzler, A. L. Velikovich, and J. H. Gardner, Phys. Plasmas **6**, 3283 (1999).
17. V. A. Smalyuk *et al*., Phys. Rev. Lett. **103**, 105001 (2009).
18. T. R. Boehly *et al*., Phys. Plasmas **16**, 056302 (2009).
19. T. R. Boehly *et al*., Phys. Plasmas **18**, 092706 (2011); Phys. Rev. Lett. **106**, 195005 (2011).
20. H. F. Robey *et al*., Phys. Plasmas **19**, 042706 (2012).
21. D. T. Michel *et al*., Phys. Rev. Lett. **109**, 155007 (2012).
22. M. J. Rosenberg *et al*., Phys. Rev. Lett. **120**, 055001 (2018).
23. M. Tabak *et al*., Phys. Plasmas **1**, 1626 (1994).
24. R. Betti *et al*., Phys. Rev. Lett. **98**, 155001 (2007).
25. W. Theobald *et al*., Phys. Plasmas **19**, 102706 (2012).
26. W. S. Varnum *et al*., Phys. Rev. Lett. **84**, 5153 (2000).
27. P. Amendt *et al*., Phys. Plasmas **9**, 2221 (2002).

28. J. Milovich *et al*., Phys. Plasmas **11**, 1552 (2004).

29. P. A. Amendt *et al*., Phys. Rev. Lett. **94**, 065004 (2005).

30. H. F. Robey *et al*., Phys. Rev. Lett. **103**, 145003 (2009).

31. D. S. Montgomery *et al*., Phys. Plasmas **25**, 092706 (2018).

32. K. Molvig *et al*., Phys. Rev. Lett. **116**, 255003 (2016).

33. E. M. Campbell and W. J. Hogan, Plasma Phys. Control. Fusion **41**, B39 (1999).

34. C. J. Randall, J. J. Thomson, and K. G. Estabrook, Phys. Rev. Lett. **43**, 924 (1979).

35. I. V. Igumenshchev *et al*., Phys. Plasmas **17**, 122708 (2010).

36. D. H. Froula *et al*., Phys. Plasmas **20**, 082704 (2013).

37. J. A. Marozas *et al*., Phys. Plasmas **25**, 056314 (2018).

38. H. Xu *et al*., Fusion Sci. Technol. **73**, 354 (2018).

39. J. D. Lindl *et al*., Phys. Plasmas **11**, 339 (2004).

40. J. Delettrez *et al*., Phys. Rev. A **36**, 3926 (1987).

41. P. B. Radha *et al*., Phys. Plasmas **12**, 056307 (2005).

42. G. P. Schurtz, Ph. D. Nicolaï, and M. Busquet, Phys. Plasmas **7**, 4238 (2000).

43. D. Cao, G. Moses, and J. Delettrez, Phys. Plasmas **22**, 082308 (2015).

44. S. X. Hu *et al*., Phys. Rev. Lett. **104**, 235003 (2010).

45. S. X. Hu *et al*., Phys. Rev. B **84**, 224109 (2011).

46. S. X. Hu *et al*., Phys. Rev. E **92**, 043104 (2015).

47. Y. H. Ding and S. X. Hu, Phys. Plasmas **24**, 062702 (2017).

48. S. X. Hu *et al*., Phys. Rev. E **90**, 033111 (2014).

49. S. X. Hu *et al*., Phys. Rev. B **96**, 144203 (2017).

50. R. Epstein *et al*., Bull. Am. Phys. Soc. **43**, 1666 (1998).

Density Measurements of the Inner Shell Release

D. Haberberger, A. Shvydky, J. P. Knauer, S. X. Hu, S. T. Ivancic, J. Carroll-Nellenback, D. Cao, V. V. Karasiev, A. V. Maximov, V. N. Goncharov, and D. H. Froula

Laboratory for Laser Energetics, University of Rochester

The material release on the back side of a CH shell was probed at conditions relevant to inertial confinement fusion (ICF). The release was found to expand further with a longer scale length than that predicted by radiation-hydrodynamic simulations. The simulations show that a relaxation of the back side of the shell consistent with measurements explains the experimentally observed reduction in ICF implosion performance—specifically reduced areal density at peak compression.

While great progress has been made over recent years in ICF experiments,[1] achieving ignition conditions remains a grand challenge. In both direct- and indirect-drive approaches to fusion, a cold layer of deuterium–tritium (DT) fuel is compressed by material ablation to form a high-areal-density confinement around an igniting central hot spot. In both approaches, several shocks are launched through an outer solid-density fuel and into a central vapor region. Once the shock breaks through the inner surface into the central region, the fuel spherically converges to form a high-areal-density confinement. By limiting the amount of material and maintaining a low temperature inside the vapor region, the implosion can reach maximum convergence and the hot-spot temperature necessary for ignition.

One of the reasons for the underperformance in the recent experiments is attributed to a reduced areal density of the fuel; 20% deficiency has been reported for most of the implosions at the National Ignition Facility.[2] Several mechanisms could contribute to the reduction in shell convergence and therefore in areal density, including mixing of the ablator material into the fuel or mixing of the fuel into the central hot spot. In addition, inaccurate modeling of the material properties of fuel interacting with multiple strong shocks could lead to an underprediction of the mass expanding from the inner surface of the main shell by material release. Such a release is created as the first shock breaks out of the main fuel into the vapor region of the target. As subsequent shocks with increasing strengths are launched into the shell at the beginning of the implosion, they travel through the rarefaction formed by the earlier shocks. The rate of material release is determined by several factors, including sound speed, ion viscosity, and thermal conduction.

Experimental signatures of the driven shell dynamics are commonly used to test hydrodynamic simulations. In implosion experiments, x-ray backlighting or self-emission measurements are used to track the shell trajectory,[3] but they give no information about the low-density material release behind the shell since the low-density material does not attenuate the high-energy x-ray photons. Optical probing with a velocity interferometer system for any reflector (VISAR) has been used to track a shock moving through a transparent material or to measure when the shock breaks out into vacuum.[4] Although these measurements are very useful for studying the equation of state (EOS) in simulation codes, no information is gained about the profile of material release when the shock breaks through the shell because at this point the optical beam is absorbed near the critical plasma density of the rarefaction wave because of its reflection geometry.

In this research, the first direct measurements of the low-density plasma released from the back side of a laser-driven shell is presented. The low-density plasma (at 10^{20} cm^{-3}) was measured to travel ~190 μm in front of the driven shell with a scale length that increased to a maximum to 63 μm over 3 ns (Fig. 1). These observations are in contrast to hydrodynamic simulations that show the plasma traveling ~80 μm away from the shell with a steep density gradient that increased to 15 μm (Fig. 2). Further investigation uncovered the sensitivity of the inner shell expansion to the initial (before the shock breakout) CH density profile. By initiating the back side of the shell with a 10-μm density gradient, release profiles matching those observed in the experiment were obtained. The more-rapid expansion results from enhanced heating of the lower-density material by the shock as it breaks out, causing a higher sound speed, and consequently, a faster post-shock expansion. This early relaxation of the CH shell boundary is consistent with estimations of preheat from x rays emanating from the hot coronal plasma. Implementing an expanded profile on the back side of the DT ice layer in direct-drive ICF implosion simulations shows a reduced convergence leading to an 18% lower areal density and a 17% smaller ion temperature.

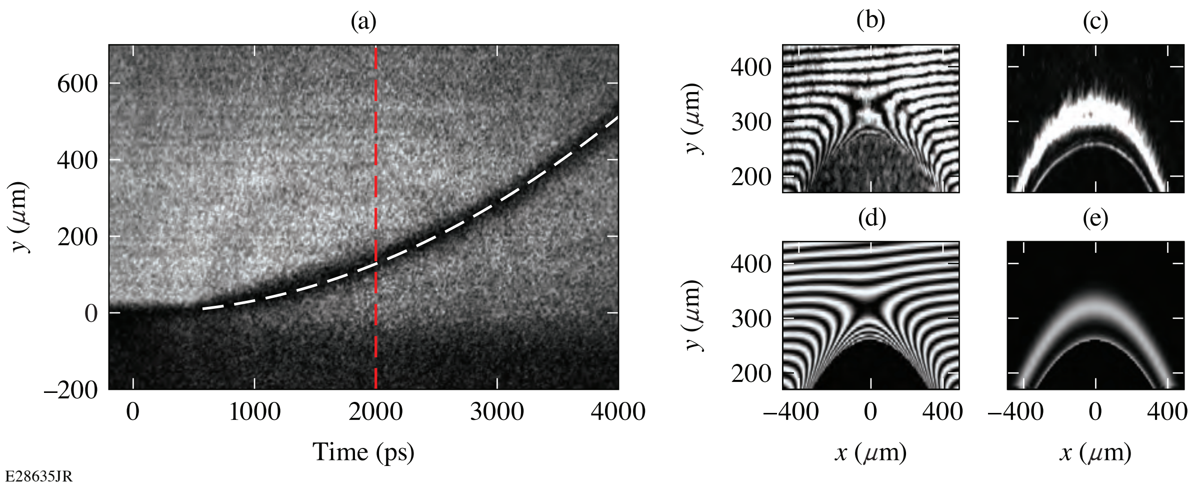

Figure 1
(a) The PJXI diagnostic measured the shell trajectory by tracking absorption of the Al He x rays traveling through the interaction region. The origins of the spatial and temporal axes represent the initial location of the center of the CH shell (spatial) at the beginning of the drive laser pulse (2% of rise, temporal). The 4ω probe diagnostic measures the density of the released plasma on the back side of the driven shell through (b) interferometry and (d) AFR at 2 ns after the drive. The synthesized response of the (c) interferometry and (e) AFR diagnostics that best match the corresponding measurements at 2 ns. The origin of the y axis corresponds to the position of shock (~120 μm) as measured by the radiography (dashed red line).

Figure 1(a) shows a radiograph where the shock is observed breaking out of the back side at t = 580±40 ps. After this time, the shell trajectory was observed to accelerate at a near-constant acceleration of ~32 μm/ns^2 (dashed white line) across ~540 μm over 4 ns. For this experimental setup, the 1.5-keV x rays provide an optimal peak absorption of ~70%. The x-ray streak-camera diagnostic had a measured spatial resolution of 20 μm, which was sufficient to track the position of the shell, although not small enough to resolve the expected shell thickness of 5 to 7 μm.

To measure the density profile in the rarefaction wave, an 8-ps-FWHM-duration, 4ω (263-nm) probe beam was used to generate interferometry[5] [Fig. 1(b)] and angular filter refractometry[6] [AFR, Fig. 1(c)] data. The two diagnostics were used in conjunction to gain confidence in the measured plasma density profiles. The interaction was probed at four times with respect to the beginning of the drive beams (2% of rise): 1 ns, 2 ns (Fig. 1), 3 ns, and 4 ns. For the probe timing of 2 ns, the shell moved ~120 μm at the center of the laser spot [Fig. 1(a)]. Figure 1(b) shows the phase change accrued from propagating through the released plasma. A measurable phase change at the center of the shell is evident for distances greater than ~290 μm; for positions less than this, the light was refracted outside of the collection optics. Refraction of the probe light from its propagation through this plasma resulted in the observation of two bands [Fig. 1(c)] of constant refraction angle corresponding to 0.75° (outer) and 3° (inner). The images were analyzed by simulating a synthetic interferogram and AFR image using an analytic function for the plasma density and iterating until the images converged to the measurements. A single exponentially decaying profile, with a transverse Gaussian function, was found to be adequate to reproduce the measurements. Other analytic profiles were tested and delivered very similar plasma profiles. The matched synthetic interferogram and AFR image for the 2-ns data are shown in Figs. 1(d) and 1(e), respectively, and correspond to a plasma density profile of $n_{\mathrm{e}}(x,y,z) = n_0 \exp\left[-y = L_y\right] \exp\left\{-\left(x^2+z^2\right) = \left[L_{\mathrm{FWHM}} \big/ 2\ln(2)\right]\right\}$, where n_0 = 3.6 ×

10^{21} cm^{-3}, L_y = 38 μm, and L_{FWHM} = 340 μm. Note, this profile is accurate only in the low-density region measured by the 4ω probe and is expected to strongly diverge from the actual plasma profile closer to the driven shell.

Figure 2 shows that the low-density plasma has expanded significantly farther than *LILAC*[7] radiation-hydrodynamic simulations predict. At the earliest measured time (1 ns), the low-density plasma is 40 μm in front of the predictions, while the position of the shell is in good agreement. Between 1 ns and 4 ns, the low-density (at 10^{20} cm^{-3}) plasma is measured to have an average velocity of ~205 μm/ns, while its scale length expanded from 10 μm to 63 μm. The average simulated expansion speed of 145 μm/ns at 10^{20} cm^{-3} was slower than the measurements, and the scale lengths increased from 2 μm to 15 μm, which are shorter than measured across the entire time span. This discrepancy was largely insensitive to the thermal transport and the EOS models used in the simulations. It was found in simulations that the position of the low-density plasma, as well as its scale length, significantly depends on the mass-density profile at the back surface of the CH shell right before the shock breaks out. The simulation results shown in Fig. 2 used an infinitely sharp boundary on the back side of the CH, as is typical in hydrodynamic simulations. These simulations significantly underestimate the plasma expansion at all times. When the back side of the CH target was relaxed over 10 μm (linear increase from zero to solid density prior to the shock breakout), the simulated trajectories are in excellent agreement with the measurements. The increased heating (from 20 eV to ~100 eV) that occurs from the shock propagating through the relaxed back side of the shell, results in a faster expansion and larger scale length than when the standard sharp interface is used. Note the trajectory of the shell was unchanged by this relaxation.

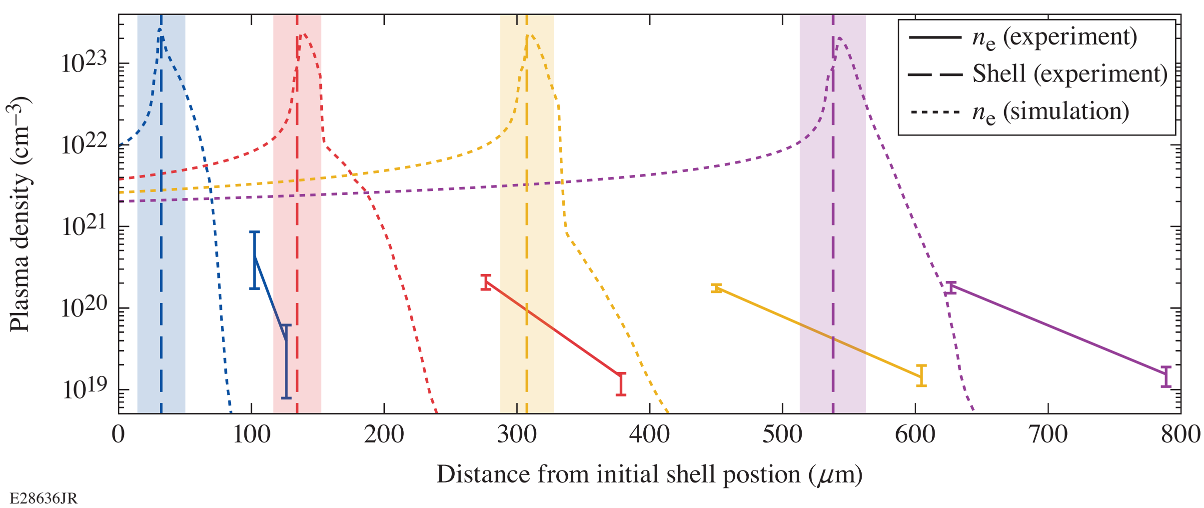

Figure 2
The measured (solid curves) and simulated (dotted curves) plasma density profiles at 1 ns (blue), 2 ns (red), 3 ns (yellow), and 4 ns (purple) are plotted. The vertical dashed lines are the peak shell position as measured by the PJXI diagnostic (with error bars shown by the shaded regions).

In summary, optical probing using interferometry and angular filter refractometry was used to study the material release from the shock breakout at conditions relevant to ICF implosions. It was observed that the position and scale length in the measured density range (10^{19} to 10^{20} cm^{-3}) of the rarefaction wave strongly depends on the density profile at the back surface of the CH before the shock passes. To match the experimental data, simulations required a relaxation that results in a neutral-density gradient on the inner surface of the CH shell before the shock pass. This lower-density material is strongly heated by the passing shock, which causes it to expand more rapidly and have a longer scale length at later times. Radiation preheat by coronal x rays can cause such a relaxation of the back surface of the CH and formation of the density gradient. Simulations of direct-drive cryogenic implosions that enhanced the inner surface release consistent with these measurements show a significant reduction in target performance, including an 18% reduction in areal density, a 17% reduction in ion temperature, and more than a factor of 2 reduction in the neutron yield.

This material is based upon work supported by the Department of Energy National Nuclear Security Administration under Award Number DE-NA0003856, the University of Rochester, and the New York State Energy Research and Development Authority

1. S. Le Pape *et al*., Phys. Rev. Lett. **120**, 245003 (2018).
2. D. S. Clark *et al*., Nucl. Fusion **59**, 032008 (2018).
3. D. T. Michel *et al*., Rev. Sci. Instrum. **83**, 10E530 (2012).
4. M. A. Barrios *et al*., Phys. Plasmas **17**, 056307 (2010).
5. A. Howard *et al*., Rev. Sci. Instrum. **89**, 10B107 (2018).
6. D. Haberberger *et al*., Phys. Plasmas **21**, 056304 (2014).
7. J. Delettrez, Can. J. Phys. **64**, 932 (1986).

The Role of Baroclinicity in the Kinetic Energy Budget

A. Lees and H. Aluie

Laboratory for Laser Energetics and Department of Mechanical Engineering, University of Rochester

The role of baroclinicity, which arises from the misalignment of pressure and density gradients, is well known in the vorticity equation, yet its role in the kinetic energy budget has never been obvious. We have shown that baroclinicity appears naturally in the kinetic energy budget after carrying out the appropriate scale decomposition. Strain generation by pressure and density gradients, both barotropic and baroclinic, also results from our analysis. These two processes underlie the recently identified mechanism of "baropycnal work,"[1–3] which can transfer energy across scales in variable density flows. We also provide numerical evidence from high-resolution (i.e., 1024 × 1024 × 1024) direct numerical simulations (DNS's) of compressible turbulence (Fig. 1).

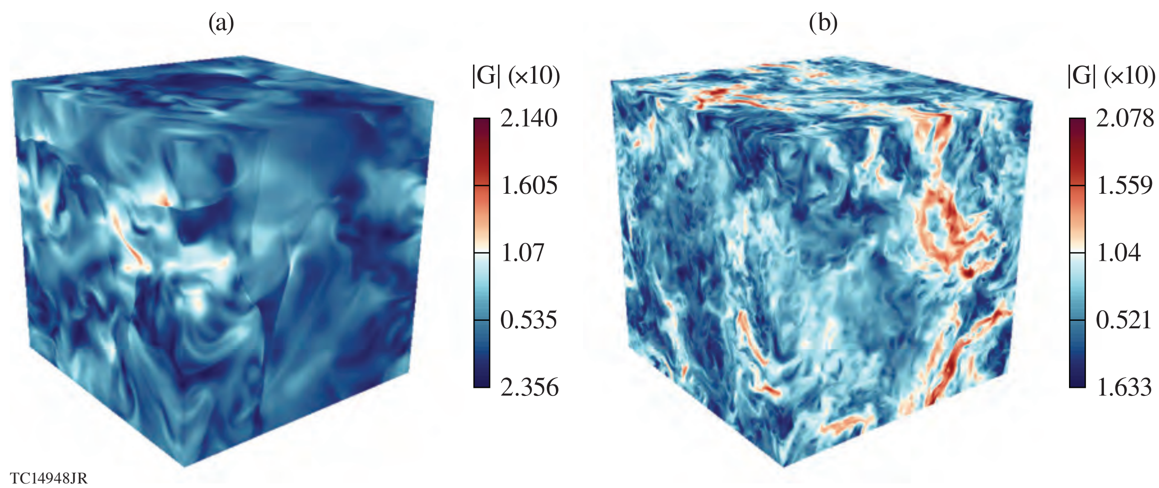

Figure 1
DNS of turbulent flows at varying levels of compressiblity using our DiNuSUR code.

To analyze the dynamics of different scales in a compressible flow, we use the coarse-graining approach. It has proven to be a natural and versatile framework for understanding and modeling scale interactions (e.g., Refs. 1–6) and is closely related to well-established physics techniques, including macroscopic electromagnetism,[7,8] where coarse graining of microscopic charge and current densities coupled with gradient expansions yield the macroscopic polarization **P** and magnetization **M** as well as higher-order multipole contributions. It is also closely related to the renormalization group (RG), especially "real-space RG,"[9,10] where a coarse-grained field is like a "block spin" and coarse-grained equations are analogous to "effective Hamiltonian/action" for the block spins with running coupling constants that depend on the scale parameter ℓ. Our approach is also intimately related to large eddy simulation (LES) in turbulence modeling.[4,11] Equations governing the dynamics of different scales can be derived relatively easily, allowing for a direct analysis of processes at those scales both analytically and using data from simulations or experiments.

For any field $a(x)$, a coarse-grained or (low-pass) filtered field, which contains modes at scales $>\ell$, is defined in n dimensions as

$$\bar{\mathbf{a}}_\ell(x) = \int d^n\mathbf{r}\, G_\ell(\mathbf{r})\,\mathbf{a}(\mathbf{x}+\mathbf{r}), \tag{1}$$

where $G(r)$ is a normalized convolution kernel and $G_\ell(r) = \ell^{-n}G(r/\ell)$ is a dilated version of the kernel having its main support over a region of diameter ℓ. The scale decomposition above is essentially a partitioning of scales in the system into large ($>\ell$), captured by $\bar{a}_\ell$, and small ($<\ell$), captured by the residual $\bar{a}'_\ell = a - \bar{a}_\ell$.

The budget for the large-scale kinetic energy can be easily derived[3] from the compressible momentum equation:

$$\partial_t\,\bar{\rho}_\ell\,\frac{\left|\tilde{\mathbf{u}}_\ell\right|^2}{2} + \nabla\cdot\mathbf{J}_\ell = -\Pi_\ell - \Lambda_\ell + \bar{P}_\ell\,\nabla\cdot\bar{\mathbf{u}}_\ell - D_\ell + \epsilon_\ell^{\mathrm{inj}}, \tag{2}$$

where $J_\ell(x)$ is space transport of large-scale kinetic energy, $\bar{P}_\ell\,\nabla\cdot\bar{u}_\ell$ is large-scale pressure dilatation, $D_\ell(x)$ is viscous dissipation acting on scales $>\ell$, and $\epsilon_\ell^{\mathrm{inj}}(x)$ is the energy injected due to external stirring. The $\Pi_\ell(x)$ and $\Lambda_\ell(x)$ terms account for the transfer of energy across scale ℓ.

Using the property of scale locality,[1] we have derived a model of Λ that shows how it transfers energy by two processes: barotropic and baroclinic generation of strain S from gradients of pressure and density ρ:

$$(\mathrm{const})\,\ell^2\rho^{-1}\left\{\left[\nabla_\rho\,(\nabla P)^T\right]:\mathbf{S}\right\} \tag{3}$$

and baroclinic generation of vorticity ω:

$$(\mathrm{const})\,\ell^2\rho^{-1}\left(\nabla_\rho\times\nabla_P\right)\cdot\omega. \tag{4}$$

While the role of pressure and density gradients in generating vorticity is well recognized, their role in strain generation has been less emphasized in the literature.

To our knowledge, this is the first direct demonstration of how baroclinicity enters the kinetic energy budget, which arises naturally from our scale decomposition and the identification of Λ as a scale-transfer mechanism (Fig. 2). Baroclinicity is often

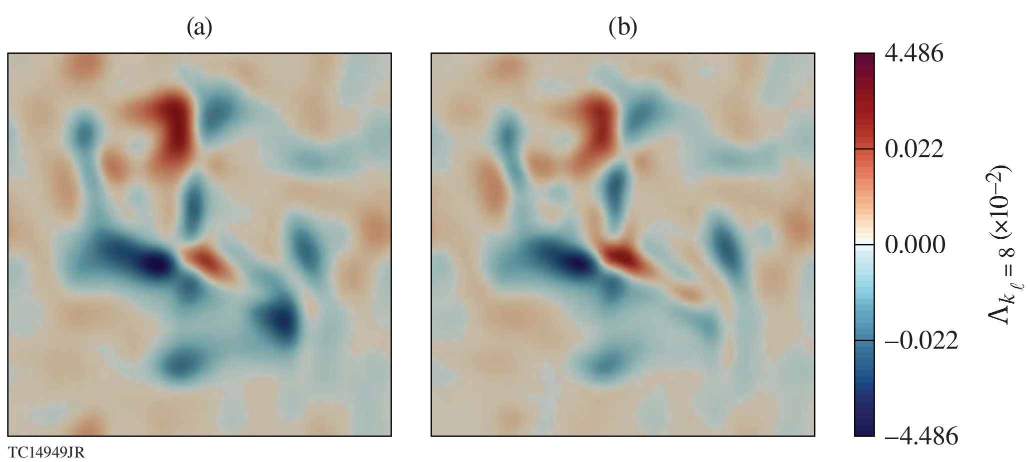

Figure 2
Visualization of a slice from our 3-D flow of the true Λ and its model that we derived, showing excellent pointwise agreement.

analyzed within the vorticity budget but its role in the energetics has never been obvious. The need for a scale decomposition in order for Λ and, as a result, baroclinic energy transfer to appear in the kinetic energy budget is similar to the scale transfer term Π, which appears in the budget only after decomposing scales due to energy conservation. In the same vein, the appearance of baroclinicity in the vorticity equation can be interpreted as being a consequence of an effective scale decomposition performed by the curl operator $\nabla\times$, which is a high-pass filter.

This material is based upon work supported by the Department of Energy National Nuclear Security Administration under Award Number DE-NA0003856, the University of Rochester, and the New York State Energy Research and Development Authority. This research was funded by DOE FES grant number DE-SC0014318. H. Aluie was also supported by NASA grant 80NSSC18K0772 and DOE grant DE-SC0019329. Computing time was provided by the National Energy Research Scientific Computing Center (NERSC) under Contract No. DE-AC02-05CH11231.

1. H. Aluie, Phys. Rev. Lett. **106**, 174502 (2011).
2. H. Aluie, S. Li, and H. Li, Astrophys. J. **751**, L29 (2012).
3. H. Aluie, Physica D **247**, 54 (2013).
4. C. Meneveau and J. Katz, Ann. Rev. Fluid Mech. **32**, 1 (2000).
5. G. L. Eyink, Physica D **207**, 91 (2005).
6. M. Germano, J. Fluid Mech. **238**, 325 (1992).
7. G. Russakoff, Am. J. Phys. **38**, 1188 (1970).
8. F. N. H. Robinson, *Macroscopic Electromagnetism*, 1st ed., International Series of Monographs in Natural Philosophy (Pergamon Press, Oxford, 1973).
9. K. G. Wilson, Rev. Mod. Phys. **47**, 773 (1975).
10. H. Burkhardt and J. M. J. van Leeuwen, eds. *Real-Space Renormalization*, Topics in Current Physics (Springer-Verlag, Berlin, 1982).
11. A. Leonard, Adv. Geophys. **18 (Part A)**, 237 (1975).

Investigation of Picosecond Thermodynamics in a Laser-Produced Plasma Using Thomson Scattering

A. S. Davies, D. Haberberger, K. Katz, S. Bucht, J. P. Palastro, R. K. Follett, and D. H. Froula

Laboratory for Laser Energetics, University of Rochester

The rapid evolution of electron density and temperature in a laser-produced plasma was measured using collective Thomson scattering. Picosecond time resolution, enabled by a pulse-front-tilt–compensated spectrometer, revealed a transition in the plasma-wave dynamics from an initially cold evolving state to a quasi-stationary equilibrium state. The equilibrium temperature was found to match the generalized heat equation's predicted scaling $T_e \propto n_e^{2/5}$ and $T_e \propto I^{1/5}$. The plasma evolution was compared to Raman gain bandwidth calculations and showed a time-dependent resonance detuning that would limit the transfer efficiency of a Raman plasma amplifier in the linear regime.

Endeavors to engineer plasmas for a number of applications rely critically on plasma conditions. Optimizing plasma devices, including laser amplifiers,[1–5] laser compressors,[6] wave plates,[7,8] polarizers,[9,10] Q plates,[11] particle accelerators,[12,13] photon accelerators,[14] high-order frequency conversion,[15,16] and photon–electron light sources,[17,18] require an accurate knowledge of plasma density and temperature dynamics. Engineering plasmas to create a laser amplifier and compressor is of particular interest because a plasma-based device can avoid the optical damage thresholds that currently limit the maximum intensity of chirped-pulse–amplification systems.[19]

A Raman plasma amplifier seeks to amplify and compress an ultrashort pulse by transferring energy from a long (tens of picoseconds), energetic pump pulse to a short (tens of femtoseconds), intense seed pulse. Raman amplification is a three-wave interaction, in which two counter-propagating laser pulses of different frequencies form a beat wave that drives an electron plasma wave through the ponderomotive force. The plasma wave facilitates the energy transfer from the higher- to the lower-frequency beam.[1] Pulse compression and efficient energy transfer require the pump pulse amplitude to be depleted within the seed pulse duration, known as the π-pulse or nonlinear regime.[6] Depleting the pump pulse amplitude within the duration of the seed requires a rapidly growing and large-amplitude plasma wave that typically forms when the Langmuir frequency is resonant with the beat frequency produced by the pump and seed beams. In the linear regime, the frequency, growth rate, and maximum amplitude of an electron plasma wave are dependent on the instantaneous electron temperature and density. Accurate prediction of the linear growth of the electron plasma wave in a Raman amplifier has been impeded by the lack of measured plasma conditions over this regime.

In a laser-produced plasma, the electromagnetic fields generate dynamic plasma conditions that evolve rapidly over the initial 50 ps. This evolution is comparable to pump durations (10 to 20 ps) that have typically been used in plasma devices. Therefore, the plasma conditions vary over the course of these experiments. During the transit of a high-intensity pump pulse through a gas, the photoionized electrons are liberated with minimal kinetic energy, resulting in an initially cold plasma. The energy supplied to the electrons by the electromagnetic field, through inverse bremsstrahlung, causes the temperature to rise rapidly until the collisionality of the plasma reduces the heating rate to a level comparable to the cooling mechanisms. Measurements of these early plasma dynamics on application-relevant time scales have been previously unattainable.

Optical Thomson scattering is a powerful diagnostic that can accurately measure plasma conditions.[20–26] A Thomson-scattering diagnostic can be used to determine localized plasma conditions by calculating the time-resolved spectra from laser light scattered off of plasma waves. The diagnostic requires a spectrometer streak-camera system to provide spectral and temporal resolution of the scattered spectra. Thomson-scattering diagnostics have not had sufficient temporal resolution to characterize the dynamics of plasma devices. Temporal resolution (>50 ps) for Thomson-scattering systems has been limited by the diagnostic's pulse-front tilt, which is inherent in the angular dispersion of the spectrometer.[27,28] In a conventional system, this pulse-front-tilt–limited resolution is more than an order of magnitude larger than the temporal resolution of present-day streak cameras (~1 ps).

Figure 1 shows measurements of the picosecond evolution of the electron temperature and density in a laser-produced plasma. The measurements were obtained by an ultrafast high-throughput spectrometer[29] that provided unprecedented temporal resolution of the electron plasma waves in the Thomson-scattering spectra.[30] These spectra were used to extract the picosecond evolution of the electron temperature and density. Hydrogen gas was ionized at an intensity near 10^{14} W/cm^2, where the electron plasma temperature was measured to rise from an initial partially ionized cold (~3-eV) plasma to a fully ionized plasma at a quasi-steady-state equilibrium temperature over ~25 ps. Figure 2 shows that the equilibrium temperatures were found to increase with higher densities and laser intensity. The measured thermodynamics were compared to generalized heat equation calculations of the equilibrium temperature. Measurements agreed with calculated equilibrium temperatures to within 15%, and the plasma condition's dependence on the density and intensity matches the heat equation's predicted scalings $T_e \propto n_e^{2/5}$ and $T_e \propto I^{1/5}$, respectively. The temporal evolution of the temperature measurements was also compared to heat equation calculations (Fig. 1), but the heating rate of the measurements was found to be slower compared to the calculations, suggesting the need to include ionization physics in the model.[31] The time dynamics of the electron plasma waves were compared to calculations of the Raman backscatter dispersion relation of the gain bandwidth. The comparisons show that the picosecond plasma evolution results in a time-dependent resonance detuning in a Raman plasma amplifier. This detuning would significantly limit transfer efficiencies in the linear regime.

The picosecond thermodynamics presented here are relevant to engineering optimum plasmas for a Raman plasma amplifier. The frequency-matching conditions necessary for laser amplification in the linear regime are dependent on the instantaneous

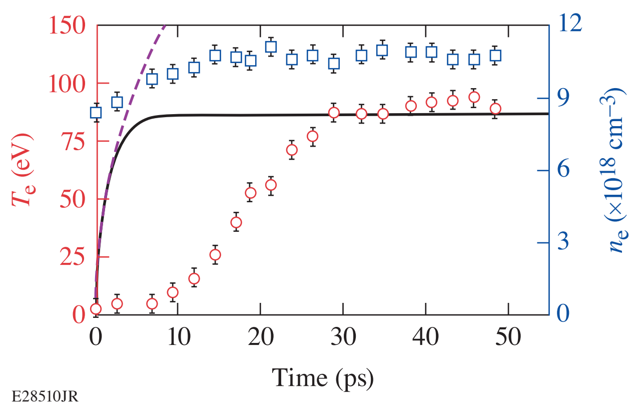

Figure 1
The measured (red circles, left axis) and calculated (solid black curve) electron temperatures are compared. The measured electron density (blue squares, right axis) is plotted as a function of time. The calculated temperature (dashed purple curve) is plotted as a function of time when the heat conduction and ion-heating terms are dropped from the generalized heat equation.

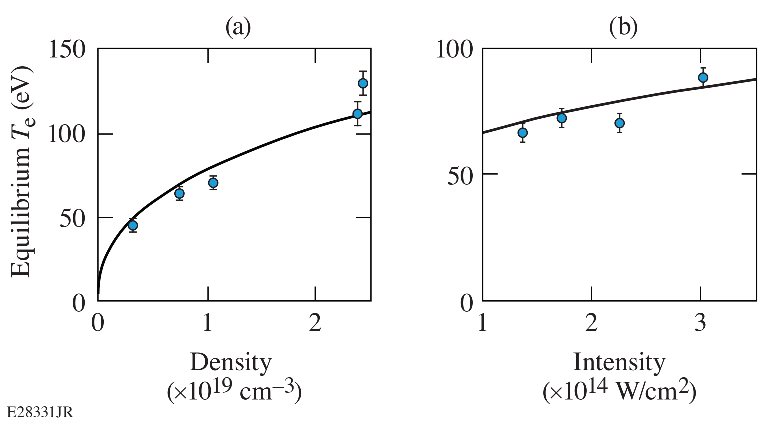

Figure 2
(a) The measured (circles) and calculated (solid curve) equilibrium temperatures are plotted versus the plasma density for an intensity of 2.2×10^{14} W/cm^2. (b) The measured (circles) and calculated (solid curve) equilibrium temperatures are plotted versus laser intensity for a density of 1.0×10^{19} cm^{-3}.

density and temperature conditions, as indicated by the Langmuir frequency. When accounting for the detuning introduced by the evolving plasma conditions (Fig. 1), the amplification regime is limited to a finite temperature range (~60 eV to ~120 eV, when the laser frequencies are chosen to be resonant at the equilibrium temperature). Outside the amplification zone, there will be zero gain due to the temperature detuning. By comparing this amplification zone to the measured temperature evolution shown in Fig. 1, it is apparent that the time dynamics of the electron plasma wave would result in time-dependent resonance detuning in a Raman plasma amplifier. In this example, the amplifier would experience zero gain until after the first 25 ps. If an 8-mm plasma channel was used to match the pump pulse duration, the first 4 mm would be wasted and the maximum possible transfer efficiency would be <50%. This example illustrates the importance of taking the plasma evolution into account when designing a Raman amplification experiment; these results can help guide future endeavors.

This material is based upon work supported by the Department of Energy National Nuclear Security Administration under Award Number DE-NA0003856, the University of Rochester, and the New York State Energy Research and Development Authority.

1. G. Shvets *et al*., Phys. Rev. Lett. **81**, 4879 (1998).
2. Y. Ping *et al*., Phys. Rev. Lett. **92**, 175007 (2004).
3. J. Ren *et al*., Nat. Phys. **3**, 732 (2007).
4. G. Vieux *et al*., Sci. Rep. **7**, 2399 (2017).
5. J. D. Sadler *et al*., Phys. Rev. E **95**, 053211 (2017).
6. V. M. Malkin, G. Shvets, and N. J. Fisch, Phys. Rev. Lett. **82**, 4448 (1999).
7. P. Michel *et al*., Phys. Rev. Lett. **113**, 205001 (2014).
8. D. Turnbull *et al*., Phys. Rev. Lett. **116**, 205001 (2016).
9. D. J. Stark *et al*., Phys. Rev. Lett. **115**, 025002 (2015).
10. D. Turnbull *et al*., Phys. Rev. Lett. **118**, 015001 (2017).
11. K. Qu, Q. Jia, and N. J. Fisch, Phys. Rev. E **96**, 053207 (2017).
12. R. Bingham, Nature **394**, 617 (1998).
13. S. M. Hooker, Nat. Photonics **7**, 775 (2013).
14. S. C. Wilks, J. M. Dawson, and W. M. Mori, Phys. Rev. Lett. **61**, 337 (1988).
15. J. J. Rocca *et al*., Phys. Rev. Lett. **73**, 2192 (1994); **75**, 1236(E) (1995).
16. A. Butler *et al*., Phys. Rev. Lett. **91**, 205001 (2003).
17. K. T. Phuoc *et al*., Nat. Photonics **6**, 308 (2012).
18. N. D. Powers *et al*., Nat. Photonics **8**, 28 (2014).
19. D. Strickland and G. Mourou, Opt. Commun. **56**, 219 (1985).
20. S. H. Glenzer *et al*., Phys. Rev. Lett. **82**, 97 (1999).
21. D. S. Montgomery *et al*., Laser Part. Beams **17**, 349 (1999).
22. J. L. Kline *et al*., Phys. Rev. Lett. **94**, 175003 (2005).
23. C. Rousseaux *et al*., Phys. Rev. Lett. **97**, 015001 (2006).
24. D. H. Froula *et al*., Phys. Rev. Lett. **93**, 035001 (2004).

25. J. S. Ross *et al*., Rev. Sci. Instrum. **81**, 10D523 (2010).

26. R. J. Henchen *et al*., Phys. Rev. Lett. **121**, 125001 (2018).

27. A. Visco *et al*., Rev. Sci. Instrum. **79**, 10F545 (2008).

28. J. Hebling, Opt. Quantum Electron. **28**, 1759 (1996).

29. J. Katz *et al*., Rev. Sci. Instrum. **87**, 11E535 (2016).

30. A. S. Davies *et al*., Phys. Rev. Lett. **122**, 155001 (2019).

31. H. P. Le, M. Sherlock, and H. A. Scott, Phys. Rev. E **100**, 013202 (2019).

Measurement and Control of Ionization Waves of Arbitrary Velocity in the Quasi-Far Field

P. Franke,[1,2] D. Turnbull,[1] J. Katz,[1] J. P. Palastro,[1] I. A. Begishev,[1] J. Bromage,[1,3] J. L. Shaw,[1] R. Boni,[1] and D. H. Froula[1,2]

[1]Laboratory for Laser Energetics, University of Rochester
[2]Department of Physics & Astronomy, University of Rochester
[3]Institute of Optics, University of Rochester

Ionization fronts with precisely controlled characteristics could help to overcome fundamental limitations in laser-plasma–based photonics applications by improving phase matching, extending interaction lengths, and facilitating better control of plasma conditions. These capabilities are particularly useful in plasma-based light manipulation processes such as photon acceleration,[1–6] Raman amplification,[7–12] and THz generation[13–15]—processes that could lead to a new generation of exotic, compact, and versatile radiation sources.

Highly controllable ionization fronts can be driven using a recently developed method called the "flying focus," in which a chirped laser pulse is focused by a hyperchromatic optic such as a diffractive lens.[16,17] The chromatic aberration causes different frequencies in the laser pulse to come to focus at different positions along the propagation axis. For a fixed focal geometry, the temporal delay between when each frequency reaches its focal position is determined by the chirp, which can be adjusted to cause the point of the maximum laser intensity to move at any velocity over distances that can greatly exceed the Rayleigh length.

When the instantaneous intensity of a flying-focus pulse exceeds the ionization intensity threshold (I_i) of a background gas an ionization front is produced that tracks the propagation of an intensity isosurface at I_i (Ref. 18). These ionization waves of arbitrary velocity (IWAV's) were experimentally demonstrated to have predictable and easily adjustable velocities equal to the expected flying-focus velocity when driven by a laser pulse with a highly uniform power spectrum in the laser far field.[19]

While modification of the power spectrum was proposed as a means to increase control of IWAV propagation,[18] previous theoretical and experimental investigations were limited to the laser far field and mainly considered flat power spectra, i.e., high-order super-Gaussians. In this parameter regime, all frequencies in the bandwidth have just enough power to ionize near their minimum spot size. Experimental observation of channels formed by IWAV propagation indicated radii ~10 μm, close to the measured far-field laser spot size. Such small-diameter IWAV's would have limited usefulness in applications because of the difficulty of coupling another beam into the IWAV, the small available cross section for interaction, and strong refraction resulting from the short transverse density scale lengths.

It is possible to increase the diffraction-limited minimum spot size by increasing the *f* number so that larger IWAV's can be driven in the laser far field. It may be experimentally favorable, however, to simply increase the total pulse power so that all wavelengths ionize before they reach their minimum spot size. Operation in this so called quasi-far-field (QFF) regime, where the transverse extent of the laser field is large compared to its diffraction-limited spot size, provides control of the IWAV radius without changing the focusing geometry. Furthermore, it offers the possibility of using nonuniform power spectra to control the dynamic behavior of the IWAV's. QFF IWAV's may be the only path forward for applications that require a significant pump intensity to exist behind the ionization front, such as flying-focus–driven plasma Raman amplification.[7,8]

This research presents the first experimental demonstration of IWAV's in the QFF and develops a new theory to predict their behavior. Figure 1 describes a simple model of IWAV propagation when the flying-focus power spectrum is nonuniform and uses it to develop an intuitive understanding of QFF IWAV's and demonstrate enhanced control of IWAV characteristics through spectral shaping. Figure 2

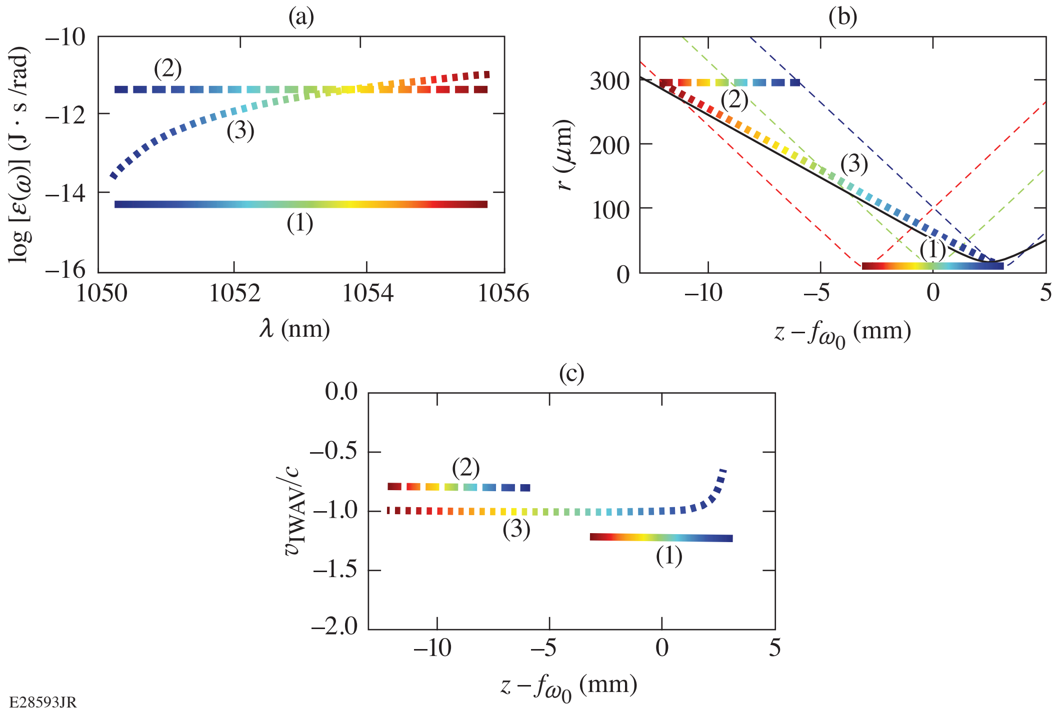

Figure 1
(a) Calculations of the IWAV (b) radius and (c) velocity are shown for the spectral energy densities. Cases (1) and (2) show the simple far-field and QFF IWAV propagations, respectively. Case (3) shows that the spectrum can be adjusted to change the IWAV radius and match the *f* number of a separate beam [black line in (b)], but still maintain a constant velocity. Case (3) also shows that the IWAV range can be increased beyond the already-extended focal region and that the IWAV can be accelerated through spectral shaping. (b) Single-frequency radii for the edges (blue and red) and center (green) of the bandwidth are shown as single-color dashed lines. (c) Velocities for cases (1) and (2) are shown offset from $v_{\text{IWAV}} = -c$ by ~20% for clarity, but all calculations were done for $v_{\text{IWAV}} = -c$.

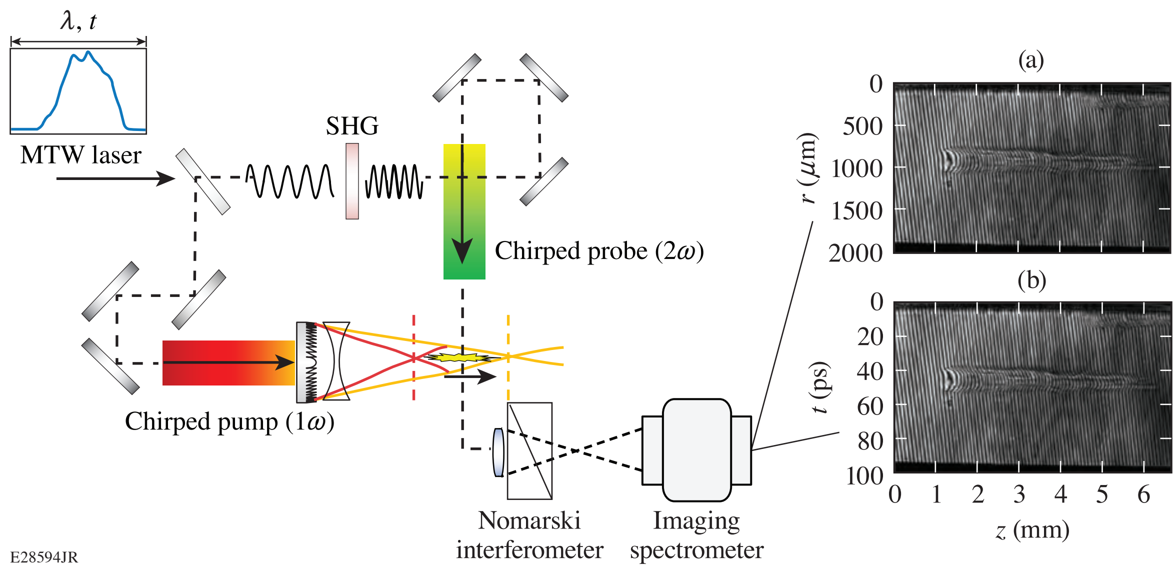

Figure 2
The Multi-Terawatt (MTW) laser was split into a 1ω pump beam that drove IWAV's in a hydrogen gas jet and a 2ω probe beam that passed through the interaction region perpendicular to the IWAV propagation with variable timing, allowing (a) conventional 2-D and (b) 1-D spectrally resolved interferograms of the IWAV propagation to be collected. The 2-D data allow for the reconstruction of the electron density as a function of radial and axial distance late in time. The 1-D and 2-D data together allow extraction of the electron density as a function of time and axial distance along the pump beam propagation axis while the IWAV is propagating through the interaction region.

describes an experimental setup that incorporates a novel spectrally resolved interferometry diagnostic that allows for the inference of IWAV characteristics such as velocity, radius, and temporal density scale length. Experimental results are compared to the theory developed in this research (Fig. 3). IWAV's with radii ~10× larger than previously observed are experimentally demonstrated. The new theory accurately predicts the observed data, even when the direct correspondence to the flying-focus theory is invalid, but obtain consistency between all theories and the data in general. The experimental ionization rates are compared to a computational model described in Ref. 18 and obtain agreement (Fig. 4), which lends experimental validation to recent predictions of the extreme frequency upshifts achievable by co-propagating a witness laser pulse with a flying-focus–driven IWAV.

This material is based upon work supported by the Department of Energy National Nuclear Security Administration under Award Number DE-NA0003856, the Fusion Energy Science under Award Numbers DE-SC0019135, DE-SC0016253, the University of Rochester, and the New York State Energy Research and Development Authority.

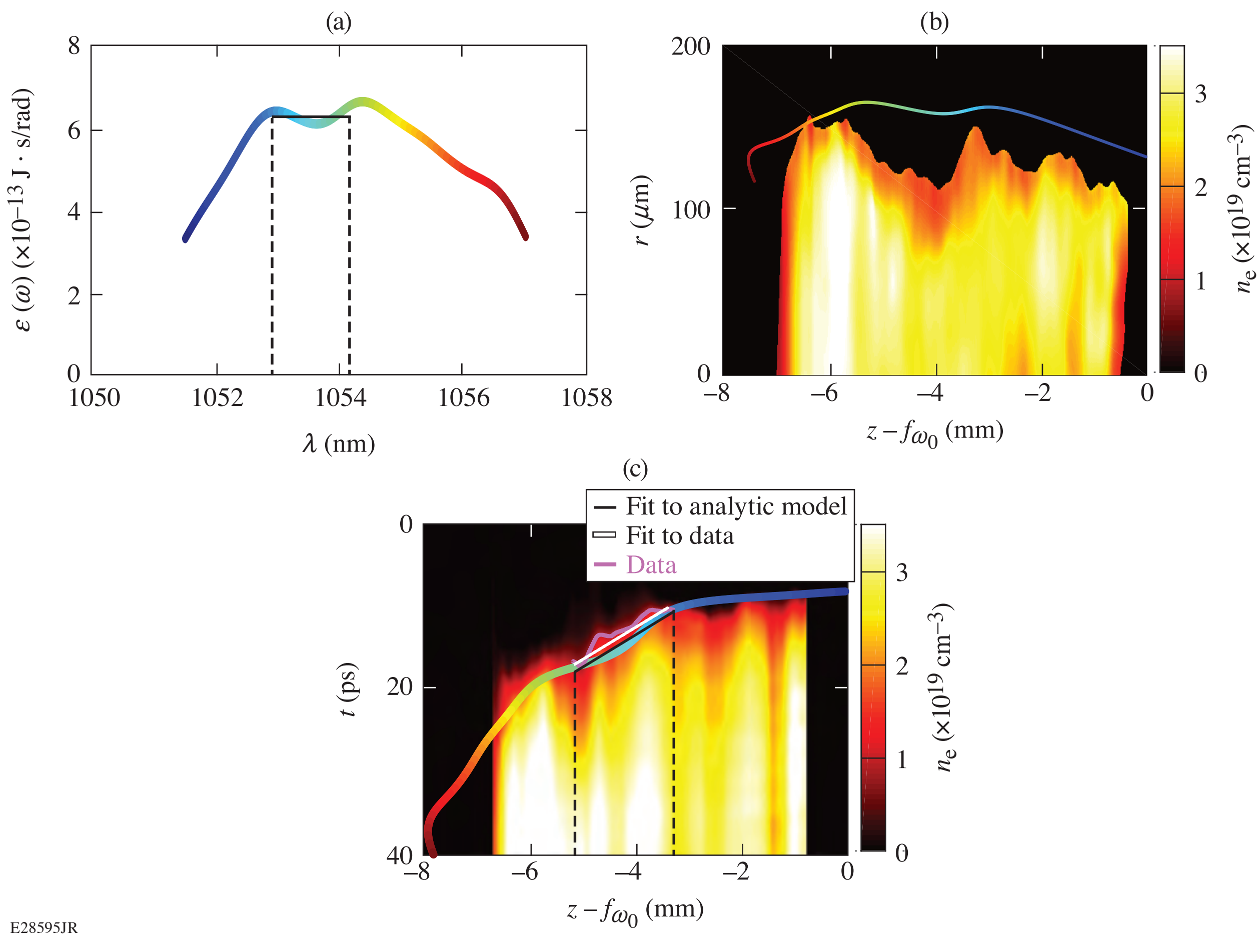

Figure 3
(a) The experimental spectral energy density was used to calculate an expected radial profile and trajectory [multicolor curves in (b) and (c), respectively], which are overlaid on the electron density data extracted from 2-D interferometry and spectrally resolved interferometry [color bar in (b) and (c), respectively]. The predicted radial profile and trajectory are in agreement with the data over the entire bandwidth. A "flat" region of the spectrum and the trajectory that corresponds to this part of the spectrum is demarcated by vertical dashed black lines in (a) and (c). In this region, the flying-focus velocity (–0.75c), the predicted IWAV velocity (–0.73c), and the measured velocity (–0.71c) are all in agreement.

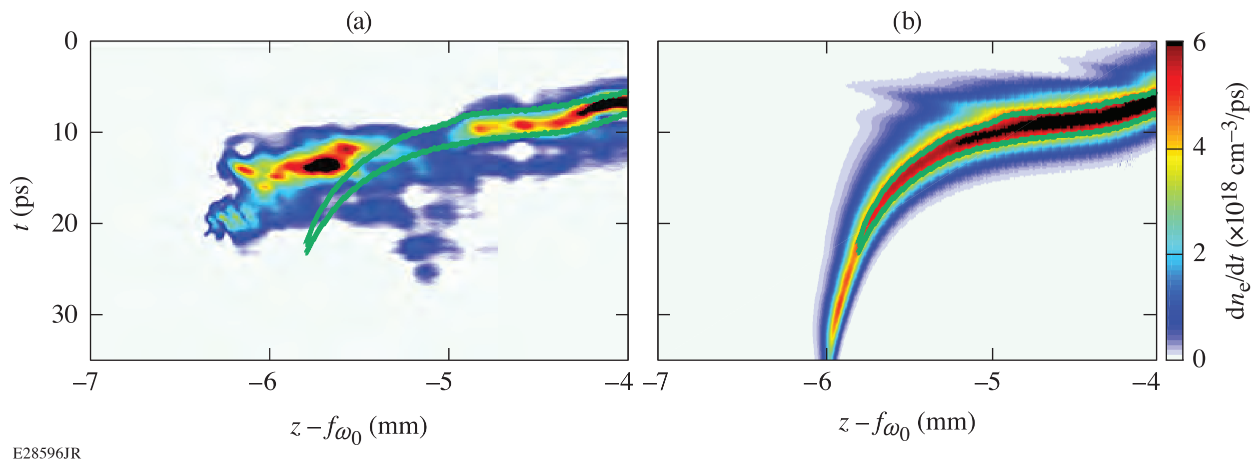

Figure 4
(a) The measured temporal density gradient (ionization rate) has values and a trajectory that are close to those predicted by simulations of ionization as a result of (b) flying-focus pulse propagation. An outline of the simulated data is shown in both (a) and (b) as a green curve.

1. A. Howard *et al*., "Photon Acceleration in a Flying Focus," to be published in Physical Review Letters.
2. S. C. Wilks *et al*., Phys. Rev. Lett. **62**, 2600 (1989).
3. J. T. Mendonça, *Theory of Photon Acceleration*, Series in Plasma Physics (Institute of Physics Publishing, Bristol, England, 2001).
4. J. M. Dias *et al*., Phys. Rev. E **66**, 056406 (2002).
5. N. C. Lopes *et al*., Europhys. Lett. **66**, 371 (2004).
6. L. Oliveria e Silva and J. T. Mendonca, IEEE Trans. Plasma Sci. **24**, 316 (1996).
7. D. Turnbull *et al*., Phys. Rev. Lett. **120**, 024801 (2018).
8. D. Turnbull *et al*., Plasma Phys. Control. Fusion **61**, 014022 (2019).
9. V. M. Malkin, G. Shvets, and N. J. Fisch, Phys. Rev. Lett. **82**, 4448 (1999).
10. V. M. Malkin, G. Shvets, and N. J. Fisch, Phys. Rev. Lett. **84**, 1208 (2000).
11. Y. Ping *et al*., Phys. Rev. Lett. **92**, 175007 (2004).
12. Y. Ping *et al*., Phys. Plasmas **16**, 123113 (2009).
13. K. Y. Kim *et al*., Opt. Express **15**, 4577 (2007).
14. P. Sprangle *et al*., Phys. Rev. E **69**, 066415 (2004).
15. C. D'Amico *et al*., Phys. Rev. Lett. **98**, 235002 (2007).
16. D. H. Froula *et al*., Nat. Photonics **12**, 262 (2018).
17. A. Sainte-Marie, O. Gobert, and F. Quéré, Optica **4**, 1298 (2017).
18. J. P. Palastro *et al*., Phys. Rev. A **97**, 033835 (2018).
19. D. Turnbull *et al*., Phys. Rev. Lett. **120**, 225001 (2018).

Photon Acceleration in a Flying Focus

A. J. Howard, D. Turnbull, A. S. Davies, P. Franke, D. H. Froula, and J. P. Palastro

Laboratory for Laser Energetics, University of Rochester

Theory and simulations demonstrate that the ionization front produced by a flying focus can upshift the frequency of an ultrashort optical pulse to the extreme ultraviolet (XUV) over a centimeter of propagation. An analytic model of the upshift predicts that this scheme could be scaled to a novel tabletop source of spatially coherent x rays.

A growing number of scientific fields rely critically on high-intensity, high-repetition-rate sources of XUV radiation (wavelengths <120 nm). These sources provide high-resolution imaging for high-energy-density physics and nanotechnology; fine-scale material ablation for nanomachining, spectrometry, and photolithography; and ultrafast pump/probe techniques for fundamental studies in atomic and molecular physics. While XUV sources have historically been challenging to produce, methods including nonlinear frequency mixing, high harmonic generation, and XUV lasing or line emission in metal-vapor and noble-gas plasmas have demonstrated promising results. Despite their successes, each of these methods introduces tradeoffs in terms of tunability, spatial coherence, divergence, or efficiency. Photon acceleration offers an alternative method for tunable XUV production that could lessen or even eliminate these tradeoffs.

Photon acceleration refers to the frequency upshift of light in response to a refractive index that decreases in time.[1] In analogy to charged-particle acceleration, the increase in photon energy, i.e., frequency, accompanies an increase in group velocity. In the context of an electromagnetic pulse, the leading phase fronts experience a higher index than adjacent, trailing phase fronts, which manifests as a local phase velocity that increases over the duration of the pulse. The trailing phase front, because of its higher phase velocity, gradually catches up with the leading front, compressing the wave period. In a medium with normal dispersion, the resulting frequency upshift translates to an increase in the local group velocity.

Plasmas, in particular, provide an ideal medium for photon acceleration: the refractive index depends on the density of free electrons, which can be rapidly increased or decreased over time through ionization and recombination or manipulated through electrostatic wave excitation. Specifically, a photon of frequency ω in an isotropic plasma experiences a refractive index $n\left(\omega = 1 - \omega_{\mathrm{p}}^2/\omega^2\right)^{1/2}$, where $\omega_{\mathrm{p}} = \left(e^2 n_{\mathrm{e}}/m\varepsilon_0\right)^{1/2}$ is the plasma frequency, n_{e} the free electron density, e the electron charge, m the electron mass, and ε_0 the permittivity of free space. An increase in the electron density over time—for example, by ionization—provides a decreasing refractive index that will accelerate the photons of a co-located pulse.

A prototypical scheme for photon acceleration involves propagating a witness pulse in an ionization front triggered by a co-propagating drive pulse. In spite of the impressive frequency shifts (>10×) predicted by theory and simulations,[1] experiments in the optical regime have met with limited success (~1.25×) (Ref. 2) as a result of witness pulse refraction and drive pulse diffraction. While these effects can be remedied by preforming a plasma or pre-shaping a gas to provide a guiding structure, two inherent limitations to the upshift remain. First, the drive pulse, and therefore the ionization front, travels at a subluminal group velocity. As the witness pulse accelerates, it quickly outpaces the ionization front, terminating the interaction. Second, the drive pulse refracts from the plasma it creates, limiting the formation of a continuous ionization front.

Here, we demonstrate, for the first time, a scheme for photon acceleration within a co-propagating ionization front that shifts an optical pulse to the XUV. The scheme utilizes a novel photonic technique known as the flying focus to overcome the aforementioned limitations.[3] An appropriately chirped drive pulse, focused through a chromatic lens, exhibits an intensity peak that counter-propagates at the speed of light in vacuum c with respect to its group velocity.[4] The peak intensity, in turn, triggers an ionization front traveling at c, which can continually accelerate the photons of a co-propagating witness pulse. A schematic is displayed in Fig. 1 for the case of a diffractive optic. The peak intensity of the drive pulse travels through the focal region $z_\mathrm{f} = (\Delta\lambda/\lambda_\mathrm{c})f$ at the focal velocity $v_\mathrm{f} = (1 + v_\mathrm{d}T/z_\mathrm{f})^{-1}\, v_\mathrm{d}$, where λ_c is the central wavelength of the drive pulse, $\Delta\lambda/\lambda_\mathrm{c}$ is its fractional bandwidth, f is the focal length of the diffractive optic at λ_c, v_d is the group velocity, and T is the stretched pulse duration.

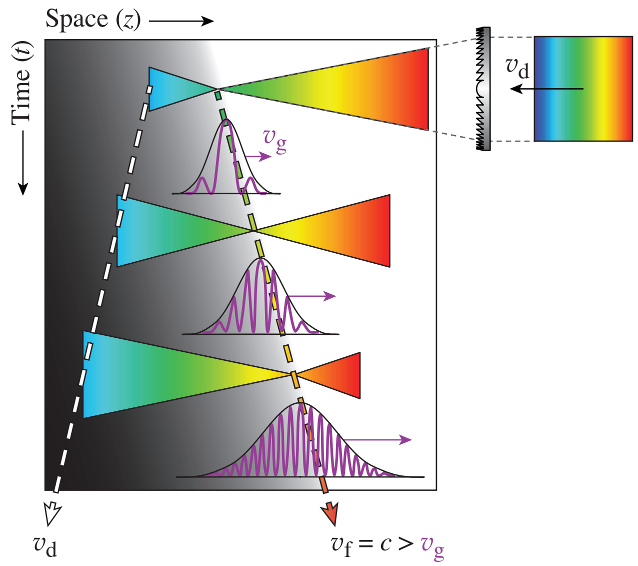

Figure 1
(a) A schematic demonstrating photon acceleration in the ionization front of a flying focus. A negatively chirped drive pulse propagating at its group velocity $v_\mathrm{d} < 0$ forms a focus that counter-propagates at the velocity $v_\mathrm{f} = c$, triggering an ionization front traveling at c. The resulting electron density is indicated by the gray shaded area. A witness pulse (purple curves) co-propagates with the ionization front at velocity and continually upshifts in frequency.

By decoupling the ionization-front velocity from the group velocity of the drive pulse, this scheme removes both of the inherent limitations of the prototypical photon accelerator. Most notably, the interaction distance is no longer limited by outpacing since the accelerated photons can never outpace a luminal (traveling at c) ionization front. Second, counter-propagating the drive pulse with respect to the ionization front mitigates ionization refraction since the focus of the drive pulse encounters only the un-ionized medium.

Figure 2 demonstrates that photon acceleration in the ionization front formed by the flying focus can upshift the frequency of an 87-fs witness pulse from the optical ($\lambda = 400$ nm) to the XUV ($\lambda = 91$ nm). The figure shows four snapshots from a photon kinetics simulation in the moving frame $\xi = ct - z$, where t is the time elapsed after injecting the witness pulse. The photons of the witness pulse enter the ionization front in Fig. 2(a), each with an initial vacuum wavelength of 400 nm. The photons continually upshift in frequency as they co-propagate with a temporal gradient in electron density as seen in Figs. 2(b) and 2(c). After ~1 cm, the photons—now upshifted to a minimum vacuum wavelength of 91 nm—approach the end of the focal region and encounter a decelerating ionization front, terminating their upshift.

Assuming an electron density profile with a constant gradient moving at c, the vacuum wavelength evolves according to $\lambda(z) = \left(1 + \omega_{\mathrm{p}0}^2 z \big/ \omega_0^2 L_T\right)^{-1/2} \lambda_0$, where λ_0 is the initial wavelength of a photon in the witness pulse, $\omega_0 = 2\pi c/\lambda_0$, and $\omega_{\mathrm{p}0}$ is the value of the plasma frequency at $\xi = L_T$. This analytic model is in good agreement with the simulation and reveals several paths to shorter wavelengths. The interaction length can be extended by increasing the bandwidth of the drive pulse or the focal length; the peak electron density can be increased by propagating within higher-density media, such as solid density targets (~10^{22} cm^{-3}); and the scale length can be decreased by increasing the intensity of the drive pulse or decreasing the effective duration of the

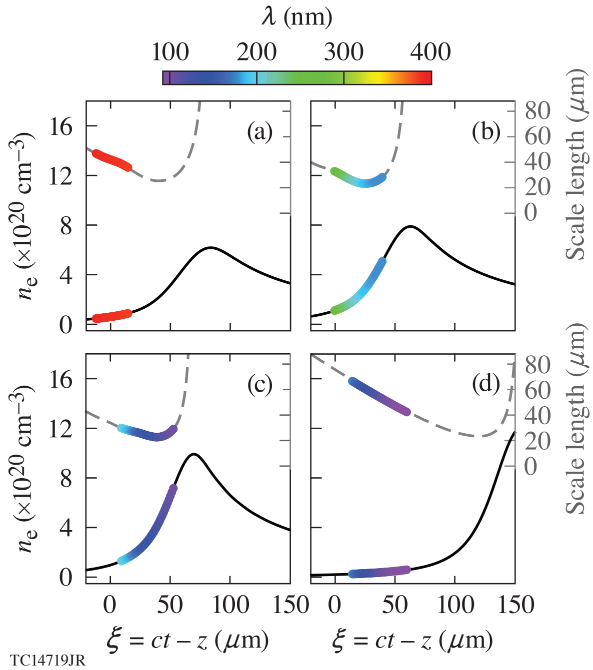

Figure 2
[(a)–(d)] A series of snapshots of an 87-fs witness pulse with an initial wavelength λ = 400 nm co-propagating with a temporal gradient in the electron density. The snapshots are taken at propagation distances of (a) 0.10, (b) 0.30, (c) 0.85, and (d) 1.05 cm and plotted in the moving frame ξ. The pulse is modeled by photons initially spaced evenly in time over 87 fs. Each photon is represented by a circle colored to correspond to its vacuum wavelength (color bar). The electron density and scale length $L = n_e / \partial_\xi n_e$ are shown as solid black and dashed gray lines, respectively.

flying focus intensity peak such that ionization occurs more rapidly. As a result, this scheme represents a promising method for the production of spatially coherent x rays at the tabletop scale.

This material is based upon the work supported by the U.S. Department of Energy Office of Fusion Energy Sciences under Contract Nos. DE-SC0016253 and DESC0019135, the Department of Energy National Nuclear Security Administration under Award No. DE-NA0003856, the University of Rochester, and the New York State Energy Research and Development Authority.

1. S. C. Wilks *et al*., Phys. Rev. Lett. **62**, 2600 (1989).

2. J. M. Dias *et al*., Phys. Rev. Lett. **78**, 4773 (1997).

3. D. H. Froula *et al*., Nat. Photonics **12**, 262 (2018).

4. J. P. Palastro *et al*., Phys. Rev. A **97**, 033835 (2018).

Evolution of the Electron Distribution Function in the Presence of Inverse Bremsstrahlung Heating and Collisional Ionization

A. L. Milder,[1,2] H. P. Le,[3] M. Sherlock,[3] P. Franke,[1,2] J. Katz,[1] S. T. Ivancic,[1] J. L. Shaw,[1] J. P. Palastro,[1] A. M. Hansen,[1,2] I. A. Begishev,[1] W. Rozmus,[4] and D. H. Froula[1,2]

[1]Laboratory for Laser Energetics, University of Rochester
[2]Department of Physics & Astronomy, University of Rochester
[3]Lawrence Livermore National Laboratory

The picosecond evolution of non-Maxwellian electron distribution functions was measured in plasmas generated by the Multi-Terawatt laser using collective electron plasma wave Thomson scattering. During the laser heating, the distribution was measured to be approximately super-Gaussian due to inverse bremsstrahlung heating. After the heating laser turned off, collisional ionization caused further modification to the distribution function while increasing electron density and decreasing temperature.

Electron velocity distributions govern most fundamental processes in plasma physics. Models of these processes often take the electron distribution function to be Maxwellian or impose small deviations from a Maxwellian. While this assumption can lead to significant errors, any significant deviation from a Maxwellian requires a kinetic understanding, which is often prohibitively challenging. As computational resources improve and experiments begin to isolate kinetic effects an understanding of non-Maxwellian electron distribution functions is becoming more tractable.

In laser-produced plasmas, inverse bremsstrahlung heating,[1–3] thermal transport,[4,5] laser–plasma instabilities,[6] and ionization recombination[7] all provide competing mechanisms that govern the shape of the electron distribution function. A recent computational study has shown the impact of atomic kinetics on inverse bremsstrahlung heating and nonlocal thermal transport, through modifications of the electron distribution function.[7] In a separate study, non-Maxwellian electron distribution functions driven by thermal transport were shown to modify Landau damping of electron plasma waves and enhance their corresponding instabilities.[5] Furthermore, most atomic physics models used to calculate x-ray emission for plasma characterization are built assuming a Maxwellian electron distribution function and deviation from a Maxwellian modifies these calculations.[2]

Although there have been numerous computational studies of kinetic effects in hydrodynamics over the last 40 years,[8] experiments have been challenged to isolate changes to the electron distribution function. In the 1990s, microwaves were used in low-temperature (~1 eV), low-density ($<10^{17}$ cm^{-3}) plasmas to investigate changes to the electron distribution function introduced by inverse bremsstrahlung heating.[9] Later in the decade, initial studies in laser plasmas suggested the existence of non-Maxwellian electron distribution functions using Thomson scattering.[10] More recently, Thomson-scattering experiments were able to show the effect of nonlocal thermal transport on electron distribution function.[4]

This research presents the first measurements of the interplay between inverse bremsstrahlung heating and ionization kinetics on the electron distribution function.[11] An ultrafast Thomson-scattering system was used to collect the electron plasma wave spectrum, which enabled the picosecond evolution of the non-Maxwellian electron distribution function to be measured in a laser-produced plasma (Fig. 1). The preferential heating of the slow electrons by the laser beam with an intensity of 2.5×10^{14} W/cm^2, coupled with atomic kinetics, resulted in a non-Maxwellian electron distribution function. The shape of the electron distribution function, 60 ps into the plasma formation, was measured to be approximately a super-Gaussian of the order of 3.4. After the laser turned off, the electron density continued to increase by 15% over the next 40 ps (~25 electron–ion collision times) due to collisional ionization.

Over this time, the electron temperature decreased from 400 eV to 300 eV [Fig. 1(c)], which is consistent with the energy required for ionization to increase the density [Fig. 1(d)]. To determine the electron distribution functions consistent with the measured Thomson-scattered spectra in this rapidly evolving plasma, Vlasov–Fokker–Planck simulations using the code K2 (Ref. 12), which included both laser heating and ionization, were required. Laser heating was found to have the largest effect on the shape of the distribution function, while atomic kinetics provided a smaller effect and allowed matching of the evolution of plasma conditions.

Figures 1(c) and 1(d) show that it is necessary to include ionization in the K2 calculations in order to match the measured plasma conditions. Including ionization also improved agreement with the Thomson-scattering spectra by altering the electron distribution function. While Fig. 1(b) shows the need for non-Maxwellian distributions driven by inverse bremsstrahlung heating to reproduce the spectra, the electron density and temperature [Figs. 1(c) and 1(d)] reveal the need to include an atomic physics model. In simulations without ionization, it is possible to alter the initial plasma conditions to achieve better agreement with the temperature, but this results in distribution functions that generate spectra with poor agreement with the measured Thomson-scattering spectra.

To determine the impact of ionization on the electron distribution function, an atomic physics model was coupled to K2. An inelastic collsional operator, sometimes called a Boltzmann operator, was used to model the changes to the distribution resulting from all atomic processes. The time evolution of the atomic states was determined through a set of coupled rate equations. The collisional rates that enter the rate matrix were obtained from direct integration of the actual distribution. The atomic data (energy levels and cross sections) were constructed based on a screened hydrogenic model using the code Cretin.[13] While the model used for these simulations includes different types of collisional and radiative processes (both bound–bound and bound–free), collisional ionization was identified as the main atomic process affecting the distribution function.[7] The simulations were performed using the experimental laser conditions. Simulations performed without the atomic physics model used a preionized plasma with an electron density of 2.2×10^{19} cm^{-3} (corresponding to an average ionization state of 9.1) and an electron temperature of 10 eV. When using the atomic physics model, ionization was self-consistently included and the simulations were initialized with a neutral density of 2.4×10^{18} cm^{-3}.

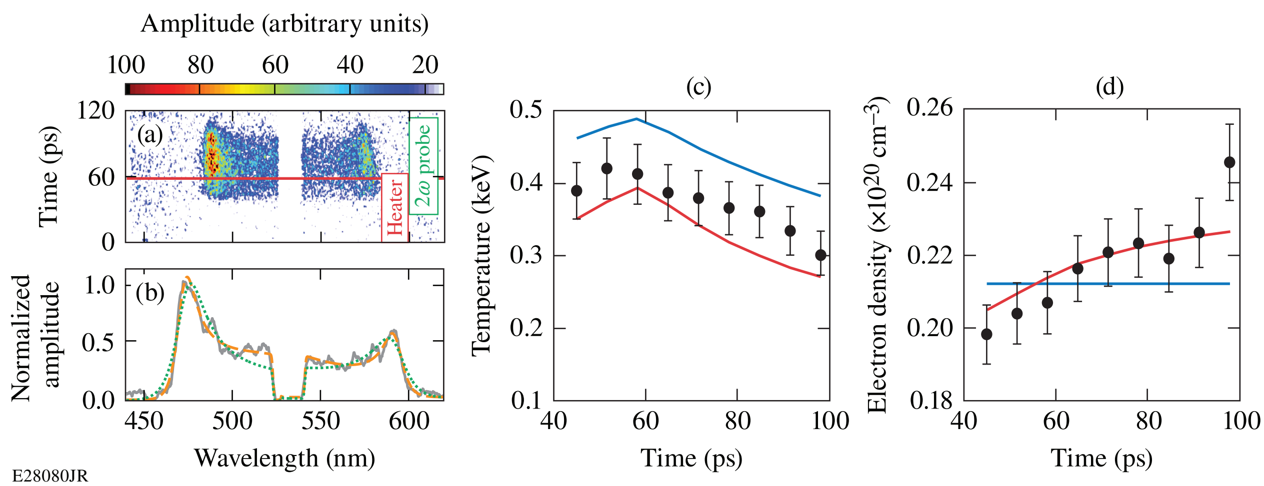

Figure 1
(a) Thomson-scattering spectrum measured from a plasma heated by an intensity of 2.5×10^{14} W/cm^2. The heater beam begins at $t = 0$ ps and the probe beam at $t = 40$ ps (inset). (b) The measured spectrum at 58 ps (solid gray curve) plotted with a spectrum calculated using Maxwellian (dotted green curve) and non-Maxwellian (dashed orange curve) electron distribution functions. The best-fit spectra determined $T_e = 428$ eV, $n_e = 2.12 \times 10^{19}$ cm^{-3}, and $m = 2$ (Maxwellian); and $T_e = 412$ eV, $n_e = 2.13 \times 10^{19}$ cm^{-3}, and $m = 3.1$ (non-Maxwellian). (c) Temperature and (d) density at nine times through the measurement are shown as solid black circles compared to K2 simulation results. The uncertainty, shown as black error bars, in the measured temperature (c) and density (d) results from repeated fitting within the noise on the spectra. The results of a K2 simulation without atomic kinetics are shown as a solid blue line. The results of a K2 simulation with atomic physics are shown as red curves.

This material is based upon work supported by the Department of Energy National Nuclear Security Administration under Award Number DE-NA0003856, the University of Rochester, and the New York State Energy Research and Development Authority.

1. A. B. Langdon, Phys. Rev. Lett. **44**, 575 (1980).
2. J. P. Matte *et al*., Plasma Phys. Control. Fusion **30**, 1665 (1988).
3. E. Fourkal *et al*., Phys. Plasmas **8**, 550 (2001).
4. R. J. Henchen *et al*., Phys. Rev. Lett. **121**, 125001 (2018).
5. W. Rozmus *et al*., Phys. Plasma **23**, 012707 (2016).
6. L. Yin *et al*., Phys. Rev. Lett. **99**, 265004 (2007).
7. H. P. Le, M. Sherlock, and H. A. Scott, Phys. Rev. E **100**, 013202 (2019).
8. H. G. Rinderknecht *et al*., Plasma Phys. Control. Fusion **60**, 064001 (2018).
9. J. M. Liu *et al*., Phys. Rev. Lett. **72**, 2717 (1994).
10. S. H. Glenzer *et al*., Phys. Plasmas **6**, 2117 (1999).
11. A. L. Milder *et al*., "Evolution of the Electron Distribution in the Presence of Inverse Bremsstrahlung Heating and Collisional Ionization," submitted to Physical Review Letters.
12. M. Sherlock, J. P. Brodrick, and C. P. Ridgers, Phys. Plasmas **24**, 082706 (2017).
13. H. A. Scott, J. Quant. Spectrosc. Radiat. Transf. **71**, 689 (2001).

Crystalline Phase Transitions and Vibrational Spectra of Silicon up to Multi-TPa Pressures

R. Paul,[1,2] S. X. Hu,[1] and V. V. Karasiev[1]

[1]Laboratory for Laser Energetics, University of Rochester
[2]Department of Mechanical Engineering, University of Rochester

This article presents the *first-principles* construction of a high pressure–temperature (*P*–*T*) phase diagram of Si up to 4 TPa and 26,000 K, which revealed new stable phases at these multi-TPa conditions. The methodology employed in this work was a combination of different first-principles approaches centered on the use of Mermin's extension of Kohn–Sham density functional theory (DFT)[1,2] and *ab initio* lattice dynamics of perfect crystals.[3]

The upper bound of the solid-state phase diagram was established using quantum molecular dynamics (QMD) simulations, within the Born–Oppenheimer approximation, with a canonical ensemble to determine the melting points. VASP[4] was used for these calculations, with the temperature being controlled via a Nosé–Hoover thermostat. Instead of using Monkhorst–Pack *k* mesh, we resorted to the use of a single special *k* point (1/4, 1/4, 1/4) for sampling the Brillouin zone (1BZ). As with all such finite-temperature computations involving electronic structure theory and lattice dynamics, however, the main challenge is the accurate determination of the effects of anharmonicity (AH) beyond the quasiharmonic (QH) approximation of phonon dynamics for the solid state, which is the principal emphasis of this work.

The anharmonic solid-state ionic-thermal contribution F_{AH}, for an optimal axial ratio γ_T at a given specific volume and temperature (V, T), was evaluated by breaking it up into two separate components and performing thermodynamic integration, with T being the ionic temperature. The first component tracks the change in Helmholtz free energy, while moving along an isochore, from T = 0 K to some finite temperature keeping the cold-curve axial ratio γ_0 constant, which is obtained from statistically averaging internal energy $U(T)$ from QMD and QH phonon calculations. The second term tracks the free energy change when the axial ratio is changed from γ_0 to γ_T at that temperature, from the anisotropic stress tensor of the ensemble. These terms are shown in Eqs. (1) and (2):

$$\left\langle F_{\mathrm{AH}}\left(V,T;\gamma=\gamma_0\right)\right\rangle\Big|_V=-T\int\left.\frac{\left\langle U(T)\right\rangle_{\mathrm{QMD}}-\left[U(T)_{\mathrm{QH}}-\frac{3}{2}N_{\mathrm{a}}k_{\mathrm{B}}T\right]}{T^2}\right|_V \mathrm{d}T, \tag{1}$$

$$F_{\mathrm{AH}}\left(V,T;\gamma_0\longrightarrow\gamma_T\right)=-\left(\frac{2V}{3\gamma_T}\right)^2\frac{\left\langle\sigma_{\mathrm{total}}^{\mathrm{anisotropic}}(T)\right\rangle\left\langle\sigma_{\mathrm{AH}}^{\mathrm{anisotropic}}(T)\right\rangle}{\left.\frac{\partial^2}{\partial\gamma^2}F_{\mathrm{QH}}(T)\right|_{\gamma_0}}. \tag{2}$$

The phase diagram (Fig. 1) shows the existence of high-pressure body-centered cubic (bcc) and simple cubic (sc) phases beyond 2.8 TPa, as well as a pocket of double hexagonal close-packed (dhcp) in the low-pressure region. The lower-symmetry orthorhombic phases of Cmce and Imma can be accurately determined only when the anharmonicity is included. The comparison to experimental results demonstrates the absolute necessity of incorporating the said effects. Similarly, the correct slope of the principal Hugoniot can be determined only when the anharmonic contribution to the Helmholtz free energy is included. The method employed in this summary presents an approach developed for the accurate construction of first-principles equation of state, phase diagrams, or deriving any property that depends on thermodynamic state variables. A remarkable observation is the increasing localization of the electron density in the face-centered cubic (fcc) phase with increasing pressure from ~100 GPa to ~2.8 TPa, leading to a dip in the electronic density of states and formation of interstitial blobs of electrons; although the dip never develops to a band gap as seen in electrides.

Supplementing the structural calculations, second- and third-order interatomic force constants were evaluated, using a combination of density functional perturbation theory (DFPT)[4] and the power spectrum constructed from phonon eigenvector-projected atomic velocities, to compute the phonon vibration modes and linewidths, respectively. This allowed for an elaborate analysis of the Raman and infrared spectra for all of the structures of silicon identified along the 500-K isotherm.

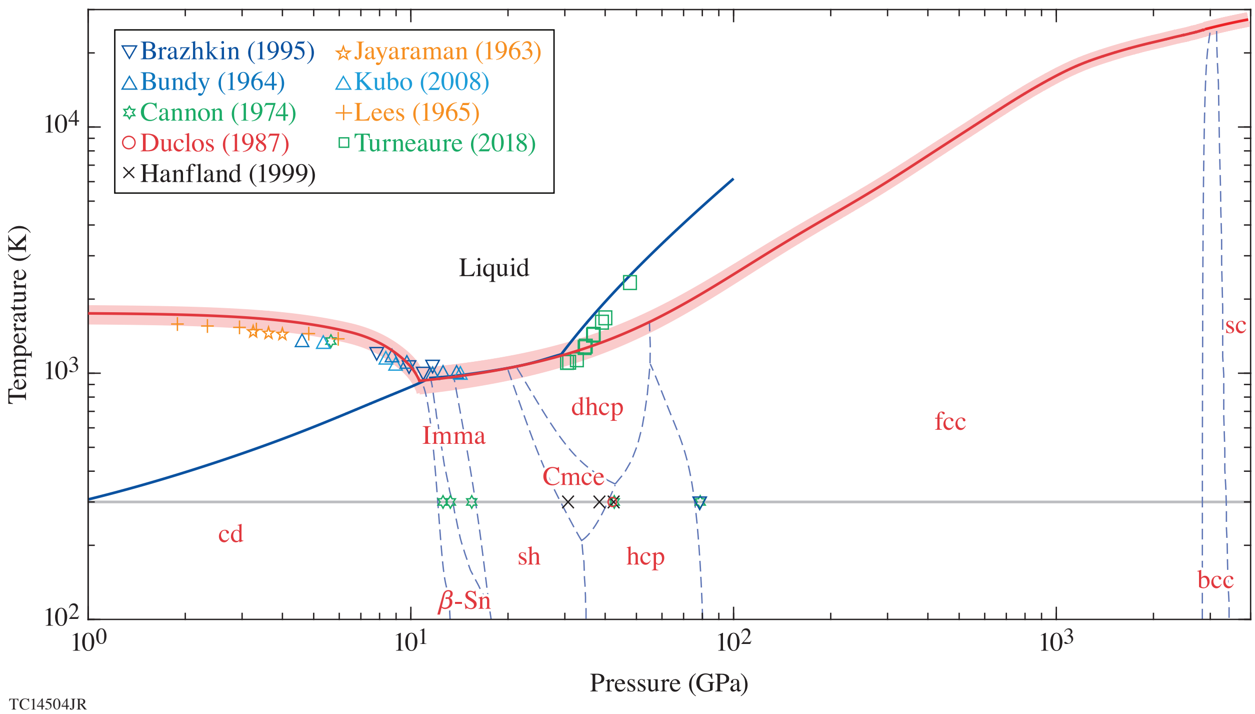

Figure 1
Pressure–temperature (P–T) phase diagram of silicon predicted using first-principles methodology. Here, the gray horizontal line represents the 300-K isotherm, whereas the solid blue line represents the principal shock Hugoniot. The discrete data points, which are also labeled in the legend, correspond to experimentally observed phase transition points.

This material is based upon work supported by the Department of Energy National Nuclear Security Administration under Award Number DE-NA0003856, the University of Rochester, and the New York State Energy Research and Development Authority.

1. W. Kohn and L. J. Sham, Phys. Rev. **140**, A1133 (1965).
2. A. Togo, F. Oba, and I. Tanaka, Phys. Rev. B **78**, 134106 (2008).
3. G. Kresse and J. Hafner, Phys. Rev. B **47**, 558 (1993); **49**, 14,251 (1994); G. Kresse and J. Furthmüller, Comput. Mater. Sci. **6**, 15 (1996); Phys. Rev. B **54**, 11,169 (1996).
4. S. Baroni *et al*., Rev. Mod. Phys. **73**, 515 (2001).

Inferred UV Fluence Focal-Spot Profiles from Soft X-Ray Pinhole Camera Measurements on OMEGA

W. Theobald, C. Sorce, W. R. Donaldson, R. Epstein, R. L. Keck, C. Kellogg, T. J. Kessler, J. Kwiatkowski, F. J. Marshall, S. Sampat, W. Seka, R. C. Shah, A. Shvydky, C. Stoeckl, L. J. Waxer, and S. P. Regan

Laboratory for Laser Energetics, University of Rochester

Laser-direct-drive inertial confinement fusion (LDD-ICF) implosions with cryogenically layered deuterium–tritium (DT) targets on OMEGA have produced hot-spot pressures >50 Gbar (Refs. 1 and 2), which is about half of the pressure required to achieve ignition conditions. Over the next several years the goal is to demonstrate an ignition-relevant hot-spot pressure of ~100 Gbar on OMEGA. The 100-Gbar Project includes improvements to the OMEGA Laser System, diagnostics, targets, and modeling, which will lead to a better understanding of the LDD-ICF physics. This requires a careful monitoring of each beam's intensity at full laser energy at the target plane, which is currently not possible, and is indirectly inferred from measurements outside the target chamber of the beam energy, the laser power, and the spot size. To characterize the focal spot of UV laser beams on target at full energy, a method was developed to image the soft x-ray emission from laser-irradiated Au planar foils. A pinhole camera with a back-thinned charge-coupled–device (CCD) detector and filtration with thin Be and Al foil filters provides images of the x-ray emission at photon energies <2 keV. This method requires a careful measurement of the relation between the applied UV fluence and the x-ray signal, which can be described by a power-law dependence. The measured exponent $\gamma \sim 2$ provides a dynamic range of ~30 for the inferred UV fluence. UV fluence profiles of selected beams were measured for 100-ps and 1-ns laser pulses and compared to directly measured profiles from an UV equivalent-target-plane (UVETP) diagnostic. The inferred spot size and super-Gaussian order from the x-ray technique agree within several percent with the values acquired by direct UV measurements. In an analogy to the UVETP technique, the method is called the x-ray target-plane (XTP) method, which is performed at full laser power inside the target chamber. UV fluence profiles were inferred for up to 11 beams equipped with SG5-850 distributed phase plates (DPP's) and were compared to directly measured UV profiles from the UVETP diagnostic for 4 of the 11 beams. Good agreement between the XTP and UVETP measurements was obtained, indicating that nonlinear optical effects from the transport in air and in the optics at the target chamber wall are likely negligible.

The experimental setup is depicted in Fig. 1(a). An OMEGA UV beam propagates from the left to the right side, passes through a distributed polarization rotator and reaches a fused-silica wedge—uncoated on the front and AR coated on the back—that picks up a 4% reflection of the full beam, which is then sent to the UVETP diagnostic. The main beam is then directed over a distance of about 18 m in air and passes through a DPP and a lens that focuses the beam onto a flat foil inside the target chamber. A similar DPP is placed in the UVETP diagnostic directly in front of an OMEGA focusing lens, mimicking the target/beam configuration. The beam is brought through focus in a vacuum tube, which is not shown in the simplified schematic; outside the tube, the expanding beam is picked up by another lens. The beam is down-collimated and attenuated, and a magnified image of the focus is produced on a CCD camera. The flat-foil target was a 20-μm-thick Si wafer with an area of 6×6 mm^2 that was coated with a 500-nm layer of Au. The target normal was aligned along the axis of an opposing port with a ten-inch manipulator (TIM). Up to five beams were focused simultaneously onto the target such that the laser spots were well separated. A pinhole camera loaded into the TIM imaged the x-ray emission with a magnification of 5.16 onto a back-thinned CCD camera.

Figure 1(b) shows example data of the laser spot of Beam 56 from XTP and compares it to Fig. 1(c), the directly measured spot from UVETP. For a quantitative comparison of the fluence profiles, both images were fitted with an elliptical 2-D super-Gaussian function given by

$$F(x,y) = F_0 \exp\left\{-\left[\left(\frac{x-x_0}{a}\right)^2 + \left(\frac{y-y_0}{b}\right)^2\right]^{n_{SG}/2}\right\} + \text{back}, \tag{1}$$

where x_0, y_0 are the coordinates of the beam center, n_{SG} is the order of the super-Gaussian function, "back" is a constant background, and a and b are the minor and major axes of the ellipse, respectively. The fitting is performed over an area of ~1.6 × 1.6 mm^2 for both the UVETP and the XTP methods. The minimum signal included in the fit is ~0.2% of the peak signal for UVETP and ~2% of the peak signal for XTP. The spot radius is defined as the arithmetic mean of a and b:

$$R_{1/e} = \sqrt{a \cdot b}, \tag{2}$$

which describes the average radius where the fluence is at the 1/e value of the peak fluence F_0. The two main parameters that are used to compare the fluence profiles are $R_{1/e}$ and n_{SG}. Figure 1(d) shows the result of the fitting process to the XTP image, while the residual (data minus fit) is shown in Fig. 1(e). The fit parameters were $R_{1/e}$ = 353.5±0.1 μm and n_{SG} = 4.86±0.01, where the errors indicate the 95% confidence band from the fitting. The ellipticity was inferred with 0.8%, which means that the beam profile is close to circular. The fitting process of the UVETP data yielded $R_{1/e}$ = 358.4±0.0 μm, n_{SG} = 5.03±0.00, and an ellipticity of 1.4%. The fitting values from XTP are slightly lower than those from UVETP; however, this is not significant. The statistical errors for $R_{1/e}$ and n_{SG} were estimated by repeating the same measurement for the same beam over multiple shots and several campaigns. The errors for the XTP method are 1.0% and 3.4% for $R_{1/e}$ and n_{SG}, respectively, and 0.1% and 1.9% for the UVETP method, respectively. Systematic errors in the XTP method include magnification errors, calibration errors, and the limitation in dynamic range, which are estimated with ~2.7% and ~4.5% for $R_{1/e}$ and n_{SG}, respectively. With respect to the estimated error budget, the UV profiles from the XTP and UVETP diagnostics are in agreement.

The XTP data from 11 beams show some spread in spot size with Beam 52 having the largest spot ($R_{1/e}$ = 365.0 μm) and Beam 61 the smallest spot ($R_{1/e}$ = 345.9 μm). The difference in spot size between the largest and the smallest beams is 19 μm

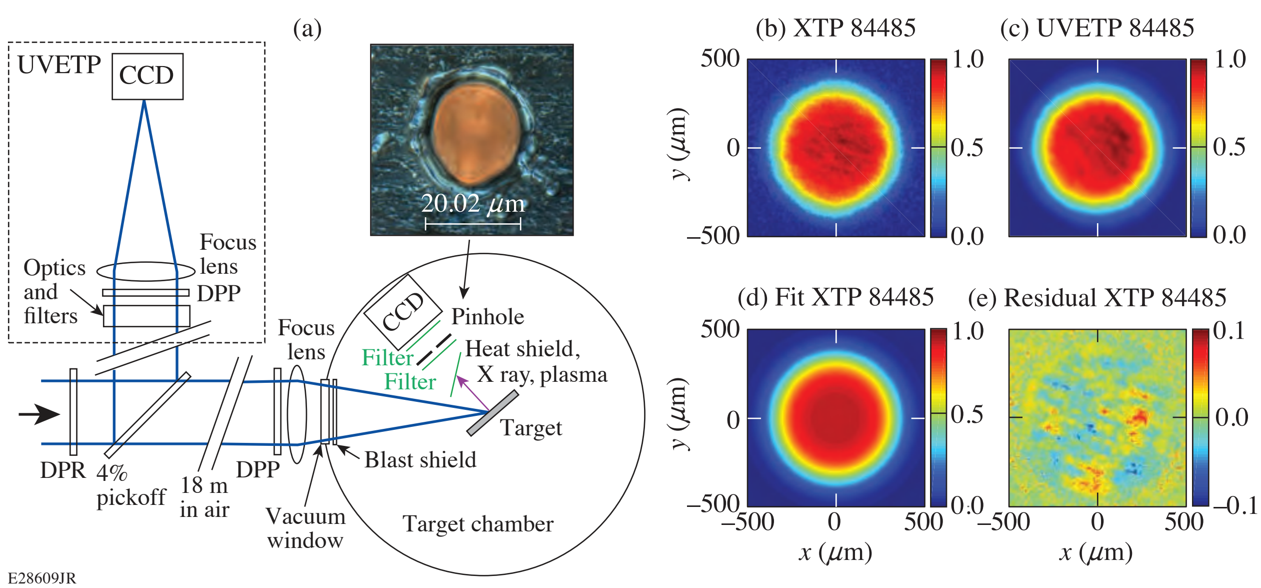

Figure 1
(a) Schematic of the experimental setup of the XTP and UVETP measurements including an optical image of a pinhole that measured the laser spots when using a 100-ps pulse. DPR: distributed polarization rotator. [(b)–(e)] UV laser-spot profiles from (b) XTP and (c) the UVETP diagnostic of Beam 56 for shot 84485. A 100-ps pulse was used. (d) The fitted 2-D super-Gaussian profile to the XTP image and (e) the residual of XTP (data minus fit).

(~5%), which is larger than the measurement error; therefore, it is likely real. The peak fluence difference on target between Beams 52 and 61 is estimated with ~11%. The average XTP values over the 11 beams resulted in $R_{1/e} = 356.6\ \mu$m and $n_{SG} = 4.92$. The average XTP values over those four beams that were covered by UVETP resulted in $R_{1/e} = 358.9\ \mu$m and $n_{SG} = 5.03$, which agree with the averaged UVETP data within the errors.

Figure 2 shows the beam-to-beam variation of the peak fluence normalized to the average value for (a) the 100-ps and (b) the 1-ns pulse measurements. The same energy was assumed on all beams. The red squares refer to the XTP diagnostic and the blue diamonds refer to the UVETP diagnostic. The yellow band indicates the acceptable rms variation (σ_{rms}) in peak fluence based on variation in beam shape, which is $\sigma_{rms} \approx 2\%$. The XTP data from the 11 beams indicate $\sigma_{rms} \approx 3\%$ for both the 100-ps and 1-ns pulse measurements, which is slightly larger than the acceptable variation. The UVETP data from the four beams result in $\sigma_{rms} \approx 1.5\%$, which is below the limit.

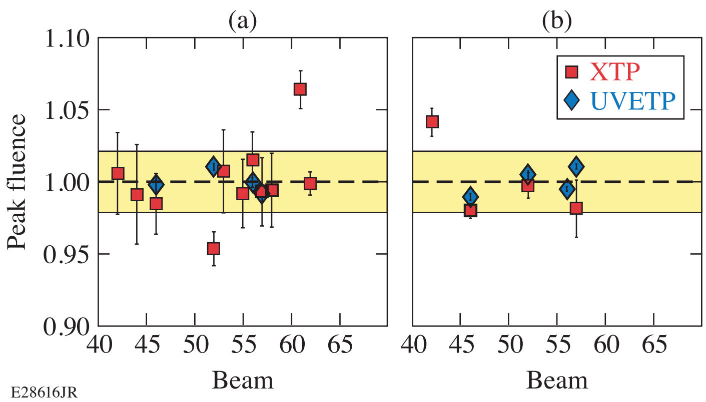

Figure 2
Beam-to-beam variation of the peak fluence normalized to the average value for (a) the 100-ps and (b) the 1-ns pulse measurements. The red squares refer to the XTP diagnostic and the blue diamonds refer to the UVETP diagnostic.

This material is based upon work supported by the Department of Energy National Nuclear Security Administration under Award Number DE-NA0003856, the University of Rochester, and the New York State Energy Research and Development Authority.

1. S. P. Regan *et al*., Phys. Rev. Lett. **117**, 025001 (2016); **117**, 059903(E) (2016).

2. A. Bose *et al*., Phys. Rev. E **94**, 011201(R) (2016).

Magnetically and Optically Tunable Terahertz Radiation from Ta/NiFe/Pt Spintronic Nanolayers Generated by Femtosecond Laser Pulses

R. Adam,[1] G. Chen,[2] D. E. Bürgler,[1] T. Shou,[3] I. Komissarov,[3] S. Heidtfeld,[1] H. Hardtdegen,[4] M. Mikulics,[1] C. M. Schneider,[1,5] and R. Sobolewski[2,3]

[1]Research Centre Jülich, Peter Grünberg Institute
[2]Materials Science Graduate Program and Laboratory for Laser Energetics, University of Rochester
[3]Department of Electrical and Computer Engineering and Laboratory for Laser Energetics, University of Rochester
[4]Research Centre Jülich, Ernst Ruska Centre for Microscopy and Spectroscopy with Electrons
[5]Department of Physics, University of California, Davis

Terahertz (THz) radiation covers the electromagnetic spectrum range between radiofrequency millimeter waves and optical far-infrared radiation, approximately 0.3 to 30 THz, and has been applied in astronomy, medical imaging, security, communication, and manufacturing[1,2] as well as a scientific tool in materials testing[3] and bio imaging,[4] or in the study of electron wakefield acceleration.[5] Among different THz sources, current extensive research focuses on emitters of ultrafast electromagnetic transients with a broad THz-range spectrum in order to control and capture spin,[6] charge,[7] or phase-transition–related processes on subpicosecond time scales. Recent observation of THz emissions from optically excited ferromagnet/metal (F/M) nanolayers[8–11] establishes a very elegant link between laser optics, spintronics, and THz radiation, merging these three very active scientific fields and having a tremendous potential for future applications. The uncomplicated fabrication of spintronic THz emitters can lead to widespread applications.

Superdiffusive spin currents generated in laser-driven demagnetization experiments have been theoretically predicted[12] and, subsequently, quickly confirmed in a number of experiments,[13–17] demonstrating their crucial role in ultrafast magnetization dynamics in a range of magnetic materials and structures. The central role of the superdiffusive currents in THz generation[9] has further strengthened their importance in laser-driven spin transient dynamics and has led to applications that are currently emerging at the border of laser physics and spin-based electronics. A simple physical mechanism has been proposed to explain the generation of THz transients from femtosecond laser-driven F/M bilayers and multilayers. THz emission is explained by the photon-driven spin current flowing from an F film to a neighboring M material. This spin current is, subsequently, converted by the inverse spin Hall effect (ISHE) into a transient charge current flowing along the M surface, thereby generating a laser-helicity independent subpicosecond electromagnetic signal.[10,18]

We have generated bursts of strong THz radiation (transient, single-picosecond-in-duration electromagnetic signals) by placing Ta/NiFe/Pt (equivalently, Ta/Py/Pt, where Py stands for permalloy: $Ni_{80}Fe_{20}$) trilayers in a static magnetic field and illuminating them with a train of 100-fs-wide laser pulses from a commercial Ti:sapphire laser (800-nm wavelength and 76-MHz repetition rate). The train of laser pulses was split into two beams with a 90:10 intensity ratio. The high-intensity branch, after bouncing from a retroreflector mounted at the delay stage, was focused at our F/M sample, while the low-intensity beam was used to excite a photoconductive low-temperature–grown GaAs (LT-GaAs) switch acting as a THz transient detector.[19] The linear motion of the delay stage in the pump beam, with a 2.5-μm-step size, allowed an optical path control with a 16.6-fs time resolution. Ta/Py/Pt samples were optically excited either by illumination of the metallic surface (direct geometry) or by laser pulses passing through the MgO substrate (reverse geometry). In addition, we used a Teflon (polytetrafluoroethylene) lens with a 5-mm diameter and 10-mm focal length to focus the THz radiation at the LT-GaAs detector operated in a photoconductive-sampling mode. The latter allowed us to reconstruct the THz transient in time domain. The external **H** field was generated either by electromagnet coils wrapped around iron yokes and supplying a variable field of up to 70 kA/m or by a pair of permanent magnets generating a fixed, ~40-kA/m field.

Our spintronic samples consisted of Ta (2-nm)/Py (2-nm)/Pt (2-nm) nanotrilayers and were deposited sequentially at room temperature by magnetron sputtering on top of optically polished 10 × 10-mm^2 MgO substrates with (100) surface orientation. The deposition thickness for each layer was monitored by a quartz crystal microbalance. The thin, 2-nm Ta buffer layer was deposited first, directly onto the MgO substrate to achieve a good adhesion and smoothness of the consecutive layers. We have chosen Pt as a top material for its relatively high spin-orbit coupling: the material-dependent parameter that, according to literature, is responsible for THz generation in magnetic nanolayers.[20]

Figure 1(a) presents a typical time-domain, subpicosecond (0.9-ps FWHM of the main peak) electromagnetic transient generated by our spintronic nanolayer emitter and detected by the LT-GaAs detector. The zero time on the time axis was chosen arbitrarily, but it was kept the same for all measurements. The measurement was done in the reverse geometry, illustrated in the left inset in Fig. 1(a) with the **H** field fixed at 55 kA/m and applied in the sample plane. The laser fluence was 7.25 μJ/cm^2. In this geometry, we have also observed (not shown here) a secondary, significantly weaker THz transient, delayed by ~10 ps with respect to the main signal. The latter signal was identified as a THz transient generated at the Py/Pt bilayer and propagating in the opposite direction with respect to the main one and, subsequently, reflected at the MgO/air interface. A fast Fourier transform (FFT) of the time-domain waveform is shown in the right inset in Fig. 1(a) as the normalized THz transient power spectrum. We note that the signal frequency content extends up to 5 THz with a 3-dB cutoff at 0.85 THz. A small dip visible in the power spectrum at about 2 THz corresponds to resonant absorption of a Teflon lens used to focus the THz beam. When we flipped the trilayer by 180° and illuminated it in the direct geometry, keeping the laser beam and **H** orientation unchanged, we recorded essentially the same time-domain transient as shown in the main panel of Fig. 1(a), but with the polarity reversed. As we discuss below, the latter indicates a reversed direction of the charge current density $\mathbf{J}_C$. Compared to the reverse geometry, the signal in direct geometry had a slightly lower amplitude (apparently caused by THz absorption by Ta and MgO) and no secondary reflected signal was

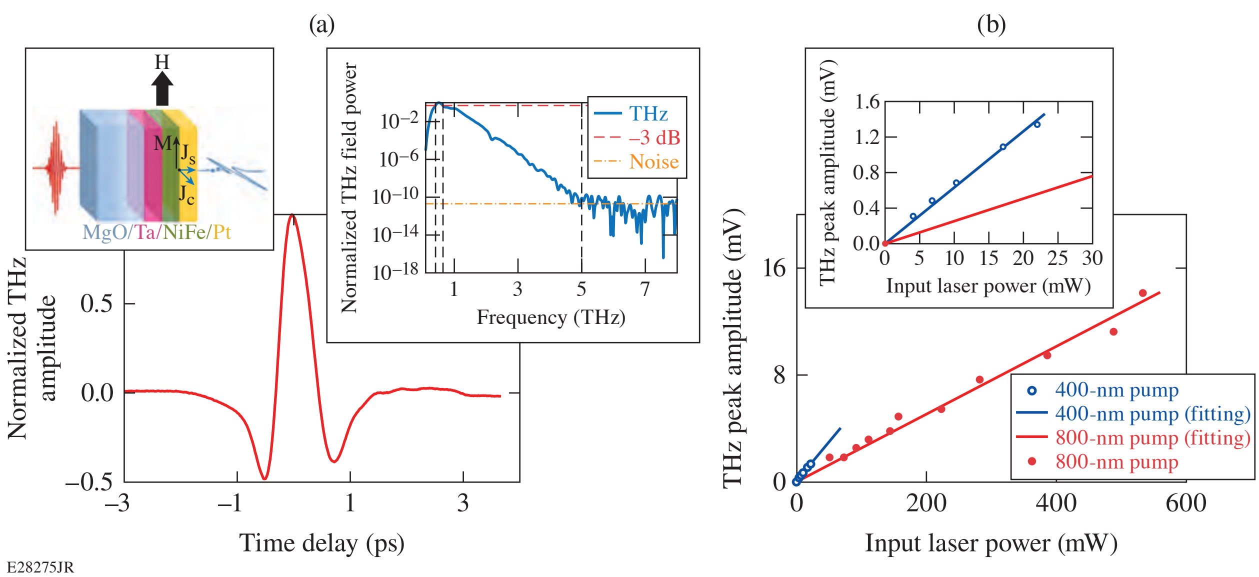

Figure 1
(a) A normalized THz transient generated by a 100-fs-wide laser pulse impinging at a Ta/Py/Pt nanotrilayer through the MgO substrate (reverse illumination geometry). The left inset shows the trilayer stacking and the schematics of the THz-generation mechanism. The right inset presents a normalized THz power spectrum that corresponds to the pulse shown in the main panel. The spectrum exhibits a 3-dB cutoff at 0.85 THz and extends to 5 THz with exponentially decreasing intensity. (b) A THz transient amplitude as a function of the incident laser beam power for both fundamental (λ = 800 nm; solid red circles) and frequency-doubled light (λ = 400 nm; open blue circles). The inset shows the available power range for the 400-nm light and demonstrates a strongly increased efficiency of THz generation at the 400-nm wavelength.

observed. Finally, we optically illuminated the Pt/Py/Ta trilayer from the Pt side at a 45° incidence angle and collected a THz transient with the detector positioned at 90° with respect to the laser beam. As expected for superdiffusive current flowing in all directions, the recorded time-domain waveform had a shape identical to the pulse shown in the main panel of Fig. 1(a). The power spectra for the direct, reverse, and 45° illumination geometries were identical to that presented in Fig. 1(a), right inset. The above observations indicate that optically triggered THz transients originate near or at the Py/Pt interface.

We have also studied the impact of varying external optical excitation on the THz signal emitted by our spintronic Ta/Py/Pt emitter. Figure 1(b) shows the maximum THz-signal amplitude A^{THz} dependence on the incident, average laser power at both the fundamental (λ = 800 nm; solid red circles) and frequency-doubled (λ = 400 nm; open blue circles) wavelengths at a constant magnetic field H = 55 kA/m. In both cases, the dependence is linear, as indicated by the corresponding linear fits. Although the range of available incident powers for the 400-nm light was quite small, limited by the efficiency of the frequency-doubling barium borate (BBO) crystal, our data clearly demonstrate that for the same laser power, 400-nm photons generate approximately 3× larger subpicosecond transients, as compared to the 800-nm photons. At the same time, the corresponding normalized time-domain waveforms (not shown) were practically the same as the one shown in Fig. 1(a), main panel, resulting in the identical THz power spectra. Although our studies seem to contradict recent results of Herapath *et al.*,[21] where no pump wavelength dependence on THz generation was reported, we stress that the measurements presented in Ref. 21 were performed not only on a different material system, but, first of all, exclusively at infrared wavelengths (900 to 1500 nm). High-energy green photons used in our studies are certainly more efficiently absorbed by metallic nanolayers and generate a significantly larger concentration of hot electrons that couple to the spins. As a result, we observe the THz amplitude enhancement as it was discussed above and presented in Fig. 1(b).

An external electromagnet in our THz setup allowed us to tune the **H** field in a range up to ±70 kA/m. For a constant laser light (λ = 800 nm) with an average laser power of 550 mW, we stepped **H** from –70 kA/m to +70 kA/m and back to –70 kA/m, and by this sequence we recorded the A^{THz} dependence on the magnitude of the in-plane **H** field applied to our Ta/Py/Pt trilayer. We observed that the $A^{\mathrm{THz}}(\mathbf{H})$ hysteresis overlaid perfectly on the shape of the static hysteresis of the magnetic moment $\mu(\mathbf{H})$ of the Py nanolayer, recorded using a commercial physical property measurement system (PPMS). Most interestingly, the measured $A^{\mathrm{THz}}(\mathbf{H})$ curve exhibited hysteresis that was significantly narrower than that of the pure Py layer.

The main question is why $A^{\mathrm{THz}}(\mathbf{H})$ for our samples follows the shape of the static hysteresis of the Py film. Our optical beam is linearly polarized, so we are in the laser-helicity independent case and the THz transient is directly proportional to $\mathbf{J}_{\mathrm{C}}$ produced by the ISHE mechanism that in turn depends on the spin current density $\mathbf{J}_{\mathrm{S}}$ and spin polarization $\boldsymbol{\sigma}$. According to, e.g., Saitoh *et al.*[22] $\mathbf{J}_{\mathrm{C}} = D_{\mathrm{ISHE}}\,(\mathbf{J}_{\mathrm{S}} \times \boldsymbol{\sigma})$, where D_{ISHE} is a coefficient representing the ISHE efficiency in a material. Therefore, we can control the ultrafast time-domain signal amplitude and polarity by controlling the $\mathbf{J}_{\mathrm{C}}$ amplitude and its direction. The $\mathbf{J}_{\mathrm{C}}$ amplitude is controlled in our case through $\boldsymbol{\sigma} \sim \mu(\mathbf{H})$, while the $\mathbf{J}_{\mathrm{C}}$ direction is controlled by the illumination geometry (direct or reverse). We note that in both geometries the superdiffusive current flows in all directions as confirmed by the experiment with laser illumination under 45° mentioned above; nevertheless, only the $\mathbf{J}_{\mathrm{C}}$ component pointing from Py to Pt matters for THz generation. For fixed directions of **H** and $\mathbf{J}_{\mathrm{S}}$, and because $\mathbf{J}_{\mathrm{C}} \sim \mu(\mathbf{H})$, one should expect that $A^{\mathrm{THz}}(\mathbf{H})$ behaves similar/identical to the $\mu(\mathbf{H})$ dependence, as, indeed, is observed in our studies. The observed significantly narrower width of the $A^{\mathrm{THz}}(\mathbf{H})$ hysteresis in the Ta/Py/Pt trilayer as compared to the $\mu(\mathbf{H})$ hysteretic dependence may arise from the fact that the static $\mu(\mathbf{H})$, measured in PPMS, represents a signal averaged over the whole sample volume. Therefore, for instance, pinning at the sample edges may contribute to the signal, while THz generation is local, defined by a laser beam spot (~50 μm in diameter). Finally, we note that in order to generate THz transients in our soft, magnetic Py-based samples with vanishing remanence, an external **H** field was always necessary. On the other hand, our preliminary measurements performed on magnetically harder materials show that after the initial magnetization, no external **H** is required to generate high-intensity THz transients. (Studies of transient THz emission from magnetically harder nanobilayers will be published separately.)

In conclusion, we have generated subpicosecond electromagnetic transients from Ta (2-nm)/Py (2-nm)/Pt (2-nm) spintronic nanotrilayers using a train of 100-fs-wide laser pulses and a static magnetic field (up to ±70 A/m) applied in the plane of a sample. Resulting power spectra of the transients extend up to 5 THz with a 3-dB cutoff at 0.85 THz. The amplitude of the transients depends linearly on the average laser power; however, for the same laser power, blue photons (400-nm wavelength) generate THz transients with amplitudes approximately 3× larger than transients resulting from excitation by infrared (800-nm-wavelength) photons. The THz amplitude of emitted signals is tunable by the **H**-field intensity and follows the hysteretic behavior of the magnetization versus **H**-field dependence of the pure Py layer, albeit $A^{\mathrm{THz}}(\mathbf{H})$ is, in practice, nonhysteretic. Finally, we note that our simple, robust, and tunable THz emitters can lead to widespread applications in compact, hand-held THz diagnostic devices, in local device-to-device communication with enormous data transfer capacity, or as sources for material and circuit testing at THz frequencies.

The work at the Research Center Jülich was performed within *Ju*SPARC (Jülich Short-pulse Particle Acceleration and Radiation Center), a strategy project funded by the BMBF. Research at Rochester has been supported in part by the grant from the HYPRES Co., and by the New York State Advanced Technology Centers for Innovative and Enabling Technologies (University of Rochester) and Advanced Sensor Technologies (Stony Brook University).

1. M. Tonouchi, Nat. Photonics **1**, 97 (2007); E. A. Williams, *National Association of Broadcasters Engineering Handbook*, 10th ed. (Elsevier, Burlington, MA, 2007).
2. R. A. Lewis, J. Phys. D: Appl. Phys. **47**, 374001 (2014).
3. A. Koroliov *et al*., Appl. Sci. **9**, 391 (2019).
4. K. Ajito and Y. Ueno, IEEE Trans. Terahertz Sci. Technol. **1**, 293 (2011).
5. E. A. Nanni *et al*., Nat. Commun. **6**, 8486 (2015).
6. S. Baierl *et al*., Nat. Photonics **10**, 715 (2016).
7. R. L. Milot *et al*., Nano Lett. **16**, 7001 (2016).
8. G. Torosyan *et al*., Sci. Rep. **8**, 1311 (2018).
9. T. Seifert *et al*., Appl. Phys. Lett. **110**, 252402 (2017).
10. T. Kampfrath *et al*., Nature Nanotechnol. **8**, 256 (2013).
11. Y. Wu *et al*., Adv. Mater. **29**, 1603031 (2017).
12. M. Battiato, K. Carva, and P. M. Oppeneer, Phys. Rev. B **86**, 024404 (2012).
13. D. Rudolf *et al*., Nat. Commun. **3**, 1037 (2012).
14. E. Turgut *et al*., Phys. Rev. Lett. **110**, 197201 (2013).
15. S. Mathias *et al*., Proc. Nat. Acad. Sci. **109**, 4792 (2012).
16. A. Eschenlohr *et al*., Nat. Mater. **12**, 332 (2013).
17. J. Sinova *et al*., Rev. Mod. Phys. **87**, 1213 (2015).
18. G. Li *et al*., J. Phys. D: Appl. Phys. **51**, 134001 (2018).
19. A. Geižutis *et al*., Opt. Mater. **30**, 786 (2008).
20. T. Seifert *et al*., Nat. Photonics **10**, 483 (2016).
21. R. I. Herapath *et al*., Appl. Phys. Lett. **114**, 041107 (2019).
22. E. Saitoh *et al*., Appl. Phys. Lett. **88**, 182509 (2006).

Investigation of Mechanisms of Laser-Induced Secondary Contamination from Metal Particles Attached on the Input Surface of Optical Components

S. G. Demos,[1] J. C. Lambropoulos,[1] R. A. Negres,[2] M. J. Matthews,[2] and S. R. Qiu[2]

[1]Laboratory for Laser Energetics, University of Rochester
[2]Lawrence Livermore National Laboratory

Laser-induced damage on large-aperture optical components exposed to high-average-power or peak-intensity laser pulses is a well-recognized issue that affects the operational parameters as well as the cost of such systems. The origin of this issue is associated with the presence of absorbing defects incorporated into the optical material during the manufacturing process or resulting from contaminant species incorporated from handling or within the operational environment. Metallic particles are commonly found contaminants on surfaces of optical components in high-energy laser systems such as at the National Ignition Facility. Researchers have made great efforts to understand the impact of these contaminants on their laser performance.[1–21] The knowledge attained from this previous work is directly applicable to the present study, which examines the dynamics of the interaction of microscale, nominally spherical metal particles attached on the input (front) surface of optics. As the momentum attained by the particle thrusts the particle against the surface, the resulting response of the particle is nontrivial. Previous work has provided only the phenomenology of the final modifications, while the intermediate steps were speculative and qualitatively described. To address this issue, the present work involves time-resolved microscopic shadowgraphy with adequate spatial and temporal resolution to resolve details of the dynamics of plasma formation, shock-wave expansion, particle ejection, and secondary contamination by small molten droplets that separated from the original particle.

The basic experimental system used in this work includes a pump laser operating at 355 nm, producing ≈8-ns (FWHM) pulses, or 1064 nm, producing ≈10-ns pulses. A different excitation geometry and substrate were used with each excitation wavelength. Specifically, excitation at 355 nm was used in combination with stainless-steel particles (316L alloy) dispersed on the input surface of a 5-cm-round, 0.5-mm-thick commercially available silica substrate. In addition, titanium particles dispersed on the surface of an ~7-μm-thick multilayer dielectric high reflector at 45° and *p* polarization were studied under excitation at 1064 nm, where the SiO_2/HfO_2 multilayer dielectric coatings were deposited on a 5-cm-round, 10-mm-thick commercially available BK7 and optimized to provide reflectivity of >99.5% at 1053 nm. In both cases, particles that were similar in diameter were selected to be exposed to the pump pulses having a diameter of the order of 20 μm. The beam profile of the pump laser impinging on the surface of the substrate was nearly flattop (with ~25% local intensity variations) and had an elliptical shape (because of the angle of incidence of the laser beam) with a minor axis of about 315 μm. The pump laser fluence was about 12.5±2 J/cm^2 under 355-nm excitation and about 17.5±2 J/cm^2 under 1064-nm excitation, both of which are relevant to the operational fluences used in large-aperture laser systems.

Two identical microscope systems providing 25× or 50× optical magnification were positioned orthogonally to each other and used to image the area containing the particle along the surface of the sample, referred to as a transmission-view (TV) microscope, and normal to the surface, referred to as a side-view (SV) microscope. Time-resolved images (Fig. 1) were acquired using pulsed illumination obtained from the probe laser operating at 532 nm, producing 180-ps (FWHM) pulses. The output of the probe beam was split to illuminate the particle parallel and orthogonally to the substrate surface, making it possible to acquire dynamic images of the particle's response to the laser pulse at predetermined delay times with respect to the time of peak intensity of the pump pulse. The probe laser fluence was of the order of 1 mJ/cm^2 and had no impact on the behavior of the particles under exposure to probe pulses alone.

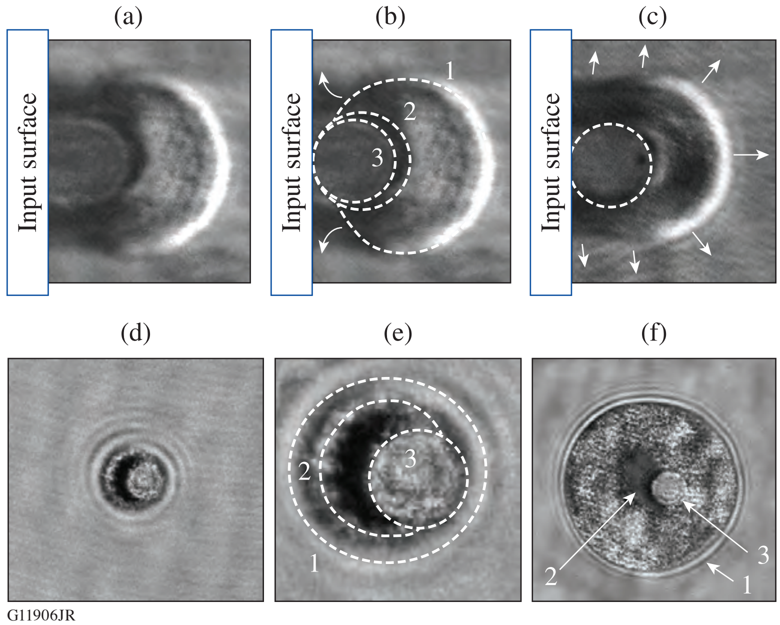

Figure 1
[(a)–(c)] Side-view images of the location of the stainless-steel particle (18-μm diameter) acquired at an ≈ –3-ns delay under a 355-nm laser exposure of ≈12 J/cm^2, capturing the position of the shock wave (1) at different stages of its expansion along with (2) the plume and (3) the particle. (a) and (c) are different events; (b) is the same as (a) with the features of interest outlined by dashed lines. The laser illuminates the particle from the right-hand side. [(d)–(f)] Transmission-view images of the location of the stainless-steel particle (17-μm diameter), acquired at about a –4-ns delay, capturing the asymmetric expansion of (1) the shock wave and (2) the plume along the substrate surface, as well as (3) the particle. (d) and (f) are different events; and (e) is a digital magnification of (d) with the features of interest outlined by dashed lines. The laser illuminates the particle from the left-hand side.

The results suggest that there are three contamination mechanisms following the interaction of laser pulses with metallic particles attached to the input surface of optics. The first mechanism is related to the initial plume expansion toward the surface, which would leave a layer of contamination around the particle. The second mechanism is related to the liquid material formed on the particle that separates during the ejection of the particle from the surface. This material is subsequently deposited around the initial particle location and mostly on the side of the particle along the direction of laser irradiation. The third mechanism is related to droplets of liquid material that separate from the particle after its ejection. As a result, these droplets can be deposited at significant distances from the initial location of the particle.

The trail of the droplets deposited on the surface via the third mechanism allows one to appreciate the direction of propagation of the particles after their ejection from the surface. For nearly spherical particles, it was observed that the particles are ejected along (or close to) the plane defined by the direction of laser beam propagation and the orthogonal direction to the surface (along the x–z plane). This is exemplified by the images shown in Fig. 2. Because the expansion of the plume is vertical to the surface, the attained momentum and direction of particle ejection depend strongly on its shape. This can be particularly important for irregularly shaped contamination particles, especially those with extended, nearly flat surfaces. The effects described here can lead to thrusting of the particle closer to the surface and subsequently an extended (spatially) contamination by liquid droplets.

The results obtained using the Ti particles dispersed on the multilayer dielectric coating surface suggest a more-severe secondary contamination compared to the contamination induced by stainless-steel particles on bare silica. This is assigned to the excitation geometry, namely the fact that laser light reflected on the coating illuminated the particle from the side, thereby increasing the total exposure fluence on the particle and creating liquified material over a larger part of its surface, including near its point of attachment on the coating surface.

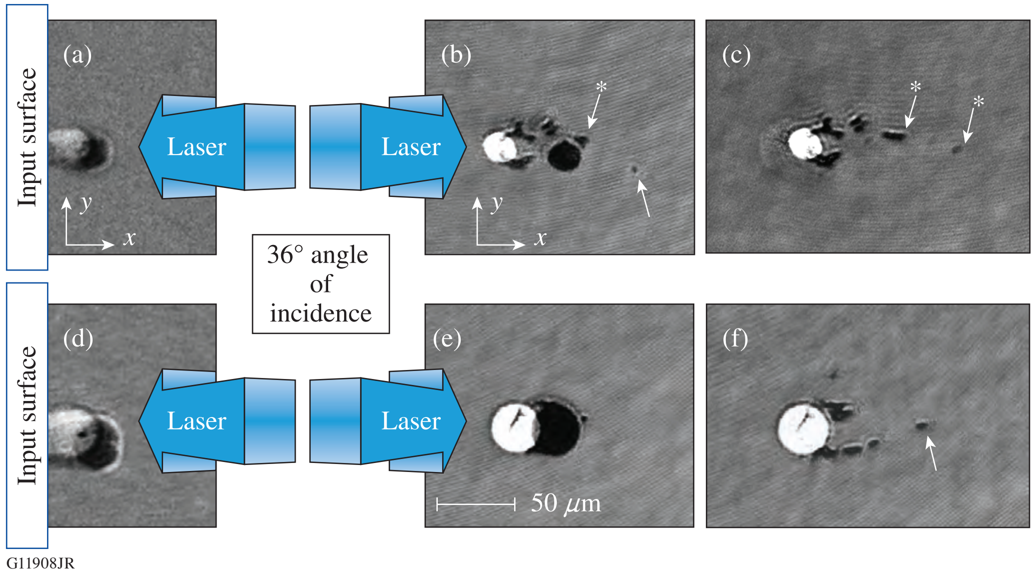

Figure 2
Two examples of the motion of stainless-steel particles at a 1025-ns delay as captured by (a) and (d) the SV microscope and (b) and (e) the TV microscope along with (c) and (f) the final TV images. [(a)–(c)] The particle is about 21 μm in diameter and exhibits motion of about 13 μm along the z axis and about 42 μm along the x axis. This means that the particle has been ejected from the surface at an angle of about 73° with respect to the z axis at a speed of about 43 m/s. Similarly, the particle in (d)–(f) was ejected at a speed of ≈32 m/s. (c) and (f) show the final images acquired at the end of the process, where only the contamination by liquid droplets that have separated from the particle is visible on the substrate surface. Comparison of the transient and final images allows one to better understand this secondary contamination process.

The behaviors observed in this work are expected to be analogous to those occurring under a wide range of excitation conditions when the interaction of the laser pulse with the particle supports an ablation event. For example, the morphology of secondary contamination under ultrashort pulsed excitation[22] is similar to that observed with the nanosecond pulses used in this work and can be fully explained using the dynamic processes described here.

This material is based upon work supported by the Department of Energy National Nuclear Security Administration under Award Number DE-NA0003856, the University of Rochester, and the New York State Energy Research and Development Authority. This work was performed in part under the auspices of the U.S. Department of Energy by Lawrence Livermore National Laboratory under Contract No. DE-AC52-07NA27344.

1. M. D. Feit *et al*., Proc. SPIE **2966**, 417 (1997).
2. F. Y. Génin, M. R. Kozlowski, and R. Brusasco, Proc. SPIE **3047**, 978 (1997).
3. F. Y. Génin *et al*., Proc. SPIE **2966**, 126 (1997).
4. D. M. Kane and D. R. Halfpenny, J. Appl. Phys. **87**, 4548 (2000).
5. S. Palmier *et al*., Proc. SPIE **5991**, 59910R (2006).
6. M. A. Norton *et al*., Proc. SPIE **5991**, 59910O (2006).
7. S. Palmier *et al*., Appl. Opt. **47**, 1164 (2008).
8. Y. Ye *et al*., Optik **123**, 1056 (2012).
9. T. Jitsuno *et al*., Proc. SPIE **8786**, 87860B (2013).
10. X. Ling *et al*., Appl. Surf. Sci. **270**, 346 (2013).

11. K. E. Gushwa and C. I. Torrie, Proc. SPIE **9237**, 923702 (2014).

12. M. J. Matthews *et al*., J. Opt. Soc. Am. B **30**, 3233 (2013).

13. F. Y. Génin *et al*., Appl. Opt. **39**, 3654 (2000).

14. E. Feigenbaum, S. Elhadj, and M. J. Matthews, Opt. Express **23**, 10589 (2015).

15. C. J. Stolz *et al*., Proc. SPIE **10691**, 106910W (2018).

16. S. R. Qiu *et al*., Appl. Opt. **54**, 8607 (2015).

17. S. R. Qiu *et al*., Opt. Eng. **56**, 011108 (2016).

18. S. G. Demos *et al*., Opt. Express **24**, 7792 (2016).

19. C. D. Harris *et al*., Opt. Lett. **40**, 5212 (2015).

20. R. N. Raman *et al*., Opt. Express **24**, 2634 (2016).

21. R. N. Raman, R. A. Negres, and S. G. Demos, Opt. Eng. **50**, 013602 (2011).

22. K. R. P. Kafka and S. G. Demos, Opt. Lett. **44**, 1844 (2019).

The 11th Omega Laser Facility Users Group Workshop

M. Koepke,[1] J. A. Frenje,[2] S. Ali,[3] A. Casner,[4] M. Gatu Johnson,[2] E. Merritt,[5] P. Tzeferacos,[6] M. S. Wei,[7] and J. P. Knauer[7]

[1]West Virginia University
[2]Massachusetts Institute of Technology
[3]Lawrence Livermore National Laboratory
[4]University of Bordeaux
[5]Los Alamos National Laboratory
[6]University of Chicago
[7]Laboratory for Laser Energetics, University of Rochester

The purpose of the Omega Laser Facility Users Group (OLUG) is to facilitate communication and exchanges among the users: from the users as a group to the facility and from the users to the broader scientific community. As a major part of OLUG's responsibility, it organizes an annual 2.5-day workshop at the end of April. The 11th OLUG Workshop was held at the Laboratory for Laser Energetics (LLE) on 24–26 April 2019. It was attended by 110 researchers, including scientists, postdoctoral fellows, and students (Fig. 1). The attendees represented institutions from four countries, including the U.S., Canada, the U.K., and

U2480JR

Figure 1
Group photo of the 11th Omega Laser Facility Users Group Workshop attendees.

France. Postdocs and students received travel support to attend the workshop from the Department of Energy's National Nuclear Security Administration. The program included talks, posters, an evening tutorial, student and post-doc sessions, and a discussion of Findings and Recommendations.

The Workshop Program

The OLUG program included the following five science talks from newly funded National Nuclear Security Administration (NNSA) Centers: "Multi-University Center for Pulsed-Power–Driven HED Science" (Cornell University), "Center for Astrophysical Plasma Properties" (University of Texas, Austin), "Center for Matters under Extreme Conditions" (University of California, San Diego), "Center for Advanced Nuclear Diagnostics and Platforms for ICF and HED Physics at Omega, NIF, and Z" [Massachusetts Institute of Technology (MIT)], and "Center for Laboratory Astrophysics" (University Michigan). The Department of Energy's (DOE's) NNSA perspective was presented by Sarah Wilk, Deputy Director of NNSA's Office of Experimental Sciences (NA-113). Other highlights included an evening tutorial session, "Non-standard Targets," offered by Chuck Sorce (LLE) and the LLE engineering team; a facility talk, "Omega Facility Update and Progress on OLUG Recommendations," by Sam Morse (LLE); a summary of the OLUG ExCom election results by Johan Frenje (MIT); summaries of the EP-OPAL Proposal Workshop (Hans Rinderknecht, LLE) and MTW-OPAL (Jake Bromage, LLE); an update on the American Physical Society's Division of Plasma Physics (APS-DPP's) Community Planning Process by Carolyn Kuranz (University of Michigan); the student and postdoc discussion panel [Michelle Marshall, Lawrence Livermore National Laboratory (LLNL)]; and a discussion of OLUG's Findings and Recommendations with LLE management, led by Maria Gatu Johnson (MIT) and Liz Merritt [Los Alamos National Laboratory (LANL)]. In addition, LLE staff organized tours of the Omega Laser Facility.

Student, postdoc, scientist, and facility posters comprised a total of 68 poster presentations that were organized in three sessions. Of the total number, 44 posters were presented by graduate students, postdocs, and undergraduate students. Two additional posters were presented by high school students who had participated in LLE's 2018 Summer High School Research Program. Although OLUG was established in 2009, the Omega Laser Facility has been building a community of science users for more than 35 years. For example, since 1979 the Omega Laser Facility has had a vigorous National Laser User Facility (NLUF) program, funded through DOE, which permits access to external users through a proposal and review process. NLUF is the oldest, continuously running DOE program to support high-energy-density (HED) science research in universities and small businesses.

Nominations and Election

In November 2018, a nominating committee formed to request January nominations for the February election of one new executive committee (EC) member. Johan Frenje (Chair, MIT), Patrick Knapp (Sandia National Laboratories), and Ryan Rygg (LLE) formed the committee. Elected from the three-candidate ballot were Sean Finnegan (LANL) to a three-year term to replace Mingsheng Wei [formerly of General Atomics (GA)] and Mario Manuel (GA) to a special one-year term to replace Channing Huntington (LLNL) who withdrew from the OLUG ExCom after the election process began. The May 2019–May 2020 EC membership of OLUG includes (a) four from U.S. university/small business: Mark Koepke (West Virginia University, Chair), Maria Gatu Johnson (MIT), Johan Frenje (MIT, Vice Chair), and Petros Tzeferacos (University of Chicago); (b) three from national laboratory/major business: Liz Merritt (LANL), Sean Finnegan (LANL), and Mario Manuel (GA); (c) one non-U.S. researcher: Alexis Casner (University of Bordeaux); (d) one from the junior researcher list: Suzanne Ali (LLNL); and (e) LLE, ex-officio: Jim Knauer. The OLUG EC is very grateful to Mingsheng Wei and Channing Huntington for their service in the EC and their contributions to the success of OLUG.

Summary of Findings and Recommendations

An important outcome of OLUG's annual workshop is the list of Findings and Recommendations that OLUG submits for consideration to LLE's management every year. The 2019 Findings and Recommendations are summarized below.

1. Implement a Shot Request Form that "auto-saves" the entered text.
2. Add diagnostic and beam information documentation to the PI (Principal Investigator) Portal.
3. Provide tools for estimating diagnostic signal levels.
4. Extend image-plate calibrations at <10 keV and 200 keV to 1 MeV.

5. Provide calibrations for spectrometer crystals.
6. Increase Dante filter and part availability.
7. Implement γ-ray spectroscopy for nuclear science.
8. Allow velocity interferometer system for any reflector (VISAR)/streaked optical pyrometer (SOP) capability on ten-inch manipulator TIM-14 (OMEGA EP).
9. Upgrade/improve VISAR/SOP.
10. Implement hardware mitigation for early-time radiation artifact on x-ray framing cameras.
11. Add CR-39 processing capability.
12. Ensure that Shot Request Form selectable setups for the streaked x-ray imager match the actual inventory.
13. Add charged-particle signal mitigation to multiple diagnostics.
14. Modify the electron–positron–proton spectrometer to measure higher-energy electrons (E_{max} ~ GeV).
15. Add a single line of sight for multiframe single-pinhole imaging.
16. Improve framing-camera pointing procedures for x-ray imaging.
17. Make Thomson scattering on DT shots compatible with the DT^3He backlighter.
18. Provide a second and/or third Thomson parabola ion energy (TPIE) analyzer.
19. Implement a more-sensitive neutron time-of-flight detector for secondary DT-n measurements.
20. Investigate upgrades to fixed x-ray pinhole cameras.
21. Provide Thomson-scattering capability on OMEGA EP.
22. Add tritium gas-fill capability into a warm spherical capsule.
23. Provide special gas fills using a variable fuel mixture, with or without tritium.
24. Install a planar cryogenics system on OMEGA EP.

The impact within the HED field of the Omega Laser Facility is broad and deep and is encountered early in one's researcher career. Omega offers tremendous opportunities for programmatic-science and basic-science research. NNSA's NLUF and Laboratory Basic Science Programs play a key student and postdoc training role at Omega. Students and postdocs publish in peer-reviewed, high-impact journals on subjects including OMEGA research on laboratory astrophysics, hydrodynamics and atomic physics, hydrodynamic instabilities, radiation hydrodynamics, materials physics and behavior of the equation of state under extreme conditions, relativistic laser–plasma interactions, magnetized plasmas, advanced/alternative inertial fusion concepts, nuclear physics, atomic physics and spectroscopy, and new diagnostics and instrumentation.

The next OLUG Workshop will be held at LLE from 29 April–1 May 2020.

This OLUG Workshop was made possible in part by the generous support of the National Nuclear Security Administration of the U.S. Department of Energy for travel expenses of students and postdocs; by MIT; and by the Laboratory for Laser Energetics at the University of Rochester for the use and availability of critical resources and support. In addition, OLUG thanks the LLE management for their responsiveness to our Findings and Recommendations. For capturing through his lens the workshop ambiance, OLUG thanks Eugene Kowaluk.

The Optics Suitcase: An Educational Outreach Tool for Inspiring Careers in Light

J. DeGroote Nelson,[1,2] T. Z. Kosc,[2,3] and P. C. Nelson[4]

[1]Optimax Systems, Inc.
[2]The Optical Society, Rochester Section
[3]Laboratory for Laser Energetics, University of Rochester
[4]Masline Electronics

Developed by the Optical Society Rochester Section (OSA-RS), the Optics Suitcase is an innovative, interactive presentation package designed to introduce middle school students to the dynamic and exciting range of concepts within the study of light. The Optics Suitcase (see Fig. 1) is an educational outreach tool developed by Dr. Stephen D. Jacobs and the OSA-RS with the busy professional in mind. It is designed to make it easy to enter a middle school classroom and excite young people about careers in technology using experiments that can be customized to highlight the presenter's interests, job, and work environment.

G12818JR

Figure 1
Photograph of the Optics Suitcase and its contents.

The Optics Suitcase contains reusable supplies and giveaway theme packets for in-class presentations that explore color in white light (see Table I). The goal is to help promote technology careers to middle school students. A detailed presentation guide is included with the suitcase to help give presenters techniques for engaging students during the presentation and making the demonstrations more interactive.

Three experiments explore the colors constituting white light in the form of diffraction (The Rainbow Peephole), polarization (Magic Stripes), and selective reflection (Magic Patch). These three experiments use giveaway theme packets that are designed to help reinforce the study of light concepts at home as students present the information they learned to their family and friends. The objective of the Optics Suitcase is to convey a sense of excitement about technology in a short period of time. To achieve this goal, the initial demonstrations serve as "ice breakers" and are intended to quickly capture the students' attention. Next, three hands-on activities use the theme packets and illustrate the overall theme of "colors in white light." They are presented at a pace best suited (as determined by the presenter) to retain the students' interest; children often enjoy taking the theme packets home and sharing with others. The presenter can customize the template take-home flyer with a name, the date, and the location of the presentation to help reinforce the message with the students. A quick review of the presentation guide and an enthusiastic attitude will result in a fun, interactive, and educational outreach activity.

Table I: List of Optics Suitcase reusable and giveaway supplies.

Quantity	Item—Reusable Supplies
1	Durable suitcase with room for other items that can be added to customize presentation
1	Instruction guide on laminated sheets
1	USB-stick with supplemental Optics Suitcase materials
1	Hot Snapz heat pad
1	Set of Arbor Scientific "Happy and Unhappy" balls
1	Slinky
1	50-mm silicon wafer, one side polished to a "mirror" finish
1	Silica glass lens
1	5-in. × 5-in. pieces of high-quality sheet polarizer
1	Transparent plastic cups
1	Set of transparent plastic tableware: knife, fork, and spoon
1	6-in. × 6-in. sheet of temperature-sensitive microencapsulated liquid crystal
Quantity	Item—Giveaway Supplies (can be restocked)
50	Rainbow Peephole: Color by Diffraction
50	Magic Stripes: Color by Polarized Transmission
50	Magic Patch: Color by Selective Reflection
50	Periodic Table of Elements

This material is based upon work supported by the Department of Energy National Nuclear Security Administration under Award Number DE-NA0003856, the University of Rochester, and the New York State Energy Research and Development Authority.

Measurement for Palladium Hydride and Palladium Deuteride Isotherms Between 130 K and 393 K

M. Sharpe,[1] W. T. Shmayda,[1] and K. Glance[2]

[1]Laboratory for Laser Energetics, University of Rochester
[2]Pittsford Sutherland High School

Palladium is a unique hydride-forming metal that finds applications in next-generation target-filling systems and isotope separation systems. The uniqueness of palladium among hydride-forming metals stems from the ability to generate significantly higher hydrogen pressures than other hydriding metals.[1] In a next-generation target-filling design, a single palladium bed could replace the existing diaphragm compressor and condensation cell. Replacing these components with a single palladium bed allows for a smaller, simpler system with fewer moving parts. The high pressures achieved using the compressor can be achieved with a palladium bed by loading the bed at low temperature and subsequently raising the temperature to release the absorbed gas. In addition to next-generation target-filling systems, palladium is currently used in the isotope separator, which is deployed in the tritium laboratory. It has been extensively demonstrated that palladium has an affinity for lower mass hydrogen isotopes. The isotope separation system at LLE exploits this affinity to separate protium (H), deuterium (D), and tritium (T) in the fuel supply, allowing for specific DT mixtures to be made.

Currently in the literature, the pressure–composition–temperature (PCT) phase diagrams for the palladium hydride system extend only to 273 K. Measurement of the PCT diagram to cryogenic temperatures is necessary for the development of next-generation systems, which intend to employ palladium as a hydriding material. The focus of the current work is to measure the PCT curves at low temperatures for both protium and deuterium.

To measure the PCT curves for palladium hydride, a small getter bed containing 2.5 g of palladium powder was utilized. This bed is connected to a manifold of calibrated volumes, which can be charged with H_2 or D_2. Absorption isotherms were measured by sequentially adding gas onto the bed from the charge volume. Hydrogen absorption onto palladium is rapid for all temperatures investigated. The data show that 99% of the gas is absorbed within 6 min.

To achieve temperatures between 130 and 240 K, a cryogenic cooler ("Q-Drive") was purchased from Chart Industries. The Q-Drive operates using an acoustically driven Stirling cycle to remove heat from a cold head. The cold head of the Q-Drive was indirectly coupled to the exterior of the Pd bed through a multilam. This multilam was in contact with a stainless-steel rod that was in direct contact with the bottom of the Pd bed. Such a design protects the cold head during high-temperature excursions, while still maintaining the capability of subambient temperatures. Temperatures greater than ambient were set by using a heater that was wrapped around the exterior of the Pd bed.

Using the above procedure and experimental setup, the PCT curves were measured for protium and deuterium from 130 to 393 K. High-temperature (≥20°C) data were measured to compare with previously reported PCT curves, while low-temperature data have not been previously reported in the literature. The measured PCT curves are shown in Fig. 1 for (a) protium and (b) deuterium. In each panel, the equilibrium pressure of each isotope is plotted against the hydrogen-to-metal (HM) ratio for an array of temperatures. The measured PCT curves display the expected three-region trend with increasing hydrogen content: the pressure initially increases rapidly (α phase), followed by a region of relatively little change in pressure (mixed α–β phase), and a second region of rapid pressure increases (β phase). The α and the β phases correspond to hydrogen diffusion into either palladium or palladium hydride, respectively. In between the α and β phases, the mixed phase exists. Here, an increasing quantity of palladium hydride is formed with an increasing hydrogen-to-palladium ratio. In general, the maximum hydrogen-to-metal ratio increases as the temperature decreases. For temperatures ≤20°C, this maximum ratio is ~0.75. The onset of the mixed α–β phase begins at HM ~ 0.08 for high-temperature isotherms and decreases to ~0.03 at ambient temperatures before increasing again at very low temperatures to ratios between 0.1 and 0.2.

A van't Hoff plot for the current data set was constructed by using the equilibrium pressures and temperatures from the measured PCT curves shown in Fig. 1. The resulting van't Hoff plot is shown in Fig. 2, which includes the protium and deuterium results from this study, along with several data sets reported in the literature.[2–4] Finally, straight-line fits to each of the data

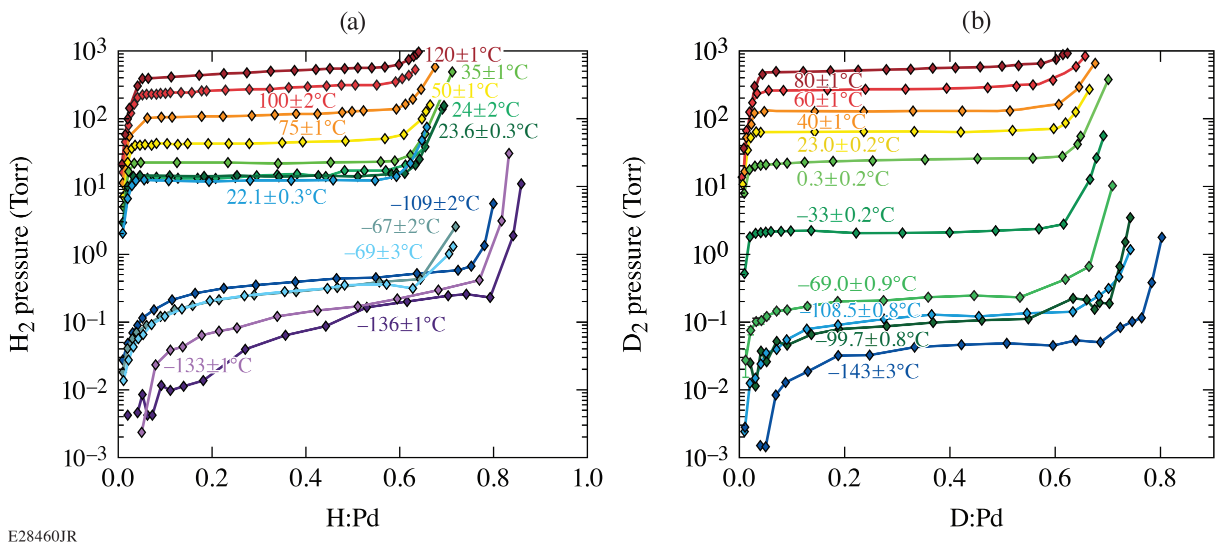

Figure 1
Pressure–composition–temperature isotherms measured using (a) hydrogen at temperatures between 296 K and 393 K and (b) deuterium at temperatures between 130 K and 353 K.

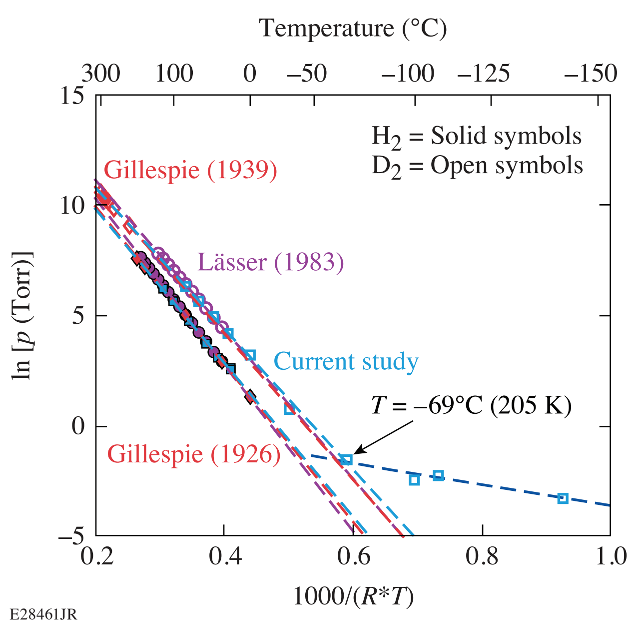

Figure 2
A van't Hoff diagram generated using equilibrium hydrogen (solid symbols) and deuterium (open symbols) pressures in the mixed region.

sets are shown as the dashed lines. The low-temperature data collected from the current work show a deviation from the high-temperature data; therefore, separate lines were fit to the low- and high-temperature data.

At low temperatures, palladium may absorb hydrogen by a mixed mechanism of hydride formation and physical adsorption. From the van't Hoff diagram (Fig. 2), a hydride forms until ~205 K. Assuming no further hydride formation occurs with lower temperature, additional pressure reductions may be due to physical adsorption of hydrogen onto palladium. The expected hydride formation and physical adsorption regions are illustrated in Fig. 3. Here, the van't Hoff diagram is reproduced with data from the present work. The shaded areas show the expectation of where a hydride forms and where physical adsorption occurs.

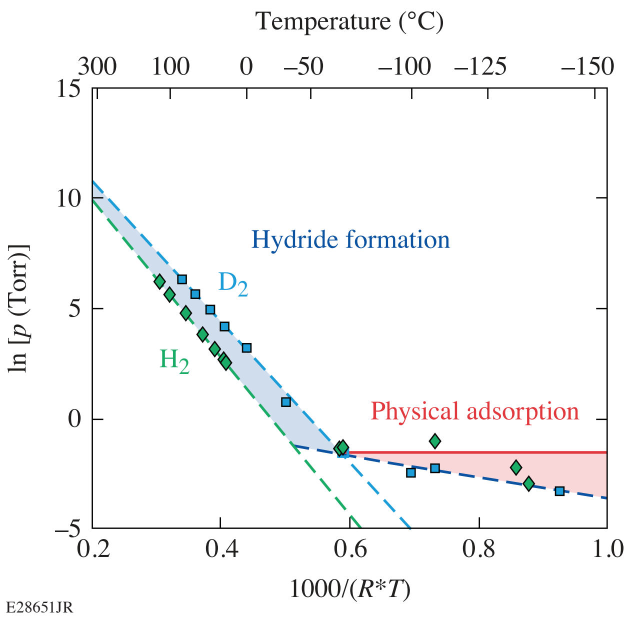

Figure 3
This van't Hoff diagram shows the different mechanisms for hydrogen absorption by palladium. The upper blue region corresponds to the pressures and temperatures at which palladium will form a hydride. The lower red region corresponds to the pressures and temperatures where hydrogen will physically adsorb onto the palladium surface.

This combination of mechanism and lower temperatures is justified by two observations: First, hydrogen and deuterium show similar equilibrium pressures at low temperatures. Similar pressures are not a result of the formation of a hydride since palladium has a greater affinity for less-massive isotopes. However, similar pressures may be a result of physical adsorption since the quantity of adsorbed gas depends primarily on the adsorbate and substrate sizes. Second, we estimate that all hydrogen loaded onto the palladium at low temperatures can be physically adsorbed into approximately six monolayers. For this estimation, it was assumed that a hydride is formed until 205 K. Below 205 K, any observed pressure reduction below the equilibrium pressure at 205 K represents hydrogen adsorbing onto the palladium's surface. Taking the "worst" case scenario, the difference between the equilibrium pressures at 205 K and 130 K is 0.174 Torr, which corresponds to 1.9×10^{-7} mol of H_2 or D_2. Assuming the specific surface area is 2 m^2/g, the total surface area is 5 m^2. The number of H_2 molecules per monolayer is given by

$$\frac{1\ H_2}{\pi r^2} = 3.4 \times 10^{-5} \frac{\text{mol } H_2}{m^2 * \text{ML}}, \tag{1}$$

where r is the radius of a hydrogen molecule. Using the results of Eq. (1), the total surface area, and the total number of moles of adsorbed hydrogen, the number of monolayers is estimated to be 10^{-3}. Such a small number of monolayers is reasonable at these low temperatures.

In summary, the palladium hydride and palladium deuteride isotherms have been measured from 130 K to 393 K. The data collected for temperatures below 273 K are the first to be reported in the literature. The measured isotherms show that an increasing quantity of palladium hydride is formed with decreasing temperatures, with a maximum hydrogen-to-metal ratio of 0.75.

These data are consistent with the literature, where the temperatures overlap. The van't Hoff diagram shows a deviation from high-temperature behavior for temperatures of less than 205 K. The data suggest that palladium can form a hydride until 205 K. Below this critical temperature, any further reduction in equilibrium pressure occurs due to physical adsorption onto the surface.

This material is based upon work supported by the Department of Energy National Nuclear Security Administration under Award Number DE-NA0003856, the University of Rochester, and the New York State Energy Research and Development Authority.

1. R. D. Penzhorn, M. Devillers, and M. Sirch, J. Nucl. Mater. **170**, 217 (1990).
2. L. J. Gillespie and F. P. Hall, J. Am. Chem. Soc. **48**, 1207 (1926).
3. L. J. Gillespie and W. R. Downs, J. Am. Chem. Soc. **61**, 2496 (1939).
4. R. Lässer and K.-H. Klatt, Phys. Rev. B **28**, 748 (1983).

A Thin-Alumina Film as a Tritium Adsorption Inhibitor for Stainless-Steel 316

C. Fagan,[1,2] M. Sharpe,[1] W. T. Shmayda,[1] and W. U. Schröder[1,2]

[1]Laboratory for Laser Energetics, University of Rochester
[2]Department of Chemistry and Physics, University of Rochester

Thin coatings of Al_2O_3 on stainless steel have been reported to suppress tritium permeation compared to uncoated steel.[1–3] However, these films are not dense; they contain microcracks, and have the potential for embedded water molecules in the film. Reducing the cracks in the alumina film may prove to further reduce permeation, and for surfaces with highly dense and uniform coatings, the permeation reduction may be improved substantially. Atomic layer deposition (ALD) is a vehicle to produce conformal, high-integrity films on hydroxylated surfaces with complex topographical features. Depositing alumina using trimethylaluminum and water is one of the most widely studied ALD reactions because of its viability as a high-κ dielectric thin-film coating. ALD of Al_2O_3 has been shown to produce conformal films with little to no surface defects as a result of the self-limiting reaction and monolayer growth mode. Atomic-layer–deposited alumina was used in this work to understand its effect on tritium absorption and to measure the tritium distribution in stainless-steel 316 (SS316) under the coating.

Samples of unmodified SS316 stock had approximately 0.86 mm of the surface machined away to remove any surface imperfections that can arise during manufacturing. These samples had an average surface roughness of 300±50 nm and are referred to from this point as 300-nm SS316. A subset of the 300-nm SS316 samples was mechanically polished to a high-mirror finish, where the average surface roughness was 5±1 nm, and is referred to as 5-nm SS316. Several polished samples were further treated by depositing 38.5±1 nm of Al_2O_3 using the ALD process and an ozone pretreatment to enhance the reactivity of the native surface oxide to the ALD reactants. These samples are referred to as ALD and have the same surface roughness as the underlying polished samples (5±1 nm). All samples were exposed to 0.5 atm of tritium gas for 24 h at room temperature. Subsequently, the samples were removed and stored in an airtight storage pod under dry helium until retrieved for the experiment.

Temperature-programmed desorption was used to determine the total quantity of tritium retained by the stainless-steel samples. The tritiated sample is placed in an oven where dry argon is purged over the sample into one of two bubblers containing water. The sample is heated to 900±1° for several hours during which the desorbed tritium is transported by the dry argon into the bubblers. The primary tritium species (HTO) is captured in the first bubbler (capture efficiency >99%), and any carryover resulting from evaporation is captured in the second bubbler. After 3 h at room temperature, the sample is allowed to cool, and the quantity of desorbed tritium is determined using liquid scintillation counting (LSC) techniques. Tritium-concentration profiles in the deposited film and metal substrate were also measured using a combination of surface washes and acid etching of stainless steel. The surface wash and acid etching procedure are reported elsewhere.[4,5] The etching procedure for the samples coated with Al_2O_3 was modified by using a selective NaOH etch that does not etch the steel substrate. The resulting solutions were neutralized to a pH = 0, mixed with an Ultima Gold™ liquid scintillation cocktail, and counted by LSC techniques using a low pH calibration curve.

The total quantity of adsorbed tritium indicates that the surface modification had influenced the total tritium adsorbed by the sample. The results of the TPD experiments are shown in Fig. 1. The data indicate that reducing the surface roughness by a factor of ~150 leads to a reduction in the total quantity of absorbed tritium, relative to the 300-nm SS316 samples. Similarly, the ALD-coated steel samples also see a decrease of ~27%. These data indicate that the ALD coating on the polished SS316 does not inhibit the absorption of tritium any further than the underlying polishing. This is likely caused by the large fraction

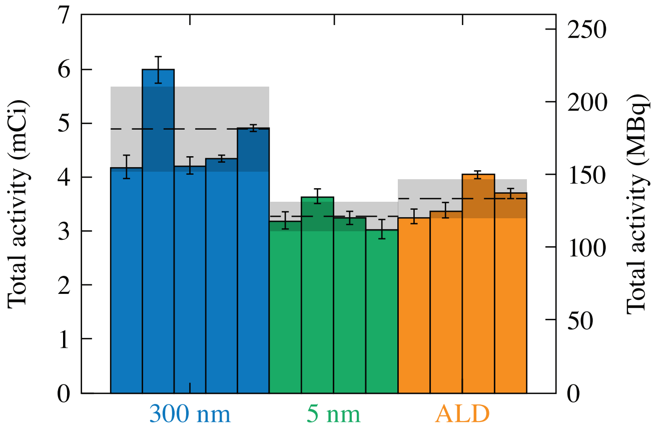

Figure 1
TPD results for the unmodified (blue bars) and modified surfaces, 5-nm SS316 (green bars) and ALD (orange bars). Each bar represents an individual sample, with the mean as dashed lines and $\pm 1\sigma$ indicated by the shaded region for each sample finish.

of $Al(OH)_2$ species present in the deposited film, which increases the total number of hydrogen binding sites relative to a pure Al_2O_3 surface film. The increase in the hydroxyl density in the deposited film increases the apparent solubility of hydrogen in the film as a result of isotope exchange with hydrogen in the hydroxides. The TPD data give an insight into the total quantity of tritium in the samples; however, the data do not speak to the distribution of tritium in the metal.

The results of the selective etching for the ALD-coated steel are shown in Fig. 2. The data suggest that high concentrations of tritium exist in the Al_2O_3 layers and that the concentration drops significantly at the steel interface. In the near-surface region ($x <$ 1 μm), the SS316 concentration is constant until a sharp drop is observed around 600 nm. To compare the concentration profiles of the ALD samples to the uncoated SS316 samples, the profiles for the uncoated steel (5 nm and 300 nm) are shifted by the alumina layer thickness (38 nm) in the concentration profile. The results show two large differences between the ALD and SS316 results. First, the ALD film contains less surface tritium compared to the uncoated samples. The second difference occurs in the near surface of the steel (~700 nm). Here, the tritium concentration is 200× less in the ALD-coated sample relative to the uncoated SS316 sample. This suggests that tritium diffusion into the metal bulk is lowered by coating steel with alumina. Even though the 5 nm and ALD samples retained the same total quantity of tritium, the distribution of the tritium in the samples is quite different. Future work will focus on making the alumina layers more ideal to determine if these films can be used as a tritium diffusion barrier on SS316.

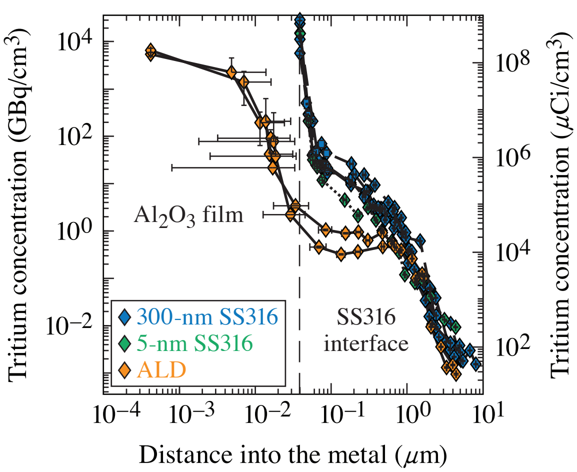

Figure 2
Tritium concentration profiles for 300-nm SS316 (blue), 5-nm SS316 (green), and ALD Al_2O_3 (orange) (Ref. 4). The uncoated samples are shifted to account for the deposited film on the ALD samples. The SS316 interface begins at the 38 nm and is indicated by the vertical dashed line.

The authors acknowledge M. Koch, S. Scarantino, and B. Ruth (University of Rochester LLE Cryogenic Tritium Facility) for their work exposing the test samples to tritium gas. This material is based upon work supported by the Department of Energy National Nuclear Security Administration under Award Number DE-NA0003856, the University of Rochester, and the New York State Energy Research and Development Authority.

1. F. Yang *et al*., J. Nucl. Mater. **478**, 144 (2016).

2. G. K. Zhang *et al*., Fusion Eng. Des. **87**, 1370 (2012).

3. T. Wang *et al*., Fusion Eng. Des. **85**, 1068 (2010).

4. M. Sharpe, C. Fagan, and W. T. Shmayda, "Distribution of Tritium in the Near Surface of 316 Stainless Steel," to be published in Fusion Science and Technology.

5. M. D. Sharpe *et al*., Fusion Eng. Des. **130**, 76 (2018).

FY19 Q3 Laser Facility Report

J. Puth, M. Labuzeta, and D. Canning

Laboratory for Laser Energetics, University of Rochester

During the third quarter (Q3) of FY19, the Omega Laser Facility conducted 357 target shots on OMEGA and 230 target shots on OMEGA EP for a total of 587 target shots (see Tables I and II). OMEGA averaged 11.6 target shots per operating day, averaging 91.7% Availability and 97.5% Experimental Effectiveness.

OMEGA EP was operated extensively in Q3 FY19 for a variety of user experiments. OMEGA EP averaged 7.9 target shots per operating day, averaging 96.7% Availability and 93.3% Experimental Effectiveness.

Additional neutron shielding is being added below the OMEGA target chamber to further limit background signal and noise on diagnostic measurements. The shielding will effectively minimize the size of the floor penetration required for cryogenic cart operations and reduce neutron scattering effects on diagnostics in the LaCave area. The shielding is being added in three phases to characterize the effectiveness and validate modeling (which will enhance calculations for future shielding design efforts). The final layer will be added in Q1 of FY20.

Table I: OMEGA Laser System target shot summary for Q3 FY19.

Program	Laboratory	Planned Number of Target Shots	Actual Number of Target Shots
ICF	LLE	82.5	99
ICF subtotal		82.5	99
HED	LLE	22	23
	LANL	44	52
	LLNL	38.5	47
	SNL	22	24
HED subtotal		126.5	146
CEA	CEA	11	13
RAL	RAL	11	9
LBS	LANL	11	10
	LLNL	33	38
	SLAC	11	13
LLE calibration	LLE	0	29
Grand total		286	357

Table II: OMEGA EP Laser System target shot summary for Q3 FY19.

Program	Laboratory	Planned Number of Target Shots	Actual Number of Target Shots
ICF	LLE	49	69
	LLNL	21	30
	NRL	7	6
ICF subtotal		77	105
HED	LLE	14	17
	LANL	7	7
	LLNL	21	25
HED subtotal		42	49
LBS	LLE	14	19
	LLNL	14	25
	SLAC	7	7
LLE calibration	LLE	0	12
Grand total		161	230

Theory of Ignition and Burn Propagation in Inertial Fusion Implosions

A. R. Christopherson,[1,2] R. Betti,[1,2,3] S. Miller,[1,2] V. Gopalaswamy,[1,2] O. M. Mannion,[1,3] and D. Cao[1]

[1]Laboratory for Laser Energetics, University of Rochester
[2]Department of Mechanical Engineering, University of Rochester
[3]Department of Physics & Astronomy, University of Rochester

A large effort is currently underway to demonstrate thermonuclear ignition in the laboratory via inertial confinement fusion (ICF).[1] ICF uses laser-driven implosions of a solid deuterium–tritium (DT) shell to achieve ignition conditions.[2,3] Ignition is a thermal instability of a DT plasma driven by the energy deposition of the alpha particles ("alpha heating") produced by the fusion reaction D + T = α(3.5 MeV) + n(14.1 MeV). Ignition has never been achieved in a laboratory plasma, and its demonstration is widely viewed as a major scientific achievement with important applications to fusion energy generation and to the stewardship of the nuclear stockpile. Unlike in steady-state plasmas, as those envisioned for magnetic confinement fusion,[4] assessing ignition in ICF is greatly complicated by the transient nature of implosions and the fact that ignition starts from the central hot region ("hot-spot ignition") and then propagates to the cold and dense surrounding fuel ("burn-wave propagation"). The fundamental mechanism at the basis of ignition is alpha heating of the DT fuel and its positive feedback on the fusion reaction rate.

Current experiments at the National Ignition Facility have demonstrated significant alpha heating, leading to amplifications of the fusion yield close to threefold.[5–7] Despite much work on assessing and measuring the degree of alpha heating, two crucial questions remain unanswered with regard to ignition: (1) What is ignition in inertial fusion; and (2) what fusion yields are required in ICF to claim that ignition has taken place. In the past, common metrics for ignition have related the fusion yield to the incident laser energy on target. The so-called *target gain* = 1 condition has been widely used as the ultimate indicator of ignition.[8] Here, target gain is the ratio of the fusion energy output to the laser energy on target. Such a metric is not rooted in the burning-plasma physics of DT fuel and is unrelated to the onset of ignition. It is motivated only by its implications to fusion energy, where an energy output greater than the input is required for any viable fusion scheme. This metric is not an indicator of the onset of the thermonuclear instability and therefore cannot be used to measure the ignition point.

In this work, we provide a physical definition of hot-spot ignition in ICF, which is of general validity for laser fusion. This definition of ignition identifies the onset of the thermal runaway within the hot spot of an ICF implosion just prior to the burn propagation in the dense fuel. To identify the ignition point, we first search for qualitative features distinguishing runaway burn in the entire fuel volume from sub-ignition alpha heating. The first distinctive feature is related to the different behavior of the yield amplification for implosions in the alpha-heating regime versus implosions with propagating burn. Here the yield amplification = $Y_\alpha / Y_{\text{no}\,\alpha}$, where Y_α is the fusion yield measured in an experiment and $Y_{\text{no}\,\alpha}$ is the estimated yield without accounting for alpha-particle energy deposition. It was shown in Ref. 9 that in the alpha-heating regime, the yield amplification depends uniquely on the dimensionless parameter f_α given by

$$f_\alpha \equiv \frac{1}{2}\frac{\theta_\alpha E_\alpha}{E_{\text{hs}}}, \tag{1}$$

where E_α is the total alpha-particle energy, θ_α is the fraction of alpha particles deposited into the hot spot, and E_{hs} is the hot-spot internal energy at bang time (when the neutron-production rate is maximized). The parameter f_α is designed to compare the deposited alpha energy to the hot-spot internal energy at bang time. In the numerator, $E_\alpha = \varepsilon_\alpha \cdot$ Yield, where $\varepsilon_\alpha = 3.5$ MeV and Yield is the neutron yield. The factor 1/2 accounts for the fact that approximately one half of all of the fusion alphas produced have deposited their energy into the hot spot at bang time. In defining E_{hs}, the hot-spot radius is the point where the neutron-production rate drops to 17% of its maximum value. The Lagrangian trajectory of this hot spot is then back calculated in time to determine the fraction of alpha particles absorbed in the hot spot, as was done in Refs. 10 and 11.

In Fig. 1, the yield amplification resulting from alpha heating is plotted as a function of f_α, where the yield amplification curves for many different targets are shown to overlap up to a critical value of $f_\alpha = 1.4$. The simulation ensemble shown here contains implosion velocities between 200 km/s and 600 km/s, laser energies between 30 kJ and 10 MJ, and adiabats between 1 and 6, where the adiabat[12] is given for DT by $\alpha = P/2.2\rho^{5/3}$, with the shell pressure P in megabars and the plasma density in g/cm^3. The database was generated by creating many ignited implosions with a variety of different target gains and then degrading them by reducing the implosion velocity, increasing the adiabat, or by applying density modulations to the inner shell surface. Ignition occurs at the critical value $f_\alpha = 1.4$ corresponding to a yield amplification due to alpha heating of about 15× to 25×. For $f_\alpha < 1.4$, alpha heating is mostly confined to the hot spot, while for $f_\alpha > 1.4$, the ablation of shell mass into the neutron-producing region significantly increases the fusion output.

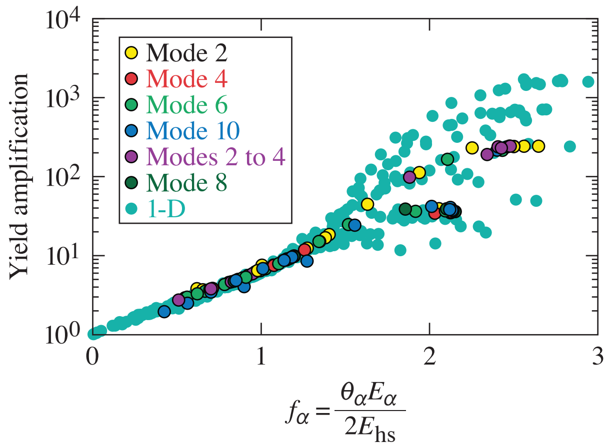

Figure 1
The yield amplification is plotted as a function of f_α for the ensemble of 1-D *LILAC*[13] and 2-D *DRACO*[14] simulations. In the alpha-heating regime ($f_\alpha < 1.4$), the yield amplification depends uniquely on f_α regardless of the target mass, areal density, and temperature. After $f_\alpha = 1.4$, shell mass and burnup fraction determine the maximum fusion yield.

This material is based upon work supported by the Department of Energy National Nuclear Security Administration under Award Number DE-NA0003856, the University of Rochester, and the New York State Energy Research and Development Authority.

1. J. Nuckolls *et al*., Nature **239**, 139 (1972).

2. S. Atzeni and J. Meyer-ter-Vehn, *The Physics of Inertial Fusion: Beam Plasma Interaction, Hydrodynamics, Hot Dense Matter*, 1st ed., International Series of Monographs on Physics, Vol. 125 (Oxford University Press, Oxford, 2004); J. D. Lindl, *Inertial Confinement Fusion: The Quest for Ignition and Energy Gain Using Indirect Drive* (Springer-Verlag, New York, 1998).

3. J. D. Lawson, Proc. Phys. Soc. Lond. B **70**, 6 (1957).

4. J. Ongena *et al*., Nat. Phys. **12**, 398 (2016); **12**, 717(E) (2016).

5. S. Le Pape *et al*., Phys. Rev. Lett. **120**, 245003 (2018).

6. T. Döppner *et al*., Phys. Rev. Lett. **115**, 055001 (2015).

7. O. A. Hurricane *et al*., Nature **506**, 343 (2014).

8. Committee on the Prospects for Inertial Confinement Fusion Energy Systems National Research Council (NRC), *An Assessment of the Prospects for Inertial Fusion Energy* (The National Academies Press, Washington, DC, 2013).

9. A. R. Christopherson *et al*., Phys. Plasmas **25**, 072704 (2018).

10. A. R. Christopherson *et al*., Phys. Plasmas **25**, 012703 (2018).

11. A. R. Christopherson and R. Betti, Phys. Rev. Lett. **99**, 021201(R) (2019).

12. M. C. Herrmann, M. Tabak, and J. D. Lindl, Nucl. Fusion **41**, 99 (2001).

13. J. Delettrez *et al*., Phys. Rev. A **36**, 3926 (1987).

14. P. B. Radha *et al*., Phys. Plasmas **12**, 056307 (2005).

Hybrid Target Design for Imprint Mitigation in Direct-Drive Inertial Confinement Fusion

L. Ceurvorst,[1] R. Betti,[2] A. Casner,[1] V. Gopalaswamy,[2] A. Bose,[2] S. X. Hu,[2] E. M. Campbell,[2] S. P. Regan,[2] C. A. McCoy,[3] M. Karasik,[4] J. Peebles,[2] M. Tabak,[5] and W. Theobald[2]

[1]Université de Bordeaux-CNRS-CEA, CELIA
[2]Laboratory for Laser Energetics, University of Rochester
[3]Sandia National Laboratories
[4]Plasma Physics Division, Naval Research Laboratory
[5]Lawrence Livermore National Laboratory

We propose a novel target design, called the hybrid direct-drive target design, for mitigating the Rayleigh–Taylor instability (RTI) in high-energy-density and direct-drive inertial confinement fusion experiments.[1] Figure 1 shows a schematic of the design in both (a) spherical and (b) planar geometries. The target is surrounded by a thin (less than 1-μm) CH membrane that is externally coated with a tens-of-nm-thick layer of Au. The membrane is offset by several hundred microns from the target's surface. A high-intensity laser picket pulse is incident on the membrane, producing smooth x-ray radiation that serves as the initial seed on the target surface and drives the first shock through the target. After giving the target time to develop its conduction zone, between a few hundred ps to ~1 ns, the main pulse propagates through the underdense plasma from the exploded membrane and drives the target itself. A proof-of-concept experiment in planar-target geometry on the OMEGA EP laser explored the performance of

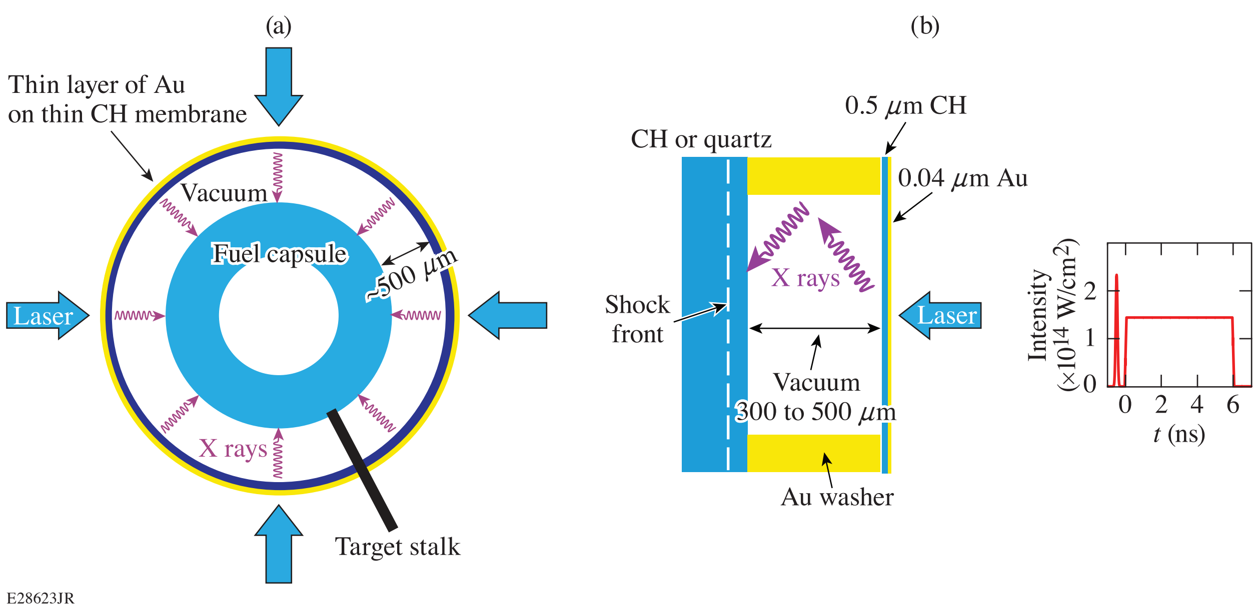

Figure 1
Schematic of (a) the spherical hybrid direct-drive target design and (b) the planar target design that was tested in the experiment.

this newly proposed concept for the first time. The experiment provided the pressure of the x-ray–driven shock wave and tested the target's imprint-mitigation capabilities. Figure 1(b) shows the design of the planar target.

A 1.5-mm-OD Au washer with a 20-μm-thick wall and a height of 300 μm or 500 μm was glued on planar quartz or polystyrene foils. The height of the washer determines the standoff distance of a 0.5-μm-thick CH membrane from the target plane. Depending on this height, the targets will be referred to as the "Hybrid300" or "Hybrid500" targets, respectively. The membrane was coated with an ~40-nm layer of Au. The space between the planar target and the membrane was held at vacuum. The Au side was irradiated with one UV beam equipped with an SG8-750 distributed phase plate. The pressure measurements used 140-μm-thick polystyrene and quartz foils. A short picket pulse (no main pulse) with a 150-ps duration and an intensity of 1 to 2 $\times$ 10^{14} W/cm^2 interacted with the Au coating to generate the x-ray pulse that created the shock wave that was observed from the target back side with a velocity interferometer system for any reflector (VISAR) diagnostic and a streaked optical pyrometer (SOP). The diagnostics measured the propagation velocity and the emission temperature, which made it possible to infer the pressure of the decaying shock wave. The Hybrid300 target obtained a pressure of ~8 Mbar at ~0.5 ns after the start of the laser pulse, while about half of the pressure was obtained at this time with the Hybrid500 target. The imprint shots applied a standard platform of time-gated face-on x-ray radiography but used a thinner 30-μm-thick planar polystyrene foil to be able to accelerate the target with a 6-ns square pulse and to amplify the seeds by RTI. No smoothing by spectral dispersion was used, causing the beam speckle pattern to serve as 3-D, multimode imprint seeds for ablative RTI. The evolution of ablative RTI was observed through face-on x-ray radiography at different times. The performance of the hybrid targets was compared to a bare 30-μm-thick polystyrene foil without an Au washer. The picket intensity was increased by about a factor of 2 in the hybrid case so that the x rays created by the picket would generate an initial shock matching the 1-D performance of the bare targets. The 1-D simulations show that the behavior of both targets is identical across designs, yielding an acceleration of 35 μm/ns^2.

Azimuthally averaged Fourier spectra of the OD modulations at different times are shown in Figs. 2(a) and 2(b) for both the bare and hybrid targets. Modulation growth was significantly reduced in both hybrid targets. The bare target reached a peak amplitude of 4.1 $\times$ 10^{-2} OD after just 3.1 ns as opposed to Hybrid300 reaching a similar level of 2.6 $\times$ 10^{-2} OD after 4.2 ns. The Hybrid500 target did not exceed noise band. The experiments show a reduction of the RTI growth and a delay in the time of target perforation by ~40% in the Hybrid300 target compared to the bare CH target. In summary, the performance of the hybrid target design

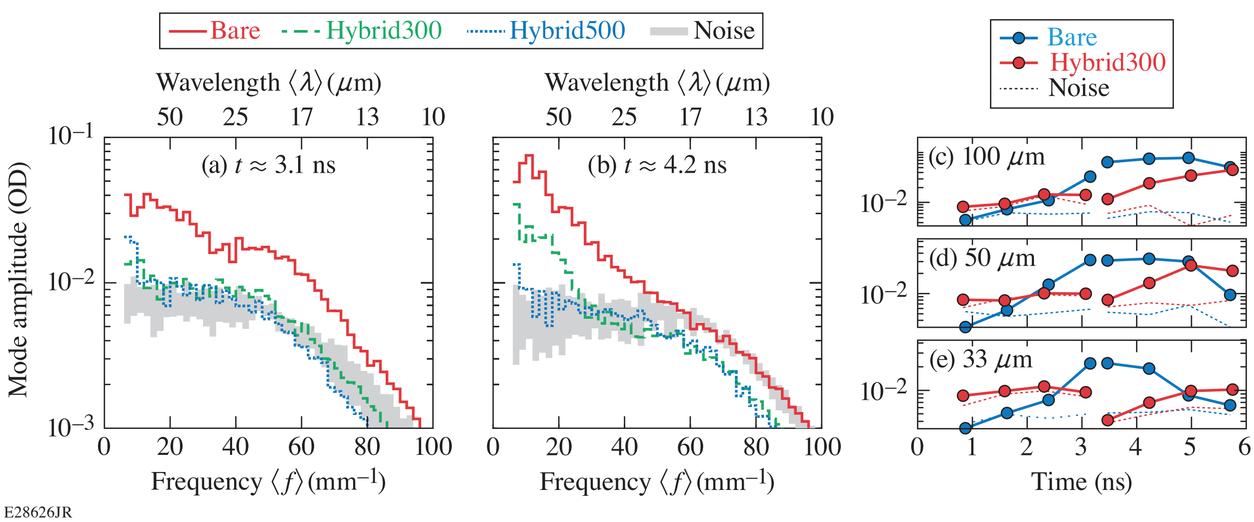

Figure 2
The azimuthally averaged Fourier spectra of the three targets and individual wavelength evolution. (a) Significant growth above noise has occurred by 3.1 ns for the bare target across the measurable spectrum. (b) The Hybrid300 target begins to exceed noise by 4.2 ns only at frequencies below ~30 mm^{-1}. [(c)–(e)] The evolution of specified wavelengths are compared between bare (blue) and Hybrid300 (red) targets. The dotted lines represent the noise levels of the corresponding target type.

has been measured for the first time through planar experiments performed on the OMEGA EP laser. Shocks were shown to be generated by the x-ray flashes with pressures that are in agreement with calculated pressures from 1-D radiation-hydrodynamic simulations using the code *LILAC*, and the growth of the ablative RTI was significantly reduced for the hybrid targets.

This material is based upon work supported by the Department of Energy National Nuclear Security Administration under Award Number DE-NA0003856, the University of Rochester, and the New York State Energy Research and Development Authority.

1. L. Ceurvorst *et al*., Phys. Rev. E **97**, 043208 (2018).

A Boundary Condition for Guderley's Converging Shock Problem

J. J. Ruby,[1,2] J. R. Rygg,[1,2,3] J. A. Gaffney,[4] B. Bachmann,[4] and G. W. Collins[1,2,3]

[1]Laboratory for Laser Energetics, University of Rochester
[2]Department of Physics and Astronomy, University of Rochester
[3]Department of Mechanical Engineering, University of Rochester
[4]Lawrence Livermore National Laboratory

The Guderley problem[1] consists of a 1-D radially converging shock wave supported to infinity. The solution consists of leveraging the group invariance of the flow equations, along with an ideal equation of state, to reduce the set of partial differential equations into a single ordinary differential equation. The result is a simplified self-similar model describing the collapse of spherical shock waves.

This model has been used for understanding the shocks in laser-driven implosions in the past.[2] In particular the model has been used to predict the neutron yield from spherical implosions.[2,3] This work sets out to make two modifications to the Guderley solution that extend its utility for understanding implosions.

The first of the modifications includes the addition of an isentropic release wave launched from some reference radius. This corresponds to the pressure no longer being supported, such as when the laser turns off in a laser-driven implosion. In this case the release wave will be launched from the ablation surface as the remaining solid density material releases into vacuum. This wave breaks the self-similarity of the solution and changes the density profile in the shocked region. The density profile of the release is

$$\rho(r) = \rho_R \left(\frac{R_{\text{out}} - r}{R_{\text{out}} - R_{\text{in}}} \right)^{\epsilon}, \tag{1}$$

with R_{out} and R_{in} referring to the inner and outer edges of the release wave, respectively. The inner edge trajectory of the release wave is known assuming it moves at the local sound speed of the material and is launched from a known location at a known time. The outer edge of the release wave is then solved for using the conservation of mass in the released region. The temperature and pressure in the released material are then solved for by using the adiabatic relationship and an ideal equation of state.

The second modification includes taking the single fluid temperature present in the Guderley solution and partitioning it between an electron fluid and an ion fluid based on their masses. Additionally, a scheme for the fluids equilibrating is introduced based on Spitzer. The temperatures are constrained to satisfy

$$T_{\text{i}} + \overline{Z} T_{\text{e}} = \left(1 + \overline{Z}\right) T_{\text{G}}, \tag{2}$$

where T_{e} and T_{i} are the electron and ion temperatures, respectively, and T_{G} is the single-fluid temperature. This leaves the single-fluid temperature unchanged, so the hydrodynamics are unperturbed. Finally, the temperatures equilibrate according to[4]

$$\frac{\mathrm{d}T_{\text{e}}}{\mathrm{d}t} = \frac{T_{\text{i}} - T_{\text{e}}}{\tau_{\text{ei}}}. \tag{3}$$

The results of the modified Guderley solution are compared to *LILAC* simulations of an 860-μm solid CH sphere driven by a 2-ns square pulse. In order to set the parameters of the Guderley solution, the initial shock pressure and the time of shock collapse were set to match the *LILAC* results. Figure 1(a) compares the trajectories from *LILAC* and the Guderley solution. The shock and release wave trajectories compare well between the two models. The shock trajectory after the release wave hits the outgoing shock is the most obvious difference between the two models. This is because the shock trajectory in the Guderley model is unchanged by the release.

Figure 1(b) compares the total x-ray yield from the shock collapse that escapes the sphere as a function of initial density of the target. As the density decreases, the release modification is less relevant because the material is much less efficient at absorbing x rays, and as the density increases, temperature equilibration is less important because the time scale for coupling is so short that the material is equilibrated instantaneously with respect to the emission time scale. Only the model that includes both modifications is able to reproduce the *LILAC* results over a broad range of the density space.

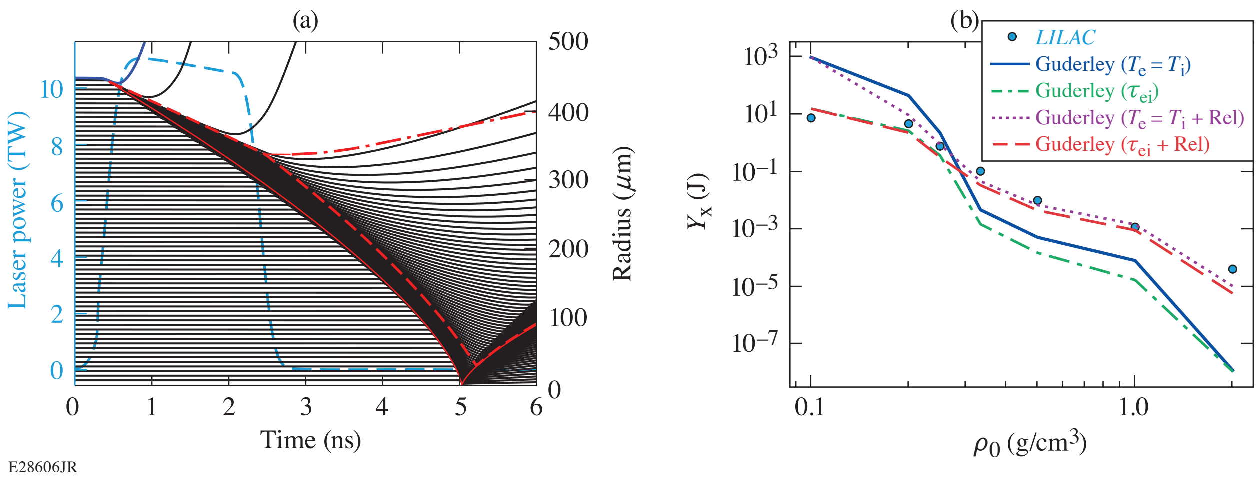

Figure 1
(a) A comparison of the wave trajectories for the modified Guderley solution (red curves) plotted over the particle trajectories from *LILAC* (black curves). The *LILAC* pulse shape is shown by blue curves. (b) A comparison of total x-ray yield in joules across different models: *LILAC* (solid circles), standard Guderley (solid blue curve), Guderley with temperature equilibration (dashed–dotted green curve), Guderley with release modification (dotted purple curve), and Guderley with release and temperature equilibration (dashed red curve). The simulations were run given the same conditions but with a scaled initial density to highlight regions where different physics played a key role.

The modified Guderley solution has proved capable of reproducing many results from *LILAC* with many fewer input parameters. This work was done with the ultimate goal of using both models to infer important physics information from spherical experiments through a Bayesian model-fitting procedure.

This material is based upon work supported by the Department of Energy National Nuclear Security Administration under Award Number DE-NA0003856, the U.S. Department of Energy, Office of Science, Office of Acquisition and Assistance under Award No. DE-SC001926, the University of Rochester, and the New York State Energy Research and Development Authority.

1. G. Guderley, Luftfahrtforschung **19**, 302 (1942).
2. J. R. Rygg, "Shock Convergence and Mix Dynamics in Inertial Confinement Fusion," Ph.D. Thesis, Massachusetts Istitute of Technology, 2006.
3. H. J. Haubold and R. W. John, Plasma Phys. **23**, 399 (1981).
4. L. Spitzer, *Physics of Fully Ionized Gases* (Interscience Publishers, New York, 1956).

Nonlinear Transmission of Laser Light Through Coronal Plasma due to Self-Induced Incoherence

A. V. Maximov, J. G. Shaw, and J. P. Palastro

Laboratory for Laser Energetics, University of Rochester

The success of direct laser-driven inertial confinement fusion (ICF) relies critically on the efficient coupling of laser light to plasma. At ignition scale, the absolute stimulated Raman scattering (SRS) instability can severely inhibit this coupling by redirecting and strongly depleting laser light. This summary describes a new dynamic saturation regime of the absolute SRS instability. The saturation occurs when spatiotemporal fluctuations in the ion-acoustic density detune the instability resonance. The dynamic saturation mitigates the strong depletion of laser light and enhances its transmission through the instability region, explaining the coupling of laser light to ICF targets at higher plasma densities.

While still in the research stage, controlled fusion could deliver an almost endless supply of power with relatively low environmental impact and a nearly inexhaustible reserve of fuel. As evidenced by active research programs throughout the world, the realization of such a technology would have lasting impact both geopolitically and for the health of our planet. In the direct-drive ICF approach, an ensemble of laser beams symmetrically illuminates a cryogenic target containing thermonuclear fuel.[1] The illumination ionizes and heats the outer shell of the target, creating a pressure that drives inward fuel compression and outward mass ejection. The mass ejection creates a region of low-density plasma, or corona, that plays a critical role in direct-drive ICF: coupling of laser light to the corona determines the strength of the ablation pressure and, ultimately, the implosion performance.[1]

Achieving efficient coupling of laser energy to the fusion target is arguably the most essential component of direct-drive ICF. A high ablation pressure requires the transmission of laser light to deep within the corona, where collisions can efficiently convert electromagnetic energy to plasma thermal energy. To get there, however, the laser light must propagate through the outer corona, where it can drive a number of parametric instabilities. In their nonlinear stage, these instabilities can redirect the incident light into unwanted directions and repartition the light energy into plasma waves. These waves can subsequently undergo local collisional damping, in which case the energy is deposited too far from the ablation surface, or collisionless damping, which creates nonthermal electrons that can preheat the fuel and reduce its compressibility.[1] In either case, the premature depletion of laser energy in this region presents a significant challenge for direct-drive ICF.

Within the U.S., the primary direct-drive program has been centered around LLE's OMEGA laser. Compared to the National Ignition Facility (NIF), the high repetition rate of OMEGA serves as an ideal platform for studying the underlying physics of direct drive. However, due to its limited laser pulse energy (30 kJ), the OMEGA laser cannot create the conditions required for a burning fusion plasma. As a result, the focus has turned to direct-drive implosions on the NIF. With its larger laser energy (>1 MJ), the NIF can drive larger capsules, which changes the characteristics of the plasma, e.g., the corona has a longer scale length and higher electron temperature. As a result, absolute SRS becomes the dominate instability[2] in contrast to OMEGA experiments in which two-plasmon decay (TPD) dominates.

In SRS, an incident laser light wave decays into a scattered Raman light wave and an electron plasma wave. In a region near the quarter-critical plasma density n_c, determined by the frequency of the laser, the SRS decay waves can grow exponentially in time as an absolute instability until they nonlinearly saturate. Recent planar-target experiments on the NIF that emulated the plasma corona of an ignition-scale direct-drive implosion showed a clear SRS feature originating from close to the quarter-critical density and no clear evidence of TPD.[2] The observations confirmed theoretical estimates that, because of the large density scale lengths in the plasma corona (of the order of few hundred microns), the threshold for absolute SRS would be exceeded. Those same estimates also suggest that the instability would strongly deplete the laser light, preventing significant transmission deep into the corona. The hydrodynamic evolution of the target was consistent, however, with the efficient conversion of laser energy into plasma thermal energy.[2] As a result, a critical question emerges: How can the laser light propagate through the absolute instability region with a high transmission rate?

The discovery of a dynamic saturation regime of the absolute SRS instability due to self-induced incoherence answers this question. As the incident light propagates through the instability region, it drives a primary SRS decay that initially depletes the laser intensity. The electron plasma waves resulting from the SRS decay then undergo a secondary instability that drives a broad spectrum of low-frequency density perturbations. The instability saturates when the density perturbations reach a high enough level to detune the primary SRS resonance, establishing a dynamic balance between the transmitted and scattered laser light. This dynamic, incoherent saturation mitigates depletion and facilitates the transmission of the laser light through the instability region, explaining how light can penetrate deep into the corona to efficiently drive ICF implosions.

To investigate the saturation of absolute SRS in the regime relevant to direct-drive implosions at the NIF scale, the laser-plasma simulation environment (*LPSE*)[3] was employed. *LPSE* applies a fluid plasma model to describe the evolution of the four waves (light, Raman, electron plasma, and ion acoustic) and the couplings between them. The simulations were performed in two spatial dimensions with *s*-polarized light. The laser light was normally incident on a plasma with linear gradient $n = n_\mathrm{c}\left(1 + x/L\right)/4$, where L is the density scale length at the quarter-critical density. The plasma parameters are as follows: laser wavelength = 0.351 μm; density scale length = 500 μm; electron temperature = 4 keV; ion temperature = 4 keV; ion charge $Z = 3.5$; ion atomic number = $2Z$; and density range from 0.21 to 0.265 n_c. At these conditions, the threshold for TPD is more than 3× higher than the threshold for absolute SRS.

Figure 1 illustrates the nonlinear saturation of absolute SRS for laser light with an incident intensity of 2×10^{14} W/cm^2 (approximately 3× greater than the theoretical instability threshold at these parameters, 6×10^{13} W/cm^2). Early in time, the laser light propagates through the plasma without scattering but undergoes a small amount of collisional absorption, about 2%; shortly thereafter, the absolute instability develops. By 5.4 ps, the instability has strongly depleted the pump [Fig. 1(a)], and the Raman light [Fig. 1(c)] has grown to an amplitude comparable to the laser light. This pump depletion stage quickly gives way, 3 ps later, to a dynamic saturation stage in which the amplitudes of both the laser and Raman light become nonstationary and spatially incoherent [Figs. 1(b) and 1(d), respectively].

Figure 2 displays the scaling of the transmission, in both the pump depletion (red circles) and dynamic saturation (blue circles) stages, as a function of laser intensity. At intensities below the absolute SRS threshold (6×10^{13} W/cm^2), the transmission is reduced by about 2% due to inverse bremsstrahlung absorption. Above the threshold, the dynamic saturation increases the transmission well above the levels determined by pump depletion alone.

The enhanced transmission explains why the temperature inferred in ignition-scale experiments agrees with radiation-hydrodynamic simulations that do not include a model for absolute SRS.[2] For example, if the intensity reaching the absorption surface was reduced by a factor of 2 due to pump depletion, radiation-hydrodynamic simulations would predict a 30% lower electron temperature.

This material is based upon work supported by the Department of Energy National Nuclear Security Administration under Award Number DE-NA0003856, the University of Rochester, and the New York State Energy Research and Development Authority.

1. R. S. Craxton *et al*., Phys. Plasmas **22**, 110501 (2015).
2. M. J. Rosenberg *et al*., Phys. Rev. Lett. **120**, 055001 (2018).
3. J. F. Myatt *et al*., Phys. Plasmas **24**, 056308 (2017).

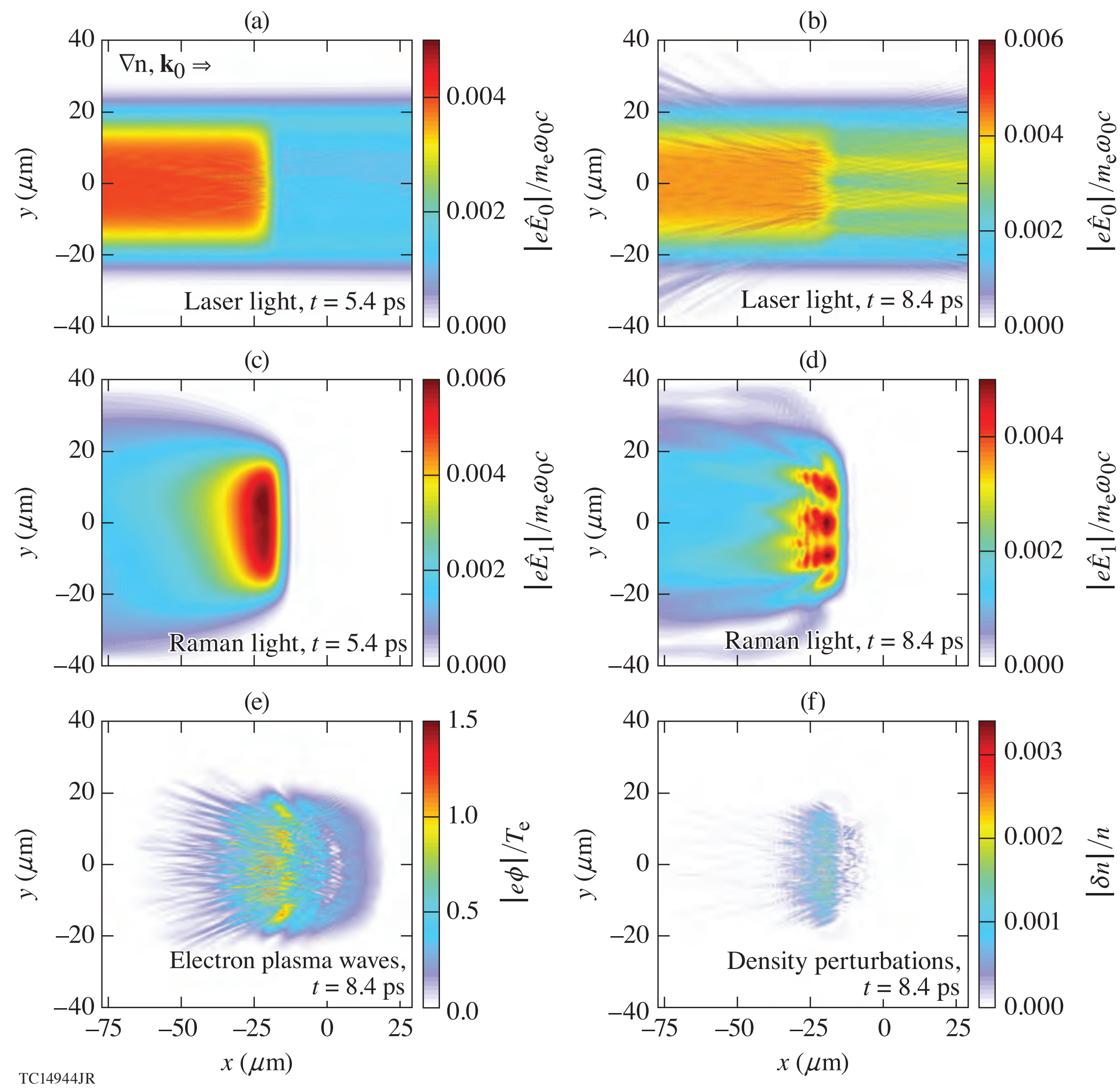

Figure 1
The amplitudes of laser and Raman light waves [(a) and (c), respectively] at 5.4 ps and [(b) and (d), respectively] 8.4 ps. (e) The amplitudes of plasma waves (in terms of wave potential energy normalized to temperature) and (f) low-frequency density perturbations at 8.4 ps.

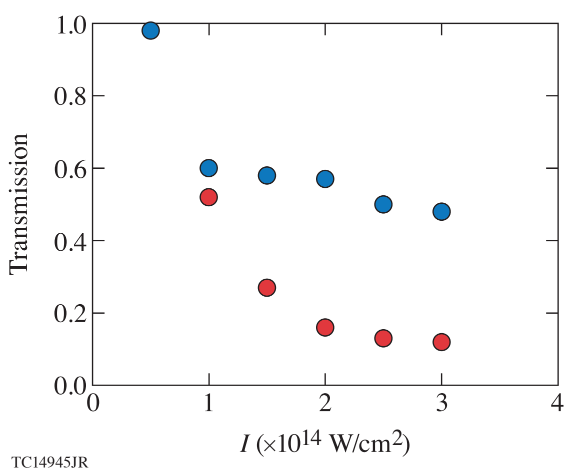

Figure 2
The scaling of light transmission at the end of the pump depletion stage (red circles) and during the dynamic saturation stage (blue circles) as a function of the incident laser intensity.

Hot-Electron Generation at Direct-Drive Ignition-Relevant Plasma Conditions at the National Ignition Facility

A. A. Solodov,[1] M. J. Rosenberg,[1] W. Seka,[1] J. F. Myatt,[2] M. Hohenberger,[3] R. Epstein,[1] C. Stoeckl,[1] R. W. Short,[1] S. P. Regan,[1] P. Michel,[3] T. Chapman,[3] J. D. Moody,[3] R. K. Follett,[1] J. P. Palastro,[1] D. H. Froula,[1] P. B. Radha,[1] and V. N. Goncharov[1]

[1]Laboratory for Laser Energetics, University of Rochester
[2]Department of Electrical and Computer Engineering, University of Alberta
[3]Lawrence Livermore National Laboratory

The direct-drive approach to laser fusion is vulnerable to hot-electron preheat as a result of the long scale length of plasma that exists near the quarter-critical density of the target [$n_{qc} = n_c/4$, where $n_c \approx 1.1 \times 10^{21}\,\lambda_0^{-2}$ cm^{-3} is the critical density and λ_0 (in μm) is the laser wavelength]. This plasma enables instabilities such as stimulated Raman scattering (SRS)[1] that generate electrostatic plasma waves capable of accelerating electrons. For full-scale, direct-drive–ignition experiments, it is estimated that the target adiabat and performance will be negatively affected if more than ~0.15% of the laser energy is coupled into the cold fuel in the form of hot electrons.[2]

An experimental platform has been fielded at the National Ignition Facility (NIF) to investigate hot-electron production from laser–plasma instabilities at direct-drive ignition-relevant conditions. Planar-target experiments, designed using the radiation-hydrodynamic code *DRACO*,[3] generate plasma and interaction conditions comparable to direct-drive–ignition designs: $I_L \sim 10^{15}$ W/cm^2, $T_e > 3$ keV, and density-gradient scale lengths of $L_n \sim 600\,\mu$m in the quarter-critical density region. Planar targets are currently the only way to achieve direct-drive ignition-relevant plasma conditions on the NIF. A schematic of the experiment and the main diagnostics are shown in Fig. 1(a). All targets—CH or Si disks with a 4.4-mm diameter and thicknesses of 1.2 mm (CH) or 0.75 mm (Si)—were placed at the NIF target chamber center and irradiated from the southern (lower) hemisphere. NIF beams used standard indirect-drive phase plates at best focus and flattop power profiles with a 2-ns linear rise and a total duration of ~7.5 ns. This configuration allowed for the variation of laser–plasma interaction (LPI) conditions by changing the number of

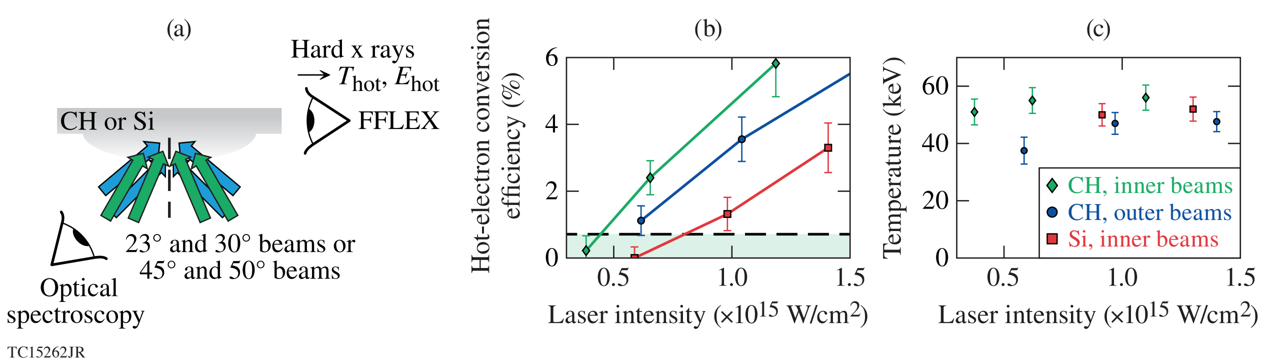

Figure 1
(a) A schematic of the experiment and the main diagnostics. (b) Laser-energy-to-hot-electron conversion efficiency and (c) hot-electron temperature versus laser intensity at the n_{qc}. The dashed horizontal line in (b) shows the hot-electron conversion efficiency of 0.7% considered to be the maximum-tolerable hot-electron preheat for divergent electron beams, as explained in the text. The preheat is tolerable in the light green region below the dashed line.

beams, single-beam intensities, and incidence angles of the beams by using beams in different cones. The higher-angle cones (45° and 50°) approximate irradiation conditions near the equator of a polar-direct-drive implosion, where the beams are incident from higher angles, while the lower-angle cones (23° and 30°) correspond to those near the poles. The use of planar targets reduces the level of cross-beam energy transfer (CBET) relative to spherical targets by excluding the outer parts of the beams, which can propagate around the target and seed CBET with beams from the opposite side.

Hot-electron production in the experiments was inferred by measuring the bremsstrahlung emission spectra using the NIF's ten-channel filter-fluorescer x-ray (FFLEX) diagnostic[4] located in the equatorial plane of the NIF chamber. The measured spectra are approximated well by the one-temperature exponential distributions. The Monte Carlo code EGSnrc[5] was used to relate the properties of hot electrons and measured hard x rays. In EGSnrc, hot electrons from 3-D Maxwellian distributions were injected from the location of the n_{qc} surface with temperatures close to the hard x-ray temperatures and with a full divergence angle of 2π toward the target.

Figure 1 shows (b) the laser-energy-to-hot-electron conversion efficiencies and (c) hot-electron temperatures inferred by comparing experiments and simulations versus the laser intensity at n_{qc} predicted by *DRACO*. The results are shown for CH targets illuminated either by inner beams (green diamonds) or outer beams (blue circles) and Si targets illuminated by inner beams (red squares). The dashed horizontal line in Fig. 1(b) shows the maximum-tolerable hot-electron conversion efficiency for divergent electron beams of 0.7%. It is obtained by estimating that with a near-2π angular divergence, only ~25% of the hot electrons will intersect the cold shell and result in preheat. Additionally, electrons at energies below ~50 keV will be stopped by the ablator. A large (near-2π) hot-electron divergence was demonstrated in previous spherical experiments on OMEGA and will be re-evaluated in the near-term implosion experiments on the NIF. Scattered-light spectrum measurements demonstrate that the most plausible mechanism of hot-electron generation in the NIF experiments is SRS.[6]

According to Figs. 1(b) and 1(c), in plastic ablators, hot-electron temperatures of ~40 keV to 60 keV and fractions of laser energy converted to hot electrons of ~0.5% to 5% were inferred when the laser intensity near the quarter-critical density increased from ~4 to 15×10^{14} W/cm^2. The intensity at n_{qc} is approximately 2× lower than the incident laser intensity due to inverse bremsstrahlung absorption. An acceptable hot-electron fraction of 0.7% of the laser energy (for divergent hot-electron beams) is exceeded if the overlapped intensity at the quarter-critical surface exceeds ~4×10^{14} W/cm^2 in plastic ablators.

Hot-electron preheat mitigation strategies are desired to extend the ignition design space to quarter-critical intensities above 4×10^{14} W/cm^2. Using mid-Z layers strategically placed in the plastic ablator materials was previously shown to suppress hot-electron generation by two-plasmon decay in smaller-scale implosions on OMEGA.[7] Our experiments using silicon planar targets demonstrate [Fig. 1(b)] that hot-electron production is also reduced in the longer-scale-length plasmas on the NIF, relevant to direct-drive ignition, in which SRS is the dominant LPI process. If the electron divergence is large, the direct-drive–ignition design space may potentially be extended to quarter-critical intensities up to ~8×10^{14} W/cm^2 by introducing silicon layers in the ablators.

This material is based upon work supported by the Department of Energy National Nuclear Security Administration under Award Number DE-NA0003856, the University of Rochester, and the New York State Energy Research and Development Authority.

1. W. Seka *et al*., Phys. Fluids **27**, 2181 (1984); H. Figueroa *et al*., Phys. Fluids **27**, 1887 (1984); C. S. Liu, M. N. Rosenbluth, and R. B. White, Phys. Fluids **17**, 1211 (1974).
2. J. A. Delettrez, T. J. B. Collins, and C. Ye, Phys. Plasmas **26**, 062705 (2019).
3. P. B. Radha *et al*., Phys. Plasmas **12**, 032702 (2005).
4. M. Hohenberger *et al*., Rev. Sci. Instrum. **85**, 11D501 (2014).
5. I. Kawrakow, Med. Phys. **27**, 485 (2000); I. Kawrakow *et al*., National Research Council Canada, Ottawa, Canada, NRCC Report PIRS-701 (May 2011).
6. M. J. Rosenberg *et al*., Phys. Rev. Lett. **120**, 055001 (2018).
7. R. K. Follett *et al*., Phys. Rev. Lett. **116**, 155002 (2016).

Three-Dimensional Particle-in-Cell Modeling of Parametric Instabilities Near the Quarter-Critical Density in Plasmas

H. Wen,[1,2] A. V. Maximov,[1,2] R. Yan,[1,2,*] J. Li,[1,2,†] C. Ren,[1,2,3] and F. S. Tsung[4]

[1]Laboratory for Laser Energetics, University of Rochester
[2]Department of Mechanical Engineering, University of Rochester
[3]Department of Physics and Astronomy, University of Rochester
[4]Department of Physics and Astronomy, University of California, Los Angeles
[*]Present Address: University of Science and Technology of China
[†]Present Address: University of California, San Diego

The interplay between two-plasmon decay (TPD) and stimulated Raman scattering (SRS) is studied using particle-in-cell (PIC) modeling in three dimensions. The TPD-related waves are mostly localized in the plane of polarization,[1] which is defined by the incident laser wave vector (in the x direction) and the laser electric-field vector (in the y direction). The SRS sidescattering develops mostly outside of the polarization plane, and its scattered-light wave vector is almost perpendicular to the incident laser wave vector.[2,3] Scattered-light waves can also propagate in the direction parallel or antiparallel to the laser wave vector (forward- and backscattering, respectively).[4] A 2-D simulation in the polarization plane (x–y) or in the perpendicular plane (x–z) will be referred to as p polarized (PP) or s polarized (SP), respectively. Two-dimensional simulations can model only the interaction where either TPD (in PP) or SRS (in SP) dominates, except for the high-frequency hybrid instability[5] case when the SRS-scattered light propagates in the backward direction and the SRS-related and TPD-related waves are in the same (x–y) plane. The 3-D simulations are required to study the interaction including both TPD and SRS. Here the results of several 3-D simulations for different plasma parameters and incident laser profiles are presented and compared with the respective 2-D simulations to illustrate that both TPD and SRS strongly influence the laser–plasma interaction near-quarter-critical density (1/4 n_c). In the 3-D modeling including both TPD and SRS, the fast-electron flux is reduced by up to an order of magnitude compared to 2-D TPD simulation results published earlier.[6]

Here we describe in detail a 3-D simulation for the parameters relevant to inertial confinement fusion (ICF) experiments.[7,8] A CH plasma is initialized with the electron temperature T_e = 2 keV and the temperatures for both ion species, T_i = 1 keV. The incident laser beam with intensity $I = 9 \times 10^{14}$ W/cm^2 propagates in the direction of density inhomogeneity (x). A linear density profile with the scale length L = 100 μm is assumed at the initial time. The size of the simulation box is 21 μm × 8.4 μm × 6.7 μm modeling the density range from 0.21 n_c to 0.26 n_c. Two 2-D simulations (PP and SP) with the same physical parameters were also performed. The TPD threshold parameter η (Ref. 1) is 1.9 (η = 1 at threshold), and the SRS backscattering threshold parameter N (Ref. 4) is 0.5 (N = 0.26 at threshold) for these simulations. The SRS sidescattering threshold[2,3] is close to the backscattering threshold. Both absolute TPD and absolute SRS instabilities are expected to grow. The threshold of the convective SRS[2] is not exceeded for the parameters described above.

The spectra of plasma waves $\left(\left|E_L\right|\right)$ obtained at a time interval between 0.3 ps and 1.0 ps in the 2-D PP and SP simulations are plotted in Figs. 1(a) and 1(b), respectively. From the 3-D simulation, the spectra of plasma waves at a time interval between 1.3 ps and 2.0 ps are plotted in Fig. 1(c) (close to the k_z = 0 plane, where TPD dominates) and in Fig. 1(d) (far away from the k_z = 0 plane, where SRS dominates). One can see from Figs. 1(c) and 1(d) that TPD and SRS coexist near 1/4 n_c. The spectra of the unstable modes for TPD and SRS are close to the linear theory results (see overlaid lines in Fig. 1).

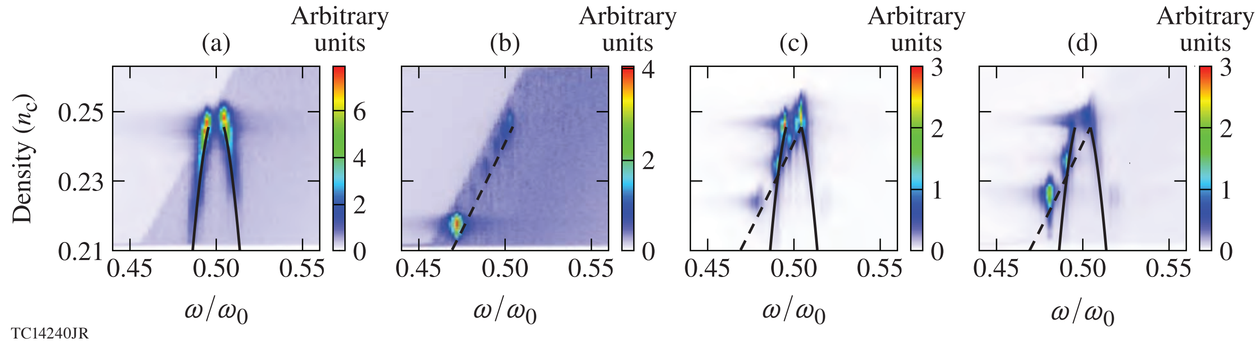

Figure 1
(a) Plasma-wave spectra in the linear instability stage as a function of plasma density and the wave frequency normalized to laser frequency in 2-D PP, (b) 2-D SP, and (c) 3-D simulation for modes with $0 \le k_z/k_0 < 0.2$ and (d) $0.2 \le k_z/k_0 < 3$. The overlaid solid black lines and the dashed black lines represent the dispersion relations satisfying the matching conditions for TPD and SRS, respectively.

As the instability evolves from the linear stage to the saturation stage, the frequency spectra shown in Fig. 1 evolve into the spectra shown in Fig. 2. One can see that the spectra in all these simulations are broader in the saturation stage compared to the linear stage. The density in Fig. 2 is calculated using the initial density profile. Compared to 2-D PP [Fig. 2(a)], the TPD is much weaker at densities lower than 0.23 n_c in the 3-D simulation [Fig. 2(c)]. The weakening of the TPD modes at these densities is also illustrated in Fig. 3(a) [and Fig. 3(b)], where the spectrum of plasma waves at densities below 0.23 n_c in the saturation stage is integrated over k_z (and k_y). There are no prominent modes along the TPD hyperbola[9] [solid black line in Fig. 3(a)] at $k_x > k_0$, which corresponds to the TPD daughter waves with larger wave vectors. Two types of low-frequency density fluctuations are identified in our simulations [see Fig. 3(c)]: one type is the ion-acoustic wave driven by the Langmuir-decay instability (LDI),[10,11] and the other type is driven with the beating of the same-frequency daughter waves of SRS and TPD. The LDI modes form a broad feature at $k_x \approx 1.7\ k_0$ (about 2× the laser wave vector in plasma) in the spectrum of the ion density fluctuations shown in Fig. 3(c). The beating of the SRS plasmons with wave vector $(k_x, k_y, k_z) = (0.87\ k_0, 0, \pm 0.2\ k_0)$ creates density perturbations $\langle \delta n \rangle$ with wave vector $(k_x, k_z) = (0, \pm 0.4\ k_0)$. The coupling between SRS plasmons and $\langle \delta n \rangle$ generates higher-order modes in the field at $k_z = \pm(0.2 + m0.4\ k_0)$, [$m$ = 1, 2 ..., see Fig. 3(b)] and in the density perturbation at $(k_x, k_z) = [0, \pm(0.4 + m0.4\ k_0)]$ [see Fig. 3(c)].

Although SRS and TPD grow independently in the linear stage, in the nonlinear stage they interact through low-frequency density perturbations. TPD growth starts from the region near 1/4 n_c and spreads to lower densities.[6] Although the peak values of $\langle \delta n \rangle$ are similar in 2-D and 3-D simulations, the peaks are reached at different densities in different simulations: in 2-D PP (without SRS) $\langle \delta n \rangle$ peaks at densities where absolute TPD modes dominate (around 0.245 n_c); in 3-D (with both SRS and TPD)

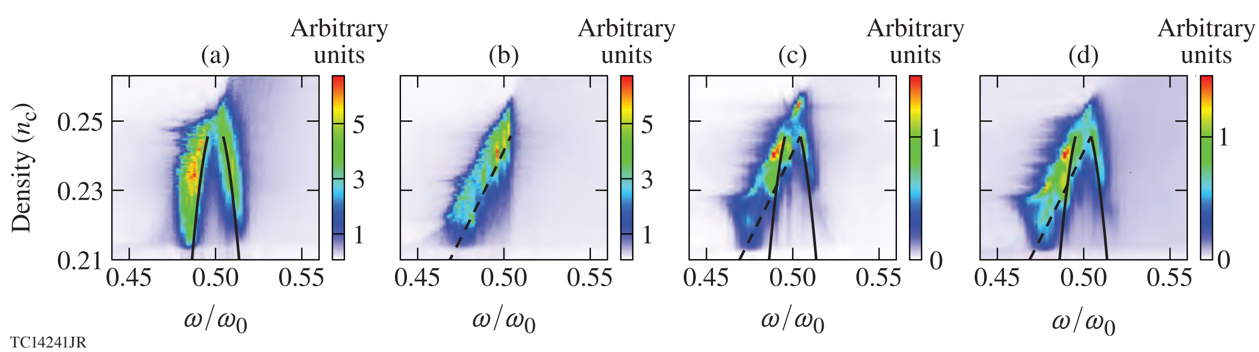

Figure 2
Plasma-wave spectra in the saturation stage in the 2-D (from 3.3 ps to 4.1 ps) and 3-D (from 2.3 ps to 3.1 ps) simulations as a function of plasma density and wave frequency. Each panel displays the same quantity as in Fig. 1.

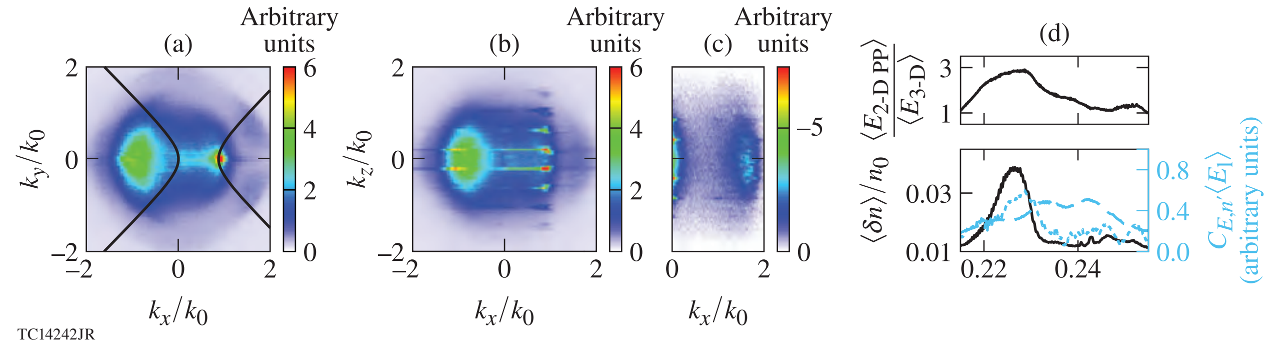

Figure 3
(a) The spectrum of plasmons in the saturation stage of 3-D simulation at densities lower than 0.23 n_c plotted in the k_x–k_y plane and (b) the k_x–k_z plane. (c) The spectrum of ion density fluctuation plotted in the k_x–k_z plane on a logarithmic scale. (d) Lower panel: Ion density fluctuations rms (root-mean-square average over the transverse direction and time) normalized to background density (solid black line), longitudinal electric field rms (dashed blue line) and caviton correlator $C_{E,n}$ (dotted blue line). Upper panel: the ratio of the electric-field amplitude of the TPD plasmons with larger wave vector between 2-D PP and 3-D simulations.

$\langle \delta n\rangle$ peaks at densities where the frequencies of TPD and SRS plasmons are close. In this region where the dispersion lines for TPD and SRS plasmons intersect [near 0.23 n_c in our simulations; see Figs. 2(c) and 3(d)] multiple pairs of SRS and TPD daughter waves have close frequencies and can drive $\langle \delta n\rangle$ through the ponderomotive force to much higher levels compared to other density regions [see the black line in Fig. 3(d)]. The level of $\langle \delta n\rangle$ near 0.23 n_c is lower in 2-D PP than in 3-D simulations. In the 3-D simulation the growth of TPD plasmons at densities below 0.23 n_c, seeded by plasmons from above 0.23 n_c, is disrupted by these enhanced ion density perturbations, as illustrated by a decrease in the level of TPD-driven plasmons below 0.23 n_c in Fig. 2(c).

The correlation between the local plasmon intensity $\left|E_L\right|^2$ and the density fluctuations δn is captured using the caviton correlator[12]

$$C_{E,n} = \left\langle -\delta n \left| E_L \right|^2 \right\rangle \Big/ \left[\left\langle (\delta n)^2 \right\rangle \left\langle E_L \right\rangle^2 \Big/ 2 \right].$$

As shown in the lower panel of Fig. 3(d), the plasma waves and the density fluctuations are weakly correlated between 0.255 n_c and 0.235 n_c: $C_{E,n}$ = 0.1 to 0.2 in spite of a significant level of plasmons in this density range. At densities close to 0.23 n_c, the lower panel of Fig. 3(d) shows the increase not only in the plasmon intensity and density fluctuations, but also in the correlation between them with $C_{E,n}$ reaching up to 0.6. The large caviton correlator indicates that the plasma waves are strongest in areas where density is depleted. The ponderomotive force of multiple pairs of SRS and TPD daughter waves with close frequencies is responsible for driving the enhanced density perturbations. The nonlinear coupling of TPD and SRS through ion perturbations leads to a lower TPD saturation level in the 3-D simulation compared to the 2-D PP simulation, which is illustrated in the upper panel of Fig. 3(d).

The fast-electron flux is defined as the energy flux carried by electrons with kinetic energy above 55 keV leaving the simulation box minus the energy flux carried by the thermal electrons injected into the simulation region from the thermal boundaries (in the x direction). Information about the hot electrons is collected during the saturation stage in each simulation for 0.5 ps. In the 3-D simulation, the fast-electron flux associated with the forward- and backward-going hot electrons was found to be 1.7% and 0.8%, respectively. The plasma-wave spectrum in the 3-D simulation corresponds to a smaller k-space domain than the spectrum in 2-D PP, which makes the staged acceleration mechanism less efficient in 3-D than in 2-D and explains a smaller number of hot electrons in the 3-D simulation compared to 2-D PP (6.6% and 3.4% in the forward and backward directions, respectively). The influence of wave breaking on the fast-electron generation is small because the maximal electric field amplitude (0.04 $m_e\omega_0 c/e$) is below the wave-breaking limit (0.1 $m_e\omega_0 c/e$) (Ref. 13).

The nonlinear regime including both TPD and SRS is also observed in simulations with the speckled laser beam[14,15] and electron–ion collision effects included. In PIC simulations with periodic boundary conditions, the limited-size simulation region effectively represents a much larger volume of plasmas and the single speckle in the simulation region mirrors itself in the transverse directions. A series of simulations has been performed to study how the speckles affect the generation of hot electrons. All parameters are the same as the simulations described previously except for the temperatures of electrons and ions being 1.5× higher. The peak intensities in the laser speckles are 1.8×10^{15} W/cm^2 (twice the average intensities). A collision package (CP) is available for the PIC code *OSIRIS*.[16] The main physics processes are observed to be the same in simulations with plane-wave beams and speckled beams.

The fast-electron flux values in simulations are listed in Table I for different incident laser beams as well as with CP turned on and off. By comparing the left and right columns of Table I, one can see that adding collisions can reduce the fast-electron flux by about 50% and in the case of plane-wave 2-D PP simulation by almost 70%. Also note that the reduction of the fast-electron flux caused by collisions affects both the forward-going electrons and backward-going electrons since the collisional damping rate affects all the plasma waves. The fast-electron flux generated in 2-D SP is much smaller than the fast-electron flux generated in 2-D PP, which indicates that the plasma waves driven by TPD are the main source of the electron acceleration.

Table I: Fast-electron flux normalized to the incident laser energy flux.

Fast-electron flux	Forward/Backward	
Collision package	On	Off
Plane wave 2-D PP	$1.6\%/1.3\%$	$5.5\%/3.8\%$
Plane wave 2-D SP	$(< 0.1\%)/0.2\%$	$(< 0.1\%)/0.5\%$
Speckle 2-D PP	$6.8\%/1.7\%$	$9.4\%/3.8\%$
Speckle 2-D SP	$(< 0.1\%)/0.3\%$	$(< 0.1\%)/0.7\%$
Speckle 3-D	$0.4\%/0.3\%$	$0.8\%/0.5\%$

The hot-electron fraction observed in the ICF experiments on the OMEGA Laser System does not exceed a few percent.[8] At the same time, in the previous PIC simulations of TPD in 2-D, the hot-electron fraction was close to an order of magnitude larger than in the experiments. The 3-D PIC simulations presented here produce the results for the hot-electron fraction that are close to the experimental levels.

Laser–plasma interaction near 1/4 n_c determines the generation of fast electrons that are crucial for the performance of ICF targets. The fast-electron flux in simulations is found to be closely related to the plasma-wave spectra. The TPD-driven plasma waves with large wave vectors are very important for accelerating electrons. At the same time, the SRS-driven plasma waves are less effective in accelerating electrons. Therefore the modeling that includes the nonlinear coupling of TPD and SRS in 3-D is the only way to correctly describe the generation of fast electrons in laser-driven ICF.

Our 3-D PIC simulations have shown the large decrease (up to an order of magnitude) in the fast-electron flux compared to 2-D TPD modeling. The reason is the nonlinear coupling between SRS and TPD, which is especially pronounced at densities lower and around 0.23 n_c. In this region, plasma waves and growing density perturbations are localized in the same areas as illustrated by the caviton correlator. Enhanced density perturbations detune and weaken the TPD-driven plasmons effective in the fast-electron generation. In addition to the TPD suppression, the plasma-wave spectra in 3-D simulations are much more narrow compared to the spectra in 2-D TPD modeling. To conclude, 3-D PIC simulations presented in this summary fully model the laser–plasma interaction near 1/4 n_c, including SRS and TPD, and obtain the fast-electron fraction level close to experimental results, resolving the large discrepancy between ICF experiments and PIC simulations that have existed for many years.

This work was supported by the Department of Energy National Nuclear Security Administration under Award Number DE-NA0003856, the University of Rochester, and the New York State Energy Research and Development Authority. We also acknowledge the support by the DOE under grant No. DE-SC0012316, and by the NSF under grant No. PHY-1314734.

1. A. Simon *et al*., Phys. Fluids **26**, 3107 (1983).
2. C. S. Liu, M. N. Rosenbluth, and R. B. White, Phys. Fluids **17**, 1211 (1974).
3. B. B. Afeyan and E. A. Williams, Phys. Plasmas **4**, 3803 (1997).
4. J. F. Drake and Y. C. Lee, Phys. Rev. Lett. **31**, 1197 (1973).
5. B. B. Afeyan and E. A. Williams, Phys. Plasmas **4**, 3845 (1997).
6. R. Yan *et al*., Phys. Rev. Lett. **108**, 175002 (2012).
7. W. Seka *et al*., Phys. Plasmas **16**, 052701 (2009).
8. D. T. Michel *et al*., Phys. Plasmas **20**, 055703 (2013).
9. J. Meyer and Y. Zhu, Phys. Rev. Lett. **71**, 2915 (1993).
10. D. F. DuBois and M. V. Goldman, Phys. Rev. **164**, 207 (1967).
11. D. F. DuBois, H. A. Rose, and D. A. Russell, Phys. Scr. **T63**, 16 (1996).
12. H. X. Vu *et al*., Phys. Plasmas **19**, 102708 (2012).
13. T. P. Coffey, Phys. Fluids **14**, 1402 (1971).
14. Y. Kato *et al*., Phys. Rev. Lett. **53**, 1057 (1984).
15. S. Skupsky *et al*., J. Appl. Phys. **66**, 3456 (1989).
16. R. A. Fonseca *et al*., in *Computational Science – ICCS 2002*, edited by P. M. A. Sloot *et al*., Lecture Notes in Computer Science, Vol. 2331 (Springer, Berlin, 2002), pp. 342–351.

An Ultrafast, Ultraviolet Metal–Semiconductor–Metal Photodetector Based on AlGaN with a Response Time Below 30 ps

Y. Zhao[1] and W. R. Donaldson[1,2]

[1]Laboratory for Laser Energetics, University of Rochester
[2]Department of Electrical and Computer Engineering, University of Rochester

Aluminum–gallium–nitride (AlGaN) photodetectors have been successfully fabricated with micrometer-scale metal–semiconductor–metal (MSM) structures and tested with ultrafast UV laser pulses. The measurements were taken with single-shot oscilloscopes. Pulse-broadening effects caused by the measurement system were systematically evaluated and reduced to resolve the intrinsic response time of the detector. The best-performing devices showed a response time of below 30 ps and dark currents below 10 pA. The devices showed linear response with the bias voltage and the laser energy.

The $Al_xGa_{(1-x)}N$ (where x denotes the fraction of substituted aluminum) ternary alloys are particularly interesting as UV detectors because of their high tolerance to extreme environments resulting from their thermal stability and radiation hardness.[1] The wide band gap of these materials comes with the unique feature of a tunable absorption edge. The wavelength of the band edge varies from 365 to 200 nm (Ref. 2) as the Al composition changes from 0% to 100%, which makes the device visible blind or even solar blind. One interesting application for the high-energy-density–physics and inertial confinement fusion (ICF) communities would be to detect Thomson scattering in a plasma, where the probe light must be at a frequency higher than the plasma frequency.[3] Currently UV probes at 263 nm and 210 nm are being considered for these applications but semiconducting detectors in this region of the spectrum are typically slow and inefficient.

MSM photodetectors based on AlGaN, however, have been commonly reported to have extremely long decay times and high dark currents[4,5] because of the poor material quality and high defect density. Recently, we successfully fabricated detectors on high-quality AlGaN wafers. The detectors had an ultrafast response time. To our knowledge, these are the fastest UV detectors fabricated on AlGaN thin films. To resolve the response time, the detectors were tested with single-shot, high-bandwidth oscilloscopes. This is the same configuration in which these devices would be used if they were employed in ICF experiments.

The intrinsic, n-type and p-type AlGaN wafers used to fabricate the devices were purchased from Kyma Technologies.[6] The ~330 nm-thick AlGaN thin films were grown on sapphire by metal–organic chemical vapor deposition (MOCVD). All of the wafers had an approximately 10% Al composition. A thin layer (~10 nm) of AlN was inserted between the substrate and the AlGaN. Acting as a buffer layer, the AlN thin film decreases the lattice constant mismatch between the AlGaN layer and the Al_2O_3 substrate, significantly reducing the density of defects and improving the quality of the materials.

The devices were designed with an interdigited finger-shaped structure. The finger width and spacing were set the same at 5 μm and the active area was 50×50 μm^2. In this work, the devices were fabricated in the Integrated Nanosystems Center (URnano) at the University of Rochester. A 120-nm-thick platinum layer was chosen for the metal contact because platinum has a high work function and has been reported to form good-quality Schottky contacts on AlGaN thin films.[7–9] A 10-nm-thick titanium layer was deposited before metallization to improve the adhesion between the platinum and semiconductor. The device fabrication involved a two-layer fabrication process and precise interlayer alignment. For some devices, the first-layer fabrication deposited a 10-nm insulating layer of SiO_2 within the compensation pad area (without covering the interdigited area). The purpose of the insulation layer was to reduce the dark current leakage from the compensation pad to the AlGaN thin film. Then, for all devices, the fabrication process deposited a metal contact that covered both the compensation area and portions of the finger-shaped area.

An ORIGAMI femtosecond laser (λ = 1053 nm with 200-fs duration) from NKT Photonics served as the main oscillator for the laser system. A single pulse from the 80-MHz pulse train was selected at a 5-Hz repetition rate by an acoustic-optic modulator and injected into an in-house–built regenerative (regen) amplifier.[10] After the regen amplifier, ~1 mJ of IR light with a FWHM of 10 ps, caused by gain-bandwidth broadening in the regen amplifier, was converted to 263 nm using nonlinear beta-barium borate crystals. The 263-nm beam with a 10-ps duration and 5-Hz repetition rate was used to test the photodetectors. We used both a 45-GHz, single-shot LeCroy oscilloscope and a 12.5-GHz Tektronix oscilloscope. When the 45-GHz oscilloscope was available, it was used in single-channel mode to access the highest digitizing rate. Otherwise, both the signal and reference signal, derived by splitting off a portion of the light and illuminating a GaAs photodiode, were acquired on the 12.5-GHz oscilloscope. The slow GaAs photodiode was used to account for fluctuations in the laser intensity. For each acquired oscilloscope trace, a portion of the trace ~100 ps wide around the peak was fitted with a Gaussian function to determine the measured FWHM, τ_{measure}.

The measurement system, including the oscilloscope, cable, transmission line-mounting fixture, and the incident laser, can cause pulse broadening in the acquired signal. The FWHM that we measured is not the intrinsic response time of our MSM detector but instead is the quadrature sum of the laser pulse width, the intrinsic response of the detector, the response of the measurement system, and the broadening effect of the measurement cable, which can be expressed in the following equation:

$$\tau_{\text{measure}} = \sqrt{\tau^2_{\text{intrinsic}} + \tau^2_{\text{oscilloscope}} + \tau^2_{\text{cable}} + \tau^2_{\text{laser}} + \tau^2_{\text{circuit}}}\,. \tag{1}$$

For the LeCroy oscilloscope, $\tau_{\text{oscilloscope}}$ is 7.8 ps. The pulse width of the laser, τ_{laser}, is 10 ps. To evaluate the broadening effect caused by the measurement circuit, a *SPICE* simulation[11] was carried out on the circuit we used for the testing. The circuit produced a FWHM of 16.9 ps with a 10-ps pulse impulse response. Therefore, the pulse broadening that the circuit could cause, τ_{circuit}, is calculated to be 13.6 ps. The cable response τ_{cable} was measured to be 22.5 ps. The measured FWHM of the signal from the AlGaN detector, as shown in Fig. 1, is 36 ps. Based on these assumption and measurements listed above, the intrinsic response of these devices is 24 ps.

We further investigated the response behavior of the detectors under different bias voltages. We changed the bias voltage from –30 V to 30 V with a B&K Precision DC Power Supply 1635, and the detector illumination remained unchanged during the test. The peak voltages under different bias voltages are plotted in Fig. 2. Clearly the detector never reached saturation, where the peak voltage was independent of the applied bias. This is unexpected behavior and may be caused by the photogenerated carri-

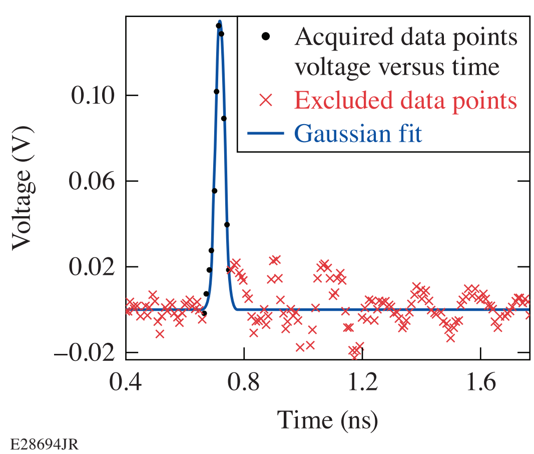

Figure 1
The response curve of the device with platinum contact fabricated on an n-type doping wafer. The finger spacing and finger width of the device are both 5 μm and the SiO_2 insulating layer is 10 nm thick. The signal is taken at a bias voltage of 15 V and a pulse energy of 52 nJ. The Gaussian fit is also plotted, while the other data points marked by red ×'s are excluded from the fit.

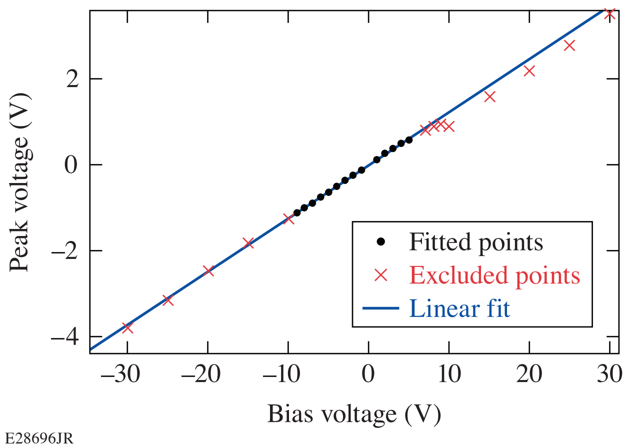

Figure 2
The peak voltage of the photodetector response under different bias voltages from –30 V to 30 V. A linear fit was made based on the data under lower biased voltage; the red ×'s points are the excluded high-voltage biased points.

ers recombining before being swept to the metal contact. As the electric field increases, the velocity of the carriers increases and more carriers reach the contact before recombining, thereby causing the peak voltage to continue to increase. Normally the peak signal is determined solely by the number of photogenerated carriers and is independent of the voltage. Since the photogenerated signal never reached the saturated regime, the responsivity could not be calculated. Further experiments are ongoing to determine the origin of the voltage dependence of the photo signal.

This material is based upon work supported by the Department of Energy National Nuclear Security Administration under Award Number DE-NA0003856, the University of Rochester, and the New York State Energy Research and Development Authority.

1. J. C. Carrano *et al*., Appl. Phys. Lett. **73**, 2405 (1998).
2. D. Walker *et al*., Appl. Phys. Lett. **74**, 762 (1999).
3. R. K. Follett *et al*., Rev. Sci. Instrum. **87**, 11E401 (2016).
4. Y. Zhao and W. R. Donaldson, J. Mater. Res. **33**, 2627 (2018).
5. Y. Zhao and W. R. Donaldson, IEEE Trans. Electron Devices **65**, 4441 (2018).
6. Kyma Technologies Inc., Raleigh, NC 27617.
7. P.-C. Chang *et al*., Thin Solid Films **498**, 133 (2006).
8. M. Brendel *et al*., Electron. Lett. **51**, 1598 (2015).
9. Y.-R. Jung *et al*., Jpn. J. Appl. Phys. **42**, 2349 (2003).
10. A. V. Okishev and J. D. Zuegel, Appl. Opt. **43**, 6180 (2004).
11. L. W. Nagel and D. O. Pederson, *SPICE (Simulation Program with Integrated Circuit Emphasis)*, EECS Department, University of California, Berkeley, Technical Report No. UCB/ERL M382 (1973).

High-Energy Parametric Amplification of Spectrally Incoherent Broadband Pulses

C. Dorrer, E. M. Hill, and J. D. Zuegel

Laboratory for Laser Energetics, University of Rochester

Large-aperture Nd:glass amplifiers that are the basis for solid-state, ignition-class laser drivers are intrinsically limited in terms of their amplification bandwidth.[1,2] Spectral gain narrowing typically reduces the optical bandwidth to a few nanometers at a central wavelength of 1053 nm (1ω), mere tenths of a percent in terms of fractional bandwidth $\Delta\omega/\omega_0$. This relatively narrow optical bandwidth limits the performance of beam-smoothing techniques used to generate a smooth, time-averaged focal spot on target. Larger fractional bandwidth of the order of 1% would decrease the asymptotic smoothing time and mitigate laser–plasma instabilities.[3] Simulations show that this bandwidth promises to vastly improve the performance of both direct- and indirect-drive inertial confinement fusion. A new broadband laser driver concept based on optical parametric amplifiers (OPA's) is being designed at LLE to deliver 3ω pulses with a fractional bandwidth greater than 1% and support experiments on the OMEGA laser. Concepts for broadband amplification and frequency conversion of spectrally incoherent pulses are being tested and compared to models.

Optical parametric amplifiers, based on a three-wave nonlinear interaction, can efficiently amplify signals over extremely large bandwidths when the wavelength-dependent phase mismatch between the high-energy pump pulse, signal to be amplified, and resulting idler wave remains small during propagation in the nonlinear crystal.[4] These amplifiers are typically used to amplify a spectrally coherent signal for which spectral components have a well-defined phase relationship, e.g., with a chirped signal in optical parametric chirped-pulse amplification (OPCPA).[5] Smoothing techniques are, however, more effective when the temporal variations of the instantaneous optical frequency are much faster than the overall pulse duration. This can be achieved, for example, with spectrally incoherent pulses originating from a random process such as amplified spontaneous emission. While these signals are effectively used in large-scale, high-energy excimer (gas) lasers,[6] demonstrating their broadband amplification in OPA's pumped by frequency-doubled lasers based on Nd-doped materials opens the path to a new generation of broadband, high-energy, ignition-class drivers based on existing solid-state laser technology and large-aperture nonlinear crystals.

We demonstrate, for the first time to our knowledge, efficient high-energy parametric amplification of broadband spectrally incoherent pulses. Because of the spatial coherence resulting from signal generation in a front end based on single-mode fibers, the amplification process is similar to what is observed with monochromatic signals. Experiments performed with the existing Multi-Terawatt laser's OPA stages, originally designed for OPCPA,[7] demonstrate the generation of spectrally incoherent waves around 1053 nm (1ω) with ~60-nm bandwidth at energies of several hundred millijoules. The large bandwidth and high conversion efficiency from the pump at 526.5 nm (2ω) to 1ω waves are the results of a collinear interaction geometry in the last OPA and generation of the seed signal at a central wavelength below 1053 nm by the fiber front end. In these conditions, the idler wave generated in the last OPA co-propagates with the signal wave and has a spectrum that is spectrally symmetric relative to the signal's spectrum with respect to 1053 nm, effectively increasing the available energy and optical bandwidth at 1ω.

Figure 1 displays the output 1ω energy after the power amplifier as a function of the 2ω pump energy. Similar amplification behavior is observed when the seed signal is a spectrally incoherent broadband signal, with the spectrum centered at 1030 nm, and a narrowband coherent signal at 1030 nm [Fig. 1(a)]. The energy in the combined signal and idler waves resulting from power-

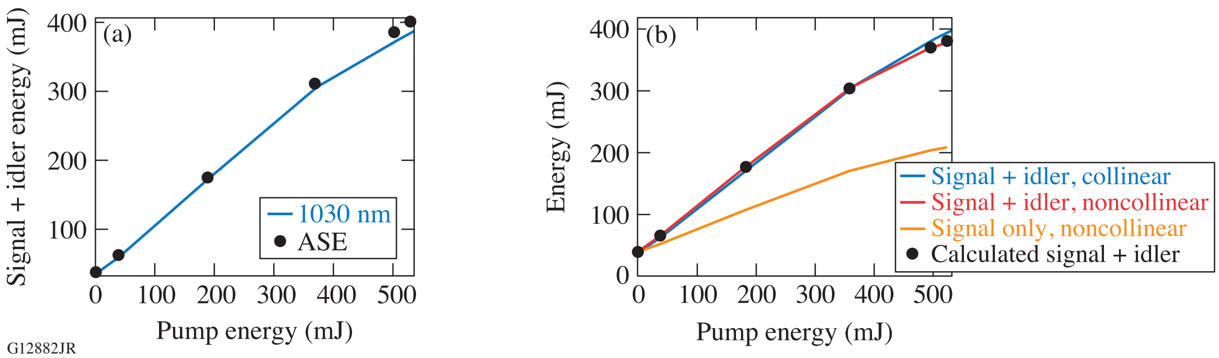

Figure 1
Amplified output energy after the power amplifier. (a) The curve corresponds to a monochromatic seed at 1030 nm and the solid black circles correspond to a spectrally broadband amplified spontaneous emission (ASE) seed. (b) The measured power-amplifier output energy is plotted for the combined signal and idler in collinear and noncollinear geometries (solid blue and red curves, respectively) and for the signal in a noncollinear geometry (solid orange curve). The energy of the combined signal and idler calculated from the signal energy is plotted with solid black circles.

amplifier operation at 530 mJ is 400 mJ, demonstrating a 70% conversion efficiency from the 2ω pump to 1ω waves considering the 30-mJ, 1ω input energy for this amplifier. Operation of the power amplifier in a collinear or slightly noncollinear geometry yields similar output energies for the combined signal and idler pulses [Fig. 1(b)]. The energy of the combined signal and idler waves calculated using the signal energy measured in a noncollinear geometry is in excellent agreement with the experimentally measured energy, showing that parasitic processes such as second-harmonic generation are not significant.[8]

The spectrum of the parametric fluorescence resulting from operation of the fully pumped OPA stages without a seed signal is shown in Fig. 2(a). The measured bandwidth, ~100 nm, is indicative of the large bandwidth that can be obtained for amplification around 1ω. Figure 2(b) shows the spectrum of the input seed signal and the spectrum of the combined signal and idler waves at the output. Because of energy conservation in the OPA pumped at 526.5 nm, amplification of signal photons at wavelengths below 1053 nm leads to the generation of idler photons at wavelengths above 1053 nm. The resulting waves have a spectral density extending over more than 60 nm, i.e., corresponding to a fractional bandwidth larger than 5% at 1ω.

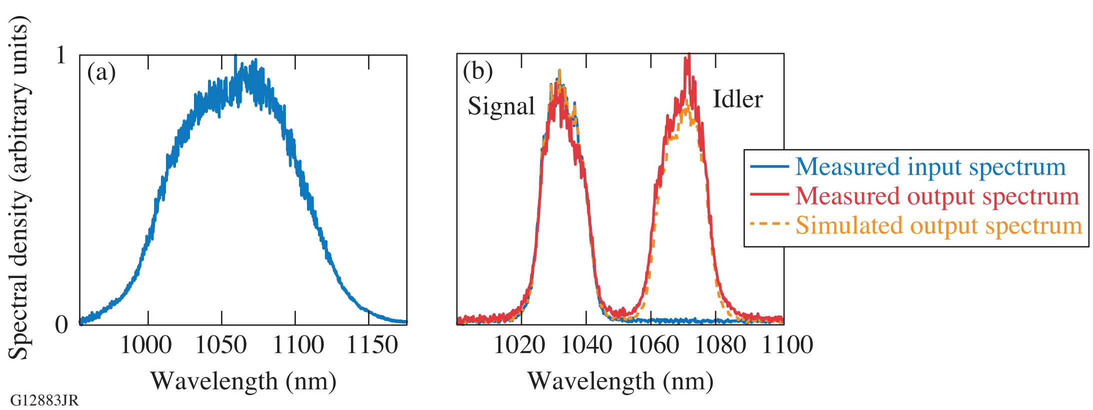

Figure 2
(a) Measured parametric fluorescence at the power-amplifier output in the absence of seed in the preamplifier; (b) input and output spectra of the power amplifier and simulated output spectrum for the ASE seed.

This material is based upon work supported by the Department of Energy National Nuclear Security Administration under Award Number DE-NA0003856, the University of Rochester, and the New York State Energy Research and Development Authority.

1. C. A. Haynam *et al*., Appl. Opt. **46**, 3276 (2007).
2. J. L. Miquel, C. Lion, and P. Vivini, J. Phys.: Conf. Ser. **688**, 012067 (2016).
3. R. K. Follett *et al*., Phys. Plasmas **26**, 062111 (2019).
4. G. Cerullo and S. De Silvestri, Rev. Sci. Instrum. **74**, 1 (2003).
5. I. Jovanovic *et al*., Appl. Opt. **41**, 2923 (2002).
6. S. Obenschain *et al*., Appl. Opt. **54**, F103 (2015).
7. V. Bagnoud *et al*., Opt. Lett. **30**, 1843 (2005).
8. J. Bromage *et al*., Opt. Express **19**, 16,797 (2011).

A Laser System Model for Enhanced Operational Performance and Flexibility on OMEGA EP

M. J. Guardalben, M. Barczys, B. E. Kruschwitz, M. Spilatro, L. J. Waxer, and E. M. Hill

Laboratory for Laser Energetics, University of Rochester

Introduction

The ability of high-energy laser systems to provide complex laser pulse shapes has growing importance in many research disciplines such as laser fusion,[1–4] high-energy-density physics,[5–8] laboratory astrophysics,[9–11] and laser conditioning of optical materials.[12] For example, x-ray diffraction of ramp-compressed crystalline solids can probe high-pressure phase transitions inaccessible with shock compression.[6] In such laser facilities, accurate, real-time predictions of laser performance are critical for maximizing experimental and operational effectiveness and flexibility. Several laser operations models that predict laser performance for high-energy laser systems have been reported.[13–22] Most of these models utilize optimization methods that comprise forward-propagation simulations with feedback to converge on the required on-target pulse power. This article reports on *PSOPS*—a MATLAB[23]-based semi-analytic model developed for the OMEGA EP[24] Laser System. *PSOPS* provides rapid and accurate predictions of OMEGA EP Laser System performance in both forward and backward directions, a user friendly interface, and rapid optimization capability between shots. The model's features have allowed real-time optimization of the laser system configuration in order to satisfy the demands of rapidly evolving experimental campaign needs and have enabled several enhancements to the accuracy and flexibility of laser system performance.

Functional Overview of *PSOPS*

The backward simulation capability of the model is used in the configuration of the system for a shot where the desired UV energy, pulse shape, expected beam profile, and beamline amplifier configuration are provided as inputs to the *PSOPS* model. The results are the required pulse shape at the input of the system, as well as the energies at each stage of the laser, from which the laser throttles and diagnostic configurations can be determined in a fast and robust manner.

During shot operations, *PSOPS* is used in the forward simulation direction to provide rapid predictions of laser-system performance using measured inputs to the amplifier chain. The measured input beam profile and real-time–measured input pulse shape are used with the expected beamline injected energy and previously measured beamline small-signal gain to predict the IR and frequency-converted UV performance at the end of the beamline. A front-end qualification shot is taken at the start of a shot day to confirm the expected injected energy and to measure the injected beam near-field distribution that is used as input to the *PSOPS* model.

Laser pulse shape, energy, and near-field beam profile are measured at several locations along the beam path. Diagnostic stages relevant to the *PSOPS* model and associated measurements are shown in Fig. 1. The output pulse shape of each beamline's regenerative amplifier is measured at a 5-Hz repetition rate using a photodiode-based pulse-stacking, pulse-shape monitor (PSM).[25] Calorimetrically calibrated charge-coupled–device (CCD) cameras (Scientific Instruments, model SI-800) are used to measure the beam's near-field profile and laser-beam energy at the beamline injection and amplified beamline output stages. A harmonic energy diagnostic (HED)[26] is used to measure the UV energy and the residual green and IR energy of the frequency-converted laser beam. Amplified IR and UV pulse shapes are measured using ROSS streak cameras.[27] These diagnostic measurements are used to calibrate the *PSOPS* model and also to determine the required stage energies and pulse shapes in both forward and backward directions when configuring for a shot.

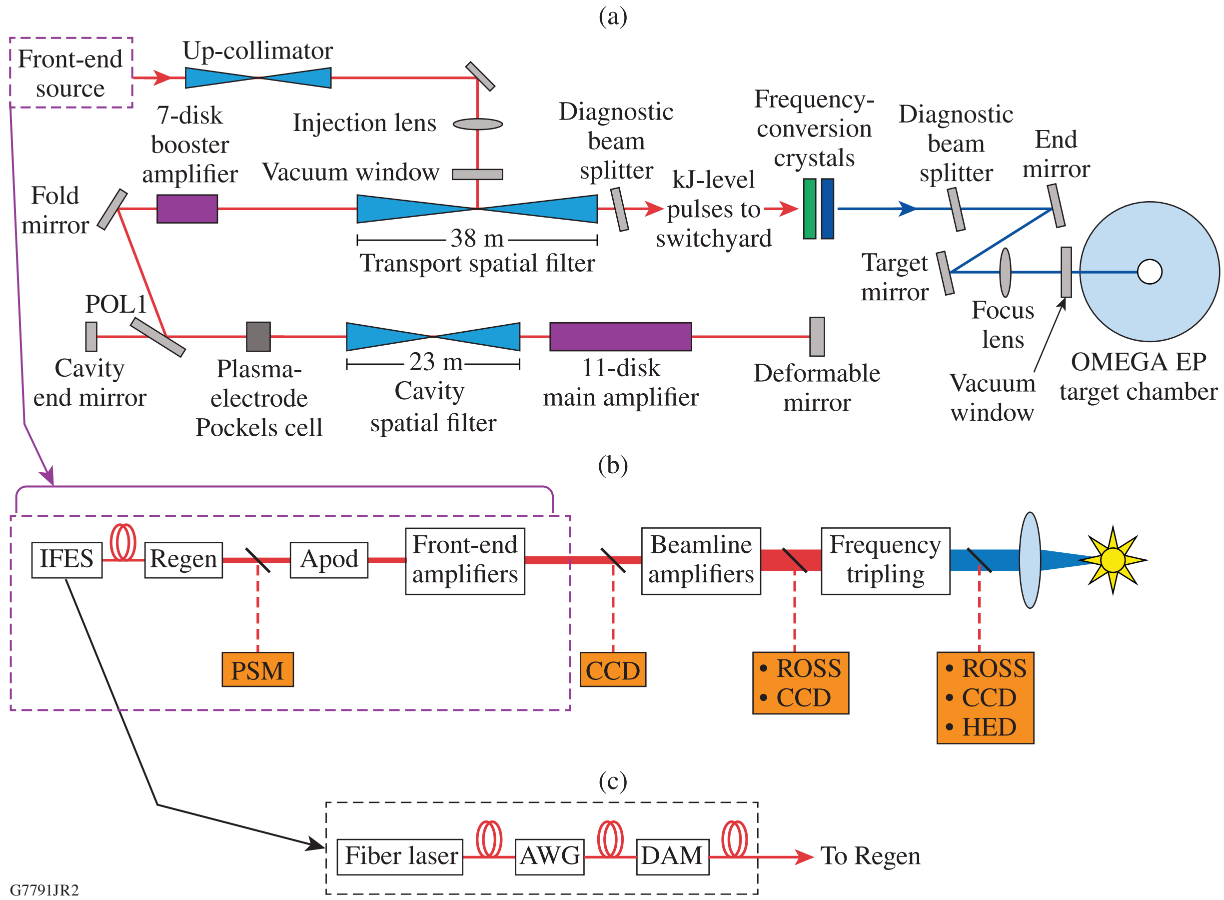

Figure 1
(a) Configuration of an OMEGA EP beamline. (b) Block diagram of (a) showing locations of pulse-shape, beam-profile, and energy-measurement diagnostics used with the *PSOPS* model. PSM: pulse-shape monitor; Apod: beam-shaping apodizer; CCD: near-field charge-coupled–device camera; ROSS: Rochester optical streak system; and HED: harmonic energy diagnostic. (c) An integrated front-end system (IFES) produces temporally shaped, 1053-nm pulses from a single-frequency, continuous-wave (cw) fiber laser. Precisely shaped temporal pulses are formed using an arbitrary waveform generator (AWG) that drives a dual-amplitude modulator (DAM).

PSOPS Model Description

Analytic solutions to the four-level, coupled-rate, and energy-transport equations for a homogeneously saturating thin slab[28] are used in *PSOPS* to determine the time-dependent gain within each LHG-8, Nd-doped laser disk at discrete locations across the laser aperture. For multipass amplification in the forward propagation direction, the output intensity of disk k is given by

$$I_k(t,x,y) = \beta^2 \cdot G_k(t,x,y) I_{k-1}(t,x,y), \tag{1}$$

where

$$G_k(t,x,y) = \frac{1}{1 - \left\{1 - \left[G_0(x,y)\right]^{-1}\right\} \exp\left[-F_k(t,x,y)/F_{\text{sat}}\right]}, \tag{2}$$

$$F_k(t,x,y) = \int_{t_0}^{t} \beta \cdot I_{k-1}(t',x,y)\,\mathrm{d}t', \tag{3}$$

where G_0 is the small-signal gain of the laser disk, F_{sat} is the saturation fluence, and a per-disk-surface loss factor β is included in the model to account for passive losses. The integral in Eq. (3) is taken in the frame of the laser pulse from the starting time of the pulse, t_0, up to the time t within the pulse. Following the repeated application of Eqs. (1)–(3) through the entire beamline, frequency conversion to the third harmonic uses look-up tables from *MIXER* calculations.[29,30] For backward prediction starting with the UV beam profile, pulse shape, and energy, these tables provide the amplified IR intensity at the end of the beamline from which the beamline input intensity is recursively calculated using Eqs. (4)–(6):

$$I_k(t,x,y) = I_{k+1}(t,x,y) \big/ \beta^2 \cdot G_k(t,x,y), \tag{4}$$

$$G_k(t,x,y) = 1 + \left[G_0(x,y) - 1\right]\exp\left[-F_k(t,x,y) \big/ F_{\text{sat}}\right], \tag{5}$$

$$F_k(t,x,y) = \int_{t_0}^{t} \left[I_{k+1}(t',x,y) \big/ \beta\right] \mathrm{d}t', \tag{6}$$

where $I_k(t,x,y)$ is the *input* intensity of the kth disk. The effective saturation fluence of the OMEGA EP beamline has been inferred from prior fits to gain-saturation data and takes into account an inhomogeneous broadening effect in the laser glass[31] and bottle-necking of the terminal level of the lasing transition for pulse widths close to the terminal-level lifetime τ_{10}, where $\tau_{10} \sim 0.25$ ns for Nd-doped phosphate laser glasses.[32,33]

Comparison of Experimental and Model Data

Spatial and temporal simulations in both forward and backward directions are in excellent agreement with measurements, as shown in Figs. 2 and 3.

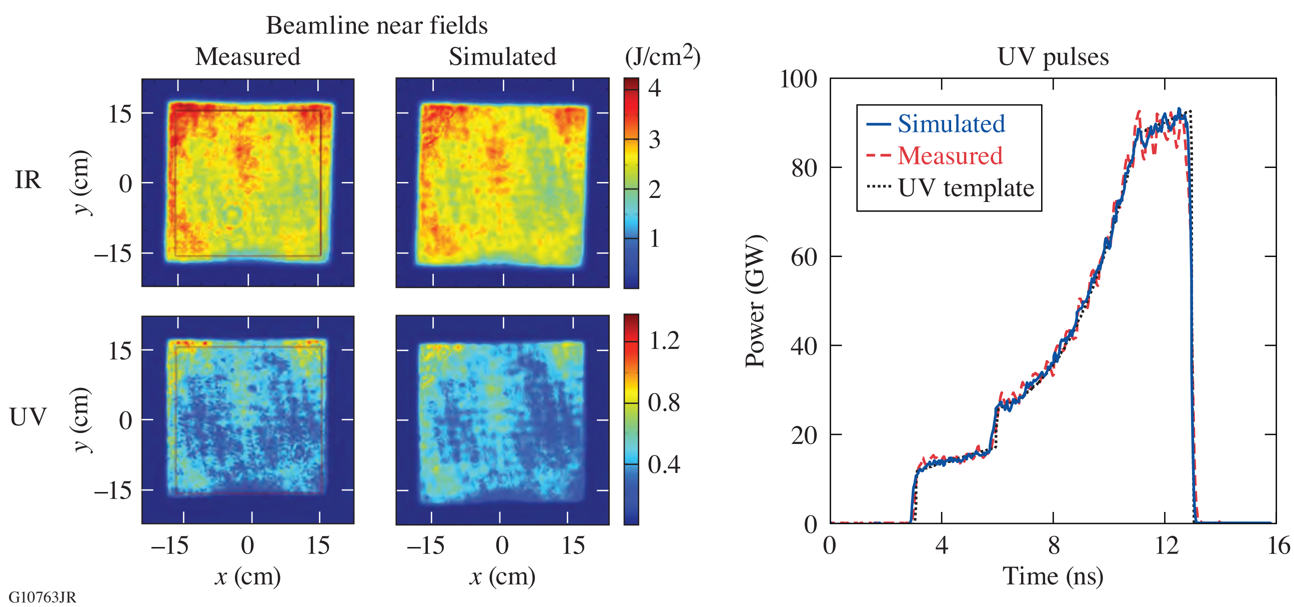

Figure 2
Comparison of *PSOPS* forward-simulated beam near fields, pulse shapes, and corresponding energies with measurements for Beamline 3, shot 20678. The forward simulation used the measured injected beam profile, pulse shape, and energy for shot 20678. IR: 3112 J measured; 3102 J simulated. UV: 453 J measured, 452 J simulated.

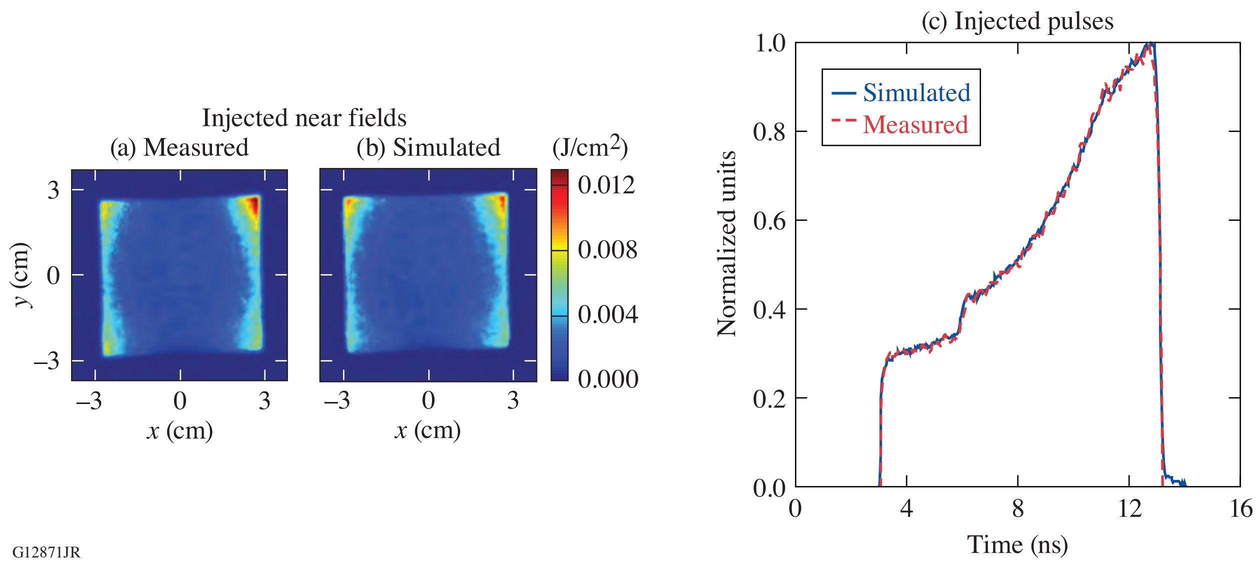

Figure 3
Comparison of *PSOPS* backward-simulated injected near-field beam profile, pulse shape, and energy with measurements for Beamline 3, shot 20678: (a) 79.5 mJ measured and (b) 76.9 mJ simulated. The backward simulation used the measured UV beam, pulse shape, and energy.

OMEGA EP Enhancements Enabled by *PSOPS*

1. Improvements to UV Energy and Pulse-Shape Accuracy

Drifts in system performance can lead to noticeable deviations between simulated and achieved pulse shapes and energies, which can be minimized with an agile system model such as *PSOPS*. For example, Fig. 4 shows how the injected pulse shape can be optimized for small changes in system performance. Figure 4(a) shows a pre-shot prediction on shot day that departs from the ideal pulse shape near the end of the pulse. Based on this prediction, the input pulse shape was modified to provide the compensated pre-shot prediction shown in Fig. 4(b). The post-shot UV simulation showed excellent agreement with the measurement [Fig. 4(c)].

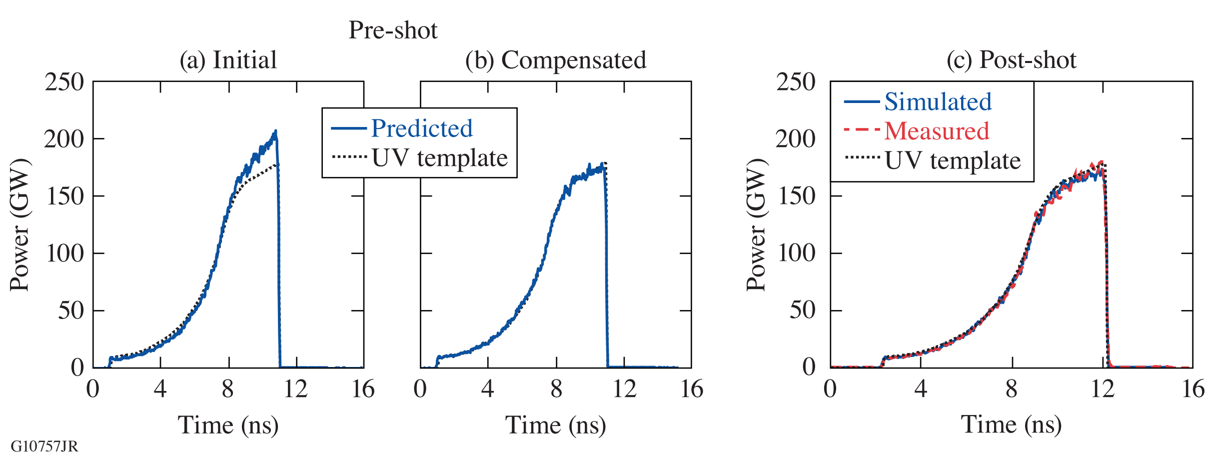

Figure 4
Predicted and requested UV pulse shapes showing how day-to-day changes in laser system performance are compensated using *PSOPS* predictions: (a) initial; (b) compensated; and (c) post-shot UV pulse simulation and measurement. On-target UV energy: 775 J requested, 751 J measured, 752 J simulated.

2. Improvements to Experimental Flexibility

PSOPS has also enhanced laser facility flexibility by enabling users to adjust requested UV pulse shapes and energies between laser shots, within a predefined range that is determined uniquely for each experimental campaign. The allowed range of energy and pulse-shape modification is assessed with respect to the laser system's fluence limits, the range of energy and pulse shapes planned for the day, and the likelihood of maintaining each beamline's 90-min shot cycle. In the example shown in Fig. 5, different energies were desired while maintaining the original normalized design pulse shape that produced 500 J of UV on-target energy. This request was accommodated in each case by adjusting the front-end pulse shape and throttles per the *PSOPS* pre-shot prediction.

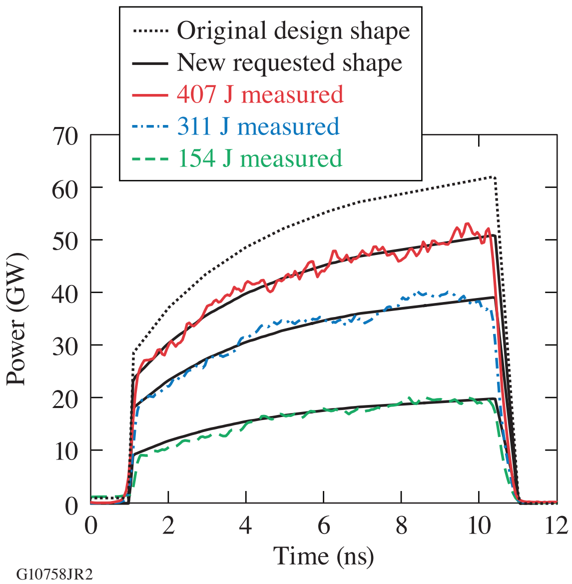

Figure 5
Example showing facility flexibility enabled by *PSOPS*. Based on a user's real-time analysis of experimental data, different energies were requested while maintaining the original normalized design pulse shape that produced 500-J on-target energy. The measured UV on-target energies are shown in the label.

3. Increased Effective Pulse-Duration Range

Currently, OMEGA EP can accommodate single-beamline pulse widths of up to 10 ns. However, improved system modeling in conjunction with precision timing allow the technique of pulse stitching to achieve up to a 4× increase in effective pulse duration. With pulse stitching, as illustrated in Fig. 6, pulse shapes from different beamlines can be precisely combined on target to form

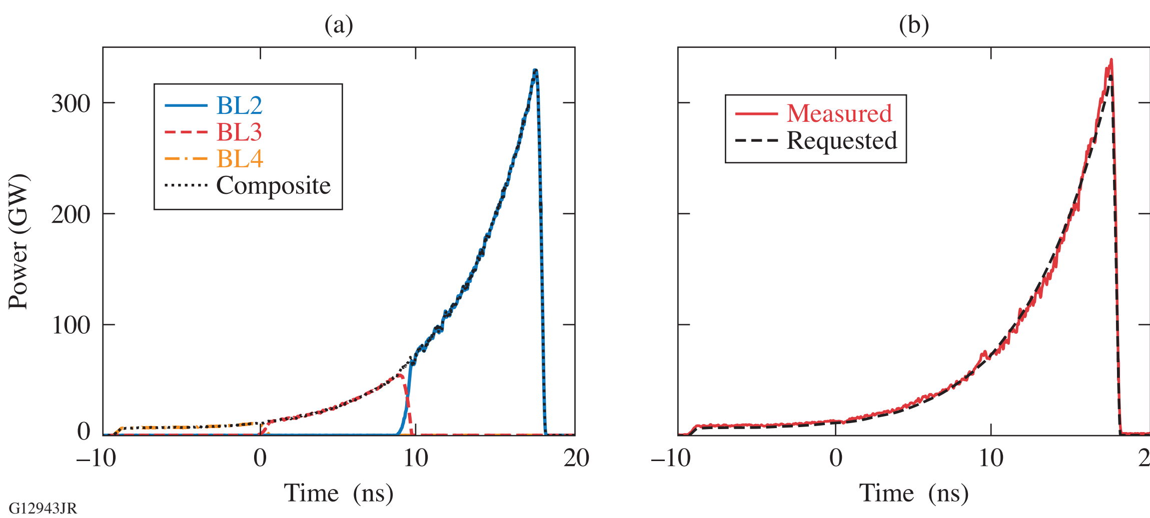

Figure 6
(a) Pre-shot prediction and (b) post-shot measurement of approximately 27-ns composite pulse shape formed by incoherent addition of the individual beamline pulse shapes and beam-to-beam timing (shot 31182).

a single composite pulse shape. In Fig. 6, the composite 27-ns ramped pulse shape shown was formed by incoherent addition of the individual pulses, separated by the temporal delay between them. Prior to the shot, *PSOPS* is used to predict the composite pulse given the specified beam-to-beam temporal delay [Fig. 6(a)]. The measured composite pulse shown in Fig. 6(b) was formed using the individual-beamline pulse-shape measurements and the measured beam-to-beam UV pulse timing.

4. Improved System Alignment

PSOPS has been used as a tool to optimize the alignment of beam-shaping apodizers[34] in the beamline front end. *PSOPS* predictions of the effect of small changes in beam centering and rotation on the amplified near-field beam uniformity can be used as a guide in the optimization of the apodizer alignment without requiring amplified shots. This has resulted in a better understanding of required tolerances for centering and rotation of both the beam-shaping apodizer and the apodized injected beam with respect to the gain profile of the beamline. As an example, Fig. 7 shows the measured effect that identifying and correcting a small error in apodizer alignment has on the amplified IR near-field beam. Using the measured injected near-field beam, *PSOPS* forward simulations were used to predict the amplified beamline output near-field profile and to correct the apodizer's alignment with respect to the gain profile of the beamline within a 10-min shot cycle. A 0.49-mm shift of the apodizer resulted in significantly improved beamline output near-field contrast and peak-to-mean fluence, as shown in Fig. 7(b). Contrast is defined as the standard deviation of the fluence divided by the mean fluence value. By limiting near-field beam fluence, fluence-limited damage may be avoided, leading to enhanced energy performance. In addition, these simulations have demonstrated that small adjustments to apodizer alignment are often sufficient to correct near-field beam nonuniformity in lieu of designing and manufacturing new apodizers.

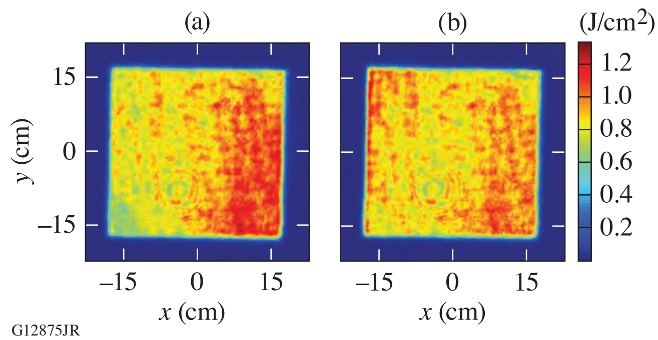

Figure 7
Measured Beamline 3 amplified IR output near-field profile (a) before moving the beam-shaping apodizer (contrast = 13.1%, peak-to-mean = 1.46:1) and (b) after moving the apodizer by 0.49 mm (contrast = 9.4%, peak-to-mean = 1.43:1). Contrast is defined in the text. The apodizer adjustment was guided by *PSOPS* simulations.

Summary

PSOPS is a semi-analytic model that is used on OMEGA EP to predict pulse shapes, stage energies, and near-field beam profiles in both forward and backward directions and has enabled accurate and rapid optimization of the laser system's performance within a small fraction of the OMEGA EP 90-min shot cycle. *PSOPS* is the key enabler of an automated capability to compute and specify the laser system's stage energies and corresponding system configurations prior to each OMEGA EP shot based upon evolving on-target pulse shape and energy requirements. The ability to calibrate the model between laser shots accounts for day-to-day system drifts without loss of shot time. Several facility enhancements have been enabled by *PSOPS*, such as improvements to UV energy and pulse-shape accuracy, improvements to experimental flexibility, increased effective pulse-duration range, and improved system alignment. An upgrade to the model currently in progress accounts for the spectral dependence of beamline gain and saturation fluence for shots that require spectrally tunable UV on-target irradiation to mitigate cross-beam energy transfer.[35]

This material is based upon work supported by the Department of Energy National Nuclear Security Administration under Award Number DE-NA0003856, the University of Rochester, and the New York State Energy Research and Development Authority.

1. S. X. Hu *et al*., Phys. Plasmas **25**, 082710 (2018).
2. D. Cao *et al*., Phys. Plasmas **25**, 052705 (2018).
3. J. Trela *et al*., Phys. Plasmas **25**, 052707 (2018).
4. A. Bose *et al*., Phys. Plasmas **25**, 062701 (2018).

5. M. Millot *et al*., Nature **569**, 251 (2019).

6. D. N. Polsin *et al*., Phys. Plasmas **25**, 082709 (2018).

7. D. N. Polsin *et al*., Phys. Rev. Lett. **119**, 175702 (2017).

8. M. C. Gregor *et al*., Phys. Rev. B **95**, 144114 (2017).

9. D. E. Fratanduono *et al*., Phys. Rev. B **97**, 214105 (2018).

10. R. F. Smith *et al*., Nat. Astron. **2**, 452 (2018).

11. F. Coppari *et al*., Nat. Geosci. **6**, 926 (2013).

12. K. R. P. Kafka, S. Papernov, and S. G. Demos, Opt. Lett. **43**, 1239 (2018).

13. M. J. Shaw *et al*., Opt. Eng. **43**, 2885 (2004).

14. M. J. Shaw *et al*., Proc. SPIE **5178**, 194 (2004).

15. R. A. Sacks *et al*., J. Phys.: Conf. Ser. **112**, 032024 (2008).

16. M. Shaw *et al*., J. Phys.: Conf. Ser. **112**, 032022 (2008).

17. D. I. Hillier, D. N. Winter, and N. W. Hopps, Appl. Opt. **49**, 3006 (2010).

18. B. J. Le Garrec and O. Nicolas, J. Phys.: Conf. Ser. **112**, 032019 (2008).

19. D. Hu *et al*., Chin. Opt. Lett. **13**, 041406 (2015).

20. K. T. Vu *et al*., Opt. Express **14**, 10,996 (2006).

21. W. Shaikh *et al*., *Central Laser Facility Annual Report 2005/2006*, 199, Rutherford Appleton Laboratory, Chilton, Didcot, Oxon., England (2005).

22. K. P. McCandless *et al*., in *Proceedings of the 14th International Conference on Accelerator & Large Experimental Physics Control Systems (ICALEPCS 2013)*, edited by C. Marshall, J. Fisher, and V. R. W. Schaa (The Joint Accelerator Conferences Website, Geneva, Switzerland, 2014), pp. 1426–1429.

23. MATLAB® R2013b, The MathWorks Inc., Natick, MA 01760-2098.

24. J. H. Kelly *et al*., J. Phys. IV France **133**, 75 (2006).

25. J. R. Marciante, W. R. Donaldson, and R. G. Roides, IEEE Photonics Technol. Lett. **19**, 1344 (2007).

26. *LLE Review Quarterly Report* **63**, 110, Laboratory for Laser Energetics, University of Rochester, Rochester, NY, LLE Document No. DOE/SF/19460-91 (1995).

27. W. R. Donaldson *et al*., Rev. Sci. Instrum. **73**, 2606 (2002).

28. A. E. Siegman, in *Lasers* (University Science Books, Mill Valley, CA, 1986), Chap. 10.

29. R. S. Craxton, Opt. Commun. **34**, 474 (1980).

30. R. S. Craxton, IEEE J. Quantum Electron. **QE-17**, 1771 (1981).

31. D. M. Pennington, D. Milam, and D. Eimerl, Proc. SPIE **3047**, 630 (1997).

32. C. Bibeau, J. B. Trenholme, and S. A. Payne, IEEE J. Quantum Electron. **32**, 1487 (1996).

33. C. Bibeau and S. A. Payne, 119, Lawrence Livermore National Laboratory, Livermore, CA, Report UCRL-LR-105820-95 (1996).

34. C. Dorrer and J. Hassett, Appl. Opt. **56**, 806 (2017).

35. B. E. Kruschwitz *et al*., Proc. SPIE **10898**, 1089804 (2019).

Toward the Reduction of Transverse Stimulated Raman Scattering in KDP/DKDP Crystals

H. Huang, T. Z. Kosc, S. G. Demos, and T. J. Kessler

Laboratory for Laser Energetics, University of Rochester

Transverse Raman generation and amplification in KDP/DKDP limit the laser power level in laser fusion systems. To properly understand the propagation and amplification of light in a birefringent crystal, a full vector model of the pump and scattering fields is required. We present a ray-tracing approximation that enables one to calculate the Raman fluence at the surface of an arbitrary crystal and pump polarization configurations. This allows one to determine the optimal configuration that minimizes the fluence peaks at the crystal edge.

Raman photons can be generated by the strong laser field (the pump) in a piece of thin crystal placed perpendicular to the path of the pump (Fig. 1). Depending on the crystal symmetry and orientation, such a signal may have significant accumulated gain when traveling parallel to the plate due to the long length of travel inside the crystal. Such transverse Raman rays have the potential to gain more energy than those parallel to the pump direction that have less distance for amplification.

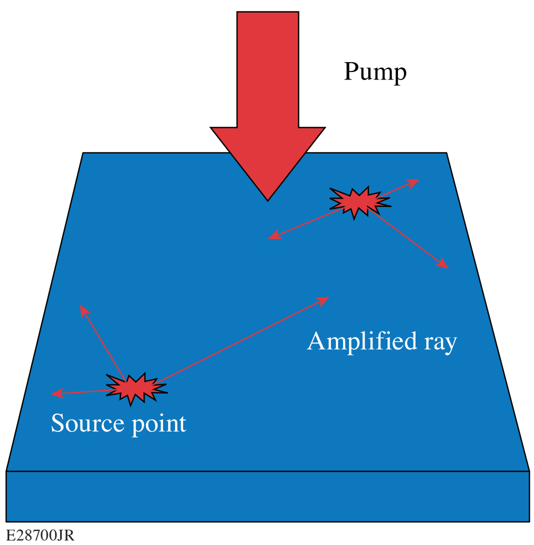

Figure 1
The pump laser excites spontaneous Raman photons in a laser crystal. The Raman is amplified as it propagates in the crystal.

The distribution of the transverse stimulated Raman scattering (TSRS) fluence at the crystal surface is not uniform. It depends on the pump laser and crystal configurations. The fluence at a surface point is the sum of all the amplified rays that arrive at this location. To calculate such fluence requires ray tracing of each such ray over the path from the spontaneous emission source point to the surface point. This requires a rigorous treatment of the ray propagating in a birefringence crystal.

The starting point of our modeling is to break each ray into the normal modes of electromagnetic waves, i.e., the o and e polarizations; similarly the pump is also broken into o and e polarizations. The Raman gain can therefore be treated as the combination of interactions between these normal modes.

An efficient code was developed following the picture of basic physics shown in Fig. 2. We were able to calculate the fluence distribution at the crystal surface for any laser and crystal configuration, including the crystal thickness and beveled-edge angle. From these calculations we can estimate the maximum laser intensity without damaging the crystal and mount, providing a guideline for the optimized crystal configuration. For example, in Fig. 3 we can see the worst-case intensity depends on the pump polarization. By selecting the correct crystal cut direction, the worst-case intensity at the crystal plate edge can be reduced.

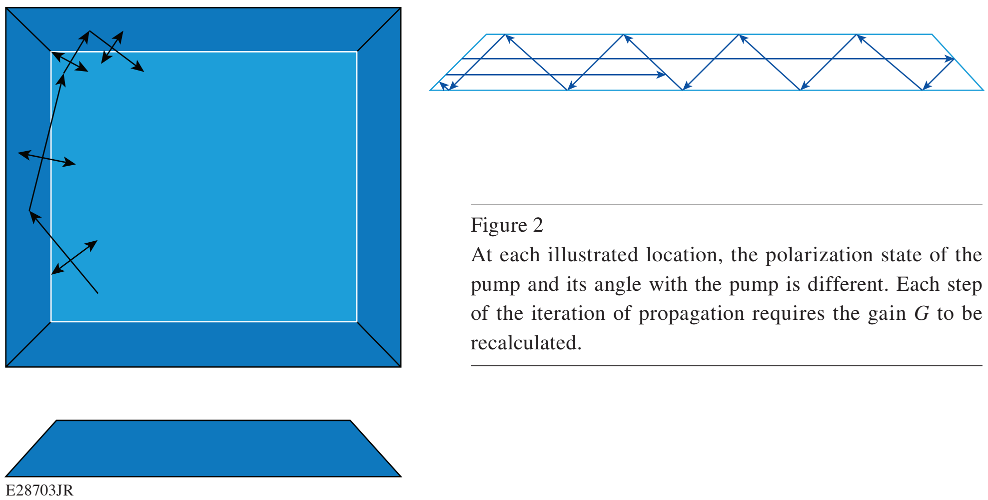

Figure 2
At each illustrated location, the polarization state of the pump and its angle with the pump is different. Each step of the iteration of propagation requires the gain G to be recalculated.

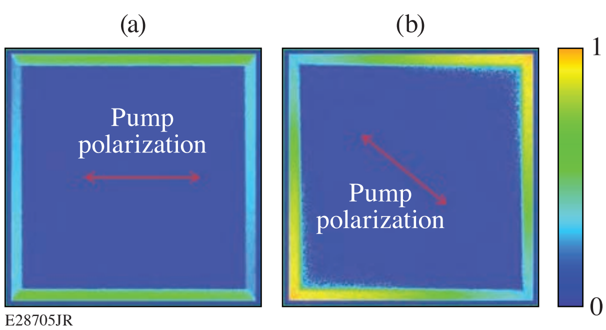

Figure 3
These plots show that the Raman distribution at the crystal surface depends on the pump polarization. (a) Pump polarization normal to the optic axis. (b) Pump polarization at an angle to the optical axis.

In summary, TSRS in laser crystal is a phenomenon we cannot completely avoid but we can find solutions to reduce the worst-case fluence at the crystal edge to avoid component damage. The key to finding such solutions is to distribute the Raman energy incoherently over polarizations and directions. The ray-tracing methods we developed provide a better understanding about how the evolution of polarization states in the crystal affect the TSRS and are a versatile tool to optimizing the design of KDP/DKDP optics including the distributed polarization rotator.

This material is based upon work supported by the Department of Energy National Nuclear Security Administration under Award Number DE-NA0003856, the University of Rochester, and the New York State Energy Research and Development Authority.

Investigation of Parameters Governing Damage Resistance of Nematic Liquid Crystals for High-Power or Peak-Intensity Laser Applications

T. Z. Kosc, A. A. Kozlov, S. Papernov, K. R. P. Kafka, S. G. Demos, and K. L. Marshall

Laboratory for Laser Energetics, University of Rochester

The damage resistance of saturated and unsaturated liquid crystals (LC's) under a wide range of laser excitation conditions, including 1053-nm pulse durations between 600 fs and 1.5 ns and nanosecond pulse excitation at 351 nm and 532 nm, has been investigated. This multiwavelength investigation probed the correlation between the electronic structure of each material and its laser-induced damage behavior by altering the excitation photon energy. The laser-induced damage threshold at all wavelengths and pulse durations was consistently higher in saturated materials than in their unsaturated counterparts.

The electronic excitation pathways in LC materials are generally known and involve a singlet ground state (S_0) and excited singlet (S_1, S_2,…S_n) and triplet states. The time scale of the transition from the singlet states to the corresponding triplet states during relaxation, or intersystem crossing, is typically >1 ns, which has been confirmed for several unsaturated LC compounds.[1,2] Because the excitation leading to laser-induced damage (breakdown) occurs during the laser pulse, transitions with lifetimes longer that the pulse duration (in our case ~1 ns) have no (or minimal) effect on laser-damage mechanisms. Consequently, we consider only the transitions between the singlet states. The accordingly modified Jablonski energy diagram in Fig. 1 describes the electronic structure in LC materials involving singlet ground state (S_0) and excited singlet (S_1, S_2,…S_n), where the energy levels are defined as multiples of the energy of a 1ω photon used in this study.

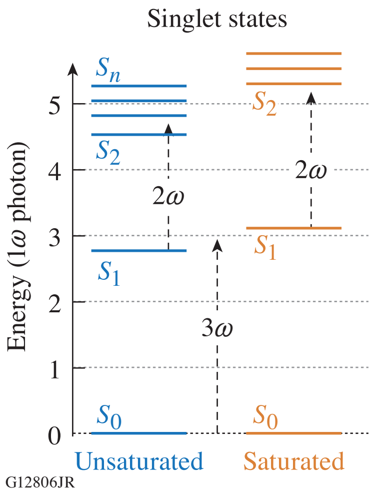

	Number of photons required to bridge the lowest excited state S_1		
Wavelength (photon energy)	351 nm (3.35 eV)	527 nm (2.36 eV)	1053 nm (1.18 eV)
Unsaturated	1	2	3
Saturated	2	2	4

Figure 1
A schematic depiction of the electronic transitions leading to laser-induced breakdown in LC materials is presented by a modified Jablonski energy diagram involving a singlet ground state (S_0) and excited singlet states (S_1, S_2,…S_n). The energy levels are referenced as multiples of a 1053-nm photon (1ω). The UV transmission edge for each material (saturated < 351 nm < unsaturated) provides insight into the order of photon absorption required to bridge the energy gap from $S_0 \longrightarrow S_1$.

The relative difference in the measured laser-induced–damage threshold (LIDT) at different wavelengths is illustrated in Fig. 2 showing the *N*-on-1 LIDT results for both saturated and unsaturated materials at all wavelengths. Comparison of the 351-nm and 527-nm results shows a difference between LIDT values of ~5× for unsaturated materials and only of ~1.5× for saturated materials. This behavior can be anticipated from the order of absorption required for electrons to undergo the $S_0 \longrightarrow S_1$ transition. Specifically, unsaturated materials require both linear absorption at 351 nm and two photon absorption at 527 nm, while for saturated materials, two-photon absorption is necessary to populate the first excited state at both wavelengths. This key difference in the electronic excitation process is reflected in the corresponding difference in the LIDT values.

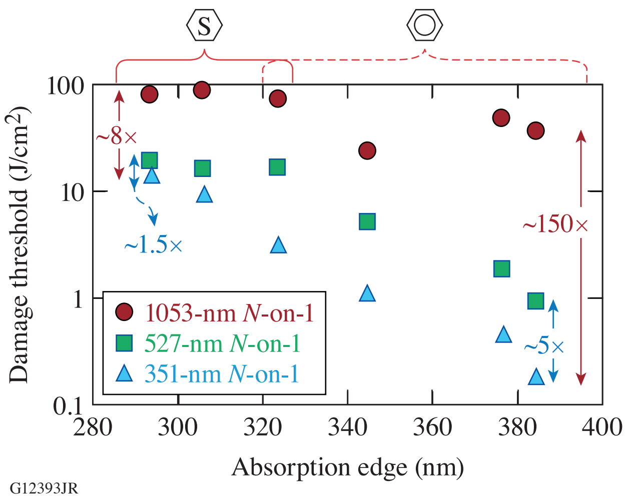

Figure 2
The *N*-on-1 LIDT values for nanosecond pulses at all three wavelengths (and 1-ns pulses) as a function of each material's absorption edge allows direct comparison of the relative differences in LIDT. The LC's investigated and their apsorption edge, as defined by $T = 98\%$, include: 1550C (294 nm), MLC-2037 (306 nm), ZLI-1646 (324 nm)PPMeOB/PPPOB (345 nm), 5CB (377 nm), and E7 (385 nm). Brackets identify saturated, unsaturated, and mixed materials. The symbols S and ○ are used to designate saturated and unsaturated materials, respectively.

Comparing LIDT results obtained under 351-nm and 1053-nm excitation, the difference in LIDT for unsaturated materials is ~150×, but only ~8× for saturated materials. The dramatic variation in LIDT differences for the two material types is arguably related to the different order of the absorption process required for the $S_0 \longrightarrow S_1$ transition. The order changes from linear absorption to a three-photon absorption process in unsaturated materials, while for saturated materials, a nonlinear process is required at both wavelengths (two-photon and four-photon processes for 351-nm and 1053-nm excitation, respectively). These results demonstrate the importance of the electronic structure of each material on the observed damage threshold and as a function of photon energy.

In summary, the experimental data suggest that key components in the laser-induced damage mechanisms in LC's involve a complex interplay of both multiphoton absorption and excited-state absorption, where their relative contributions vary with wavelength. Future work will concentrate on extending and applying these findings to both glassy and polymer LC materials systems and developing improved passive and active devices that offer polarization, phase, and intensity control for high-peak-power and average-power laser applications.

This material is based upon work supported by the Department of Energy National Nuclear Security Administration under Award Number DE-NA0003856, the University of Rochester, and the New York State Energy Research and Development Authority.

1. R. Sander, V. Herrmann, and R. Menzel, J. Chem. Phys. **104**, 4390 (1996).

2. G. E. O'Keefe *et al.*, Liq. Cryst. **21**, 225 (1996).

Glancing-Angle–Deposited Silica Films for Ultraviolet Wave Plates

S. MacNally, C. Smith, J. Spaulding, J. Foster, and J. B. Oliver

Laboratory for Laser Energetics, University of Rochester

Glancing-angle deposition (GLAD) is a coating process where the incident vapor condenses on a substrate oriented at a high incidence angle θ relative to the substrate normal, forming microscopic nuclei (experimental setup is shown in Fig. 1). Self-shadowing occurs at this high angle, shaping the nuclei into individual columns that tilt toward the vapor source.[1] These anisotropic structures create birefringence in the film, allowing for the creation of wave plates when depositing a film of the proper thickness.

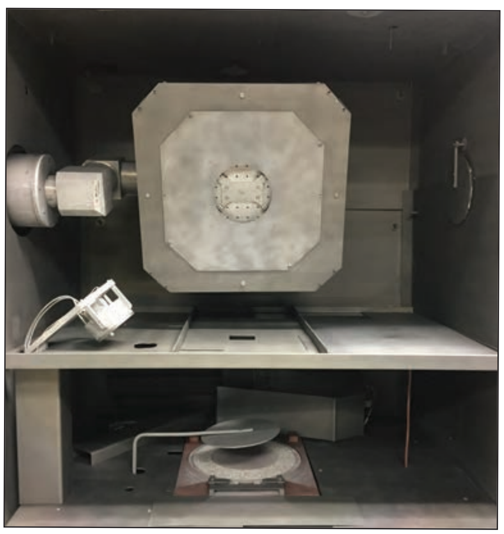

G12902JR

Figure 1
Angstrom Engineering GLAD stage mounted in a 1.2-m vacuum chamber. Each coating deposition included a 100-mm-diam fused-silica substrate or two 50-mm-diam substrates: a silicon wafer and a fused-silica witness sample. Substrates remain in the center of the stage as it flips to the programmed $\pm\theta$. An electron-beam gun is mounted directly below the aperture, and an Inficon Crystal 12 sensor is mounted on the side to measure the deposition rate/thickness.

With a lack of shadowing in the substrate tilt-axis direction, there is a progressive fanning of the column cross section along with a chaining together of adjacent columns, which can lead to greater light scattering in the film. To reduce this column broadening and limit scatter, an all-silica, multilayer GLAD structure was implemented. Alternating layers of birefringent and dense SiO_2 were deposited during a single-coating deposition by alternating the substrate angle (0° for the dense layers and 73° for the birefringent layers). The number of birefringent and dense groupings was based on the desired retardance value for a quarter- or half-wave plate at a wavelength of 351 nm. Dense layers provide a base for the growth of a new birefringent layer and were inserted throughout the coating at intervals less than 400 nm since the width of individual silica columns was found to increase only beyond that thickness.[2] An antireflective coating was then added as a final layer in the design, which consisted of a single GLAD layer deposited at 82°.

The refractive indices and thickness of each layer in the design had to be precisely calibrated with a Woollam variable-angle spectroscopic ellipsometer (VASE®) since these values change with substrate deposition angle and deposition time.[3] Scanning electron microscope (SEM) and spectrophotometer measurements were also used to corroborate the index and thickness data.

Photometric performance was evaluated using a 351-nm laser and a 4-in. integrating sphere with a silicon detector. The quarter-wave plate exhibited a reflectance of 3.9% and a transmittance of 95.8%, yielding a loss of 0.3%, while the half-wave plate exhibited a reflectance of 4.2% and a transmittance of 95.3%, yielding a loss of 0.5%. Both reflectance measurements include the uncoated back surface of the substrate. This multilayer design helped to decrease scatter loss compared to previous SiO_2 single-layer coating runs (with an optical scatter loss of 10% to 15%) (Ref. 4). SEM and spectrophotometer measurements for a multilayer quarter-wave plate are shown in Fig. 2.

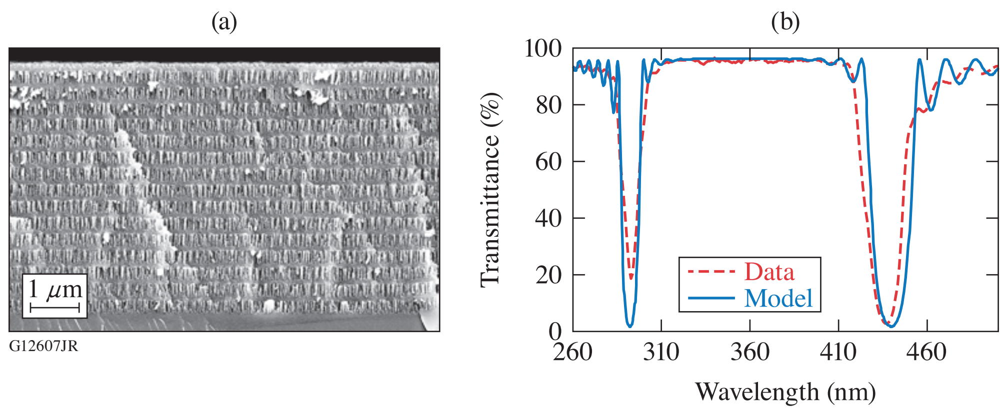

Figure 2
(a) SEM image of a 31-layer quarter-wave–plate coating. (b) Theoretical transmittance through the quarter-wave design with back-side reflection (solid blue curve) overlaid with spectrophotometer data (dashed red curve).

The multilayer design also helped to limit scatter loss over time. Eight months after deposition, the scatter detected in single-layer quarter- and half-wave–plate samples increased 16% and 48%, respectively, while the scatter increase in multilayer wave plates remained under 1% (as shown in Fig. 3).

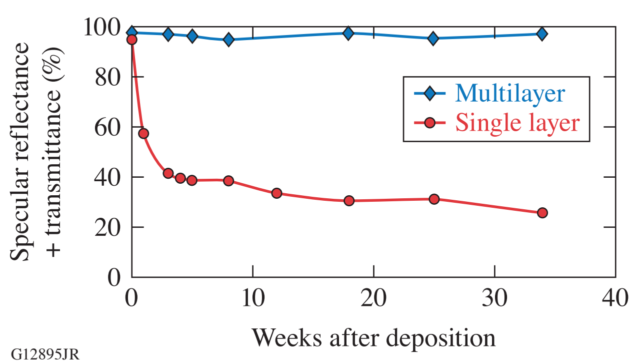

Figure 3
Scatter measurements for a single-layer and multilayer half-wave plate. Eight months after deposition, multilayer scatter has remained approximately the same and single-layer scatter has increased 48%.

Retardance was measured with a Hinds Instruments Exicor® 450XT Mueller Matrix Polarimeter and found to be uniform across all 50-mm and 100-mm samples. The wave plates also exhibited a high laser-induced–damage threshold (LIDT). The LIDT for a multilayer quarter-wave–plate coating, performed on polished fused silica processed with an "advanced mitigation process," was found to be 12.51±0.51 J/cm^2 in a 1:1 testing protocol and 36.31±3.74 J/cm^2 in an *N*:1 testing protocol. This is an improvement from previous silica single-layer LIDT measurements (~11 J/cm^2 in both a 1:1 and *N*:1 testing protocol).[4]

In the future, we hope to deposit these multilayer wave plates on larger substrates (up to ~400 mm in diameter), while maintaining the same low-loss, high-LIDT, wide-design bandwidth achieved with this current experiment.

This material is based upon work supported by the Department of Energy National Nuclear Security Administration under Award Number DE-NA0003856, the University of Rochester, and the New York State Energy Research and Development Authority.

1. M. M. Hawkeye, M. T. Taschuk, and M. J. Brett, *Glancing Angle Deposition of Thin Films: Engineering the Nanoscale*, Wiley Series in Materials for Electronic & Optoelectronic Applications (Wiley, Chichester, United Kingdom, 2014), pp. 6,7, 53–60, 237–240.

2. L. Grinevičiūtė *et al*., Phys. Stat. Sol. A **214**, 1770175 (2017).

3. C. Smith, S. MacNally, and J. B. Oliver, "Modeling of Serially Bi-Deposited Glancing-Angle–Deposition Coatings," to be published in Applied Optics.

4. J. B. Oliver *et al*., Opt. Express **22**, 23,883 (2014).

Stress Compensation by Deposition of a Nonuniform Corrective Coating

J. B. Oliver, B. Charles, and J. Spaulding

Laboratory for Laser Energetics, University of Rochester

Thin-film stresses distort the surface flatness of a coated optic in a convex or concave manner for compressive or tensile films, respectively. While traditional evaporated optical coatings typically lead to the formation of low-magnitude tensile stresses, more-energetic processes such as ion-beam sputtering,[1] magnetron sputtering,[2] and plasma-ion–assisted deposition[3] generally form highly compressive films with significant distortion of the optical surface. Such stress-induced curvature can be mitigated by using thicker substrates, coating the back surface of the optic to yield an equivalent deformation in the opposite direction,[4] or by prefiguring the optic surface to counteract the effects of the film stress.[5] These modifications can be costly, while process modifications to alleviate highly compressive stresses often lead to porous, environmentally unstable films.

A unique approach was developed to prefigure the optic surface by depositing a radially nonuniform film using the same deposition process as the optical coating. The corrective coating is deposited beneath the functional optical coating, on the same surface of the substrate, with a thickness profile designed using finite-element analysis to correct for the anticipated surface-flatness deformation resulting from the eventual optical coating deposition from the as-fabricated flat substrate surface. This approach is depicted in Fig. 1.

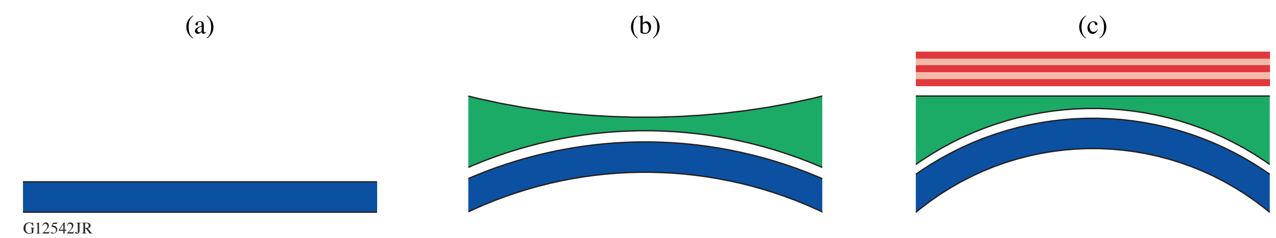

Figure 1
Mitigation of a high compressive film stress by deposition of a gradient compensation layer is illustrated, with (a) the as-fabricated flat substrate; (b) the addition of a compressive, radially graded layer leading to a concave surface, even though the substrate has been deflected in a convex manner; and (c) the combination of the gradient compensation layer and the optical coating leading to a nominally flat coated surface.

This method was used to compensate the stress-induced deformation of a 3.3-μm-thick optical coating on a 100-mm-diam × 3-mm-thick fused-silica substrate. The coating was deposited using plasma-ion–assisted electron-beam evaporation, with alternating layers of hafnium dioxide and silicon dioxide. The calculated compensation layer consisted of a gradient-thickness silica layer with zero physical thickness at the optic center and increasing in a cubic manner to a thickness of approximately 6.7 μm at the edge. The graded coating was fabricated by depositing the corrective layer directly on the substrate through a mask centered on the rotating optic. The mask blocked all deposition flux from reaching the center of the optic, then gradually increased the open space and corresponding thickness, in a cubic manner, until the full thickness was reached at the optic edge. For the purposes of this proof-of-concept demonstration, the chamber was then vented, the mask removed, and the system evacuated once again in order to deposit the multilayer (non-graded) optical coating. Surface-flatness measurements were taken at each stage of the deposition process to quantify the changes from the individual process steps. To implement this in a production process, the mask insertion/removal would be automated while the chamber remains under vacuum.

Surface-flatness measurements were performed using a Zygo Verifire 633-nm interferometer of the uncoated substrate, the substrate with the gradient compensation layer, and the finished component after deposition of both the compensation layer and the multilayer mirror. To improve surface-flatness measurement accuracy, the non-graded mirror coating was designed and fabricated with a center wavelength of 633 nm to reduce errors resulting from nonuniformity of the reflected phase of the coating. After process qualification and the development of a suitable compensation profile to yield a flat coated surface, the deformation from any uniform coating deposition could be compensated. The measurement of the uncoated substrate was removed from that of the stress-compensation layer and the overall component to evaluate only the impact of this stress-compensation approach. An additional control substrate was also included in the multilayer deposition to evaluate the anticipated deformation without the use of the compensating layer. The results are shown in Fig. 2.

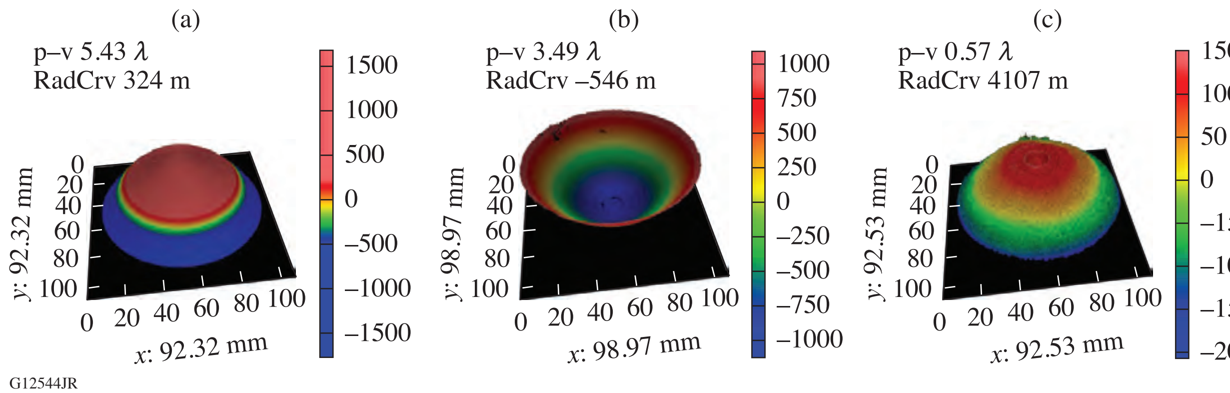

Figure 2
Change in the surface figure of a 100-mm-diam, 3-mm-thick fused-silica substrate as a result of coating with an all-dielectric mirror coating with or without a silica stress-compensation layer (as-fabricated surface flatness subtracted from all subsequent measurements). (a) The control (mirror coating only) surface figure, at 5.4 waves of deviation from flat (λ = 633 nm). (b) After coating with the silica compensation layer, the surface is 3.5 waves concave. (c) Once the high reflector coating is deposited, the combination of the two coatings results in a nominally flat optic, with the change in surface flatness ~10% of that resulting from the high reflector alone. A slightly thicker compensation layer could further improve the surface flatness. p–v: peak to valley.

The surface deformation of the coated optic with the corrective layer is reduced by nearly 90% relative to that of the coated control substrate without the graded corrective layer [Fig. 2(a) at 5.43 waves versus Fig. 2(c) at 0.57 waves at 633 nm]. It is also clear that a slight increase in the thickness of the corrective layer would further improve the surface flatness, since Fig. 2(c) is still dominated by a spherical-like term with a low edge and a high center (as would result from a compressive film stress, which is the compensation the gradient layer would provide). This stress-mitigation approach significantly reduces the deformation of an optic coated with a compressively stressed film while allowing deposition on a single substrate surface. As demonstrated, a cubic-thickness gradient silica layer can reduce the surface deformation of a compressively stressed optical coating by an order of magnitude.

This material is based upon work supported by the Department of Energy National Nuclear Security Administration under Award Number DE-NA0003856, the University of Rochester, and the New York State Energy Research and Development Authority.

1. G. W. DeBell, Proc. SPIE **5991**, 599116 (2005).
2. M. Scherer *et al*., Proc. SPIE **5963**, 596319 (2005).
3. J. B. Oliver *et al*., Appl. Opt. **50**, C19 (2011).
4. M. Bischoff *et al*., Appl. Opt. **53**, A212 (2014).
5. S. Gensemer and M. Gross, Opt. Express **23**, 31,171 (2015).

Design and Alignment of an All-Spherical Unobscured, Four-Mirror Image Relay for an Ultra-Broadband Subpetawatt Laser

E. M. Schiesser,[1,2] S.-W. Bahk,[1] J. Bromage,[1,2] and J. P. Rolland[2]

[1]Laboratory for Laser Energetics, University of Rochester
[2]Institute of Optics, University of Rochester

LLE is developing an ultra-broadband optical parametric chirped-pulse–amplified laser system.[1] This laser, the Multi-Terawatt Optical Parametric Amplifier Line (MTW-OPAL),[2] is designed to produce 7.5-J, 15-fs pulses with a 200-nm bandwidth from 810 nm to 1010 nm through multiple stages of noncollinear optical parametric amplifiers (NOPA's). Image relays between NOPA's preserve the beam quality and sequentially magnify the beam size according to its amplified energy level to keep the maximum fluence below the damage threshold. The final relay after the last NOPA stage (referred to as NOPA5 since it is the fifth amplifier) requires an all-reflective, unobscured optical relay to avoid introducing additional longitudinal chromatic aberration, also known as radial group delay (RGD).[3–5] RGD refers to the fact that refractive image relays delay the pulse in the center of the beam with respect to the pulse in the outer edge of the beam as the center beam goes through thicker material in the lens. This RGD is of the order of hundreds of femtoseconds so it is significantly larger than the ideal 15-fs design pulse width and would greatly reduce the focused intensity. The final all-reflective image relay, also referred to as an achromatic image relay (AIR), removes the longitudinal chromatic aberrations and RGD by avoiding lenses in favor of using mirrors. The AIR for NOPA5 performs two roles: it acts as a beam expander to create a 90×90-mm beam from the 45×45-mm output from NOPA5, and it relays the NOPA5 (N5) output to the fourth grating (G4) in the grating compressor chamber (GCC). These two roles must be achieved simultaneously; consequently, two sets of conjugate planes must be simultaneously realized: the "far-field" (FF) collimation planes and the "near-field" (NF) pupil imaging planes. This simultaneous dual-conjugate imaging case has been investigated for two refractive elements and four refractive elements by Wang *et al*.[6]

In optical design, there is often a trade-off between complexity and performance. Off-axis conic sections are the most obvious choice for unobscured, small-FOV (field-of-view) designs like the AIR, as we have previously reported.[7] However, it is important to understand if we can achieve our goals with simpler spherical optics since this reduces complexity and therefore the cost. Instead of field-bias or aperture offset as in an off-axis conic design, one can tilt the optical components to avoid obscuration. Buchroeder[8,9] details many examples of tilted component telescopes, some of which have only spherical components. These designs use tilted components to avoid obscuration, but the relative tilts must be chosen to balance the resulting aberrations. Steven and Dubra[10] describe the design of a two-mirror relay using tilted spherical components.

The design detailed in the present work is a four-mirror all-spherical design that tilts the mirrors to avoid obscuration. We show the theoretical basis for the correction of field-constant coma and field-constant astigmatism using two of the mirror tilts. We then show the alignment of the design in a test-bed setup.

There are nine first-order parameters for this four-mirror system: the input and output working distances, the three distances between the mirrors, and the four radii of curvature of each mirror. The magnification constraint, NF imaging requirement, and FF collimation requirement determine three of these variables. The other six variables are available to meet the layout and space requirements. To meet those requirements, the five distances are specified within a certain range based on the space constraints in the GCC, leaving only one truly free variable: the curvature of the first mirror. This variable is constrained by the stay-out zone created by the damage threshold of the mirrors, which constrains the size of the beam on the mirrors.

With the first-order parameters determined, the next step was to create an unobscured configuration. To do so, we can tilt the components appropriately; however, tilting spherical components results in aberrations. Buchroeder showed that these types of designs, known as tilted-component telescopes, can correct the aberrations caused by the tilts by appropriately tuning the tilts of the mirrors.[8,11] In addition, Rogers showed the same using the nodal aberration theory (NAT) for two and three mirrors for extended fields of view.[12] Because the FOV for the AIR is small at 0.14°, we can achieve the required correction while maintaining enough freedom in the design to keep the AIR within the space constraints of the GCC.

Given the minimum tilt angle of M1 required to remove the obscuration of M2, we can use the theoretical framework of NAT to predict the M3 and M4 tilts necessary to correct the field-constant astigmatism and field-constant coma induced from the tilts of M1 and M2. The system of equations involves two NAT aberration terms composed in terms of the sigma vectors of each surface. The sigma vectors are then related to the tilts of each surface. Because of the quadratic dependence of field-constant astigmatism on the sigma vector, there are two solutions; however, only one solution is unobscured, shown in Fig. 1. The angles from the theoretical analysis were ultimately optimized to balance the aberrations and reduce the overall rms wavefront error.

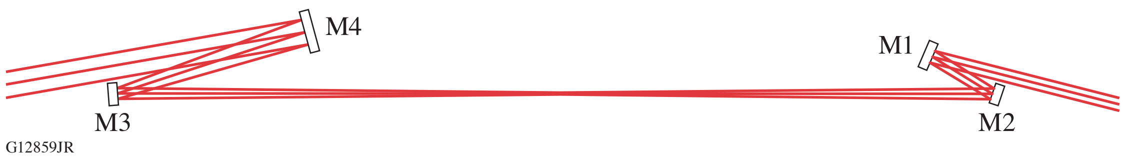

Figure 1
The final layout of the AIR mirrors, showing the ray path from the central field point.

An alignment plan for the AIR has been developed and tested. The alignment procedure consists of two stages: course alignment and fine alignment. The course alignment stage uses the arm of a precision coordinate-measuring machine (CMM) to place precision-machined pinhole jigs. The CMM arm is a FARO Gage Plus, from which we achieved of the order of 100-μm placement accuracy of the pinholes.[13] Passing a pencil beam from an alignment laser diode through the pinholes establishes a line that serves as the optical axis. Since the mirrors are spherical, guiding the pencil beam through the pinholes using tip/tilt and z travel on each mirror can be used to position the center of curvature close to the nominally designed position. All four mirrors can be coarsely aligned sequentially with this method. Tolerance analysis assuming 100-μm accuracy in the mirror placement of the AIR design shows that the coarse alignment using the pinholes is adequate to position the mirrors accurately enough such that fine alignment of M4 tip, tilt, and defocus can correct any residual defocus and astigmatism still present after course alignment. Additionally, M3 tip/tilt can be used to correct residual coma, if necessary.

To test the feasibility of the alignment plan and to troubleshoot possible difficulties before the final alignment in the GCC, we developed a test bed to replicate the *in-situ* alignment before the final system is aligned at LLE. The essential components of the test bed are a 532-nm laser diode, a custom wavefront sensor,[14] a polarizing beam splitter, a beam expander, and several planar mirrors.

The NOPA5 crystal outputs a 45 × 45-mm collimated beam. To replicate this in the test bed, we use two beam expanders as shown in Fig. 2: The first is a 4× beam expander that focuses the output of a laser diode into a 25-μm pinhole used as a spatial filter. The resulting Gaussian beam is then collimated and truncated using a square apodizer before passing through a polarizing beam splitter (PBS). The second beam expander then enlarges the beam to 45 × 45 mm. A quarter-wave plate at the focus of the 10× beam expander rotates the polarization of the return beam from vertical to horizontal to reduce spurious reflections from PBS. Additionally, an adjustable iris is used to create a pencil beam for the course alignment step. The return beam reflects off the PBS interface to a wavefront sensor and a blank mirror substrate with a wedge acting as a second beam splitter. The second return beam is directed into a focusing lens and charge-coupled–device camera used to maintain alignment.

The subsequent wavefront after the course alignment routine using the pinholes is shown in Fig. 3(a). The dominant aberration in the wavefront after the course alignment step appears to be defocused. Figure 4 shows the peak-to-valley (p–v) and rms

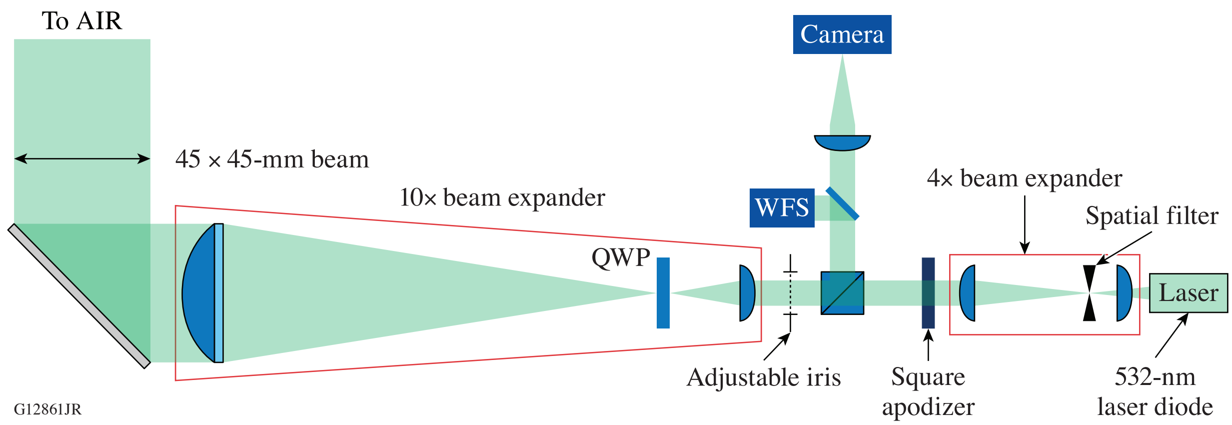

Figure 2
The test-bed components to produce a 45 × 45-mm beam and to measure the return wavefront. QWP: quarter-wave plate; WFS: wavefront sensor.

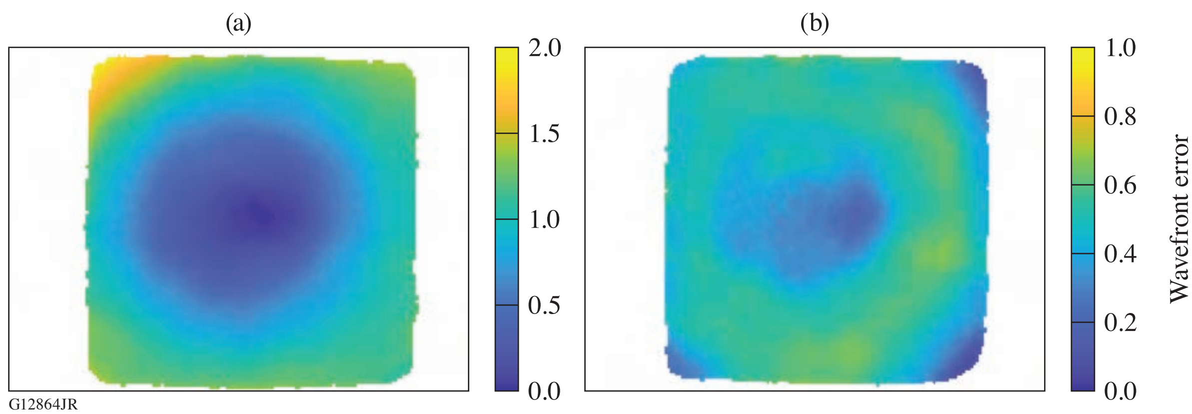

Figure 3
The double-pass wavefront given in waves at 532 nm for (a) after the course alignment step and (b) after the fine alignment steps. Note that the color scale ranges from [0,2] waves for (a) and from [0,1] waves for (b).

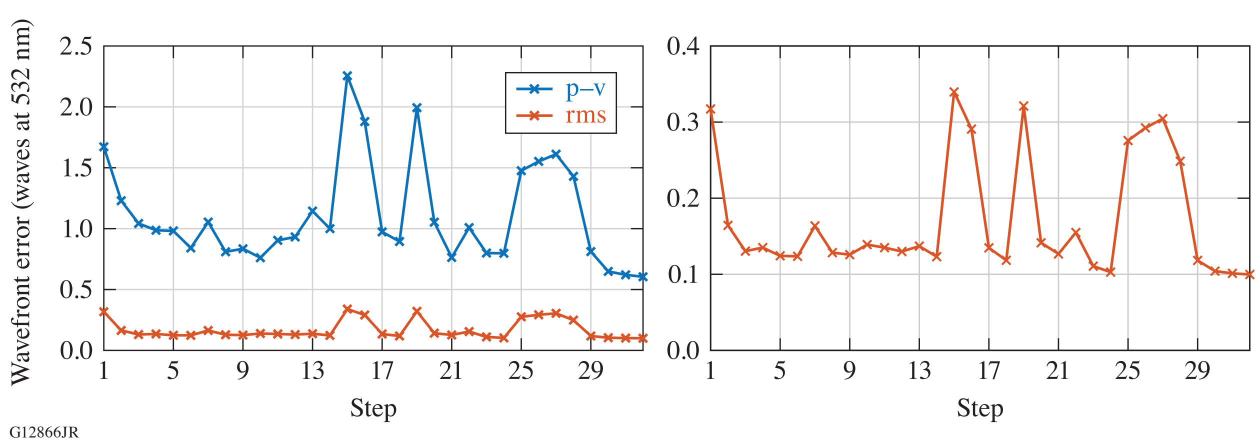

Figure 4
(a) The p–v and rms values of the wavefront at each step; (b) the rms WFE values of the wavefront at each step.

wavefront error (WFE) of the wavefront at each step in the fine alignment process. This defocus was more than predicted by the tolerances of the CMM coarse alignment stage—a clue to another issue that will be addressed later.

Figure 3(b) shows the measured wavefront error after fine alignment. There is residual spherical aberration, as predicted by the ray-tracing model. Additionally, there is still some coma (Z7/8) present and higher-order modes are also becoming dominant. Since we reached the desired p–v and rms WFE targets, however, we stopped the alignment process. With the aid of the program used to decompose the wavefront and predict the adjustments, the fine alignment routine can be completed in less than 1 h. After completing fine alignment, the resulting wavefront p–v at 532 nm was 0.61 waves and the rms WFE was 0.10 waves in double pass. Applying the reduction factor of 3.42 to the measured wavefronts in Fig. 3, we have 0.176 waves p–v and 0.029 waves rms. Therefore, we can expect a wavefront p–v of less than 0.2 waves and rms WFE of less than 0.05 waves at 910 nm at the output of the AIR using this method.

After the wavefront was aligned, the magnification of the beam was measured. Minimizing magnification error is important for laser systems with large beams. For the AIR, the magnification was required to be –2.00±2%. To measure the magnification in the test bed, a mask with holes was placed at the object plane and the distance between the images of the holes was measured in the image. The relative distance between the holes was measured.

The result was a magnification of –2.13±2%, which is a +7.5% change from the required value of –2.00±2%. At first, this error was suspected to be caused by uncertainties in the alignment process. However, the course and fine alignment processes were repeated multiple times to test this suspicion, and the magnification was remeasured each time. The measured value of the magnification varied by less than 1% between alignments. To bring the magnification back into spec, the position of another mirror besides M4 must be adjusted; however, the same space constraints in the design process also restrict us here: M2 is already very close to the GCC wall. Although there is some room to move M1, moving it would require changing the input angle of the beam from N5, which is not ideal. M3, being the only mirror left, is the best candidate to move. To test how far was required, the location of M3 was moved by 75 mm toward M2 to shorten the focal length of the M3/M4 pair in the model with the measured radii, which reduced the magnification by 3.5%. This adjustment reduced the output working distance to the image plane (G4) by 75 mm. This change was reproduced in the test bed, and the magnification was remeasured to be 2.07, bringing the magnification error down from 7.5% to 3.5%. Based on the model, to bring the magnification error down another 3.5%, we could move the M3 mirror by another 75 mm. Since the test-bed optics likely do not have exactly the same radii as the *in-situ* AIR optics, this final M3 mirror adjustment was not performed on the test bed. The actual compensation will be based on the measurements of the *in-situ* AIR mirrors.

The design of an unobscured reflective laser relay comprising four tilted spherical mirrors has been described. We showed the theoretical basis for such a four-mirror design using first-order optical matrix methods and NAT. We then described the process of aligning the design in a test bed to demonstrate an effective alignment method for such a design. We were able to achieve a nominal design that met our specifications and also successfully align the design in a test-bed environment to achieve our target wavefront error of less than 0.25 waves p–v and 0.07 waves rms.

This material is based upon work supported by the Department of Energy National Nuclear Security Administration under Award Number DE-NA0003856, the University of Rochester, and the New York State Energy Research and Development Authority.

1. S.-W. Bahk, J. Bromage, and J. D. Zuegel, Opt. Lett. **39**, 1081 (2014).
2. J. Bromage *et al*., High Power Laser Sci. Eng. **7**, e4 (2019).
3. Z. Bor, Opt. Lett. **14**, 119 (1989).
4. Zs. Bor and Z. L. Horváth, Opt. Commun. **94**, 249 (1992).
5. H.-M. Heuck *et al*., Appl. Phys. B **84**, 421 (2006).
6. D. Y. Wang, D. M. Aikens, and R. E. English, Jr., Opt. Eng. **39**, 1788 (2000).

7. E. M. Schiesser *et al*., Opt. Lett. **43**, 4855 (2018).

8. R. A. Buchroeder, Appl. Opt. **9**, 2169 (1970).

9. R. A. Buchroeder, Optical Sciences Center, University of Arizona, Tucson, AZ, Optical Sciences Technical Report 68 (1971).

10. S. Steven, J. Bentley, and A. Dubra, Opt. Express **27**, 11205 (2019).

11. R. A. Buchroeder, "Titled Component Optical Systems," Ph.D. thesis, University of Arizona, 1976.

12. J. R. Rogers, Opt. Eng. **39**, 1776 (2000).

13. FARO Gage & Gage-PLUS, 20 February 2009, http://www.dirdim.com/pdfs/DDI_FARO_Gage.pdf.

14. S.-W. Bahk and C. Dorrer, in *Imaging and Applied Optics*, OSA Technical Digest (online) (Optical Society of America, Washington, DC, 2013), Paper CM3C.4.

Ellipsometric Modeling of Serially Bi-Deposited Glancing-Angle–Deposition Coatings

C. Smith, S. MacNally, and J. Oliver

Laboratory for Laser Energetics, University of Rochester

Glancing-angle–deposition (GLAD) coatings have been in development at LLE for a variety of applications. When produced using serial bi-deposition,[1] a birefringence is created due to the difference in coating density along perpendicular axes in the coating plane, as shown in Fig. 1. The higher-density direction corresponds to the coating flip axis, while the lower-density region is created due to the self-shadowing nature of the GLAD coating process.

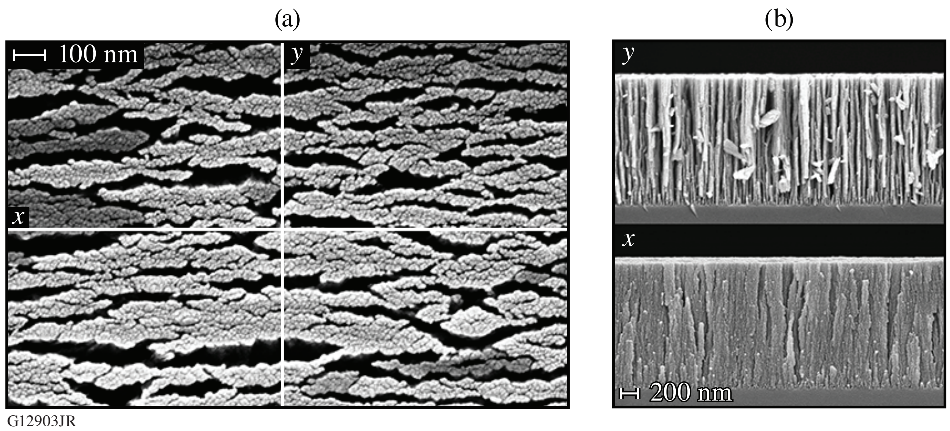

Figure 1
The birefringence of these coatings is achieved because of the microstructure produced in the GLAD serial bi-depostion process. The scanning electron micrograph of (a) the top view of the coating shows the directionality of the density difference, while (b) the side view shows the magnitude.

The birefringence created in this process makes ellipsometric modeling difficult due to the number of fit parameters, leaving unconstrained variables. Incorrect models produce unreliable dispersion curves, making coating design nearly impossible. In this work, a process was developed combining ellipsometric measurement techniques with well-established optical coating design methods to create precise index models. This enabled the development of complex optical coatings using only a single material.

In this experiment, a coating was designed using alternating GLAD and amorphous silica layers. To create these multilayer coatings, a methodical approach was taken. Short, single-layer GLAD coatings were created and measured on a Woollam VASE® ellipsometer in multiple orientations. This made precise characterization possible, resulting in high-quality dispersion curves. Due to the deposition process used in this experiment, the multilayer coating was presumed to have a slightly different density than the single-layer coatings. To correct for this, the single-layer dispersion curves were used to design a seven-layer calibration coating described by Baumeister.[2] This coating is highly sensitive to changes in optical thickness and is commonly used for material characterization or process corrections. When this coating was evaluated (Fig. 2) and optimized using the thin-film design software OptiRE, new dispersion curves were created that closely matched the measured performance.

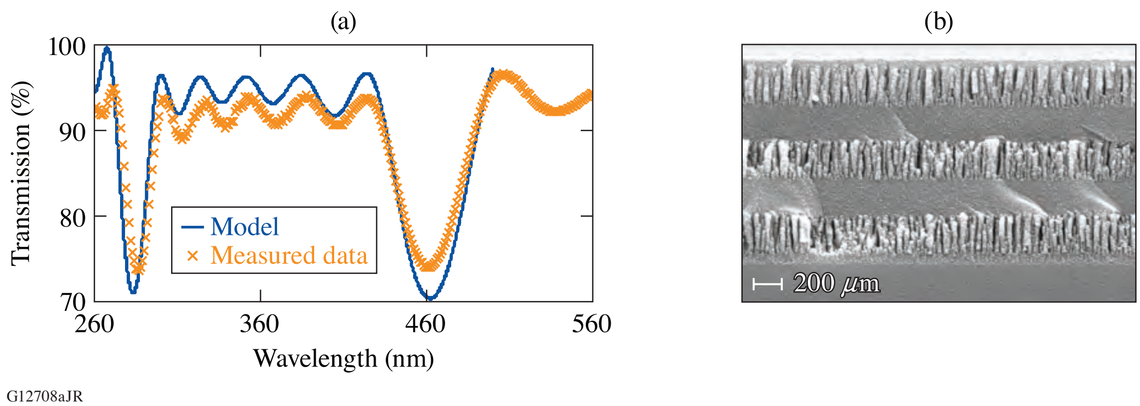

Figure 2
(a) Spectral design versus measured data used to create the seven-layer coating; (b) SEM micrograph of the calibration coating.

Additionally, this experiment required an antireflective (AR) overcoat. A three-layer coating was designed to mimic the density of the final three layers of the multilayer. This coating was evaluated using the same techniques described above, and a dispersion curve for the final layer was found. Using these data, along with the data from the seven-layer coating, a 31-layer wave plate was created (Fig. 3).

This experiment used only three different coating parameters to alter the index of the material and create a final product with only three indices, but the technique described is sufficient for the design and production of a limitless number of indices using a single material. Future work will focus on expanding these capabilities.

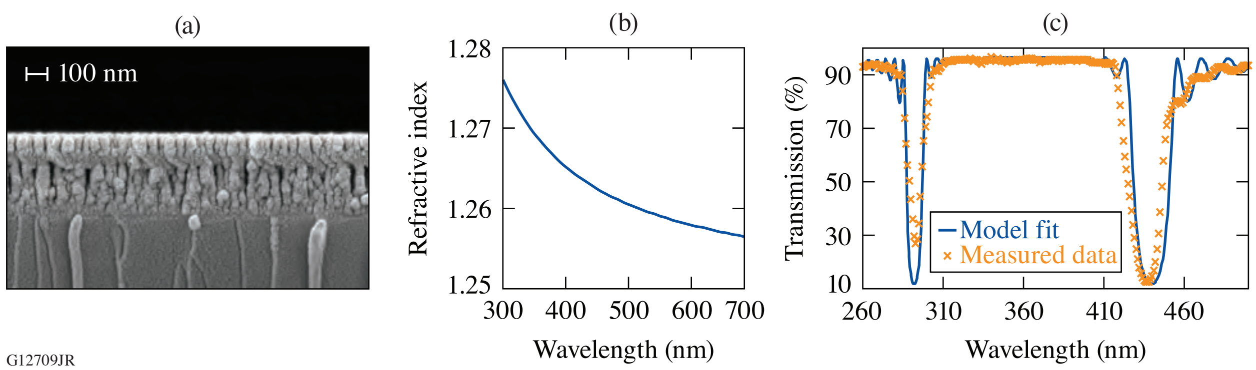

Figure 3
(a) A three-layer coating closely approximating the last three layers of the wave plate; (b) dispersion curve calculated for the final AR layer; (c) spectral measurement versus measured data used to create the 31-layer coating.

This material is based upon work supported by the Department of Energy National Nuclear Security Administration under Award Number DE-NA0003856, the University of Rochester, and the New York State Energy Research and Development Authority.

1. S. MacNally *et al.*, in *Optical Interference Coatings Conference (OIC) 2019*, OSA Technical Digest (OIC) 2019 (Optical Society of America, 2019), Paper MD.2.
2. P. Baumeister, *Optical Coating Technology* (SPIE Optical Engineering Press, 2004), pp. 9-56–9-57.

Modeling Variable-Impedance, Magnetically Insulated Transmission Lines

R. B. Spielman and A. B. Sefkow

Laboratory for Laser Energetics, University of Rochester

The design of very-low-inductance, magnetically insulated transmission lines (MITL's) is a critical part of building low-inductance vacuum transmission lines and load configurations. It becomes more difficult to build low-impedance (low-inductance), constant-impedance MITL's when the MITL's must operate at high voltage. This is due to the increase in the fraction of the electrical current carried in vacuum electron flow in the MITL's at high voltage. Vacuum electron flow can be lost at downstream locations with impedance mismatches and at vacuum convolutes. We describe the design of a variable-impedance, disk MITL that allows us to reduce the inductance of disk MITL's. In this design, the impedance of the MITL at a radius of r = 150 cm is at 1.5 Ω, while the impedance of the MITL at a radius of r = 30 cm is 2 Ω. The impedance transition between these two radial locations can be done many ways but this summary uses a simple linear change in gap from the outer 1.5-Ω MITL to the inner 2.0-Ω MITL. Two-dimensional, electromagnetic (EM) particle-in-cell (PIC) simulations of this variable-impedance MITL will show electron flow and losses.

Our variable-impedance MITL is a conical disk MITL that starts at a radius of r = 150 cm and proceeds inward to a radius of r = 30 cm (see Fig. 1). The initial geometric impedance is 1.5 Ω (at 150 cm) with a gap of dz = 3.76 cm. The final geometric impedance is 2 Ω (at 30 cm) with a gap of dz = 1 cm. The inductance of this variable-impedance, disk MITL is 6.52 nH, a reduction of 1.55 nH when compared with an 8.07-nH, 2-Ω disk MITL. We now clearly see the reason for a variable-impedance MITL—lower inductance leading to higher efficiencies. The 2-Ω MITL design was described by Spielman and Reisman,[1] where a Z-flow model was used to quantify the vacuum electron flow at peak MITL voltage. The circuit code *Screamer*[2] was used to model

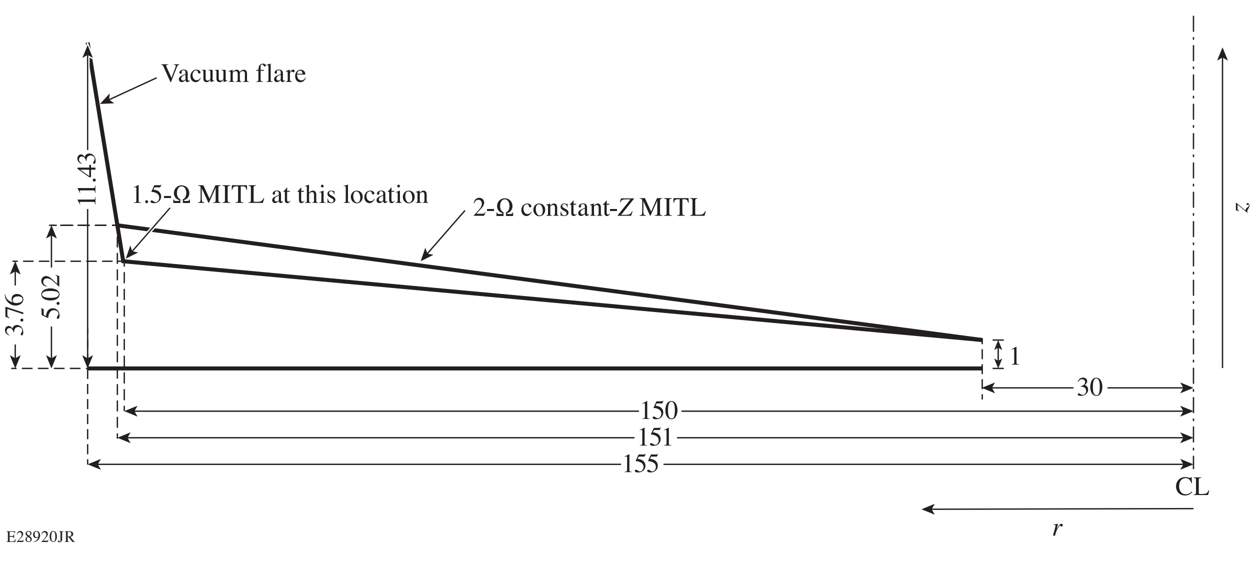

Figure 1
We show a schematic of a conical-disk MITL having a constant, 2-Ω impedance MITL profile and a similar conical-disk MITL having a variable, 1.5-Ω to 2-Ω impedance MITL profile. The figure shows a slice of the MITL at a single rotational angle around the marked center line. All units are in cm. CL: center line.

the qualitative MITL performance in Ref. 1. Herein, we model electron losses that will occur in a well-behaved, superinsulated variable-impedance disk MITL operating with equilibrium, vacuum electron flow. While we know that *any* variable-impedance MITL will have losses,[3] we assert that the real question is the magnitude of such losses.

The analytic approach to modeling electron losses in a variable-impedance MITL is based on the Z_{flow} model for MITL's described by Ottinger *et al.*[4] We assume as a worst case that any change in vacuum electron flow in excess of the retrapping current seen in the constant, the 2-Ω impedance case is lost at each segment transition. A 2-Ω MITL, as modeled here, has a slowly dropping vacuum electron flow moving inward due the nonmatched load. This forces retrapping of some of the vacuum electron flow. In reality, these loss currents are not at the discrete segment boundaries but are distributed over the entire MITL. The peak vacuum flow in the variable-impedance case is ~4% of the total anode current (in the outer MITL segment). The loss currents range from 3.4 kA on the outer segment to 6.2 kA on the inner segment. Importantly, the increase in total current due to the reduced inductance exceeds the increase in vacuum flow by 3×.

This particular impedance profile (linear in gap, not linear in Z) is not the optimum profile for pushing electron losses radially outward, where they have less impact due to the larger surface area. Various impedance profiles are possible and some of these have lower inductance than others. It is important to note that these predicted variable-impedance loss currents are significantly lower than the current losses seen during the setup of magnetic insulation.[1] It should be obvious that a variable-impedance MITL with a larger change in impedance (e.g., 1 Ω to 2 Ω) would suffer larger electron losses. Eventually, the losses in a variable-impedance MITL due to large impedance changes would approach the current losses seen during the setup of magnetic insulation and possibly result in MITL failure due to anode heating.

A 2-D EM PIC code can provide a more-quantitative picture of the electron losses in a variable-impedance MITL. For numerical accuracy, the number of macroparticles must be kept large (poor run time). The *LSP* code[5] is used to model the electron flow in the MITL's.

In *LSP*, the voltage waveforms generated in *Screamer* calculations are used as input to the simulation. The physical geometry of the MITL is as described earlier in Fig. 1. *LSP* invokes a unipolar, Child–Langmuir emission model that starts electron emission from the cathode at 200 kV/cm. An adaptive particle management routine is used to maintain about 100 particles per cell, resulting in a few million total macroparticles in the calculation. Radial resolution is ~1000 μm and axial resolution is ~100 μm.

We first ran a simulation with a constant-impedance 2-Ω MITL. In this case we do not expect losses in the constant-impedance section of the MITL. Figure 2 shows a snapshot of the electron density in the simulation at 100 ns, the time where the voltage is maximum and the current has reached half its peak. The Z-flow MITL theory predicts this MITL is perfectly insulated at peak voltage with no electron losses. The dz thickness of the vacuum sheath will decrease slightly as one moves from larger to smaller radius. The simulation is then rerun with identical electrical parameters except for the geometric boundary change of the variable-impedance disk MITL. The MITL impedance varies from 1.5 Ω at R = 150 cm and 2 Ω at R = 30 cm. For comparison, Fig. 3 shows the analogous snapshot of the variable-impedance MITL simulation at 100 ns.

One can now compare the two simulations. First, the small vortices that form in Fig. 2 appear to be influenced by the stairstep profile found on the MITL anode. Use of a surface-conformal meshing technique in these simulations would allow full clarification of this point. An examination of the electron flow in Fig. 3 shows similar vortices that are larger in amplitude and shorter in wavelength than those in Fig. 2. One can see that the thickness of the electron sheath at large radius is thicker in Fig. 3 than in Fig. 2. This is expected since the lower-impedance MITL modeled in Fig. 3 should have the larger sheath. Examination of multiple time steps of both simulations shows that these vortices have rotational flow (counterclockwise). It is interesting to note that the thickness of the electron sheath between the vortices is as expected in Fig. 3. The higher impedance at smaller radius results in the same electron sheath thickness as the constant 2-Ω case.

Importantly, there are no increased electron losses to the anode at the time of peak voltage in the variable-impedance case. This is true even though we have used a poor impedance profile with radius, where the use of a geometric straight line has greater dZ/dr at smaller radius and so should develop more losses at smaller radii. More-favorable dZ/dr profiles would reduce or eliminate the dZ/dr at small radius and push the changes in Z to larger radii, where losses are significantly less consequential.

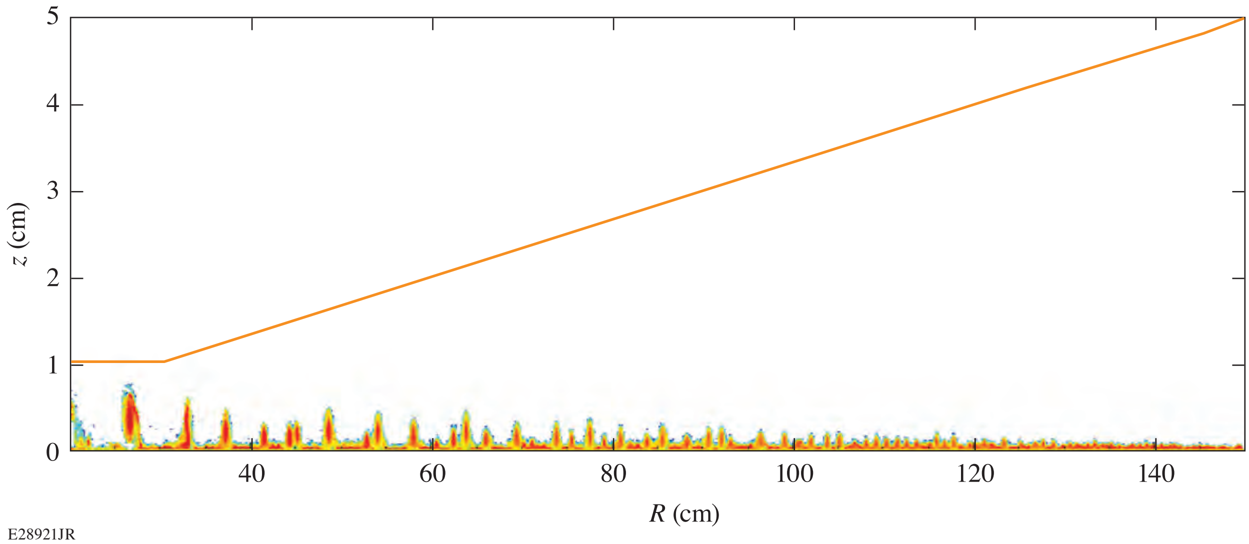

Figure 2
A snapshot of constant-impedance (2-Ω) MITL performance at $t = 100$ ns, where the simulation is at peak voltage and 0.5× maximum current.

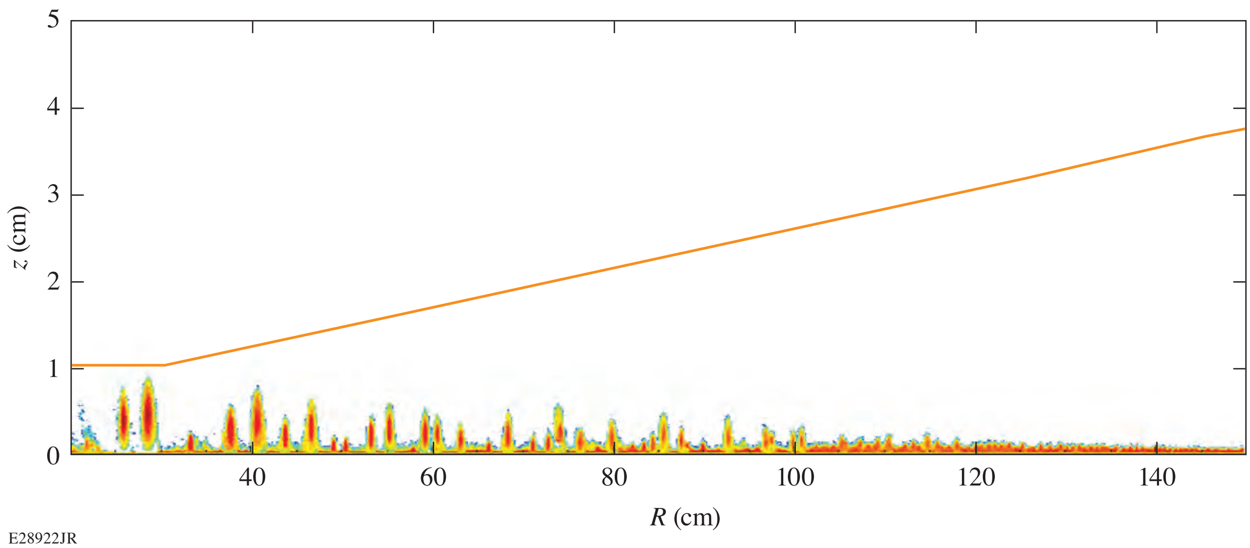

Figure 3
A snapshot of variable-impedance (1.5-Ω to 2-Ω) MITL performance at $t = 100$ ns, where the simulation is at peak voltage and 0.5× maximum current.

This material is based upon work supported by the Department of Energy National Nuclear Security Administration under Award Number DE-NA0003856, the University of Rochester, and the New York State Energy Research and Development Authority.

1. R. B. Spielman and D. B. Reisman, Matter Radiat. Extremes **4**, 027402 (2019); **4**, 049901(E) (2019).

2. R. B. Spielman and Y. Gryazin, in *2015 IEEE Pulsed Power Conference (PPC)* (IEEE, Piscataway, NJ, 2015).

3. T. D. Pointon and M. E. Savage, in *2005 IEEE Pulsed Power Conference* (IEEE, Piscataway, NJ, 2005), pp. 151–154.

4. P. F. Ottinger *et al.*, in *17th IEEE International Pulsed Power Conference*, edited by R. D. Curry (IEEE, Piscataway, NJ, 2009), pp. 1176–1179.

5. D. V. Rose *et al.*, Phys. Rev. Spec. Top., Accel. Beams **18**, 030402 (2015).

LLE's Summer High School Research Program

R. S. Craxton

Laboratory for Laser Energetics, University of Rochester

During the summer of 2019, 14 students from Rochester-area high schools participated in the Laboratory for Laser Energetics' Summer High School Research Program. This was the 31st year of the program, which started in 1989. The goal of the program is to excite a group of high school students about careers in the areas of science and technology by exposing them to research in a state-of-the-art environment. Too often, students are exposed to "research" only through classroom laboratories, which have prescribed procedures and predictable results. In LLE's summer program, the students experience many of the trials, tribulations, and rewards of scientific research. By participating in research in a real environment, the students often become more excited about careers in science and technology. In addition, LLE gains from the contributions of the many highly talented students who are attracted to the program.

The students spent most of their time working on their individual research projects with members of LLE's technical staff. The projects were related to current research activities at LLE and covered a broad range of areas of interest including experimental diagnostic development, computer modeling of implosion physics, cryogenic target characterization, experimental design, irradiation uniformity, physical chemistry, and optical materials characterization (see Table I).

The students attended weekly seminars on technical topics associated with LLE's research. Topics this year included laser physics, fusion, fission, pulsed power, holography, and LLE's cryogenic target program. The students also received safety training, learned how to give scientific presentations, and were introduced to LLE's resources, especially the computational facilities.

The program culminated on 28 August with the "High School Student Summer Research Symposium," at which the students presented the results of their research to an audience including parents, teachers, and LLE staff. The students' written reports will be made available on the LLE Website and bound into a permanent record of their work that can be cited in scientific publications.

Three hundred and ninety-one high school students have now participated in the program. This year's students were selected from just over 40 applicants.

At the symposium LLE presented its 23rd annual William D. Ryan Inspirational Teacher Award to Mrs. Rebecca Berardino, a mathematics teacher at Barker Road Middle School in Pittsford. This award is presented to a teacher who motivated one of the participants in LLE's Summer High School Research Program to study science, mathematics, or technology and includes a $1000 cash prize. Teachers are nominated by alumni of the summer program. Mrs. Berardino was nominated by Margaret Rudnick, a participant in the 2018 program. Margaret wrote, "Mrs. Berardino is the single most instrumental person that caused me to fall in love with the intricacies of complex problems, ultimately leading me to pursue a STEM-related field in college and probably as a career." When Margaret encountered Mrs. Berardino in seventh grade, she was shocked to find that Mrs. Berardino refused to give her the answers she wanted but told her to work out the problem for herself: "I still vividly remember the panic I felt when Mrs. Berardino said, 'I'm not going to feed you the answer with a silver spoon.'" Margaret had no choice but to persevere. After "an inordinate amount of approaches and thought processes," she came to the answer on her own: "I had never experienced that moment of sincere joy and triumph after mentally crawling to the top of a mountain…This moment changed my life." After

Mrs. Berardino's classes, Margaret was inspired to sign up for the most rigorous science and math classes available and "constantly seek the excitement of advanced learning…I realized that I absolutely do not want to be fed with a silver spoon." Other students in Mrs. Berardino's class were also inspired: "She opened our eyes to the wonder of not just mathematics, but the world, making sure to enrich our theoretical learning with cool examples of math in nature." Margaret concluded by saying, "So much of my love for science is owed to Mrs. Berardino, and looking back, her amazing classes are the part of middle school I remember the best."

This material is based upon work supported by the Department of Energy National Nuclear Security Administration under Award Number DE-NA0003856, the University of Rochester, and the New York State Energy Research and Development Authority.

Table I: High School Students and Projects—Summer 2019.

Name	High School	Supervisor	Project Title
Henry Berger	Brighton	C. J. Forrest	Design of a Single-Hit Neutron Spectrometer for Long-Duration Fusion Reactions
Adelyn Carney	Webster Schroeder	H. G. Rinderknecht	Optimization of X-Ray Prepulse Geometry for Imprint Mitigation in Directly Driven Implosions
Ji-Mi Jang	Pittsford Mendon	T. Z. Kosc	Micro Raman Spectroscopy of Silica and Hafnia Laser Damage Sites
Christopher "Jude" Kukla	Pittsford Mendon	F. J. Marshall and S. T. Ivancic	Evaluation of Fresnel Zone Plate X-Ray Imagers for Inertial Confinement Fusion Applications
Michele Lin	Attica	M. McCluskey	A Comparative Study of the Effects of Methanol and Ethanol Solutions on the Bulk Etch Rate of CR-39
Anthony Mazzacane	Pittsford Mendon	P. B. Radha, O. M. Mannion, and S. Miller	Using *IRIS3D* to Simulate the Effects of Smoothing by Spectral Dispersion on Cryogenic Implosions
George Morcos	Rush Henrietta	K. L. Marshall	Glassy Liquid Crystals Based on Natural Products for High-Peak-Power Laser Optics
Adam Mroueh	Pittsford Sutherland	D. Broege	Schlieren Diagnostic for the Imaging of Thermal Turbulence
Ka-Hyun Nam	Brighton	C. Fagan and W. T. Shmayda	Comparative Analysis of Oxygen Uptake in Nickel and Copper-Zinc Beds
Simon Narang	Pittsford Sutherland	M. D. Wittman and D. Bredesen	Application for Filling Cryogenic Targets at an Arbitrary Viewing Angle
Max Neiderbach	Geneseo	M. Sharpe, V. Anand, and R. Peck	Enhancements to the Calorimetric Measurement System on the OMEGA Laser
Stephen Rosa	Eastridge	W. T. Shmayda and M. D. Sharpe	Investigations of the Hydrogen-Palladium and Deuterium-Palladium Systems
William Wang	Pittsford Sutherland	R. S. Craxton	Development of a Beam Configuration for the SG4 Laser to Support both Direct and Indirect Drive
Hanna Wiandt	Pittsford Mendon	R. S. Craxton	Optimization of the Uniformity of 12-Quad Targets for the National Ignition Facility

FY19 Q4 Laser Facility Report

J. Puth, M. Labuzeta, and D. Canning

Laboratory for Laser Energetics

During the fourth quarter of FY19, the Omega Facility conducted 421 target shots on OMEGA and 201 target shots on OMEGA EP for a total of 622 target shots (see Tables I and II). OMEGA averaged 11.1 target shots per operating day, averaging 95.7% Availability and 95.4% Experimental Effectiveness.

OMEGA EP was operated extensively in Q4 FY19 for a variety of user experiments. OMEGA EP averaged 8.0 target shots per operating day, averaging 96.4% Availability and 93.8% Experimental Effectiveness.

Table I: OMEGA Laser System target shot summary for Q4 FY19.

Program	Laboratory	Planned Number of Target Shots	Actual Number of Target Shots
ICF	LLE	143	155
	LANL	22	24
	LLNL	16.5	15
	NRL	11	7
ICF Subtotal		192.5	201
HED	LLE	22	21
	LANL	44	46
	LLNL	33	35
HED Subtotal		99	102
CEA	CEA	11	14
LBS	LLE	33	38
	LLNL	27.5	35
	Oxford	11	8
LLE Calibration	LLE	0	23
Grand Total		374	421

Table II: OMEGA EP Laser System target shot summary for Q4 FY19.

Program	Laboratory	Planned Number of Target Shots	Actual Number of Target Shots
ICF	LLE	24.5	32
	LANL	14	22
ICF Subtotal		38.5	54
HED	LLE	28	32
	LANL	7	8
	LLNL	42	42
HED Subtotal		77	82
CEA	CEA	7	11
LBS	LANL	7	5
	LLE	14	17
	LLNL	7	14
	Oxford	3.5	7
LLE Calibration	LLE	7	11
Grand Total		161	201

National Laser Users' Facility and External Users' Programs

M. S. Wei

Laboratory for Laser Energetics, University of Rochester

Under the facility governance plan implemented in FY08 to formalize the scheduling of the Omega Laser Facility as a National Nuclear Security Administration (NNSA) User Facility, Omega Laser Facility shots are allocated by programs following NNSA guidance. The majority (~69%) of the Omega target shots each year are committed to the national Inertial Confinement Fusion (ICF) Program and the High-Energy-Density (HED) Program conducted by scientists from Lawrence Livermore National Laboratory (LLNL), Los Alamos National Laboratory (LANL), Sandia National Laboratories (SNL), the Naval Research Laboratory (NRL), and LLE. In FY19, about 78% of the total Omega shots were delivered for the ICF and HED campaigns.

The Fundamental Science program at the Omega Laser Facility with projects selected through open-call and peer-reviewed processes, is typically allotted between 25% to 29% of the total Omega Laser Facility shots. The program has two distinct components: (1) the NLUF grant program awarded to an individual principal investigator (PI) on a two-year cycle with the associated Omega Laser Facility time (~18% of the overall facility time each year) for experiments led by U.S. academia and business; and (2) the Laboratory Basic Science (LBS) Program for basic science experiments (~11% of the facility time) conducted by the NNSA ICF laboratories including LLNL, LANL, SNL, NRL, LLE, and some of the Office of Science laboratories such as SLAC, Princeton Plasma Physics Laboratory (PPPL), and Lawrence Berkeley National Laboratory (LBNL). In FY19, the Fundamental Science Program obtained a total of 416 target shots that accounted for 18% of the overall 2320 Omega Laser Facility shots. The relative lower fraction of the Fundamental Science shots in FY19 is due to the postponed NLUF solicitation for the 2019 and 2020 periods that resulted in no new NLUF projects. Some of the shot time reserved for the NLUF allocation in FY19 was redistributed to LBS, ICF, and HED.

The Omega Laser Facility was also used for several campaigns (a total of 78 target shots) led by teams from the Commissariat à l'énergie atomique et aux énergies (CEA) of France, CELIA at the University of Bordeaux of France, and the joint Rutherford Appleton Laboratory (RAL) and University of York of the United Kingdom. These externally funded experiments are conducted at the facility on the basis of special agreements put in place by the UR/LLE and participating institutions with the endorsement by NNSA.

The facility users during this year included eight collaborative teams participating in the NLUF Program with the Omega Laser Facility shot allocation from the FY17–FY18 awards; 25 teams led by scientists from LLNL, LANL, LLE, and SLAC participating in the LBS Program; many collaborative teams from the national laboratories (LLNL and NRL) and LLE conducting ICF experiments; investigators from LLNL, LANL, SNL, and LLE conducting experiments for HED programs; and scientists and engineers from CEA, the University of Bordeaux, and RAL/York.

FY19 National Laser Users' Facility Program

M. S. Wei

Laboratory for Laser Energetics, University of Rochester

During the second and third quarters of FY19, the National Nuclear Security Administration (NNSA) and the Office of Science jointly completed a funding opportunity announcement (FOA), review, and selection process for National Laser Users' Facility (NLUF) experiments to be conducted at the Omega Laser Facility during FY20 and FY21. Seventeen proposals were successfully submitted in response to this FOA. After peer review by an independent proposal review committee for scientific and technical merit and the feasibility review by the Omega Laser Facility team, NNSA selected 11 proposals for funding and Omega shot allocation with a total of 22.5 and 23.5 shot days for experiments in FY20 and FY21, respectively. It was noted that a large number of NLUF grant proposals failed during the initial administrative review due to unexpected submission errors and were deemed nonresponsive. Following NNSA's guidance, LLE made a one-time additional open-call late in FY19 to receive Omega Laser Facility time proposals for Academic and Industrial Basic Science (AIBS) experiments to fulfill the remaining NLUF shot allocation in FY20–FY21. Based on the merit review committee's recommendation, ten new projects were selected for Omega beam-time awards with a total of 11 and 10 shot days for AIBS experiments in FY20 and FY21, respectively. Table I shows the list of NLUF grant projects and AIBS beam-time awards approved for Omega shot allocations in FY20–FY21.

During the first and second quarters of FY19, eight NLUF projects that had been approved during the previous NLUF cycle (calendar year 2017–2018) completed 127 target shots. The NLUF experiments conducted at the facility during FY19 are summarized in this section.

A critical part of the NLUF program is the education and training of graduate students in plasma and HED physics. In addition, graduate students can also access the Omega Facility for shots through their collaborations with national laboratories and LLE. There were more than 60 graduate students from 18 universities involved in the external user-led research programs supported by NLUF/LBS and/or with experiments conducted at the Omega Laser Facility (see Table II), among which ten students successfully defended their Ph.D. theses during FY19 (see the highlighted names in Table II).

Structure of $MgSiO_3$ Under Ramp Compression to 368 GPa

Principal Investigator: T. S. Duffy (Princeton University)
Co-investigators: D. Kim and S. Han (Princeton); R. F. Smith and F. Coppari (LLNL), and J. K. Wicks (Johns Hopkins University)

In Earth's lower mantle, enstatite [$(Mg,Fe)SiO_3$] transforms into the perovskite-structured mineral known as bridgmanite. This phase is considered to be the most abundant mineral in the entire earth, making up as much as 80% of the volume of the vast lower mantle. Near the base of the mantle, bridgmanite undergoes a further phase transition to the post-perovskite (ppv, $CaIrO_3$-type) structure. The ppv phase is expected to play a major role in the interiors of large terrestrial exoplanets due to the higher internal pressures of these bodies. It is therefore necessary to understand the behavior of enstatite at extreme conditions to develop models for the mineralogy, structure, and dynamics of such exoplanets.

We carried out experiments on OMEGA on several different enstatite starting materials, including a low-Fe enstatite $\left[Mg/(Mg+Fe) \sim 0.99\right]$ from Sri Lanka, a high-Fe enstatite $\left[Mg/(Mg+Fe) \sim 0.61\right]$ from India, and a synthetic $MgSiO_3$ glass

(MDI, Inc.). All samples were ground to a few microns in size, pressed into a foil using a diamond-anvil cell, and assembled into target packages. Experiments were performed on both OMEGA and OMEGA EP using ramp compression and x-ray diffraction with the powder x-ray diffraction image-plate (PXRDIP) diagnostic. These experiments are especially challenging due to the relatively weak scattering and low symmetry of high-pressure silicate phases.

Table I: Eleven NLUF grant projects (in blue) and ten AIBS beam-time awards (in gray) approved for the FY20–FY21 Omega Laser Facility shot allocations.

Principal Investigator	Institution	Title
F. N. Beg	University of California, San Diego	Charged-Particle Transport and Energy Deposition in Warm Dense Matter With and Without an External Magnetic Field
C. M. Krauland	General Atomics	Characterization of the Nonlinear Laser–Plasma Interaction in Electron-Assisted Shock Ignition
K. Krushelnick	University of Michigan	The Dynamics of Strong Magnetic Fields Generated by Relativistic Laser–Plasma Interactions Using OMEGA EP
E. Liang	Rice University	Collision of Two Magnetized Jets Created by Hollow Ring Lasers
R. Mancini	University of Nevada, Reno	A Laboratory Photoionized Plasma Experiment on OMEGA EP
C. McGuffey	University of California, San Diego	Driving Compressed Magnetic Fields to Exceed 10 kT in Cylindrical Implosions on OMEGA
R. Petrasso	Massachusetts Institute of Technology	High-Energy-Density Physics, Laboratory Astrophysics, and Student Training on OMEGA
P. Tzeferacos	University of Chicago	Fundamental Astrophysical Processes in Radiative Supersonic MHD Turbulence
M. Vaddivia	Johns Hopkins University	Demonstration of Monochromatic Talbot–Lau X-Ray Deflectometry (TXD) Electron Density Diagnostic in Laser–Target Interactions
J. Wicks	Johns Hopkins University	High Pressure and Temperature Polymorphism of a Key Super-Earth Mantle Material: MgO
L. Willingale	University of Michigan	Direct Laser Acceleration of Electrons for Bright, Directional Radiation Sources
M. Cappelli	Stanford University	Hydrodynamic versus Kinetic Atomic Mix in Deflagrating Converging Plasmas
T. Duffy	Princeton University	Phase Transitions in Planetary Materials at Ultrahigh Pressures
W. Fox	Princeton University	Magnetic Reconnection in High-Energy-Density Plasmas
R. Jeanloz	University of California, Berkeley	Multi-Compression and Chemical Physics of Planetary Interiors
H. Ji	Princeton University	Study of Particle Acceleration from Magnetically Driven Collisionless Reconnection at Low Plasma Beta Using Laser-Powered Capacitor Coils
C. Kuranz	University of Michigan	Experimental Astrophysics on the OMEGA Laser
M. Manuel	General Atomics	B-Field Effects on Laser–Plasma Instabilities
D. Schaeffer	Princeton University	Particle Heating by Collisionless Shocks in Magnetized High-Energy-Density Plasmas
B. Srinivasan	Virginia Tech	Investigation of Feasibility of the 11B(P,3α) Reaction in ICF Settings
W. Theobald	University of Rochester	Quantifying Turbulent Rayleigh–Taylor Mixing with X-Ray Phase Contrast Imaging

Table II: Graduate students from other universities who have conducted research utilizing the Omega Laser Facility through NLUF and LBS or via collaborations with national laboratories and LLE in FY19. Ten students successfully defended their Ph.D. thesis during FY19 (see shaded cells).

Name	University	Academic Advisor	Notes
Patrick Adrian	MIT	Petrasso	
Timothy Mark Johnson	MIT	Petrasso	
Neel Kabadi	MIT	Petrasso	
Justin Kunimune	MIT	Petrasso	
Brandon Lahmann	MIT	Petrasso	
Jacob Pearcy	MIT	Petrasso	
Raspberry Simpson	MIT	Petrasso	
Benjamin Reichelt	MIT	Petrasso	
Hong Sio	MIT	Petrasso	Graduated October 2018; postdoc at LLNL
Graeme Sutcliffe	MIT	Petrasso	
Abraham Chien	Princeton	Ji	
Cole Holcomb	Princeton	Spitkovsky	Graduated December 2018; data scientist at The Estée Lauder Companies
Jack Matteucci	Princeton	Bhattacharjee/Fox	Graduated January 2020
Donghoon Kim	Princeton	Duffy	
Sirus Han	Princeton	Duffy	
Ian Ocampo	Princeton	Duffy	New
Connor Krill	JHU	Wicks	New; through LLNL-led LBS
Juliette Lamoureux	JHU/NASA Goddard	Wicks	New
Tylor Perez	JHU	Wicks	New
Zixuan Ye	JHU	Wicks	New
Melissa Sims	Stonybrook	Wicks	Defended in March 2019; postdoc at JHU
Dylan Cliché	University of Nevada, Reno	Mancini	LLE collaboration
Enac Gallardo	University of Nevada, Reno	Mancini	LLE collaboration
Daniel Mayes	University of Nevada, Reno	Mancini	
Kyle Swanson	University of Nevada, Reno	Mancini	
Patrick Belancourt	University of Michigan	Drake	Through collaboration with LLE including LBS shots
Shane Coffing	University of Michigan	Drake/Kuranz	
Laura Elgin	University of Michigan	Drake/Kuranz	Through collaboration with national labs; graduated September 2019; postdoc at SNL
Raul Melean	University of Michigan	Kuranz/McBride	Collaboration with JHU's NLUF (P. Valdivia)
Heath Lefevre	University of Michigan	Kuranz/Drake	
Joseph Levesque	University of Michigan	Drake/Kuranz	

Table II: Graduate students from other universities who have conducted research utilizing the Omega Laser Facility through NLUF, LBS, or via collaborations with national labs and LLE in FY19. Ten students successfully defended their Ph.D. thesis during FY19 (see shaded cells) (continued).

Name	University	Academic Advisor	Notes
Alex Rusmas	University of Michigan	Kuranz/Drake	Through collaboration with. LANL; defended in April 2019, now a postdoc at LANL
Robert Vandervort	University of Michigan	Drake	
Paul Campbell	University of Michigan	Krushelnick/Willingale	Defended October 2019; now a FES Postdoc Fellow at the University of Michigan
Amina Hussein	University of Michigan	Krushelnick/Willingale	Defended in June 2019; now UC President Postdoc Fellow
Peter Kordell	University of Michigan	Krushelnick	Defended in May 2019; now at Northrop Grumman
Brandon Russell	University of Michigan	Krushelnick/Willingale	
Hongmei Tang	University of Michigan	Krushelnick/Willingale	New
Krish Bhutwala	University of California, San Diego	Beg	
Rui Hua	University of California, San Diego	Beg	Through LLNL-led LBS (PI Ping); defended in September 2019; imaging scientist at Cannon Medical Research USA
Shu Zhang	University of California, San Diego	Beg	Through GA-led NLUF
Kaitlyn Amodeo	University of California, Davis	Stewart	Through LLNL-led LBS (PI Millot)
Erik Davies	University of California, Davis	Stewart	Through LLNL-led LBS (PI Millot)
Paul King	University of Texas, Austin	Hegelich	Through LLNL-led LBS (PI Albert)
Dara Hok	Stanford	Gleason-Holbrook	Through LLNL-led LBS (PI Krygier)
Yongchao Lu	Rice University	Liang	Rice-led NLUF and also through LANL collaboration
Kevin Meaney	University of New Mexico	Gilmore	Through LANL collaboration
Brett Scheiner	University of Iowa	Baalrud	Through LANL collaboration
Oliver Vaxirani	Virginia Tech	Srinivasan	Through LANL collaboration
Archie Bott	Oxford	Gregori	Through University of Chicago-led NLUF (PI Lamb); graduated 2019; postdoc at Princeton University
Oliver Karnbach	Oxford	Gregori/Wark	Through LLNL-led LBS (PI Chen)
Hannah Poole	Oxford	Gregori	Collaboration with LLE
Jacob Topp-Myfflestone	Oxford	Gregori	Collaboration with LLE
Gabriel Perez-Callejo	Oxford	Rose	Through LLNL-led LBS and HED (PI Marley)

Table II: Graduate students from other universities who have conducted research utilizing the Omega Laser Facility through NLUF, LBS, or via collaborations with national labs and LLE in FY19. Ten students successfully defended their Ph.D. thesis during FY19 (see shaded cells) (continued).

Name	University	Academic Advisor	Notes
Jocelain Trela	University of Bordeaux	Batani	Through LLE-led LBS (PI Theobald); graduated June 2019; scientist at CEA
Matthew Khan	University of York	Woolsey	Through LLE-led LBS (PI Theobald)
Gabriel Rion	Ecole Polytechnique, Palaiseau		Through LLE-led LBS (PI Theobald)
Victorien Bouffetier	University of Bordeaux		Through LLE-led LBS (PI Theobald) and JHU-led NLUF
Olena Turianska	University of Bordeaux		Through LLE-led LBS (PI: Theobald)
Thibault Goudai	University of Bordeaux		Through LLNL-led LBS (PI: Khan)

JHU: Johns Hopkins University
MIT: Massachusetts Institute of Technology

Nine successful experiments have been conducted in total (five Fe-poor, two Fe-rich, and two $MgSiO_3$ glass). For the crystalline samples, the drive energies ranged from 207 to 597 J and the resulting pressures were 118 to 277 GPa. The experiments used Cu or Fe backlighters paired with pinholes made from W or Ta. For the glass samples, the drive energies ranged from 607 to 912 J and the resulting pressures were 274 to 368 GPa. In the experiments on the crystalline samples, one to three sample diffraction lines were observed in seven shots. The diffraction lines from all shots produced a consistent d spacing trend as a function of pressure, and all samples yielded diffraction lines with similar d spacings, suggesting transformation to the same phase. Interestingly, the positions of the observed diffraction lines are not consistent with the major peaks of the post-perovskite phase, which is expected to be stable at these pressures. The peaks are also not consistent with bridgmanite or akimotoite, two forms of (Mg,Fe) SiO_3 stable under lower pressure conditions. We commenced a search among metastable $MgSiO_3$ phases that have been reported in diamond-anvil cell experiments and obtained a tentative match with a phase known as β-postopx (post-orthopyroxene). Our group had previously observed this phase in single-crystal, 300-K diamond anvil cell experiments above 50 GPa. The structure consists of alternating Mg-O and Si-O layers. The Mg-O layers are pyroxene-like, whereas the Si-O layers transform toward akimotoite-like sheets with 4 + 1 and sixfold coordination of silicon with oxygen.

Our results (Fig. 1) indicate that ramp compression of a silicate at 1 to 2 Mbar may produce a metastable phase. Furthermore, it indicates that the same high-pressure phases may be generated in low-temperature static experiments and rapid dynamic experiments, further demonstrating the complementarity of the two techniques. Our results also show that we can potentially place constraints on high-pressure phases in weakly diffracting, low-symmetry silicate systems under extreme pressures. Future experiments will be aimed at better constraining the crystal structure by enhancing the diffraction signal. X-ray diffraction under shock compression will also be performed to compare structures obtained under different loading conditions.

This material is based upon work supported by the Department of Energy National Nuclear Security Administration through the National Laser Users Facility Program under Award Number DE-NA0003611.

Properties of Magnetohydrodynamic Turbulence in Laser-Produced Plasmas

Principal Investigator: D. Lamb University of Chicago
Co-investigators: G. Gregori and P. Tzeferacos (University of Chicago and Oxford University); C. Palmer, A. Bott, L. Chen, and J. Meinecke (Oxford); D. H. Froula and J. Katz (LLE); H.-S. Park (LLNL); and R. D. Petrasso, C. K. Li, and A. Birkel (MIT)

Astronomical observations that are based on Faraday rotation and polarization measurements, the Zeeman effect, magneto-bremsstrahlung, and *in-situ* measurements of proximal astrophysical objects reveal how space is permeated by magnetic fields[1] that play crucial roles in myriad astrophysical phenomena. Despite the broad consensus among astronomers that magnetic-field

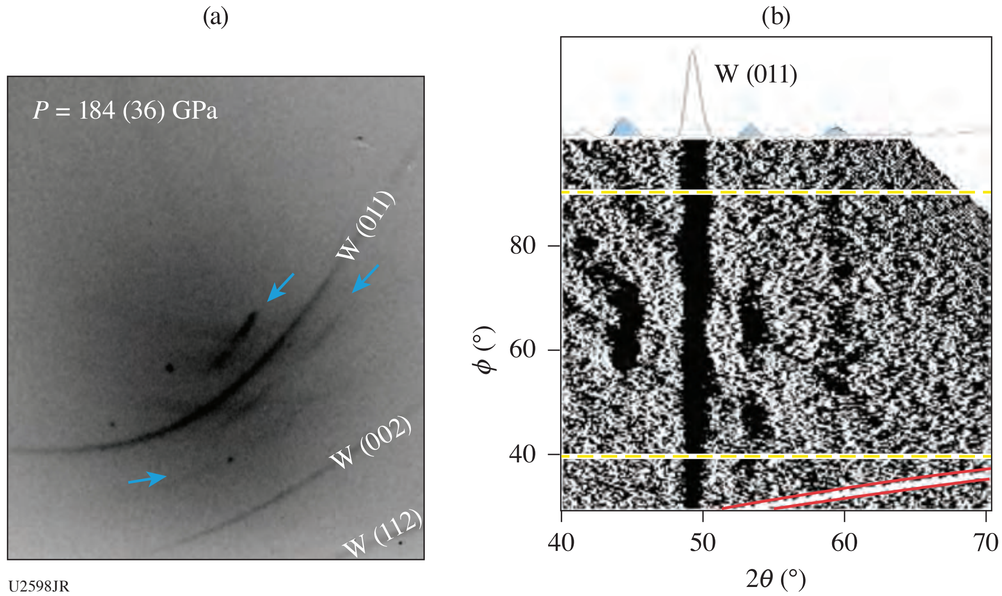

Figure 1
Diffraction data for $MgSiO_3$ at 183(36) GPa. (a) One of the image plates for OMEGA EP shot 27426. Lines from the enstatite sample are indicated by blue arrows. (b) Image-plate data transformed to ϕ–2θ coordinates, where ϕ is the azimuthal angle around the incident x-ray beam and 2θ is the diffraction angle. A lineout from the region between the yellow horizontal dashed lines is shown at the top. Peaks from the high-pressure phase of $MgSiO_3$ are shaded in blue.

amplification via turbulent dynamo is behind observed cosmic magnetism, theoretical considerations and numerical modeling have unavoidably resorted to simplifying assumptions that do not necessarily reflect the properties of astrophysical turbulence. Turbulent dynamo theoretical and numerical studies have largely focused on incompressible turbulence, and simulations are typically restricted to magnetic Prandtl numbers Pm ~ 1 due to resolution constraints,[2] rarely considering systems of equations that go beyond resistive magnetohydrodynamics (MHD). Only in the last few years have theoretical and numerical efforts begun to tackle highly compressible magnetized turbulence[3,4]—an important step forward, given that most astrophysical systems in the interstellar and intergalactic mediums exhibit signs of high compressibility [i.e., large sonic Mach (M) numbers]. Supersonic turbulence plays a critical role in determining the star formation rate,[5] the star formation efficiency,[6] and the stellar mass distribution.[7]

Supersonic magnetized turbulence and turbulent dynamo were the astrophysical processes we targeted on the third shot day of the TDYNO NLUF Experimental Campaign, "Properties of Magnetohydrodynamic Turbulence in Laser-Produced Plasmas." The shot day was carried out on 12 December 2018 and included the 30,000th shot of OMEGA, an important facility milestone. We prototyped and deployed a platform [Fig. 2(a)] similar to the one we fielded on OMEGA for our previous successful TDYNO Campaigns (FY15–FY18), during which we (1) demonstrated nonlinear amplification by turbulent dynamo for the first time in a laboratory environment;[8,9] (2) quantified the diffusion of energetic charged particles through magnetized turbulence;[10] and (3) characterized the growth rates in the kinematic and nonlinear phases of the turbulent dynamo mechanism.[11] Guided by simulation campaigns using the *FLASH* code[12–15] [Fig. 2(b)] on one of the nation's leadership supercomputers, we modified the original TDYNO platform to achieve supersonic turbulence. The configuration consists of two diametrically opposed chlorinated CH foil targets and a pair of grids supported by cylindrical shields. The foil targets are backlit with temporally stacked beams, delivering 5 kJ of energy on each side in a 5-ns ramp-up. The beams drive a pair of counter-propagating, high-Rm plasma flows that carry the seed magnetic fields generated by a Biermann battery. The flows propagate through a pair of grids that destabilize the flow and define the driving scale of the turbulence. The flows then meet at the center of the chamber to form a hot, turbulent interaction region where the magnetic fields are amplified to saturation values [Fig. 2(c)]. The chlorine dopant increases the radiative cooling efficiency of the turbulent plasma. This results in a decrease in the temperature and the sound speed of the plasma, making it supersonic [Fig. 2(d)]. However, our design enabled us to retain high-enough temperatures in the turbulent plasma to achieve supercritical Rm values for dynamo to operate [Fig. 2(e)].

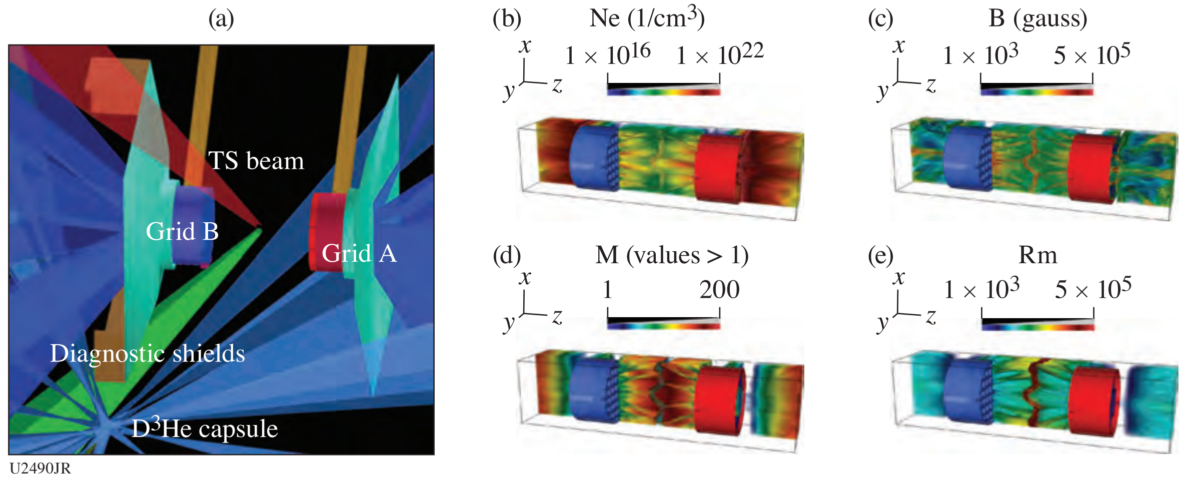

Figure 2
Supersonic turbulent dynamo on OMEGA. (a) VisRad schematic of the supersonic TDYNO platform for OMEGA. (b) *FLASH* simulation of the CHCl platform we will field on OMEGA (electron number density rendering). (c) Magnetic-field strength in the *FLASH* simulation, indicating amplification to hundreds of kG. (d) Mach number of the plasma flows and the turbulent region, showing only values above unity. The turbulent plasma is robustly supersonic. (e) The Rm values in the *FLASH* simulations are above RmC, in the many hundreds.

The primary goals of this shot day were to determine the energy cascade of the supersonic MHD turbulence by measuring the spectrum of both the magnetic field and plasma fluctuations and to characterize and map out the time history and saturation of turbulent dynamo in the supersonic regime. The shots yielded a wealth of experimental data, and preliminary analysis indicates that we were, in fact, able to generate compressible magnetized turbulence, characterize the plasma state, and measure the magnetic-field amplification using the suite of diagnostics we fielded previously. More specifically, we used x-ray imaging [Fig. 3(a)] to visualize the formation and evolution of the magnetized turbulence and to reconstruct the density power spectrum from the x-ray intensity fluctuations [Fig. 3(b)]. Moreover, the 4ω Thomson-scattering diagnostic yielded detailed information on the plasma state (ion and electron temperatures, bulk flow velocity, turbulent velocity, and electron density) at different times. During this first attempt at a 4ω probe, the diagnostic performed remarkably well. Finally, we employed proton radiography [Fig. 4(a)] on all shots and reconstructed the path-integrated magnetic fields[16,17] [Fig. 4(b)], thereby measuring the magnetic-field amplification.

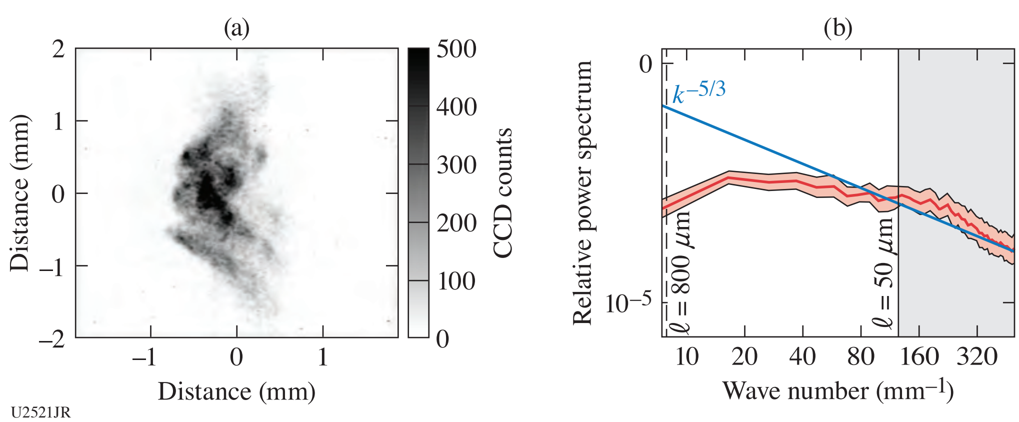

Figure 3
(a) X-ray image of supersonic radiative turbulence on OMEGA. (b) The shallow power spectrum from the x-ray fluctuations of (a) shows a departure from Kolmogorov and more power at small scales, consistent with supersonic turbulence.

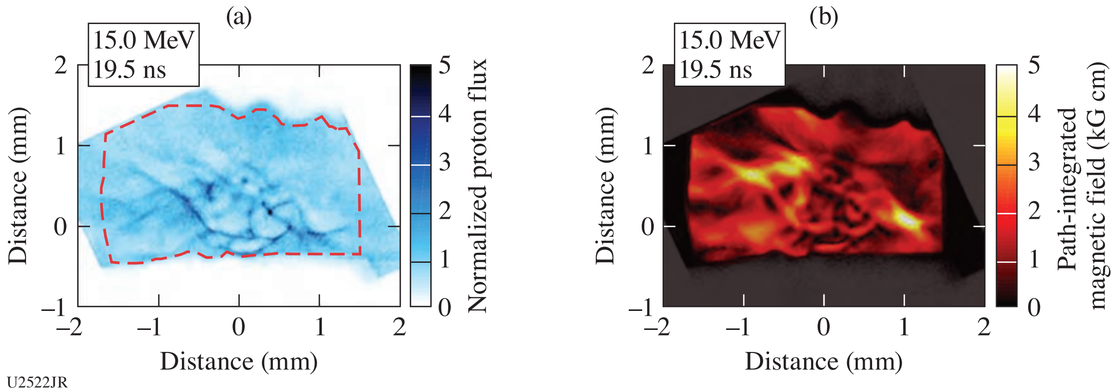

Figure 4
(a) Proton radiography of the turbulent interaction region at the same time as Fig. 3(a). (b) Path-integrated magnetic field from the proton radiograph in (a).

Despite the complexity of the experimental platform, the alignment procedures we developed, with the help of personnel from LLE and General Atomics, enabled us to perform 14 shots during our third shot day. The experimental data are currently being analyzed and promise to further our understanding of magnetized astrophysical turbulence in the supersonic regime.

The research leading to these results has received funding from the European Research Council under the European Community's Seventh Framework Programme (FP7/2007-2013)/ERC grant agreements no. 256973 and 247039, the U.S. Department of Energy under Contract No. B591485 to Lawrence Livermore National Laboratory, Field Work Proposal No. 57789 to Argonne National Laboratory, Subcontract No. 536203 with Los Alamos National Laboratory, Subcontract B632670 with Lawrence Livermore National Laboratory, and grants no. DE-NA0002724, DE-NA0003605, and DE-SC0016566 to the University of Chicago. We acknowledge support from the National Science Foundation under grants PHY-1619573 and PHY-1903430. Awards of computer time were provided by the U.S. Department of Energy ASCR Leadership Computing Challenge (ALCC) program. This research used resources of the Argonne Leadership Computing Facility at Argonne National Laboratory, which is supported by the Office of Science of the U.S. Department of Energy under contract DE-AC02-06CH11357. Support from AWE plc., the Engineering and Physical Sciences Research Council (grant numbers EP/M022331/1, EP/N014472/1 and EP/P010059/1) and the Science and Technology Facilities Council of the United Kingdom is also acknowledged, as well as funding from grants 2016R1A5A1013277 and 2017R1A2A1A05071429 of the National Research Foundation of Korea. This material is based upon work supported by the Department of Energy National Nuclear Security Administration under Award Number DE-NA0003856, the University of Rochester, and the New York State Energy Research and Development Authority.

An Experiment to Observe Photoionization Fronts in the Laboratory

Principal Investigator: H. J. LeFevre (University of Michigan)
Co-investigators: W. J. Gray, J. S. Davis, R. Gillespie, S. R. Klein, C. C. Kuranz, and R. P. Drake (University of Michigan); and P. A. Keiter (LANL)

When there is a sustained ionizing radiation source incident on a medium, such as the end of the cosmic dark ages and present-day star-forming regions, heat fronts propagate out from the source until the heating and cooling rate reach a steady state.[18] In the examples from cosmology and astrophysics listed above, photoionization (PI) is the process driving the heating, and the heat front formed is called a PI front. PI-front physics is also relevant to the capsule implosions in indirect-drive inertial confinement fusion experiments. Since there has been no observation of this type of front in astrophysics or the laboratory, an experiment to understand their properties is of interest.

Work by Drake and Gray[19,20] shows that it is possible to generate the appropriate conditions for a PI front using a laser-irradiated Au foil[21] on the OMEGA laser. They parameterize the experiment to the atomic physics of the problems with two dimensionless parameters:

$$\alpha = \frac{n_{\mathrm{i}+1}}{n_{\mathrm{i}}} \frac{n_{\mathrm{e}} R_{\mathrm{i}+1,\mathrm{i}}}{\Gamma_{\mathrm{i},\mathrm{i}+1}}, \tag{1}$$

$$\beta = 1 + \frac{n_{\mathrm{i}}}{n_{\mathrm{i}+1}} \frac{\langle \sigma v \rangle_{\mathrm{i,i}+1}}{R_{\mathrm{i}+1,\mathrm{i}}}, \tag{2}$$

where n_{i} is the population density of the ith ionization state, n_{e} is the electron density, $R_{\mathrm{i+1,i}}$ is the total recombination rate, $\Gamma_{\mathrm{i,i+1}}$ is the photoionization rate, and $\langle \sigma v \rangle_{\mathrm{i,i+1}}$ is the electron collisional ionization rate. In order to produce a PI front, Eq. (1) must be much less than 1 and Eq. (2) should be ~1. An ~80-eV quasi-blackbody source possible on OMEGA[21] incident on an 8.5-atm N gas cell should be sufficient to drive a front that has dimensionless parameters in the correct regime.[19,20]

The gas cell used in these experiments had a 3-mm inner diameter and a 7-mm length with a 750-nm-thick plastic window supported by a 100-μm-thick stainless-steel grid and a 500-nm-thick Au foil with a 3-mm diameter that was 300 μm from the gas cell window. Ten beams using SG5 phase plates drive the Au foil with an intensity of 10^{14} W/cm^2 by using pairs of beams with 1-ns pulse shapes to create 5 ns of total drive duration.

The primary measurement in this experiment is absorption spectroscopy of a 1% Ar dopant in the N gas cell. Irradiating a glow-discharge polymer capsule with an 850-μm outer diameter and a 9-μm wall thickness using 20 beams each with a 1-ns square pulse shape implodes the capsule, which produces a 220-ps-duration, continuum x-ray source in the spectral range of the Ar K shell from 2.9 to 3.3 keV. The capsule location was 10 mm from the axis of the gas cell with a 100-μm W aperture offset by 5 mm to restrict the source-size broadening of the spectrum. This measurement will provide the temperature, density, and ionization states of the Ar dopant, which one would then correlate to the plasma parameters in the N. To measure the spectrum through the gas cell, an x-ray spectrometer (XRS) was fielded in a ten-inch manipulator (TIM-3) with a PET crystal in position 2 with a 4° tilt to a central angle of 19.56°. Another XRS in TIM-1 with the same crystal configuration pointed at an unobstructed surface of the crystal recorded the unattenuated spectrum on each shot. A framing camera in TIM-2 recorded the capsule source size during the x-ray flash, a soft x-ray framing camera in TIM-6 observed the capsule emission size from an about orthogonal view, and a framing camera in TIM-5 observed the front surface emission of the Au foil. Additionally, Dante ran on these shots to observe the time-resolved capsule flux and characterize the Au foil emission on a dedicated shot.

Of the nine total shots during the campaign, three types of null shots evaluated the noise sources present during the measurement: only capsule, only capsule with gas cell present, and only driven gas cell. The remaining six shots included a repeat capsule-only null shot and five integrated physics shots. This resulted in a thorough characterization of the capsule backlighter used as an absorption source. However, there were emission lines in the capsule data, shown in Fig. 5(a), caused by contaminants in the capsule that affected the data analysis on shot day. Additionally, the gas cell acts to collimate the capsule emission [shown in Figs. 5(b) and 5(c)], which limits the spectral range of the absorption measurement, and the anticipated Ar absorption lines lie outside this narrow range. The crystal tilt was meant to adjust for this collimation, but this configuration was not well constrained. As a result, the shot day did not produce absorption spectra of PI fronts.

The positive result, considered the success of this shot day, is that this was the first shot day using this platform and the changes necessary to produce the desired measurements were minimal. In future experiments, a rotation of the target should allow for a standard configuration of the XRS diagnostics, which would remove the concerns about collimation. Holding the capsules at vacuum until minutes before placing them in the chamber should reduce the contamination levels in the capsule spectra. It should also be possible to add measurements, such as x-ray Thomson scattering or x-ray fluorescence, to this platform to allow for more-direct observation of the N. This would allow for redundant measurements that would confirm models for multiple diagnostics. Additionally, with a longer-duration backlighter and a streaked spectrometer, it will be possible to capture the propagation of the PI front with this platform.

This material is based upon work supported by the Department of Energy National Nuclear Security Administration under Award Number DE-NA0003856, the University of Rochester, and the New York State Energy Research and Development Authority.

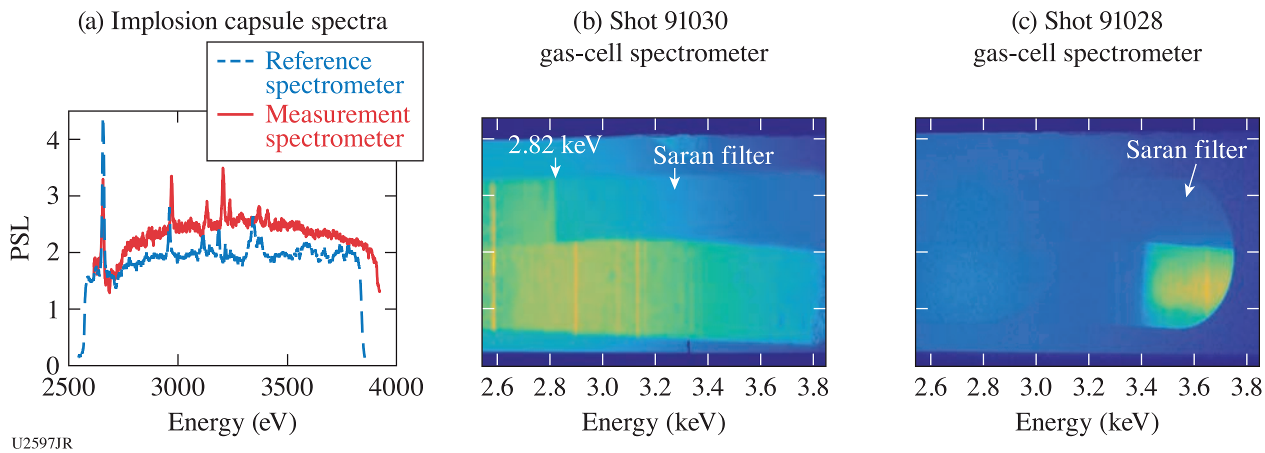

Figure 5
(a) The combined spectral data from both spectrometers on a capsule-only shot. This allows one to compare the emission from the capsule using different lines of sight and shows that it only varies by about 15%. This also shows that the contaminants are not localized to a single location. (b) Raw data from the spectrometer in TIM-3 without a gas cell collimating the capsule emission. It shows a region covered by a Saran filter, which acts as a spectral fiducial from the Cl K edge. (c) The emission seen by the spectrometer in TIM-3 when a gas cell is present demonstrates the collimation of the backlighter and subsequent reduction of the spectral range.

MIT FY19 NLUF Work on High-Energy-Density Physics and Student Training at Omega

Principal Investigator: R. D. Petrasso (MIT)
Co-investigators: C. K. Li, J. A. Frenje, M. Gatu Johnson, F. H. Séguin, and A. Bose (MIT)
Graduate students: P. Adrian, T. Johnson, N. Kabadi, J. Kunimune, B. Lahmann, J. Pearcy, B. Reichelt, R. Simpson, H. Sio, and G. Sutcliffe (MIT)
Undergraduate students: R. Przybocki and H. Propp (MIT)

MIT NLUF work in FY19 included a wide range of experiments applying charged-particle spectrometry, time-history study of inertial confinement fusion (ICF) nuclear and x-ray production, and monoenergetic charged-particle radiography methods developed by MIT and collaborators to the study of ICF plasmas, laboratory astrophysics, and high-energy-density physics (HEDP). Specific major topics where research has produced important results include kinetic and multi-ion-fluid effects on ICF implosion dynamics; ion–electron equilibration in ICF; ion stopping around the Bragg peak in weakly coupled D^3He plasmas; ion stopping in warm dense matter; and nuclear reactions and products relevant to stellar and big-bang nucleosynthesis. Twenty papers about NLUF-related research were published or submitted in FY19,[10,22–40] including seven with MIT first authors.[22,23,32–34,38,40] There were also many invited talks and contributed talks presented at conferences.

Much of the work was done by MIT graduate and undergraduate students in the group; during the last year, the group welcomed two new graduate students (J. Kunimune and B. Reichelt) as part of MIT's long-term program of recruiting and training outstanding Ph.D. students in HEDP and ICF science. Two undergraduates (R. Przybocki of MIT and H. Propp of Cornell) worked with the group and have expressed interest in continuing work in HEDP.

Graduate student H. Sio, after completing his Ph.D. thesis ("Using Time-Resolved Nuclear Diagnostics to Probe Kinetic/Multi-Ion Physics and Shock Dynamics on OMEGA and the NIF"), stayed on as a postdoc to work with student N. Kabadi and LLE collaborators on the development of the particle-x-ray temporal diagnostic (PXTD) that measures the time history of multiple nuclear burn products and multiple energy bands of x-ray emissions in ICF implosions. Dr. Sio has been nominated for the 2020 *Rosenbluth Outstanding Doctoral Thesis Award* for this work. Use of the PXTD has led to the first time-resolved quantitative assessment of the dynamics of fuel-ion species separation in DT^{3}He gas-filled capsule implosions by using simultaneously measured D^{3}He and DT reaction histories.[23,32] These reaction histories captured the relative timing of the nuclear burn histories with unprecedented precision (~10 ps), as seen in Fig. 6(a). Average-ion hydrodynamic simulations, shown in Fig. 6(b), cannot explain the 50±10-ps earlier D^{3}He reaction history relative to DT, even for hydrodynamic-like implosions. The ^{3}He/T fuel ratio in the early phase of the shock burn, inferred from time-resolved D^{3}He/DT yield ratio, is an order of magnitude higher than the initial ^{3}He/T gas-fill ratio and therefore indicates species separation, which obviously cannot be captured by average-ion simulations. As shown in Fig. 6(c), an *LSP* multi-ion simulation captures the timing of these reaction histories. Proposed future efforts will advance these initial studies by exploring the dynamics of kinetic/multi-ion fluid effects and ion-thermal decoupling in D^{3}He and D_2 (with trace T) in shock-driven and ablatively driven implosions.

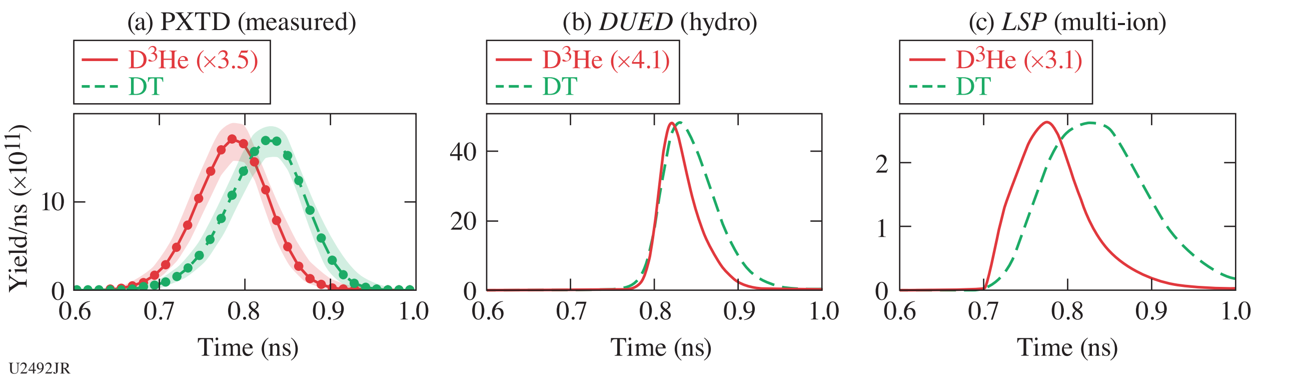

Figure 6
(a) Absolute D^{3}He (red) and DT (green) reaction histories measured with PXTD, (b) simulated by the average-ion hydro-code *DUED*, and (c) *LSP* multi-ion code for OMEGA shot 82615. The D^{3}He reaction histories are amplitude scaled to match the DT histories for clarity. The measured D^{3}He-bang time is 50±10 ps earlier than the DT-bang time. Uncertainties in the PXTD data are indicated by the shaded regions in (a). This work was recently published by former MIT Ph.D. student H. Sio in Physical Review Letters.[32]

Two significant new diagnostic methods that have evolved from students' NLUF science experiments this year will be very important for many future experiments on OMEGA. The first is "cryoPXTD," which is the PXTD modified with improved optics for cryogenic ICF experiments; it will have 10-ps relative timing accuracy of nuclear-burn and x-ray-emission measurements, and it will provide measurements of electron temperature as a function of time. The second method is an extension of the monoenergetic-charged-particle radiography technique for imaging and analyzing plasmas and their self-generated electromagnetic fields, originally developed by MIT scientists C. K. Li, R. D. Petrasso, and F. H. Séguin (who received the 2017 *John Dawson Award for Excellence in Plasma Physics Research* for this NLUF work done on OMEGA). This radiography technique previously utilized a backlighter that supplied 3- and 14.7-MeV protons, but student G. Sutcliffe is developing a new tri-particle backlighter that supplies mono-energetic 9.5-MeV deuterons in addition to the 3- and 14.7-MeV protons. This new backlighter makes it possible to simultaneously record three radiographs (one for each particle type) and thereby provide new options for uniquely identifying the separate effects of self-generated electric and magnetic fields in plasmas imaged with radiography. Student J. Pearcy has already done preliminary work on deducing the spatial distributions of magnetic fields observed indirectly in some of these new radiographs.

Other individuals in the Division have carried out other important new physics studies and received important awards. For example, scientist M. Gatu Johnson (see Fig. 7) was selected as the 2019 recipient of the American Physical Society's prestigious *Katherine E. Weimer Award* for outstanding plasma science research by a woman physicist in the early stages of her career. The citation on her certificate reads, "For significant contributions to Inertial Fusion Sciences and pioneering work in Stellar Nucleosynthesis through nuclear measurements," and much of her work was done on OMEGA through the NLUF program.

Scientist C. K. Li did innovative breakthrough studies on astrophysically relevant, electromagnetic collisionless shocks in the laboratory. These studies led to the definitive demonstration that the structure and dynamics of astrophysical collisionless shocks can be modeled in the laboratory and provided new insight into the role of the Weibel instability in electron heating and shock

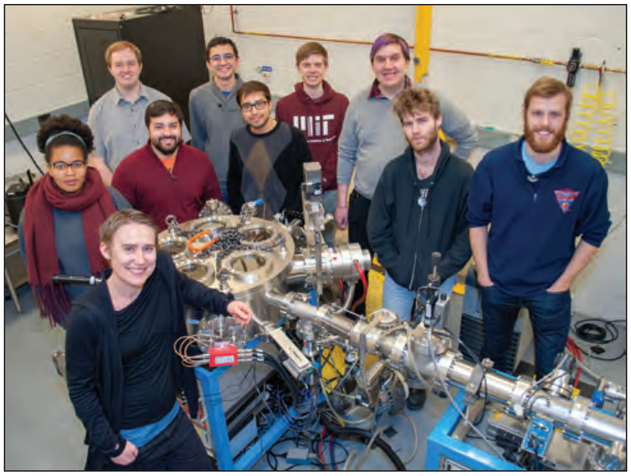

U2494JR

Figure 7
M. Gatu Johnson, 2019 *Weimer Award* recipient, shown with MIT graduate students and MIT's accelerator that is used for ICF diagnostic development.

mediation. Collisionless shocks are ubiquitous in the universe as a consequence of supersonic plasma flows sweeping through interstellar and intergalactic media, and the generation of electromagnetic collisionless shocks in the laboratory has been an important goal during the last several decades for elucidating large-scale astrophysical phenomena (e.g., supernova remnants and protostellar jets), accreting compact objects, and studying a broad range of fundamental physics phenomena. Sponsored by the NLUF program, laboratory experiments led by MIT demonstrated the formation of a quasi-perpendicular, magnetized collisionless shock. The collisionless shock was responsible for electron acceleration to energies exceeding the average energy by two orders of magnitude. These results were recently published by Physical Review Letters.[22]

This material is based upon work supported by the Department of Energy National Nuclear Security Administration under Award Numbers DE-NA0003539 and DE-NA0003539, the University of Rochester, and the New York State Energy Research and Development Authority.

Demonstration of Talbot–Lau X-Ray Deflectometry (TXD) Electron Density Diagnostic in Laser–Target Interactions
Principal Investigators: M. P. Valdivia Leiva (Johns Hopkins University)
Graduate students: M. Trantham and H. Le Fevre (University of Michigan); M. Vescovi (Universidad Catolica de Chile); and V. Bouffetier (University of Bordeaux)

A Talbot–Lau x-ray deflectometer (TXD) electron density diagnostic[41] has been implemented on the OMEGA EP laser. The task was preceded by preparatory experiments on the Multi-Terawatt (MTW) laser. Moiré imaging was demonstrated using a laser-based x-ray backlighter to backlight a static object and a laser-produced plasma object. Measurement of electron density gradient maps of above-quarter-critical density in ablating plasmas (i.e., plasmas actively irradiated by an intense laser) through TXD was pursued.

The OMEGA EP experiment was carried out on 5 December 2018 and tested the TXD technique. The experimental design was carried out in collaboration with Dr. P. Keiter (now at LANL), Dr. P. Drake, and graduate students from the University of Michigan, who also supported the design, preparation, and execution of the OMEGA EP experiment. The irradiated foil experiment was designed along with the diagnostic adaptation for OMEGA EP.

The experiment required design and implementation of a TXD diagnostic platform compatible with the OMEGA EP laser. The project was supported by C. Mileham and C. Stoeckl, among many other science and engineering LLE staff. From the original concept design submitted by Johns Hopkins University and considering TXD diagnostic requirements, LLE's engineering team proposed a rail-like TXD design compatible with a TIM diagnostic setup, which is one of the front ends to the OMEGA EP laser x-ray charge-coupled–device (CCD) imaging camera diagnostic. The final design by J. Zou allows for interferometer alignment using a laboratory x-ray source outside the OMEGA EP chamber. The setup maintains the geometrical conditions once the diagnostic is placed inside the vacuum chamber. The design allows for fine adjustments for potential grating tilting, precise and independent rotation of gratings, as well as small displacement in xyz, with a wider range of motion in the z direction (see Fig. 8).

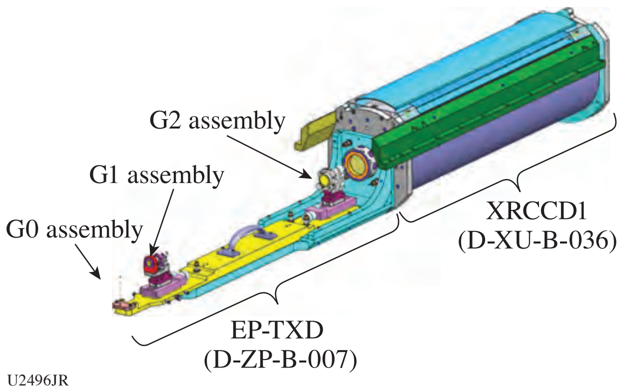

Figure 8
OMEGA EP TXD diagnostic schematic.

Simulations of propagating density profiles from laser–matter interaction of plastic foils were performed [Fig. 9(a)] to better understand thermal electron transport in laser-produced plasmas. Propagation density profiles from laser–matter interaction of plastic (CH) foils were simulated and provided ablation profiles of the laser-irradiated planar foil above critical density. Synthetic Moiré patterns were generated from the simulated electron density profiles and analyzed through the TXD methods. The foil ablation profile expands along the direction shown in Fig. 9(b). TXD imaging will provide an x–y map, and an electron density profile will be detected along the y direction. It should be noted that the Moiré image will also provide vertical electron density information for the radial expansion of the foil along x, albeit with spatial resolution limited by a fringe period. The foil and ablation-front orientation with respect to the grating bars is shown in Fig. 9(c).

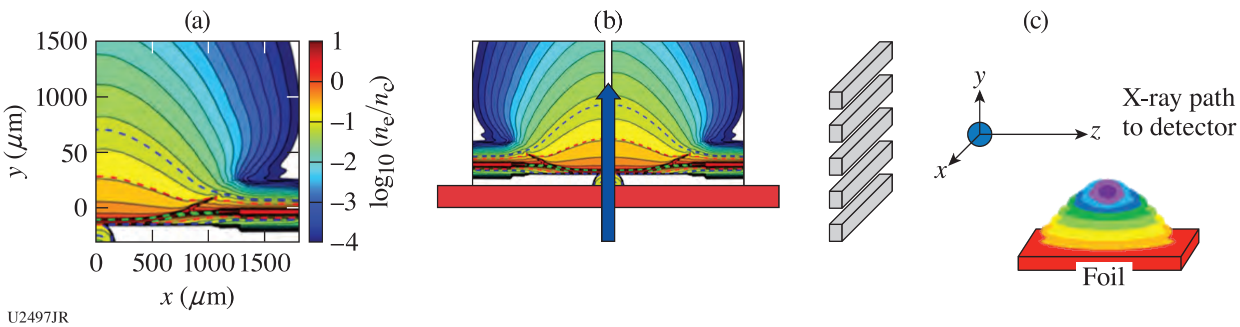

Figure 9
(a) Electron density *CRASH* 2-D simulation; (b) ablation expansion diagram; and (c) measurement schematics for the OMEGA EP experiment showing source grating bars orientation.

The OMEGA EP experiment aimed to demonstrate grating survival for x-ray laser backlighting of <100 J as well as fringe formation. This goal was accomplished, demonstrating laser-based Moiré imaging. A Moiré image was obtained with a 48.7-J, 10-ps, 70-μm-spot-size backlighter beam. A fringe contrast of ~12% to 15% was measured for a backlighter foil to a source grating distance of 2 mm, compared to the 26% to 28% obtained with a Cu x-ray tube. Hard hits reached a level of <21,000 counts, with ~1.8 signal-to-noise ratio. Figure 10 shows a 200-μm × 1.75-mm × 0.5-mm Ta slab. A FWHM of 60.3±2.0 μm was measured by the edge method.

A second goal of the EP-TXD experiment was to obtain electron density profiles from an ablation plasma front. In addition to demonstrating TXD capabilities as an advanced diagnostic for HEDP plasmas, these results were expected to benchmark radiation hydrodynamic codes that fail to predict ablation dynamics in laser-produced plasmas. Following the results shown in Fig. 10, the CH foil was irradiated with three UV beams at maximum energy with a backlighter beam pulse of 48.7 J, 10 ps, and 70-μm spot size. An electromagnetic pulse caused an error in the CCD electronics readout, which rendered the detector unavailable for the remaining laser shots. The x-ray CCD was replaced with image plates; however, since their x-ray energy response is high for higher energies, no discernible fringes were observed, and no Moiré images were recorded from an irradiated foil

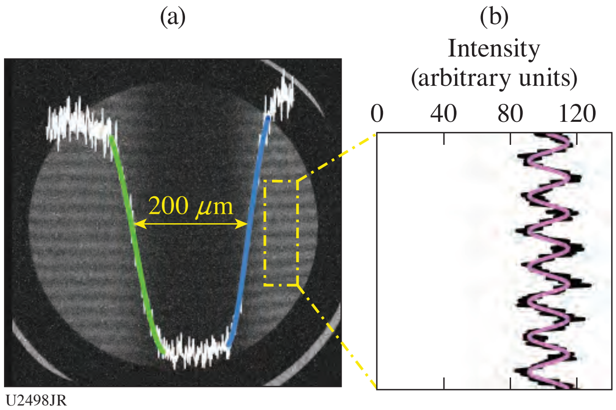

Figure 10
(a) Moiré image of a Ta test object (200 μm × 1.75 mm × 1.5 mm) recorded with the x-ray CCD and (b) the Moiré fringe contrast plot.

ablation front. Therefore, the second goal was not accomplished given that electron density mapping of a plasma object was not achieved. Nevertheless, these results served as a detector capability test for a future EP-TXD diagnostic that will suppress the high-energy component by means of refractive optics. With that goal in mind, a multilayer mirror configuration will be explored in our upcoming NLUF grant.

1. E. N. Parker, *Cosmical Magnetic Fields: Their Origin and Their Activity*, The International Series of Monographs on Physics (Clarendon Press, Oxford, 1979).
2. A. Brandenburg and Å. Nordlund, Rep. Prog. Phys. **74**, 046901 (2011).
3. C. Federrath *et al*., Astrophys. J. **797**, L19 (2014).
4. C. Federrath, J. Plasma Phys. **82**, 535820601 (2016).
5. M. R. Krumholz and C. F. McKee, Astrophys. J. **630**, 250 (2005).
6. C. Federrath and R. S. Klessen, Astrophys. J. **763**, 51 (2013).
7. P. Padoan and A. Nordlund, Astrophys. J. **576**, 870 (2002).
8. P. Tzeferacos *et al*., Phys. Plasmas **24**, 041404 (2017).
9. P. Tzeferacos *et al*., Nat. Commun. **9**, 591 (2018).
10. L. E. Chen *et al*., "Stochastic Transport of High-Energy Particles Through a Turbulent Plasma," submitted to Physical Review Letters.
11. A. F. A. Bott *et al*., to be submitted to Proceedings of the National Academy of Sciences.
12. B. Fryxell *et al*., Astrophys. J. Suppl. Ser. **131**, 273 (2000).
13. A. Dubey *et al*., Parallel Comput. **35**, 512 (2009).
14. P. Tzeferacos *et al*., High Energy Density Phys. **17**, 24 (2015).
15. Flash Center for Computational Science, University of Chicago, Chicago, IL 60637, http://flash.uchicago.edu/site/.
16. C. Graziani *et al*., Rev. Sci. Instrum. **88**, 123507 (2017).
17. A. F. A. Bott *et al*., J. Plasma Phys. **83**, 905830614 (2017).
18. B. Strömgren, Astrophys. J. **89**, 526 (1939).
19. R. P. Drake *et al*., Astrophys. J. **833**, 249 (2016).
20. W. J. Gray et al., Phys. Plasmas **26**, 052901 (2019).

21. J. S. Davis *et al*., Phys. Plasmas **25**, 073304 (2018).
22. C. K. Li *et al*., Phys. Rev. Lett. **123**, 055002 (2019).
23. H. Sio *et al*., Phys. Plasmas **26**, 072703 (2019).
24. D. B. Schaeffer *et al*., Phys. Rev. Lett. **122**, 245001 (2019).
25. T. R. Joshi *et al*., Phys. Plasmas **26**, 062702 (2019).
26. P. Mabey *et al*., Sci. Rep. **9**, 8157 (2019).
27. P.-E. Masson-Laborde *et al*., Phys. Rev. E **99**, 053207 (2019).
28. A. S. Liao *et al*., Phys. Plasmas **26**, 032306 (2019).
29. L. Gao *et al*., Astrophys. J. Lett. **873**, L11 (2019).
30. Y. Lu *et al*., Phys. Plasmas **26**, 022902 (2019).
31. V. Gopalaswamy *et al*., Nature **565**, 581 (2019).
32. H. Sio *et al*., Phys. Rev. Lett. **122**, 035001 (2019).
33. M. Gatu Johnson *et al*., Phys. Plasmas **26**, 012706 (2019).
34. J. A. Frenje *et al*., Phys. Rev. Lett. **122**, 015002 (2019).
35. A. M. Saunders *et al*., Phys. Rev. E **98**, 063206 (2018).
36. G. Kagan *et al*., Contrib. Plasma Phys. **59**, 181 (2019).
37. P. T. Springer *et al*., Nucl. Fusion **59**, 032009 (2019).
38. M. Gatu Johnson *et al*., Phys. Rev. E **98**, 051201(R) (2018).
39. O. M. Mannion *et al*., Rev. Sci. Instrum. **89**, 10I131 (2018).
40. M. Gatu Johnson *et al*., Rev. Sci. Instrum. **89**, 10I129 (2018).
41. M. P. Valdivia *et al*., Rev. Sci. Instrum. **91**, 023511 (2020).

FY19 Laboratory Basic Science Program

M. S. Wei

Laboratory for Laser Energetics, University of Rochester

In FY19, a total of 25 Laboratory Basic Science (LBS) projects were allocated a total of 27.5 shot days for experiments at the Omega Laser Facility, which included five additional projects selected from the FY19 LBS proposals based on their ranking to back fill some of the National Laser Users' Facility allocations. A total of 289 target shots were conducted for the LBS experiments led by scientists from Lawrence Livermore National Laboratory (LLNL), Los Alamos National Laboratory (LANL), LLE, SLAC, and Princeton Plasma Physics Laboratory (PPPL) (see Table I). The FY19 LBS experiments are summarized here.

Table I: LBS experiments conducted at the Omega Laser Facility in FY19.

Principal Investigator	Institution	Title
F. Albert	LLNL	Laser Wakefield Electron Acceleration and Betatron Radiation on OMEGA EP
H. Chen	LLNL	Exploring the Applications of Laser-Produced Relativistic Electron–Positron Pair-Plasma Jets
H. Chen	LLNL	Laboratory Model of Particle Acceleration in Supernova Shocks
K. Flippo	LANL	Characterizing Magnetized Turbulent Plasmas: Toward Generating Laboratory Dynamo
C. J. Forrest	LLE	Evaluation of Neutron-Induced Breakup with Light-Z Nuclei at E_n = 14.03 MeV at the Omega Laser Facility
W. Fox	PPPL	Turbulent Transport in Magnetized HED Plasmas
D. E. Fratanduono	LLNL	Investigating Giant Impacts Between Rocky Planets with High-Pressure Melting and Shock Equation-of-State Measurements on Complex Silicates
A. Gleason	SLAC	Viscosity Measurements Using Tracer Particles
S. Glenzer	SLAC	High-Yield Neutron Pulses from Deflagrating Convergence in Hohlraums
X. Gong	LLE	Structure and Melting of High-Pressure Sodium and Potassium
M. Gorman	LLNL	Phase Transformation Kinetics—Strain Rate Tuning of the Peierls Distortion in Ramp-Compressed BCT Sn
B. J. Henderson	LLE	Optical Spectroscopy of High-Pressure Sodium
S. X. Hu	LLE	Uncharted Territory: Testing the Predictions of Density Functional Theory (DFT) in Warm and Extremely Dense Plasmas
L. C. Jarrott	LLNL	Using Line Intensity Enhancements to Characterize NLTE Plasmas
S. Jiang	LLNL	Characterizing Pressure Ionization in Ramp-Compressed Materials with Fluorescence and Absorption Spectroscopy
G. Kagan	LANL	Probing Electron Distribution in Spherical Implosions with Hard X-Ray Spectroscopy

Table I: LBS experiments conducted at the Omega Laser Facility in FY19 (continued).

Principal Investigator	Institution	Title
S. Khan	LLNL	Absolute EOS Measurements of Low-Density Foams Toward Studying the Landau–Darrieus Instability in HED Conditions
A. Krygier	LLNL	The Strength of Fe and Fe-Si 16 wt% at the Conditions in Earth's Core
E. Marley	LLNL	Radiative Properties of an Open L-Shell, Non-LTE Plasma
M. Millot	LLNL	A Journey to the Center of Uranus and Neptune: Using X-Ray Diffraction to Unravel the Atomic Structure of New Solid and Superionic Ices at Multi-Megabar Pressures
Z. L. Mohamed	LLE	Study of Gamma Ray Products from Reactions Relevant to Big Bang Nucleosynthesis
J. Moody	LLNL	Developing an Ultrahigh Magnetic Field Laboratory for HED Science
H. G. Rinderknecht	LLNL	Structure and Scaling of Strong Collisional Plasma Shocks
R. Saha	LLE	Measurements of Warm Dense Matter Based on Angularly and Spectrally Dispersed X-Ray Scattering
W. Theobald	LLE	X-Ray Phase-Contrast Imaging of Strong Shocks in Foam Targets

During FY19, LLE issued a solicitation for LBS proposals for beam time in FY20. A total of 36 proposals were submitted requesting a total of 57.5 shot days, 274% exceeding the LBS allocation, showing strong interest and high demand of Omega Laser Facility time for basic high-energy-density (HED) experiments from both National Nuclear Security Administration inertial confinement fusion (ICF) labs and Office of Science laboratories. An independent LBS Proposal Review Committee consisting of 12 experts from university, national laboratories, and industry reviewed and ranked the proposals. Based on the Review Committee's recommendation, 22 proposals, including one led by Lawrence Berkeley National Laboratory, were selected and allocated a total of 21.5 shot days for experiments at the Omega Laser Facility in FY20 as shown in Table II.

Table II: LBS experiments approved for target shots at the Omega Laser Facility in FY20.

Principal Investigator	Institution	Title
F. Albert	LLNL	X-Ray Radiation Driven by Laser Wakefield Acceleration at OMEGA EP
H. Chen	LLNL	Develop a Magnetic Mirror Trap for Laser-Produced Relativistic Electron–Positrons
F. Coppari	LLNL	The Atomic Structure and Melting of New Solid and Superionic Water Ices at Multi-Megabar Pressures: Searching for Ice XIX
T. Döppner	LLNL	Experimental Measurement of Mutual Diffusivity in Warm Dense Matter
K. A. Flippo	LANL	Quantifying the Path to Saturation in a Turbulent Magnetic Dynamo (TMD)
W. Fox	PPPL	Turbulent Transport in Magnetized HED Plasmas
D. E. Fratanduono	LLNL	Investigating Giant Impacts between Rocky Planets with High-Pressure Melting and Shock Equations-of-State Measurements on Complex Silicates
L. Gao	PPPL	Effect of Laser Parameters on Magnetic Field Generation with Laser-Powered Capacitor Coils
A. Gleason	SLAC	Viscosity Measurements Using Tracer Particles
S. Jiang	LLNL	Characterizing Pressure Ionization in High Density with X-Ray Line Emission Spectroscopy
O. M. Mannion	LLE	Measuring the Gamow Energy Shift of Fusion Products in High-Temperature Plasmas
M. Millot	LLNL	Peering Into the Ice Giant Planets Using Shocks on Precompressed Water–Ammonia Mixtures: Superionic Ammonia Hydrates

Table II: LBS experiments approved for target shots at the Omega Laser Facility in FY20 (continued).

Principal Investigator	Institution	Title
Z. L. Mohamed	LLE	Study of Gamma Ray Products from Reactions Relevant to Big Bang Nucleosynthesis
P. M. Nilson	LLE	Terra Incognita: Testing the Predictions of Density Functional Theory (DFT) in Warm and Extremely Dense Plasmas
A. Pak	LLNL	Proton Radiography of Target Normal Sheath Acceleration Fields in the Long-Pulse Regime
H. G. Rinderknecht	LLE	Measuring the Triton Breakup Reaction T(n,2n)D
R. Saha	LLE	Optical and X-Ray Scattering Measurements of Dense Lithium
R. Smith	LLNL	The Effect of Alloying on High-Pressure Phase Transformations: Diffusion Time Scales and Kinetics
C. Stoeckl	LLE	Development of New Experimental Platform LIANS on OMEGA/OMEGA EP for Deuteron and Triton-Induced Nuclear Reactions
G. Swadling	LLNL	An Investigation of Magnetic Fields Generated by Instability Microphysics in Collisionless Plasmas Flow Interactions Using Optical Thomson Scattering
S. Zhao	LBNL	Extreme Deformation and Failure of High Entropy Alloys by Laser Shock-Induced Compression and Tension
A. B. Zylstra	LLNL	Implosions for Studying Solar CNO Reactions

Laser Wakefield Acceleration on OMEGA EP

Principle Investigator: F. Albert, LLNL
Co-investigators: N. Lemos,* J. Williams, and H. Chen (LLNL); and J. L. Shaw, D. Haberberger, and D. H. Froula (LLE)
Graduate student: P. King (LLNL/University of Texas, Austin)
*Postdoc

This series of shots was designed to accelerate electrons in the self-modulated laser wakefield acceleration (SMLWFA) regime, in collaboration with LLE. The Wakefield-EP-19A shot day was coupled with other LLE-led campaigns (PlasmaLensEP and AdvRadEP), with an overall goal to accelerate high-charge, relativistic electrons beyond 100 MeV. This laser wakefield acceleration platform will serve future applications (development and use of novel x-ray sources) on OMEGA EP and the National Ignition Facility's (NIF's) Advanced Radiographic Capability (ARC) laser.

The shot day alternatively used the backlighter and sidelighter beams in their best compression configuration (0.7-ps pulse duration), focused onto the newly commissioned OMEGA EP ten-inch manipulator (TIM)–based gas-jet system. The gas jet provided plasma electron densities in the 3×10^{18} to 1×10^{19} cm^{-3} range. Since laser wakefield acceleration benefits from longer focal lengths, we used apodizers to increase the effective focal length to *f*/6 (*f*/10) on the backlighter (sidelighter) from the original *f*/2 geometry. This resulted in a maximum energy on target of 95 J (24 J). We used 6-mm-long and 10-mm-long nozzles and varied the laser intensity between 3×10^{18} and 6×10^{19} W/cm^2.

The campaign successfully measured Maxwellian electron beam spectra up to 200 MeV with the electron–proton–positron spectrometer (EPPS) as well as the beam profile, using two image plates with a hole placed in front of the diagnostic, as shown in Fig. 1. Beam profiles with divergences <100 mrad were measured, with a total charge above 100 nC, which is the highest charge recorded in a self-modulated laser wakefield accelerator to date.

Analysis of the campaigns is ongoing, and the results of the shot day, coupled to the LLE-led campaigns, were presented in an invited talk[1] at the annual 2019 APS-DPP meeting.

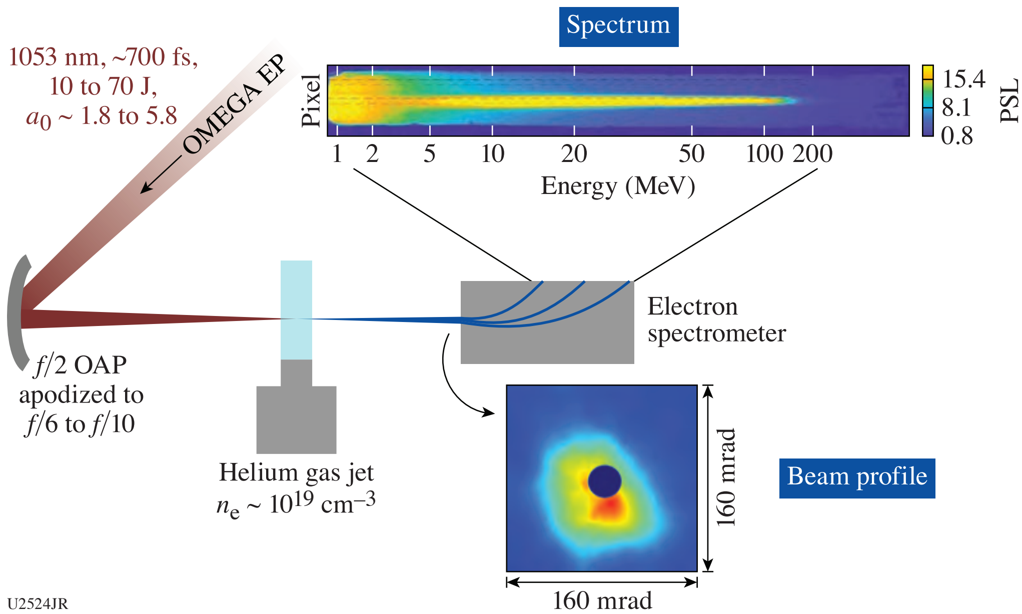

Figure 1
Experimental configuration for Wakefield-EP-19A, with examples of a measured electron spectrum and beam profile.

Exploring the Applications of Laser-Produced Relativistic Electron–Positron Pair-Plasma Jets
Principle Investigator: H. Chen (LLNL)
Co-investigators: J. Kim (UCSD); M. Manuel (GA); and S. Kerr,* A. Macphee, and A. Link (LLNL)
*Postdoc

In FY19, this team completed one LBS shot day on OMEGA EP, alternating the two OMEGA EP short-pulse beams to produce jets of electron–positron antimatter pairs. These 14 FY19 shots used novel targets to explore the laser–target interaction and to seek enhanced pair production. The experiment focused on (1) enhancing the pair yield using nanostructured targets and (2) collimating or focusing positron jets by shaping the rear target surface to modify the sheath potential. The experiments successfully demonstrated both yield enhancement and positron focusing. The data strengthened prospects for future experiments on laboratory astrophysics using the pair jet–plasma interaction to drive beam instabilities.

The OMEGA EP short-pulse beams (~1 kJ in 10 ps) irradiated 1-mm-thick Au targets, with and without (1) a parabolic cone on the front of the target and (2) a convex-shaped back surface. It was found that for the same laser energy, positron yields and acceleration were both increased by using the parabolic cones, with a trend similar to that found on NIF ARC experiments.[2] This finding is important as well as unexpected because the OMEGA EP laser has a smaller *f* number ($f \sim 2$) compared to that of ARC ($f \sim 60$). The underlying physics remain to be investigated. We also repeated the results obtained in FY18 that used a hemispherical-shaped back surface to focus the positron jets through the sheath field,[3] similar to that observed in proton focusing. This observation is important because it demonstrated that higher pair density can be achieved by reducing their volume, which may enable the development of instabilities predicted by theory.

The prior experiments showed that quasi-monoenergetic relativistic positron jets are formed during high-intensity irradiation of thick gold targets,[4,5] and that these jets can be strongly collimated[6] using the magneto-inertial fusion electrical delivery system (MIFEDS).[7] The external field produces a 40-fold increase in the peak positron and electron signals.[5] The positron yield was found to scale as the square of the laser energy.[8,9] The FY15 results revealed another dimension of scaling on the target materials.

The favorable scaling would enable the laboratory study of relativistic pair plasmas that are important to understanding some of the most exotic and energetic systems in the universe.[9,10]

Laboratory Model of Particle Acceleration in Supernova Shocks

Principle Investigator: H. Chen (LLNL)
Co-investigators: C. A. J. Palmer,* A. R. Bell, A. Bott,* G. Gregori, and J. Matthews* (Oxford); D. Lamb and P. Tzeferacos (University of Chicago); A. Birkel and C. K. Li (MIT); and H.-S. Park (LLNL)
Graduate student: O. Karnbach (Oxford)
*Postdoc

This shot day studied the growth of the nonresonant hybrid instability in a turbulent magnetized plasma driven by a high-current proton beam. The TDYNO target platform[11] is used to produce a turbulent magnetized plasma. This is generated by colliding the flow of two plasma jets, each of which has had its flow disrupted by passage through a mesh. The jets are produced by ten OMEGA beams with 2 kJ of energy arranged into a 10-ns-long drive. Previous shot days have demonstrated that this can produce plasmas embedded with stochastic magnetic fields with strengths up to 4 kG. One of the OMEGA EP short-pulse beams (2 kJ in 100 ps) was used to produce a proton beam from a thin (50-μm) metal target. This target was positioned 3 mm from the central axis of the turbulent plasma (Fig. 2). The OMEGA EP beam was fired 20 ns after the OMEGA beams so that the low-energy TNSA proton beam would interact with the turbulent plasma.

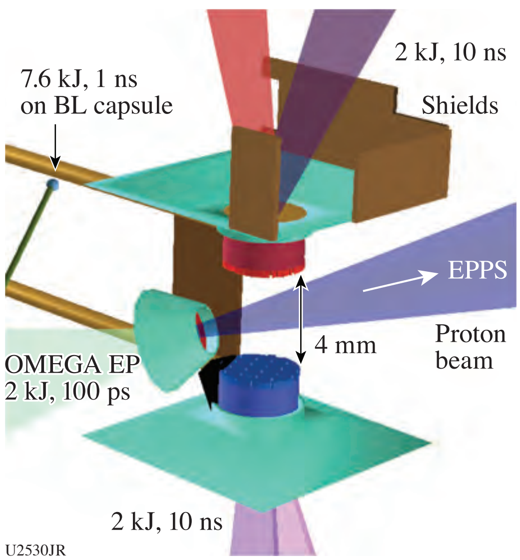

Figure 2
Experimental configuration. BL: backlighter.

The main diagnostics included an x-ray framing camera to measure self-emission from the turbulent plasma, proton radiography using a D^3He capsule irradiated with 17 OMEGA beams (450 J/beam, 1 ns) to probe the magnetic field structure of the plasma, and the EPPS to measure the energy spectrum of the TNSA proton beam. The EPPS was also equipped with a thin (<3-mm) RCF/CR39 stack in the front holder to measure the spatial profile of the beam. The streaked Thomson-scattering measurements indicate that the colliding plasma conditions are similar to previous experiments with electron temperatures of the order of 300 eV. The XRFC indicated fluctuations in plasma density in the collision region [Figs. 3(a)–3(c)] from which the density spectrum will be extracted. This can be compared with the spectrum of fluctuations in the plasma magnetic field, which will be extracted from the PRAD (proton radiography data) [Figs. 3(d) and 3(e)]. Qualitative study of the PRAD indicates modulated magnetic fields with small-scale structures visible at early times but not at later times. In addition to the displayed data, the EPPS indicates some energy-dependent transverse momentum imparted to the OMEGA EP proton beam as it transits the turbulent plasma.

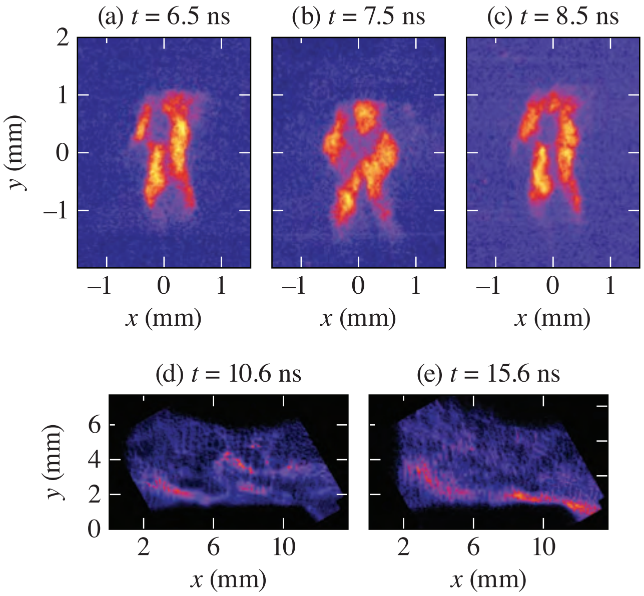

U2531JR

Figure 3
[(a)–(c)] Time series of XRFC images and [(d) and (e)] raw PRAD images where the brighter signal indicates higher proton flux. In both cases, time given is relative to nominal collision time of two ablation plasmas.

Inelastic Reactions of ^{7}Li from 14-MeV Neutrons Using an Inertial Confinement Fusion Platform

Principal Investigator: C. J. Forrest (LLE)

Co-investigators: J. P. Knauer, P. B. Radha, V. Yu. Glebov, O. M. Mannion, Z. L. Mohamed, S. P. Regan, T. C. Sangster, and C. Stoeckl (LLE); and W. U. Schröder (LLE and Dept. Chemistry and Physics, University of Rochester

HEDLP (high-energy-density laboratory plasmas) is an established experimental platform that is used to address opportunities in a number of fields of scientific research.[12] Recently, HEDLP's generated on the OMEGA laser[13] have been used to conduct basic nuclear science experiments. These facilities present viable and interesting alternatives to experimental accelerator-based platforms. In fact, primary yields are at the levels required to begin investigating fundamental nuclear reactions including neutron-induced breakup reactions of light nuclei. For these reasons, new fields of scientific exploration have been initiated for both nuclear interactions and high-energy-density plasmas.

Low-energy nuclear reactions involving light nuclei (for example, the breakup of a deuteron) represent one of the most attractive cases to study nucleon–nucleon interaction due to it being one of the simplest systems to evaluate.[14] Experiments that inferred the double-differential cross section from the breakup of the deuteron have been compared to past measurements performed using accelerator-based platforms and *ab initio* calculations performed by A. Deltuva, which are in good agreement with the recent measurements achieved on OMEGA.[15] This measurement is currently the only data available that spans nearly the entire energy range from 1 to 10.5 MeV.

The production ^{7}Li nuclei play an important role in primordial nucleosynthesis, nuclear astrophysics, and fusion energy generation. Recent calculations using the no-core shell model with continuum (NCSMC) method are being applied to light nuclei to describe bound and scattering states such as ^{7}Be and ^{7}Li (Ref. 16). These calculations provide predictions for a resonance S-wave state for ^{6}He + p at a very low energy above the reaction threshold, which is relevant for astrophysics.

Recent experiments on OMEGA using the bright neutron source to irradiate ^{7}Li have measured the inelastic reaction cross sections as shown in Fig. 4. An enhanced peak at E_n = 3.4 MeV (E_x = 10.1 MeV) has been observed and might be the resonance from the ^{6}He + p $\langle - \rangle$ state predicted using the NCSMC model. The next step is to submit another LBS proposal and to perform these experiments with both ^{6}Li and ^{7}Li to verify this resonance state.

This material is based upon work supported by the Department of Energy National Nuclear Security Administration under Award Number DE-NA0003856, the University of Rochester, and the New York State Energy Research and Development Authority.

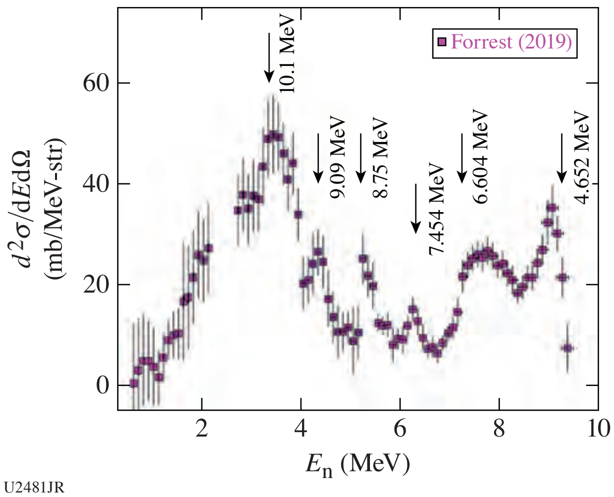

Figure 4
The double-differential cross section has been measured using a high-yield 14-MeV neutron source incident on ^{7}Li. Several of the known excited states are listed. The predicted state E_x = 10.1 MeV is from ^{6}He + p ⟨–⟩ ^{7}Li using the NCSMC analysis.

Turbulent Transport in Magnetized High-Energy-Density Plasmas
Principal Investigator: W. Fox (PPPL)
Co-investigators: D. Schaeffer, A. Bhattacharjee, and A. Spitkovsky (Princeton University); G. Fiksel (University of Michigan); and P. Knapp (SNL)

We have developed a new platform to study turbulent transport in magnetized laser plasmas on the OMEGA 60-beam laser. Anomalously fast diffusion of plasma across magnetic fields has long been recognized in magnetic fusion devices and laser plasmas. Microinstabilities driven by gradients in plasma parameters give rise to convective flow patterns on meso- to global scales, which leads to correspondingly enhanced diffusion coefficients. While some experiments have demonstrated aspects of anomalous transport in high-energy-density (HED) plasmas, many aspects remain unknown, and this physics is typically not included in magnetohydrodynamic (MHD) design codes for inertial confinement fusion (ICF). A key question when applying magnetic fields to HED plasmas is to understand the role of transport processes, in particular the processes that cause particles and field to mix and diffuse with respect to one another. These processes determine the time and space scales over which plasma heat can be effectively confined by the magnetic field. When plasmas are not created with embedded magnetic fields, diffusion is also a key step in "mixing" the field and plasma—a step that is important for creating large magnetized volumes of plasma for laboratory astrophysics experiments.[17,18]

A particularly important example of magnetized confinement of HED plasma is the magnetized liner inertial fusion (MagLIF)[19] approach to magneto-inertial fusion. The crucial questions of how well the hot plasma is insulated from the liner by the field and how ideally the field is compressed have not been addressed. These experiments also aim to help study the efficacy of magnetic insulation and flux compression that are essential to the scaling of the MagLIF concept.[20]

During this LBS experiment we successfully carried out one shot day on OMEGA 60. We adapted a MIFEDS-based platform that we have previously used to study magnetic reconnection and shocks.[17,18] To study turbulent transport, a plasma was ablated from a plastic target into a pre-existing magnetic field powered by MIFEDS. The interaction of the plasma with the field was diagnosed with 2-D proton radiography to map the magnetic-field topology. Protons measuring 3 and 15 MeV were produced by the implosion of a D^{3}He backlighter capsule and captured on CR-39. A Ni mesh was placed between the backlighter capsule and the plasma in order to make quantitative measurements of the magnetic-field deflection by tracking distortions in the mesh grid. Fiducial markings on the mesh allow for unambiguous identification of target chamber center (TCC). Image plates were also placed behind the CR-39 stack to capture x rays from the backlighter implosion. The resulting x-ray image provides another reference of the undistorted mesh for every shot. Additionally, local plasma parameters were measured with 2ω, spatially resolved Thomson scattering. The interaction of the laser plasma with the background field was measured for different laser energies and different target orientations relative to the field.

Figure 5 shows example proton radiography images, including a reference vacuum image [Fig. 5(a)] and 3- and 15-MeV images [Figs. 5(b) and 5(c), respectively] taken 12 ns after the laser plasma was ablated. With the plasma the mesh is heavily distorted in the 3-MeV image, indicating some turbulent structures. Figure 5(d) shows the path-integrated magnetic field $\int B \times dl$ from the 15-MeV reference (shot 92505) and plasma (shot 92515) images. The profiles taken across the midplane at two locations (above and below TCC) illustrate measurement noise. The vacuum profiles (blue curve) agree well with the expected signal from a model of the MIFEDS-generated field. The expansion of the plasma (red curve) creates a strong diamagnetic cavity, which evacuates most of the field. The results indicate that the cavity is still expanding or has recently stagnated. Furthermore, the measured field profiles, along with the density and temperature measured with Thomson scattering, confirm that these experiments are in a dimensionless regime similar to that of the MagLIF preheat conditions, with $\beta > 1$ and unmagnetized ions ($\nu_{ii}\omega_{ci} > 1$) and magnetized electrons ($\nu_{ei}\omega_{ce} > 1$), where $\nu_{e,i}$ are the collision frequencies and $\omega_{ce,i}$ are the gyrofrequencies. Additional measurements in an upcoming shot day will explore later times when the cavity starts collapsing.

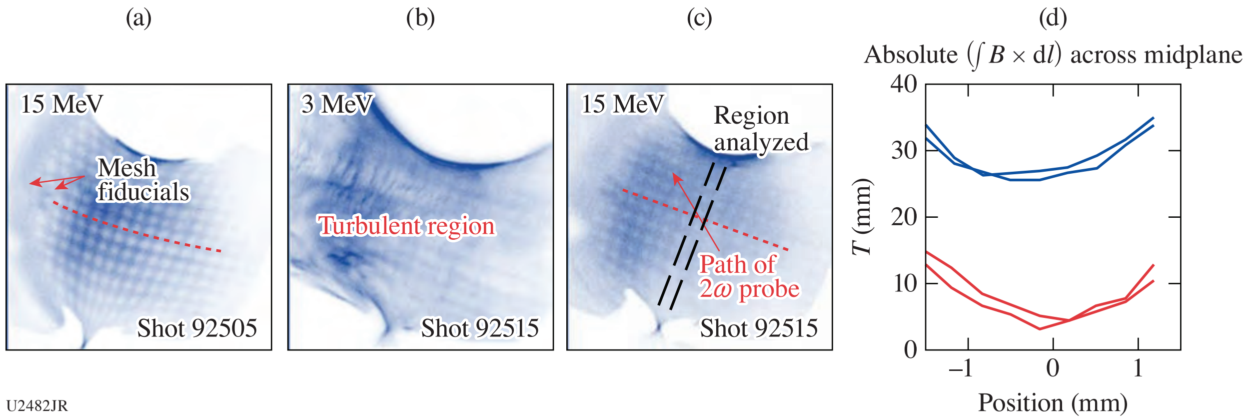

Figure 5
Example proton radiography images. (a) Reference image taken in vacuum. The mesh pattern is distorted by the MIFEDS magnetic field, but it can be referenced against fiducials. (b) A 3-MeV image taken 12 ns after the laser plasma is ablated. (c) A 15-MeV image taken on the same shot as (b). The mesh pattern is still visible, allowing for quantitative analysis. (d) Comparison of measured path-integrated magnetic-field profiles from the reference (blue curve) and plasma (red curve) images. The region analyzed for both images is shown in (c).

Investigating Giant Impacts Between Rocky Planets with High-Pressure Melting and Shock Equation-of-State Measurements on Complex Silicates—SilicateEOS-EP-19

Principal Investigators: D. E. Fratanduono and M. Millot (LLNL)
Co-investigators: B. Chidester,* D. Spaulding, and S. Stewart, (University of California, Davis); J. Li (University of Michigan); and J. Townsend* (SNL)
Graduate students: E. Davies and K. Amodeo (University of California, Davis)
*Postdoc

We conducted experiments to investigate the melting behavior and pressure–density–temperature (P–ρ–T) shock equation of state (EOS) and document bonding changes in hot liquid states of complex silicate minerals using ultrafast velocimetry and pyrometry measurements up to 2 TPa. Our goal is to address one of the most puzzling questions in planetary sciences: How did energetic collisions in the early solar system result in the physical structures and chemical compositions of the terrestrial planets? We also wish to document the structure and melting processes of multicomponent liquids, which is fundamental to both planetary sciences and HED physics.

Because it is necessary to constrain the thermodynamic response of the planet-forming materials to understand the dynamics of sub-giant and giant collisions and to examine the potential for chemical equilibration between the target and the impactor, we concentrated our effort on natural samples from the olivine [$(Mg,Fe)_2SiO_4$] and orthopyroxene [$(Mg,Fe)SiO_3$] mineral families, which constitute the majority of the silicate mantles of the terrestrial planets (e.g., Earth, Mars) by volume.

This shot day completed 14 shots on the OMEGA EP laser, alternating beams to increase the shot rate. Velocity interferometry and optical pyrometry with decaying shocks (Fig. 6) measured the shock temperature and the intersection of the Hugoniot with the melting curve for two minerals: olivine [$(Mg_{90},Fe_{10})_2SiO_4$] and bronzite [$(Mg_{90},Fe_{10})SiO_3$]. After detailed analysis and upcoming complementary experiments in FY20, these data will be used to develop improved EOS models for hydrodynamic simulations of impact events and interior structure models. In particular, the olivine data will be compared to previous experiments at the Omega Laser Facility on the pure end-member mineral forsterite: (Mg_2SiO_4) reported in Ref. 21. The bronzite data will complement the previous work on $MgSiO_3$ enstatite described in Ref. 22.

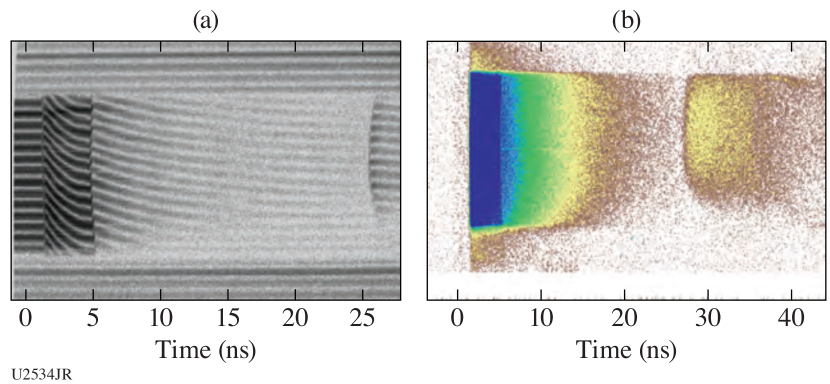

Figure 6
(a) Example active shock breakout (ASBO) and (b) streaked optical pyrometer (SOP) data for the SilicateEOS-EP-19 Campaign showing a decaying shock traveling though the multilayer package to reveal the optical and thermodynamic properties of bronzite in the Mbar range.

Phase Transformation Kinetics—Strain Rate Tuning of the Peierls Distortion in Ramp-Compressed Body-Centered Tetragonal Tin

Principal Investigators: M. Gorman and R. Smith (LLNL)

The goal of the SnKinetics-19A/B/C experiments on OMEGA was to develop a ramp-compression platform to determine the crystal structure of tin (Sn) up to 70 GPa at several different compression rates. These observations will be compared to shock and static measurements on Sn and are expected to confirm a previously unreported mechanism responsible for altering crystal structure evolution under dynamic compression conditions.

In the target design shown in Fig. 7 we use a plasma piston design[23] to ramp compress a 6-μm-thick Sn layer, which is directly coated onto a LiF window. To minimize the heat transfer from the plasma to the Sn sample, we incorporate a 6-μm-thick preheat shield. A 50-μm-thick, 50-g/cm^3 additive manufactured foam (AMFoam) layer is used to temporally shape the ramp and pressure hold profile experienced by the Sn layer.[24] The OMEGA VISAR (velocity interferometer system for any reflector) active shock breakout (ASBO) measures the Sn/LiF particle velocity from which the sample pressure as a function of time can be determined.[25] These experiments combine nanosecond x-ray diffraction[25] and ramp compression to dynamically compress and determine the crystal structure of Sn/LiF to peak pressures within the 10- to 70-GPa range. Using the OMEGA powder x-ray diffraction image-plate (PXRDIP) diagnostic,[25] the compressed Sn sample is probed with a 1-ns He$_\alpha$ x-ray source to determine crystal structure at a well-defined sample pressure (VISAR). Figure 8 shows an example of the data, with information on the high-pressure body centered cubic (bcc) phase of Sn. Also observed are peaks from the ambient pressure W pinhole that serve to calibrate diffraction angle.

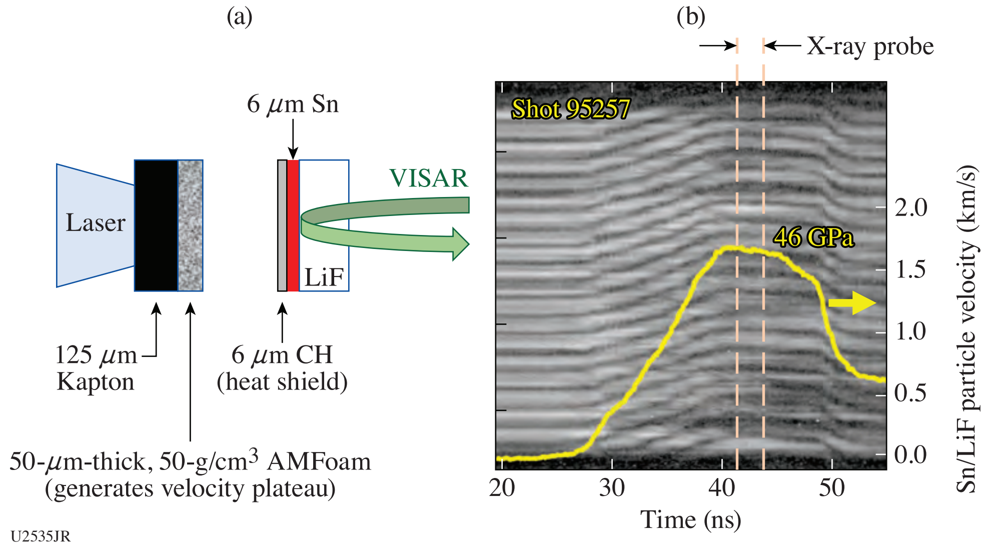

Figure 7
(a) Target design for ramp-compression experiments of Zr using the OMEGA laser. (b) Raw VISAR data with extracted Sn/LiF particle velocity profile. As indicated a Cu He$_{\alpha}$ x-ray source is timed to probe the sample at peak compression. For shot 95257 (as shown) the peak sample pressure for Sn is 46 GPa.

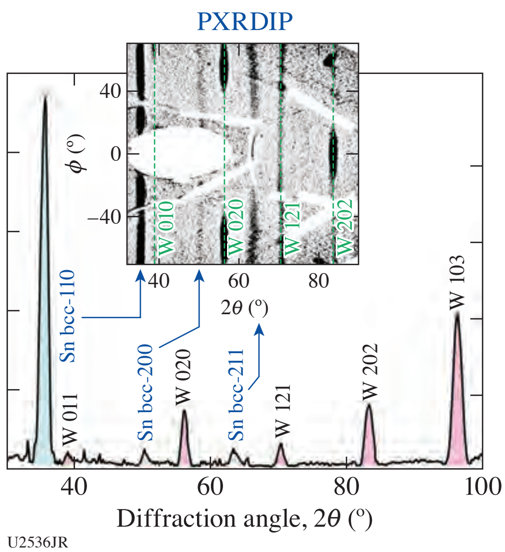

Figure 8
Diffraction pattern for ramp-compressed Sn up to peak pressures of 46 GPa. Here the Sn bcc phase is observed along with the ambient pressure W-pinhole calibration peaks.[25]

Implementation of a Broadband Optical Spectroscopy Diagnostic for OMEGA EP

Principal Investigator: B. J. Henderson (LLE and Dept. of Physics and Astronomy, UR)

Co-investigators: J. R. Rygg (LLE, Dept. of Physics and Astronomy, UR); J. Katz, C. Sorce, J. Kendrick, A. Sorce, T. R. Boehly, and M. Zaghoo (LLE); and G. W. Collins (LLE and Dept. of Mechanical Engineering, UR)

Matter, when subject to extreme pressures and temperatures, can experience significant changes in optical, structural, and electronic properties. These transitions often manifest themselves through changes in optical transport properties, the most readily observable being reflectance and absorption. Experiments on OMEGA EP have sought to measure reflectance with the monochromatic VISAR diagnostic.[26] While single-wavelength reflectivity measurements can be used to identify phase transitions, they lack the required spectral dependence to determine properties such as plasma frequency and band gap. Our work shows (1) a proof of principle for recovering a reflected broadband signal from compressed aluminum and (2) the system's ability to accurately measure temperature in high-pressure shocks.

Aluminum's ambient band structure contains parallel bands that preferentially absorb near 1.5 eV (~825 nm). Under the effects of compression, the energy gap between these bands expands, shifting interband absorption to higher photon energies with increasing pressure.[27] To examine this high-pressure behavior, we submitted an LBS proposal to investigate electronic structure changes in matter at extreme conditions. Figure 9 shows a reflected broadband signal from an isentropically compressed Al–LiF interface. The broadband probe is generated by a CH–quartz–SiO_2 foam target and redirected to the back side of the sample via an in-chamber optical train. Analysis of these results is still ongoing.

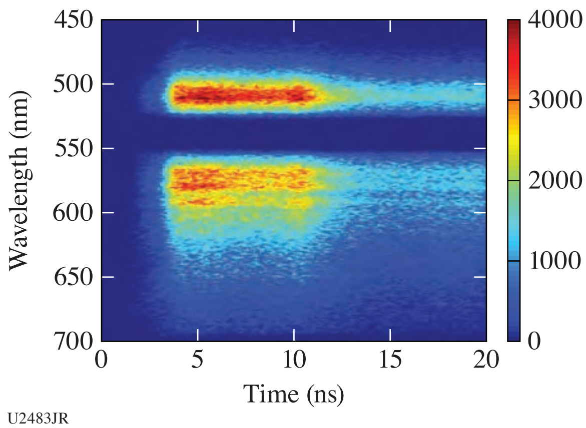

Figure 9
Streak image of a reflected broadband signal from shot 30375. The backlighter is driven at 2 ns, the shock enters the quartz pusher at 3.5 ns, and the backlighter achieves a temporally flat brightness profile at 6 ns in the SiO_2 foam. A significant decrease in signal observed at 11 ns is due to changes in optical properties in the compressed target.

Additionally, this diagnostic was proposed as a powerful tool for high-accuracy temperature measurements in strongly shocked materials. For systems with unknown shock pressure–temperature scaling, quartz is the typical reference for new measurements. The quartz P–T scaling for shock compression has been reported[28] and is widely used in many HED experiments. The uncertainty in this scaling remains quite large, however, primarily due to the use of spectrally integrating diagnostics to measure shock brightness. With spectral resolution, we can directly observe the Planck's law scaling of thermal emission with temperature. Figure 10 shows the recorded emission spectrum of a decaying shock in quartz. This data will be used to refine quartz's ability to function as a temperature standard in future HED experiments.

This material is based upon work supported by the Department of Energy National Nuclear Security Administration under Award Number DE-NA0003856, the University of Rochester, and the New York State Energy Research and Development Authority.

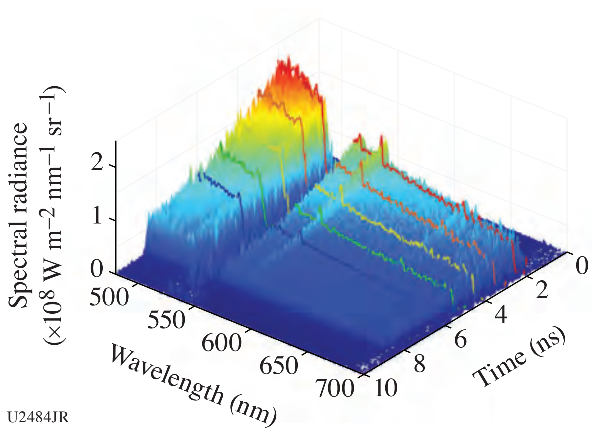

Figure 10
Emission spectrum from a decaying shock in quartz from shot 30378. Single-time lineouts (many colors) are fit with a Planck's Law function to determine the temperature. "Spikes" and "troughs" in the spectrum are due to filters in the VISAR–SOP relay.

Developing Inverted-Corona Fusion Targets as Neutron Sources

Principal Investigators: M. Hohenberger (LLNL) and S. Glenzer (SLAC)
Co-investigators: N. B. Meezan and A. J. Mackinnon (LLNL); and M. Cappelli (Stanford)
Graduate students: W. Riedel (Stanford); N. Kabadi (MIT); and F. Treffert (SLAC)

These experiments explored the feasibility of inverted-corona targets as fusion-neutron sources for HED applications. In inverted-corona targets, laser beams directly ablate a layer of fusion fuel on the inner surface of a target, e.g., a CD-lined capsule.[29,30] As the ablative flows converge at the target's center, the plasma particles transition from long-range interactions to collisional stagnation, heating the ions and generating fusion reactions. The fusionable material may also be provided as a gas fill, where, similar to an exploding pusher, the laser-driven ablation launches a centrally converging shock into the gas, thereby heating it to fusion conditions.

The experimental setup is shown schematically in Fig. 11. Target capsules with a 1.8-mm inner diameter and 25-μm-thick walls had one (or two) laser entrance holes (LEH's) and were laser irradiated by 19 (or 39) beams with 1-ns square pulses at up to 500 J/beam. CH capsules with 1.5 atm of D_2-gas fill were fielded, as well as vacuum, CD-lined CH capsules with varying liner thickness or liner depth (see Fig. 12).

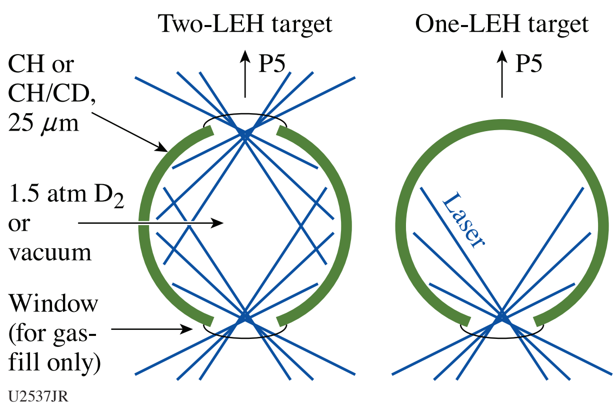

Figure 11
Experimental setup.

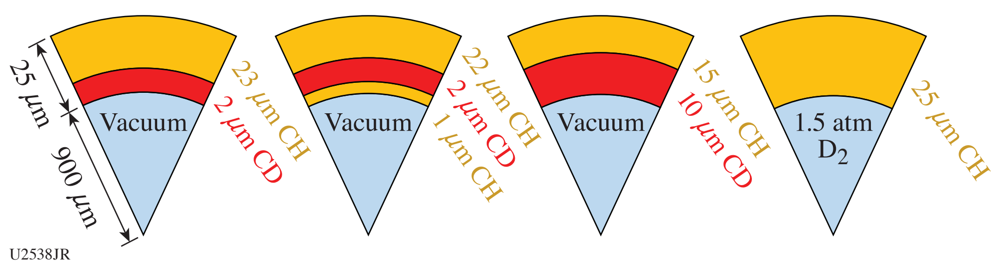

Figure 12
Target types.

Generally, 2-D *HYDRA* calculations predicted a linear scaling of yield with incident laser energy, while the 1- or 2-LEH configuration had little performance impact. With a calculated yield of up to ~10^{11} neutrons at 18 kJ of incident energy, *HYDRA* 2-D simulations predicted the highest yields for the gas-filled capsules. For the vacuum targets, *HYDRA* predicted most of the D–D fusion to occur in the stagnating ablation plasma from the innermost 1-μm layer of CD liner, with little increase in yield beyond that thickness, and peak neutron yield of ~5×10^{10} at 18 kJ of incident energy. Recessing the CD liner 1 μm into the wall decreased calculated yield by >30×.

This is in contrast to the experimental neutron yields, which are plotted in Fig. 13 on a logarithmic scale and as a function of laser energy. While these data also follow a linear trend with energy, the experiments generally underperformed compared to the simulations, with $Y/Y_{2\text{-D}}$ between ~5% to ~15%. Furthermore, the experimental data exhibit a strong dependence of yield on liner thickness, with an ~15× increase in yield from the 2-μm (circles) to the 10-μm CD liner (triangles), with the latter giving the highest performance of ~1.5×10^{10}. This indicates significant mixing in the ablative plasma, confirmed by the minor drop in yield for the recessed 2-μm CD liner (diamonds).

With a detailed data analysis in progress, these experiments support promising applications; e.g., neutron radiography at the NIF requiring a total yield of ~10^{14} should be possible using a DT-gas–filled, single-LEH target and few-hundred-kJ driver energies.

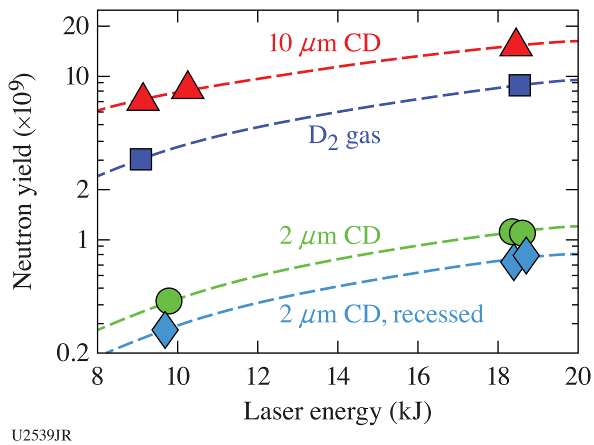

Figure 13
Neutron yields.

Characterizing Pressure Ionization in Ramp-Compressed Materials with Fluorescence and Absorption Spectroscopy
Principal Investigators: S. Jiang and Y. Ping (LLNL)
Co-investigators: A. Lazicki, P. Sterne, P. Grabowski, H. Scott, R. Smith, R. Shepherd, B. Bachmann, and J. Eggert (LLNL); and S. B. Hansen (SNL)

This pressure ionization campaign comprised a half-day on OMEGA and one day on OMEGA EP during FY19. Following the previous FY18 campaign, which for the first time provided a direct benchmark between various isolated-atom and average-atom ionization models by measuring K-shell fluorescence emission of Co, the FY19 campaign extended the measurement to study a possible K-edge shift and began an investigation of L-shell emission lines.

On OMEGA, we have measured the K edge of compressed Co as a function of density. A schematic of the experimental setup is displayed in Fig. 14(a). The high pressure in Co was achieved by ramp compression using the long-pulse drivers to keep the temperature low during the compression process. The pulses were designed to mimic the drive used on OMEGA EP during the FY18 campaign. The pressure history was characterized with on-shot VISAR measurements. Under two different drive energies, 1500 J and 6600 J, the sample reached 1.5× and 2.1× compression, correspondingly. We used a foil x-ray backlighter and measured the absorption spectra using a high-resolution spectrometer IXTS. No obvious Co K-edge shift was observed [Fig. 14(b)], which is consistent with the prediction of average-atom models but disagrees with the commonly used isolated-atom models. We were also able to measure the EXAFS [Fig. 14(c)] to confirm low temperature in compressed Co.

On OMEGA EP, the L-shell fluorescence emission of Sn was observed using the IXTS spectrometer configured with a lower-energy PET (pentaerythritol) crystal. In this experiment a short-pulse laser beam irradiated a secondary Be target that was directly attached to a Sn foil. The hot electrons generated by the laser–Be interaction could transport to the Sn layer and induce fluorescence. Sn L_β spectra with different Be thicknesses are shown in Fig. 15. The L_β line shifts to higher energy with increasing temperature (thinner Be). Detection of this L_β line under compression proved more challenging due to backgrounds generated by the long-pulse beams but is promising for future work.

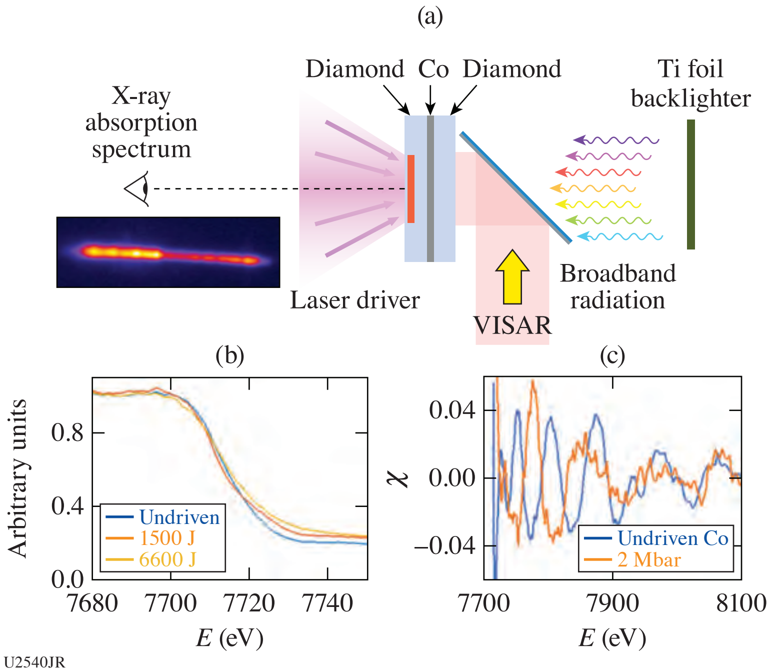

Figure 14
(a) Experimental schematic and [(b) and (c)] results on OMEGA.

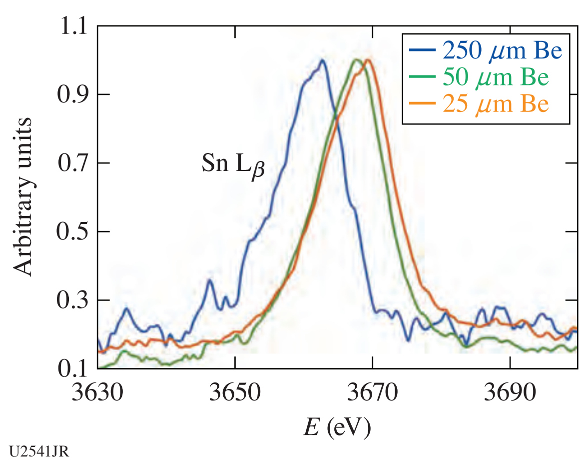

Figure 15
Sn L_β fluorescence spectra.

Shock Trajectory in Low-Density Carbonized Resorcinol-Formaldehyde Foams for the Landau–Darrieus Instability
Principal Investigator: S. F. Khan (LLNL)
Co-investigators: A. Casner, L. Masse, L. Ceurvorst, T. Goudal, D. Martinez, and V. A. Smalyuk (LLNL)

The objective of these OMEGA EP experiments is to measure the shock trajectory into driven carbonized resorcinol-formaldehyde (CRF) foams in order to select the optimum material density and drive laser intensity for NIF Discovery Science experiments to study the Landau–Darrieus instability (LDI) in laser ablation. Two CRF densities were tested, nominally 50 mg/cm^3 and 100 mg/cm^3. The tested drive laser intensities were 5×10^{12} W/cm^2, 1×10^{13} W/cm^2, and 2×10^{13} W/cm^2. The shock trajectory was tracked using side-on radiography and the shock breakout was measured using VISAR face-on (see Fig. 16). The side-on radiography was imaged onto an x-ray framing camera using a V backlighter. The shock was clearly visible in most

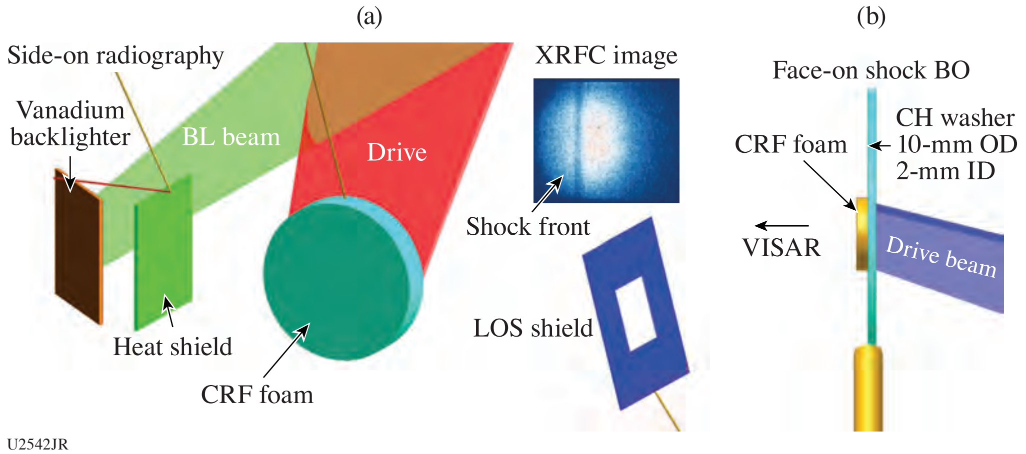

Figure 16
Experimental layout with primary measurements: (a) side-on radiography and (b) face-on shock breakout using VISAR.

of the frames and the shock breakout was clear. For the 100-mg/cm^3 CRF foam driven at 5×10^{12} W/cm^2, side-on radiography measured a velocity of 25 to 30 km/s, the shock breakout measurement gave a velocity of 21 km/s, while initial 2-D simulations gave 16 km/s. However, considering these results, 3-D simulations (see Fig. 17) were performed with actual laser spot size and incidence angle that show a much better agreement. For the NIF Discovery Science experiments, the 100-mg/cm^3 density was chosen to be driven with an intensity of 1.25×10^{12} W/cm^2. We used a lower laser intensity to observe the LDI before the shock breakout and Rayleigh–Taylor instabilities were generated.

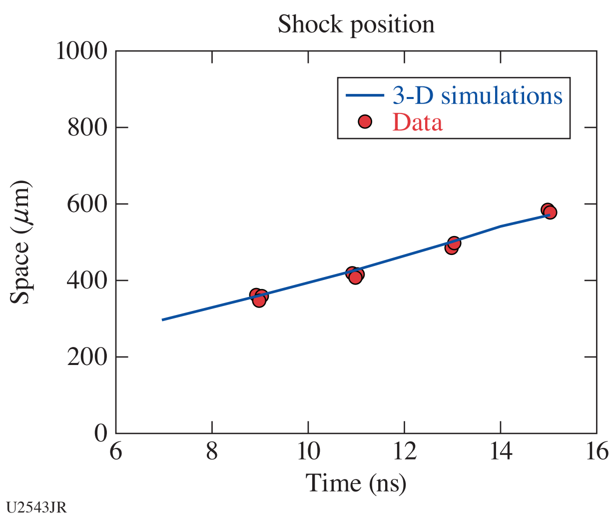

Figure 17
Shock position as a function of time.

Development of the New Forward–Backward X-Ray Diffraction Diagnostic
Principal Investigator: A Krygier
Co-investigators: C. E. Wehrenberg and A Gleason (SLAC); and H.-S. Park and J. H. Eggert (LLNL)

This LBS experiment, as shown in Fig. 18, was the first effort to collect simultaneous transmission and reflection diffraction from a sample driven to high pressure with the new forward–backward x-ray diffraction (FBXRD) diagnostic. By using two monochromatic x-ray sources, we simultaneously probed the sample in multiple geometries, maximizing coverage of the range of angles between the diffraction plane and applied stress direction. This capability will be able to constrain the *in-situ* strain anisotropy induced by material strength in a polycrystalline sample.

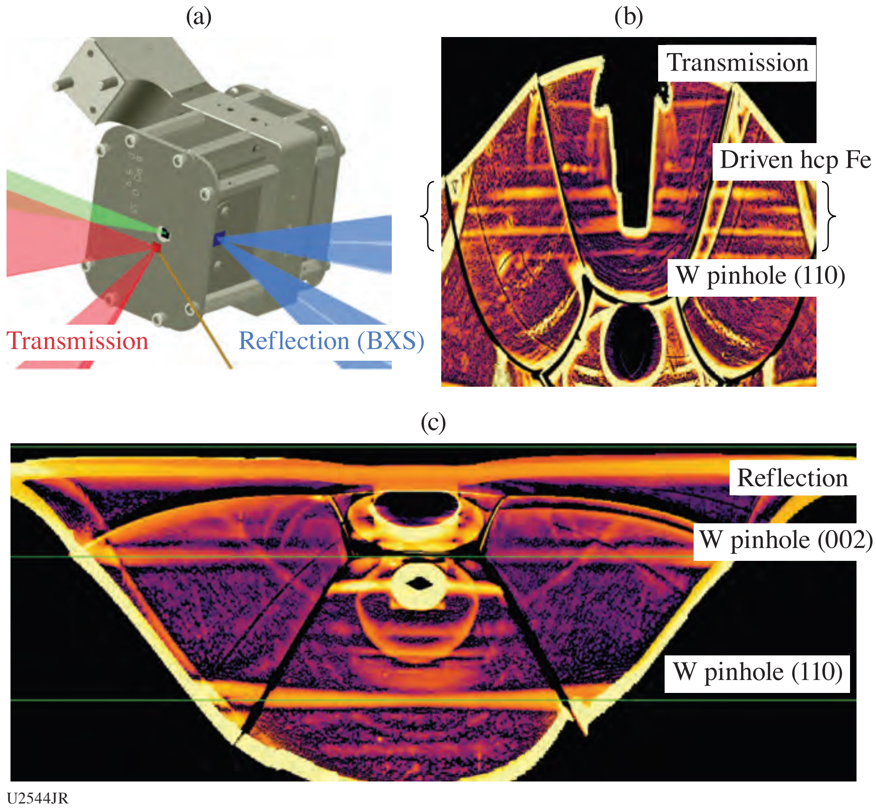

Figure 18
(a) Experimental setup; (b) driven x-ray diffraction in the transmission geometry showing high-pressure Fe hcp phase reflections; and (c) reflection geometry x-ray diffraction. The bright lines shown are from the W pinhole.

Many of the shots on this campaign were dedicated to optimizing the backlighter, shielding, and pinhole configuration. We performed a scan of reflection backlighter laser illumination energies and spot sizes using diffraction quality as the ultimate judge of each configuration. We found that a range of conditions produces high-quality diffraction. We also tested several conical shielding configurations for the backward x-ray scattering (BXS) reflection diffraction setup, including tungsten, stainless steel, and plastic; tungsten worked best. We have identified several sources of background signal that confound a full interpretation of the diffraction signal.

Time-Resolved Measurement of Germanium L-Shell Emission Using a Buried Layer Platform
Principal Investigator: E. V. Marley (LLNL)
Co-investigators: D. Bishel, M. Frankel, Y. Ehrlich, Z. Shpilman, M. B. Schneider, G. E. Kemp, R. F. Heeter, M. E. Foord, D. A. Liedahl, K. Widmann, and J. Emig (LLNL)

This campaign was designed to measure the emitted L-shell germanium spectra from a well-characterized and uniform plasma for comparison to atomic kinetic models. Recent studies have shown a discrepancy between atomic kinetic models and high-*Z* M-shell spectral data. This study was conducted to test the accuracy of models for L-shell emission.

Planar, buried-layer targets were illuminated equally on both sides (Fig. 19) to heat the sample. The sample used in the campaign was a 2000-Å-thick Ge/Sc mixture designed to burn through completely before the end of the laser pulse, providing uniform plasma conditions to measure the L-shell emission of the germanium. The samples were buried between two 5-μm-thick layers of Be, which acted as an inertial tamp slowing the expansion of the sample.

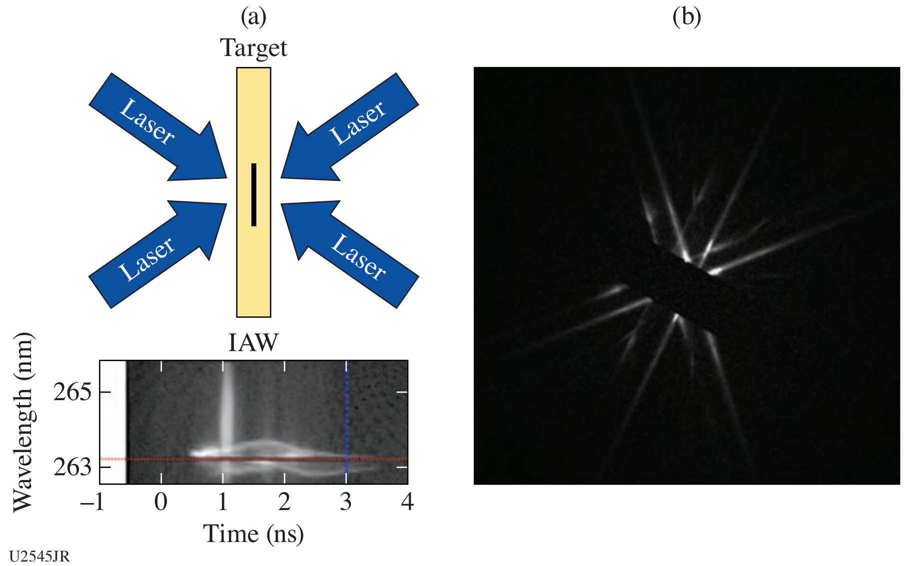

Figure 19
(a) Experimental configuration; (b) Thomson-scattering data of shot 94085; and (c) TGS data of Ge and Sc L-shell spectra.

Time-resolved 2-D images of the target's x-ray emission, viewed both face-on and side-on, were recorded using pinhole cameras coupled to framing cameras. The 4ω probe beam and Thomson spectrometer were also used to measure the scatter off the electron and ion acoustic features [see Fig. 19(b)]. A new filter package was used during the campaign to filter out the self-emission and unconverted light, providing high-quality scattering data. The K-shell spectra from the Sc were used to determine the electron temperature of the plasma. The time-resolved spectra were recorded using a crystal spectrometer coupled to a framing camera. A crystal spectrometer was used to record the Ge L-shell emission, also time resolved. All of the framing cameras, those used for imaging as well as those used for spectroscopy, were co-timed so the plasma conditions could be determined for the measured Ge L-shell emission.

The Soreq transmission grating spectrometer (TGS), as part of the ongoing LLNL/Soreq collaboration, was used to record the absolutely calibrated time-integrated germanium and scandium L-shell emission onto an x-ray charge-coupled device.

A single pulse shape was used during the campaign: a 3.0-ns square pulse with a 100-ps picket arriving 1 ns before the main pulse. A complete (all six diagnostics, correctly timed and pointed) set of data was recorded during the campaign at temperatures of ~2 keV.

A Journey to the Center of Uranus and Neptune: Using X-Ray Diffraction to Unravel the Atomic Structure of New Solid and Superionic Ices at Multimegabar Pressures

Principal Investigators: M. Millot and F. Coppari (LLNL)
Co-investigators: D. E. Fratanduono and S. Hamel (LLNL); S. Stanley (Johns Hopkins University); and M. Bethkenhagen (Postdoc, Rostock University, Germany)

We conducted an OMEGA EP one-day campaign to investigate the structure and equation of state of solid and superionic water at Uranus's and Neptune's deep interior conditions with a combination of ultrafast x-ray diffraction and optical diagnostics using new laser dynamic compression techniques.

This work expands on our recent discovery of superionic water ice at the Omega Laser Facility (LBS Campaign on Extreme Chemistry, FY13) reported in Ref. 31 and the subsequent discovery of a new superionic water ice XVIII (LBS Campaign on

SolidWater, FY14 described in Ref. 32). Superionic ices, a new exotic state of matter, are characterized by fluid-like diffusing hydrogen ions (protons) within a solid lattice of oxygen ions, which could dominate the interiors of icy giant planets such as Uranus, Neptune, and their extra-solar cousins.

We successfully commissioned the new platform for x-ray diffraction of initially liquid samples on the OMEGA EP laser and collected excellent quality data on eight system shots using two UV beams to compress the water sample layer and two UV beams to generate an x-ray source flash for the x-ray diffraction measurement (Fig. 20). Preliminary analysis suggests that the use of longer pulse duration allowed us to explore lower-temperature compression paths to search for predicted new phases of solid ices of pure water.[33]

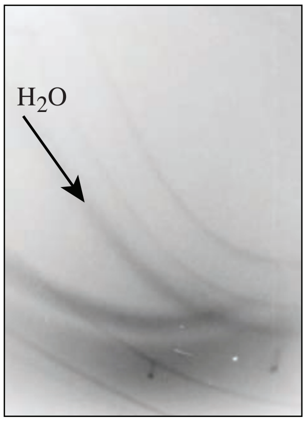

U2546JR

Figure 20
Raw PXRDIP data showing the successful observation of x-ray diffraction from Mbar water ice on OMEGA EP.

We also explored higher-temperature compression paths that reproduce the pressure–temperature conditions inside Neptune and Uranus to constrain the melting line near 1 Mbar and document the atomic structure and transport properties of pure water at these conditions.

Changes in the Electronic Structure of Dense, High-Temperature Matter
Principal Investigators: P. M. Nilson and S. X. Hu (LLE); and S. B. Hansen (SNL)
Graduate Students: D. A. Chin, J. J. Ruby (LLE)

The goal of this campaign is to test atomic-scale models that are used to estimate changes in the electronic structure of compressed materials. How atomic physics may be altered in these conditions is of fundamental importance to the study of stellar interiors, planetary cores, and inertial fusion. To measure detailed x-ray absorption features and fluorescent line emission from dense, high-temperature matter, a self-backlit, spherical-implosion platform is being developed on the OMEGA Laser System.

The experiment uses a 30-μm-thick plastic shell that contains a metal-doped layer. The inset of Fig. 21 shows the target design. The spherical target has three layers: a 17-μm CH ablator, a 10-μm CH layer doped with 2 or 4 at. % Cu, and an inner 3-μm CH layer. A slow, moderate-convergence implosion is used to assemble the material under study and to backlight its properties using continuum emission generated in the core at bang time. The target is driven by direct laser ablation using a 27-kJ, 1-ns drive. To provide information on the imploded-core conditions, the target contains a 20-atm D_2 Ar (0.1 or 1 at. %) fill.

Figure 21 shows an example of time-integrated x-ray emission and absorption spectrum from these experiments. The data show the Cu K-edge shape and spectral shift, in addition to the Cu K_α emission and resonant 1*s*–3*p* and 1*s*–2*p* self-absorption features. These x-ray spectroscopic features were time resolved in the experiment using a streaked x-ray spectrometer (not shown). Detailed analysis of the simultaneous time-integrated and time-resolved x-ray emission and absorption spectra is underway for comparison with model predictions. The ultimate goal is to use these data to constrain the ionization balance and investigate the importance of density effects on the conditions that are generated. Future work will apply these techniques to both closed- and open-shell systems.

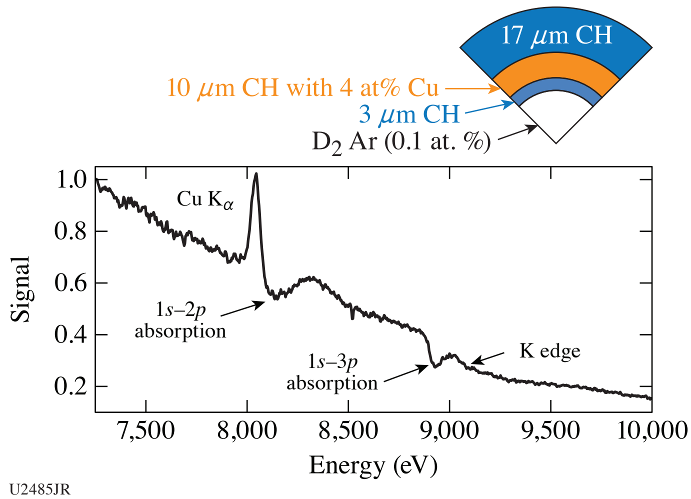

Figure 21
Example of time-integrated x-ray absorption features and fluorescent line emission from a laser-driven implosion containing a Cu-doped layer. The target design, shell composition, and core fill are shown in the inset.

The Effects of the Plasma Geometry on the K-Shell Spectrum of Mid-Z (21–26) Ions

Principal Investigator: G. Pérez-Callejo (student, University of Oxford)
Co-investigators: E. V. Marley,* M. B. Schneider, G. E. Kemp, M. E. Foord, R. F. Heeter, D. A. Liedahl, G. V. Brown, and J. Emig
Students: D. Bishel (LLE)
*Postdoc

This campaign was designed to measure the K-shell spectra of mid-*Z* atoms in well-defined and uniform plasmas in order to characterize how the flux from optically thick lines depends on the geometry of the plasma. This idea has been studied mainly in astrophysics, but the aim of this study was to take advantage of said geometric effects for characterizing the plasma conditions in dot spectroscopy experiments on the NIF. On two shot days, planar buried layer targets were illuminated evenly on both sides to heat the sample [Fig. 22(a)], which consisted of a Ti-only disk for the first shot day, and were changed to a 1:1 mixture of Sc and V for the second shot day. This change minimized the presence of Be impurities in the spectra, as well as the optical depth of the disk. The sample was tamped on both sides by 5-μm-thick layers of Be to slow the sample's expansion and provide radial confinement to maintain its cylindrical shape.

In both shot days, the pulse shape was kept the same, a 2.7-ns square pulse to maintain the maximum possible uniformity. A complete (all six diagnostics, correctly timed) set of data was recorded during the campaign at temperatures ~1.5 keV. The initial data look promising.

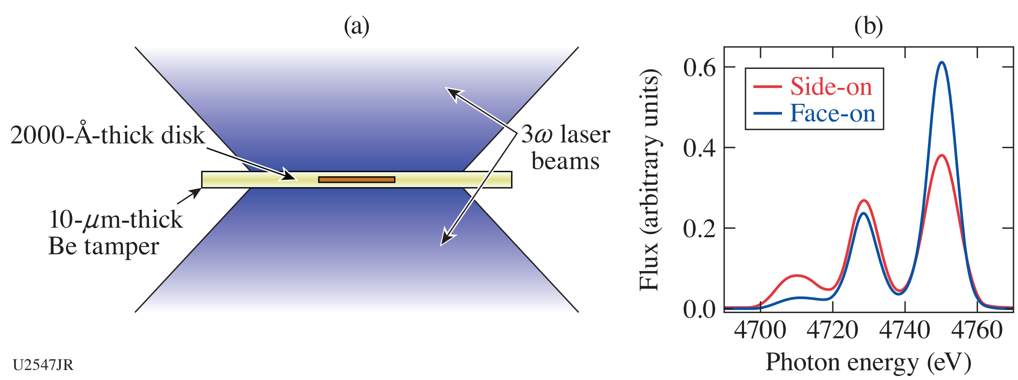

Figure 22
(a) Experimental configuration and (b) time-resolved Ti H_α spectra with data inset at 2.7 ns of shot for both face-on and side-on configurations.

Time-resolved 2-D images of the targets' x-ray emission viewed both face-on and side-on were recorded using gated pinhole imagers. The K-shell spectra were measured in four time windows using crystal spectrometers, with focus on the He_{α} complex [Fig. 22(b)]. The temperature of the plasma was determined from the optically thin spectra lines using a genetic algorithm approach. For the second day, the ratio of isoelectronic lines provide a more accurate measurement of the temperature. The plasma density was obtained from the measured size of the plasma at every time by imposing a conservation of particles condition.

On the first shot day, a high-resolution double-crystal spectrometer with spatial resolution was fielded on OMEGA to study possible uniformities in the plasma. On the second shot day, this spectrometer was replaced with a streak camera to study the heating processes of the Sc and V in a continuous manner. In both shot days, a TGS from the Soreq Institute, Israel, was fielded to check, against hydrodynamic simulations, how the plasma was being heated as the laser burned through the Be tamper.

Viscosity Measurements Using Tracer Particles

Principal Investigator: J. Shang (Dept. Mechanical Engineering, University of Rochester)
Co-investigators: D. N. Polsin, H. Aluie,* D. Kelley,* J. R. Rygg, R. Betti,* J. F. Myatt, J. Zhang,* R. W. Short, A. V. Maximov,* W. Seka, D. H. Froula,† D. H. Edgell, D. T. Michel, and I. V. Igumenshchev (LLE); A. Gleason (SLAC National Accelerator Laboratory and Stanford University); and D. E. Hinkel, P. Michel, and J. D. Moody (LLNL)
*Also Dept. Mechanical Engineering, University of Rochester
†Also Dept. of Physics and Astronomy, University of Rochester

Most numerical models in HED applications such as ICF do not include the viscosity for materials being simulated.[34,35] Yet, it is well known that viscosity plays an important role in the evolution of hydrodynamic instabilities and the mixing between materials, especially at early times at scales smaller than 100-μm diameter. Our objective was to measure viscosity in an HED polymer, such as CH, which is commonly employed in target fabrication for ICF and basic science experiments. In this experiment, we aimed to shock-compress the CH and track the movement of small, high-*Z* particles embedded in the CH over time. The viscosity plays a role in how well a particle tracks the surrounding fluid and can be inferred by comparing trajectories of particles of different sizes and/or density after a shock has passed.

Our target bulk was composed of particle-seeded epoxy; as a CH material, we have a reasonable understanding of how it will behave under shock compression, and high-*Z* particles (Ti, W) can be introduced before it cures. The final targets for this campaign have manually positioned particles, with their positions consistent between targets within 50 μm. Ideally, the bulk medium would be homogeneous; however, to position the particles reproducibly, a support structure of amorphous silica supports the epoxy layer; because of the density difference between the epoxy and the silica, this likely produced a nonuniform shock that will affect the particle dynamics.

The experiments used area backlighting to track particle motion over four time slices as recorded on an XRFC (Fig. 23). Here, two laser beams irradiated a plastic ablator at the front of the target using 1100-μm distributed phase plates, driving a shock through the material. As the CH started to flow during the shock process, the idea was that the embedded particles should move enough that we can track them in the flow. An additional beam irradiated a Cu backlighter foil with a 1-ns square pulse to illuminate the sample and track the motion as captured on the XRFC's positioned opposite the backlighter. During the 0.1-ns gate duration of the framing camera, we collected snapshots of the bead positions (Fig. 24) in combination with VISAR and SOP. We demonstrated in this LBS shot day that (1) the targets can be made with sufficient precision to have the beads placed in precise locations; (2) the beads can be resolved with the number of photons generated via area backlighting; and (3) pressures achieved with CH are suitable to generate flow. A driven bead shot was collected, but bead location and preliminary analysis are ongoing. It could be that the beads melted at the shock-compression conditions achieved. The time delay between framing strips was set to intervals over which we anticipated a modest but detectable displacement of the particles.

These results have been shared by a graduate student at poster sessions at the HED Summer School (August 2019) and at the Division of Plasma Physics Meeting (October 2019).

This work was performed under the auspices of the U.S. Department of Energy under Grant DE-SC0019329 within the joint HEDLP program.

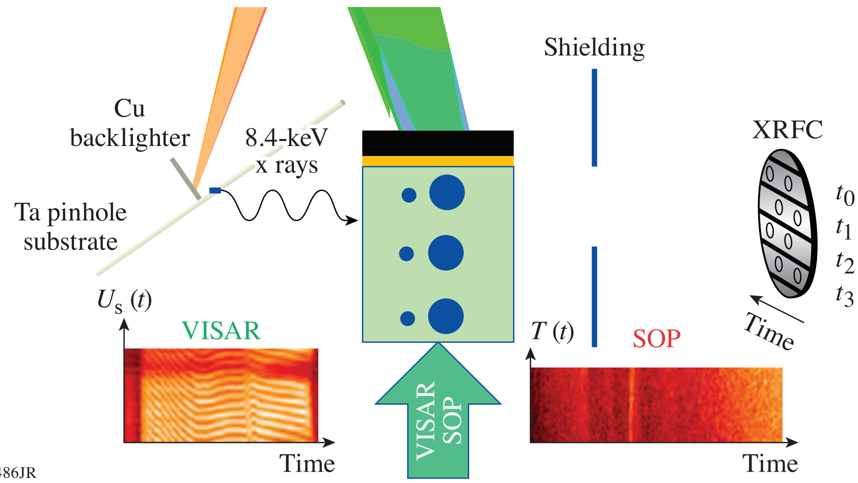

Figure 23
Schematic of a particle-tracking experiment conducted at LLE to date using an area backlighter and x-ray framing camera. The primary diagnostics are VISAR, XRFC, and SOP.

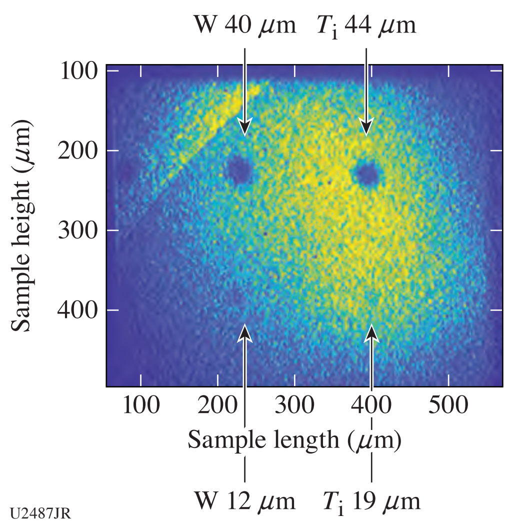

Figure 24
Image of high-Z beads placed along the side of the target.

X-Ray Phase-Contrast Imaging of Strong Shocks on OMEGA EP
Principal Investigator: W. Theobald (LLE)
Co-investigators: P. M. Nilson, A. Kar, R. Betti, and M. S. Wei, (LLE); L. Antonelli, M. Khan, and N. Woolsey (University of York, UK); R. Scott and K. Glize (RAL, UK); V. Bouffetier, L. Ceurvorst, A. Casner, O. Turianska, D. Batani, and F. Barbato (CELIA, University of Bordeaux, France); G. Rigon (Ecole Polytechnique, Palaiseau, France); and S. Atzeni (University of Rome "La Sapienza," Italy)

X-ray phase contrast imaging (XPCI) is a technique that is widely used in biology and medicine. It is based on the phase shift induced by a density gradient in matter. When a density gradient is present perpendicularly to the propagation direction of the x ray, it deflects the x-ray beam in the opposite direction with respect to the density gradient. If we consider a density edge, the resulting XPCI image of this edge is located between a maximum and a minimum of the intensity profile. This effect is able to highlight every density interface and is not density dependent. Strong density gradients of very different densities can be probed at the same time. This makes this diagnostic more versatile compared to standard x-ray absorption radiography. Moreover, XPCI works with both monochromatic and broadband sources, which makes this technique an interesting tool for warm dense matter and HED physics studies. X-ray free-electron lasers and synchrotrons are the usual platform for XPCI experiments due to the high-energy flux and the coherence of the beams. However, incoherent x-ray radiation sources can also be used for XPCI thanks to the lateral coherence, which is defined as

$$l_t \approx R\frac{\lambda}{s}, \tag{1}$$

where R is the source-object distance, λ is the photon wavelength, and s is the source size. It is clear from this formula that if one is able to use a small source size, not-too-hard x rays (several keV), and a setup that maximizes the source–object distance (which might be limited by the photon flux and other technical constraints), phase-contrast enhancement can be achieved. Moreover, if high-energy x rays are used, it is possible to shield the detector from target self-emission and focus the attention on the hydrodynamic evolution of the target. A successful proof-of-principle experiment was performed by some of the co-authors at the PHELIX laser at GSI, Germany, with a laser-driven bremsstrahlung source that provided experimental images of both the shock front and the rarefaction wave.[36] This was followed by an experiment (XPCI-EP-19A) that demonstrated x-ray phase contrast imaging on OMEGA EP, which is described here. The experiment developed the XPCI technique on OMEGA EP with short-pulse backlighters and used this technique to measure the density profile of a strong shock in a cylindrical CH target. Various backlighter targets containing Cu material were tested in order to optimize the x-ray phase contrast source. The experiment demonstrated a spatial resolution of ~15 μm at sufficient photon energies (~8 to 9 keV) so that the images are not affected by the strong x-ray self-emission from the plasma corona. Figure 25 shows images of (a) a single and (b) a double laser-induced shock wave. Figure 25(c) shows the experimental setup. The two UV (λ = 0.35-μm) laser beams (B3, B4) provided an energy of 1250 J/beam in a 2-ns square pulse and were focused on the front side of a CH cylinder with a diameter of 1 mm and a length of 1 mm. The beams were equipped with SG8-0750 distributed phase plates that produced a laser spot with a diameter of 750 μm (1/e value of peak fluence) and fluence distribution envelope that is well described by a super-Gaussian function with an order of 6.4.

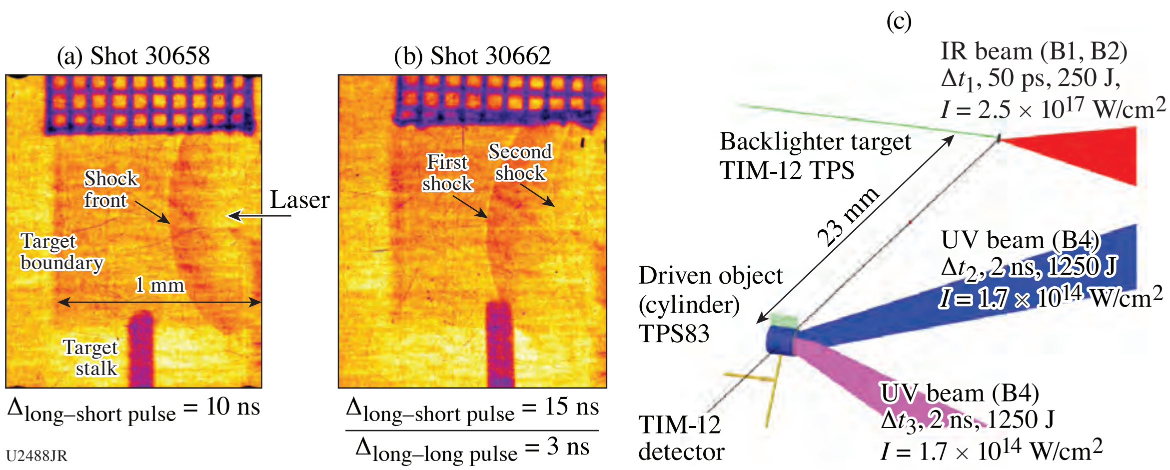

Figure 25
XPCI data of (a) a single and (b) a double laser-induced shock wave on OMEGA EP. (c) Setup of the XPCI experiment on OMEGA EP. The radiograph shown in (a) was taken 10 ns after the start of the UV beam, and the shock wave has propagated over several hundred microns in the CH target. The radiograph shown in (b) was taken at 15 ns after the start of the first UV pulse. The second UV pulse was launched at a 3-ns delay with respect to the first UV pulse.

The backlighter target consisted of a 5 × 30 × 300-μm^3 small strip of Cu foil glued onto a 10-μm-thick CH substrate. Either IR beam B1 or B2 was focused normal onto the Cu strip with the strip aligned along the axis to TIM-14, which contained a passive imaging plate detector in a heavymet shielded box (LLDI). The backlighter produced a strong emission between 8 and 9 keV predominately from the He$_\alpha$ and Ly$_\alpha$ resonance lines. The distance from backlighter to CH cylinder was 2.3 cm, and the distance from the CH cylinder to the IP detector was 1.4 m, providing a magnification of 60×.

Resolution Au grids mounted on the top of the cylinder provide a spatial fiducial and are used to infer the spatial resolution, which was found to be 15 μm in the horizontal direction and 18 μm in the vertical direction. The spatial resolution was limited by the source size and how well the strip target could be aligned. The images show many scratches on the image plate (IP), which somehow degraded the image quality. The IP's were used multiple times before the experiment and the scratches accumulated from prior use. Future experiments will request fresh IP's in order to avoid these scratches.

The data were successfully reproduced by simulations of the UV beam interaction using the 2-D radiation hydrodynamic code *DUED*.[37] Figure 26(a) compares the experimental data (top) from the double-shock experiment and the simulated x-ray phase contrast image (bottom), showing good agreement of the general signal level and also the positions of both shock fronts. Figure 26(b) shows lineouts along the horizontal axis of the experimental data and the simulated data, showing the typical signal excursions that are caused by the phase enhancement. The hydrodynamic simulation results were post-processed with an XPCI code that is described in Ref. 36. The shock wave is not perfectly symmetric because both beams are not interacting with the target surface at normal incidence but with an angle of incidence of 23° with respect to the target normal from different directions. The data analysis is ongoing with planned comparison to other hydrodynamic codes, improvements of image filtering to enhance the image quality, and possible comparison with other XPCI codes. The XPCI-EP-19A experiment on OMEGA EP demonstrated x-ray phase-contrast imaging of strong shocks with sufficient contrast in a low-Z material.

This material is based upon work supported by the Department of Energy National Nuclear Security Administration under Award Number DE-NA0003856, the University of Rochester, and the New York State Energy Research and Development Authority.

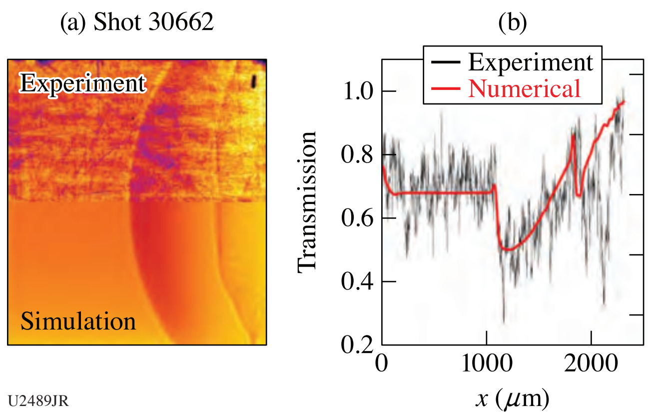

Figure 26
(a) Comparison of the experimental data (top) from the double-shock experiment and the simulated x-ray phase contrast image (bottom) shows good agreement of the general signal level and the positions of both shock fronts. (b) Lineouts along the horizontal axis of the experimental data and the simulated data show the typical signal excursions that are caused by the phase enhancement.

1. J. L. Shaw *et al*., presented at the 61st Annual Meeting of the APS Division of Plasma Physics, Fort Lauderdale, FL, 21–25 October 2019.
2. G. J. Williams *et al*., presented at the International Conference on High Energy Density Science (ICHED), Oxford, UK, 31 March–5 April 2019.
3. J. Kim *et al*., "Dynamic Focusing of Laser Driven Positron Jets by Self-Generated Fields," submitted to New Journal of Physics.
4. H. Chen *et al*., Phys. Rev. Lett. **102**, 105001 (2009).
5. H. Chen *et al*., Phys. Rev. Lett. **105**, 015003 (2010).
6. H. Chen *et al*., Phys. Plasmas **21**, 040703 (2014).
7. O. V. Gotchev *et al*., Rev. Sci. Instrum. **80**, 043504 (2009).
8. H. Chen *et al*., Phys. Rev. Lett. **114**, 215001 (2015).
9. H. Chen *et al*., Phys. Plasmas **22**, 056705 (2015).
10. H. Chen *et al*., High Energy Density Phys. **7**, 225 (2011).
11. P. Tzeferacos *et al*., Nat. Commun. **9**, 591 (2018).
12. *Report of the Workshop on High Energy Density Laboratory Physics Research Needs*, Office of Science and National Nuclear Security Administration, U.S. Department of Energy, Washington, DC (15–18 November 2009).

13. T. R. Boehly *et al*., Opt. Commun. **133**, 495 (1997).

14. H. Witała and W. Glöckle, Phys. Rev. C **83**, 034004 (2011).

15. C. J. Forrest *et al*., Phys. Rev. C **100**, 034001 (2019).

16. M. Vorabbi *et al*., Phys. Rev. C **100**, 024304 (2019).

17. G. Fiksel *et al*., Phys. Rev. Lett. **113**, 105003 (2014).

18. D. B. Schaeffer *et al*., Phys. Rev. Lett. **119**, 025001 (2017).

19. S. A. Slutz *et al*., Phys. Plasmas **17**, 056303 (2010).

20. D. D. Ryutov *et al*., Phys. Plasmas **19**, 062706 (2012).

21. D. E. Fratanduono *et al*., Phys. Rev. B **97**, 214105 (2018).

22. S. Root *et al*., Geophys. Res. Lett. **45**, 3865 (2018).

23. R. F. Smith *et al*., Phys. Rev. Lett. **101**, 065701 (2008).

24. J. S. Oakdale *et al*., Adv. Funct. Mater. **27**, 1702425 (2017).

25. J. K. Wicks *et al*., Sci. Adv. **4**, eaao5864 (2018).

26. D. Polsin, *LLE 2018 Annual Report, October 2019-September 2018*, 240, Laboratory for Laser Energetics, University of Rochester, Rochester, NY, LLE Document No. DOE/NA/1944-1450 (March 2019).

27. H. Tups and K. Syassen, J. Phys. F: Met. Phys. **14**, 2753 (1984).

28. S. Brygoo *et al*., J. Appl. Phys. **118**, 195901 (2015).

29. H. Daido *et al*., Appl. Phys. Lett. **51**, 2195 (1987).

30. G. Ren *et al*., Phys. Rev. Lett. **118**, 165001 (2017).

31. M. Millot *et al*., Nat. Phys. **14**, 297 (2018).

32. M. Millot *et al*., Nature **569**, 251 (2019).

33. B. Militzer and H. F. Wilson, Phys. Rev. Lett. **105**, 195701 (2010).

34. V. A. Thomas and R. J. Kares, Phys. Rev. Lett. **109**, 075004 (2012).

35. D. S. Clark *et al*., Phys. Plasmas **23**, 056302 (2016).

36. L. Antonelli *et al*., Europhys. Lett. **125**, 35002 (2019).

37. S. Atzeni *et al*., Comput. Phys. Commun. **169**, 153 (2005).

FY19 Lawrence Livermore National Laboratory Experimental Programs at the Omega Laser Facility

R. F. Heeter,[1] F. Albert,[1] S. J. Ali,[1] L. R. Benedetti,[1] N. Candeias Lemos,[1] H. Chen,[1] F. Coppari,[1] A. Fernandez Pañella,[1] D. E. Fratanduono,[1] M. Ginnane,[2] M. Gorman,[1] M. Hohenberger,[1] S. Jiang,[1] G. E. Kemp,[1] S. F. Khan,[1] P. King,[1] A. Krygier,[1] A. E. Lazicki,[1] T. Ma,[1] M. J. MacDonald,[1] D. Mariscal,[1] E. V. Marley,[1] M. C. Marshall,[1] D. A. Martinez,[1] M. A. Millot,[1] C. A. J. Palmer,[3] H. S. Park,[1] J. Park,[4] G. Perez Callejo,[3] Y. Ping,[1] B. B. Pollock,[1] P. L. Poole,[1] J. Ralph,[1] A. M. Saunders,[1] G. F. Swadling,[1] R. Tommasini,[1] K. Widmann,[1] A. Zylstra,[1] O. L. Landen,1 [1] W. W. Hsing,[1] and A. S. Wan[1]

[1]Lawrence Livermore National Laboratory
[2]Laboratory for Laser Energetics, University of Rochester
[3]Oxford University
[4]University of California, San Diego

In fiscal year 2019 (FY19), Lawrence Livermore National Laboratory's (LLNL's) High-Energy-Density (HED) Physics and Indirect-Drive Inertial Confinement Fusion (ICF-ID) Programs conducted numerous campaigns on the OMEGA and OMEGA EP Laser Systems. This was the 21st year of national laboratory collaborative experiments at the Omega Laser Facility since the Nova Laser at LLNL shut down in 1999 (Ref. 1), building upon prior collaborations. In FY19 overall, these LLNL programs led 465 target shots, with 283 shots using only the OMEGA Laser System, 172 shots using only the OMEGA EP Laser System, and 10 joint shots using both lasers together. Approximately 28% of the total number of shots (60 OMEGA shots and 71 OMEGA EP shots) supported the ICF-ID Campaign. The remaining 72% (223 OMEGA-only shots, 101 OMEGA EP-only shots, and 10 joint shots) were dedicated to experiments for HED physics. Highlights of the various HED and ICF-ID campaigns are summarized in the following reports.

In addition to these experiments, LLNL Principal Investigators (PI's) led a variety of Laboratory Basic Science (LBS) campaigns using OMEGA and OMEGA EP, including 99 target shots using only OMEGA and 39 shots using only OMEGA EP. The highlights of these campaigns are summarized in the LBS section (p. 257).

Overall, LLNL PI's led a total of 603 shots at LLE in FY19. In addition, LLNL PI's supported 47 National Laser Users' Facility (NLUF) shots on OMEGA and 31 NLUF shots on OMEGA EP in collaboration with the academic community.

Indirect-Drive Inertial Confinement Fusion Experiments

Hydrodynamic Response from Nonuniformities in High-Density Carbon Ablators

Principal Investigator: S. Ali
Co-investigators: P. M. Celliers, A. Fernandez Pañella, C. Weber, S. W. Haan, and V. A. Smalyuk

Performance and yield from fusion capsules at the National Ignition Facility (NIF) are highly dependent on the uniformity of the capsule implosion. Hydrodynamic instabilities are a significant source of performance degradation during the implosion and can arise from, among other reasons, intrinsic heterogeneity within the capsule material. High-density carbon (HDC) is a polycrystalline diamond material that has a complex microstructure, as well as being acoustically anisotropic, which can lead to variations in the shock speed in crystallites of different orientations, potentially seeding instabilities. Additional sources of heterogeneous response include the behavior of the grain boundary material, which is often of a different bonding character than the crystallites, voids in the deposited material, and static internal stresses in the polycrystalline structure. The current strategy for reducing the impact of internal heterogeneities is to fully melt the ablator material on the first shock, requiring >12 Mbar for HDC.[2–4] This strong shock also raises the entropy of the fuel, making it more difficult to reach the high densities required for ignition. As part of the effort to understand both the origin and impact of the velocity nonuniformities in HDC, we have conducted 2-D velocimetry experiments on planar foils under conditions near the first shock in HDC.

The goal of the Capseed Campaign is to measure shock-front velocity nonuniformities in ICF ablator materials and quantify the level of nonuniformity caused by intrinsic effects. This is done by using the OMEGA high-resolution velocimeter (OHRV) to obtain velocity maps of the optically reflecting shock front following release of the ablator material into either PMMA for the warm experiments or cryogenic deuterium for the cryo experiments. As part of our attempt to move toward more capsule-like targets, as opposed to the planar foils that have been used for past Capseed Campaigns, we have been moving toward using large-diameter (4.5 to 5 mm) capsules for our two half-day campaigns in FY19. Unfortunately, due to the complexity involved in fabricating these large spheres, the 5-mm HDC spheres were not complete in time for 19B, but a secondary goal of measuring the effect of grain size on the nonuniformity was achieved. Relative to the microcrystalline HDC, the onset of velocity uniformity in the 10- to 20-m/s range occurred at just under 10 Mbar, as shown in Fig. 1. This suggests that nanocrystalline capsules can be driven on a lower adiabat than larger grain size capsules while still remaining relatively free of instabilities. This work is ongoing, and target fabrication has made great strides in fabricating the larger-diameter spheres, so the plan remains to move toward the capsule-like samples while still investigating other potential sources of perturbation.

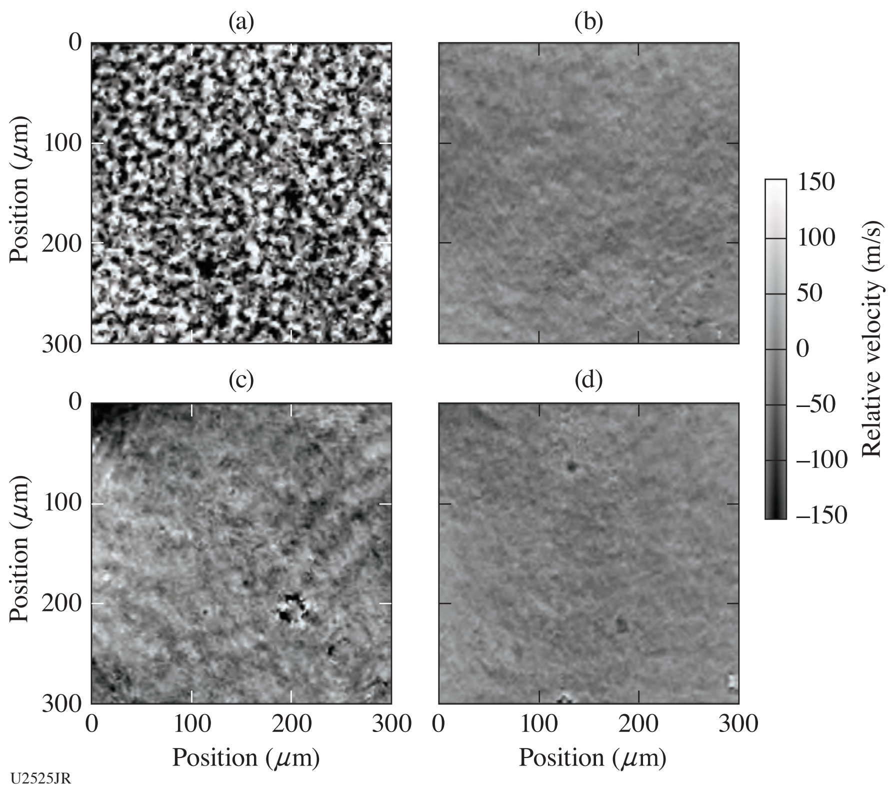

Figure 1
Velocity maps from nanocrystalline HDC releasing into cryogenic D_2 at (a) ~7 Mbar with rms 100 m/s, (b) ~8 to 9 Mbar with rms 45 m/s, (c) ~10 Mbar with rms 14 m/s, and (d) ~12 Mbar with rms 12 m/s. The diagnostic detection limit is 10 m/s for (b) and 5 m/s for (a), (c), and (d).

Determination of EOS and Melt Line of W-Doped Diamond Between 6 and 12 Mbar
Principal Investigator: A. Fernandez Pañella
Co-investigators: M. Millot and P. M. Celliers

This half day on OMEGA EP was designed to collect high-quality data on the melt line and equation of state (EOS) of W-doped diamond (0.3 at. %) in the multi-Mbar range. W-doped HDC is used in ICF capsules on the NIF, but only a scarce amount of EOS data is available, and little is known about what effect the doping has on the diamond melt line. Molecular dynamics (MD) simulations by S. Bonev predict that the melt temperature of HDC decreases with increasing Si dopant concentration. Similar effects are expected with W dopant, but experimental verification is required.

The W-doped HDC-19A Campaign used planar targets and a direct-drive configuration with a Be ablator, a quartz pusher, and two samples side by side: one being W-doped HDC and pure HDC glued together and the other being a quartz witness (see Fig. 2). The velocity profiles were recorded using VISAR (velocity interferometer for any reflector) and the emissivity using SOP (streaked optical pyrometry) (see Fig. 3). Throughout the day, the laser drive energy was changed to probe different shocked pressure states in the diamond.

We obtained six good data points from 600 to 1200 GPa. The experimental design was successful, and shocks were steady, as indicated by the quartz witness velocity history. The W-doped HDC target at 0.3 at. % is completely opaque at the VISAR

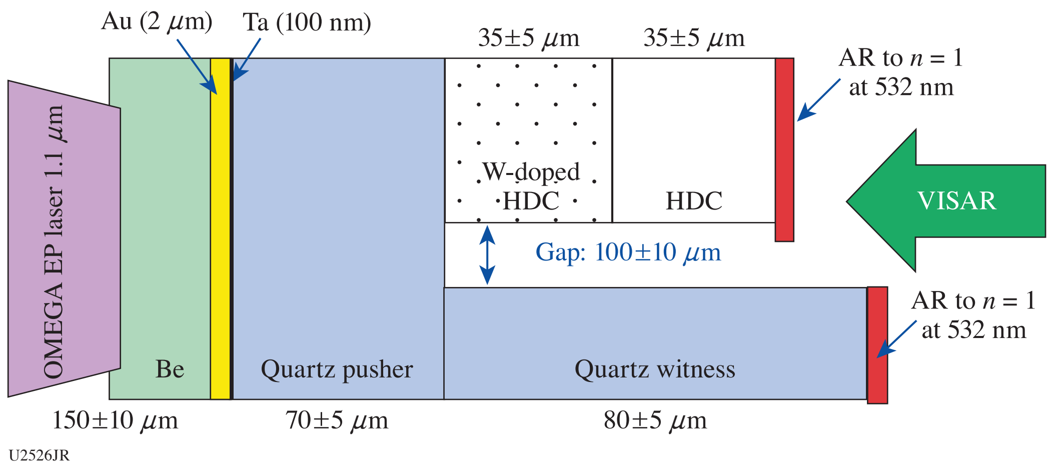

Figure 2
Experimental setup and target design for the W-doped HDC-19A Campaign.

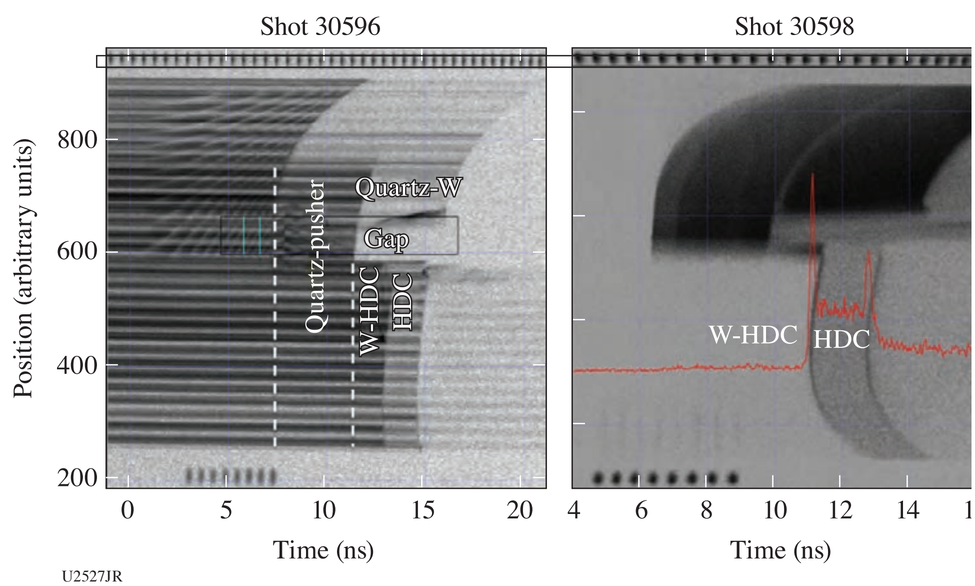

Figure 3
VISAR and SOP data from shot 30596, corresponding to 9.5 Mbar. Neither fringe movement nor emission is observed in the W-HDC sample.

and SOP wavelengths. Transit time analysis will be used to infer EOS data. Furthermore, we will also use the SOP data from the pure and transparent HDC to constrain its temperature along the melt line of pure diamond. Once the data are analyzed, we will be able to constrain the EOS of W-doped HDC in a pressure range relevant for ICF experiments.

Study of the Melting Temperature of Diamond with Pyrometry
Principal Investigator: M. Millot
Co-investigator: P. M. Celliers

This series of shots aims at measuring the shock temperature of diamond over a broad pressure range from 5 Mbar to 40 Mbar. To do this, the approach builds on the previous work by Eggert *et al*. carried out on OMEGA in 2005–2006 and reported in Ref. 5. Namely, the idea is to launch a strong, unsupported shock in a thick sample of diamond and track simultaneously the shock velocity and reflectivity with a VISAR velocimetry instrument [active shock breakout (ASBO)] and the spectral radiance with the SOP.[6] A gray-body approximation using the measured reflectivity to determine the emissivity then allows one to obtain the variation of the shock temperature as a function of shock velocity, which one can relate to pressure using a previously determined U_S–u_p equation-of-state relationship.

With excellent laser performance and support, we collected eight system shots in the half-day allocation, returning excellent-quality data. In particular, the new optical telescope with improved achromaticity and therefore enhanced spatial resolution resulted in noticeably higher-quality SOP (see Fig. 4).

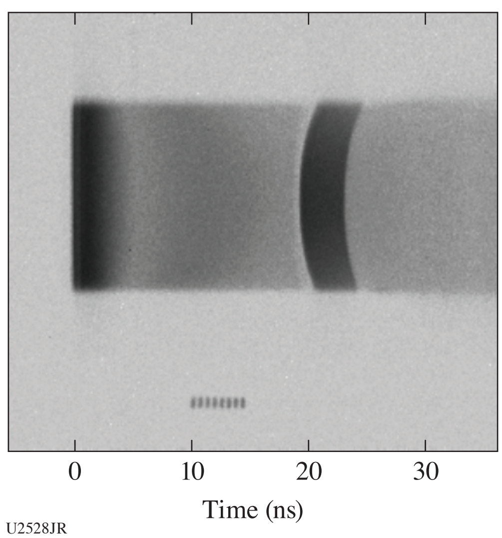

Figure 4
Example SOP data for the Diamond Melt 19A Campaign.

The ongoing data analysis will be used to improve our understanding of the thermodynamic properties of diamond near the pressure–temperature conditions that are relevant for ICF experiments using HDC ablators.[7]

Investigation of the Atomic Structure of Dense Carbon with X-Ray Diffraction
Principal Investigator: M. Millot
Co-investigators: F. Coppari, A. Fernandez Pañella, J. Emig, V. Rekow, and P. M. Celliers

This series of shots aims at measuring the atomic structure of diamond in the multi-megabar range and near the pressure–temperature conditions achieved during the initial stage of ICF implosions using HDC ablators on the NIF.[7] In particular, we aim to unravel how shock-compressed diamond transforms to a conducting fluid above 11 Mbar as expected from previous experiments, numerical simulations, and theoretical modeling. Further, we hope to elucidate if dense fluid carbon formed by shock compression could solidify upon decompression and the link with a possible maximum in the melting curve of carbon near 5 Mbar (Ref. 8).

This campaign on OMEGA EP used a combination of ultrafast x-ray diffraction and optical diagnostics using new laser dynamic compression techniques. We collected excellent-quality data on eight system shots using one UV beam to compress the water sample layer and three UV beams to generate an x-ray source flash for the x-ray diffraction measurement. Preliminary analysis suggests that we successfully managed to record high-quality x-ray diffraction data (see Fig. 5) and scan a broad range of pressure from 5 to 12 Mbar.

The ongoing data analysis and upcoming experiments on OMEGA EP in FY20 and on the NIF will be used to improve our understanding of the microscopic and thermodynamic properties of carbon at extreme conditions, build improved constitutive models and provide information for future designs for ICF at the NIF. In particular, we hope to resolve the discrepancy between current EOS and experimental data unveiled by the analysis of shock-timing experiments on the NIF and described in Ref. 9.

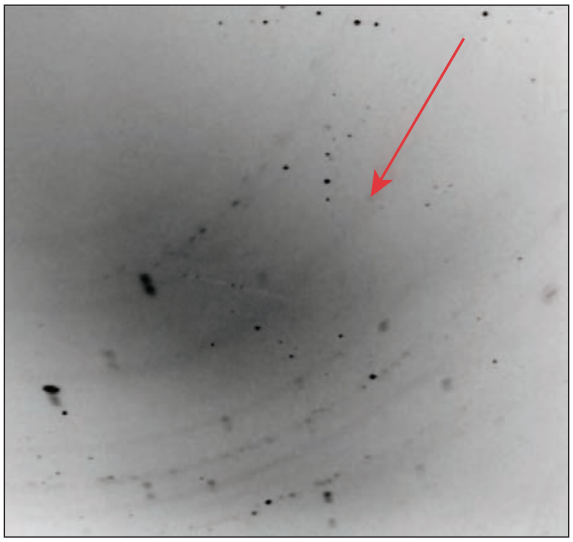
U2529JR

Figure 5
Example of raw powder x-ray diffraction image-plate (PXRDIP) data showing the x-ray diffraction pattern of diamond shock-compressed near 8 Mbar (red arrow), together with the calibration line.

Proton Radiography Measurements Using DT^{3}He–Filled Exploding Pushers as Proton and Deuteron Sources
Principal Investigator: B. B. Pollock
Co-investigators: G. Sutcliffe, C. Li, and J. D. Moody

MagHohlMultiPBL-19A is the first experiment in a campaign to probe hohlraum-relevant physics with protons and deuterons from a DT^{3}He-filled exploding-pusher source.

Figure 6 shows the general experimental geometry. The backlighter capsule location and drive were the same for all shots on the day, but the fill varied between DT^{3}He and D^{3}He. The capsules were driven by 39 beams of OMEGA, while the others were used for driving foil targets and for Thomson scattering. Two foil configurations were studied during the shot day. The first irradiated flat CH foils in both foil locations with six beams each, where protons (and deuterons if the capsule contained T) probed the electric and magnetic field structures at the target surface either through or tangential to the target face. In this configuration, 2ω Thomson scattering was performed at various locations relative to the surface of one of the target foils in order to measure electron density and temperature for comparison with simulations of the expanding surface plasma. The second configuration used Au foils in both locations, one flat and one curved; both foils were probed edge on with the protons and deuterons from the pusher. The maximum number of beams was reduced to either three or five, depending on the foil geometry, and the on-shot beam orientation was varied by dropping one or more beams from each shot. By changing the effective beam spacing, the resulting field structures are also affected and can be distinguished using the (up to) three charged particles emitted from the pusher. The proton data are still being processed, but initial estimates of the deuteron yield from the capsules containing T are approximately 3$\times$ less than initial estimates based on scaling from prior experiments. This discrepancy is being investigated further, and future experiments will attempt to drive the capsules with more energy to achieve higher yields.

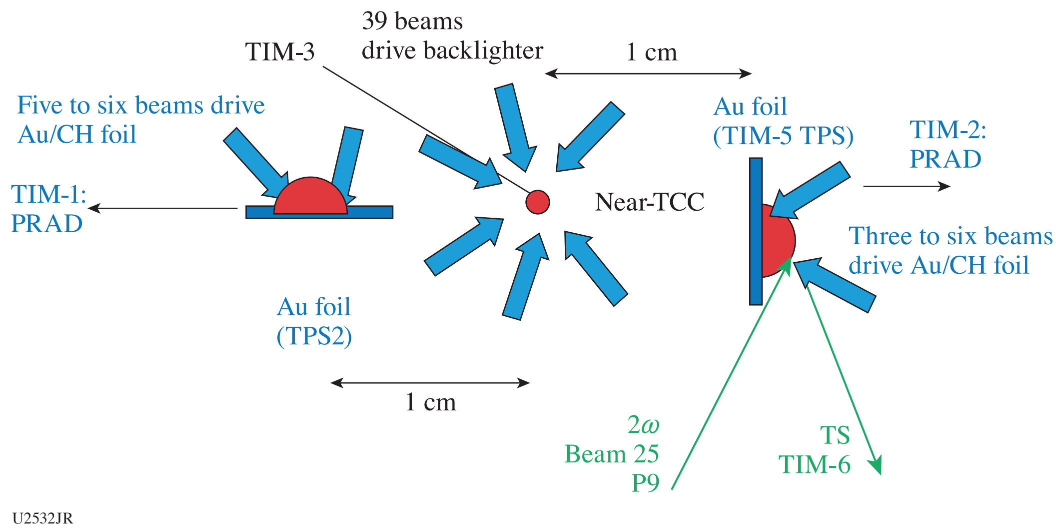

Figure 6
Experimental configuration for MagHohlMultiPBL-19A. Two foils are placed ~1 cm away from an exploding-pusher capsule target positioned near target chamber center (TCC). The capsule is filled with either DT^3He or D^3He. When compressed, both capsule fills produce 3.0- and 14.7-MeV protons; with T present in the fill, 9.5-MeV deuterons are also produced. These particles probe the electric- and magnetic-field structures either across or through the foil targets depending on the foil orientation. Protons and deuterons are recorded on CR-39 detectors.

Characterization of Compressed MIFEDS Fields in Cylindrical Targets

Principal Investigator: B. B. Pollock
Co-investigators: J. R. Davies and J. Peebles (LLE); and J. D. Moody (LLNL)

BFieldAmp-19A and 19B were the first experiments in this campaign to attempt to characterize compressed magnetic fields in cylindrical geometries on OMEGA.

Figure 7 shows the general experimental geometry for BFieldAmp-19A and 19B. The target for both shot days was an empty plastic tube of ~600 μm diameter with a 30-μm-thick wall. The tube is irradiated around its waist to drive >10× convergence of the tube diameter. Provided the inner wall of the tube is sufficiently ionized from x rays produced by the laser–wall interaction

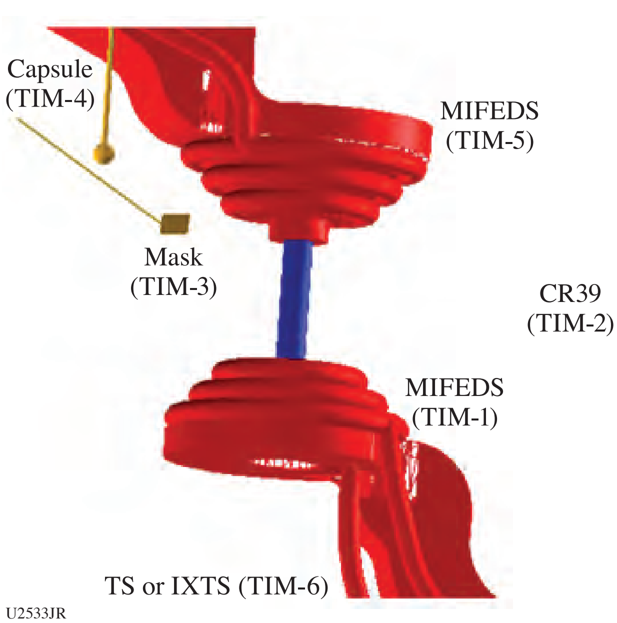

Figure 7
Experimental configuration for BFieldAmp experiments. A plastic tube (blue) is attached to one MIFEDS coil, while a second coil is inserted on the opposing side to allow for up to 30-T magnetic-field production at the center of the tube. The tube is irradiated with 40 beams around its waist to drive it radially inward from an initial diameter of ~600 μm to a final diameter of ~50 μm. Protons are produced from the implosion of a D^3He-filled capsule target, some of which are collected on a CR-39 detector on the opposite side of the tube from the capsule. The mask was present only in 19B and partially blocks the proton line of sight to the CR-39 on only one side of the tube. The optical Thomson-scattering collection system was used to measure plasma emission on 19A, while the imaging x-ray Thomson spectrometer (IXTS) system was used to measure x-ray emission on 19B.

on the exterior of the tube, the magnetic field should compress with the tube wall and result in an increased B-field strength proportional to the square of the tube's convergence ratio. The strength of the applied magneto-inertial fusion electrical discharge system (MIFEDS) magnetic field was varied from 5 to 30 T between the two shot days, and optical and x-ray emission measurements were taken to look for evidence of the magnetic-field compression. However, the proton data from these experiments are currently inconclusive about the compression of the initial magnetic field during the tube implosion, as are the spectroscopic measurements. Further analysis is underway, and future experiments will add a gas fill to the tube similar to that of the mini-MagLIF (magnetized liner inertial fusion) experiments of J. Davies *et al*.[10] The initial gas fill will provide the tube with material to push against, potentially reducing the convergence ratio, but in this configuration the gas has been shown to be able to be ionized by the x rays produced during the implosion and should therefore be more robust for entraining the initial magnetic field and compressing it as the tube implodes. Following a successful characterization of B-field compression, additional future work will use the high-field region at the compressed tube center as a platform for ultrahigh magnetic-field experiments.

Characterization of Laser-Driven Magnetic Fields

Principal Investigator: B. B. Pollock

Co-investigators: S. Fujioka, H. Morita, K. Law, and J. D. Moody

BFieldLoop-19A is a continuation of the laser-driven magnetic-field experimental campaign on OMEGA EP. The goals for 19A were to study current diffusion in the loop targets, as well as to examine the B-field dependence on target material choice for the loops.

Figure 8 shows data from four different shots on the day. Figure 8(a) is a radiograph of the loop target without driving the magnetic field. The loop target and the x-ray shield blocking the line of sight to the proton generation foil can be seen clearly in the image. The top of the target shows shadowed regions at the edges, corresponding to the location of the thin strap pieces that connect the front and back rectangular plate portions of the target, which are intended to restrict the ability of the current to diffuse away from the target edges. This configuration also produces a magnetic reconnection geometry between the straps, which may be investigated further in future experiments.

Figure 8(b) shows the result of driving a Au target with 0.5 TW of laser power for 3 ns, consistent with previous experimental configurations with complete loop sections at the target top. The lateral width of the shadowed region outside the outline cor-

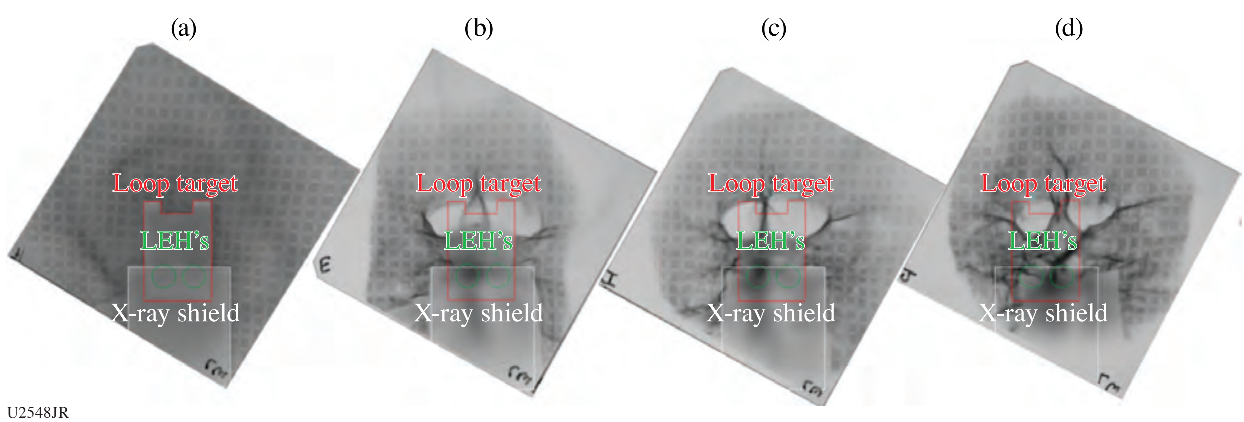

Figure 8
Proton radiography images for (a) undriven Au, (b) driven Au, (c) driven Cu, and (d) driven Al targets. The targets are foils folded to produce parallel rectangular plate sections that are 1.1 mm wide and 1.5 mm tall, with 300-μm-wide, 250-μm-radius straps at the edges connecting the plates (which are separated by 500 μm). The B field is produced by irradiating the target interior through one of the laser entrance holes (LEH's, typically the left side in these images), which generates a voltage difference between the plates, driving a current through the straps, resulting in a magnetic field around the top portion of the target. The x-ray shield blocks the line of sight from the LEH's back to a 10-μm-thick Au foil, which is irradiated by the 1-ps backlighter pulse on OMEGA EP at 200 J to produce the probing protons via the TNSA (target normal sheath acceleration) mechanism. A Cu mesh between the TNSA foil and the B-field target produces the grid structure in the images.

responding to the undriven target location is correlated with the strength of the magnetic field being produced around the straps, but there is also significant additional structure developing on the interior part of the target between the straps. Changing the target material to Cu shows an enhancement in this structure, as well as enhanced caustic features at the edges of the proton shadows around the straps. Reducing the target Z even further by using an Al target shows more structure still compared to the Cu and Au targets. These additional materials were initially chosen to study the effect of different conductivities and specific heats on current diffusion processes; the enhanced structures around the target location need further analysis to determine the full impact of target material choice on the current and B-field generation processes. These data are still being analyzed, but future experiments will measure the B-field structure in the non-Au targets at earlier evolution times as well as after the end of the pulse (as has been done previously with Au).

Experiments to Address Laser Transport in Magnetized Plasmas
Principal Investigator: D. Mariscal
Co-investigators: G. E. Kemp, E. Marley, and K. Tummel

Simulations using *HYDRA* with magnetohydrodynamic (MHD) packages predict enhanced laser propagation and plasma temperatures when magnetic fields are imposed along the laser axis, as seen in Fig. 9. These experiments explore parameters that produce magnetized plasmas (electrons) where these effects can be examined and used to determine which MHD terms are important for reproducing results in *HYDRA*.

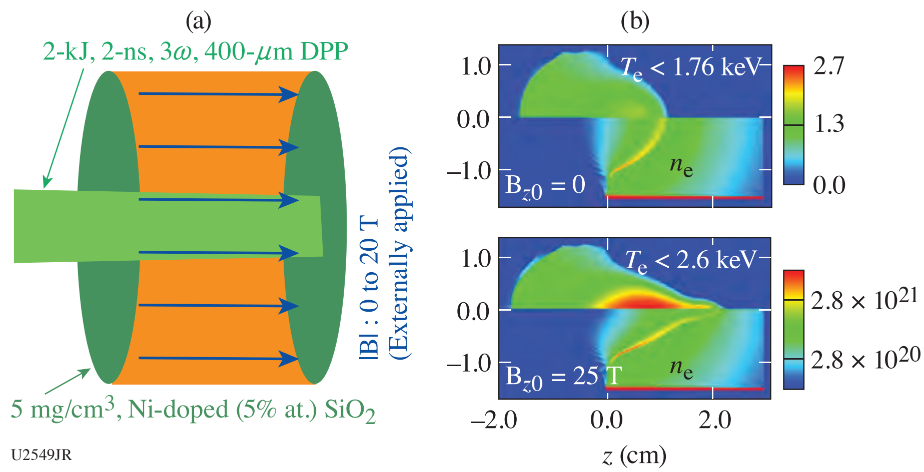

Figure 9
(a) Experiment and simulation setup in *HYDRA* showing orientation of axial B field along laser axis, cylindrical foam targets, and laser parameters. (b) Results from 2-D *HYDRA* calculations (K. Tummel) showing significant differences in both electron density and temperature profiles at 1.5 ns into the laser pulse.

Targets in these experiments were 3-mm-diam, 3-mm-long, 5-mg/cm^3 SiO_2 foams [see Fig. 9(a)] that were doped with Ni at ~5% atomic fraction in order to perform spectral measurements of the plasma temperature. These foams were mounted within MIFEDS coils with a quasi-Helmholtz geometry to provide a nearly uniform spatial profile magnetic field up to ~20 T [see Fig. 10(a)]. The targets were then driven by a single UV beam on OMEGA EP with ~2 kJ of laser energy in a 2-ns super-Gaussian pulse. Two geometries were employed such that either Beam 1 or Beam 4 was used to drive the targets, with each beam using a 750-μm or 400-μm distributed phase plate (DPP) providing ~2×10^{14} or ~1×10^{15} W/cm^2 laser intensity. With these parameters, the plasma density is $\sim 0.2\, n_e/n_c$ with temperatures of ~2 keV and as seen in Fig. 10(b), allows one to explore plasma Hall parameters up to ~1. The multipurpose spectrometer (MSPEC) was used to acquire spatially and temporally resolved x-ray data along the laser axis [see Fig. 10(c)], while an x-ray framing camera (XRFC) was used to image the heat-front propagation [Fig. 10(d)].

Over two shot days, 17 target shots were completed, resulting in both a successful platform demonstration and a data set scanning two intensities and four B-field values (0, 5, 10, and 19 T). Preliminary analysis seems to indicate a dip in propagation velocity in

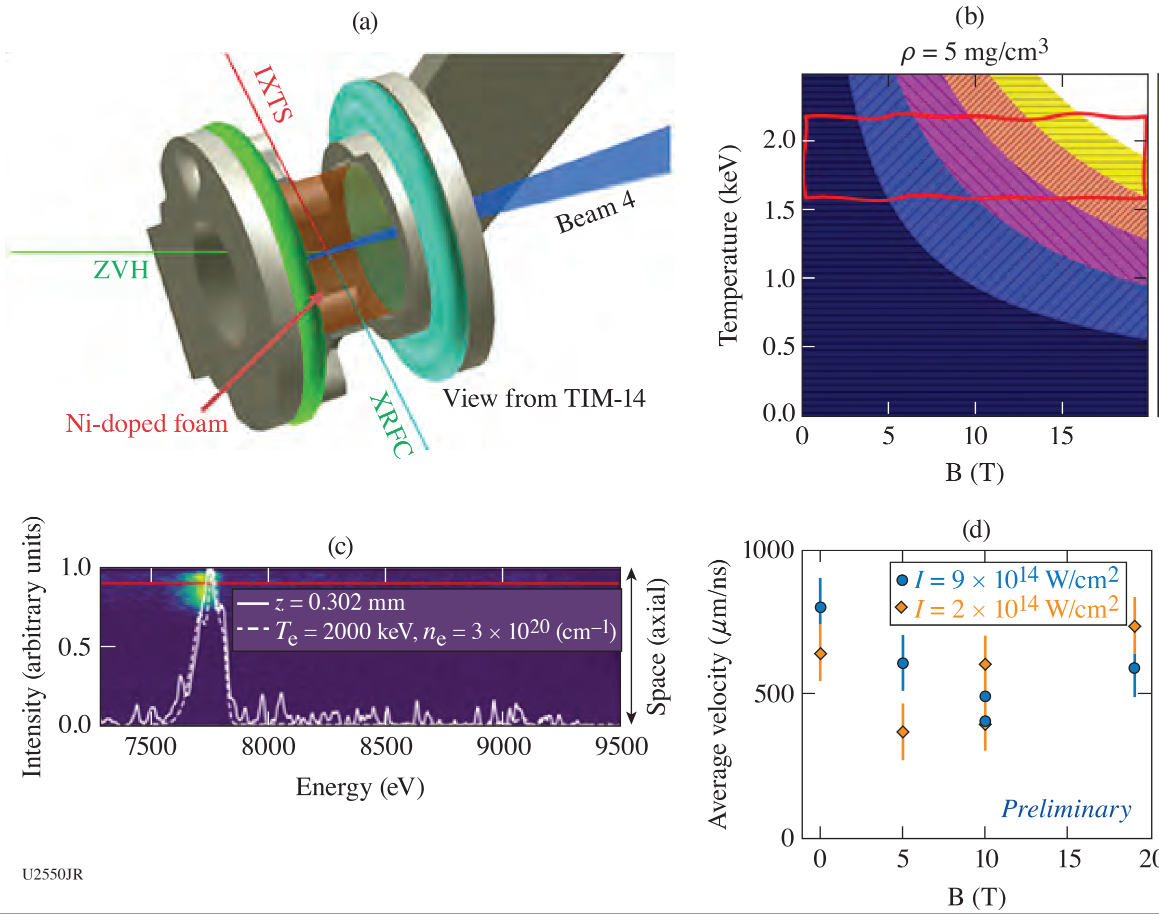

Figure 10
(a) Experimental setup showing MIFEDS coils and diagnostic locations. (b) The red box shows $\omega_{ce}\tau_{ei}$ space for the present experimental parameters at a fixed density. (c) Example MSPEC data, lineout, and corresponding fit. (d) Experimentally measured velocities showing a slowing of laser heat front near 5 to 10 T.

the neighborhood of 5 to 10 T. *HYDRA* simulations are underway to compare against this data set that should provide important insight regarding the importance of B fields in hydrodynamic calculations of laser-driven experiments at ICF-relevant conditions.

Experiment Study of Laser Entrance Hole Dynamics
Principal Investigator: J. Ralph
Co-investigators: M. Tabak, W. Farmer, O. L. Landen, and P. Amendt

These experiments tested several designs of the hohlraum LEH for use in advanced next-generation hohlraums. In total, 14 shots were performed to compare the LEH closure, hohlraum drive, and backscatter when using a variety of LEH types. The 1-mm-diam hohlraums were aligned to the H4–H17 axis; the surrounding six beams at 21.5° were focused at the 400- or 500-μm-diam LEH and incident on a 25-mm-thick Au plate located at about the middle of the hohlraum. The laser pulse used on all experiments is the 2-kJ pulse shown in Fig. 11(b). The x-ray framing camera timing (blue arrows) is shown relative to the laser pulse. We tested four types of LEH's: a simple opening; a 0.5-μm polyimide window; a CH-lined Au plate with a polyimide window; and, finally, a 100-μm-thick Au foam with a polyimide window.

All experiments used the same laser pulse. The mains results are summarized in Fig. 12. Here we see the 400-μm x-ray framing camera data from ten-inch manipulator TIM-3, looking in through the LEH, and TIM-2, looking at the hohlraum emission. The LEH-side framing camera measures the LEH closure as a function of time as shown in Fig. 12. We find the CH liner maintains the complete opening of 400 μm throughout the pulse. The TIM-2 framing-camera data shown in Fig. 12 provides a measure of the peak hohlraum emission using a 2° Ge mirror combined with a 1-μm Zn filter. From this data, the Au foam seems erratic, low at early time and high later in the pulse. The remaining LEH designs show an overall decline with time. Neglecting the Au foam data, it appears that during the middle of the pulse, the CH-lined LEH results in about 25% more emission. These results will provide information for future experiments and designs on the NIF.

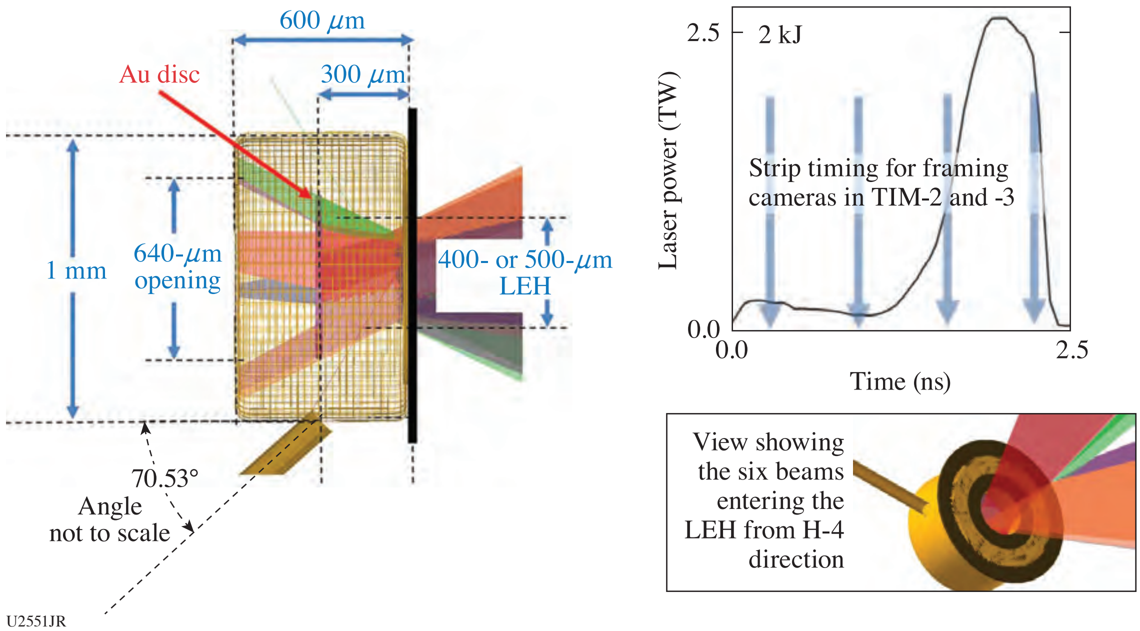

Figure 11
Target and experimental configuration.

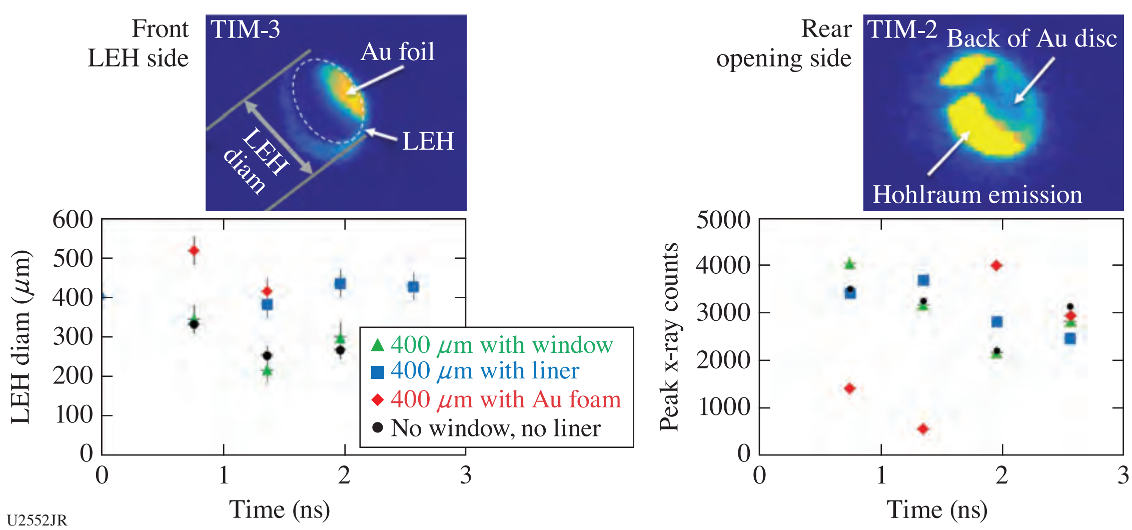

Figure 12
X-ray framing camera data.

Assessing Heat Transport in the Transition Between Local and Nonlocal Regimes

Principal Investigator: G. F. Swadling
Co-investigators: W. Farmer, M. Sherlock, M. Rosen, and B. B. Pollock (LLNL); D. H. Edgell (LLE); and C. Bruulsema and W. Rozmus (UA)

In the BeSphere-19A Campaign, we performed experiments that heated beryllium-coated spheres in a direct-drive geometry. The experiments were diagnosed using the OMEGA Thomson-scattering system (TSS), scatter calorimeters, and the Dante x-ray spectrometer. The aim of these experiments was to make quantitative measurements of the parameters of the blow-off plasma produced from these spherical targets. Seven target shots were completed in the half-day.

The data from these experiments are currently being used to benchmark heat-transport models. Using beryllium as the target material eliminates complications introduced by the high radiative losses and complex atomic physics of gold. To further simplify comparisons between experiment and simulation, the targets were heated at comparatively low intensities of 1 to 2.5 $\times 10^{14}$ W/cm^2; at these intensities, coupling the laser to the target was shown to be better than 90%.

The Thomson-scattering diagnostic measured the time-resolved spectrum of light scattered by fluctuations in n_e with wave vectors $\vec{k}$ tangential to the surface of the sphere. The size of the scattering volume, defined by the overlap of the probe beam and collection cone, was ~(50 μm)^3. Measurements were made at locations 200, 300, and 400 μm from the sphere surface. The diagnostic recorded scattering from both high-frequency electron plasma wave fluctuations (EPW, T_e, n_e) and low-frequency ion-acoustic wave fluctuations (IAW, T_e, T_i, v_{flow}). Examples of the data recorded are shown in Fig. 13. Fitting these measured spectra results in quantitative measurements of the plasma parameters, which may be compared with the results of numerical modeling. As an example, the T_e and T_i profiles measured in the experiment are compared with those calculated in a *LASNEX* run in Fig. 13, illustrating that good agreement was achieved.

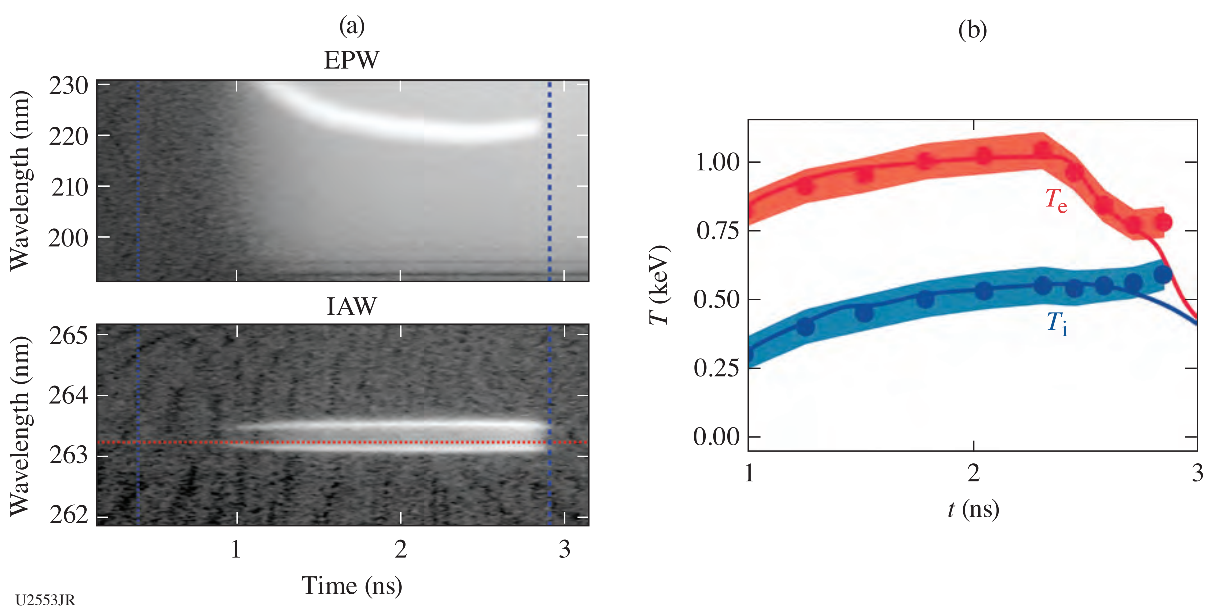

Figure 13
(a) Raw IAW and EPW Thomson-scattering spectra. (b) Example of a comparison between plasmas parameters measured by fitting the Thomson data and those calculated in a *LASNEX* simulation of the experiment. The circles are measurements, the shaded band indicates experimental uncertainly, and the solid lines show the *LASNEX* values.

Generation of TNSA Short-Pulse Laser-Accelerated Deuterons with up to 30-ps Pulse Length

Principal Investigator: J. Park (UCSD)
Co-investigators: J. Kim and F. N. Beg (UCSD); and T. Ma, D. Mariscal, G. Cochran,* and A. Zylstra (LLNL)
Graduate student: R. Simpson (MIT)
*Postdoc

This series of shots investigated the generation of proton and deuteron beams via short-pulse laser acceleration using the TNSA mechanism in the multi-ps regime. CD foils of 35-μm thickness were illuminated by OMEGA EP short-pulse beams with a varying pulse length (1 to 30 ps) and intensity (10^{17} to 10^{18} W/cm^2), relevant to NIF ARC (Advanced Radiographic Capability) laser conditions. Over the course of the day, the two OMEGA EP short-pulse beams were alternated in single-beam shots: Beam 1 delivered between 100 J and 300 J of energy on targets over 1- or 3-ps pulse length, while Beam 2 delivered between 625 J and 1250 J of energy over 10 ps or 30 ps. Both beams were defocused, ~45 μm R/80, to achieve the desired laser intensity. Several target shots utilized a novel configuration of combining both beams to provide a temporally shaped pulse to test proton and deuteron generation.[11] On this shot, the two beams were spatially overlapped on the target, but Beam 1 (3 ps) arrived prior to Beam 2 (30 ps) by ~45 ps. Three diagnostics were used to measure proton, deuteron, and electron spectra with varying laser conditions: radiochromic film (RCF) along the target rear normal, a Thomson parabola ion energy (TPIE) analyzer, and an electron spectrometer (E-spec) at 45° from the target rear normal (Fig. 14).

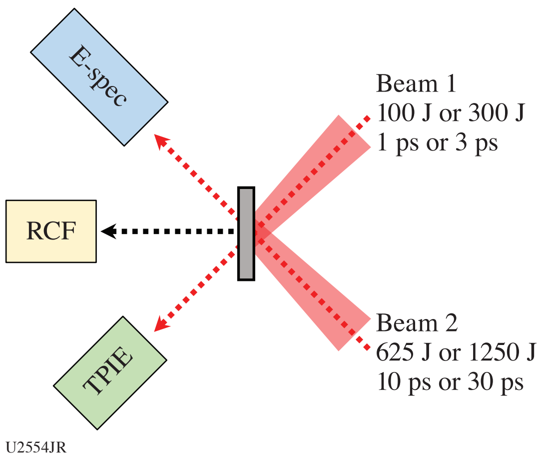

Figure 14
Top-down view of the experimental setup.

It was observed (Fig. 15) that there is a strong scaling of the ion flux and maximum ion energy with laser energy when a single beam is utilized; a 3-ps-long pulse with 100 J generated protons up to 3.6 MeV but no observable deuterons, while a 30-ps-long pulse with 625 J generated protons up to 5.1 MeV and deuterons up to 1.8 MeV. When both beams were simultaneously used, the maximum energy increased to 6.8 MeV and 4.9 MeV for protons and deuterons, respectively. The electron flux was also significantly increased by up to 7× when comparing single-beam to dual-beam configurations. The increase in the maximum ion energy due to this increased electron flux or the electron temperature is still under investigation.

Increasing Laser-Accelerated Particle Energies with "Shaped" Short Pulses

Principal Investigator: D. Mariscal
Co-investigators: T. Ma and G. Cochran* (LLNL); and J. Park* and J. Kim* (UCSD)
*Postdoc

Newer kJ-class, short-pulse (ps) lasers such as the NIF's ARC laser have recently been shown to be able to accelerate protons to energies that far exceed conventional scalings. While these results are encouraging, the proton energies necessary for probing indirectly driven ICF experiments are 2× higher than currently achievable with ARC. A new concept inspired by a unique ARC capability—the ability to deliver multiple short-pulse beams to the same location with specified delays—was tested on OMEGA EP by delivering both short-pulse beams to a single target in order to create pseudo-shaped short laser pulses.

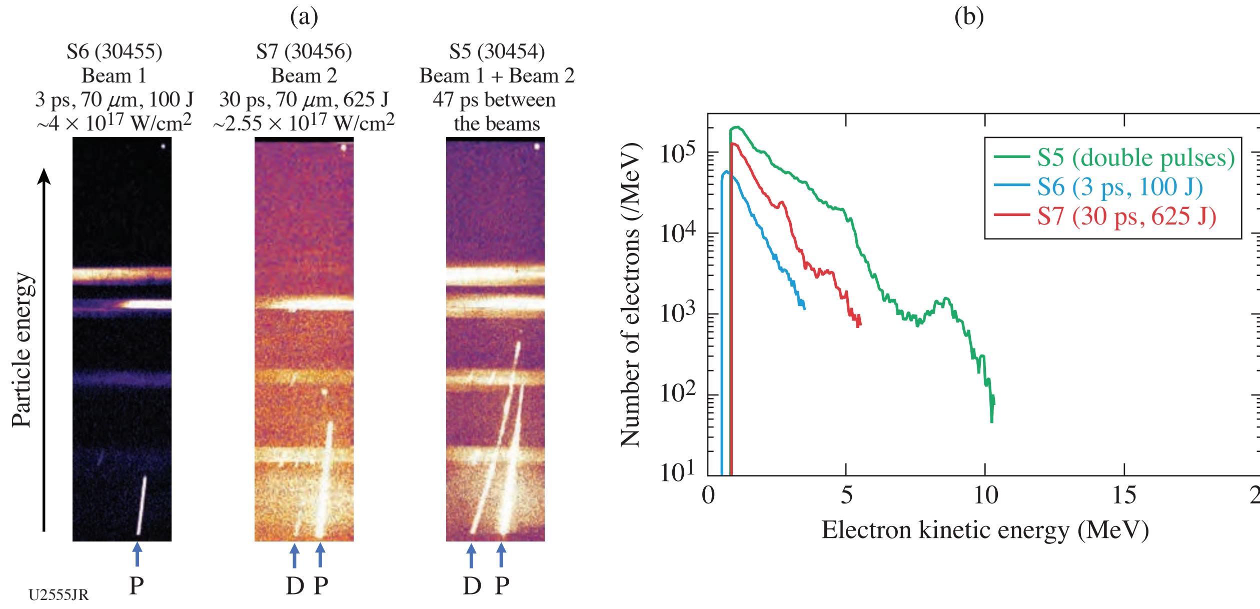

Figure 15
(a) Raw data from TPIE and (b) electron spectra from CD targets with three different laser configurations.

The experimental geometry is shown in Fig. 16. Both short-pulse beams were defocused to $R_{80} \sim 45\ \mu$m in order to simulate ARC-like laser conditions. One beam delivered 550 J at 4 ps, while the trailing beam delivered 1.6 kJ at 30 ps. Simple flat Cu foils (1 mm diam × 35 μm thick) were used as targets. The choice of Cu enabled the use of the spherical crystal imager (SCI) instrument to monitor spatial overlap of the two beams on target, while the ultrafast x-ray streak (UFXRS) camera and time-resolved channel of the high-resolution spectrometer (HRS) monitored the relative timing of the beams on target. Particle diagnostics including RCF and the electron positron proton spectrometer (EPPS) were used to monitor the particle characteristics for each shot. Particle spectra were recorded from single-beam shots before combining the beams and varying the relative timing between the two throughout the day.

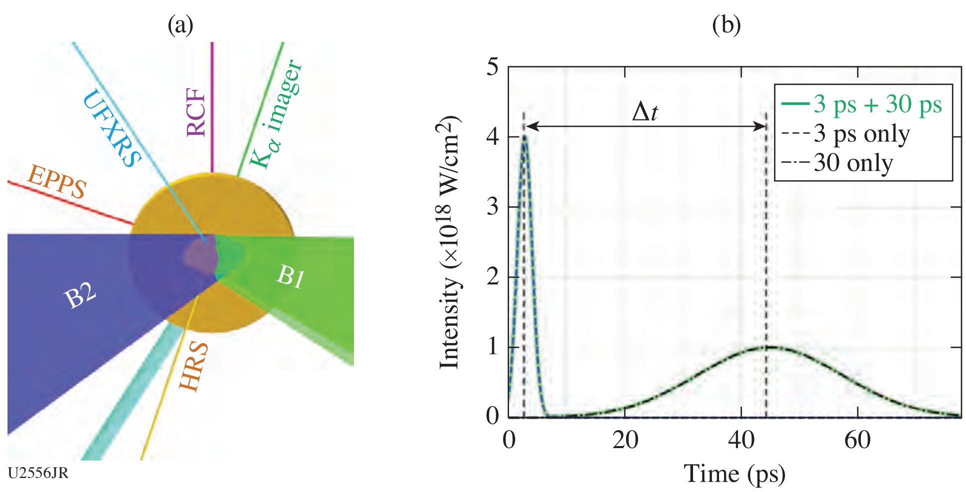

Figure 16
(a) Experimental configuration showing the two short-pulse beams incident on the foil target and the location of the diagnostics; and (b) an example of the pulse shapes and definition of Δt for Fig. 17.

A successful day with nine data shots was completed (four single beam + five combined beam). A preliminary look at the data (Fig. 17) indicates that electron temperatures and yields were significantly increased when pulse combinations were used, with a factor-of-2+ increase in total conversion efficiency into hot (>1-MeV) electrons, 50% increase in electron temperature, and a corresponding 50% increase in maximum proton energy. These data suggest that the use of shaped short pulses could increase the energy and efficiency of MeV particle sources driven by the NIF's ARC by manipulating time-dependent particle acceleration physics at the picosecond level. These novel results stimulated follow-up experiments now scheduled in FY20.

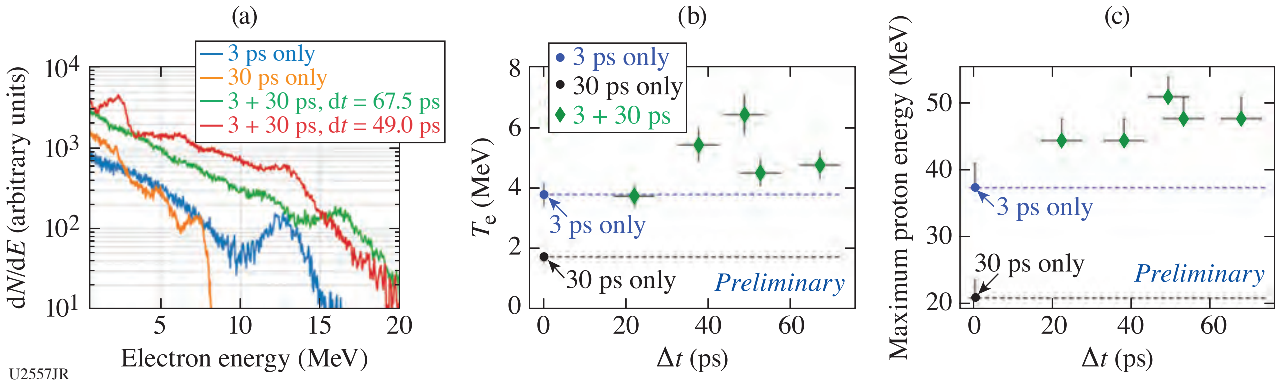

Figure 17
(a) Several electron spectra from the EPPS spectrometer and analysis showing (b) the exponential temperature fits to the data and (c) the maximum proton energy from RCF stacks for each case. All data are plotted versus the delay between the two beams.

Development of Improved Backlighters Using* In-Situ *Plasma Reflectors
Principal Investigator: R. Tommasini
Co-investigators: J. Park, L. Divol, and A. Kemp

The SmallSpotBL-EP-19 Campaign continued the development and testing of novel small-source x-ray backlighters that started with the prior campaign, SmallSpotBL-EP-17. The concept is to use *in-situ* plasma mirrors to enhance the laser energy coupling on microwire backlighters that can be used as point sources in high-energy x-ray radiography and at the same time increase the tolerance to laser pointing jitter.

In this campaign we introduced an improvement of the plasma mirror geometry by using 25-μm-diam Au microwires at the vertex of parabolic-like CH profiles, for brevity U-shaped PM (Fig. 18).

The 30-ps-long, 1-kJ energy pulses from the OMEGA EP sidelighter beam were pointed at the vertex of the plasma mirror profile. The x-ray yield and source size were measured along the line of sight aligned parallel with the gold wire, by radiographing a tantalum step wedge and a calibrated tungsten sphere, 200 μm in diameter.

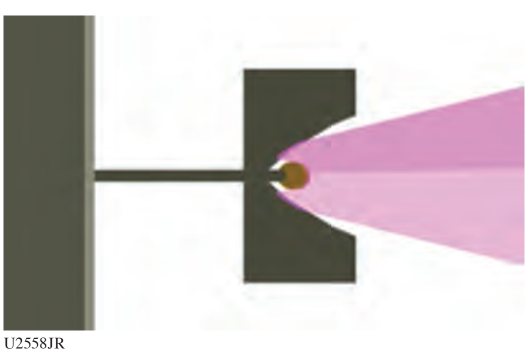

Figure 18
End-on view of 25-μm-diam Au wire in a U-shaped plasma mirror, illuminated by the OMEGA EP sidelighter beam.

We also performed shots with the original V-shaped CH profiles (V-shaped PM) and with bare Au wires. The results have confirmed a 2× to 3× increase in conversion efficiency when using the V-shaped plasma mirror configuration as compared to bare wires, and a 4× to 5× increase when using the U-shaped plasma mirror configuration. We also reported reduced statistical variation in x-ray yield between shots. The backlighter source size when using plasma mirrors has measured similar or smaller in size with respect to bare microwires and always very close to the wire diameter.

These novel backlighters are ideal for hard x-ray radiography of ICF implosions and make it possible to reduce the backlighter size in order to record radiographs with higher spatial resolution while maintaining sufficient signal-to-noise ratio. They have been used to record Compton radiographs of the imploding fuel on two layered THD shots on the NIF.

High-Energy-Density Experiments

1. Material Equation of State and Strength Measured Using Diffraction

X-Ray Diffraction of Shock-Ramped Platinum

Principal Investigators: A. E. Lazicki (LLNL) and M. Ginnane (LLE)
Co-investigators: R. Kraus, J. H. Eggert, M. Marshall, and D. E. Fratanduono (LLNL); D. N. Polsin, X. Gong, T. R. Boehly, J. R. Rygg, and G. W. Collins (LLE); and J.-P. Davis, C. McCoy, C. Seagle, and S. Root (SNL)

This campaign seeks to determine the structure of platinum (Pt) at high temperatures and pressures. Platinum is of interest because it is often used as a pressure calibration standard in diamond anvil cell experiments due to its low reactivity and wide pressure–temperature stability. Shock-ramp experiments on Sandia's Z machine have suggested evidence of a phase transition occurring at ~150 GPa. The inverse Z method applied to Pt by L. Burakovsky[12] suggests a solid–solid phase transition in a similar pressure region. The goal of this experiment was to use x-ray diffraction (XRD) to study the crystal structure at the pressure regime where a new phase is suggested. A series of measurements was carried out using the powder x-ray diffraction image-plate (PXRDIP) platform on OMEGA EP. The target package consisted of a Be ablator, a 25-μm Al foil, a 7-μm Pt foil sample, and a 130-μm LiF window. The thickness of the Be ablator was varied between shots in order to reach different shock pressures (50 to 200 GPa). Two 10-ns UV beams were combined to create a 20-ns drive that shocked the sample and then ramp compressed to various pressures, up to ~500 GPa. A Ge backlighter foil was driven to create a 1-ns flux of 10.25-keV x rays that were diffracted by the target package and collected on the image plates shown in Fig. 19. The ASBO telescope was focused at the sample/LiF interface and used to infer a pressure history in the Pt.

Six of the seven shots had either three or four solid diffraction lines, consistent with the face-centered cubic (fcc) phase. In the remaining shot, liquid diffraction is believed to have been observed, but blanking in ASBO means the exact pressure is unable to be determined using the usual method. Initial hydrodynamic simulations suggest the Pt was shocked to >800 GPa. This last shot will provide information for an upcoming shot day to determine where Pt melts on the Hugoniot.

Laue Diffraction from Ta Using a Cu Foil Backlighter

Principal Investigator: A. Krygier
Co-investigators: C. E. Wehrenberg and H.-S. Park

The TextureDiff-19A experiment investigated deformation in [100] and [110] single-crystal tantalum at high pressure. Twinning has been found to play an important role in deformation under some conditions in tantalum, and this experiment was motivated to investigate this effect in single-crystal samples. Additionally, previous measurements of diffraction from single-crystal samples have not been able to constrain the *in-situ* density due to the nature of the technique. This experiment developed a new technique to simultaneously measure density and strain anisotropy in single-crystal samples (Fig. 20).

A shock wave was driven into the samples using direct laser ablation. The strength of the material produces strain anisotropy, where the sample is more compressed in the loading direction than the transverse directions. We probed this with white-light x-ray diffraction. Previous measurements of this sort used a capsule implosion to produce the smooth, high-flux, short-duration x-ray

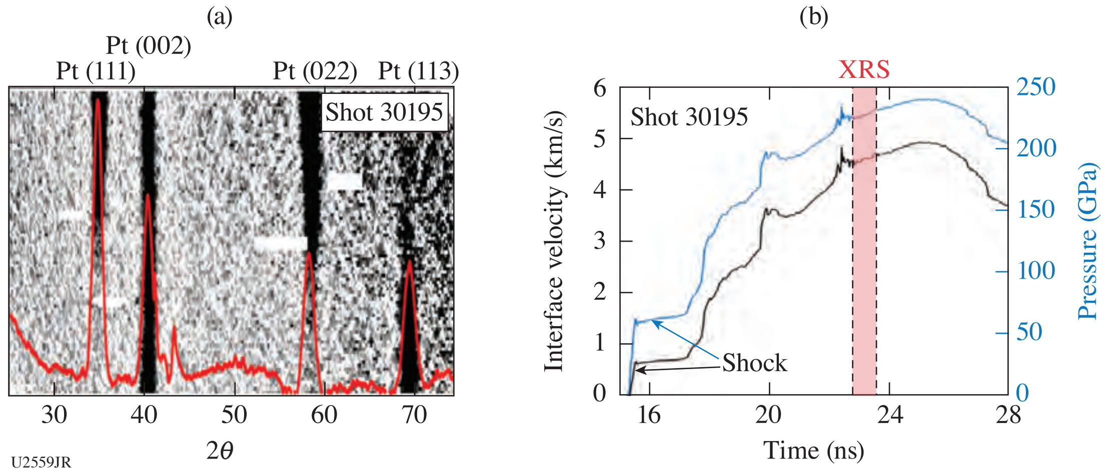

Figure 19
(a) Example diffraction data showing four lines generated by solid Pt in the fcc phase. (b) The sample particle velocity, inferred pressure profile, and timing of the x-ray source (XRS) obtained from VISAR.

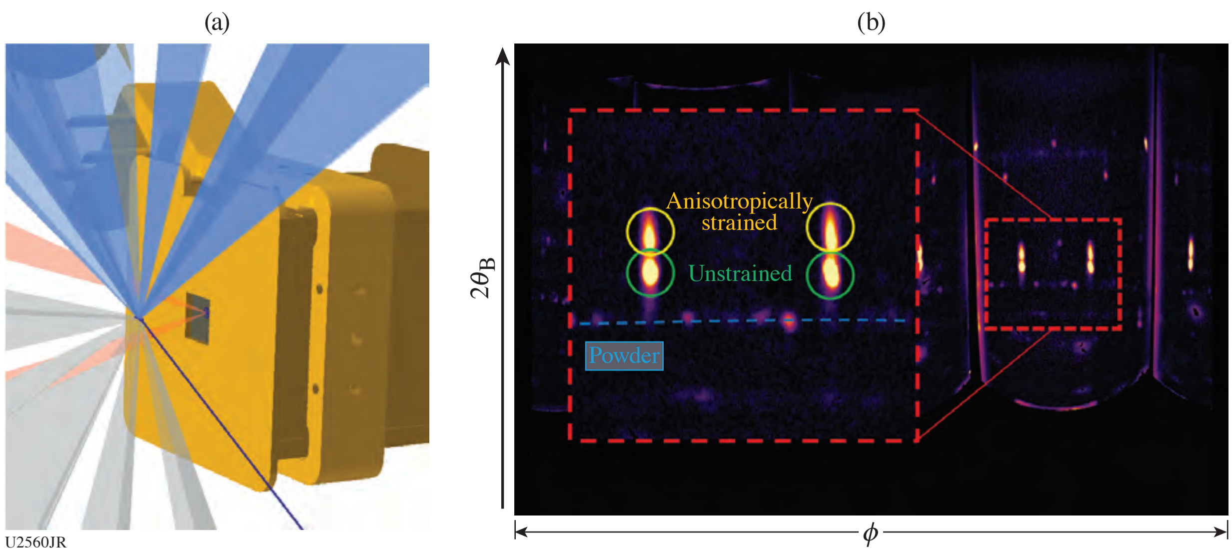

Figure 20
(a) One to two beams drive a shock wave into the Ta sample package. Nineteen beams heat a Cu or Au–Cu foil to produce white-light + He$_\alpha$ x-ray pulse. (b) Example data from [100] Ta. In the inset, green circles show the undriven Laue reflections; yellow circles show the anisotropically strained reflection that arises due to strength at high pressure. The dashed blue line shows powder diffraction from the monochromatic Cu He$_\alpha$.

pulse. We additionally probed the sample velocity using the ASBO diagnostic. We tested using a foil backlighter for this purpose, based on observation of x-ray flux enhancement made by the Extended X-Ray Absorption Fine Structure (EXAFS) Campaign. By using a copper foil backlighter, the x-ray spectrum has both a broad white-light feature useful for measuring strain anisotropy with Laue diffraction, as well as quasi-monochromatic He$_\alpha$ emission that is used to measure density with powder diffraction from polycrystalline samples and geometrically allowed single-crystal reflections. We also tested Au–Cu foils to compare bremsstrahlung emission but found this dramatically increased unwanted probe heating to the sample. This capability has the added bonus of enabling the use of PXRDIP instead of BBXRD, which improves the quality of the diffraction due to the geometry.

Probing the High-Pressure Crystal Structure of Lithium Fluoride
Principal Investigator: M. Gorman
Co-investigators: R. Smith and C. E. Wehrenberg

These experiments explored the high-pressure phase diagram of lithium fluoride. A structural transformation from the B1 phase to the B2 phase has been predicted.[13] Observing this transition may explain why nonlinear corrections to the refractive index of LiF are required in ramp-compression experiments on the NIF.[14] The target design is shown in Fig. 21(a). A 50-μm polycrystalline LiF sample was sandwiched between a 40-μm diamond ablator and a 100-μm MgO window. The OMEGA VISAR (ASBO) measures the LiF/MgO particle velocity from which the sample pressure as a function of time can be determined[15] as shown in Fig. 21(b). In these experiments we combine nanosecond x-ray diffraction[15] and ramp compression to dynamically compress and determine the crystal structure of LiF to peak pressures up to 600 GPa. Using the OMEGA PXRDIP diagnostic,[15] the compressed LiF sample is probed with a 2-ns He$_\alpha$ x-ray source to determine crystal structure at a well-defined sample pressure (VISAR). An example of the quality of the data obtained is shown in Fig. 21(c). Here we obtain information on the high-pressure B1 phase of LiF. Also observed are peaks from the ambient pressure Ta pinhole, which serve to calibrate diffraction angle. We find that LiF remains in the B1 phase up to at least 600 GPa along a quasi isentrope.

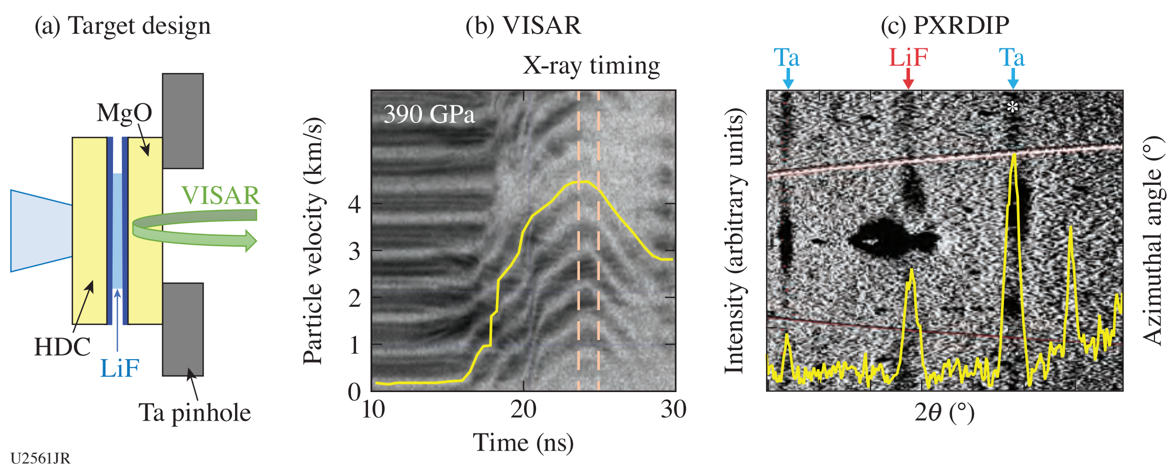

Figure 21
(a) Typical target design with a 40-μm diamond ablator, a 50-μm polycrystalline LiF sample, and a 100-μm single-crystal MgO window. (b) Raw VISAR fringe data with analyzed velocity profile overlaid. (c) De-warped PXRDIP diffraction data with 1-D lineout overlaid. The profile shows diffraction from the B1 phase of LiF at 390 GPa.

Development of a Time-Resolved X-Ray Diffraction Platform on OMEGA EP
Principal Investigator: L. R. Benedetti
Co-investigators: F. Coppari (LLNL); and D. N. Polsin, J. R. Rygg, and C. Sorce (LLE)

Based on the work performed in 2018, in which we learned that there was substantial electromagnetic pulse upset caused by the proximity of the large PXRDIP box to the x-ray streak camera, we completely redesigned the OMEGA EP time-resolved diffraction test platform. In the new platform [Fig. 22(a)], we removed the PXRDIP box (and associated image plates) and replaced it with a baffle/shield that prevents light from the backlighter from directly hitting any diagnostic. We are now also testing an XRFC for imaged diffraction (in addition to the x-ray streak camera) because the XRFC may be better shielded than the x-ray streak camera. As with the x-ray streak camera, dedicated hardware is required to maneuver the XRFC to an appropriate location to collect diffraction.

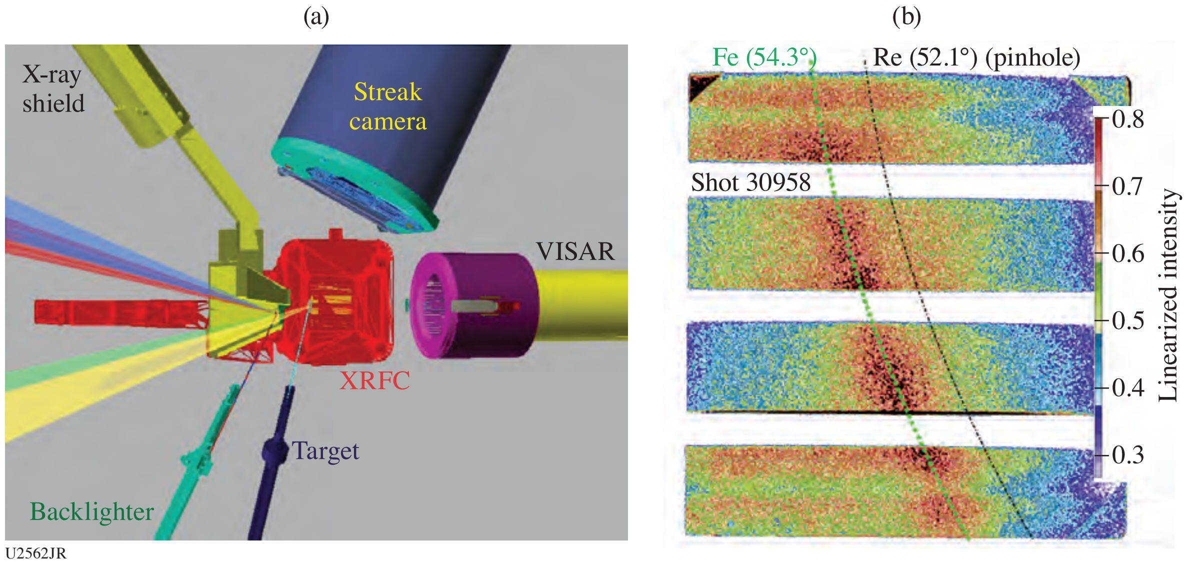

Figure 22
Imaged x-ray diffraction on OMEGA EP. (a) Updated experimental setup that maximizes distance between shielding elements and SSCA. (b) X-ray diffraction to XRFC of undriven Fe. Calculated diffraction is shown as an overlay.

We used this experimental setup on two shot days in FY19, during which we collected two diffraction patterns of undriven iron onto the XRFC [Fig. 22(b)]. Ongoing challenges are alignment accuracy, photometrics, and still-unexplained background signals along the streak camera's line of sight.

New Approach to Pressure Determination in Diffraction Experiments Using an* In-Situ *Pressure Standard
Principal Investigator: F. Coppari
Co-investigators: J. H. Eggert and R. Kraus (LLNL); and M. Vasquez (CalPoly, summer student at LLNL)

The goal of the *In-Situ* Pressure Campaign is to develop a new way to determine pressure in diffraction experiments based on the use of an *in-situ* pressure gauge. By measuring the diffraction signal of a standard material (whose pressure–volume equation of state is known) compressed together with the sample, one can determine the pressure upon ramp compression from the volume determined from the measured diffraction pattern.

Currently the pressure is determined by measuring the diamond free-surface velocity or particle velocity through a transparent window (such as LiF) using VISAR. This method is in some cases ambiguous (lack of reflectivity or shock formation) or relies on assumptions and equation-of-state models for the window materials. Cross-checking the VISAR measurement with *in-situ* pressure determination using the diffraction signal of a standard material will improve the diffraction platform by providing a complementary way of determining the pressure state within the sample, with great impact to the programmatic effort of determining structures and phase transitions at high pressure and temperature. In addition, combining pressure determination from VISAR and from the *in-situ* gauge can give us information about the temperature of the sample by measuring the calibrant thermal expansion.

We collected 12 successful shots in two half-days on the OMEGA laser, where we continued the work started in the previous FY, pushing it to higher pressure. The targets consisted of diamond ablators, Au/Ta or Pt/W coatings as *in-situ* pressure standards, and a diamond or LiF window [Fig. 23(a)]. We reached pressures as high as ~600 GPa and collected very good quality diffraction data (12 shots) in two half-days [Fig. 23(b)]. Simultaneous VISAR data were also collected. Data analysis is being finalized and comparison of the pressures obtained from VISAR and diffraction will provide information on the accuracy of the VISAR method as well as the existence of preheating. If successful, this platform will be implemented into a real diffraction experiment to be used as either a complementary or an alternative way to determine pressure and will also be developed on other experimental facilities such as NIF, XFEL, and synchrotrons.

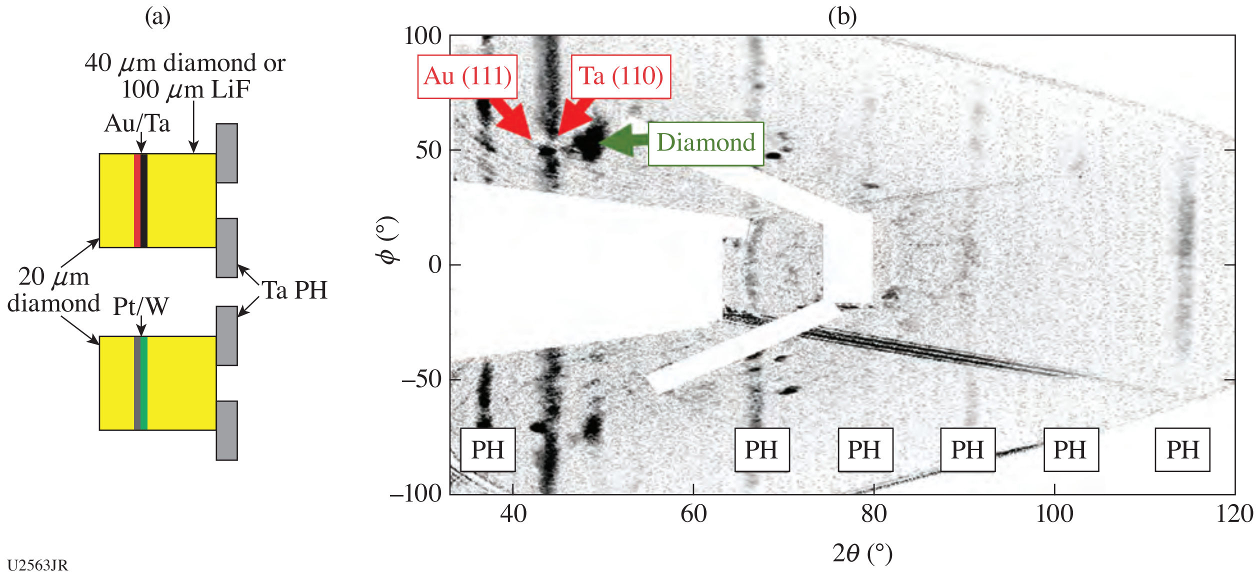

Figure 23
(a) Schematic of the target assembly. Diamond or LiF windows were coated with 1-μm-thick Au/Ta or Pt/W pairs used as pressure standards in the diffraction experiment. All targets had a 20-μm diamond ablator and were mounted on Ta pinholes. (b) Diffraction data collected in one of the experiments using Au/Ta as standards. At least one peak from compressed Au or Ta is visible, as well as lines from the Ta pinhole (PH) used to calibrate the diffraction geometry and single-crystal Laue spots due to the diamond. Cu He$_\alpha$ radiation (~8.4 keV) was used to obtain the diffraction data.

Development of the New Forward/Backward X-Ray Diffraction Diagnostic
Principal Investigator: A Krygier
Co-investigators: C. E. Wehrenberg, H.-S. Park, and J. H. Eggert (LLNL)

This experiment was the first effort at development of the new forward/backward x-ray diffraction diagnostic (Fig. 24). By using two monochromatic x-ray sources, we will be able to constrain the *in-situ* strain anisotropy induced by material strength in a polycrystalline sample. In this experiment we tested several design features: First, we measured the first reflection diffraction on OMEGA using a floating Fe microfoil with no pinhole. Second, we optimized the reflection x-ray cone shield, finding that a larger cone performed significantly better, with low background. Third, we tested a U-6 wt% Nb sample pinhole used in transmission

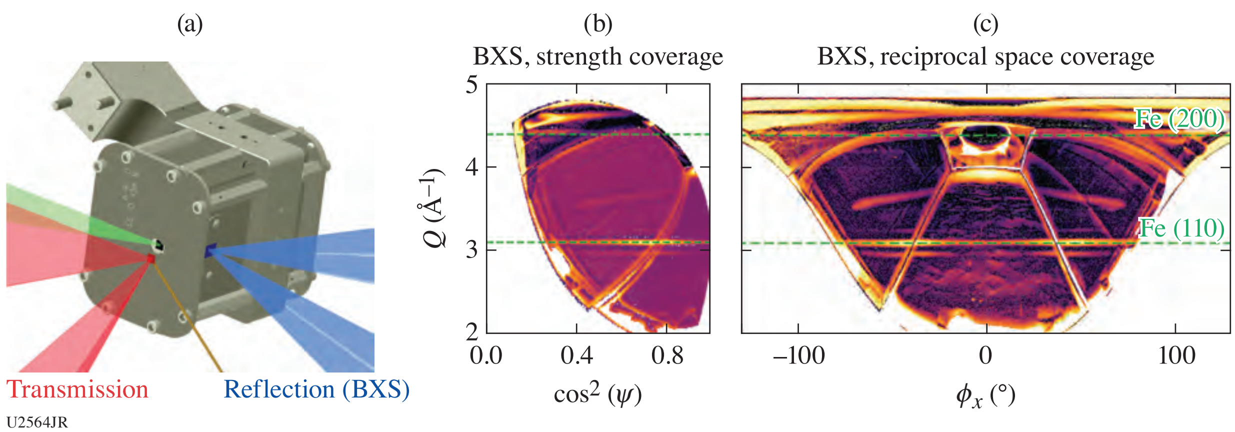

Figure 24
(a) Experimental setup. (b) Reflection diffraction from undriven Fe, displayed versus cos$^2\psi$, the important parameter for strength; ψ is the angle between the diffracting plane and the applied stress. (c) The same data projected in reciprocal lattice–azimuthal coordinates. Extra reflections are from multiple emission lines from the Ti backlighter. An extraneous signal is also seen between the [110] and [200] Fe reflections.

diffraction on the NIF, finding that it produces unwanted x-ray diffraction in the reflection geometry. Finally, we confirmed high-quality diffraction in the transmission configuration with the extra features required for reflection diffraction (shield cone, etc.).

2. Material Equation of State Using Other Techniques

Equation-of-State Measurements Using Laser-Driven Mo Flyer-Plate Impacts
Principal Investigator: F. Coppari
Co-investigators: R. London, P. M. Celliers, M. Millot, A. Lazicki, and J. H. Eggert

The goal of the campaign is to develop a platform for absolute EOS measurements by laser-accelerated symmetric flyer-plate impacts.

The conceptual design is to use ramp compression to accelerate a molybdenum (Mo) flyer across a vacuum gap through indirect laser ablation and observe the flyer impact on a same-material sample, mounted side-by-side to a quartz window [Fig. 25(b)]. Velocity interferometry measurements with VISAR allow us to measure the flyer acceleration (U_{fs}) through the transparent quartz window, providing a measure of U_{p_impact} (for a symmetric impact: $U_{p\_impact} = 0.5 * U_{fs\_impact}$). The resulting shock state in the Mo sample is determined via transit time by measuring the time difference between the impact (t_{Mo_impact}) and the shock breakout (t_{Mo_BO}). The shock velocity U_s is then determined from $U_s = T_{Mo} / (t_{Mo\_BO} - t_{Mo\_impact})$, where T_{Mo} is the accurately measured thickness of the Mo sample. Using the Rankine–Hugoniot equations, one can then determine pressure and density of Mo *absolutely* (e.g., without needing a known pressure reference), enabling one to develop an EOS standard.

This platform will be extremely useful to all programmatic activities interested in EOS and Hugoniot measurements at pressures of tens of Mbar, where currently there are no materials whose EOS has been experimentally determined.

This campaign built upon the results obtained in the past fiscal years. Very good quality data [Fig. 25(b)] were obtained in all 14 shots, also thanks to improvements in the target fabrication procedure that allowed us to obtain many planar targets and therefore more-accurate measurements of the shock velocity.

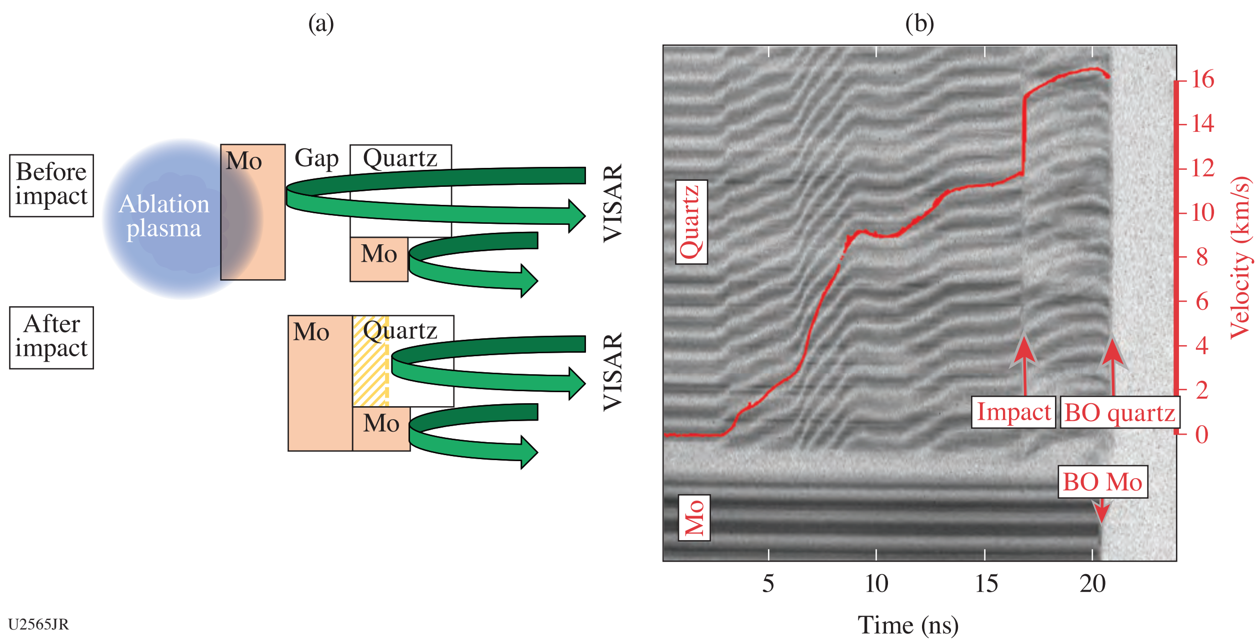

Figure 25
(a) Schematic representation of the experimental setup. A Mo foil is accelerated across a vacuum gap and impacted on a transparent quartz window, mounted side-by-side to a Mo foil. The simultaneous measurement of the flyer velocity and shock velocity upon impact with VISAR gives a measurement of the Mo EOS, without the need to rely on the EOS of a reference material. (b) Representative VISAR record. The main events are indicated by arrows.

The Mo EOS was explored up to U_s =16 km/s corresponding to about 12 Mbar. In-depth data analysis will allow us to determine if this platform represents a viable path toward absolute EOS measurements.

Developing a Conically Convergent Platform for Measuring Hugoniot Equation of State in the 100-Mbar to Gbar Pressure Regime
Principal Investigator: A. E. Lazicki
Co-investigators: F. Coppari, D. Swift, R. London, D. Erskine, H. Whitley, and J. Nilsen

This campaign was designed to develop a platform for measuring Hugoniot EOS of arbitrary (including high-*Z*) materials at pressures much higher than can be achieved using a standard planar drive. This platform is intended to collect data in the >100-Mbar pressure regime, where currently very little data exist for any material, for the purpose of constraining EOS models. To achieve the desired pressure amplification, we launched converging shock waves into a plastic cone inset in a halfraum. For appropriate cone angles, nonlinear reflections of the shock wave result in the formation of a Mach stem: a planar high-pressure shock that propagates along the axis of the cone.

Previous OMEGA shot days from FY16–FY19 tested design concepts in preparation for shots on the NIF. We have not previously been able to generate a Mach wave on OMEGA with sufficient steadiness, planarity, and surface area to perform an EOS measurement of sufficient accuracy because of limitations in pulse energy and length, but we have successfully tested the effects of a wide range of optimization concepts, including cone material, height and angle, hohlraum size and gas fill, laser pulse length and energy, and various schemes for heat shielding.

The shots in FY19 (3 half-days for a total of 20 shots) were specifically aimed toward testing a new scale of hohlraum (0.85-mm length, 1.15-mm diameter) midway between the standard, larger-scale EOS hohlraum (1×1.3 mm), which produced insufficiently supported Mach waves, and a smaller scale (0.7×1 mm) tested in FY18, which resulted in supported Mach waves but with insufficient surface area, and very high levels of hard x-ray preheat, presumably from hohlraum laser–plasma instability (LPI). We also tested a new concept for constraining target preheat levels by measuring time-resolved x-ray fluorescence, pumped by the hohlraum radiation, from a thin layer of Cu placed in contact with the physics package.

The mid-scale hohlraum produced Mach waves with a slightly reduced area compared to the large-scale hohlraum, but they were better supported, steadier, and more planar. We generated pressures up to ~180 Mbar in an Au stepped target, over an ~170-μm planar area (Fig. 26). We also tested the effects of changing Mach cone angle in the mid-scale hohlraum and can clearly

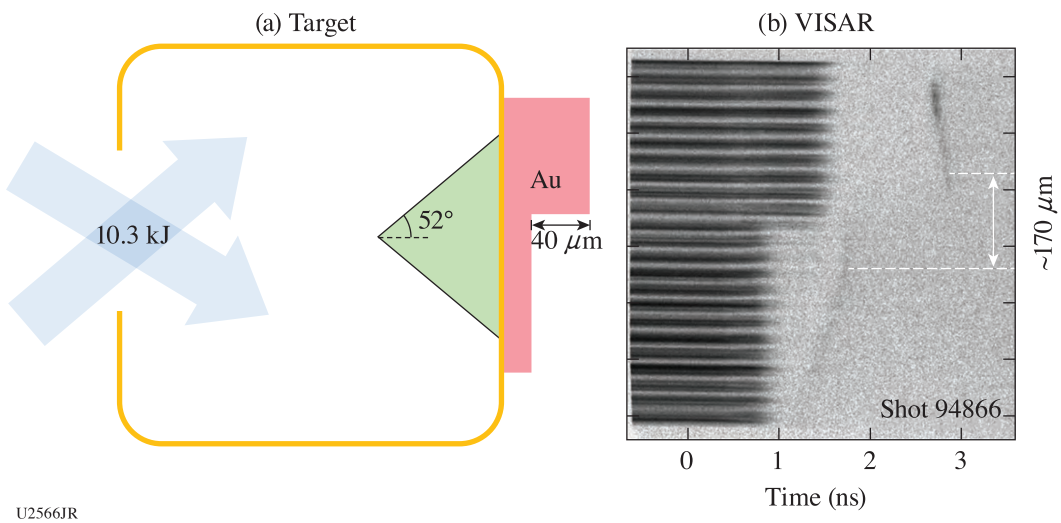

Figure 26
Mach wave generated in a CH cone and propagated through an Au stepped target. Average shock speeds of ~36.4 km/s were achieved in the Au. The VISAR reflectivity is lost about 1 ns before the shock wave breaks out, indicating that the free surface of Au melted. Shock-wave breakout is indicated by a flash of light from thermal emission.

confirm a predicted trend toward higher Mach wave pressure and smaller area with decreasing cone angle. Because of the large columnar volume of very high pressure material generated in a Mach cone, on shot days 19A and 19B we tested the Mach cone as a neutron generator by making the cones out of deuterated plastic. We generated up to ~2×10^8 D–D yield with a pure CD cone and an order of magnitude lower when a CH ablator was deposited on the CD cone.

Liquid–Ice VII Phase-Transition Kinetics in Ramp-Compressed Water
Principal Investigator: M. C. Marshall
Co-investigators: M. Millot, D. E. Fratanduono, and R. F. Smith

RampWaterEP-19A studied the liquid–ice VII phase transition in ramp-compressed water at ultrahigh strain rates ($>10^6$ s^{-1}). The principal isentrope of water crosses the liquid–ice VII equilibrium phase boundary at ~2.5 GPa; however, ramp-compression experiments at the Sandia Z machine observed the phase transition at 7 GPa (Ref. 16). We are testing the metastability limit of liquid water by ramp compressing over ~10× higher compression rates than the Z experiments.

We completed one day on OMEGA EP with a total of 13 target shots. A shocked CH reservoir released across a vacuum gap and isentropically loaded the water cell shown in Fig. 27(a). A thin water layer (~15 μm), created using a sapphire diving board inside the water cell, was ramp compressed to ~15 GPa. The experiments were designed to observe two signatures of the phase transition using VISAR: The first was a stress release on the rear sapphire window of the thin water layer caused by volume collapse during the transition (ice VII is 60% more dense than liquid water). The second was a coincident dip in transmission through the water layer from optical scattering of the coexisting liquid and ice phases with different refractive indices.

Preliminary analysis suggests that freezing occurred in several shots at pressures ranging from 7 to 9 GPa. An example of the stress-release signature of freezing is shown in Fig. 27(b). No clear evidence for transient opacity has been identified. Analysis is ongoing, and a follow-up campaign that uses a variety of windows (sapphire, quartz, and PMMA) on the thin water layer is scheduled on OMEGA EP in FY20. Data will be compared to predictions using SAMSA, an LLNL kinetics code.

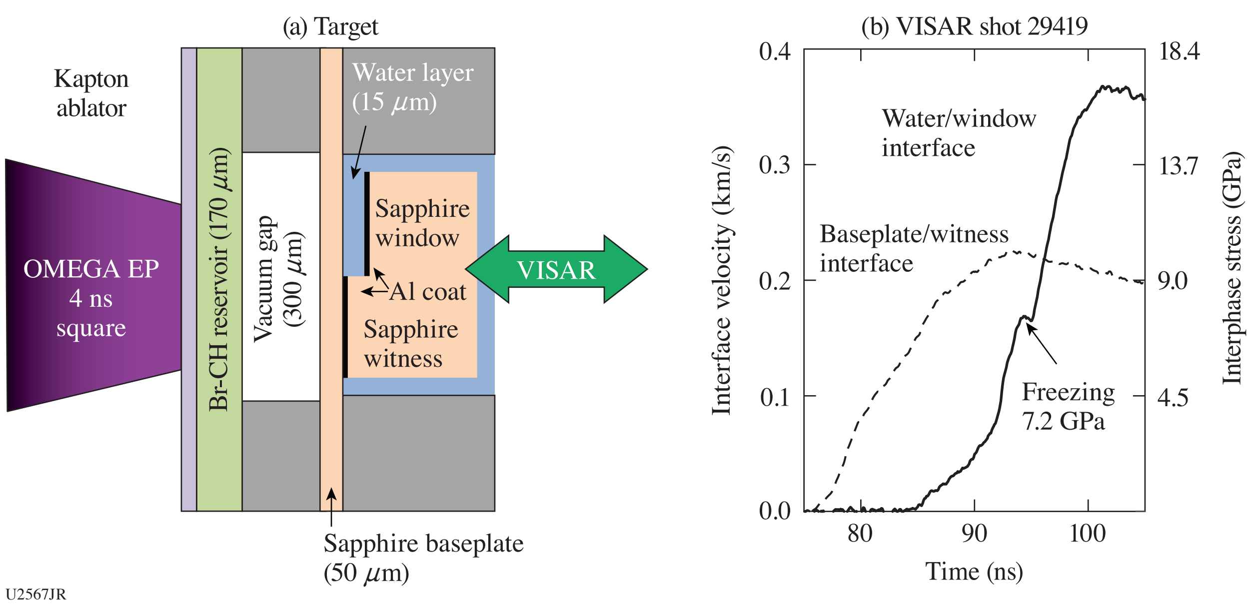

Figure 27
(a) Target design for a stress-release measurement and (b) interface velocity and stress as determined from VISAR. The velocity of the baseplate/Al/witness interface (dashed curve) provided a drive measurement for each target shot. The stress release on the water/Al/window is indicative of freezing (solid curve).

EXAFS Measurements Using Foil Backlighters and a Focusing Spectrometer
Principal Investigator: Y. Ping
Co-investigators: F. Coppari, A. Krygier, J. McNaney, and J. H. Eggert

In previous OMEGA shots, we discovered that foil backlighters are brighter than the implosion backlighter at x-ray energies >10 keV. This series of shots demonstrated the feasibility of EXAFS measurements using foil backlighters and a focusing spectrometer, and the results supported the associated NIF design.

The experimental setup is shown in Fig. 28. The foil backlighter (Ti, Ag, or Au) was irradiated by ~20 beams marked as green and pink in Fig. 28. The main target was a Fe foil sandwiched between diamond plates, mounted in a 3-D–printed plastic enclosure with a VISAR mirror and shield. For high-pressure shots, the Fe package was driven by five beams (blue) stacked in time to simulate a ramp drive. The focusing spectrometer was an imaging x-ray Thomson spectrometer (IXTS) with a toroidal crystal for 1-D spatially resolved x-ray spectra in Johann geometry, where the resolution is insensitive to the x-ray source size.

The Fe EXAFS spectrum was observed as shown in Fig. 29(a). The resolution was lower than expected due to an unexpected error in the radius of curvature of the toroidal crystal. In FY20 the position of the detector inside the IXTS will be adjusted to

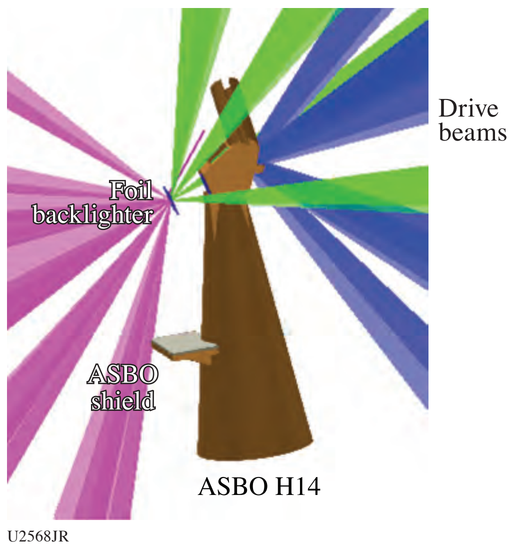

Figure 28
Experimental configuration.

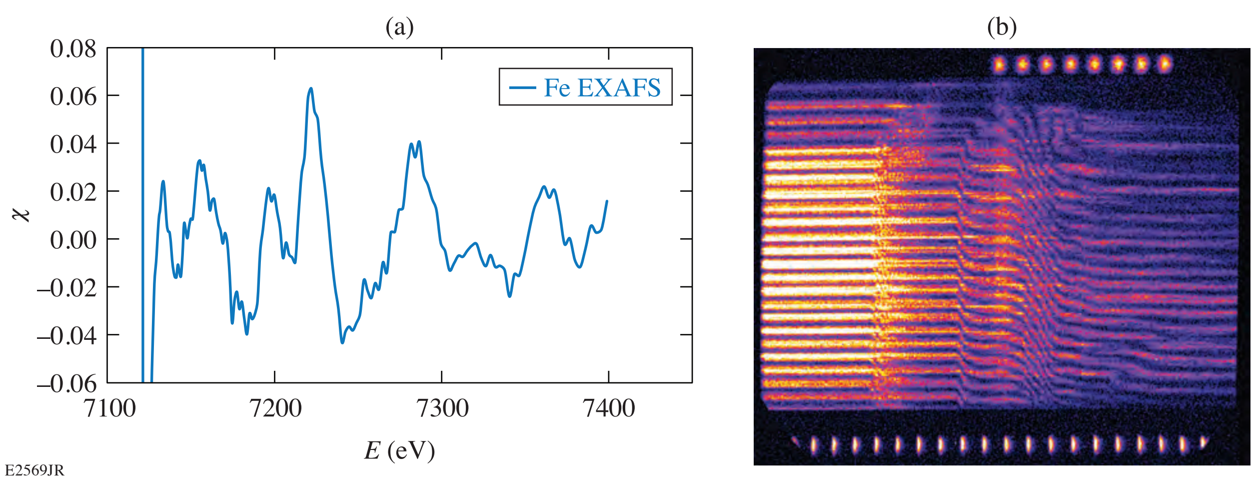

Figure 29
(a) Fe EXAFS spectrum from the IXTS with a Ti foil backlighter and (b) VISAR data for an ~5-Mbar drive.

match the actual radius of the crystal to improve the resolution. VISAR measurements were also demonstrated for the first time simultaneously with EXAFS measurements on OMEGA by adding a shield to block the direct line of sight from the backlighter to the ASBO lens as shown in Fig. 28. A typical VISAR raw image is displayed in Fig. 29(b). In comparison to prior implosion backlighters, foil backlighters require fewer laser beams and produce more photons above 10 keV. The new focusing geometry provides much higher signals on the image plate detector, providing a promising platform for x-ray absorption spectroscopy measurements.

Backlighter Development for EXAFS Measurements at High Energy on the OMEGA Laser
Principal Investigator: F. Coppari
Co-investigators: A. Do, Y. Ping, A. Krygier, and J. McNaney

EXAFS measurements require a bright, smooth, broadband x-ray source. X-ray radiation emitted by a capsule implosion meets these requirements and is currently used in laser-based EXAFS experiments. The x-ray emission decays quickly, however, at higher energies, making EXAFS measurements above 10 keV very challenging. For high-quality, higher-energy EXAFS measurements, there is a need for different x-ray sources. The bremsstrahlung radiation emitted by laser-irradiated higher-Z materials has the potential to be successfully used as such an x-ray source, provided the loss of spectral resolution in the measured EXAFS spectra due to source size effects can be mitigated. This can be accomplished by either collimating the x rays using a slit (although this will also reduce the total flux) or using a focusing spectrometer to measure the EXAFS signal.

During our two half-day campaigns we collected a total of 14 shots where we looked at different backlighter materials [Ti, Ag (including Ag foams), Au, Ge], varied the laser-drive conditions, and characterized the spectra in a wide energy range using combinations of different spectrometers (the flat x-ray Rowland spectrometer[17] and the dual-crystal spectrometer[18]).

We found that (1) the brightest spectra were measured for laser irradiance of the order of 10^{17} W/cm^2 and (2) Ti emits the brightest spectrum in the energy range below 25 keV, after which Au becomes brighter. Ti represents, therefore, a promising choice as a backlighter for EXAFS measurements at energies higher than 10 keV, where its spectrum is smooth and free from line emissions (see Fig. 30). A combination of a Ti foil backlighter and a focusing spectrometer is expected to significantly improve the EXAFS platform on the OMEGA laser and represents the point design for the development of the EXAFS diagnostic on the NIF. This configuration will be tested further during the next fiscal year on OMEGA.

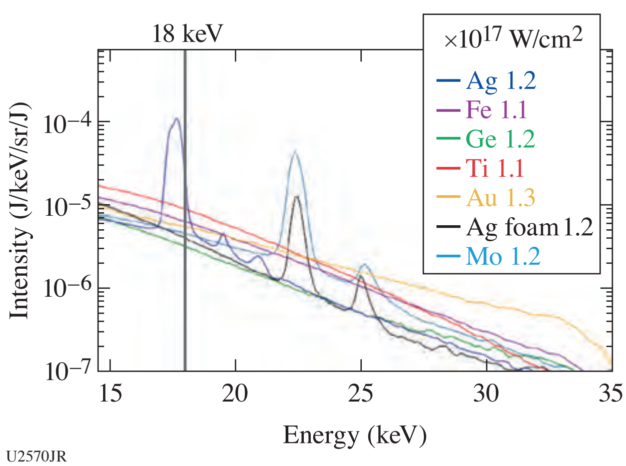

Figure 30
Spectra measured with the dual-channel spectrometer (DCS) for the backlighter materials studied in this campaign (also including data obtained on Ag and Mo in 2016) for laser irradiation of the order of 10^{17} W/cm^2. Our data clearly show that Ti is brighter than any other material looked at in this study for energies below 25 keV.

Isentrope Measurements of Isochorically Heated Materials
Principal Investigator: A. Saunders
Co-investigators: Y. Ping, A. Jenei, H. Whitley, J. Nilsen, and J. H. Eggert (LLNL); and M. Hill (AWE)

The aim of this new series of shots is to measure the release isentrope of heated materials. The isochoric heating was achieved by fast proton beams generated by high-intensity short laser pulses as illustrated by Fig. 31. The primary diagnostics are streaked

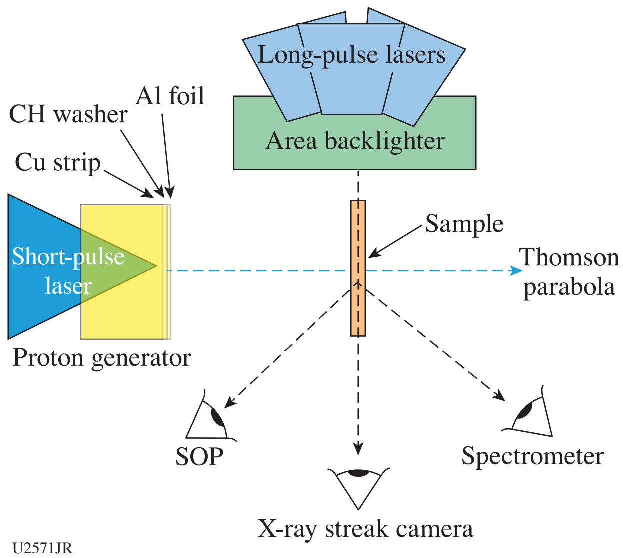

Figure 31
Experimental configuration.

x-ray radiography for time-resolved density profiles and SOP for initial temperature after the fast heating. The pressure is obtained from the density measurements using an analytical method developed by Foord *et al.*[19] The target was a 50-μm-sq ribbon of diamond, CH, or Al to allow radiography and SOP along two orthogonal axes. Other diagnostics, such as Thomson parabola and soft x-ray spectrometer VSG, were also fielded to provide the energy spectra of the proton beam and x-ray fluorescence spectra of the heated sample.

High-quality data have been obtained from both primary diagnostics as shown in Fig. 32. The x-ray radiograph clearly shows the expansion of the target. The SOP shows that there is some preheat by the x-ray backlighter, which was reduced in the second shot day by increasing the distance between the backlighter and the sample. Detailed data analysis is underway, and a paper on this new platform has been written for submission to Review of Scientific Instruments. Figure 32(c) shows two isentropes from two different EOS's: L130 and *SESAME* 3718 for Al at 2 eV. The large discrepancy between the two models, especially at lower densities, indicates a strong need of experimental data in this warm-dense-matter regime.

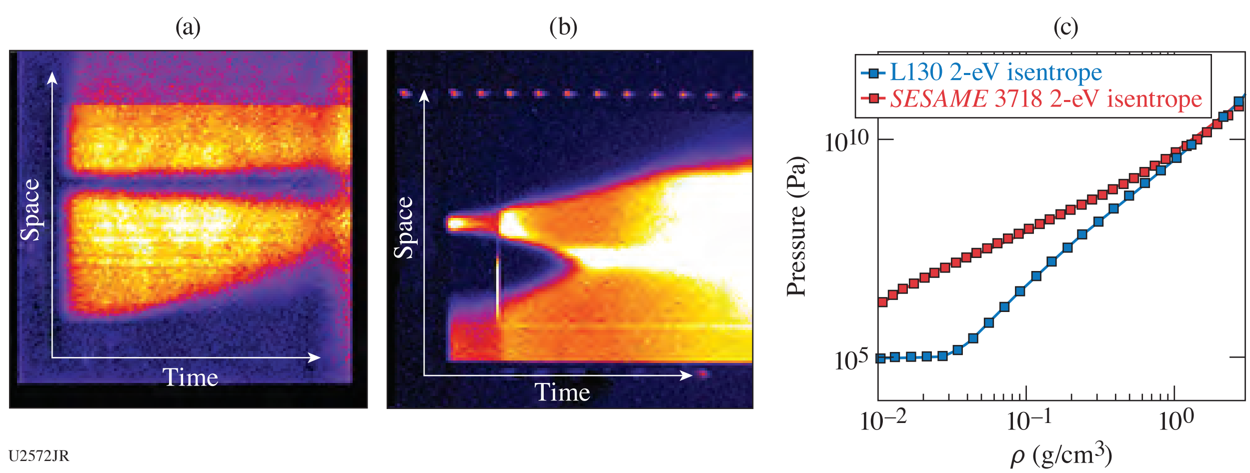

Figure 32
Streaked x-ray radiograph for (a) Al, (b) a SOP image, and (c) two isentropes from two EOS models: L130 and *SESAME* 3718 for Al heated to 2 eV.

Measurements of the Single-Crystal TATB Hugoniot to 80 GPa
Principal Investigator: A. Fernandez Pañella
Co-investigators: M. Marshall,* T. Myers, J. H. Eggert, T. Bunt, L. Lauderbach, and L. D. Leininger
*Postdoc

The purpose of the HEEOSEP-19A Campaign was to complete the Hugoniot measurements (initiated in FY18) of TATB (triamino-trinitrobenzene) shocked to a high pressure. TATB is a high explosive known for its insensitivity to high temperatures and impacts. Experiments were done on the OMEGA EP laser, where TATB was shocked to a range of pressures (15 to 80 GPa) over eight shots, filling up the gaps from the previous campaign. Hugoniot data were obtained by impedance matching relative to an aluminum standard. Planar targets had a Kapton ablator, aluminum base plate (standard), single-crystal TATB sample, and LiF witness used to correct for shock unsteadiness. Two laser beams with total energies of 580 to 2300 J were stacked in time, producing a 20-ns drive to support a nearly steady shock in the TATB. VISAR was used to measure interface velocities and shock transit times needed for the impedance-matching analysis. These results have been used to complete the single-crystal Hugoniot measurements of TATB (shown in Fig. 33). A manuscript has been written about these two campaigns.

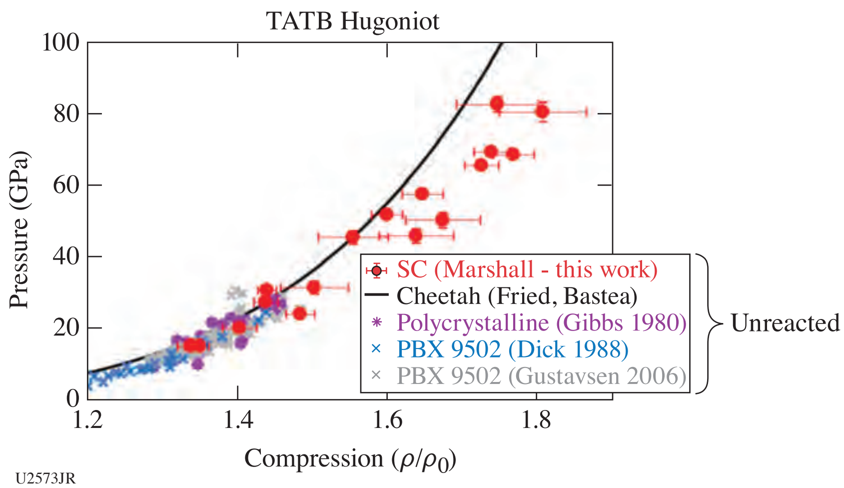

Figure 33
Single-crystal TATB Hugoniot. Pressure versus compression in a pressure range from 15 to 80 GPa covering unreacted and overdriven states.

Phase Transformations and Chemical Reaction in Shock-Compressed TATB
Principal Investigator: M. C. Marshall
Co-investigators: A. Fernandez Pañella, M. G. Gorman,* T. Myers, B. Yancey, J. H. Eggert, and L. D. Leininger (LLNL); and D. N. Polsin (LLE)
*Postdoc

The purpose of the HEXRDEP-19A campaign was to measure phase transformations and chemical reaction products in shocked TATB (triamino-trinitrobenzene) using x-ray diffraction. TATB ($C_6H_6N_6O_6$) is an insensitive high explosive that chemically reacts into inert gases and solid carbon species.

Experiments were done on the OMEGA EP laser, where TATB was shocked to pressures ranging 10 to 90 GPa over eight shots. The planar targets had an epoxy ablator, single-crystal TATB sample, and a Ti-coated LiF window mounted on a tungsten pinhole. Two laser beams with total energies of 190 to 1090 J were stacked in time, producing a 20-ns drive to support a nearly steady shock in the TATB. The two remaining beams were incident on a Fe backlighter foil, producing He$_\alpha$ emission to probe the crystal structure of the shocked TATB. X-ray diffraction data were obtained using the PXRDIP diagnostic, and VISAR was used to measure the TATB/LiF interface velocities needed to determine the shocked TATB pressure.

Initial results indicate that the TATB single crystals remain highly textured solids to ~40 to 50 GPa. A change in the x-ray diffraction pattern is observed when TATB is shocked over ~55 GPa. A new powder line, consistent with diffraction from the

(111) plane of diamond, is observed at 90 GPa (Fig. 34). Analysis is ongoing and a follow-up shot day using higher-energy Cu backlighters is scheduled for FY20. Data will be used to improve predictive modeling of chemical reactions in TATB-based explosives.

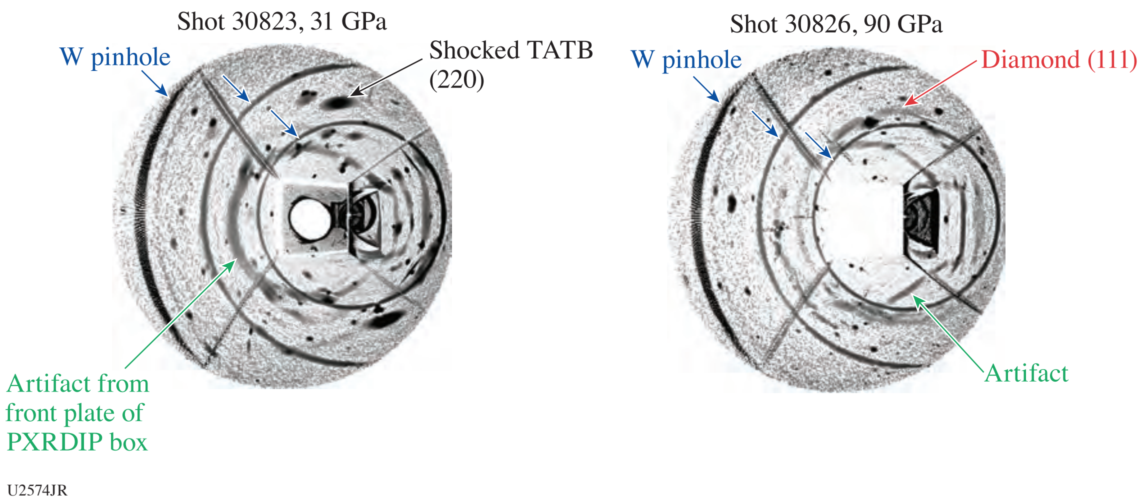

Figure 34
Stereographic projections of PXRDIP data for two shots.

3. Material Dynamics, Strength, and Ejecta Physics

Strength Experiments Using Direct-Drive Rayleigh–Taylor (DDRT) Growth Rates
Principal Investigator: A. Zylstra
Co-investigators: H.-S. Park, C. Stan,* D. Swift, T. Lockard, and J. McNaney (LLNL); and M. Hill and P. Graham (AWE)
*Postdoc

This campaign consisted of two OMEGA EP shot days with a total of 11 shots. The goal of this campaign is to measure the growth of pre-imposed ripples at a Rayleigh–Taylor (RT) unstable interface on a material sample of interest. Since the material strength will suppress the RT growth rate, strength in the HED regime can be inferred from the measured growth rate.

New in FY19 is the use of a direct-drive configuration on OMEGA EP, unlike previous indirect-drive strength experiments performed on OMEGA[20] or the NIF. The major advantages of a direct-drive platform are twofold: first, the pressure history on the sample can be changed by modifying the pulse shape, unlike the indirect-drive technique, which requires modifications to the target (through the "reservoir"); second, a direct inference of the growth rate can be performed by comparing the rippled sample in both driven and undriven regions.

The experimental configuration is shown in Fig. 35. Three long-pulse UV beams (2, 3, and 4) with 1.8-mm phase plates are used to drive the physics package. The beams are staggered in time to create a 30-ns drive using individualized and stitched pulse shapes to compress the sample to ~1 Mbar. The physics package is placed 14 mm toward TIM-12, which holds the primary diagnostics. For the RT growth measurements, the sidelighter beam shoots a microflag or microwire target placed 5 mm away from TCC to create a high-energy x-ray point-projection backlighter. The sidelighter uses 1000 J of energy in a 100-ps pulse. This campaign starts out using VISAR as the primary diagnostic to measure the shock propagation through a surrogate physics package, which characterizes the drive and sample conditions; then the diagnostic is switched to the LLNL Laue diffraction imager for radiography.

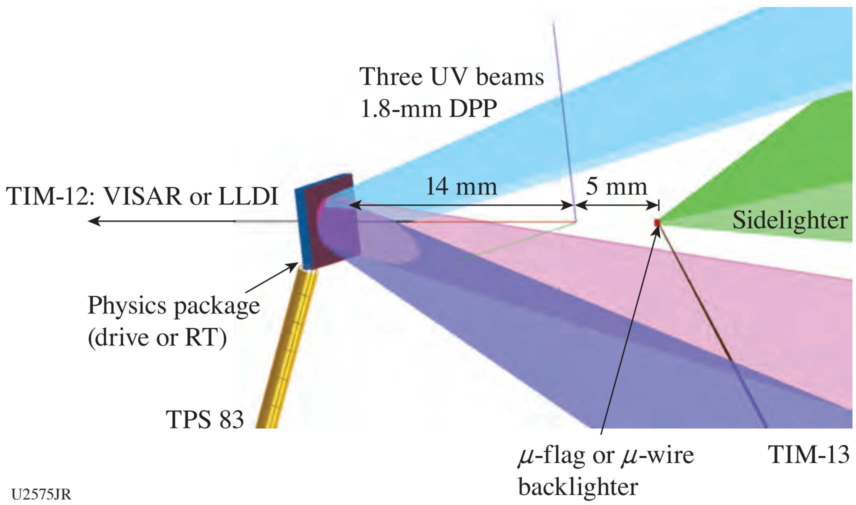

Figure 35
Experimental configuration.

The first shot day, DDRT used tantalum as the material to enable comparison to Ref. 20 and develop the platform. Excellent radiography data were obtained; the results are being interpreted and prepared for publication. Sample radiographs are shown in Fig. 36. Initial indications are that the new analysis method enabled by the direct-drive platform can substantially reduce the uncertainties associated with the strength growth factor measurements. On the second day, the material was switched to tin. An example radiograph is also shown in Fig. 36. Measuring the strength of tin at HED conditions will provide data needed for a tri-lab project on material strength. Good data were obtained early in time; at the latest sample times, the data appear compromised by instability growth at a Au/Re preheat shield layer between the ablator and the tin sample. Data analysis is still in progress, and the platform will be adapted for improved measurements in FY20 toward meeting the tri-lab goals.

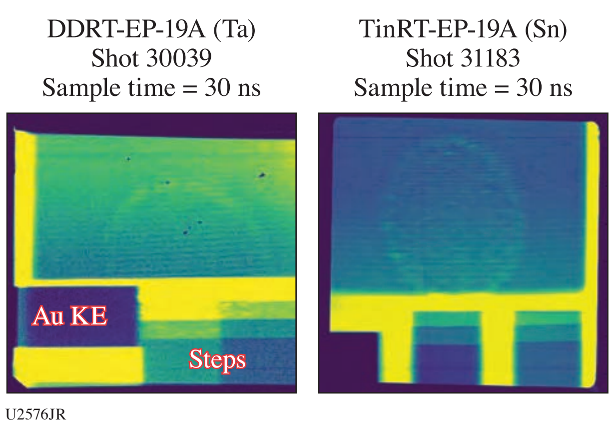

Figure 36
Raw radiographs from each shot day; the growth factor analysis and interpretation is in progress.

Spall and Recollection in Ramp-Compressed Tin

Principal Investigator: S. J. Ali

Co-investigators: A. Saunders, H.-S. Park, J. H. Eggert, A. Fernandez Pañella, F. Najjar, T. Haxhimali, B. Morgan, Y. Ping, and C. Huntington (LLNL); and H. G. Rinderknecht (LLE)

In dynamically compressed materials undergoing ductile failure, the formation and coalescence of voids due to high-rate tensile stress induce spallation—the formation of one or more 2-D sheets that detach from the bulk material. Eventually, the material behind the sheets may catch up and recollection can occur, potentially resulting in the closure of the voids or fractures and, depending on the mechanical response of the material, healing of the surface. The formation and recollection of spall layers is a leading hypothesis to explain the origin of spatially heterogenous reflectivity loss and recovery observed in-line VISAR results for free-surface dynamic compression experiments. In ramp-compression experiments on polycrystalline tin on the NIF with small initial shock, this reflectivity loss and late-time recovery are observed in free-surface experiments where the initial shock is below the bct to bcc phase transition, as shown in Fig. 37, but no longer observed when the initial shock is higher. This suggests that the reflectivity loss is due to damage and breakup of the surface during spallation, and that the subsequent impact of either additional spall layers or the bulk, as indicated by the observed acceleration of the material, contributes to the healing or repair of the observed surface. To determine the microphysical nature of the damage, it is necessary to resolve both the spatial distribution of the ejected material fragments and their velocities.

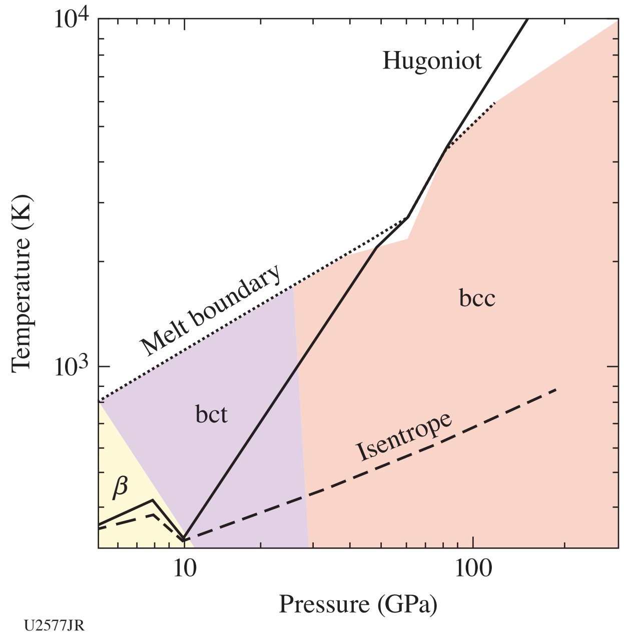

Figure 37
Tin phase diagram.

We used the OHRV, a 2-D velocimetry diagnostic, to simultaneously image and measure the velocity of ramp-compressed tin. Over the course of two half-day campaigns, we were successful in smoothly ramp compressing tin to a peak pressure of 50 to 100 GPa, through the bct–bcc phase transition. While we observed spall-like behavior, shown in Fig. 38, and fracture along grain boundaries, we did not observe the reflectivity recovery and acceleration seen in NIF experiments. Ramp compression was accomplished using a plasma-piston drive, which allows for less flexibility in pulse shaping; and our current hypothesis is that the behavior observed in the NIF experiments is more sensitive to drive than initially suspected. Further work will be required to understand this sensitivity.

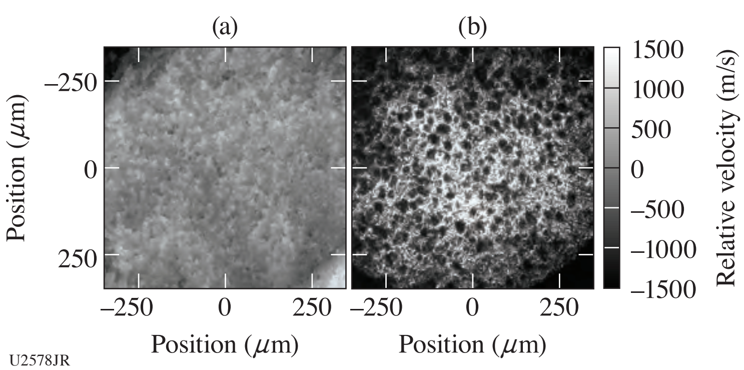

Figure 38
OHRV results from a shot ramping tin to ~70 GPa. An OHRV probe was on compression at ~50 GPa. Both (a) a velocity map and (b) an image show round features indicative of solid material spall.

Development of High-Power Laser Platforms to Study Metal Ejecta Interactions

Principal Investigator: A. Saunders
Co-investigators: S. J. Ali, H.-S. Park, J. H. Eggert, F. Najjar, T. Haxhimali, B. Morgan, Y. Ping, and C. Huntington (LLNL); and H. G. Rinderknecht (LLE)

High-velocity ejecta and dust grain interactions are of great interest to the Stockpile Stewardship Program as well as interstellar and interplanetary science. Ejecta particles are generated by the Richtmyer–Meshkov (RM) instability when a strong shock wave interacts with surface defects while breaking out at a metal interface into vacuum or gas. Ejecta formation has been studied extensively, but ejecta particle transport, interaction, and recollection are still poorly understood. This project has been working to apply to this topic novel experimental techniques and diagnostics that have been developed for high-energy laser studies. Specifically, we have used x-ray radiography, as well as 1-D and 2-D VISAR to explore the details of ejecta transport, interaction, and recollection.

We developed a platform for the OMEGA laser to measure the areal mass density emerging from surface perturbations on tin foils. The platform uses the previously developed target fixture designed to make concurrent 1-D and 2-D VISAR measurements, allowing us to quantify the conditions in the tin upon shock release and provide data about the areal mass density of the ejecta jets. The target package is shown in Fig. 39(a) and consists of an ablator, a tin sample with multiple divots, and a silicon-nitride collection plate. The silicon nitride is 100 nm thick and reflects a fraction of visible light such that it provides a reflective surface for the VISAR measurements. Jets emerging from the tin divots impact on the silicon nitride window, causing it to accelerate. One-dimensional VISAR measures the motion of the silicon nitride and tracks the velocity as a function of time. Through the equations for momentum conservation, one can solve for the areal mass density of the ejecta jets in terms of the velocity of the SiN window.[21] The 2-D VISAR provides an image of the jets impacting the SiN, as well as the velocity as a function of position, as shown in Fig. 40.

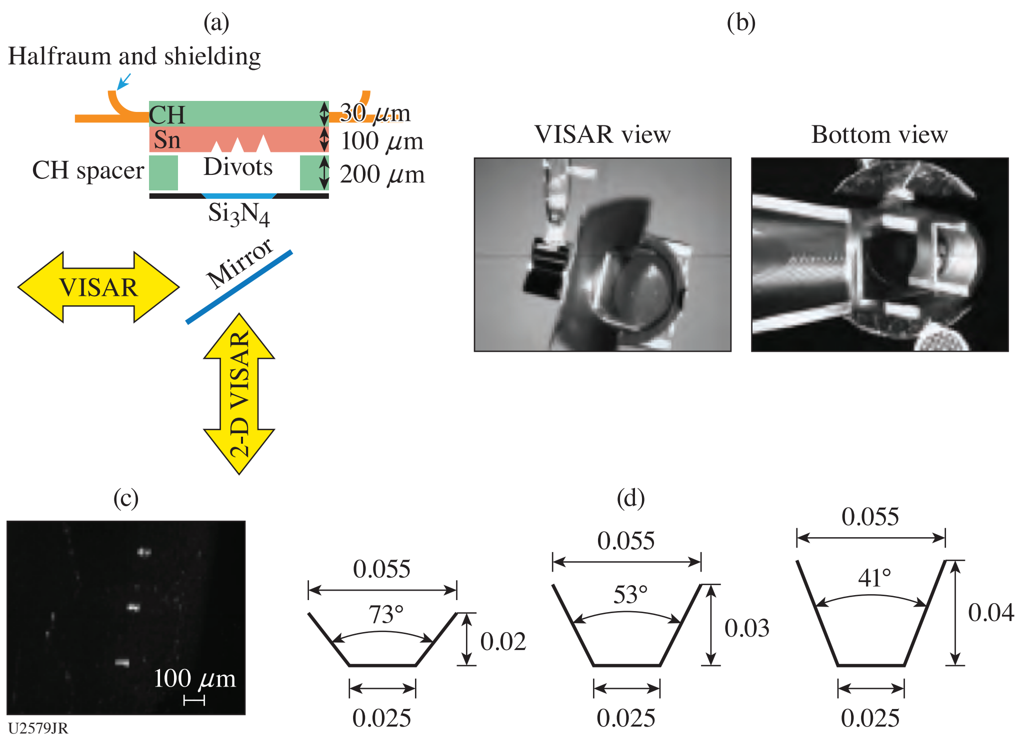

Figure 39
(a) Target schematic; (b) photos of the actual target from the 1-D VISAR view and the bottom view; and (c) image of the divots on the tin surface; and (d) divot schematics.

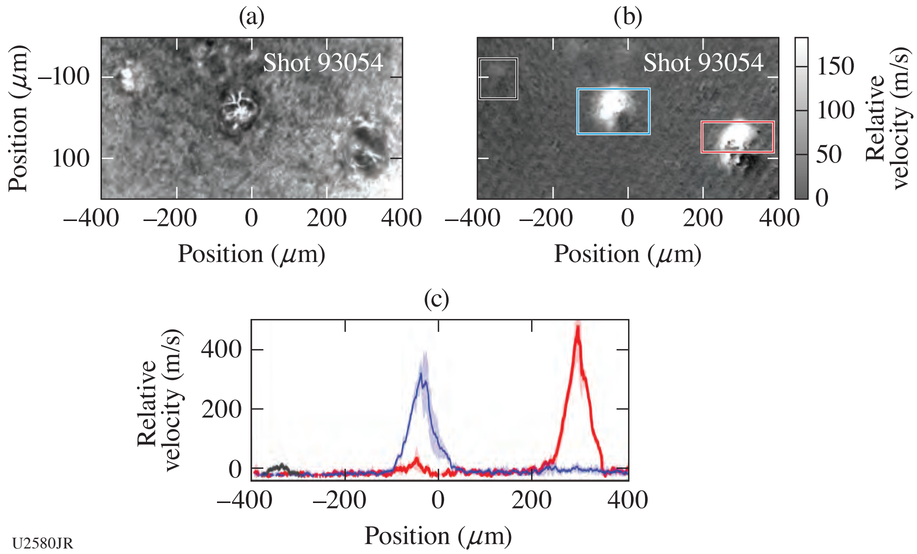

Figure 40
Two-dimensional VISAR results from one ejecta shot with three divots with varying depths showing (a) an image of the ejecta interacting with the SiN, (b) velocity of the ejecta/SiN interaction, and (c) lineouts of the velocity for each divot.

Study of Metal Ejecta Recollection, Interactions, and Transport on OMEGA EP
Principal Investigator: A. Saunders
Co-investigators: H.-S. Park, S. Ali, J. H. Eggert, T. Haxhimali, K. MacKay,* B. Morgan, F. Najjar, Y. Ping, and C. Stan* (LLNL); H. G. Rinderknecht (LLE); and P. Tzeferacos (University of Chicago)
*Postdoc

This campaign consisted of three shot days with a total of 27 shots to develop a laser-driven experimental platform to understand ejecta properties, especially during their recollection, interactions, and transport processes. Ejecta are submicron to micron particles that can travel at hyper velocities (1 to 10 km/s). Understanding ejecta interactions has broad relevance to many fields of science including impact material physics and debris shielding.

In FY19, the OMEGA EP Ejecta-Interact Campaigns focused on creating ejecta in both solid and liquid stages, measuring their jet velocities, and developing a radiography platform to understand their morphology and evolution. Figure 41 shows the experimental configuration. The target was a 30-μm-thick ablator with a 100-μm-thick Sn metal foil. The Sn had a long 45-μm-

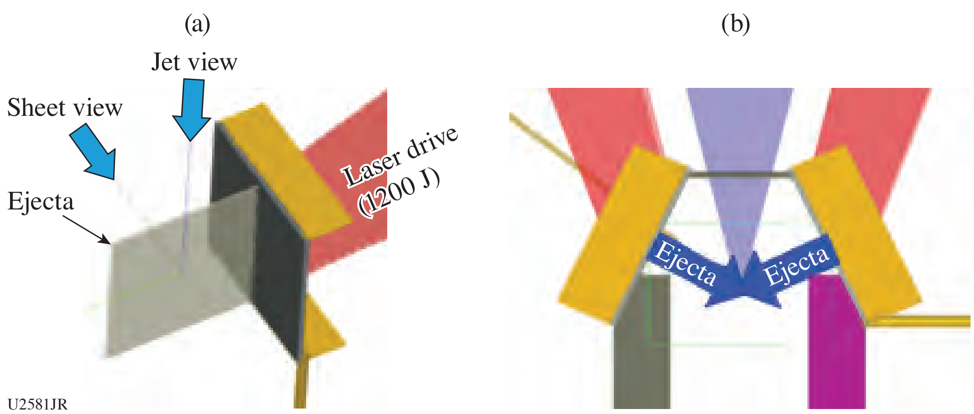

Figure 41
Experimental configuration: (a) single jet platform; (b) interacting jet platform.

deep groove with a 60° opening in the middle of the surface. The laser drive shocks the Sn target. Release of the shock onto the free surface generates RM instabilities from the surface perturbation, and ejecta jets are created. Figure 41(a) is the platform for the single jet and (b) is the interacting jet configuration.

The drive used 1.8-mm-diam phase plates and an 8-ns square pulse with varying laser energies. We tried three different laser energies to control the ejecta phase (i.e., liquid and solid.) The drive was measured by the VISAR diagnostic on separate shots. From the free-surface velocity measurements, the particle velocities were calculated. From these particle velocities, using the well-known Hugoniot EOS table for Sn, the shock velocities and the shock pressure were derived. The ~1120-J laser energy resulted in an ~100-GPa shock pressure that was well above the Hugoniot melt line; therefore, the ejecta were in the liquid state. At ~300 J, we measured ~42 GPa, which is still in the liquid state; at ~70 J, we measured a shock pressure of ~16 GPa, which is well below the melt line. These drive calibration shots were crucial to understanding the ejecta state.

For radiography, we used the short-pulse–driven Ti microwire backlighter that generates predominantly 4.5-keV K_{α} x-ray photons with ~10-μm spatial resolution. The target geometry was varied such that the radiography was viewing two different orthogonal angles, the "jet" view and "sheet" view of the ejecta jet. Figure 42 shows the resulting single ejecta jet evolution from both jet and sheet view radiography. For these shots, we used a 1200-J drive that created melted Sn ejecta at ~100-GPa shock pressure. The initial analysis indicates that the ejecta jet velocity was ~5.3 km/s; the bulk surface was ~2.5 km/s. The radiometric data show that the areal mass density was ~0.3 mg/cm^2 (Ref. 21). The ejecta front travels at a faster velocity than the bulk surface of the tin that can be seen preceding the bulk surface in the radiography.

For the EjectaInteract-EP-19C Campaign, we created solid-state Sn ejecta jets using ~70 J of drive laser energy that delivered ~16 GPa of shock pressure. Figure 43 shows the resulting radiography in the jet and sheet views. The sheet view shows interest-

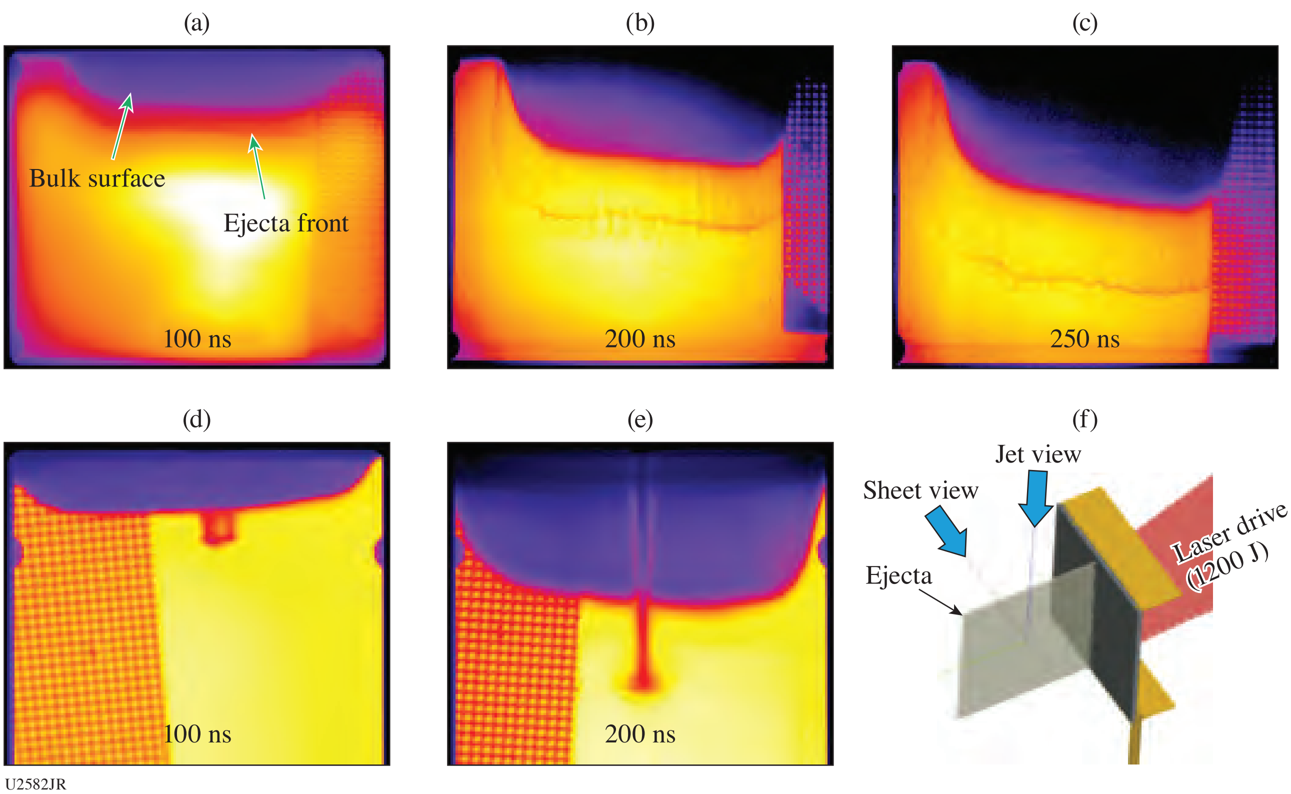

Figure 42
Raw radiographs of expanding liquid Sn ejecta jets taken at different delay times. The top row is the "sheet" view; the bottom row is the "jet" view.

ing layered features that could be spalling. From these views, the solid Sn ejecta jet velocity is ~2 km/s. The interacting jets are created by shocking two targets in opposite directions. The interacting jet view is shown in the third panel. The lineout of the interacting region shows more obscuration of the signal, indicating that the ejecta density was piling up from inelastic scattering.

Future campaigns will study more details of the interacting ejecta properties and the effect of different materials and different groove shapes. In addition, particle-plate interactions will be studied.

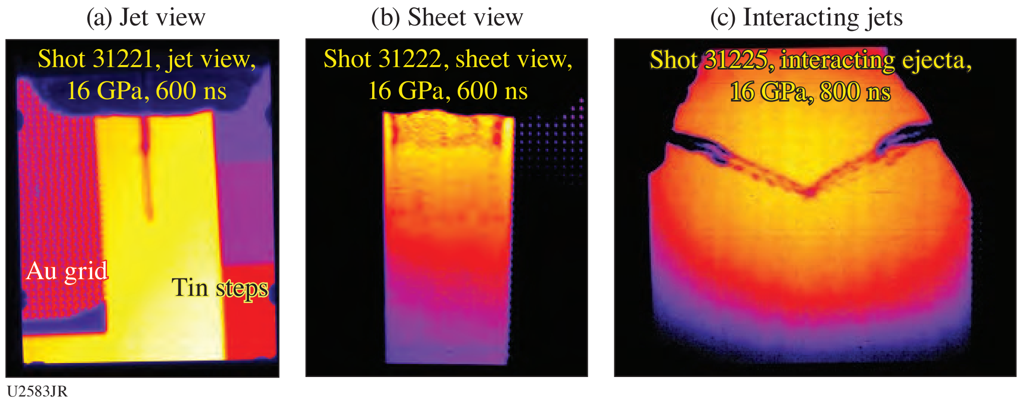

Figure 43
Raw radiographs of expanding solid Sn ejecta jets with (a) "jet" and (b) "sheet" views. (c) The interacting jets are created by two opposing targets. Density pile-up was observed in the interaction region.

4. National Security Applications

SolarCellESD: Solar Cell Electrostatic Discharge Experiments
Principal Investigator: K. Widmann
Co-investigators: P. Jenkins and J. Lorentzen (NRL); S. Seiler (DTRA); and J. Emig, P. Poole, and B. Blue (LLNL)

To determine experimentally whether prompt x rays can induce failure modes in solar arrays remains the key goal of the SolarCellESD Campaign. The main difference in vulnerability of an array compared to a single solar cell is the presence of a voltage difference between neighboring cells that can be up to hundreds of volts depending on the overall layout of the array. For the experiments on OMEGA, we continue to field the smallest-possible array, i.e., 2 × 1 cells with electronic controls that allow us to dial in a voltage difference (bias voltage) between the two cells and, therefore, to study the failure modes as a function of incident x-ray flux and bias voltage, respectively.

For the FY19 campaign we deployed a new solar cell coupon design, with a new mechanical support structure that made it easier to exchange the solar cell coupons between shots. We continued using the electromagnetic interference (EMI) enclosure, but fielded two of the four Langmuir probes in the "shadow" of the EMI enclosure, i.e., away from the line of sight of the incident x rays (see Fig. 44). The goal of this arrangement was to investigate if the Langmuir probe signal is partly generated by a possible x-ray–induced blow-off plasma from the solar cells. Measurements from the probes in the shadow showed no significant signal above the noise level and, therefore, validated our interpretation of the signal from the Langmuir probes that remained in the line of sight of the x-ray source.

We were able to bracket the threshold conditions for the onset of an electrostatic discharge and for the development of sustained arcing for a fixed bias setting. We observed significant variation, however, in the breakdown response based on the view angle for the azimuthally asymmetric laser drive (azimuthal with respect to the hohlraum axis). This important finding will determine the geometry of the experimental setup for upcoming SolarCellESD Campaigns. We also tested a high-temperature hohlraum rather than halfraum as the x-ray source. Unfortunately, a failure of the Dante gate valve prevented us from measuring the performance of this new x-ray source, but we plan to repeat the test of the new source in FY20.

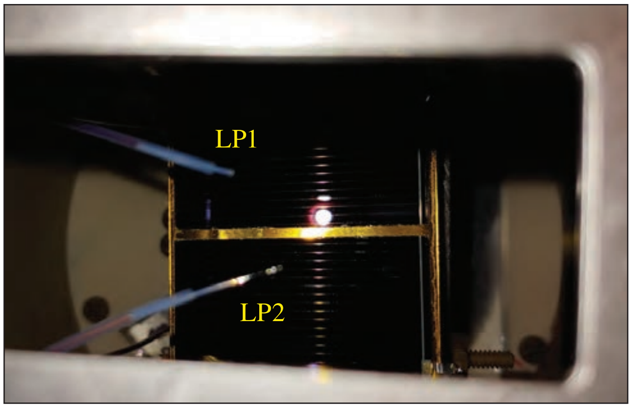

Figure 44
View of the gap between the two solar cells of the 2 × 1 mini array as seen through the aperture of the EMI enclosure. The two features on the left (LP1, LP2) are the Langmuir probes that are in the line of sight of the x-ray source. These probes are several centimeters above the surface of the solar cells.

Plasma-Instability Control to Generate a High-Energy Bremsstrahlung X-Ray Source
Principal Investigator: P. L. Poole
Co-investigators: R. Kirkwood, S. C. Wilks, M. May, K. Widmann, and B. E. Blue

FY19 continued a campaign to develop a high-fluence x-ray source in the 30- to 100-keV range by optimizing plasma instabilities. High-fluence sources at lower energies are currently used for materials effects studies in extreme environments, but no good source exists for >30-keV x rays. This project aims to enhance laser conversion to plasma instabilities like stimulated Raman scattering (SRS) and two-plasmon decay (TPD), which accelerate electrons in plasma waves that will convert to high-energy x rays via bremsstrahlung in the high-*Z* hohlraum wall.

Two half-day campaigns during FY19 attempted to optimize and prolong the duration of plasma conditions that have been found favorable for strong plasma-wave generation. Experiments from previous years demonstrated x-ray yield enhancement from two hohlraum fills (inner CH liner and low-density CH foams) that also enhanced different plasma instabilities and therefore different components of the x-ray spectrum. A natural evolution for FY19 was to study these effects in combination: the insets in Fig. 45 show the usual Au hohlraum with 1-μm-thick CH "windows," which could be ablated by the initial prepulse just like the inner liner, but this redesign allowed CH foam to be fielded as well between the windows to maintain sufficient plasma density as the laser ablated away material. This design was also fielded with foam layers increasing in density toward the center of the

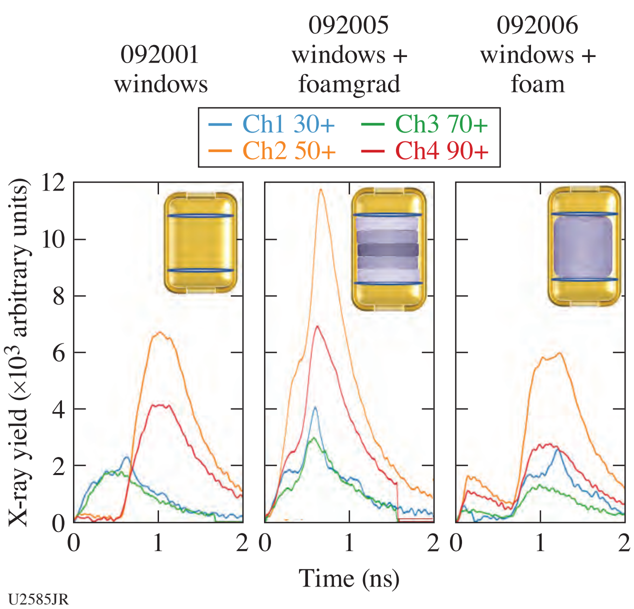

Figure 45
Hard x-ray detector signal from three shots (target type indicated by inset). Enhancement of the desired >50-keV channel (orange curve) is observed for the windowed hohlraums, with further increases (factor-of-4 integrated yield) for the windowed, layered foam hohlraums.

hohlraum. Hard x-ray detector signals (Fig. 45) showed enhancement of the desired >50-keV x rays (orange) with the CH window designs and a further 4× enhancement in total yield for targets that also contained the foam layers.

The results from the OMEGA campaign were used to design a complementary NIF shot day in Q2 FY19, which demonstrated an increase in the hot-electron temperature distribution and thereby the >50-keV hard x-ray signal over FY18 results. These successes have enabled the first shots of materials in high-fluence, hard x-ray environments on the NIF and are being fielded on more campaigns in FY20, even as optimizations continue. This new x-ray source represents a large capability increase for national security applications and related materials under extreme condition studies, with the additional benefit of broadening the understanding of plasma instability control for fusion and other applications.

Enhancing Multi-KeV Line Radiation from Laser-Driven Nonequilibrium Plasmas Through the Application of External Magnetic Fields

Principal Investigator: G. E. Kemp
Co-investigators: D. A. Mariscal,* P. L. Poole,* J. D. Colvin, M. J. May, and B. E. Blue (LLNL); A. Dasgupta, A. L. Velikovich, and J. Giuliani (NRL); and C. K. Li and A. Birkel (MIT)
*Postdoc

A recent LLNL Laboratory Directed Research and Development effort (17-ERD-027) has been studying the influence of externally applied magnetic fields on laser-driven x-ray sources—like those typically used for high-fluence radiography or backlighters—with the ultimate goal of improving multi-keV x-ray conversion efficiency through thermal transport inhibition. The goal of this series of shots was to test and qualify a platform for fielding externally generated magnetic fields on previously fielded x-ray sources on the OMEGA laser. This platform is intended to collect data in the 20-T magnetic-field regime, where currently very little data exist for such high-Z, non-LTE (local thermodynamic equilibrium), magnetized plasma conditions. The collected data will be used to constrain thermal transport inhibition and MHD models currently used in the multi-physics radiation-hydrodynamic code *HYDRA*.

The experimental configuration is illustrated in Fig. 46. Thin-walled, cylindrical Kr gas pipes (1.5 atm) were driven by 20 kJ of laser energy in a 1-ns pulse (40 beams) as typical sources of ~13-keV K-shell line radiation. A total of six shots were taken, half of which had externally imposed B fields. A dual-MIFEDS design was adopted to reach ~20-T field strengths (compared to ~13 T from MagXRSA-18A). Quantifying changes in x-ray emission with increasing external B-field strength was the primary goal of the shots, recorded with Dante (0 to 20 keV), hard x-ray detectors (20 to 500 keV), pinhole cameras (>2 keV), and the DCS (11 to

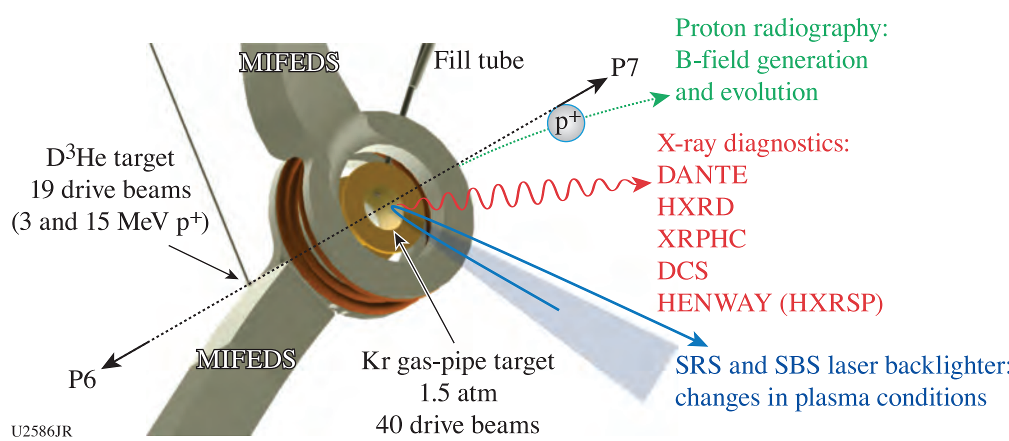

Figure 46
Experimental configuration for MagXRSA-19A. X-ray emission, laser backscatter, and proton radiography data were simultaneously obtained to quantify the evolution and influence of external B fields in these interactions.

45 keV). Secondary diagnostics included proton radiography and stimulated Raman/Brillouin laser backscatter. A D^3He backlighter capsule provided a source of 3- and 15-MeV protons. Analysis is ongoing, but initial results suggest ~50% enhancements in multi-keV Kr emission (>8 keV) when the 20-T B field was present, consistent with the pre-shot modeling.[22] Enhancements of 2.6× were also observed in the >80-keV emission, suggesting B fields could also be used to enhance continuum emission.

Preliminary results from this campaign have led to additional shot time in FY20. With the recent MIFEDS hardware upgrades, we anticipate fields in excess of 40 T in the dual-MIFEDS configuration. These promising results have also justified parallel NIF platform development later in FY20, where we will explore magnetized Ag and Xe K-shell x-ray sources.

5. Plasma Properties

Development of a Platform to Benchmark Atomic Models for X-Ray Spectroscopy of Shock-Heated Materials

Principal Investigator: M. J. MacDonald

Co-investigators: A. M. Saunders, T. Döppner, C. M. Huntington, K. B. Fournier, H. A. Scott, and T. Baumann (LLNL); S. R. Klein, K. Ma, H. J. Lefevre, C. C. Kuranz, and E. Johnsen (University of Michigan); and R. W. Falcone (University of California, Berkeley)

The FoamXRFTS-19A Campaign was the second shot day to develop a platform using simultaneous x-ray fluorescence (XRF) spectroscopy and x-ray Thomson scattering (XRTS) to measure the equation of state of shocked foams. The goal of this platform is to provide XRF spectroscopy data from shock-heated materials at known temperatures, measured independently using XRTS, to benchmark atomic models for future XRF diagnostics.

This platform uses a planar shock wave to heat a cylinder of foam doped with a mid-Z element, similar to previous results published from the Trident Laser Facility at Los Alamos National Laboratory,[23] with the addition of an XRTS diagnostic. A laser-driven Zn He_α backlighter induced K-shell fluorescence from the Co-doped foam and also served as the x-ray source for XRTS. The IXTS spectrometer recorded spatially resolved Co K_β XRF, measuring the density profile of the shock wave in the foam in addition to resolving XRF spectra from the shocked and unshocked regions of the foam. This campaign successfully demonstrated the ability to measure Co K_β spectra from the shock-heated layer at a range of drive conditions, as shown in Fig. 47(a). Initial estimates of the peak temperature in the shocked layer from the Co K_β spectra as a function of drive energy are shown in Fig. 47(b). The temperatures are from simulated emission spectra calculated using Cretin,[24] an atomic kinetics and radiation code developed at LLNL. Although the XRTS data collected in these experiments will be difficult to interpret due to noise in the data, the results will be helpful in improving the experimental setup for future campaigns.

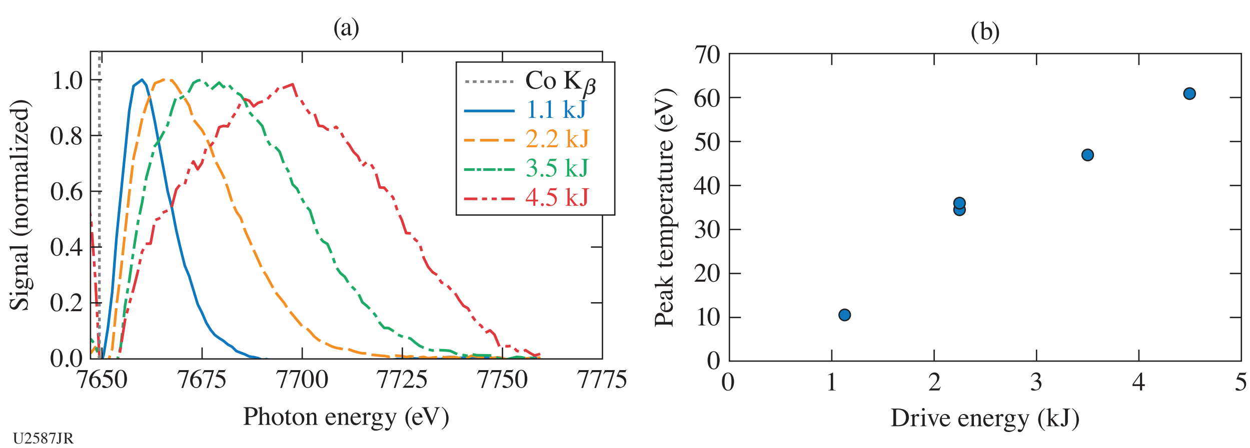

Figure 47
(a) Co K_β spectra taken at different drive energies after removing the contribution from unshocked material. (b) Peak temperatures in the shock-heated foam determined by fitting Co K_β emission to Cretin simulations.

Measurement of Au M-Shell Emission Using A Buried Layer Platform

Principal Investigator: E. V. Marley
Co-investigators: R. F. Heeter, M. B. Schneider, G. E. Kemp, M. E. Foord, D. A. Liedahl, K. Widmann, and J. Emig (LLNL); D. Bishel (LLE); and G. Perez-Callejo (University of Oxford)

This campaign was designed to measure the emitted M-shell gold spectra from a well-characterized and uniform plasma for comparison to atomic kinetic models. The buried-layer target geometry used for this experiment is capable of generating plasmas with an electron temperature of ~2 keV at electron densities of 10^{21} electrons per cubic centimeter. These are also the conditions found inside gold hohlraums used on experiments on the NIF, providing a stable laboratory setting for radiation transport and atomic kinetic studies.

Planar, buried-layer targets were illuminated equally on both sides [Fig. 48(a)] to heat the sample. The sample used in the campaign was a 1300-Å-thick Au/V mixture designed to burn through completely before the end of the laser pulse, providing uniform plasma conditions to measure the M-shell emission of the gold. The samples were buried between two 5-μm-thick layers of Be, which acted as an inertial tamp slowing the expansion of the sample. The targets were designed so that the sample would be concentric with the Be tamp. However, they were not laser cut to spec and only one of the targets had a sample concentric with its Be tamp.

Time-resolved 2-D images of the target's x-ray emission, viewed both face on and side on, were recorded using pinhole cameras coupled to framing cameras. The 4ω probe beam and Thomson spectrometer were also used to measure the scatter off of the electron and ion-acoustic features [see Fig. 48(b)]. A new filter package was used during the campaign to filter out the self-emission and unconverted light, which has been an issue in the past with high-Z targets, and good quality data were obtained. The K-shell spectra from V were used to determine the electron temperature of the plasma. The time-resolved spectra were recorded using a crystal spectrometer coupled to a framing camera. Two crystal spectrometers were used to record the full range of the Au M-shell emission, also time resolved. All of the framing cameras used, those for imaging as well as those for spectroscopy, were co-timed so the plasma conditions could be determined for the measured Au M-shell emission.

A single pulse shape was used during the campaign: a 3.0-ns square pulse with a 100-ps picket arriving 1 ns before the main pulse. A complete (all six diagnostics, correctly timed) set of data was recorded during the campaign at temperatures ~2 keV.

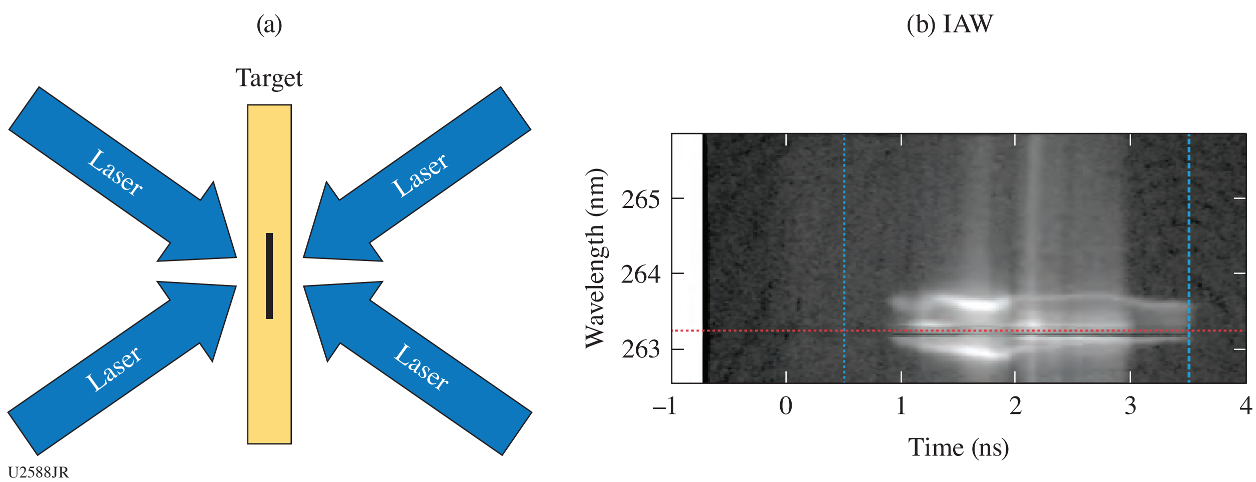

Figure 48
Experimental configuration and Thomson-scattering data of shot 93556.

6. Hydrodynamics

Performance Verification of Ta_2O_5 Foams for Hydro Experiments
Principal Investigator: D. A. Martinez
Co-investigators: M. Rubery and S. McAlpin (AWE); and S. Prisbrey (LLNL)

Foam targets are used on a variety of experiments on the NIF, and verification of the EOS of specific foams is necessary for accurate experimental design and analysis. In this experiment on OMEGA, we tested the Ta_2O_5 foam at a 0.85-g/cm^3 density over the course of five laser target experiments. The experiment consisted of a gold hohlraum heated with 15 drive beams with a 1-ns pulse at 360 J/beam. The heated hohlraum indirectly drove a polyimide ablator, which was used to simultaneously drive a quartz sample and a Ta_2O_5 sample. Using VISAR and SOP we can verify the drive on the plastic ablator using the quartz sample and use the information to calibrate our post-shot simulations so we can compare the shock breakout time of the Ta_2O_5 foam sample through an SOP measurement. Additionally, the Ta_2O_5 foam produced a reflecting shock while the shock was traversing through the Ta_2O_5, allowing the VISAR diagnostic to provide an additional measurement to verify the accuracy of our Ta_2O_5 equation-of-state tables. Figure 49 shows the velocity measurements inferred from the VISAR diagnostic. The Ta_2O_5 used the index of refraction reported from Miller.[25] The post-shot simulation results shown used only the laser drive to determine the shock velocity in the quartz. The experiments provided useful information for our team to calibrate our models for future NIF experiments.

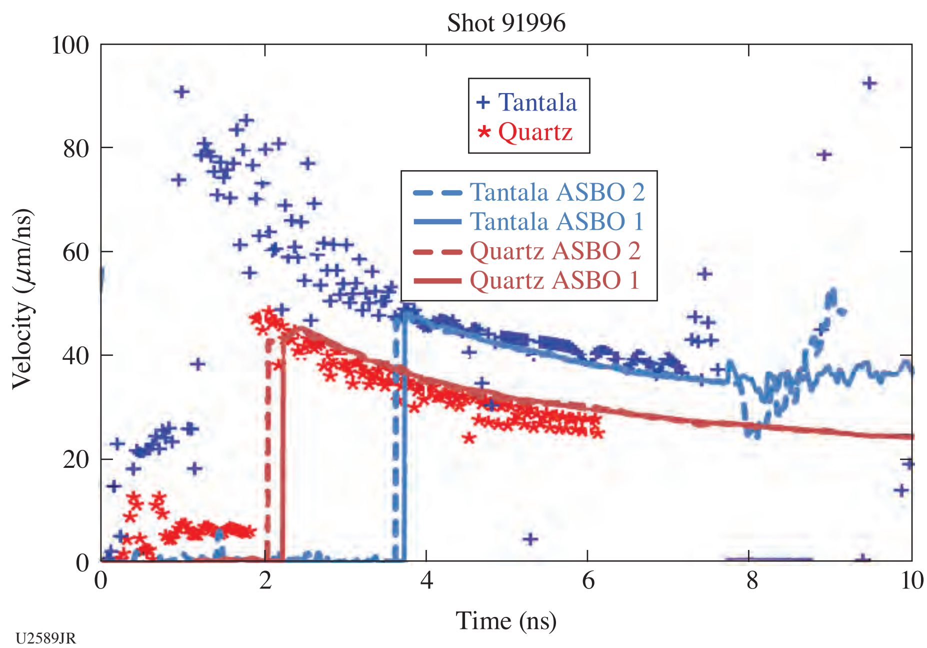

Figure 49
The measured velocity of the reflecting shock from the VISAR diagnostic. Both legs of the diagnostic are reported as active shock breakout (ASBO) 1 and 2.

Mitigating Crosstalk Between High-Energy Backlighters with Shielding
Principal Investigator: S. F. Khan
Co-investigators: D. A. Martinez, S. C. Wilks, S. Prisbrey, D. Kalantar, and A. J. Mackinnon

The objective of these OMEGA EP experiments is to test three shield designs to mitigate the cross interaction of a dual wire backlighter system with a long delay. Previous OMEGA EP experiments (Dbl-HEBL-18A) showed that fratricide between the wires significantly degraded the resolution of the second wire for delays above 4 ns. The experiments used two 12.5-μm-diam W wires with a separation of 4 mm. Shields between the wires consisting of gold (375 μm), plastic (500 μm), and their combination were tested. Each wire was illuminated by infrared 50-ps, 1-kJ short pulses with time intervals of 0, 10, and 15 ns. Source size of each wire was inferred by a radiograph of a gold test grid. Shadowgraphs of the second wire were recorded using the fourth-harmonic probe laser beam and qualitatively illustrates the expansion of the wire (see Fig. 50).

The tested shields show that for a 10-ns time separation, the source size of the second wire was essentially the same as the first wire within measurement uncertainties. Since the plastic shield is transparent to x rays above 10 keV, this indicates that the electrons or very soft x-rays from the initial wire are the primary mechanism for degradation. The results from this experiment are being used in backlighter development experiments on the NIF.

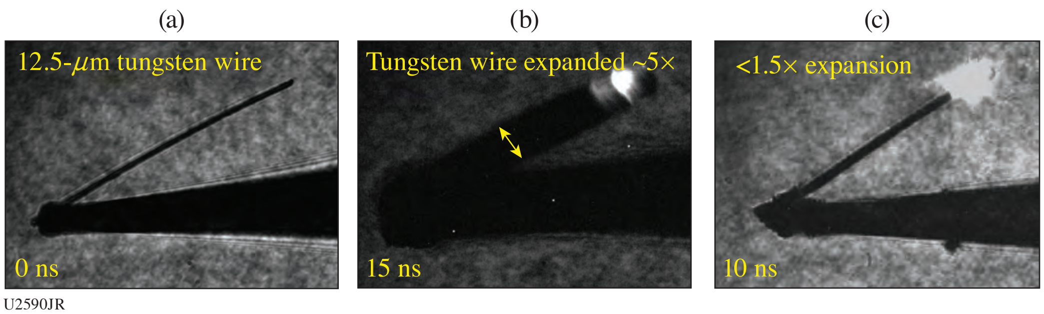

Figure 50
Shadowgraphs of the second wire using the fourth-harmonic probe beam. (a) The wire before either of the wires is illuminated; (b) the second wire 15 ns after the first wire was illuminated with no shielding in between; and (c) the second wire with a 500-μm polyimide shield in between the wires and 10-ns delay. The polyimide shield mitigates the expansion.

Broadband MeV Gamma-Ray Source Development
Principal Investigator: N. Lemos
Co-investigators: A. Pak, D. Rusby, J. Williams, and A. Mackinnon

Following 2011 OMEGA EP experiments,[26] we have begun to investigate the potential of laser-driven MeV radiography. A series of shots was designed to reproduce the past results using one OMEGA EP short-pulse beam and to improve those by coupling the two OMEGA EP short-pulse beams into the same target. We successfully reproduced the past results and showed an improvement when coupling the two beams into the same target.

This experiment had three objectives: (1) reproduce the results presented in Ref. 26; (2) study fratricide by separating both beams in space and time; and (3) maximize x-ray yield by overlapping both beams in space and time. The setup used to achieve the three objectives is shown in Figs. 51(a)–51(c), respectively. For all these configurations the laser beams had an energy of 900 J per pulse and a pulse duration of 10 ps, the electron beam temperature was measured, and a high-density object [image quality indicator (IQI)] was radiographed. The electron beam temperature was used to optimize the x-ray emission since it directly relates to the x-ray spectrum temperature,[27] and the IQI was used to characterize the x-ray source imaging capabilities.

Figure 52 shows the measured electron temperature for all three experimental setups. The highest electron temperature was achieved when overlapping both beams in time and space (green circle), i.e., maximum intensity on target. The second-hottest

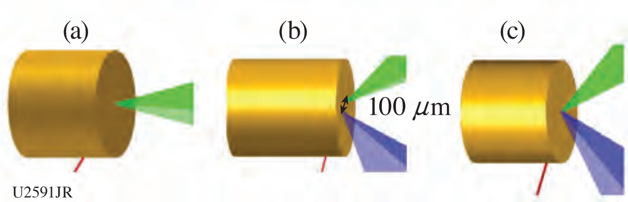

Figure 51
Three experimental setups used in this experiment.

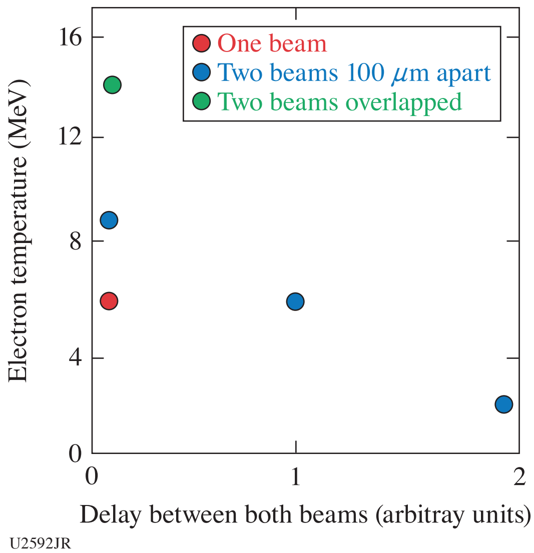

Figure 52
Electron beam temperature for the three experimental setups versus delay between both beams.

electron spectrum was achieved when both beams were separated by ~100 μm (blue circles) followed by the single-beam shot (red circle). To study fratricide we separated both beams by ~100 μm and delayed both beams up to 2 × 5 ns (blue circles). It is clear that when both beams are delayed in time, fratricide is occurring since the electrons' beam temperature starts to drop.

Figure 53(a) shows a CAD drawing of a section of the IQI, and Fig. 53(b) shows the highest-quality radiograph of the IQI with an areal density of 13 g/cm^2 obtained when using the experimental setup in Fig. 51(c). Here we summed the signal recorded in 12 image plates in order to increase the signal-to-noise ratio. Results of this campaign are being used to optimize a similar platform that is being developed on the NIF-ARC.

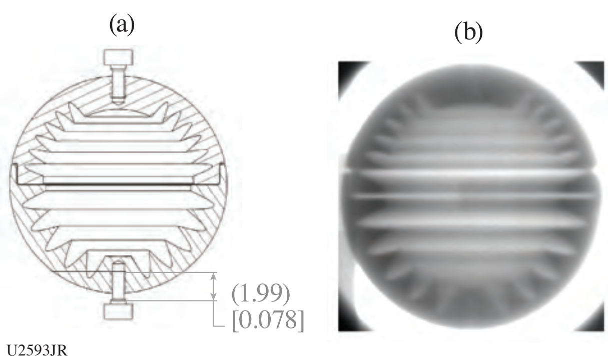

Figure 53
(a) CAD section of the IQI and (b) x-ray image of the IQI.

This work was performed under the auspices of the U.S. Department of Energy by Lawrence Livermore National Laboratory under Contract DE-AC52-07NA27344.

1. *LLE 1999 Annual Report, October 1998–September 1999*, 222, Rochester, NY, LLE Document No. DOE/SF/19460-332 (2000).

2. D. K. Bradley *et al*., Phys. Plasmas **16**, 042703 (2009).

3. D. K. Bradley *et al*., Phys. Rev. Lett. **102**, 075503 (2009).

4. S. W. Haan *et al*., Phys. Plasmas **18**, 051001 (2011).

5. J. H. Eggert *et al*., Nat. Phys. **6**, 40 (2010).

6. M. Millot, Phys. Plasmas **23**, 014503 (2016).

7. S. Le Pape *et al*., Phys. Rev. Lett. **120**, 245003 (2018).

8. L. X. Benedict *et al*., Phys. Rev. B **89**, 224109 (2014).

9. M. Millot *et al*., Phys. Rev. B **97**, 144108 (2018).

10. J. R. Davies *et al*., Phys. Plasmas **24**, 062701 (2017).

11. J. Kim *et al*., Phys. Plasmas **25**, 083109 (2018).

12. L. Burakovsky *et al*., J. Phys.: Conf. Ser. **500**, 162001 (2014).

13. P. C. Myint *et al*., J. Phys. Chem. Phys. **150**, 074506 (2019).

14. L. E. Kirsch *et al*., J. Appl. Phys. **125**, 175901 (2019).

15. J. K. Wicks *et al*., Sci. Adv. **4**, eaao5864 (2018).

16. D. H. Dolan *et al*., Nat. Phys. **3**, 339 (2007).

17. D. B. Thorn *et al*., Rev. Sci. Instrum. **89**, 10F119 (2019).

18. J. F. Seely *et al*., High Energy Density Phys. **3**, 263 (2007).

19. M. E. Foord, D. B. Reisman, and P. T. Springer, Rev. Sci. Instrum. **75**, 2586 (2004).

20. H. S. Park *et al*., Phys. Rev. Lett. **114**, 065502 (2015).

21. A. M. Saunders *et al*., Lawrence Berkeley National Laboratory, Livermore, CA, Report LLNL-PROC-783445 (2019).

22. G. E. Kemp *et al*., Phys. Plasmas **23**, 101204 (2016).

23. M. J. MacDonald *et al*., J. Appl. Phys. **120**, 125901 (2016).

24. H. A. Scott, J. Quant. Spectrosc. Radiat. Transf. **71**, 689 (2001).

25. J. E. Miller, "High-Pressure Equation-of-State of Porous-Ta_2O_5," Ph.D. thesis, University of Rochester, 2007.

26. C. Courtois *et al*., Phys. Plasmas **18**, 023101 (2011).

27. A. Compant La Fontaine, C. Courtois, and E. Lefevre, Phys. Plasmas **19**, 023104 (2012).

FY19 Los Alamos National Laboratory Experimental Campaigns at the Omega Laser Facility

P. A. Keiter. S. Palaniyappan, B. Scheiner, A. Rasmus, H. Johns, K. Meaney, K. Flippo, and Y. Kim

Los Alamos National Laboratory

Rayleigh–Taylor Instability Growth Measurements of Engineered Perturbations in Cylindrical Implosions

Principal Investigators: S. Palaniyappan, J. P. Sauppe, B. J. Tobias, C. F. Kawaguchi, K. A. Flippo, S. H. Batha, P. A. Bradley, E. N. Loomis, L. Kot, D. W. Schmidt, T. H. Day, R. Gonzales, and J. L. Kline (LANL); A. B. Zylstra and O. L. Landen (LLNL); D. Shvarts (Ben-Gurion University and NRCN); E. Malka (NRCN); and N. N. Vazirani (Virginia Tech)

Inertial confinement fusion (ICF) implosions require high convergence [convergence ratio (CR) of 17 for direct-drive implosions and CR of 30 to 35 for indirect-drive implosions] to achieve the required fuel density and temperature for ignition to occur. Radiation-hydrodynamic (rad-hydro) codes are an indispensable tool for designing current ICF experiments and a guide for future designs. Hydro-instability growth in ICF implosions is one of the major issues with the current ICF implosions that do not reach the predicted performances. The rad-hydro codes and the underlying physics models have not been validated against precise hydro-growth measurements at high convergence because such measurements simply do not exist. We have chosen cylindrical implosions to make precise hydro-growth measurements that can be used to validate the rad-hydro codes. We have performed cylindrical implosions with a CR of 2.5 at the University of Rochester's Omega Laser Facility. We are planning to increase the CR using higher driver energy at Lawrence Livermore's National Ignition Facility (NIF).

In FY19, we had two CylDRT shot days at the Omega Laser Facility. The first shot day was 14 March 2019, and the second shot day was 19 September 2019. The CylDRT platform was developed to measure the Rayleigh–Taylor (RT) growth of the engineered sine-wave initial perturbations on the inner side of an aluminum marker layer in cylindrical geometry. Both face-on and side-on x-radiographies were used as main diagnostics. Figure 1 shows the axial and transverse views of the nominal cylindrical target. The cylinder was 2.5 mm long and had a 986-μm outer diameter; the inner diameter of the cylinder was 860 μm. In the middle of the cylinder, there was a 500-μm-long aluminum marker band on the inner side of the cylinder. In addition, the inner aluminum layer had engineered sine-wave perturbations. Figure 2 shows the experimental geometry. The cylinder was driven by 40 beams with a 1-ns square pulse. A nickel backlighter was attached to the TIM-4 (ten-inch manipulator) end of the cylinder. An x-ray framing camera was used for face-on radiography in TIM-6. We used 12× magnification with a 10-μm pinhole onto a four-strip charge-coupled device [x-ray framing camera (XRFC3)]. We also used a TIM-2–TIM-3 side imaging of the target to see the uniformity of the implosion with a 6× magnification.

Figure 2 shows the experimental geometry from the VisRad. The cylinder is aligned along the P6–P7 axis. The TIM-4 backlighter is attached to the main cylinder target. The cylinder was inserted via TPS2 (Target Positioning System). The TIM-2–TIM-3 axis was used for the sidelighter imaging with a vanadium sidelight.

During the CylDRT19A shot day on 8 March, we measured the RT growth of single mode-20 initial sine-wave perturbations (Fig. 3). The measured growth rate of these engineered perturbations agrees well with the *xRAGE* hydro simulations. During the CylDRT19B shot day on 19 September, we measured the RT growth of surface roughness (200-nm and 500-nm) perturbations. This data have yet to be analyzed.

This material is based upon work supported by the Department of Energy National Nuclear Security Administration under Award Number DE-NA0003856, the University of Rochester, and the New York State Energy Research and Development Authority.

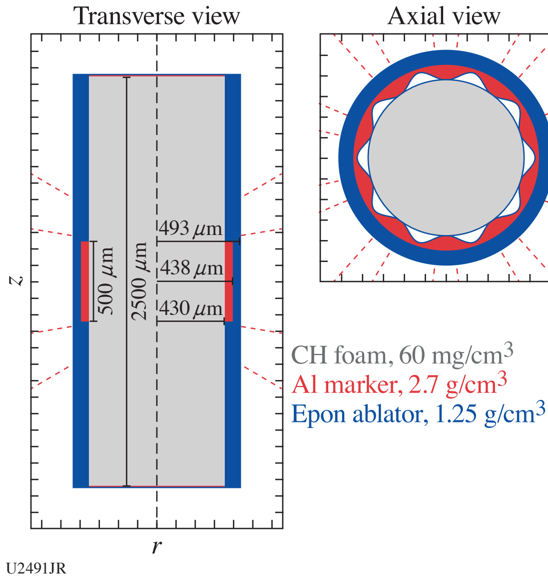

Figure 1
Sketch of transverse and axial views of the target.

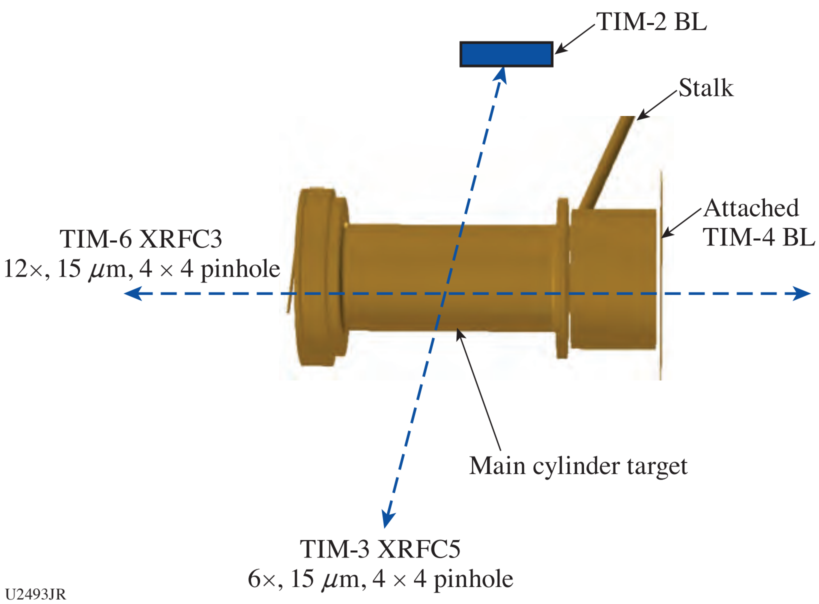

Figure 2
Experimental geometry for cylinder platform. BL: backlighter.

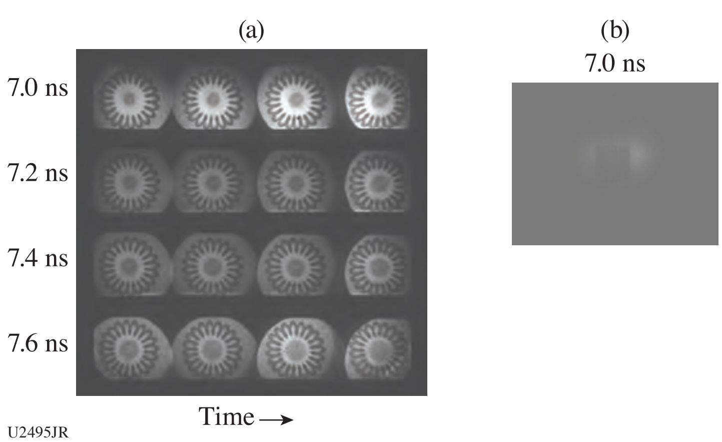

Figure 3
X-radiograph of the mode-20 sine-wave perturbation at a late time (7 to 7.8 ns). (a) Face-on view and (b) side-on view.

Evaluation of Revolver *Shell Collisions*

Principal Investigators: B. S. Scheiner (LANL and University of Iowa); M. J. Schmitt, S. C. Hsu, D. W. Schmidt, K. Molvig, N. Krasheninnikova, and C. Wilde (LANL); and F. J. Marshall, P. M. Nilson, D. N. Polsin, and T. R. Boehly (LLE); and J. G. Mance (Nevada National Security Site)

The Revolver-19A/B Campaigns evaluated the ablator-driver intershell collision relevant to the outer two shells of the *Revolver* triple shell direct-drive–ignition design.[1] Using scaled direct-drive double-shell, cone-in targets [Fig. 4(a)], these experiments aimed to validate the post-collision inner shell velocity predictions from the radiation-hydrodynamic code *HYDRA* using backlit images of the inner shell [Fig. 4(b)]. The measured inner shell velocity of 7.52±0.59 cm/μs was in excellent agreement with the 7.19-cm/μs value predicted by *HYDRA* [Fig. 4(e)] without the need for any adjustable parameters in the simulation.[2] These experiments provide confidence in the modeling capability currently being used for the *Revolver* triple-shell ignition design, in particular, the ability to accurately model the shell collision process.

In addition to evaluating shell collisions, Revolver-19A/B developed a platform that is optimal for evaluating the feedthrough of RT unstable growth, seeded by drive asymmetries and engineering features, to the inner shell. High-resolution (~2.5-μm) images of the outer interface of the inner shell were obtained in Revolver-19B [Figs. 4(c) and 4(d)] through a collaboration between the LANL *Revolver* team and LLE. These images were the first obtained for a dynamic implosion using the newly commissioned Fresnel zone plate imager. Preliminary analysis of the sharp edge between the high-opacity inner shell and surrounding low-

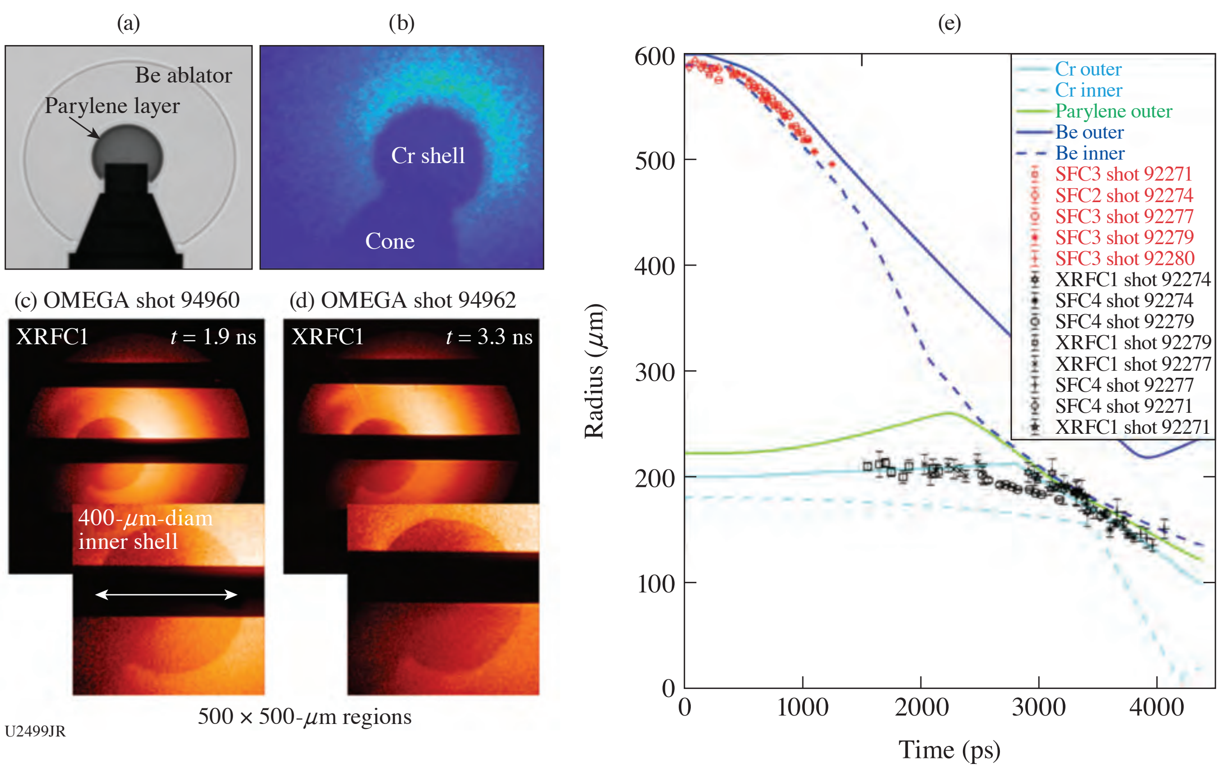

Figure 4
Summary of experimental and simulation data from Revolver-19A/B. (a) A pre-shot radiograph of the cone-in-shell target showing the target construction. (b) A backlit image of the inner shell after the collision with the outer shell corresponding to one of the black data points in (e). (c) A ~2.5-μm–resolution backlit Fresnel zone plate image of the inner shell from Revolver-19B at t = 1.9 ns before the shell collision. (d) Similar to (c) but after the shell collision. (e) The measured outer radius from ablator self-emission images and inner shell backlit images compared with simulation predictions.

opacity tamping layer suggests that Legendre modes in excess of $\ell = 50$ can be obtained from such images. Previously, such high-mode studies would have only been possible using much larger capsules at the NIF. These advances will allow the timely evaluation of mitigation schemes for high-mode growth in multishell targets due to drive asymmetries and engineering features using subscale targets on the OMEGA Laser.

This research was supported by the Laboratory Directed Research and Development Program of Los Alamos National Laboratory under project number 20180051DR.

Discrete Vortex Model and ModCons

Principal Investigators: A. Rasmus, C. Di Stefano, K. Flippo, E. Merritt, F. Doss, A. Strickland, and D. Schmidt (LANL)

In FY19, the discrete vortex model (DVM) and ModCons EP were built on diagnostic development successes from FY18, increasing our ability to resolve instability evolution. DVM and ModCons utilize a shared experimental platform to study different aspects of hydrodynamic-instability growth on interfaces (see Fig. 5). Three long-pulse beams are used to create a semi-sustained shock, which drives instability growth. These campaigns utilize a Mn He$_\alpha$ (6.2-keV) backlighter, which is used in conjunction with a spherical crystal imager to create x-ray radiographs of interface evolution.

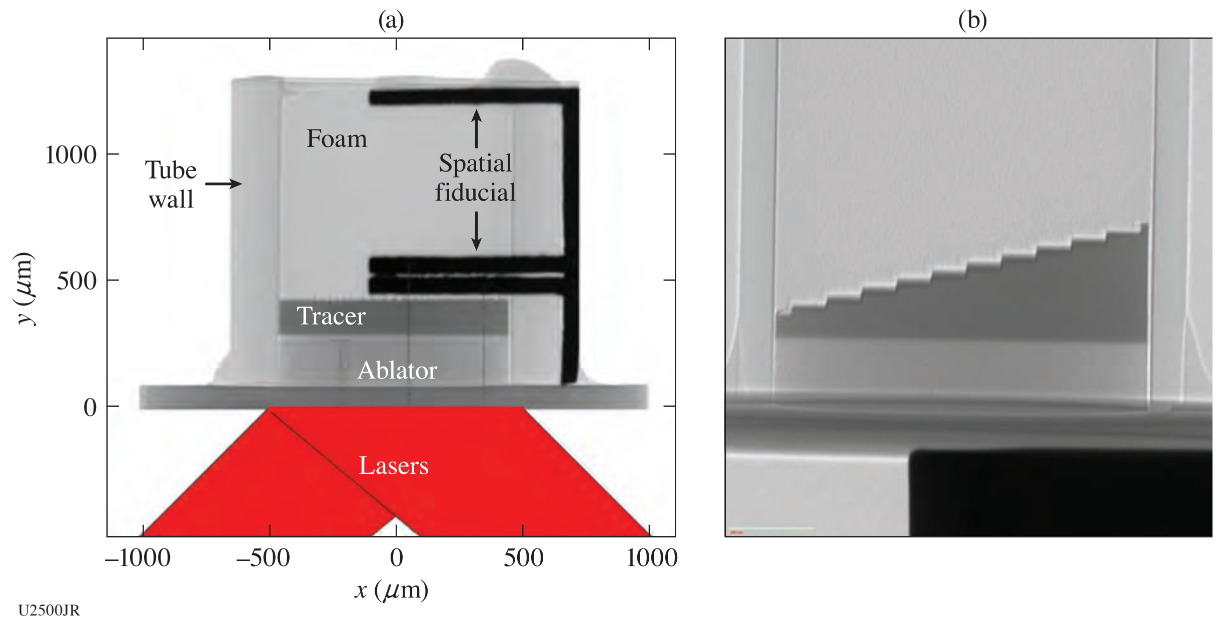

Figure 5
(a) A pre-shot radiograph of a ModCons target and (b) a pre-shot radiograph of a DVM target. Three lasers irradiate the ablator, driving a shock into the target. Hydrodynamic instability growth takes place at the interface between the tracer and foam.

ModCons-19A and ModCons-19B measured the evolution of Richtmyer–Meshkov (RM) growth, with delayed-onset Rayleigh–Taylor (RT), for a broadband perturbation [see Fig. 6(a)]. This yielded good measurements of coupled RM growth during the linear phase of instability evolution. These measurements will yield insight into how initially laminar multimode interfaces become nonlinear and eventually turbulent.

DVMEP-19A measured the evolution of a staircase perturbation [Fig. 6(b)]. This campaign is designed to show that whether the discrete vortex model describes the post-shock evolution of an interface depends on the vorticity distribution along the post-shock interface, rather than the type of vorticity. We also performed proof-of-concept shots for a target type that should allow us to measure the rate at which information about a vorticity distribution propagates through the post-shock system.

Figure 6
Experimental radiographs showing hydrodynamic instability growth: (a) ModCons and (b) DVM.

Radishock: The Evolution of Radiation Flow Across a Dynamic Boundary Provided by a Counter-Propagating Shock Using a Time Series of Shots of Space-Resolved Spectra and Radiography to Obtain Temperature and Density
Principal Investigators: H. M. Johns, P. Kozlowski, S. Wood, A. Liao, T. S. Perry, C. Fryer, C. J. Fontes, P. Hakel, J. P. Colgan, T. Urbatsch, and M. Douglas (LANL); and J. W. Morton and C. R. D. Brown (Atomic Weapons Establishment)

Radishock conducted three shot days on OMEGA this year: Radishock-19A, Radishock-19B, and Radishock-19C. The Radishock Campaign studies the interaction between a supersonic Marshak wave (generated by a hohlraum) and a counter-propagating shock (generated using a directly driven Be ablator). This system is a laboratory analogue to core–shell interactions in Type IIn, IIp, and superluminous supernovae. Additionally, this serves as a physics-based test of the COAX diagnostic platform. When the radiation flow meets the leading edge of the counter-propagating shock, we observe a temperature spike that is larger than the uncertainties we expect in the COAX Platform in simulations (see Fig. 7). As in COAX, we measure the temperature using absorption spectra generated when our Ti-laden aerogel foam is ionized by our radiation front to a temperature of 100 to 150 eV. When we backlight this plasma with 4.5- to 5.5-keV x rays generated by our Kr capsule backlighter, the L-shell Ti ions absorb those photons, resulting in 1*s*–2*p* and 1*s*–3*p* K-shell spectra that are very temperature sensitive due to their source in L-shell ions.

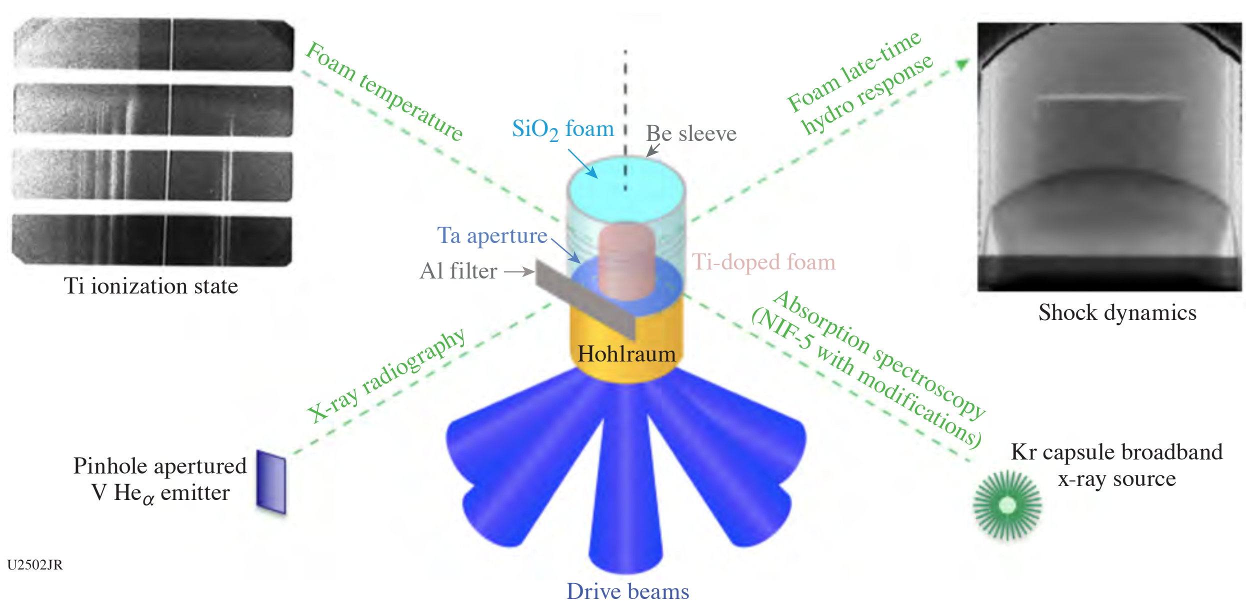

Figure 7
COAX Platform image showing quasi-perpendiular spectroscopic and hydrodynamic axes.

The other axis of our system enables us to view the hydrodynamic behavior and determine the location and eventual density of the shock. In this case we backlight the target with a V-foil backlighter attached to a substrate with a pinhole in it. In both cases we are using point-projection backlighting. Figure 8 shows the platform with the Radishock physics target.

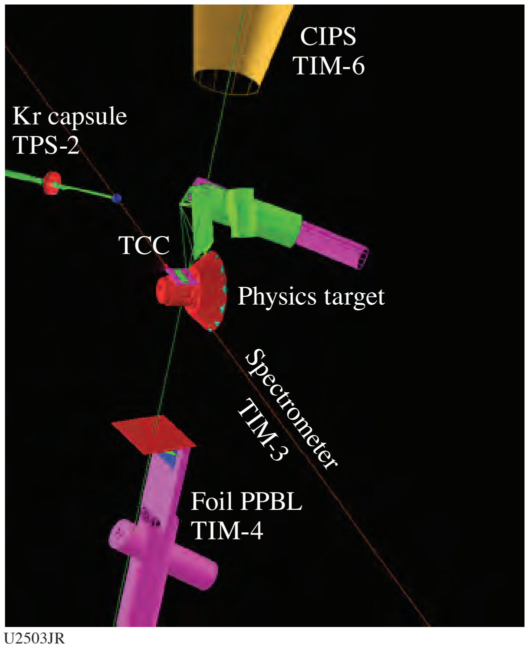

Figure 8
Radishock platform in VisRad. PPBL: point-projection backlighter.

Time zero in Radishock is the start of the ablator drive. The hohlraum drive starts at 4 ns after the ablator drive, but instead of being a single 1-ns square pulse, the 12 beams are divided into two sets of six beams, where the second set is delayed by 1 ns (starting at 5 ns) with respect to the first set. While this reduces the temperature achieved, this longer drive helps the radiation flow to stay supersonic longer, which maximizes the amount of time we have to conduct our experiment. To record spectroscopic or radiography data at different times, we change the relative timing between when we fire the capsule or V-foil backlighter so that we can record spectra or radiographs at different times in the evolution of this system, but the relative hohlraum timing or ablator timing remain unchanged. Figure 9 shows simulations of Radishock at 5, 6, 7, and 8 ns after the ablator drive. These

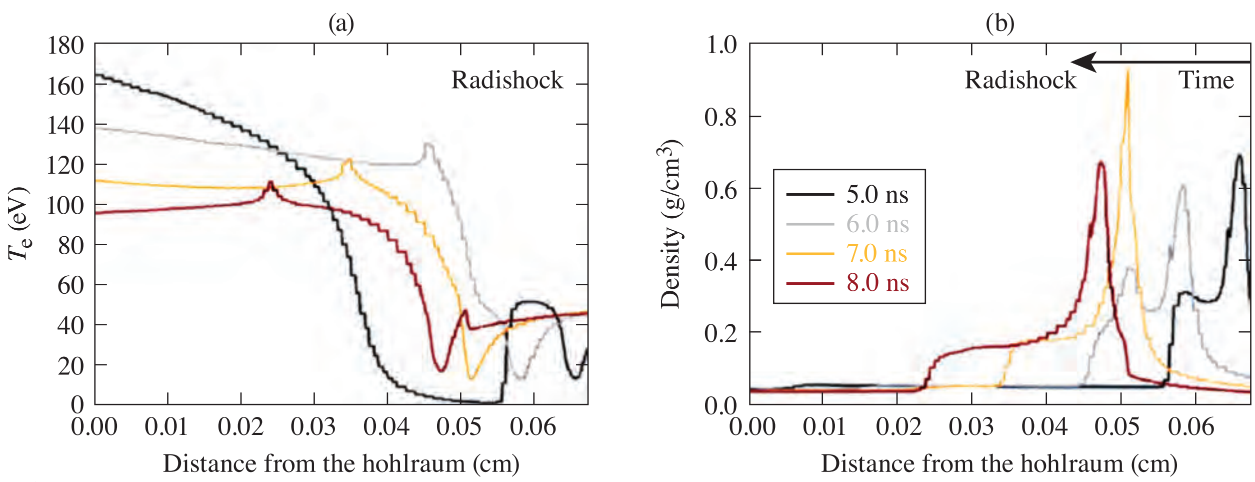

Figure 9
Simulations of Radishock experiment (a) T_e and (b) density at different data collection times.

represent times at which we could collect data to observe pre-interaction (5 ns), start of interaction (6 ns), peak density (7 ns), and late-time interaction (8 ns). These simulations show temperature for the radiation front interacting with the shock on the left and density on the right.

In Fig. 10, the hohlraum is positioned at 0 cm on the left, and the clipper is on the right side. The distance between the two is about 650 μm.

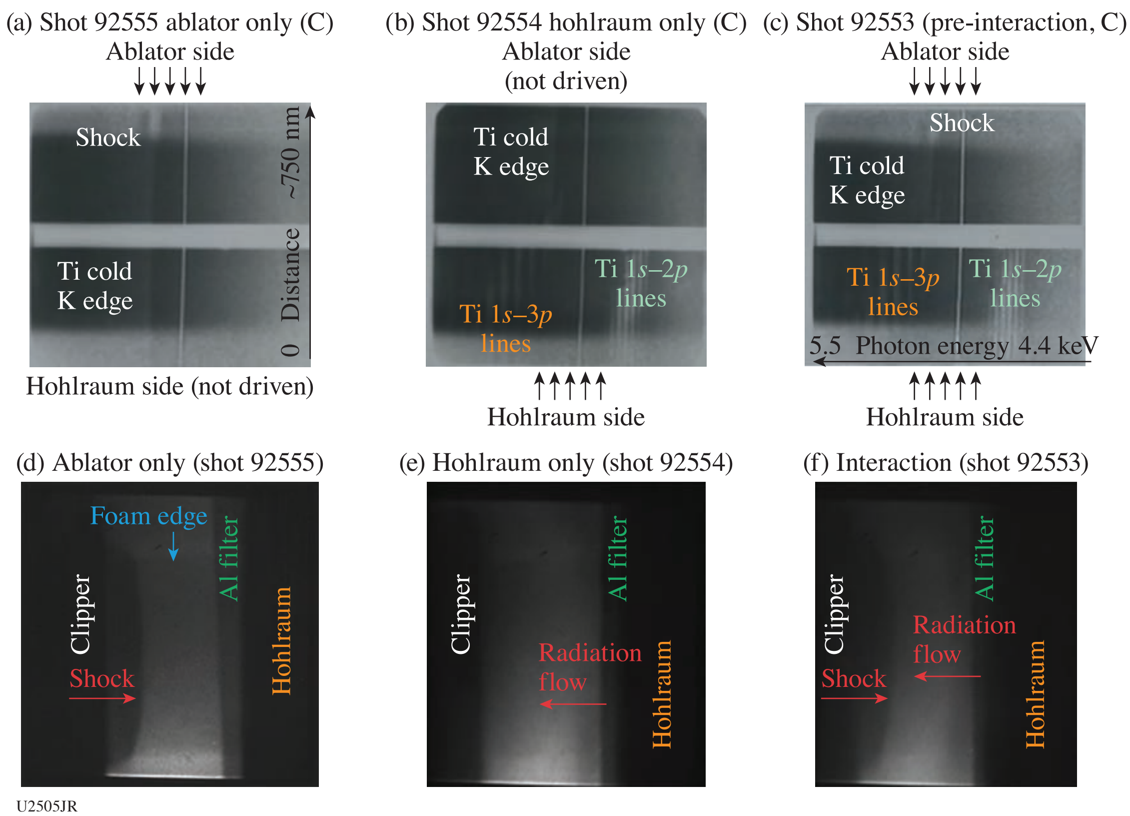

Figure 10
[(a)–(c)] Spectra, [(d)–(f)] radiography from Radishock-19A for the [(a),(d)] ablator only, [(b),(e)] radiation-flow only, and [(c),(f)] interaction. Radiography was taken at ~5.8 ns for these three shots.

Table I summarizes the types of data collected in Radishock-19A, 19B, and 19C, where 19B was a characterization day instead of a nominal characterization day. In Radishock-19A we focused on the start of interaction and peak density. In Radishock-19C we focused on peak density and late-time behavior. In FY18 we had a problem with our radiography involving an early-light effect, which we have determined was due mostly to a mix between soft x rays generated by the CH tube that contains the Radishock

Table I: Data type of shots collected and total number of shots/shot day in FY19.

Day	Date	Spectra	Radiography	DANTE and SOP	V-foil spectra	Number of shots
19A	1/31/19	5 ns, 6.2 ns	5.8 ns, 7.2 ns	–	–	14
19B	9/12/19	–	–	2 COAX and 7 Radishock hohlraums	4 shots	13
19C	8/15/19	7.2 ns, 8.2 ns	4.7 ns, 8.3 ns	–	–	12

SOP: streaked optical pyrometer

foam and blowoff from the Be ablator. In Radishock-19A we added a cone to block the x rays from the ablator blowoff from being recorded by the close-in ported snout (CIPS's) tip and added additional Be shielding on the target on the radiography side to block soft x rays from the CH tube from being recorded by the radiograph. Radishock-19A was the first time we fielded these platform changes, which successfully ameliorated the early light.

In Radishock-19B (12 September 2019) we instead collected data to characterize our hohlraums and our radiography backlighter. We collected nine shots of hohlraum data for DANTE and streaked optical pyrometer (SOP) [with the OATEL (off-axis active shock breakout telescope) in the P1–P12 configuration]. DANTE was used to collect data from the hohlraum laser entrance hole, same as for our nominal configurations, but with the hohlraum near target chamber center (TCC) and no other sources (such as backlighters) in the chamber. We added a single-beam timing fiducial on a 2-mm V square, viewable by DANTE, to provide a small, short-duration signal that we could use to co-time the DANTE channels. The hohlraum included an Al foil on the radiation entrance holes that the hohlraum would heat, and we used the SOP to record the temperature of that plate to serve as a sanity check for simulations attempting to produce synthetic DANTE. Because nominal Radishock days have high incidence for DANTE and the hohlraum is not near TCC, and other radiation sources are present while the hohlraum is active, it becomes extremely challenging to analyze our DANTE data accurately. We intend to use the data from this 19B day to help us better understand what the hohlraum looks like alone, so that we can accurately separate out our hohlraum signal and backlighters on our nominal day. We also collected four shots of data on our V-foil backlighter spectrum to better identify which of the V $K_{\alpha,\beta}$ lines are actually providing the backlighting for our experiment and also confirmed that the emission did not last past the laser drive of our foil backlighter. We discovered that all three $K_{\alpha,\beta}$ are active, but the highest energy provides the strongest source. This will also be of help to better extract density from our radiographs. For these shots, we used the x-ray streak camera with the streaked x-ray spectrometer snout and XRS1 (Rowland x-ray spectrometer). We left DANTE on with no changes to identify any potential signal from the V-foil backlighters. There is a very small signal from this backlighter on several channels, but it is likely not detectable when the hohlraum is active. Figure 11 shows example lineouts from our SOP data for our Radishock hohlraums. Figure 12 shows examples of analyzed spectral data. The spectra shown are 1*s*–3*p* Ti K-shell spectra generated by L-shell ions. Each spectral feature is a blended set of transitions from a single ionization state. Higher photon energy features are from higher ionization stages; as such, more absorption in features at higher photon energy equates to a higher temperature. Whether the temperature difference is consistent with simulations shown in Fig. 9 at this time (6.2 ns) will require further analysis to determine. If the temperature spike is not present, however, we would expect the trend to be reversed—the radiation flow becomes cooler with distance from the hohlraum instead of hotter. Therefore, the deeper absorption observed at larger distances from the hohlraum is consistent with the existence of the temperature spike.

This work was performed under the auspices of the U.S. Department of Energy at Los Alamos National Laboratory under Contract No. 8923318CNA000001.

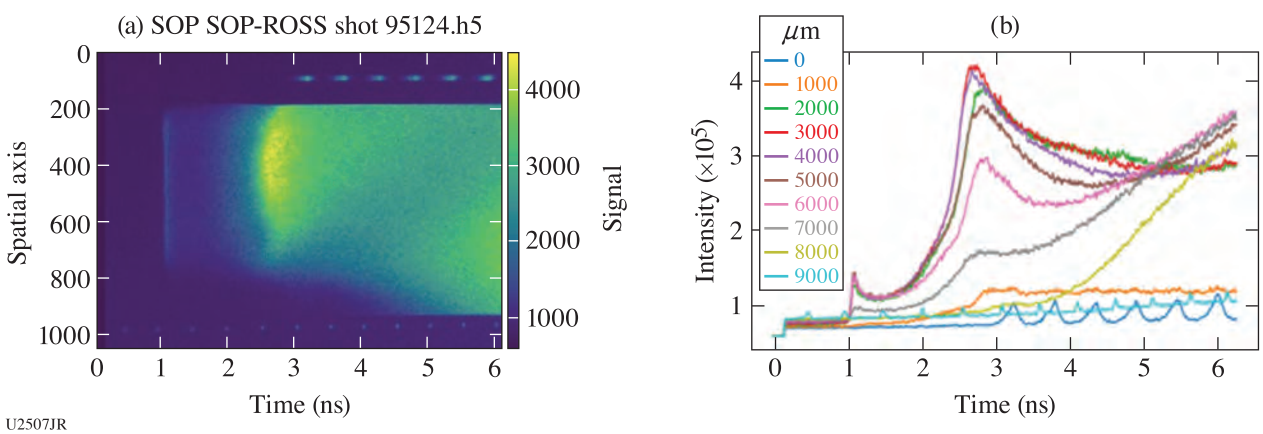

Figure 11
(a) SOP data with (b) lineouts in time showing peak emission at just before 3 ns after the start of the hohlraum drive. ROSS: Rochester Optical Streak System.

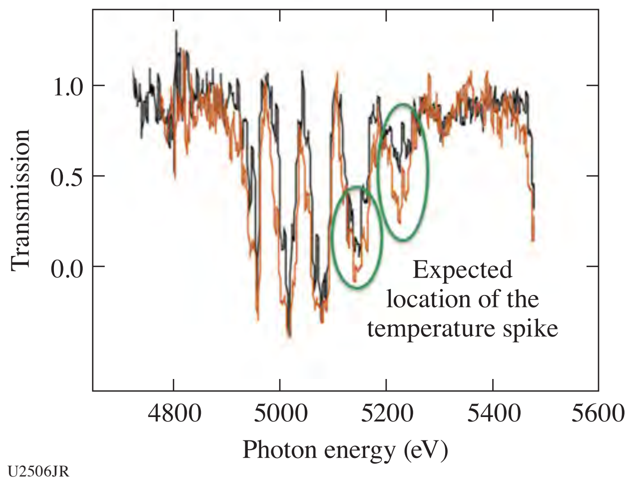

Figure 12
Transmission spectra from 19A interaction at 6.2 ns, at and behind the temperature spike.

High-Spatial-Resolution Separated Reaction Mix Measurements

Principal Investigators: K. D Meaney, Y. H. Kim, H. Herrmann, R. Gonzales, V. Garcia, and H. Geppert-Kleinrath (LANL); A. Leatherland (AWE); and A. Zylstra (LLNL)

Understanding the complex mixing processes that occur in ICF and high-energy-density systems is vital to improving performance. An OMEGA shot series in 2017 used a separated reactant platform to study mix but used very thin (150-nm) placed layers of deuterium fuel in 15-μm-thick CH plastic ablator shells around a hydrogen–tritium fuel in order to give a highly specific spatial location of shell mixture into the fuel. Previous separated reactant experiments had used 1-μm-thick or larger deuterium layers. The 2017 data revealed that 15-μm OMEGA capsules had two distinct mix measurements. When the layer was located right up against fuel, a high amount of mix was observed; when it was recessed just 0.3 μm and 0.6 μm away from the fuel, no mix of the shell was observed. This rapid dropoff of mix is believed to be caused by a diffusion-dominated mix state, which can occur when the yield is mostly shock dominated and hydrodynamic instabilities, such as Rayleigh–Taylor, do not have time to develop a turbulent mix layer. Interestingly, when the placed layer was recessed ever further to 0.9 μm, a significant amount of mix was again observed. This "inversion" mix suggests some mix mechanism that preferentially pulls material deeper away from the fuel.

Two OMEGA shot days in 2019 were executed to better understand the results from the 2017 shots. The shots in 2019 used a capsule design similar to that of 2017: spherical capsules with a placed deuterium layer (Fig. 13). First, to verify the hypothesis about the diffusion mix layer, a middle recession depth of 0.15 μm was placed between the high-mix layer (0-μm recession depth) and the no-mix layer (0.3 μm) to determine the diffusion length scale. The 2019 data show a sharp drop-off of mix, consistent with diffusion-dominated mix, but not as sharp as observed in 2017, possibly due to the capsules being 1 keV cooler than the

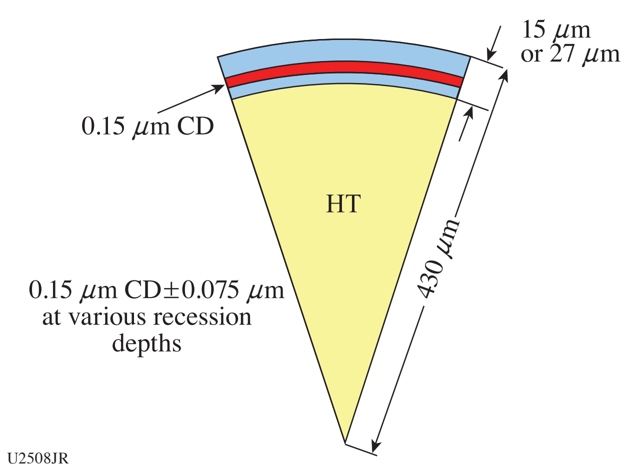

Figure 13
Diagram of the 2019 gamma-mix campaign capsules. All have <0.1% D fill.

2017 shots. Simulations of these cooler capsules to help understanding is ongoing. Second, by moving to thicker shells (27 μm) with different laser pulse shapes, the plasma conditions would be varied into a cooler but denser hot-spot condition (more NIF cryo DT-like), which are well understood to have a fully developed turbulent mix layer. By varying the plasma conditions, we should see a decrease in the steepness of the mixing layer as the capsules transition from diffusion dominated to hydrodynamically dominated. The 2019 data see a shallower mix drop-off as the capsules become cooler and denser. The summary of this data is shown in Fig. 14.

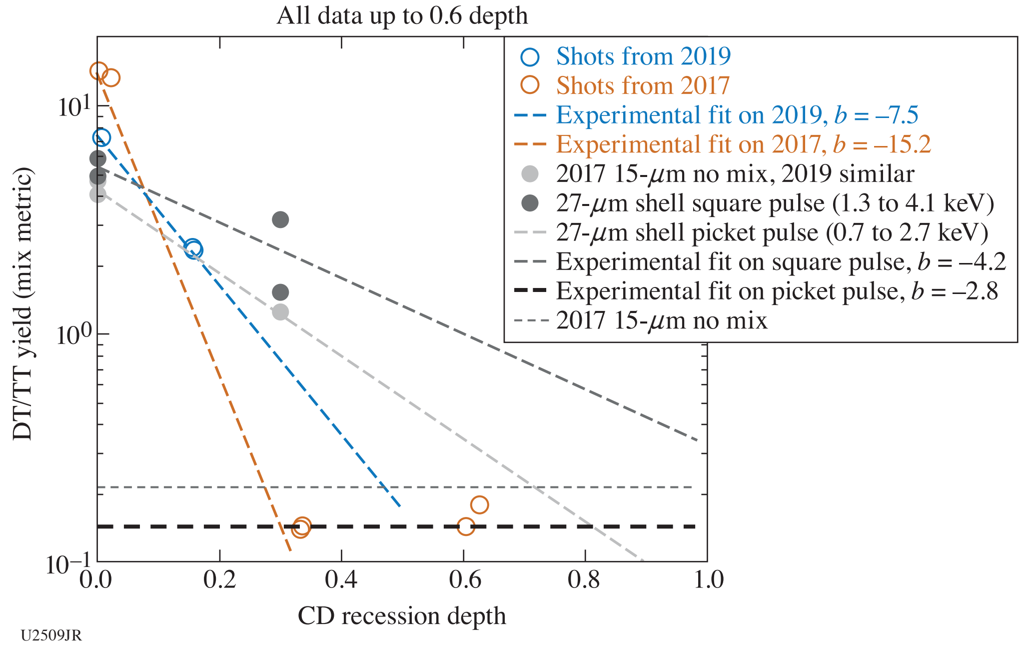

Figure 14
Comparison of how quickly the mix of the shell drops off at different temperature conditions.

The 2019 data also investigated the cause of the observed inversion mix seen at the 0.9-μm recession depth. Our initial hypothesis was that either a P1 asymmetry or a stalk-induced jet may cause preferential mixing further away from the fuel, pulling shell material from further out. This was tested by intentionally causing a larger P1 asymmetry by physically offsetting the capsules 50 and 100 μm from the target and laser center. The stalk was tested by placing multiple (two and four total) stalks called porcupine targets. Both of these variations observed no more increase in the mix at the 0.9-μm recession depth, suggesting neither has a substantial effect on the observed mix. Further recession depths were also tested at 1.4 μm and 2 μm and saw a further decreasing mix signal. All the data observed in both 2017 and 2019 are shown in Fig. 15.

The 2019 OMEGA data were successful in understanding complex mix mechanisms observed in 2017, but questions on the exact nature of the "mix dip" in the 0.3- and 0.6-μm recession depth and the relevance of diffusion dominated mix to NIF-like systems still remain and continue to be investigated.

The MShock Platform Studied Preheat Mitigation Strategies and Defect Evolution

Principal Investigators: K. A. Flippo, E. Merritt, T. Desjardins, F. Doss, C. Di Stefano, and A. Rasmus (LANL)

The MShock Campaign on OMEGA is a developmental test bed and design space for our premier hydrodynamic platform NIF MShock, a successor and derivative of the successful OMEGA and NIF Shock–Shear platform. The MShock Campaign vies to develop a versatile system for studying complex interfaces under the effects of successive shocks—either in co-propagating or counter-propagating geometries, or both combined. Here we can test ideas and develop techniques at a relatively low risk on a

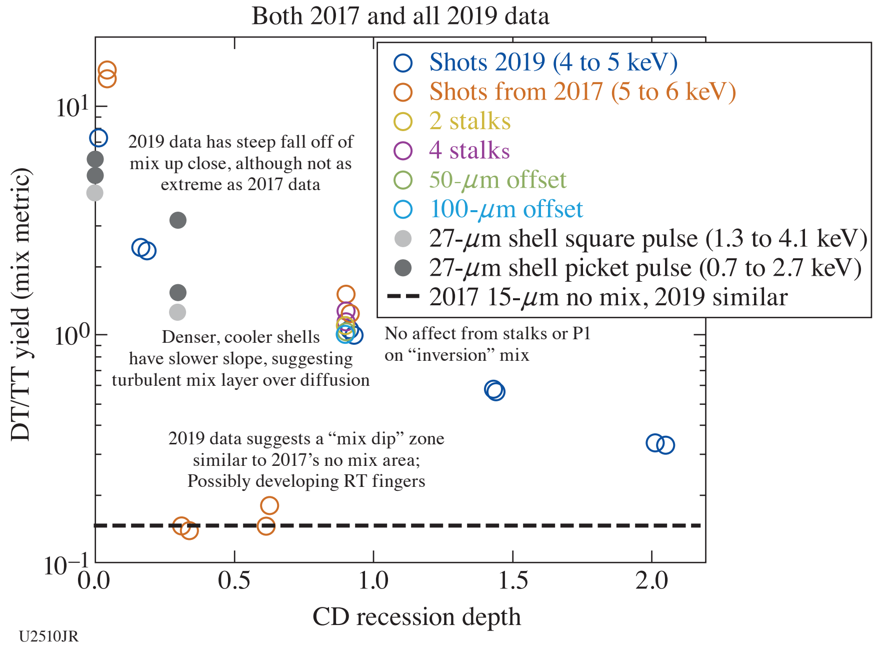

Figure 15
Summary of the mix data observed in 2019 with the data in 2017.

per-shot basis. This year we had three main goals: to test preheat mitigation strategies, develop a heating platform, and test jetting/defect concepts on the MShock platform.

We have tested several preheat mitigation strategies for the MShock platform with the secondary goal of minimizing the effects of those strategies on the shock strength, timing, and shape that drive the physics. We have tested a number of ablator types with various dopings and buried gold layers to damp hot electrons and x rays from the drive beams. This will be less necessary with the new phase plates that can accommodate our design needs; however, mitigation is still needed for higher drive strengths. The main ablator types tested where 1% to 3% iodine-doped CH, 1% to 3% Si-doped CH, and buried Au layers of 2 to 6 μm on the ablator surface inside the target or buried in the drive side. The iodine doping was shown to actually increase hot-electron production with the no-phase-plate drive configuration, so it was not useful. The thicker 5-μm Au layer slowed the shock down by about 3 ns compared to the no-Au layer but little preheat was observed (see Fig. 16). The thinner Au preheat layer did not slow the shock down significantly, but it also did not stop the preheat.

Another consequence of using the thicker 5-μm Au layer on the inside of the ablator was that at late time, the Au tended to obscure the physics [see Fig. 17(a)]. The layer was moved 65 μm inside the ablator to allow for more time before it would cloud the experiment, which worked well [Fig. 17(b)].

In conjunction, we have also been testing heating strategies to preheat our physics package at a time of our choosing, which requires us to have minimal preheat from the main drives. To this end, we have developed an MShock heater platform to study the effects of adding extra energy to the layer before and after initial shock or re-shock on OMEGA. The OMEGA version of the platform at this time is limited to shock and counter-propagating reshock. The layer expanded by a nearly a factor of 5× after heating and before first shock, indicating a temperature of several tens of eV.

The third goal was to test the jet/defect platform. We used a doped central section with a divot to produce a jet from the shocked interface. The scaling of the layer thickness driven by a scaled problem led to the shock taking almost 10 ns to propagate across the PAI defect layer. This limited the growth of the jet in the geometry but did produce jetting from the divot and useful data to improve the platform (see Fig. 18).

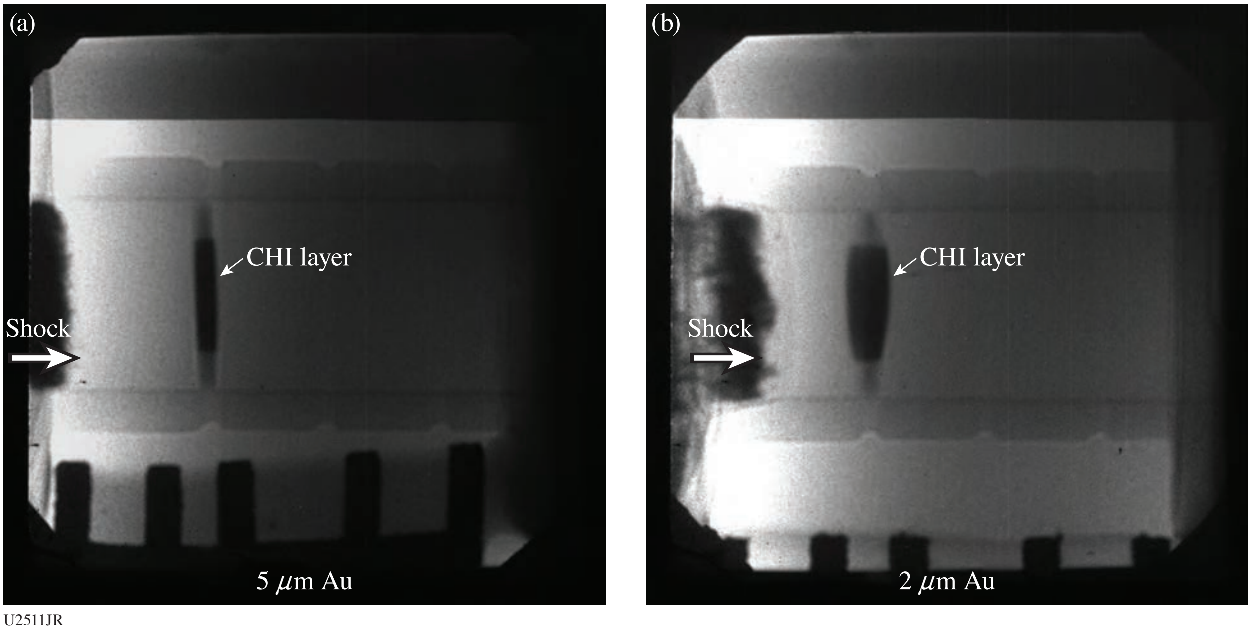

Figure 16
(a) The 5-μm Au layer delays the shock by ~3 ns (4.5 ns after drive) with little preheat compared to (b) the 2-μm Au layer, which shows little delay but significant preheat. CHI: iodine-doped CH.

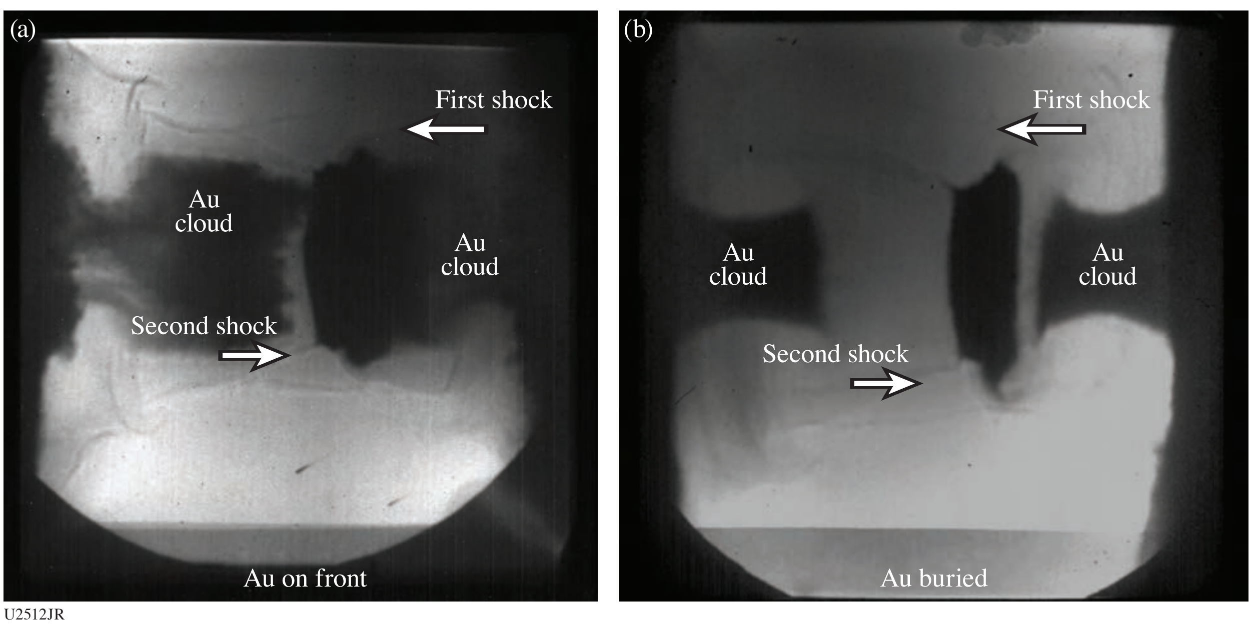

Figure 17
(a) The 5-μm Au design suffered from excessive Au clouding the physics. (b) When the Au was moved back into the ablator 65 μm, the Au was delayed sufficiently to allow one to see the physics of the interaction.

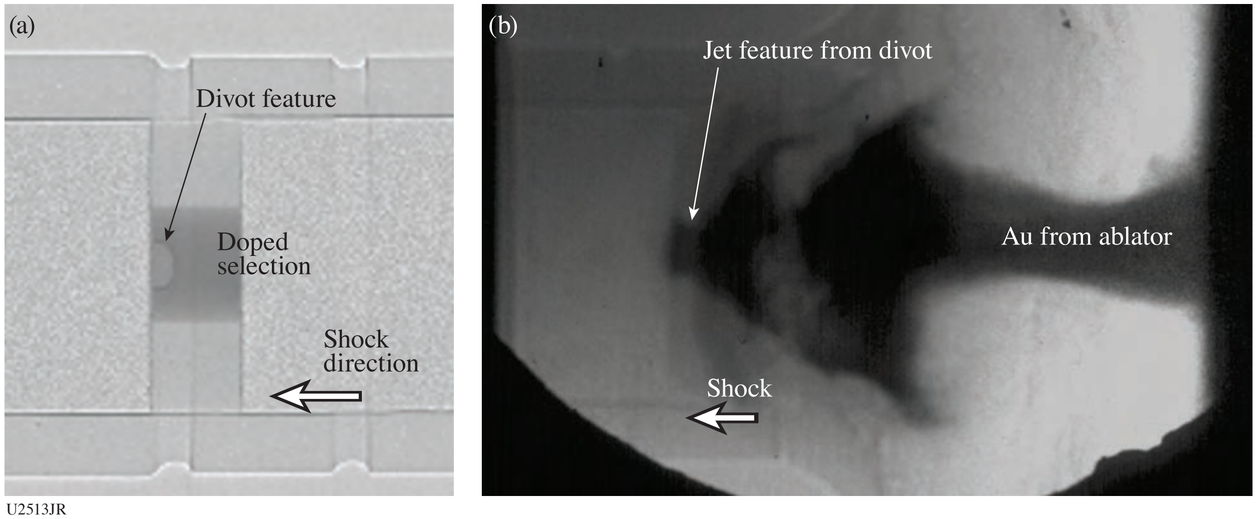

Figure 18
(a) Jet/divot target driven by (b) a strong shock.

The HEDB Campaign Explores If Magnetic Fields Change Turbulent Evolution of HED Systems

Principal Investigators: K. A. Flippo, Y. Lu, S. Li, D. H. Barnak,* H. Li, K. Kelso, A. Liao, A. Rasmus, N. Vazirani, and C. Fiedler Kawaguchi (LANL); E. Liang (Rice University); and C. K. Li, A. Birkel, and B. Lahmann (Massachusetts Institute of Technology)
*Currently at LLE

The HEDB Campaign is looking to quantify the scale and magnitude of self-generated B fields in high-energy-density (HED) systems and specifically to answer the question if these fields can change the turbulent evolution of these systems. This year's campaign focused on using D^3He implosions to produce protons for monoenergetic (14.7-MeV) proton radiography of HED-relevant platforms. We used a modified version of the Shock-Shear platform, where a set of two shocks counter-propagate across a layer, splitting the shock tube in half. This sets up a very strongly sheared layer with strong flows on either side for study. In these experiments we intentionally made a layer with slots in it so the shock can interact more strongly and lead to turbulence and B-field generation more quickly and of a large magnitude so that we would be sure to see them. We cut windows in the shock tube to allow the 14.7-MeV protons to traverse the internal structure, where the physics is occurring, without too much scattering; however, even with this help, the scattering is significant. To mitigate this effect, we employed a mask for the proton source, so that we would have an easier time differentiating scattering from B-field deflection. The mask is known as a "pepper pot." The HEDB experiment is shown in Fig. 19. In Fig. 19(a) the Be or CH shock tube is at the center with two gold cones on either side to prevent scattered light from the driver interaction from contaminating the x-ray imaging. The proton source is a D^3He capsule imploded 1 cm away from the main target, sending protons through the pepper-pot foil, through the "windows," and into the experiment. Proton radiography (pRad) images are shown in two columns: [(b) and (d)] show the synthetic pRad images using *FLASH* simulation results; [(c) and (e)] contain the experimental data. The top row [(b) and (c)] shows images with no fields present (turned off in *FLASH*) and an undriven target from the experiment. The bottom row [(d) and (e)] shows simulated fields of about 50 T from the *FLASH* results and the experimental results from a driven target. We estimate ~30 T from the measured deflection for the self-generated fields in the tube from these results. The next steps would be to improve the radiography by using a higher-flux short-pulse source from the OMEGA EP beamline into OMEGA on a joint shot day.

The LabDynamoEP Campaign Successfully Produced a Turbulent Magnetic Dynamo

Principal Investigators: K. A. Flippo, A. Liao, D. H. Barnak,* Y. Lu, S. Li, H. Li, A. Rasmus, K. Kelso, and C. Fiedler Kawaguchi (LANL); and C. C. Kuranz (University of Michigan)
*Currently at LLE

The LabDynamoEP Campaign is a turbulent magnetic dynamo (TMD) experiment using a simple cone design to produce a turbulent plume of plasma. For a TMD to form, the Reynolds number of the flow and the magnetic Reynolds number of the

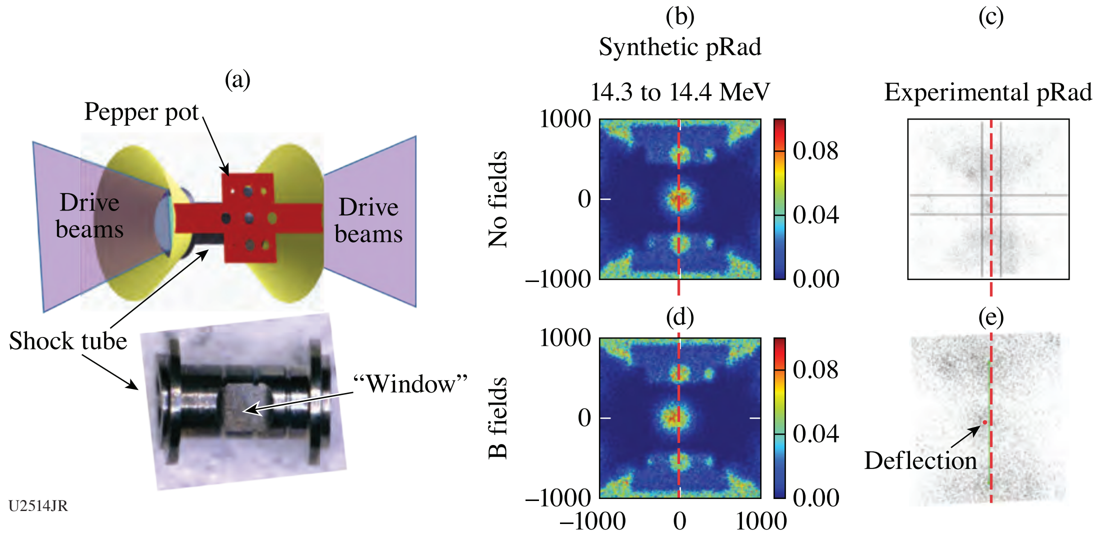

Figure 19
(a) HEDB setup; [(b)–(e)] Proton radiography (pRad). [(b),(c)] The pRad images have no fields (scattering only) and show no deflection off the center line (dashed red line); [(d),(e)] the pRad images have a 50-T field (synthetic) and an estimated 30-T field from experiment.

plasma must be both high and comparable. The ratio of these two numbers is known as the Prandtl number (Rm/Re), which can be rewritten as momentum diffusivity over thermal diffusivity or, alternatively, viscosity over thermal conductivity. When this ratio is of order unity or larger, then the TMD can operate. This platform is designed to achieve this goal on OMEGA EP (see Ref. 3).

We have obtained a series of proton radiographs using the fourth beam on OMEGA EP, which produced a target normal sheath accelerated (TNSA) proton beam. The proton radiographs can then be Fourier transformed into modal information to produce a power spectrum of the magnetic field modes (as in Fig. 20) following C. Graziani *et al.*[4] Figure 21 shows the same for the experimental data from FY19 shots on OMEGA EP, with (a) proton radiographs and (b) reduced data. The solid colored curves represent different times in the *FLASH* simulation, and the dotted curves show the same for the experimental data. Both sets show the clear trend of growth of all modes, indicating the existence of a turbulent dynamo in action.

Preheat Effects on Macro-Pore MARBLE Foams

Principal Investigators: Y. Kim, P. Kozlowski, T. J. Murphy, T. H. Day, D. N. Woods, B. M. Haines, C. Di Stefano, and B. J. Albright (LANL)

In FY19, two Marble Void Collapse Campaigns on OMEGA were performed to provide supporting data for the Marble Implosion Campaign on the NIF. The NIF Marble capsules consist of deuterated foam whose pores are filled with tritium gas. Initial pore sizes are varied to adjust mix morphology. During the capsule implosion, however, hohlraum-driven x rays may increase the foam temperature, thereby reducing pore size and potentially wiping out macropore initial conditions. Diagnosing the preheat effects on the Marble foam on the NIF was not easily accessible; two OMEGA experiments were performed to assess and mitigate the effects of preheat on the Marble foam. The first approach was to develop an indirect-drive platform to identify the amount of x-ray preheat and the amount of shock-driven preheat. The second approach was to develop a direct-drive platform to measure the evolution of single-pore size, while varying the high-Z gas pressure in it.

Figure 22(a) shows the experimental setup utilizing a beryllium shock tube with an inner diameter of 500 μm. The ends of the tube are capped with Rexolite ablators that can be doped with mid-Z materials such as up to 3% silicone. The ablator is irradiated by x-ray flux produced inside a gold hohlraum. To generate an x-ray drive, 20 beams of the 1-ns laser (total 10 kJ) are pointed at the inner wall of the gold hohlraum. The shock tube is filled with two pieces of low-density CH foams (40 mg/cm^3). A thin layer of plastic disk (40 μm thick) separates the two foam layers. The expansion of the thin layer hints at the amount of

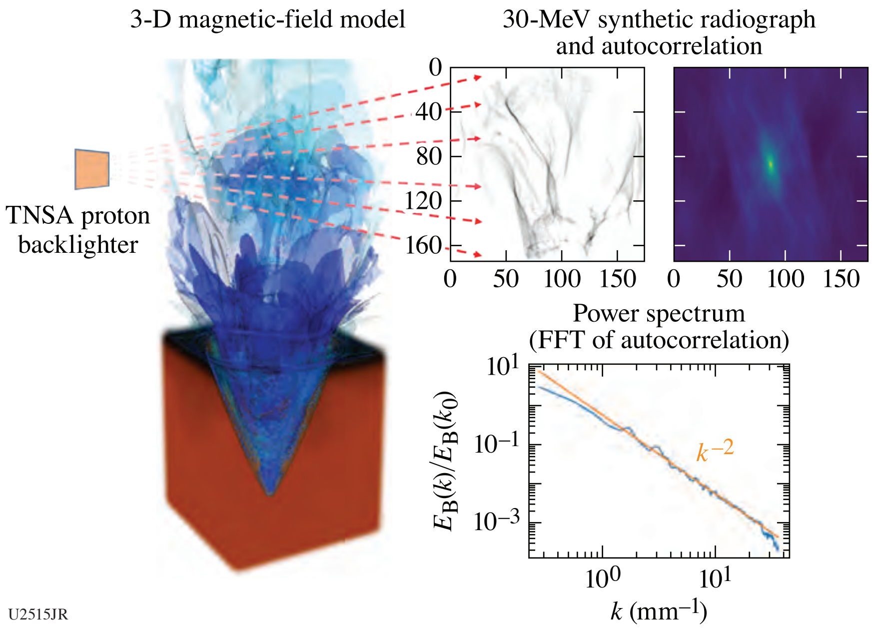

Figure 20
The LabDynamoEP setup is a simple cone of a few millimeters in size. Three OMEGA EP beams irradiate the cone nonuniformly to produce a turbulent plume of plasma. The lasers additionally heat the area above the cone, keeping the turbulent plasma hot and driving a turbulent magnetic dynamo. These data are a *FLASH* simulation with synthetically produced proton radiography (from the *FLASH* package) showing the k^{-2} spectrum one would expect from a turbulent compressible flow. FFT: fast Fourier transform.

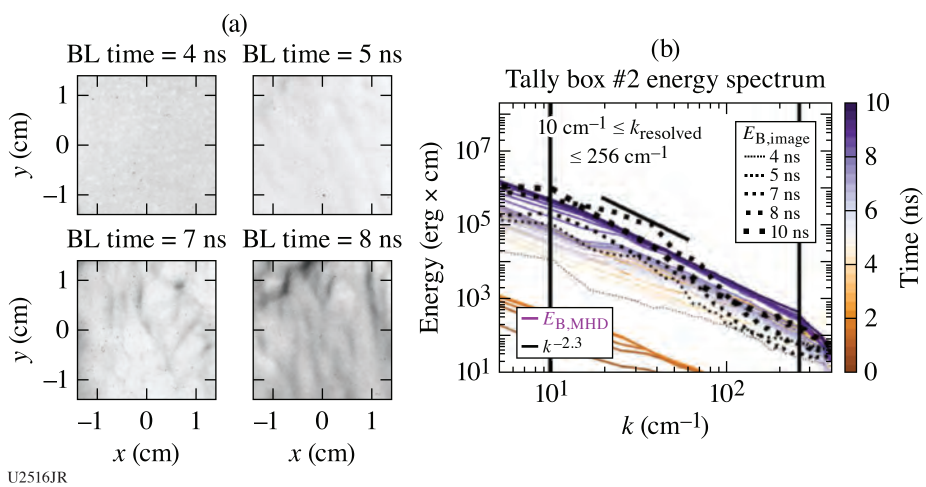

Figure 21
(a) Experimental proton radiographs of the TMD in action analyzed into (b) a power spectrum in time showing the growth of all modes in time (the solid colored curves are *FLASH* simulation results and the dotted curves are experiment data), indicating the dynamo in action magnifying the magnetic fields.

preheat deposited in the foam. Using a point-projection radiographic technique, expansion of the plastic disk has been observed. Figure 22(b) shows a net growth width (L–L_0) of the plastic disk as a function of time, where the initial thickness L_0 is 40 μm and the measured width is L. Within a diagnostic time period (0 to 8 ns), the expansion of the plastic disk showed two distinct behaviors: In early times (up to 4 ns), the expansion rate is approximately 3 μm/ns (~0.2-eV equivalent temperature). Between 4 and 8 ns, the expansion rate increased significantly (~10 μm/ns or 2-eV equivalent temperature). Currently, a LANL *xRAGE* simulation is underway to identify the amount of preheat from a hohlraum-driven x ray and a shock-driven radiation.

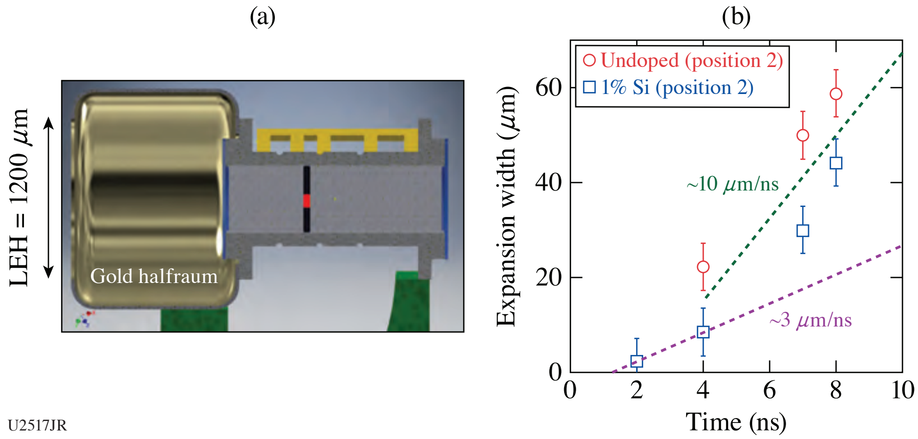

Figure 22
(a) Experimental schematics of indirect-drive preheat platform. (b) In early times (up to 4 ns), the expansion rate is approximately 3 μm/ns (~0.2 eV equivalent temperature). Between 4 and 8 ns, the expansion rate increased significantly (~10 mm/ns or 2-eV equivalent temperature).

Adding high-*Z* gas into the NIF Marble capsule showed the ability to control the degree of heterogeneous mix by preserving initial pore size of the Marble foam. However, the geometry and highly heterogeneous structure make it difficult to confirm this. Therefore, the single-void collapse platform (previously filled with foam, now filled with krypton gas) was modified to test how a void collapses and deforms under different high-*Z* gas pressure conditions. Figure 23 shows the chlorine backlighter images taken with a mixture of 3 atm of krypton gas and 3 atm of hydrogen. Figure 23(a) shows an image taken before the shock reaches the initial gas-filled void, which appears to have substantially compressed even prior to shock arrival. This is expected according to simulations. Figure 23(b) shows a late-time image taken after the shock reaches the void, which is flattened during interaction with the shock. Our target leaking during the shot presented an experimental challenge. In the future, high-pressure target designs will require further refinement.

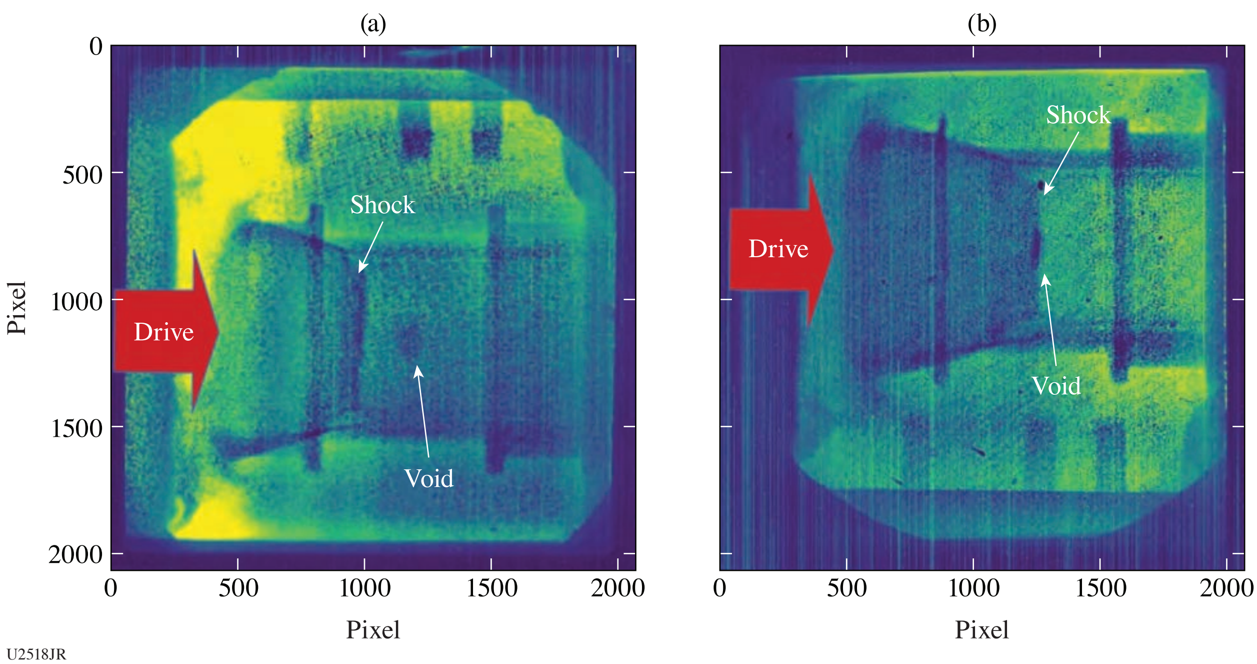

Figure 23
(a) An image taken before the shock reaches the initial gas-filled void and (b) an image taken after the shock reaches the initial gas-filled void.

This work was performed under the auspices of the U.S. Department of Energy by the Triad National Security, LLC, at Los Alamos National Laboratory. MARBLE is supported by the DOE NNSA Office of Experimental Science (NA-113) SAT and PAT Programs.

1. K. Molvig *et al*., Phys. Rev. Lett. **116**, 255003 (2016).

2. B. Scheiner *et al*., Phys. Plasmas **26**, 072707 (2019).

3. A. S. Liao *et al*., Phys. Plasmas **26**, 032306 (2019).

4. C. Graziani *et al*., Rev. Sci. Instrum. **88**, 123507 (2017).

FY19 Sandia National Laboratories Progress Report on Omega Laser Facility Experiments

B. A. Aguirre,[1] W. J. Martin,[1] and S. M. Neville[2]

[1]Sandia National Laboratories
[2]U.S. Air Force Nuclear Weapons Center

The Energetic Neutrons Campaign led by Sandia National Laboratories (SNL) had a successful year testing electronic devices under 14-MeV neutron irradiation at the Omega Laser Facility. During FY19 SNL employees were trained to take over new responsibilities while visiting LLE, continued collaborating with external organizations, and generated knowledge that supports SNL's national security mission.

In FY19 SNL trained a new engineer to become the Principal Investigator (PI) of the Energetic Neutrons Campaign. The transfer of knowledge and skills between the old and new PI's was seamless and enhances SNL's capability to test multiple setups by having more trained personnel during test campaigns at Omega. Also, the number of Omega-certified SNL radiation workers increased from one to three, allowing SNL to increase the number and complexity of the test campaigns at the facility.

In FY19 SNL collaborated with the U.S. Air Force Nuclear Weapons Center and others during the Energetic Neutrons Campaigns. SNL hosted engineers and scientists from these organizations at the Omega Laser Facility and supported experiments related to radiation effects in semiconductor devices. During FY19 SNL also provided an opportunity for others to collaborate on experiments at Los Alamos National Laboratory, Massachusetts Institute of Technology, LLE, Atomic Weapons Establishment, and Commissariat à l'énergie atomique et aux énergies.

SNL continued using the last two generations of neutron effects diagnostics [NED's, Fig. 1(a)] designed and built in previous years to field passive and active semiconductor devices and integrated circuits. The instant response of electronic devices to 14-MeV neutrons produced on OMEGA was monitored before, during, and after the irradiations, and the device physics of the

(a) (b)

U2520JR

Figure 1
(a) The Gen 3 NED used at Omega; (b) the photon shielding designed for a Gen 3 NED.

irradiated devices was explored with post-irradiation characterization tools at SNL. Irradiations on OMEGA supported a 14-MeV neutron flux effect study on silicon-based devices (Fig. 2) and an ionization effect study on semiconductor devices exposed to high-flux neutron irradiations [Fig. 1(b)]. Some of the results were presented at the Hardened Electronics and Radiation Technology (HEART) Conference in the spring of 2019; the remainder of the results were used internally.

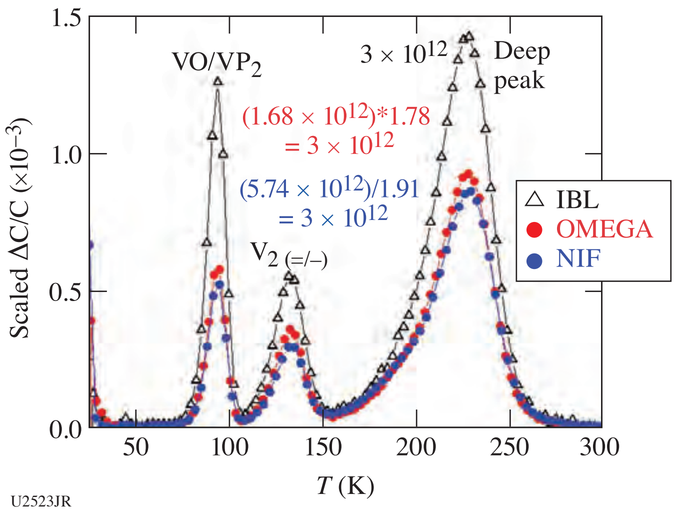

Figure 2
Radiation-induced defects for different 14-MeV neutron facilities. IBL: Ion Beam Laboratory; NIF: National Ignition Facility.

This work was performed at Sandia National Laboratories, a multimission laboratory managed and operated by National Technology and Engineering Solutions of Sandia LLC, a wholly owned subsidiary of Honeywell International Inc. for the U.S. Department of Energy's National Nuclear Security Administration under contract DE-NA0003525. The views expressed in the article do not necessarily represent the views of the U.S. Department of Energy or the United States Government. SAND2019-13909 R.

FY19 Naval Research Laboratory Report on Omega Laser Facility Experiments

M. Karasik

Naval Research Laboratory

Naval Research Laboratory (NRL) researchers in collaboration with LLE conducted tests of the high-Z coating hybrid drive with spherical shells on OMEGA. Building on data and insight from NIKE and OMEGA EP experiments, the shot day experiments (see Fig. 1) focused on coating pre-expansion needed for effective imprint suppression with the coating and on shell radiography for measuring the areal mass perturbations at the early stages of implosions. Two methods of coating pre-expansion were tested: direct low-power laser beam prepulse and indirect soft x-ray–driven pre-expansion. The low-power laser prepulse required a nonstandard beamline operation with amplification stages turned off (developed by the LLE laser operators for these shots).

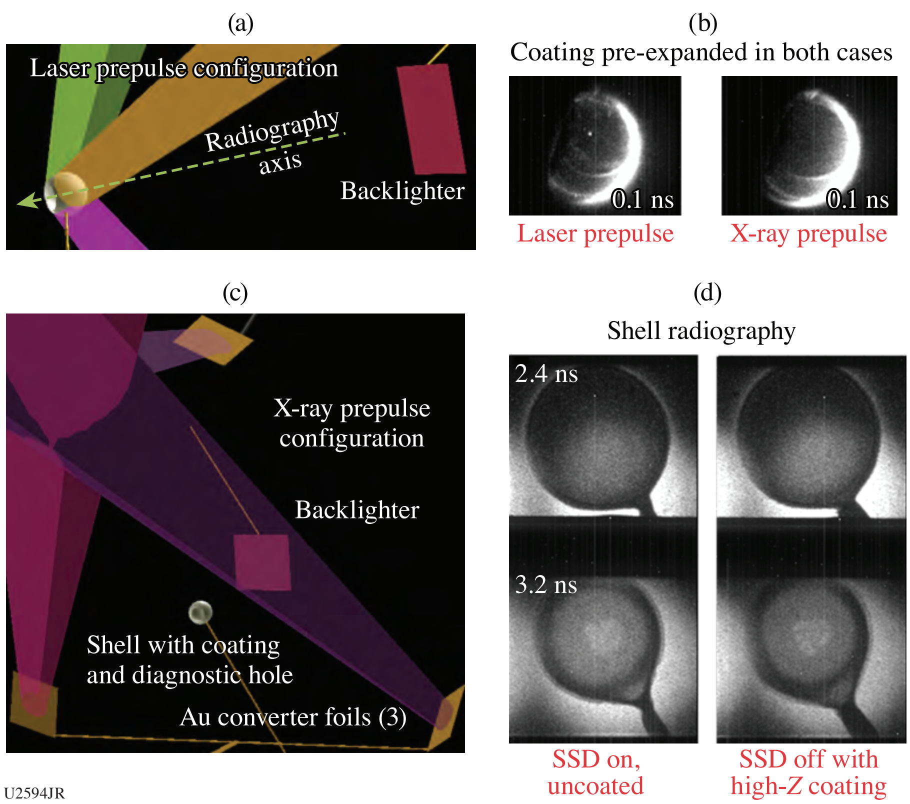

Figure 1
[(a),(b)] Two experimental configurations for high-Z coating pre-expansion: (a) direct laser prepulse and (b) x-ray prepulse (bottom left). (c) Self-emission shows coating was expanded in both laser prepulse and x-ray prepulse configurations. (d) Example shell radiography for two shots: an uncoated shell with maximally smoothed SSD drive and a shell with high-Z coating pre-expanded by the x-ray prepulse with no SSD smoothing.

The x-ray prepulse utilized a converter foil design developed on our OMEGA EP experiments. Self-emission images of coating dynamics show that successful coating pre-expansion was achieved with both methods. Data were obtained on hydrodynamic growth of pre-imposed target perturbations. Radiography images show similar results for the case of maximum smoothing using the smoothing by spectral dispersion (SSD) drive on an uncoated shell and for the case of no SSD on a high-*Z*–coated shell. Detailed analysis is underway.

FY19 CELIA Report on Omega Laser Facility Experiments

Wire Point-Projection X-Ray Radiography of Rayleigh–Taylor Instabilities on OMEGA EP

Principal Investigators: A. Casner, V. Bouffetier, and L. Ceurvorst (CELIA, University of Bordeaux); G. Rigon, P. Mabey, and M. Koenig (Ecole Polytechnique); L. Antonelli, M. Khan, and N. Woolsey (University of York); R. Scott and K. Glize (Rutherford Appleton Laboratory); and W. Theobald (LLE)

The advent of MJ-class laser facilities such as the National Ignition Facility (NIF) and Laser Mégajoule's (LMJ's) PETAL makes it possible to explore states of matter in the laboratory that are relevant for astrophysics and high-energy-density (HED) plasmas under extreme conditions of pressure. For the case of high-Mach-number turbulent flows, the NIF and LMJ-PETAL are unique energy drivers because targets can be accelerated over larger areas and longer time periods than previously achieved on any other laser facilities. This enables hydrodynamic instabilities, such as the Rayleigh–Taylor instability (RTI) or Kelvin–Helmholtz instability, to be driven into their turbulent stage of development. However, even if x-ray imaging diagnostics for hydrodynamic instabilities experiments have improved over the past two decades, further developments are still needed to elevate our understanding and simulations of turbulent flows in HED plasmas.[1]

We report here on a novel planar RTI platform that takes advantage of OMEGA EP short-pulse beams to perform wire point-projection x-ray radiography.[2] The platform was first developed at the LULI2000 Laser Facility in France.[3] The experimental configuration is shown in Fig. 1. The drive laser intensity was $I \sim 2 \times 10^{14}$ W/cm^2 at 2ω with a pulse duration of 1.5 ns. The

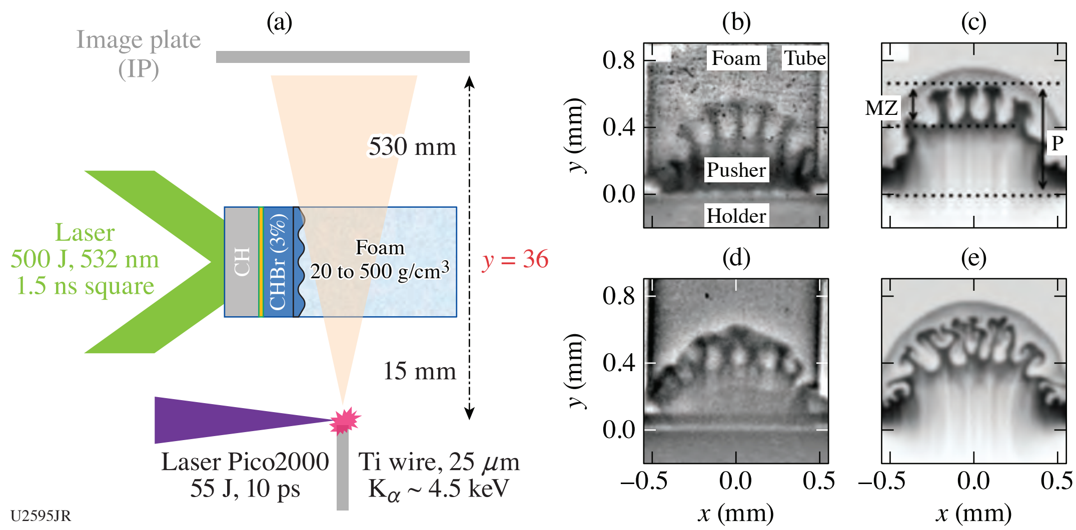

Figure 1
(a) Sketch of target composition and materials for deceleration-phase RTI experiments on LULI2000. [(b)–(e)] Comparison of [(b) and (d)] experimental and [(c) and (e)] synthetic radiographs taken at t = 30 ns for a foam with a density of 100 mg/cm^3. The mixing zone (MZ) is defined as the distance between peak and bubble.[2]

Pico2000 beam (55 J, 10 ps) was used in bottom-up geometry[2] to acquire snapshots of RTI during the linear and highly nonlinear phases. RTI is triggered during the deceleration phase with modulated targets embedded within low-density resorcinol formaldehyde foam ($C_{15}H_{12}O_4$).

The modulated package (monomode or multimode) decelerates into the lighter-foam medium, typically with densities ranging from 50 to 500 mg/cm^3. Typical radiographs acquired for foam with 100 mg/cm^3 are shown in Fig. 2. The initial perturbation wavelength and the amplitude were λ = 120 μm and 20 μm peak-to-valley, respectively. The highly nonlinear regime of the RTI was reached, as can be seen by the development of mushrooms at the spike heads. *FLASH* simulations[3] agreed fairly well with the experimental radiographs [see Figs. 1(c) and 1(e)].

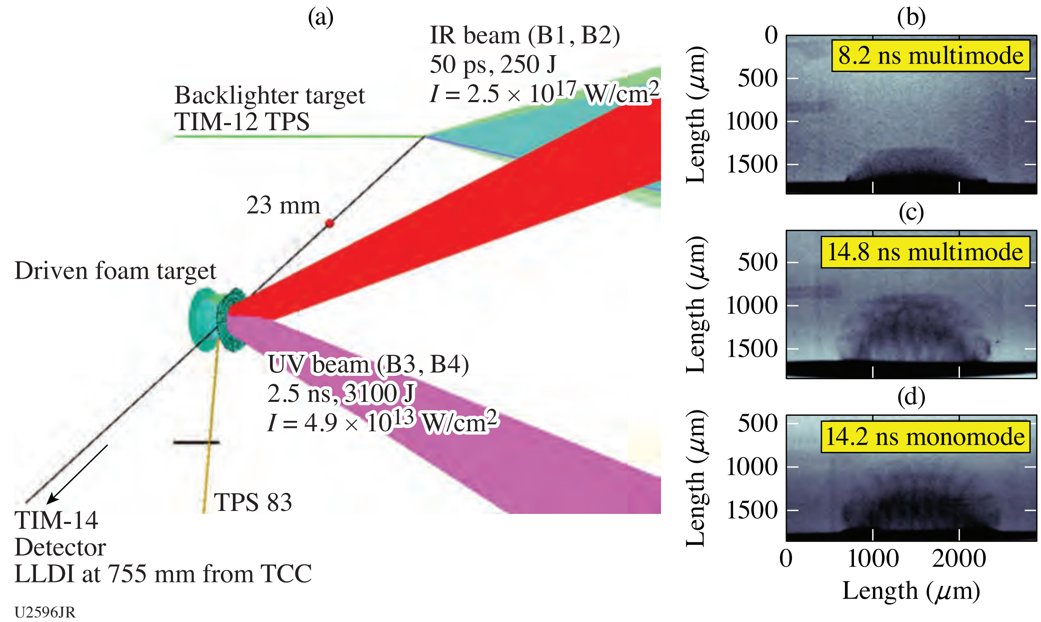

Figure 2
(a) TurboHEDP-EP-19A setup and [(b)–(d)] experimental data; [(b),(c)] multimode initial condition at t = 8.2 and 14.8 ns, respectively. TIM: ten-inch manipulator; TPS: Target Positioning System; TCC: target chamber center.

A scaled-up version of the LULI2000 platform was successfully commissioned on OMEGA EP in May 2019. Going to a larger facility such as OMEGA EP allowed the modulated CH/foam targets to be driven at higher laser energies with better beam quality. Figure 2(a) shows the experimental setup. The two driving UV (λ = 0.35 μm) laser beams (B3, B4) provided an energy of 1550 J/beam in a 1.25-ns-sq pulse and were focused on a CH ablator (10 μm thick) with a diameter of 3.1 mm. Behind the CH ablator, a preheat shield protects a modulated CHBr (5% atomic fraction) in contact with a cylinder (1.8-mm internal diameter, 1.5 mm in length) filled with a foam at 20 mg/cm^3 to trigger RTI growth in deceleration. The UV beams were equipped with SG8-1100 distributed phase plates that produced a laser spot with a diameter of 930 μm (1/e value of peak fluence) and a fluence distribution envelope that is well described by a super-Gaussian function with an order of 6.0. The UV laser intensity was 2×10^{14} W/cm^2 per beam. The IR beams B1 or B2 were focused normal onto the Ti wire with the wire aligned along the axis to TIM-14, which contained a passive imaging-plate detector plate in a heavimet shielded box [LLNL Laue diffraction imager (LLDI) located at 755 mm from target chamber center]. The wire backlighter produced a strong emission between 4.5 and 5.5 keV, predominately from the He$_\alpha$ and Ly$_\alpha$ resonance lines. The distance from backlighter to CH/foam cylinder was 2.3 cm, and the distance from the CH/foam cylinder to the IP detector was 74 cm, providing a 38$\times$ magnification. Resolution Au grids were mounted on top of the cylinder and were used to infer the spatial resolution, which was found to be 33 μm.

Preliminary results of nonlinear RTI are shown in Figs. 2(b)–2(d) for the two different initial conditions (single-mode and two-mode pattern). The quality of the data is not as high as that acquired on LULI2000. A deliberate choice was also made to work with targets nearly twice as large in diameter (1.8 mm instead of 1 mm), which induces tight constraints on target alignment. Nevertheless, these preliminary data compare reasonably well with ongoing *FLASH* calculations. A follow-up campaign is envisioned for XPCI imaging of RT instabilities.

This material is based upon work supported by the Agence Nationale de la Recherche under the ANR project TurboHEDP (ANR-15-CE30-0011).

1. A. Casner *et al*., High Power Laser Sci. Eng. **6**, e44 (2018).
2. E. Brambrink *et al*., High Power Laser Sci. Eng. **4**, e30 (2016).
3. G. Rigon *et al*., Phys. Rev. E **100**, 021201 (2019).

FY19 Rutherford Appleton Laboratory Report on Omega Laser Facility Experiments

Evaluation of New Laser Direct-Drive Pulse Shapes on OMEGA

Principal Investigators: R. H. H. Scott and K. Glize (Rutherford Appleton Laboratory); L. Antonelli, M. Khan, and N. Woolsey (University of York); W. Theobald, C. Stoeckl, M. S. Wei, and R. Betti (LLE); J. A. Frenje (Massachusetts Institute of Technology); and A. Casner and D. Batani (CELIA)

The laser direct-drive approach to inertial fusion employs complex pulse shapes that are shaped in time. This temporal shaping dictates many implosion parameters including the implosion "adiabat" (ratio of the pressure to the Fermi pressure), the velocity, the growth rate of the Rayleigh–Taylor instability, etc.

HYADES[1] simulations of a large OMEGA DT cryo data set show very good agreement to a wide range of experimental implosion parameters, despite being limited to one spatial dimension (D) as shown in Fig. 1. A surprising finding from this work is that, according to *HYADES*, the low-adiabat, triple-picket pulse shapes that were originally designed to be highly performing would not perform well even in 1-D. The *HYADES* code was used to design a new high-performing pulse shape. The evaluation of this new pulse shape was the primary goal of this experiment. A secondary goal was the evaluation of a novel hot-electron divergence measurement methodology using a buried Cu fluor layer within the target.

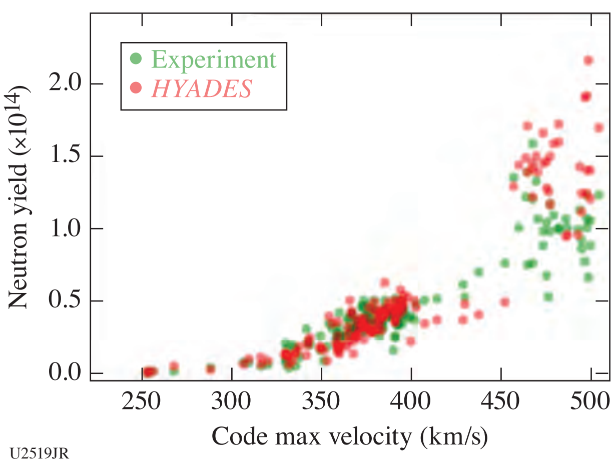

Figure 1
Experimental neutron yield (green points) versus *HYADES* predicted yields. The *HYADES* predictions show a good predictive capability up to ~475 km/s.

The targets employed were 860-μm-outer-diam CH shells with 27-μm wall thickness. Some of the targets also had a 1.5-μm-wide, 4% (by atom number) Cu dopant layer offset 1 μm from the shell's inner surface. In all cases the targets were filled with 20 atm of deuterium gas.

By varying the initial picket amplitude and the delay between the picket and foot of the pulse, the calculated adiabat of the implosion was varied. Yield over clean (YOC) is defined as the experimental yield divided by the 1-D yield. In this experiment we found a strong scaling of YOC with calculated implosion adiabat, with the highest adiabats having a YOC of 0.89. Although analysis of this work is ongoing, this initial experiment indicates that were an implosion to be fielded on an OMEGA DT cryogenic implosion employing this new pulse shape, it would exceed current performance levels.

Generally, the OMEGA laser performed excellently. The major issue on the day was that we lost a number of targets, apparently due to vibrations in the target insertion system. Diagnostics performed excellently except for the gated spherical crystal imager, which could not be timed and therefore yielded no data.

This work was supported by EPSRC grants EP/P023460/1 and EP/P026796/1.

1. Cascade Applied Sciences Inc., Longmont, CO 80503, http://casinc.com/index.html.

Publications and Conference Presentations

Publications

R. Adam, G. Chen, D. E. Bürgler, T. Shou, I. Komissarov, S. Heidtfeld, H. Hardtdegen, M. Mikulics, C. M. Schneider, and R. Sobolewski, "Magnetically and Optically Tunable Terahertz Radiation from Ta/NiFe/Pt Spintronic Nanolayers Generated by Femtosecond Laser Pulses," Appl. Phys. Lett. **114**, 212405 (2019).

H. Aluie, "Convolutions on the Sphere: Commutation with Differential Operators," Int. J. Geomath. **10**, 9 (2019).

S.-W. Bahk, "Current Status of Chirped–Pulse Amplification Technology and Its Applications," Phys. High Technol. **27**, 16 (2018).

K. A. Bauer, M. Heimbueger, S. Sampat, L. J. Waxer, E. C. Cost, J. H. Kelly, V. Kobilansky, J. Kwiatkowski, S. F. B. Morse, D. Nelson, D. Weiner, G. Weselak, and J. Zou, "Comparison of On-Shot, In-Tank, and Equivalent-Target-Plane Measurements of the OMEGA Laser System Focal Spot," Proc. SPIE **10898**, 108980G (2019).

I. A. Begishev, M. Romanofsky, S. Carey, R. Chapman, G. Brent, M. J. Shoup III, J. D. Zuegel, and J. Bromage, "High-Efficiency, Large-Aperture Fifth-Harmonic–Generation of 211-nm Pulses in Ammonium Dihydrogen Phosphate Crystals for Fusion Diagnostics," Proc. SPIE **10898**, 108980N (2019).

X. Bian and H. Aluie, "Decoupled Cascades of Kinetic and Magnetic Energy in Magnetohydrodynamic Turbulence," Phys. Rev. Lett. **122**, 135101 (2019).

W. A. Bittle, M. Bock, R. Boni, J. Kendrick, A. Sorce, and C. Sorce, "A Rate-Doubled 10-GHz Fiducial Comb Generator for Precision Optical Timing Calibration," Rev. Sci. Instrum. **90**, 035103 (2019).

D. Broege and J. Bromage, "Measurements of Heat Flow from Surface Defects in Lithium Triborate," Opt. Express **27**, 10,067 (2019).

D. Broege, S. Fochs, G. Brent, J. Bromage, C. Dorrer, R. F. Earley, M. J. Guardalben, J. A. Marozas, R. G. Roides, D. Weiner, J. Sethian, X. Wang, D. Weiner, J. Zweiback, and J. D. Zuegel, "The Dynamic Compression Sector Laser: A 100-J UV Laser for Dynamic Compression Research," Rev. Sci. Instrum. **90**, 053001 (2019).

J. Bromage, S.-W. Bahk, I. A. Begishev, C. Dorrer, M. J. Guardalben, B. N. Hoffman, J. B. Oliver, R. G. Roides, E. M. Schiesser, M. J. Shoup III, M. Spilatro, B. Webb, D. Weiner, and J. D. Zuegel, "Technology Development for Ultraintense All-OPCPA Systems," High Power Laser Sci. Eng. **7**, e4 (2019).

S. Bucht, D. Haberberger, J. Bromage, and D. H. Froula, "Methodology for Designing Grism Stretchers for Idler-Based Optical Parametric Chirped-Pulse-Amplification Systems," J. Opt. Soc. Am. B **36**, 2325 (2019).

D. Cao, R. C. Shah, S. P. Regan, R. Epstein, I. V. Igumenshchev, V. Gopalaswamy, A. R. Christopherson, W. Theobald, P. B. Radha, and V. N. Goncharov, "Interpreting the Electron Temperature Inferred from X-Ray Continuum Emission for Direct-Drive Inertial Confinement Fusion Implosions on OMEGA," Phys. Plasmas **26**, 082709 (2019).

M. Chorel, S. Papernov, A. A. Kozlov, B. N. Hoffman, J. B. Oliver, S. G. Demos, T. Lanternier, É. Lavastre, L. Lamaignère, N. Roquin, B. Bousquet, N. Bonod, and J. Néauport, "Influence of Absorption-Edge Properties on Subpicosecond Intrinsic Laser-Damage Threshold at 1053 nm in Hafnia and Silica Monolayers," Opt. Express **27**, 16,922 (2019).

A. R. Christopherson, R. Betti, and J. D. Lindl, "Thermonuclear Ignition and the Onset of Propagating Burn in Inertial Fusion Implosions," Phys. Rev. E **99**, 021201(R) (2019).

A. Colaïtis, J. P. Palastro, R. K. Follett, I. V. Igumenshchev, and V. Goncharov, "Real and Complex Valued Geometrical Optics Inverse Ray-Tracing for Inline Field Calculations," Phys. Plasmas **26**, 032301 (2019).

A. S. Davies, D. Haberberger, J. Katz, S. Bucht, J. P. Palastro, W. Rozmus, and D. H. Froula, "Picosecond Thermodynamics in Underdense Plasmas Measured with Thomson Scattering," Phys. Rev. Lett. **122**, 155001 (2019).

J. R. Davies, D. H. Barnak, R. Betti, E. M. Campbell, V. Yu. Glebov, E. C. Hansen, J. P. Knauer, J. L. Peebles, and A. B. Sefkow, "Inferring Fuel Areal Density from Secondary Neutron Yields in Laser-Driven Magnetized Liner Inertial Fusion," Phys. Plasmas **26**, 022706 (2019).

J. DeGroote Nelson, T. Z. Kosc, and P. C. Nelson, "The Optics Suitcase: Educational Outreach Tool for Inspiring Careers in Light," Proc. SPIE **11143**, 111432N (2019).

J. A. Delettrez, T. J. B. Collins, and C. Ye, "Determining Acceptable Limits of Fast-Electron Preheat in Direct-Drive-Ignition-Scale Target Designs," Phys. Plasmas **26**, 062705 (2019).

S. G. Demos, B. N. Hoffman, C. W. Carr, D. A. Cross, R. A. Negres, and J. D. Bude, "Mechanisms of Laser-Induced Damage in Absorbing Glasses with Nanosecond Pulses," Opt. Express **27**, 9975 (2019).

S. G. Demos, J. C. Lambropoulos, R. A. Negres, M. J. Matthews, and S. R. Qiu, "Dynamics of Secondary Contamination from the Interaction of High-Power Laser Pulses with Metal Particles Attached on the Input Surface of Optical Components," Opt. Express **27**, 23,515 (2019).

Y. H. Ding, A. J. White, S. X. Hu, O. Certik, and L. A. Collins, "*Ab Initio* Studies on the Stopping Power of Warm Dense Matter with Time-Dependent Orbital-Free Density Functional Theory," Phys. Rev. Lett. **121**, 145001 (2018).

W. R. Donaldson and A. Consentino, "Co-Timing UV and IR Laser Pulses on the OMEGA EP Laser System," Proc. SPIE **10898**, 108980O (2019).

C. Dorrer, "Spatiotemporal Metrology of Broadband Optical Pulses," IEEE J. Sel. Top. Quantum Electron. **25**, 3100216 (2019).

C. Dorrer and S.-W. Bahk, "Spatio-Spectral Characterization of Broadband Fields Using Multispectral Imaging," Opt. Express **26**, 33,387 (2018).

C. Dorrer and R. J. Brown, "Stable Low-Repetition-Rate Time-Lens Picosecond Seed Source," IEEE Photonics Technol. Lett. **30**, 1854 (2018).

C. Dorrer and J. Qiao, "Direct Binary Search for Improved Coherent Beam Shaping and Optical Differentiation Wavefront Sensing," Appl. Opt. **57**, 8557 (2018).

T. Filkins and J. Katz, "Design of a Free-Space Image-Relay Optical Time Domain Reflectometer to Measure Fiber-Optic Time Delays at Inertial Confinement Fusion Relevant Wavelengths," Proc. SPIE **11114**, 1111417 (2019).

R. K. Follett, J. G. Shaw, J. F. Myatt, V. N. Goncharov, D. H. Edgell, D. H. Froula, and J. P. Palastro, "Ray-Based Modeling of Cross-Beam Energy Transfer at Caustics," Phys. Rev. E **98**, 043202 (2018).

C. J. Forrest, A. Deltuva, W. U. Schröder, A. V. Voinov, J. P. Knauer, E. M. Campbell, G. W. Collins, V. Yu. Glebov, O. M. Mannion, Z. L. Mohamed, P. B. Radha, S. P. Regan, T. C. Sangster, and C. Stoeckl, "Deuteron Breakup Induced by 14-MeV Neutrons from Inertial Confinement Fusion," Phys. Rev. C **100**, 034001 (2019).

D. H. Froula, J. P. Palastro, D. Turnbull, A. Davies, L. Nguyen, A. Howard, D. Ramsey, P. Franke, S.-W. Bahk, I. A. Begishev, R. Boni, J. Bromage, S. Bucht, R. K. Follett, D. Haberberger, G. W. Jenkins, J. Katz, T. J. Kessler, J. L. Shaw, and J. Vieira, "Flying Focus: Spatial and Temporal Control of Intensity for Laser-Based Applications," Phys. Plasmas **26**, 032109 (2019) (invited).

R. Ghosh, O. Swart, S. Westgate, B. L. Miller, and M. Z. Yates, "Antibacterial Copper–Hydroxyapatite Composite Coatings via Electrochemical Synthesis," Langmuir **35**, 5957 (2019).

V. Yu. Glebov, M. J. Eckart, C. J. Forrest, G. P. Grim, E. P. Hartouni, R. Hatarik, J. P. Knauer, A. S. Moore, S. P. Regan, T. C. Sangster, D. J. Schlossberg, and C. Stoeckl, "Testing a Cherenkov Neutron Time-of-Flight Detector on OMEGA," Rev. Sci. Instrum. **89**, 10I122 (2018).

V. Gopalaswamy, R. Betti, J. P. Knauer, N. Luciani, D. Patel, K. M. Woo, A. Bose, I. V. Igumenshchev, E. M. Campbell, K. S. Anderson, K. A. Bauer, M. J. Bonino, D. Cao, A. R. Christopherson, G. W. Collins, T. J. B. Collins, J. R. Davies, J. A. Delettrez, D. H. Edgell, R. Epstein, C. J. Forrest, D. H. Froula, V. Y. Glebov, V. N. Goncharov, D. R. Harding, S. X. Hu, D. W. Jacobs-Perkins, R. T. Janezic, J. H. Kelly, O. M. Mannion, A. Maximov, F. J. Marshall, D. T. Michel, S. Miller, S. F. B. Morse, J. Palastro, J. Peebles, P. B. Radha, S. P. Regan, S. Sampat, T. C. Sangster, A. B. Sefkow, W. Seka, R. C. Shah,

W. T. Shmayda, A. Shvydky, C. Stoeckl, A. A. Solodov, W. Theobald, J. D. Zuegel, M. Gatu Johnson, R. D. Petrasso, C. K. Li, and J. A. Frenje, "Tripled Yield in Direct-Drive Laser Fusion Through Statistical Modelling," Nature **565**, 581 (2019).

L. Guazzotto and R. Betti, "Two-Fluid Burning-Plasma Analysis for Magnetic Confinement Fusion Devices," Plasma Phys. Control. Fusion **61**, 085028 (2019).

H. Habara, T. Iwawaki, T. Gong, M. S. Wei, S. T. Ivancic, W. Theobald, C. M. Krauland, S. Zhang, G. Fiksel, and K. A. Tanaka, "A Ten-Inch Manipulator (TIM) Based Fast-Electron Spectrometer with Multiple Viewing Angles (OU-ESM)," Rev. Sci. Instrum. **90**, 063501 (2019).

E. C. Hansen, D. H. Barnak, P.-Y. Chang, R. Betti, E. M. Campbell, J. R. Davies, J. P. Knauer, J. L. Peebles, S. P. Regan, and A. B. Sefkow, "Optimization of Laser-Driven Cylindrical Implosions on the OMEGA Laser," Phys. Plasmas **25**, 122701 (2018).

E. C. Hansen, P. Hartigan, A. Frank, A. Wright, and J. C. Raymond, "Simulating Radiative Magnetohydrodynamical Flows with ASTROBEAR: Implementation and Applications of Non-Equilibrium Cooling," Mon. Not. R. Astron. Soc. **481**, 3098 (2018).

D. R. Harding, M. J. Bonino, W. Sweet, M. Schoff, A. Greenwood, N. Satoh, M. Takagi, and A. Nikroo, "Properties of Vapor-Deposited and Solution-Processed Targets for Laser-Driven Inertial Confinement Fusion Experiments," Matter and Radiation at Extremes **3**, 312 (2018).

R. J. Henchen, M. Sherlock, W. Rozmus, J. Katz, P. E. Masson-Laborde, D. Cao, J. P. Palastro, and D. H. Froula, "Measuring Heat Flux from Collective Thomson Scattering with Non-Maxwellian Distribution Functions," Phys. Plasmas **26**, 032104 (2019) (invited).

A. J. Howard, D. Turnbull, A. S. Davies, P. Franke, D. H. Froula, and J. P. Palastro, "Photon Acceleration in a Flying Focus," Phys. Rev. Lett. **123**, 124801 (2019).

S. X. Hu, V. N. Goncharov, P. B. Radha, S. P. Regan, and E. M. Campbell, "Microphysics Studies for Direct-Drive Inertial Confinement Fusion," Nucl. Fusion **59**, 032011 (2019).

I. V. Igumenshchev, A. L. Velikovich, V. N. Goncharov, R. Betti, E. M. Campbell, J. P. Knauer, S. P. Regan, A. J. Schmitt, R. C. Shah, and A. Shvydky, "Rarefaction Flows and Mitigation of Imprint in Direct-Drive Implosions," Phys. Rev. Lett. **123**, 065001 (2019).

K. R. P. Kafka and S. G. Demos, "Interaction of Short Laser Pulses with Model Contamination Microparticles on a High Reflector," Opt. Lett. **44**, 1844 (2019).

A. Kar, T. R. Boehly, P. B. Radha, D. H. Edgell, S. X. Hu, P. M. Nilson, A. Shvydky, W. Theobald, D. Cao, K. S. Anderson, V. N. Goncharov, and S. P. Regan, "Simulated Refraction-Enhanced X-Ray Radiography of Laser-Driven Shocks," Phys. Plasmas **26**, 032705 (2019).

V. V. Karasiev, S. X. Hu, M. Zaghoo, and T. R. Boehly, "Exchange-Correlation Thermal Effects in Shocked Deuterium: Softening the Principal Hugoniot and Thermophysical Properties," Phys. Rev. B **99**, 214110 (2019).

V. V. Karasiev, S. B. Trickey, and J. W. Dufty, "Status of Free-Energy Representations for the Homogeneous Electron Gas," Phys. Rev. B **99**, 195134 (2019).

K. Kopp and S. G. Demos, "Microscopy with Ultraviolet Surface Excitation (MUSE) Enables Translation of Optical Biopsy Principles to Enhance Life Science Education," Proc. SPIE **10873**, 108731D (2019).

A. Koroliov, G. Chen, K. M. Goodfellow, A. N. Vamivakas, Z. Staniszewski, P. Sobolewski, M. El Fray, A. Łaszcz, A. Czerwinski, C. P. Richter, and R. Sobolewski, "Terahertz Time-Domain Spectroscopy of Graphene Nanoflakes Embedded in Polymer Mix," Appl. Sci. **9**, 391 (2019).

A. A. Kozlov, J. C. Lambropoulos, J. B. Oliver, B. N. Hoffman, and S. G. Demos, "Mechanisms of Picosecond Laser-Induced Damage in Common Multilayer Dielectric Coatings," Sci. Rep. **9**, 607 (2019).

B. E. Kruschwitz, J. Kwiatkowski, C. Dorrer, M. Barczys, A. Consentino, D. H. Froula, M. J. Guardalben, E. M. Hill, D. Nelson, M. J. Shoup III, D. Turnbull, L. J. Waxer, and D. Weiner, "Tunable UV Upgrade on OMEGA EP," Proc. SPIE **10898**, 1089804 (2019).

A. Lees and H. Aluie, "Baropycnal Work: A Mechanism for Energy Transfer Across Scales," Fluids **4**, 92 (2019).

O. M. Mannion, V. Yu. Glebov, C. J. Forrest, J. P. Knauer, V. N. Goncharov, S. P. Regan, T. C. Sangster, C. Stoeckl, and

M. Gatu Johnson, "Calibration of a Neutron Time-of-Flight Detector with a Rapid Instrument Response Function for Measurements of Bulk Fluid Motion on OMEGA," Rev. Sci. Instrum. **89**, 10I131 (2018).

A. L. Milder, S. T. Ivancic, J. P. Palastro, and D. H. Froula, "Impact of Non-Maxwellian Electron Velocity Distribution Functions on Inferred Plasma Parameters in Collective Thomson Scattering," Phys. Plasmas **26**, 022711 (2019).

S. C. Miller, J. P. Knauer, C. J. Forrest, V. Yu. Glebov, P. B. Radha, and V. N. Goncharov, "Fuel-Shell Interface Instability Growth Effects on the Performance of Room Temperature Direct-Drive Implosions," Phys. Plasmas **26**, 082701 (2019).

J. P. Palastro, J. G. Shaw, R. K. Follett, A. Colaïtis, D. Turnbull, A. V. Maximov, V. N. Goncharov, and D. H. Froula, "Resonance Absorption of a Broadband Laser Pulse," Phys. Plasmas **25**, 123104 (2018).

S. Papernov, "Spectroscopic Setup for Submicrometer-Resolution Mapping of Low-Signal Absorption and Luminescence Using Photothermal Heterodyne Imaging and Photon-Counting Techniques," Appl. Opt. **58**, 3908 (2019).

R. Paul, S. X. Hu, and V. V. Karasiev, "Anharmonic and Anomalous Trends in the High-Pressure Phase Diagram of Silicon," Phys. Rev. Lett. **122**, 125701 (2019).

J. L. Peebles, S. X. Hu, W. Theobald, V. N. Goncharov, N. Whiting, P. M. Celliers, S. J. Ali, G. Duchateau, E. M. Campbell, T. R. Boehly, and S. P. Regan, "Direct-Drive Measurements of Laser-Imprint-Induced Shock Velocity Nonuniformities," Phys. Rev. E **99**, 063208 (2019).

B. W. Plansinis, W. R. Donaldson, and G. P. Agrawal, "A Time-to-Frequency Converter for Measuring the Shape of Short Optical Pulses," Rev. Sci. Instrum. **90**, 083106 (2019).

S. P. Regan, V. N. Goncharov, T. C. Sangster, E. M. Campbell, R. Betti, J. W. Bates, K. Bauer, T. Bernat, S. Bhandarkar, T. R. Boehly, M. J. Bonino, A. Bose, D. Cao, L. Carlson, R. Chapman, T. Chapman, G. W. Collins, T. J. B. Collins, R. S. Craxton, J. A. Delettrez, D. H. Edgell, R. Epstein, M. Farrell, C. J. Forrest, R. K. Follett, J. A. Frenje, D. H. Froula, M. Gatu Johnson, C. R. Gibson, L. Gonzalez, C. Goyon, V. Yu. Glebov, V. Gopalaswamy, A. Greenwood, D. R. Harding, M. Hohenberger, S. X. Hu, H. Huang, J. Hund, I. V. Igumenshchev, D. W. Jacobs-Perkins, R. T. Janezic, M. Karasik, J. H. Kelly, T. J. Kessler, J. P. Knauer, T. Z. Kosc, R. Luo, S. J. Loucks, J. A. Marozas, F. J. Marshall, M. Mauldin, R. L. McCrory, P. W. McKenty, D. T. Michel, P. Michel, J. D. Moody, J. F. Myatt, A. Nikroo, P. M. Nilson, S. P. Obenschain, J. P. Palastro, J. Peebles, R. D. Petrasso, N. Petta, P. B. Radha, J. E. Ralph, M. J. Rosenberg, S. Sampat, A. J. Schmitt, M. J. Schmitt, M. Schoff, W. Seka, R. Shah, J. R. Rygg, J. G. Shaw, R. Short, W. T. Shmayda, M. J. Shoup III, A. Shvydky, A. A. Solodov, C. Sorce, M. Stadermann, C. Stoeckl, W. Sweet, C. Taylor, R. Taylor, W. Theobald, D. P. Turnbull, J. Ulreich, M. D. Wittman, K. M. Woo, K. Youngblood, and J. D. Zuegel, "The National Direct-Drive Inertial Confinement Fusion Program," Nucl. Fusion **59**, 032007 (2019).

B. S. Rice, J. Ulreich, and M. J. Shoup III, "Prediction of Deuterium–Tritium Ice-Layer Uniformity in Direct-Drive Confinement Fusion Target Capsules," in *Proceedings of NAFEMS World Congress 2019* (NAFEMS, Glasgow, Scotland 2019).

M. J. Rosenberg, R. Epstein, A. A. Solodov, W. Seka, J. F. Myatt, P. A. Michel, M. A. Barrios, D. B. Thorn, M. Hohenberger, J. D. Moody, and S. P. Regan, "X-Ray Spectroscopy of Planar Laser-Plasma Interaction Experiments at the National Ignition Facility," Phys. Plasmas **26**, 012703 (2019).

M. J. Rosenberg, D. B. Thorn, N. Izumi, D. Williams, M. Rowland, G. Torres, M. Haugh, P. Hillyard, N. Adelman, T. Schuler, M. A. Barrios, J. P. Holder, M. B. Schneider, K. B. Fournier, D. K. Bradley, and S. P. Regan, "Image-Plate Sensitivity to X Rays at 2 to 60 keV," Rev. Sci. Instrum. **90**, 013506 (2019).

M. Sadek and H. Aluie, "Extracting the Spectrum of a Flow by Spatial Filtering," Phys. Rev. Fluids **3**, 124610 (2018).

S. Sampat, T. Z. Kosc, K. A. Bauer, R. D. Dean, W. R. Donaldson, J. Kwiatkowski, R. Moshier, A. L. Rigatti, M. H. Romanofsky, L. J. Waxer, and J. H. Kelly, "Power Balancing the Multibeam OMEGA Laser," Appl. Opt. **57**, 9571 (2018).

S. Sampat, T. Z. Kosc, K. A. Bauer, R. D. Dean, W. R. Donaldson, J. Kwiatkowski, R. Moshier, A. L. Rigatti, M. H. Romanofsky, L. J. Waxer, and J. H. Kelly, "Power Balancing a Multibeam Laser," Proc. SPIE **10898**, 108980A (2019).

E. M. Schiesser, S.-W. Bahk, J. Bromage, and J. P. Rolland "Gaussian Curvature and Stigmatic Imaging Relations for the Design of an Unobscured Reflective Relay," Opt. Lett. **43**, 4855 (2018).

J. Serafini, A. Hossain, R. B. James, S. B. Trivedi, and R. Sobolewski, “Time-Resolved, Nonequilibrium Carrier and Coherent Acoustic Phonon Dynamics in (Cd,Mg)Te Single Crystals for Radiation Detectors,” Semicond. Sci. Technol. **34**, 035021 (2019).

R. V. Shapovalov, G. Brent, R. Moshier, M. Shoup, R. B. Spielman, and P.-A. Gourdain, “Design of 30-T Pulsed Magnetic Field Generator for Magnetized High-Energy-Density Plasma Experiments,” Phys. Rev. Accel. Beams **22**, 080401 (2019).

R. B. Spielman and D. B. Reisman, “On the Design of Magnetically Insulated Transmission Lines for *Z*-Pinch Loads,” Matter Radiat. Extremes **4**, 027402 (2019).

C. Stoeckl, T. Filkins, R. Jungquist, C. Mileham, N. R. Pereira, S. P. Regan, M. J. Shoup III, and W. Theobald, “Characterization of Shaped Bragg Crystal Assemblies for Narrowband X-Ray Imaging,” Rev. Sci. Instrum. **89**, 10G124 (2018).

C. Stoeckl, C. J. Forrest, V. Yu. Glebov, S. P. Regan, T. C. Sangster, W. U. Schröder, A. Schwemmlein, and W. Theobald, “A Platform for Nuclear Physics Experiments with Laser-Accelerated Light Ions,” Nucl. Instrum. Methods Phys. Res. B **453**, 41 (2019).

M. Stoeckl and A. A. Solodov, “Refining Instrument Response Functions with 3-D Monte Carlo Simulations of Differential Hard X-Ray Spectrometers,” Nucl. Instrum. Methods Phys. Res. A **931**, 162 (2019).

W. Theobald, C. Sorce, M. Bedzyk, S. T. Ivancic, F. J. Marshall, C. Stoeckl, R. C. Shah, M. Lawrie, S. P. Regan, T. C. Sangster, E. M. Campbell, T. J. Hilsabeck, K. Engelhorn, J. D. Kilkenny, D. Morris, T. M. Chung, J. D. Hares, A. K. L. Dymoke-Bradshaw, P. Bell, J. Celeste, A. C. Carpenter, M. Dayton, D. K. Bradley, M. C. Jackson, L. Pickworth, S. R. Nagel, G. Rochau, J. Porter, M. Sanchez, L. Claus, G. Robertson, and Q. Looker, “The Single-Line-of-Sight, Time-Resolved X-Ray Imager Diagnostic on OMEGA,” Rev. Sci. Instrum. **89**, 10G117 (2018).

D. Turnbull, S.-W. Bahk, I. A. Begishev, R. Boni, J. Bromage, S. Bucht, A. Davies, P. Franke, D. Haberberger, J. Katz, T. J. Kessler, A. L. Milder, J. P. Palastro, J. L. Shaw, and D. H. Froula, “Flying Focus and Its Application to Plasma-Based Laser Amplifiers,” Plasma Phys. Control. Fusion **61**, 014022 (2019).

L. J. Waxer, K. A. Bauer, E. C. Cost, M. Heimbueger, J. H. Kelly, V. Kobilansky, S. F. B. Morse, D. Nelson, R. Peck, R. Rinefierd, S. Sampat, M. J. Shoup III, D. Weiner, G. Weselak, and J. Zou, “In-Tank, On-Shot Characterization of the OMEGA Laser System Focal Spot,” Proc. SPIE **10898**, 108980F (2019).

B. Webb, M. J. Guardalben, C. Dorrer, S. Bucht, and J. Bromage, “Simulation of Grating Compressor Misalignment Tolerances and Mitigation Strategies for Chirped-Pulse–Amplification Systems of Varying Bandwidths and Beam Sizes,” Appl. Opt. **58**, 234 (2019).

K. M. Woo, R. Betti, D. Shvarts, O. M. Mannion, D. Patel, V. N. Goncharov, K. S. Anderson, P. B. Radha, J. P. Knauer, A. Bose, V. Gopalaswamy, A. R. Christopherson, E. M. Campbell, J. Sanz, and H. Aluie, “Impact of Three-Dimensional Hot-Spot Flow Asymmetry on Ion-Temperature Measurements in Inertial Confinement Fusion Experiments,” Phys. Plasmas **25**, 102710 (2018).

J. Xin, R. Yan, Z.-H. Wan, D.-J. Sun, J. Zheng, H. Zhang, H. Aluie, and R. Betti, “Two Mode Coupling of the Ablative Rayleigh-Taylor Instabilities,” Phys. Plasmas **26**, 032703 (2019).

M. Zaghoo, T. R. Boehly, J. R. Rygg, P. M. Celliers, S. X. Hu, and G. W. Collins, “Breakdown of Fermi Degeneracy in the Simplest Liquid Metal,” Phys. Rev. Lett. **122**, 085001 (2019).

M. Zaghoo, R. J. Husband and I. F. Silvera, “Striking Isotope Effect on the Metallization Phase Lines of Liquid Hydrogen and Deuterium,” Phys. Rev. B **98**, 104102 (2018).

H. Zhang, R. Betti, R. Yan, D. Zhao, D. Shvarts, and H. Aluie, “Self-Similar Multimode Bubble-Front Evolution of the Ablative Rayleigh-Taylor Instability in Two and Three Dimensions,” Phys. Rev. Lett. **121**, 185002 (2018).

X. Zhang and M. Z. Yates, “Controllable Synthesis of Hydroxyapatite-Supported Palladium Nanoparticles with Enhanced Catalytic Activity,” Surf. Coat. Technol. **351**, 60 (2018).

X. Zhang, Y. Zhang, and M. Z. Yates, “Hydroxyapatite Nanocrystal Deposited Titanium Dioxide Nanotubes Loaded with Antibiotics for Combining Biocompatibility and Antibacterial Properties,” MRS Advances **3**, 1703 (2018).

Omega External Users' Publications

R. Aboushelbaya, A. F. Savin, L. Ceurvorst, J. Sadler, P. A. Norreys, A. S. Davies, D. H. Froula, A. Boyle, M. Galimberti, P. Oliviera, B. Parry, Y. Katzir, and K. Glize, "Single-Shot Frequency-Resolved Optical Gating for Retrieving the Pulse Shape of High Energy Picosecond Pulses," Rev. Sci. Instrum. **89**, 103509 (2018).

F. Albert, N. Lemos, J. L. Shaw, P. M. King, B. B. Pollock, C. Goyon, W. Schumaker, A. M. Saunders, K. A. Marsh, A. Pak, J. E. Ralph, J. L. Martins, L. D. Amorim, R. W. Falcone, S. H. Glenzer, J. D. Moody, and C. Joshi, "Betatron X-Ray Radiation in the Self-Modulated Laser Wakefield Acceleration Regime: Prospects for a Novel Probe at Large Scale Laser Facilities," Nucl. Fusion **59**, 032003 (2019).

A. Antikainen and G. P. Agrawal, "Soliton Supermode Transitions and Total Red Shift Suppression in Multi-Core Fibers," Opt. Lett. **44**, 4159 (2019).

R. L. Berger, C. A. Thomas, K. L. Baker, D. T. Casey, C. S. Goyon, J. Park, N. Lemos, S. F. Khan, M. Hohenberger, J. L. Milovich, D. J. Strozzi, M. A. Belyaev, T. Chapman, and A. B. Langdon, "Stimulated Backscatter of Laser Light from BigFoot Hohlraums on the National Ignition Facility," Phys. Plasmas **26**, 012709 (2019).

L. Berzak Hopkins, S. LePape, L. Divol, A. Pak, E. Dewald, D. D. Ho, N. Meezan, S. Bhandarkar, L. R. Benedetti, T. Bunn, J. Biener, J. Crippen, D. Casey, D. Clark, D. Edgell, D. Fittinghoff, M. Gatu-Johnson, C. Goyon, S. Haan, R. Hatarik, M. Havre, D. Hinkel, H. Huang, N. Izumi, J. Jaquez, O. Jones, S. Khan, A. Kritcher, C. Kong, G. Kyrala, O. Landen, T. Ma, A. MacPhee, B. MacGowan, A. J. Mackinnon, M. Marinak, J. Milovich, M. Millot, P. Michel, A. Moore, S. R. Nagel, A. Nikroo, P. Patel, J. Ralph, H. Robey, J. S. Ross, N. G. Rice, S. Sepke, V. A. Smalyuk, P. Sterne, D. Strozzi, M. Stadermann, P. Volegov, C. Weber, C. Wild, C. Yeamans, D. Callahan, O. Hurricane, R. P. J. Town, and M. J. Edwards, "Toward a Burning Plasma State Using Diamond Ablator Inertially Confined Fusion (ICF) Implosions on the National Ignition Facility (NIF)," Plasma Phys. Control. Fusion **61**, 014023 (2019).

E. G. Blackman and J. A. Tarduno, "Mass, Energy, and Momentum Capture from Stellar Winds by Magnetized and Unmagnetized Planets: Implications for Atmospheric Erosion and Habitability," Mon. Not. R. Astron. Soc. **481**, 5146 (2018).

A. Casner, C. Mailliet, G. Rigon, S. F. Khan, D. Martinez, B. Albertazzi, T. Michel, T. Sano, Y. Sakawa, P. Tzeferacos, D. Lamb, S. Liberatore, N. Izumi, D. Kalantar, P. Di Nicola, J. M. Di Nicola, E. Le Bel, I. Igumenshchev, V. Tikhonchuk, B. A. Remington, J. Ballet, E. Falize, L. Masse, V. A. Smalyuk, and M. Koenig, "From ICF to Laboratory Astrophysics: Ablative and Classical Rayleigh–Taylor Instability Experiments in Turbulent-Like Regimes," Nucl. Fusion **59**, 032002 (2019).

S. Chawla, M. Bailly-Grandvaux, H. S. McLean, P. K. Patel, M. S. Wei, and F. N. Beg, "Effect of Target Material on Relativistic Electron Beam Transport," Phys. Plasmas **26**, 033111 (2019).

A. Chien, L. Gao, H. Ji, X. Yuan, E. G. Blackman, H. Chen, P. C. Efthimion, G. Fiksel, D. H. Froula, K. W. Hill, K. Huang, Q. Lu, J. D. Moody, and P. M. Nilson, "Study of a Magnetically Driven Reconnection Platform Using Ultrafast Proton Radiography," Phys. Plasmas **26**, 062113 (2019).

D. T. Cliche and R. C. Mancini, "Impact of 3D Effects on the Characteristics of a Multi-Monochromatic X-Ray Imager," Appl. Opt. **58**, 4753 (2019).

A. Colaïtis, R. K. Follett, J. P. Palastro, I. Igumenshchev, and V. Goncharov, "Adaptive Inverse Ray-Tracing for Accurate and Efficient Modeling of Cross Beam Energy Transfer in Hydrodynamics Simulations," Phys. Plasmas **26**, 072706 (2019).

A. L. Coleman, M. G. Gorman, R. Briggs, R. S. McWilliams, D. McGonegle, C. A. Bolme, A. E. Gleason, D. E. Fratanduono, R. F. Smith, E. Galtier, H. J. Lee, B. Nagler, E. Granados, G. W. Collins, J. H. Eggert, J. S. Wark, and M. I. McMahon, "Identification of Phase Transitions and Metastability in Dynamically Compressed Antimony Using Ultrafast X-Ray Diffraction," Phys. Rev. Lett. **122**, 255704 (2019).

C. N. Danson, C. Haefner, J. Bromage, T. Butcher, J.-C. F. Chanteloup, E. A. Chowdhury, A. Galvanauskas, L. A. Gizzi, J. Hein, D. I. Hillier, N. W. Hopps, Y. Kato, E. A. Khazanov, R. Kodama, G. Korn, R. Li, Y. Li, J. Limpert, J. Ma, C. H. Nam, D. Neely, D. Papadopoulos, R. R. Penman, L. Qian, J. J. Rocca, A. A. Shaykin, C. W. Siders, C. Spindloe, S. Szatmari, R. M. G. M. Trines, J. Zhu, P. Zhu, and J. D. Zuegel, "Petawatt and Exawatt Class Lasers Worldwide," High Power Laser Sci. Eng. **7**, e54 (2019).

C. A. Di Stefano, F. W. Doss, A. M. Rasmus, K. A. Flippo, and B. M. Haines, "The Modeling of Delayed-Onset Rayleigh–Taylor and Transition to Mixing in Laser-Driven HED Experiments," Phys. Plasmas **26**, 052708 (2019).

L. Divol, D. P. Turnbull, T. Chapman, C. Goyon, and P. Michel, "An Analytical Study of Non-Resonant Transient Cross-Beam Power Transfer Relevant to Recent Progress in Plasma Photonics," Phys. Plasmas **26**, 043101 (2019).

R. P. Drake, "A Journey Through High-Energy-Density Physics," Nucl. Fusion **59**, 035001 (2019).

R. P. Drake and F. W. Doss, "Regimes of the Vishniac–Ryu Decelerating Shock Instability," Astrophys. J. **868**, 23 (2018).

G. Duchateau, S. X. Hu, A. Pineau, A. Kar, B. Chimier, A. Casner, V. Tikhonchuk, V. N. Goncharov, P. B. Radha, and E. M. Campbell, "Modeling the Solid-to-Plasma Transition for Laser Imprinting in Direct-Drive Inertial Confinement Fusion," Phys. Rev. E **100**, 033201 (2019).

T. S. Duffy and R. F. Smith, "Ultra-High Pressure Dynamic Compression of Geological Materials," Front. Earth Sci. **7**, 23 (2019).

K. Engelhorn, T. J. Hilsabeck, J. Kilkenny, D. Morris, T. M. Chung, A. Dymoke-Bradshaw, J. D. Hares, P. Bell, D. Bradley, A. C. Carpenter, M. Dayton, S. R. Nagel, L. Claus, J. Porter, G. Rochau, M. Sanchez, S. Ivancic, C. Sorce, and W. Theobald, "Sub-Nanosecond Single Line-of-Sight (SLOS) X-Ray Imagers," Rev. Sci. Instrum. **89**, 10G123 (2018) (invited).

C.-H. Fann, J. Zhang, M. ElKabbash, W. R. Donaldson, E. M. Campbell, and C. Guo, "Broadband Infrared Plasmonic Metamaterial Absorber with Multipronged Absorption Mechanisms," Opt. Express **27**, 27,917 (2019).

A. Fernandez-Pañella, M. Millot, D. E. Fratanduono, M. P. Desjarlais, S. Hamel, M. C. Marshall, D. J. Erskine, P. A. Sterne, S. Haan, T. R. Boehly, G. W. Collins, J. H. Eggert, and P. M. Celliers, "Shock Compression of Liquid Deuterium up to 1 TPa," Phys. Rev. Lett. **122**, 255702 (2019).

W. Fox, J. Matteucci, C. Moissard, D. B. Schaeffer, A. Bhattacharjee, K. Germaschewski, and S. X. Hu, "Kinetic Simulation of Magnetic Field Generation and Collisionless Shock Formation in Expanding Laboratory Plasmas," Phys. Plasmas **25**, 102106 (2018).

D. E. Fratanduono, M. Millot, A. Fernandez Pañella, P. A. Sterne, G. W. Collins, D. G. Hicks, J. H. Eggert, T. R. Boehly, and P. M. Celliers, "Measurement of the Sound Speed in Dense Fluid Deuterium Along the Cryogenic Liquid Hugoniot," Phys. Plasmas **26**, 012710 (2019).

J. A. Frenje, R. Florido, R. Mancini, T. Nagayama, P. E. Grabowski, H. Rinderknecht, H. Sio, A. Zylstra, M. Gatu Johnson, C. K. Li, F. H. Séguin, R. D. Petrasso, V. Yu. Glebov, and S. P. Regan, "Experimental Validation of Low-Z Ion-Stopping Formalisms Around the Bragg Peak in High-Energy-Density Plasmas," Phys. Rev. Lett. **122**, 015002 (2019).

L. Gao, B. F. Kraus, K. W. Hill, M. Bitter, P. Efthimion, M. B. Schneider, A. G. MacPhee, D. B. Thorn, J. Kilkenny, J. Ayers, R. Kauffman, H. Chen, and D. Nelson, "Absolute Calibration of a Time-Resolved High Resolution X-Ray Spectrometer for the National Ignition Facility," Rev. Sci. Instrum. **89**, 10F125 (2018) (invited).

L. Gao, E. Liang, R. K. Follett, H. Sio, P. Tzeferacos, D. H. Froula, A. Birkel, C. K. Li, D. Lamb, R. Petrasso, W. Fu, M. Wei, and H. Ji, "Mega-Gauss Plasma Jet Creation Using a Ring of Laser Beams," Astrophys. J. Lett. **873**, L11 (2019).

M. Gatu Johnson, B. D. Appelbe, J. P. Chittenden, A. Crilly, J. Delettrez, C. Forrest, J. A. Frenje, V. Yu. Glebov, W. Grimble, B. M. Haines, I. V. Igumenshchev, R. Janezic, J. P. Knauer, B. Lahmann, F. J. Marshall, T. Michel, F. H. Séguin, C. Stoeckl, C. Walsh, A. B. Zylstra, and R. D. Petrasso, "Impact of Imposed Mode 2 Laser Drive Asymmetry on Inertial Confinement Fusion Implosions," Phys. Plasmas **26**, 012706 (2019).

M. Gatu Johnson, B. D. Applebe, J. P. Chittenden, J. Delettrez, C. Forrest, J. A. Frenje, V. Yu. Glebov, W. Grimble, B. M. Haines, I. Igumenshchev, R. Janezic, J. P. Knauer, B. Lahmann, F. J. Marshall, T. Michel, F. H. Séguin, C. Stoeckl, C. Walsh, A. B. Zylstra, and R. D. Petrasso, "Impact of Asymmetries on Fuel Performance in Inertial Confinement Fusion," Phys. Rev. E **98**, 051201(R) (2018).

M. Gatu Johnson, J. Katz, C. Forrest, J. A. Frenje, V. Yu. Glebov, C. K. Li, R. Paguio, C. E. Parker, C. Robillard, T. C. Sangster, M. Schoff, F. H. Séguin, C. Stoeckl, and R. D. Petrasso, "Measurement of Apparent Ion Temperature Using the Magnetic Recoil Spectrometer at the OMEGA Laser Facility," Rev. Sci. Instrum. **89**, 10I129 (2018).

C. G. R. Geddes and J. L. Shaw, "Summary of Working Group 1: Laser-Plasma Wakefield Acceleration," in *2018 IEEE Advanced Accelerator Concepts Workshop (AAC 2018)* (IEEE, New York, 2018), pp. 1–5.

M. R. Gomez, S. A. Slutz, P. F. Knapp, K. D. Hahn, M. R. Weis, E. C. Harding, M. Geissel, J. R. Fein, M. E. Glinsky, S. B. Hansen, A. J. Harvey-Thompson, C. A. Jennings, I. C. Smith, D. Woodbury, D. J. Ampleford, T. J. Awe, G. A. Chandler, M. H. Hess, D. C. Lamppa, C. E. Myers, C. L. Ruiz, A. B. Sefkow, J. Schwarz, D. A. Yager-Elorriaga, B. Jones, J. L. Porter, K. J. Peterson, R. D. McBride, G. A. Rochau, and D. B. Sinars, "Assessing Stagnation Conditions and Identifying Trends in Magnetized Liner Inertial Fusion," IEEE Trans. Plasma Sci. **47**, 2081 (2019).

M. G. Gorman, A. L. Coleman, R. Briggs, R. S. McWilliams, A. Hermann, D. McGonegle, C. A. Bolme, A. E. Gleason, E. Galtier, H. J. Lee, E. Granados, E. E. McBride, S. Rothman, D. E. Fratanduono, R. F. Smith, G. W. Collins, J. H. Eggert, J. S. Wark, and M. I. McMahon, "Recovery of Metastable Dense Bi Synthesized by Shock Compression," Appl. Phys. Lett. **114**, 120601 (2019).

M. G. Gorman, A. L. Coleman, R. Briggs, R. S. McWilliams, D. McGonegle, C. A. Bolme, A. E. Gleason, E. Galtier, H. J. Lee, E. Granados, M. Śliwa, C. Sanloup, S. Rothman, D. E. Fratanduono, R. F. Smith, G. W. Collins, J. H. Eggert, J. S. Wark, and M. I. McMahon, "Femtosecond Diffraction Studies of Solid and Liquid Phase Changes in Shock-Compressed Bismuth," Sci. Rep. **8**, 16927 (2018).

P.-A. Gourdain, M. B. Adams, M. Evans, H. R. Hasson, R. V. Shapovalov, J. R. Young, and I. West-Abdallah, "Enhancing Cylindrical Compression by Reducing Plasma Ablation in Pulsed-Power Drivers," Phys. Plasmas **26**, 042706 (2019).

P.-A. Gourdain, A. B. Sefkow, and C. E. Seyler, "The Generation of Warm Dense Matter Using a Magnetic Anvil Cell," IEEE Trans. Plasma Sci. **46**, 3968 (2018).

E. C. Hansen, P. Hartigan, A. Frank, A. Wright, and J. C. Raymond, "Simulating Radiative Magnetohydrodynamical Flows with ASTROBEAR: Implementation and Applications of Non-Equilibrium Cooling," Mon. Not. R. Astron. Soc. **481**, 3098; **483**, 2123(E) (2019).

D. P. Higginson, J. S. Ross, D. D. Ryutov, F. Fiuza, S. C. Wilks, E. P. Hartouni, R. Hatarik, C. M. Huntington, J. Kilkenny, B. Lahmann, C. K. Li, A. Link, R. D. Petrasso, B. B. Pollock, B. A. Remington, H. G. Rinderknecht, Y. Sakawa, H. Sio, G. F. Swadling, S. Weber, A. B. Zylstra, and H.-S. Park, "Kinetic Effects on Neutron Generation in Moderately Collisional Interpenetrating Plasma Flows," Phys. Plasmas **26**, 012113 (2019).

D. M. H. Hung, E. G. Blackman, K. J. Caspary, E. P. Gilson, and H. Ji, "Experimental Confirmation of the Standard Magnetorotational Instability Mechanism with a Spring-Mass Analogue," Commun. Phys. **2**, 7 (2019).

V. V. Ivanov, A. V. Maximov, R. Betti, L. S. Leal, R. C. Mancini, K. J. Swanson, I. E. Golovkin, C. J. Fontes, H. Sawada, A. B. Sefkow, and N. L. Wong, "Study of Laser Produced Plasma in a Longitudinal Magnetic Field," Phys. Plasmas **26**, 062707 (2019).

T. R. Joshi, S. C. Hsu, P. Hakel, N. M. Hoffman, H. Sio, and R. C. Mancini, "Progress on Observations of Interspecies Ion Separation in Inertial-Confinement-Fusion Implosions via Imaging X-Ray Spectroscopy," Phys. Plasmas **26**, 062702 (2019).

G. Kagan, O. L. Landen, D. Svyatskiy, H. Sio, N. V. Kabadi, R. A. Simpson, M. Gatu Johnson, J. A. Frenje, R. D. Petrasso, R. C. Shah, T. R. Joshi, P. Hakel, T. E. Weber, H. G. Rinderknecht, D. Thorn, M. Schneider, D. Bradley, and J. Kilkenny, "Inference of the Electron Temperature in Inertial Confinement Fusion Implosions from the Hard X-Ray Spectral Continuum," Contrib. Plasma Phys. **59**, 181 (2019).

M. F. Kasim, A. F. A. Bott, P. Tzeferacos, D. Q. Lamb, G. Gregori, and S. M. Vinko, "Retrieving Fields from Proton Radiography Without Source Profiles," Phys. Rev. E **100**, 033208 (2019).

P. M. King, N. Lemos, J. L. Shaw, A. L. Milder, K. A. Marsh, A. Pak, B. M. Hegelich, P. Michel, J. Moody, C. Joshi, and F. Albert, "X-Ray Analysis Methods for Sources from Self-Modulated Laser Wakefield Acceleration Driven by Picosecond Lasers," Rev. Sci. Instrum. **90**, 033503 (2019).

J. L. Kline, S. H. Batha, L. R. Benedetti, D. Bennett, S. Bhandarkar, L. F. Berzak Hopkins, J. Biener, M. M. Biener, R. Bionta, E. Bond, D. Bradley, T. Braun, D. A. Callahan, J. Caggiano, C. Cerjan, B. Cagadas, D. Clark, C. Castro, E. L. Dewald, T. Döppner, L. Divol, R. Dylla-Spears, M. Eckart, D. Edgell, M. Farrell, J. Field, D. N. Fittinghoff, M. Gatu Johnson, G. Grim, S. Haan, B. M. Haines, A. V. Hamza, E. P. Hartouni, R. Hatarik, K. Henderson, H. W. Herrmann,

D. Hinkel, D. Ho, M. Hohenberger, D. Hoover, H. Huang, M. L. Hoppe, O. A. Hurricane, N. Izumi, S. Johnson, O. S. Jones, S. Khan, B. J. Kozioziemski, C. Kong, J. Kroll, G. A. Kyrala, S. LePape, T. Ma, A. J. Mackinnon, A. G. MacPhee, S. MacLaren, L. Masse, J. McNaney, N. B. Meezan, J. F. Merrill, J. L. Milovich, J. Moody, A. Nikroo, A. Pak, P. Patel, L. Peterson, E. Piceno, L. Pickworth, J. E. Ralph, N. Rice, H. F. Robey, J. S. Ross, J. R. Rygg, M. R. Sacks, J. Salmonson, D. Sayre, J. D. Sater, M. Schneider, M. Schoff, S. Sepke, R. Seugling, V. Smalyuk, B. Spears, M. Stadermann, W. Stoeffl, D. J. Strozzi, R. Tipton, C. Thomas, R. P. J. Town, P. L. Volegov, C. Walters, M. Wang, C. Wilde, E. Woerner, C. Yeamans, S. A. Yi, B. Yoxall, A. B. Zylstra, J. Kilkenny, O. L. Landen, W. Hsing, and M. J. Edwards, "Progress of Indirect Drive Inertial Confinement Fusion in the United States," Nucl. Fusion **59**, 112018 (2019).

P. F. Knapp, M. R. Gomez, S. B. Hansen, M. E. Glinsky, C. A. Jennings, S. A. Slutz, E. C. Harding, K. D. Hahn, M. R. Weis, M. Evans, M. R. Martin, A. J. Harvey-Thompson, M. Geissel, I. C. Smith, D. E. Ruiz, K. J. Peterson, B. M. Jones, J. Schwarz, G. A. Rochau, D. B. Sinars, R. D. McBride, and P.-A. Gourdain, "Origins and Effects of Mix on Magnetized Liner Inertial Fusion Target Performance," Phys. Plasmas **26**, 012704 (2019).

A. Krygier, F. Coppari, G. E. Kemp, D. B. Thorn, R. S. Craxton, J. H. Eggert, E. M. Garcia, J. M. McNaney, H.-S. Park, Y. Ping, B. A. Remington, and M. B. Schneider, "Developing a High-Flux, High-Energy Continuum Backlighter for Extended X-Ray Absorption Fine Structure Measurements at the National Ignition Facility," Rev. Sci. Instrum. **89**, 10F114 (2018).

G. A. Kyrala, J. E. Pino, S. F. Khan, S. A. MacLaren, J. D. Salmonson, T. Ma, L. Masse, R. Tipton, P. A. Bradley, J. R. Rygg, J. E. Field, R. Tommasini, J. E. Ralph, D. P. Turnbull, A. J. Mackinnon, L. R. Benedetti, D. K. Bradley, S. Nagel, P. M. Celliers, E. Dewald, T. R. Dittrich, L. Berzak Hopkins, N. Izumi, M. L. Kervin, J. Kline, C. Yeamans, R. Hatarik, D. Sayre, E. P. Hartouni, A. Pak, K. C. Chen, and D. E. Hoover, "Using a 2-Shock 1D Platform at NIF to Measure the Effect of Convergence on Mix and Symmetry," Phys. Plasmas **25**, 102702 (2018).

S. Le Pape, L. Divol, A. MacPhee, J. McNaney, M. Hohenberger, D. Froula, V. Glebov, O. L. Landen, C. Stoeckl, E. Dewald, S. Khan, C. Yeamans, P. Michel, M. Schneider, J. Knauer, J. Kilkenny, and A. J. Mackinnon, "Optimization of High Energy X Ray Production Through Laser Plasma Interaction," High Energy Density Phys. **31**, 13 (2019).

T.-G. Lee, M. Busquet, M. Klapisch, J. W. Bates, A. J. Schmitt, S. X. Hu, and J. Giuliani, "Radiative and Atomic Properties of C and CH Plasmas in the Warm-Dense-Matter Regime," Phys. Rev. E **98**, 043203 (2018).

N. Lemos, P. King, J. L. Shaw, A. L. Milder, K. A. Marsh, A. Pak, B. B. Pollock, C. Goyon, W. Schumaker, A. M. Saunders, D. Papp, R. Polanek, J. E. Ralph, J. Park, R. Tommasini, G. J. Williams, H. Chen, F. V. Hartemann, S. Q. Wu, S. H. Glenzer, B. M. Hegelich, J. Moody, P. Michel, C. Joshi, and F. Albert, "X-Ray Sources Using a Picosecond Laser Driven Plasma Accelerator," Phys. Plasmas **26**, 083110 (2019).

C. K. Li, V. T. Tikhonchuk, Q. Moreno, H. Sio, E. D'Humières, X. Ribeyre, Ph. Korneev, S. Atzeni, R. Betti, A. Birkel, E. M. Campbell, R. K. Follett, J. A. Frenje, S. X. Hu, M. Koenig, Y. Sakawa, T. C. Sangster, F. H. Seguin, H. Takabe, S. Zhang, and R. D. Petrasso, "Collisionless Shocks Driven by Supersonic Plasma Flows with Self-Generated Magnetic Fields," Phys. Rev. Lett. **123**, 055002 (2019).

A. Liao, P. Hartigan, G. Fiksel, B. Blue, P. Graham, J. Foster, and C. Kuranz, "Using the ROSS Optical Streak Camera as a Tool to Understand Laboratory Experiments of Laser-Driven Magnetized Shock Waves," High Power Laser Sci. Eng. **6**, e22 (2018).

A. S. Liao, S. Li, H. Li, K. Flippo, D. Barnak, K. Van Kelso, C. F. Kawaguchi, A. Rasmus, S. Klein, J. Levesque, C. Kuranz, and C. K. Li, "Design of a New Turbulent Dynamo Experiment on the OMEGA-EP," Phys. Plasmas **26**, 032306 (2019).

J. D. Lindl, S. W. Haan, O. L. Landen, A. R. Christopherson, and R. Betti, "Progress Toward a Self-Consistent Set of 1D Ignition Capsule Metrics in ICF," Phys. Plasmas **25**, 122704 (2018).

Y. Lu, P. Tzeferacos, E. Liang, R. K. Follett, L. Gao, A. Birkel, D. H. Froula, W. Fu, H. Ji, D. Lamb, C. K. Li, H. Sio, R. Petrasso, and M. S. Wei, "Numerical Simulation of Magnetized Jet Creation Using a Hollow Ring of Laser Beams," Phys. Plasmas **26**, 022902 (2019).

A. Macrander, N. Pereira, C. Stoeckl, X. Huang, and E. Kasman, "Quartz Conditioning Crystal for X-Ray Rocking Curve Topography," J. Appl. Cryst. **52**, 115 (2019).

C. Mailliet, E. Le Bel, L. Ceurvorst, S. F. Khan, D. Martinez, Th. Goudal, N. Izumi, D. Kalantar, P. Di Nicola, J. M. Di Nicola, I. Igumenshchev, V. T. Tikhonchuk, B. Remington,

V. A. Smalyuk, L. Masse, and A. Casner, "Long-Duration Direct Drive Hydrodynamics Experiments on the National Ignition Facility: Platform Development and Numerical Modeling with CHIC," Phys. Plasmas **26**, 082703 (2019).

M. J.-E. Manuel, A. B. Sefkow, C. C. Kuranz, A. M. Rasmus, S. R. Klein, M. J. MacDonald, M. R. Trantham, J. R. Fein, P. X. Belancourt, R. P. Young, P. A. Keiter, B. B. Pollock, J. Park, A. U. Hazi, G. J. Williams, H. Chen, and R. P. Drake, "Magnetized Disruption of Inertially Confined Plasma Flows," Phys. Rev. Lett. **122**, 225001 (2019).

P.-E. Masson-Laborde, S. Laffite, C. K. Li, S. C. Wilks, R. Riquier, R. D. Petrasso, G. Kluth, and V. Tassin, "Interpretation of Proton Radiography Experiments of Hohlraums with Three-Dimensional Simulations," Phys. Rev. E **99**, 053207 (2019).

C. A. McCoy, M. C. Marshall, D. N. Polsin, D. E. Fratanduono, P. M. Celliers, D. D. Meyerhofer, and T. R. Boehly, "Hugoniot, Sound Velocity, and Shock Temperature of MgO to 2300 GPa," Phys. Rev. B **100**, 014106 (2019).

P. Michel, M. J. Rosenberg, W. Seka, A. A. Solodov, R. W. Short, T. Chapman, C. Goyon, N. Lemos, M. Hohenberger, J. D. Moody, S. P. Regan, and J. F. Myatt, "Theory and Measurements of Convective Raman Side Scatter in Inertial Confinement Fusion Experiments," Phys. Rev. E **99**, 033203 (2019).

M. Millot, F. Coppari, J. R. Rygg, A. Correa Barrios, S. Hamel, D. C. Swift, and J. H. Eggert, "Nanosecond X-Ray Diffraction of Shock-Compressed Superionic Water Ice," Nature **569**, 251 (2019).

A. Pak, S. Kerr, N. Lemos, A. Link, P. Patel, F. Albert, L. Divol, B. B. Pollock, D. Haberberger, D. Froula, M. Gauthier, S. H. Glenzer, A. Longman, L. Manzoor, R. Fedosejevs, S. Tochitsky, C. Joshi, and F. Fiuza, "Collisionless Shock Acceleration of Narrow Energy Spread Ion Beams from Mixed Species Plasmas Using 1 μm Lasers," Phys. Rev. Accel. Beams **21**, 103401 (2018).

J. Peebles, A. V. Arefiev, S. Zhang, C. McGuffey, M. Spinks, J. Gordon, E. W. Gaul, G. Dyer, M. Martinez, M. E. Donovan, T. Ditmire, J. Park, H. Chen, H. S. McLean, M. S. Wei, S. I. Krasheninnikov, and F. N. Beg, "High-Angle Deflection of the Energetic Electrons by a Voluminous Magnetic Structure in Near-Normal Intense Laser-Plasma Interactions," Phys. Rev. E **98**, 053202 (2018).

N. R. Pereira, A. T. Macrander, C. Stoeckl, and E. O. Baronova, "On Evaluating X-Ray Imaging Crystals with Synchrotron Radiation," Rev. Sci. Instrum. **89**, 10G126 (2018).

K. Prestridge, "Experimental Adventures in Variable-Density Mixing," Phys. Rev. Fluids **3**, 110501 (2018).

A. M. Rasmus, C. A. Di Stefano, K. A. Flippo, F. W. Doss, C. F. Kawaguchi, J. L. Kline, E. C. Merritt, T. R. Desjardins, T. Cardenas, D. W. Schmidt, P. M. Donovan, F. Fierro, L. A. Goodwin, J. I. Martinez, T. E. Quintana, J. S. Zingale, and C. C. Kuranz, "Shock-Driven Hydrodynamic Instability of a Sinusoidally Perturbed, High-Atwood Number, Oblique Interface," Phys. Plasmas **26**, 062103 (2019).

A. E. Raymond, C. F. Dong, A. McKelvey, C. Zulick, N. Alexander, A. Bhattacharjee, P. T. Campbell, H. Chen, V. Chvykov, E. Del Rio, P. Fitzsimmons, W. Fox, B. Hou, A. Maksimchuk, C. Mileham, J. Nees, P. M. Nilson, C. Stoeckl, A. G. R. Thomas, M. S. Wei, V. Yanovsky, K. Krushelnick, and L. Willingdale, "Relativistic-Electron-Driven Magnetic Reconnection in the Laboratory," Phys. Rev. E **98**, 043207 (2018).

T. P. Remington, E. N. Hahn, S. Zhao, R. Flanagan, J. C. E. Mertens, S. Sabbaghianrad, T. G. Langdon, C. E. Wehrenberg, B. R. Maddox, D. C. Swift, B. A. Remington, N. Chawla, and M. A. Meyers, "Spall Strength Dependence on Grain Size and Strain Rate in Tantalum," Acta Mater. **158**, 313 (2018).

E. Ruskov, V. Yu. Glebov, T. W. Darling, F. J. Wessel, F. Conti, J. C. Valenzuela, H. U. Rahman, and F. N. Beg, "Gated Liquid Scintillator Detector for Neutron Time of Flight Measurements in a Gas-Puff Z-Pinch Experiment," Rev. Sci. Instrum. **90**, 073505 (2019).

A. M. Saunders, B. Lahmann, G. Sutcliffe, J. A. Frenje, R. W. Falcone, and T. Döppner, "Characterizing Plasma Conditions in Radiatively Heated Solid-Density Samples with X-Ray Thomson Scattering," Phys. Rev. E **98**, 063206 (2018).

J. P. Sauppe, B. M. Haines, S. Palaniyappan, P. A. Bradley, S. H. Batha, E. N. Loomis, and J. L. Kline, "Modeling of Direct-Drive Cylindrical Implosion Experiments with an Eulerian Radiation-Hydrodynamics Code," Phys. Plasmas **26**, 042701 (2019).

D. B. Schaeffer, W. Fox, R. K. Follett, G. Fiksel, C. K. Li, J. Matteucci, A. Bhattacharjee, and K. Germaschewski, "Direct Observations of Particle Dynamics in Magnetized Collisionless

Shock Precursors in Laser-Produced Plasmas," Phys. Rev. Lett. **122**, 245001 (2019).

B. Scheiner, M. J. Schmitt, S. C. Hsu, D. Schmidt, J. Mance, C. Wilde, D. N. Polsin, T. R. Boehly, F. J. Marshall, N. Krasheninnikova, K. Molvig, and H. Huang, "First Experiments on Revolver Shell Collisions at the OMEGA Laser," Phys. Plasmas **26**, 072707 (2019).

A. Shimony, W. C. Wan, S. R. Klein, C. C. Kuranz, R. P. Drake, D. Shvarts, and G. Malamud, "Construction and Validation of a Statistical Model for the Nonlinear Kelvin-Helmholtz Instability Under Compressible, Multimode Conditions," Phys. Plasmas **25**, 122112 (2018).

H. Sio, J. A. Frenje, A. Le, S. Atzeni, T. J. T. Kwan, M. Gatu Johnson, G. Kagan, C. Stoeckl, C. K. Li, C. E. Parker, C. J. Forrest, V. Glebov, N. V. Kabadi, A. Bose, H. G. Rinderknecht, P. Amendt, D. T. Casey, R. Mancini, W. T. Taitano, B. Keenan, A. N. Simakov, L. Chacón, S. P. Regan, T. C. Sangster, E. M. Campbell, F. H. Seguin, and R. D. Petrasso, "Observations of Multiple Nuclear Reaction Histories and Fuel-Ion Species Dynamics in Shock-Driven Inertial Confinement Fusion Implosions," Phys. Rev. Lett. **122**, 035001 (2019).

H. Sio, O. Larroche, S. Atzeni, N. V. Kabadi, J. A. Frenje, M. Gatu Johnson, C. Stoeckl, C. Li, C. J. Forrest, V. Glebov, P. J. Adrian, A. Bose, A. Birkel, S. P. Regan, F. H. Séguin, and R. D. Petrasso, "Probing Ion Species Separation and Ion Thermal Decoupling in Shock-Driven Implosions Using Multiple Nuclear Reaction Histories," Phys. Plasmas **26**, 072703 (2019).

H. Sio, C. Li, C. E. Parker, B. Lahmann, A. Le, S. Atzeni, and R. D. Petrasso, "Fuel-Ion Diffusion in Shock-Driven Inertial Confinement Fusion Implosions," Matter Radiat. Extremes **4**, 055401 (2019).

P. T. Springer, O. A. Hurricane, J. H. Hammer, R. Betti, D. A. Callahan, E. M. Campbell, D. T. Casey, C. J. Cerjan, D. Cao, E. Dewald, L. Divol, T. Doeppner, M. J. Edwards, J. E. Field, C. Forrest, J. Frenje, J. A. Gaffney, M. Gatu-Johnson, V. Glebov, V. N. Goncharov, G. P. Grim, E. Hartouni, R. Hatarik, D. E. Hinkel, L. Berzak Hopkins, I. Igumenshchev, P. Knapp, J. P. Knauer, A. L. Kritcher, O. Landen, A. Pak, S. Le Pape, T. Ma, A. G. MacPhee, D. H. Munro, R. C. Nora, P. K. Patel, L. Peterson, P. B. Radha, S. P. Regan, H. Rinderknecht, C. Sangster, B. K. Spears, and C. Stoeckl, "A 3D Dynamic Model to Assess the Impacts of Low-Mode Asymmetry, Aneurysms and Mix-Induced Radiative Loss on Capsule Performance Across Inertial Confinement Fusion Platforms," Nucl. Fusion **59**, 032009 (2019).

J. Strehlow, P. Forestier-Colleoni, C. McGuffey, M. Bailly-Grandvaux, T. S. Daykin, E. McCary, J. Peebles, G. Revet, S. Zhang, T. Ditmire, M. Donovan, G. Dyer, J. Fuchs, E. W. Gaul, D. P. Higginson, G. E. Kemp, M. Martinez, H. S. McLean, M. Spinks, H. Sawada, and F. N. Beg, "The Response Function of Fujifilm BAS-TR Imaging Plates to Laser-Accelerated Titanium Ions," Rev. Sci. Instrum. **90**, 083302 (2019).

J. D. Styron, C. L. Ruiz, K. D. Hahn, G. W. Cooper, G. A. Chandler, B. Jones, B. R. McWatters, C. J. Forrest, J. Vaughan, J. Torres, S. Pelka, J. Smith, and C. Weaver, "Average Neutron Time-of-Flight Instrument Response Function Inferred from Single D-T Neutron Events Within a Plastic Scintillator," Rev. Sci. Instrum. **89**, 10I119 (2018).

D. B. Thorn, F. Coppari, T. Döppner, M. J. MacDonald, S. P. Regan, and M. B. Schneider, "X-Ray Spectrometer Throughput Model for (Selected) Flat Bragg Crystal Spectrometers on Laser Plasma Facilities," Rev. Sci. Instrum. **89** (10), 10F119 (2018).

M. P. Valdivia, F. Veloso, D. Stutman, C. Stoeckl, C. Mileham, I. A. Begishev, W. Theobald, M. Vescovi, W. Useche, S. P. Regan, B. Albertazzi, G. Rigon, P. Mabey, T. Michel, S. A. Pikuz, M. Koenig, and A. Casner, "X-Ray Backlighter Requirements for Refraction-Based Electron Density Diagnostics Through Talbot-Lau Deflectometry," Rev. Sci. Instrum. **89**, 10G127 (2018).

X. Wang, P. Rigg, J. Sethian, N. Sinclair, N. Weir, B. Williams, J. Zhang, J. Hawreliak, Y. Toyoda, Y. Gupta, Y. Li, D. Broege, J. Bromage, R. Earley, D. Guy, and J. Zuegel, "The Laser Shock Station in the Dynamic Compression Sector. I," Rev. Sci. Instrum. **90**, 053901 (2019).

A. J. White, O. Certik, Y. H. Ding, S. X. Hu, and L. A. Collins, "Time-Dependent Orbital-Free Density Functional Theory for Electronic Stopping Power: Comparison to the Mermin-Kohn-Sham Theory at High Temperatures," Phys. Rev. B **98**, 144302 (2018).

J. Xin, R. Yan, Z.-H. Wan, D.-J. Sun, J. Zheng, H. Zhang, H. Aluie, and R. Betti, "Two Mode Coupling of the Ablative Rayleigh-Taylor Instabilities," Phys. Plasmas **26**, 032703 (2019).

R. P. Young, C. C. Kuranz, D. Froula, J. S. Ross, and S. Klein, "Observation of Collisionless-to-Collisional Transition in Colliding Plasma Jets with Optical Thomson Scattering," Phys. Plasmas **26**, 012101 (2019).

S. Zhang, A. Lazicki, B. Militzer, L. H. Yang, K. Caspersen, J. A. Gaffney, M. W. Däne, J. E. Pask, W. R. Johnson, A. Sharma, P. Suryanarayana, D. D. Johnson, A. V. Smirnov, P. A. Sterne, D. Erskine, R. A. London, F. Coppari, D. Swift, J. Nilsen, A. J. Nelson, and H. D. Whitley, "Equation of State of Boron Nitride Combining Computation, Modeling, and Experiment," Phys. Rev. B **99**, 165103 (2019).

W. Zhang and E. M. Campbell, "Progress and Prospect," Matter and Radiation at Extremes **4**, 013001 (2019).

S. Zhao, R. Flanagan, E. N. Hahn, B. Kad, B. A. Remington, C. E. Wehrenberg, R. Cauble, K. More, and M. A. Meyers, "Shock-Induced Amorphization in Silicon Carbide," Acta Mater. **158**, 206 (2018).

H. Zhou and E. G. Blackman, "Calculating Turbulent Transport Tensors by Averaging Single-Plume Dynamics and Application to Dynamos," Mon. Not. R. Astron. Soc. **483**, L104 (2019).

Conference Presentations

The following presentations were made at the CEA–NNSA Joint Diagnostic Meeting, Le Barp, France, 2–3 October 2018:

S. P. Regan, C. J. Forrest, W. Theobald, C. Sorce, C. Danly, I. V. Igumenshchev, V. N. Goncharov, F. J. Marshall, V. Yu. Glebov, T. C. Sangster, E. M. Campbell, P. Volegov, T. Murphy, C. Wilde, J. Kline, O. Landoas, T. Caillaud, B. Rosse, M. Briat, I. Thfoin, J. L. Bourgade, T. Dautremer, E. Barat, and J. D. Kilkenny, "OMEGA Neutron Imaging Project."

W. Theobald, "3-D Hot-Spot X-Ray Imaging for OMEGA DT Cryogenic Implosions."

The following presentations were made at the CELIA Seminar, Bordeaux, France, 3 October 2018:

S. X. Hu, W. Theobald, J. L. Peebles, S. P. Regan, P. B. Radha, D. T. Michel, Y. H. Ding, V. N. Goncharov, T. R. Boehly, R. Epstein, E. M. Campbell, G. Duchateau, A. Casner, V. Tikhonchuk, L. A. Collins, J. D. Kress, and B. Militzer, "Understanding ICF Implosions on OMEGA: From Intrinsic Material Properties to Laser Imprint."

M. S. Wei, C. M. Krauland, S. Muller, S. Zhang, J. Li, J. L. Peebles, F. N. Beg, W. Theobald, E. Borwick, C. Ren, C. Stoeckl, D. Haberberger, T. Filkins, D. Turnbull, R. Betti, E. M. Campbell, J. Trela, D. Batani, K. Glize, R. Scott, and L. Antonelli, "Laser–Plasma Instabilities and Hot-Electron Generation in the Shock-Ignition Intensity Regime."

The following presentations were made at the First LMJ–PETAL User Meeting, Bordeaux, France, 4–5 October 2018:

E. M. Campbell, "A Perspective on the Future of ICF and HEDP Research."

W. Theobald, R. Betti, A. Bose, S. X. Hu, E. M. Campbell, S. P. Regan, C. McCoy, A. Casner, L. Ceurvorst, and M. Karasik, "The Hybrid Target Approach: A Promising Path Forward to Mitigate Laser Imprint in Direct-Drive Inertial Confinement Fusion."

M. S. Wei and J. M. Soures, "Overview of the Omega Laser Facility and Basic Science User Program."

E. M. Campbell, "Fusion: Making a Star on Earth and the Quest for the Ultimate Energy Source to Power the Planet," presented at the AEFM Seminar, Rochester, NY, 11 October 2018.

Y. Zhao, "AlGaN Metal–Semiconductor–Metal UV Photodetectors," presented at Industrial Associates, Rochester, NY, 19 October 2018.

The following presentations were made at the 4th International Conference on High Energy Density Physics, Ningbo, China, 21–25 October 2018:

R. Betti, V. Gopalaswamy, J. P. Knauer, A. R. Christopherson, D. Patel, K. M. Woo, A. Bose, K. S. Anderson, T. J. B. Collins, S. X. Hu, V. Yu. Glebov, A. V. Maximov, C. Stoeckl, F. J. Marshall, M. J. Bonino, D. R. Harding, R. T. Janezic, J. H. Kelly, S. Sampat, T. C. Sangster, S. P. Regan, E. M. Campbell, M. Gatu Johnson, J. A. Frenje, C. K. Li, R. D. Petrasso, and O. A. Hurricane, "Progress Toward Ignition and Burn in Inertial Confinement Fusion."

D. H. Froula, J. P. Palastro, D. Turnbull, T. J. Kessler, A. Davies, A. Howard, L. Nguyen, D. Ramsey, G. W. Jenkins, S.-W. Bahk, I. A. Begishev, R. Boni, J. Bromage, S. Bucht, R. K. Follett, D. Haberberger, J. Katz, and J. L. Shaw, "Flying Focus: Spatiotemporal Control of Intensity for Laser-Based Applications."

J. P. Knauer, R. Betti, V. Gopalaswamy, M. J. Bonino, E. M. Campbell, T. J. B. Collins, C. J. Forrest, V. Yu. Glebov, V. N. Goncharov, D. R. Harding, O. M. Mannion, J. A. Marozas, F. J. Marshall, P. W. McKenty, D. T. Michel, P. B. Radha, S. P. Regan, T. C. Sangster, C. Stoeckl, M. Gatu Johnson, and J. A. Frenje, "Direct-Drive, High-Adiabat, Cryogenic Implosion Results from the OMEGA Laser System" (invited).

K. Luo, D. Mejia-Rodriguez, V. V. Karasiev, J. Dufty, and S. B. Trickey, "Development of Free Energy Density Functional Theory: Predictive Power of First Principles Approximations for Warm Dense Matter."

The following presentations were made at Tritium Focus Group-Sandia, Albuquerque, NM, 22–25 October 2018:

D. Bassler, C. Fagan, W. T. Shmayda, and W. U. Schröder, "Tritium Interactions with Thin Films of Al_2O_3 on Stainless-Steel 316."

C. Fagan, M. Sharpe, W. T. Shmayda, and W. U. Schroder, "Low-Pressure, Radio-Frequency–Generated Plasma for Tritium Desorption from Metals."

M. Sharpe, C. Fagan, and W. T. Shmayda, "Influence of Microstructure on the Absorption of Tritium into Gold-Plated 316 Stainless Steel."

W. T. Shmayda, N. P. Redden, and R. Earley, "Enhancing Gas Chromatography Performance."

P. B. Radha, "Overview and Status of Direct-Drive Inertial Confinement Fusion in the United States," presented at the 27th IAEA Fusion Energy Conference (FEC 2018), Ahmedabad, India, 22–27 October 2018.

The following presentations were made at the NIF VISAR Workshop, Livermore, CA, 23–24 October 2018:

M. K. Ginnane, A. Sorce, J. D. Kendrick, R. Boni, B. Saltzman, D. Weiner, M. Zaghoo, D. N. Polsin, B. J. Henderson, J. Zou, M. Couch, C. M. Rogoff, M. C. Gregor, T. R. Boehly, J. R. Rygg, and G. W. Collins, "Improvements to the VISAR and Streaked Optical Pyrometer at the Omega Laser Facility."

J. L. Peebles, S. X. Hu, V. N. Goncharov, N. Whiting, P. M. Celliers, S. J. Ali, G. Duchateau, E. M. Campbell, T. R. Boehly, and S. P. Regan, "First Direct-Drive Measurements of Laser-Imprint-Induced Shock-Velocity Nonuniformities on OMEGA."

The following presentations were made at the U.S.-Japan Workshop on Theory and Simulations of High-Field and High-Energy-Density Physics, Portland OR, 3–4 November 2018:

A. Howard, D. Turnbull, A. Davies, D. H. Froula, and J. P. Palastro, "Photon Acceleration in the Ionization Front of a Flying Focus."

P. M. Nilson, F. Ehrne, C. Mileham, D. Mastrosimone, C. Taylor, R. K. Jungquist, R. Boni, J. Hassett, C. R. Stillman, S. T. Ivancic, D. J. Lonobile, R. W. Kidder, M. J. Shoup III, A. B. Sefkow, A. A. Solodov, W. Theobald, C. Stoeckl, S. X. Hu, D. H. Froula, K. W. Hill, L. Gao, M. Bitter, P. Efthimion, I. Golovkin, and D. D. Meyerhofer, "High-Resolving-Power, Streaked X-Ray Spectroscopy of Picosecond-Scale Relativistic Laser–Matter Interactions on the OMEGA EP Laser System."

J. L. Peebles, J. R. Davies, D. H. Barnak, A. B. Sefkow, P. A. Gourdain, R. Betti, and A. Arefiev, "Characterizing Magnetic and Electric Fields from Laser-Driven Coils Using Axial Proton Probing."

H. Rinderknecht, H.-S. Park, J. S. Ross, P. A. Amendt, D. P. Higginson, S. C. Wilks, R. K. Follett, D. Haberberger, J. Katz, D. H. Froula, N. M. Hoffman, G. Kagan, B. Keenan,

A. Simakov, L. Chacon, and E. Vold, “Ion-Velocity Structure in Strong Collisional Plasma Shocks.”

The following presentations were made at the 60th Annual APS Division of Plasma Physics, Portland OR, 5–9 November 2018:

K. S. Anderson, C. J. Forrest, O. M. Mannion, D. T. Michel, R. C. Shah, J. A. Marozas, P. B. Radha, F. J. Marshall, J. P. Knauer, R. Epstein, V. Gopalaswamy, M. Gatu Johnson, and S. Laffite, “Modeling of Target Offset in Warm Implosions on OMEGA.”

D. Cao, R. C. Shah, S. P. Regan, C. Sorce, R. Epstein, I. V. Igumenshchev, V. Gopalaswamy, A. R. Christopherson, W. Theobald, P. B. Radha, and V. N. Goncharov, “Using the 10 to 20 keV X-Ray Spectrum to Infer an Electron Temperature (T_e) as an Implosion Diagnostic on OMEGA.”

D. A. Chin, P. M. Nilson, G. W. Collins, T. R. Boehly, J. R. Rygg, F. Coppari, Y. Ping, D. Trail, I. Szumila, and M. Harmand “Interpreting EXAFS Spectra: Toward Ramp-Compression Studies of Iron Oxide (FeO).”

A. R. Christopherson, R. Betti, S. Miller, V. Gopalaswamy, D. Cao, D. Keller, and J. D. Lindl, “Thermonuclear Ignition and the Onset of Propagating Burn in Inertial Fusion.”

G. W. Collins, J. R. Rygg, T. R. Boehly, M. Zaghoo, D. N. Polsin, B. J. Henderson, X. Gong, L. Crandall, R. Saha, J. J. Ruby, G. Tabak, M. Huff, Z. Sprowal, A. Chin, M. K. Ginnane, P. M. Celliers, J. H. Eggert, A. Lazicki, R. F. Smith, R. Hemley, F. Coppari, B. Bachman, J. Gaffney, D. E. Fratanduono, D. G. Hicks, Y. Ping, D. Swift, D. G. Braun, S. Hamel, M. Milllot, M. Gorman, R. Briggs, S. Ali, R. Kraus, M. McMahon, S. Brygoo, R. Jeanloz, R. Falcone, F. N. Beg, C. Bolme, A. Gleason, S. H. Glenzer, H. J. Lee, T. Duffy, J. Wang, J. Wark, and G. Gregori, “Matter at Extreme Energy Density: Exotic Solids to Inertial Fusion” (invited).

T. J. B. Collins, C. Stoeckl, R. Epstein, R. Betti, J. A. Delettrez, W. Bittle, C. J. Forrest, V. Yu. Glebov, V. N. Goncharov, D. R. Harding, I. V. Igumenshchev, D. W. Jacobs-Perkins, R. T. Janezic, J. H. Kelly, T. Z. Kosc, C. Mileham, D. T. Michel, R. L. McCrory, P. W. McKenty, F. J. Marshall, S. F. B. Morse, P. B. Radha, S. P. Regan, B. Rice, T. C. Sangster, M. J. Shoup III, W. T. Shmayda, C. Sorce, W. Theobald, J. Ulreich, M. D. Wittman, J. A. Frenje, M. Gatu Johnson, and R. D. Petrasso, “Cryogenic Target Performance and Fuel-Ablator Perturbation Growth.”

L. Crandall, J. R. Rygg, G. W. Collins, T. R. Boehly, M. Zaghoo, P. M. Celliers, D. E. Fratanduono, M. C. Gregor, A. Jenei, M. Millot, J. H. Eggert, and D. Spaulding, “Equation-of-State Measurements of Precompressed CO_2.”

R. S. Craxton, Y. Yang, E. M. Garcia, P. W. McKenty, M. J. Schmitt, and K. Molvig, “*Revolver* Designs for the National Ignition Facility Using Current and Optimized Phase Plates.”

A. Davies, J. Katz, S. Bucht, D. Haberberger, J. P. Palastro, I. A. Begishev, J. L. Shaw, D. Turnbull, R. Boni, D. H. Froula, and W. Rozmus, “Ultrafast Thomson Scattering and the Effects of Collisions on the Electron Plasma Wave Feature.”

J. R. Davies, D. H. Barnak, R. Betti, P.-Y. Chang, V. Yu. Glebov, E. C. Hansen, J. P. Knauer, J. L. Peebles, A. B. Sefkow, K. J. Peterson, and D. B. Sinars, “Laser-Driven Magnetized Liner Inertial Fusion on OMEGA” (invited).

Y. H. Ding, S. X. Hu, A. J. White, O. Certik, and L. A. Collins, “*Ab Initio* Studies on Stopping Power of Warm Dense Matter with Time-Dependent Orbital-Free Density Functional Theory.”

D. H. Edgell, R. K. Follett, J. Katz, J. P. Palastro, D. Turnbull, and D. H. Froula, “Density Profile Measurements on OMEGA Using the CBET Beamlets Diagnostic.”

R. Epstein, C. Stoeckl, P. B. Radha, T. J. B. Collins, P. W. McKenty, D. Cao, R. C. Shah, D. Cliche, and R. C. Mancini, “Inferring Shell Nonuniformity in OMEGA Implosions by Self-Emission Radiography.”

R. K. Follett, J. G. Shaw, D. H. Edgell, D. H. Froula, C. Dorrer, J. Bromage, E. M. Campbell, E. M. Hill, T. J. Kessler, J. P. Palastro, J. F. Myatt, J. W. Bates, and J. L. Weaver, “Suppressing Parametric Instabilities with Laser Frequency Detuning and Bandwidth” (invited).

C. J. Forrest, K. S. Anderson, V. Yu. Glebov, V. Gopalaswamy, V. N. Goncharov, J. P. Knauer, O. M. Mannion, P. B. Radha, S. P. Regan, T. C. Sangster, R. C. Shah, C. Stoeckl, J. A. Frenje, and M. Gatu Johnson, “Evaluating the Residual Kinetic Energy in Direct-Drive Cryogenic Implosions on OMEGA.”

P. Franke, D. Turnbull, J. P. Palastro, J. Katz, I. A. Begishev, R. Boni, J. Bromage, A. L. Milder, J. L. Shaw, and D. H. Froula, "Ionization Waves of Arbitrary Velocity."

D. H. Froula, J. P. Palastro, D. Turnbull, T. J. Kessler, A. Davies, P. Franke, A. Howard, L. Nguyen, D. Ramsey, G. W. Jenkins, S.-W. Bahk, I. A. Begishev, R. Boni, J. Bromage, S. Bucht, R. K. Follett, D. Haberberger, J. Katz, J. L. Shaw, F. A. Hegmann, D. Purschke, N. Vafaei-Najafabadi, J. Vieira, and F. Quéré, "Flying Focus: Spatial and Temporal Control of Intensity for Laser Based Application" (invited).

M. K. Ginnane, A. Sorce, J. D. Kendrick, R. Boni, B. Saltzman, D. Weiner, M. Zaghoo, D. N. Polsin, B. J. Henderson, J. Zou, M. Couch, C. M. Rogoff, M. C. Gregor, T. R. Boehly, J. R. Rygg, and G. W. Collins, "Improvements to the VISAR and Streaked Optical Pyrometer at the Omega Laser Facility."

V. Yu. Glebov, C. J. Forrest, J. P. Knauer, O. M. Mannion, S. P. Regan, T. C. Sangster, C. Stoeckl, M. J. Eckart, G. P. Grim, A. S. Moore, and D. J. Schlossberg, "DT Yield and Ion Temperature Measurement with a Cherenkov Neutron Time-of-Flight Detector on OMEGA."

V. N. Goncharov, "Perturbation Evolution at Early Stages of Inertial Confinement Fusion Implosions."

X. Gong, D. N. Polsin, L. Crandall, M. Huff, B. J. Henderson, J. R. Rygg, T. R. Boehly, G. W. Collins, A. Jenei, M. G. Gorman, R. Briggs, J. H. Eggert, and M. I. McMahon, "X-Ray Diffraction of Ramp-Compressed Potassium."

V. Gopalaswamy, R. Betti, J. P. Knauer, K. M. Woo, D. Patel, A. R. Christopherson, A. Bose, N. Luciani, F. J. Marshall, C. Stoeckl, V. Yu. Glebov, S. P. Regan, D. T. Michel, W. Seka, D. H. Edgell, R. C. Shah, D. Cao, V. N. Goncharov, J. A. Delettrez, I. V. Igumenshchev, P. B. Radha, T. J. B. Collins, T. C. Sangster, E. M. Campbell, M. Gatu Johnson, R. D. Petrasso, C. K. Li, and J. A. Frenje, "Optimization of Direct-Drive Inertial Fusion Implosions Through Predictive Statistical Modeling" (invited).

D. Haberberger, A. Shvydky, J. P. Knauer, S. X. Hu, V. N. Goncharov, S. T. Ivancic, and D. H. Froula, "Density Measurements of the Inner Shell Release."

A. M. Hansen, D. Turnbull, D. Haberberger, J. Katz, D. Mastrosimone, A. Colaïtis, A. B. Sefkow, R. K. Follett, J. P. Palastro, and D. H. Froula, "Cross-Beam Energy Transfer Platform Development on OMEGA."

R. J. Henchen, J. Katz, D. Cao, J. P. Palastro, D. H. Froula, M. Sherlock, and W. Rozmus, "Direct Measurements of Nonlocal Heat Flux by Thomson Scattering" (invited).

B. J. Henderson, T. R. Boehly, M. Zaghoo, J. R. Rygg, D. N. Polsin, X. Gong, L. Crandall, M. Huff, M. K. Ginnane, G. W. Collins, S. Ali, and P. M. Celliers, "Broadband Reflectivity Diagnostic Development for Dynamic Compression Experiments on OMEGA EP."

A. Howard, D. Turnbull, A. Davies, D. H. Froula, and J. P. Palastro, "Photon Acceleration in the Ionization Front of a Flying Focus."

S. X. Hu, R. Epstein, V. N. Goncharov, and E. M. Campbell, "Direct-Drive-Ignition Designs with Gradient-Density Double Shells."

M. Huff, J. R. Rygg, G. W. Collins, T. R. Boehly, M. Zaghoo, D. N. Polsin, B. J. Henderson, L. Crandall, D. E. Fratanduono, M. Millot, R. F. Smith, J. H. Eggert, P. M. Celliers, M. C. Gregor, and C. A. McCoy, "Measurements of Sound Speed in Iron Shock-Compressed to ~1 TPa."

I. V. Igumenshchev, R. C. Shah, R. Betti, E. M. Campbell, V. N. Goncharov, J. P. Knauer, S. P. Regan, A. Shvydky, A. L. Velikovich, and A. J. Schmitt, "Mitigating Imprint in Direct-Drive Implosions Using Rarefaction Flows."

V. V. Karasiev, S. X. Hu, M. Zaghoo, and T. R. Boehly, "Study of the Exchange-Correlation Thermal Effects for Transport and Optical Properties of Shocked Deuterium."

J. P. Knauer, C. Stoeckl, R. Betti, V. Gopalaswamy, K. S. Anderson, D. Cao, M. J. Bonino, E. M. Campbell, T. J. B. Collins, C. J. Forrest, V. Yu. Glebov, V. N. Goncharov, D. R. Harding, J. A. Marozas, F. J. Marshall, P. W. McKenty, P. B. Radha, S. P. Regan, T. C. Sangster, and R. C. Shah, "Burn-Rate Measurements from the High-Performance Cryogenic Implosion Campaign on OMEGA."

L. S. Leal, A. V. Maximov, A. B. Sefkow, R. Betti, and V. V. Ivanov, "Modeling of a Laser-Generated Plasma in MG Magnetic Fields."

O. M. Mannion, K. S. Anderson, C. J. Forrest, V. Yu. Glebov, J. P. Knauer, Z. L. Mohamed, S. P. Regan, T. C. Sangster, R. C. Shah, C. Stoeckl, and M. Gatu Johnson, "Integrated Analysis of Nuclear Measurements from the Target-Offset Campaign on OMEGA."

J. A. Marozas, G. D. Kerbel, M. M. Marinak, and S. Sepke, "Implementation of the Low-Noise, 3-D Ray-Trace Inverse-Projection Method in the Radiation-Hydrodynamics Code *HYDRA*."

F. J. Marshall, V. N. Goncharov, J. H. Kelly, T. Z. Kosc, and A. Shvydky, "*In Situ* Measurements of Direct-Drive Illumination Uniformity on OMEGA."

A. V. Maximov, J. G. Shaw, R. W. Short, and J. P. Palastro, "Saturation of Stimulated Raman Scattering in Inhomogeneous Plasma."

P. W. McKenty, T. J. B. Collins, J. A. Marozas, E. M. Campbell, K. Molvig, and M. J. Schmitt, "Numerical Investigation of Laser Imprint Mitigation in *Revolver* Ignition Designs."

A. L. Milder, P. Franke, J. Katz, J. P. Palastro, S. T. Ivancic, J. L. Shaw, A. S. Davies, I. A. Begishev, R. H. Cuffney, M. Spilatro, and D. H. Froula, "Measurement of the Langdon Effect in Laser-Produced Plasma Using Collective Thomson Scattering."

S. C. Miller, J. P. Knauer, C. J. Forrest, V. Yu. Glebov, O. M. Mannion, W. T. Shmayda, T. J. B. Collins, J. A. Marozas, K. S. Anderson, P. B. Radha, and V. N. Goncharov, "Deceleration-Phase Rayleigh–Taylor Growth Effects on the Performance of Direct-Drive Implosions."

Z. L. Mohamed, J. P. Knauer, C. J. Forrest, and M. Gatu Johnson, "Wave-Function Amplitude Analysis of the ^{5}He Resonance in the TT Neutron Spectrum."

P. M. Nilson, F. Ehrne, C. Mileham, D. Mastrosimone, C. Taylor, R. K. Jungquist, R. Boni, J. Hassett, C. R. Stillman, S. T. Ivancic, D. J. Lonobile, R. W. Kidder, M. J. Shoup III, A. B. Sefkow, A. A. Solodov, W. Theobald, C. Stoeckl, S. X. Hu, D. H. Froula, K. W. Hill, L. Gao, M. Bitter, P. Efthimion, I. E. Golovkin, and D. D. Meyerhofer, "High-Resolving-Power, Streaked X-Ray Spectroscopy on the OMEGA EP Laser System."

J. P. Palastro, T. M. Antonsen, Jr., L. Nguyen, A. Colaïtis, R. K. Follett, D. Turnbull, J. Vieira, and D. H. Froula, "Cherenkov Radiation from a Plasma."

D. Patel, R. Betti, V. Gopalaswamy, J. P. Knauer, K. M. Woo, S. P. Regan, T. C. Sangster, C. Stoeckl, and F. J. Marshall, "A Novel Double-Spike Pulse Shape for OMEGA Cryogenic Implosions."

R. Paul, S. X. Hu, and V. V. Karasiev, "High-Pressure Phase Diagram of Silicon."

J. L. Peebles, J. R. Davies, D. H. Barnak, A. B. Sefkow, P. A. Gourdain, R. Betti, and A. V. Arefiev, "Characterizing Magnetic and Electric Fields from Laser-Driven Coils Using Axial Proton Probing."

D. N. Polsin, X. Gong, G. W. Collins, M. Huff, L. Crandall, T. R. Boehly, J. R. Rygg, A. Jenei, M. Millot, J. H. Eggert, and M. I. McMahon, "X-Ray Diffraction of Ramp-Compressed Sodium."

S. P. Regan, V. N. Goncharov, D. Cao, R. Epstein, R. Betti, M. J. Bonino, T. J. B. Collins, E. M. Campbell, C. J. Forrest, V. Yu. Glebov, D. R. Harding, J. P. Knauer, J. A. Marozas, F. J. Marshall, P. B. Radha, T. C. Sangster, R. C. Shah, C. Stoeckl, R. W. Luo, M. E. Schoff, and M. Farrell, "Dependence of Hot-Spot Mix in DT Cryogenic Implosions on the Design Adiabat."

H. G. Rinderknecht, D. T. Casey, R. Bionta, R. Hatarik, A. Moore, E. P. Hartouni, D. Scholssberg, G. P. Grim, O. L. Landen, and P. K. Patel, "Signatures of Systematic Azimuthal Asymmetry in Nuclear Diagnosis of ICF Implosions on the NIF."

M. J. Rosenberg, A. A. Solodov, R. K. Follett, W. Seka, S. P. Regan, R. Epstein, A. R. Christopherson, R. Betti, A. V. Maximov, T. J. B. Collins, V. N. Goncharov, R. W. Short, D. Turnbull, D. H. Froula, P. B. Radha, J. F. Myatt, P. Michel, M. Hohenberger, L. Masse, G. Swadling, J. S. Ross, T. Chapman, J. D. Moody, J. W. Bates, and A. J. Schmitt, "Laser–Plasma Interaction Experiments at Direct-Drive Ignition-Relevant Scale Lengths at the National Ignition Facility."

J. J. Ruby, J. R. Rygg, C. J. Forrest, V. Yu. Glebov, D. A. Chin, G. W. Collins, B. Bachmann, J. A. Gaffney, Y. Ping, H. Sio, and N. V. Kabadi, "Measurement of Plasma Conditions at Shock Collapse on OMEGA."

R. Saha, J. Topp-Mugglestone, G. Gregori, T. White, S. P. Regan, G. W. Collins, and J. R. Rygg, "Atomic and Electronic Structure of Warm Dense Silicon."

J. L. Shaw, Z. Barfield, D. Haberberger, A. M. Hansen, J. Katz, D. Mastrosimone, D. H. Froula, F. Albert, P. M. King, N. Lemos, J. Williams, P. Fan, and Y. Lu, "Laser Wakefield Acceleration Platform for OMEGA EP."

A. Shvydky, D. Haberberger, J. Carroll-Nellenback, D. Cao, D. H. Froula, V. N. Goncharov, S. X. Hu, I. V. Igumenshchev, J. P. Knauer, J. A. Marozas, A. V. Maximov, P. B. Radha, S. P. Regan, and T. C. Sangster, "Numerical Simulations of Shock-Release OMEGA EP Experiments."

A. A. Solodov, M. J. Rosenberg, W. Seka, R. Epstein, R. W. Short, R. K. Follett, A. R. Christopherson, R. Betti, P. B. Radha, S. P. Regan, D. H. Froula, V. N. Goncharov, J. F. Myatt, P. Michel, M. Hohenberger, T. Chapman, J. D. Moody, J. W. Bates, and A. J. Schmitt, "Hot-Electron Generation and Preheat in Direct-Drive Experiments at the National Ignition Facility."

C. Stoeckl, T. J. B. Collins, R. Epstein, V. N. Goncharov, R. K. Jungquist, C. Mileham, P. B. Radha, S. P. Regan, T. C. Sangster, and W. Theobald, "Investigating Small Scale Mix in Direct-Drive Cryogenic DT Implosions with Radiography on OMEGA."

G. Tabak, M. Millot, T. R. Boehly, L. Crandall, B. J. Henderson, M. Zaghoo, S. Ali, P. M. Celliers, D. E. Fratanduono, S. Hamel, A. Lazicki, D. Swift, P. Loubeyre, R. Kodama, K. Miyanishi, T. Ogawa, N. Ozaki, T. Sano, R. Jeanloz, D. G. Hicks, G. W. Collins, J. H. Eggert, and J. R. Rygg, "Equation of State and Metallization of Methane Shock-Compressed to 400 GPa."

W. Theobald, R. Betti, A. Bose, S. X. Hu, E. M. Campbell, S. P. Regan, C. A. McCoy, A. Casner, L. Ceurvorst, and M. Karasik, "The Hybrid Target Approach: A Promising Path Forward to Mitigate Laser Imprint in Direct Drive Inertial Confinement Fusion."

D. Turnbull, P. Franke, S.-W. Bahk, I. A. Begishev, R. Boni, J. Bromage, S. Bucht, A. Davies, D. Haberberger, J. Katz, T. J. Kessler, A. L. Milder, J. P. Palastro, J. L. Shaw, D. H. Froula, M. Edwards, Q. Jia, K. Qu, N. Fisch, N. Vafaei-Najabadi, J. Vieira, and F. Quéré, "Ionization Waves of Arbitrary Velocity."

K. M. Woo, R. Betti, O. M. Mannion, D. Patel, V. N. Goncharov, K. S. Anderson, P. B. Radha, J. P. Knauer, V. Gopalaswamy, A. R. Christopherson, E. M. Campbell, H. Aluie, D. Shvarts, J. Sanz, and A. Bose, "Impact of Three-Dimensional Hot-Spot Flow Asymmetry on Ion-Temperature Measurements in Inertial Confinement Fusion Experiments."

M. Zaghoo, G. W. Collins, T. R. Boehly, J. R. Rygg, V. V. Karasiev, S. X. Hu, and P. M. Celliers, "Breakdown of Fermi Degeneracy in the Simplest Liquid Metal" (invited).

H. Zhang, R. Betti, D. Zhao, H. Aluie, R. Yan, and D. Shvarts, "Self-Similar Multimode Bubble-Front Evolution of the Ablative Rayleigh–Taylor Instability in Two and Three Dimensions."

J. L. Peebles, J. R. Davies, D. H. Barnak, R. Betti, V. Yu. Glebov, E. C. Hansen, J. P. Knauer, K. J. Peterson, and D. B. Sinars, "Scaled Neutron-Yield Enhancement Using the Laser-Driven MagLIF Platform on the OMEGA Laser," presented at the MagLIF Meeting, Portland OR, 5–9 November 2018.

M. S. Wei, "Status of FY18 OLUG Findings and Recommendations," presented at OLUG Meeting at APS Division of Plasma Physics, Portland OR, 6 November 2018.

The following presentations were made at Technology of Fusion Energy 2018, Orlando, FL, 11–15 November 2018:

C. Fagan, M. Sharpe, W. T. Shmayda, and W. U. Schröder, "Tritium Retention in Hexavalent Chromate-Conversion–Coated Aluminum Alloy."

J. L. Peebles, J. R. Davies, D. H. Barnak, R. Betti, V. Yu. Glebov, E. C. Hansen, J. P. Knauer, K. J. Peterson, and D. B. Sinars, "Pulsed-Power and Laser-Driven Magnetized Liner Inertial Fusion."

M. Sharpe, C. Fagan, and W. T. Shmayda, "Distribution of Tritium in the Near Surface of 316 Stainless-Steel."

W. T. Shmayda, C. R. Shmayda, and J. Torres, "Tritium Extraction from Water."

T. C. Sangster, "Status of Laser-Direct-Drive Fusion in the U.S.," presented at the Institute of Applied Physics and Computational Mathematics, Beijing, China, 29–30 November 2018.

D. H. Froula, C. Dorrer, E. M. Hill, R. K. Follett, A. A. Solodov, J. P. Palastro, D. Turnbull, D. H. Edgell, J. Bromage, T. J. Kessler, J. G. Shaw, A. M. Hansen, A. L. Milder, J. Katz, R. Boni, J. D. Zuegel, V. N. Goncharov, E. M. Campbell, P. Michel, D. Strozzi, M. Glensky, K. Peterson, J. W. Bates, A. Schmitt, J. L. Weaver, and J. F. Myatt, "Innovative Science and Broadband Lasers at LLE—A Path to an Expanded ICF Design Space," presented at Fusion Power Associates 39th Annual Meeting and Symposium, Washington, DC, 4–5 December 2018.

The following presentations were made at the Joint U.S./Israel Workshop on High-Energy-Density Physics, Tel Aviv, Israel, 10–12 December 2018:

R. Betti, "Fusion Research at LLE: Direct Drive and Magnetized Targets."

T. R. Boehly, "High-Energy-Density Physics Research at LLE."

E. M. Campbell, "NIF—An Unexpected Journey, Lessons Learned to Secure "Projects of Scale" and the Future of ICF Research."

T. C. Sangster, "Overview of the Laboratory for Laser Energetics."

J. D. Zuegel, C. Dorrer, E. M. Hill, R. K. Follett, A. A. Solodov, J. P. Palastro, D. Turnbull, D. H. Edgell, J. Bromage, T. J. Kessler, J. G. Shaw, A. M. Hansen, A. L. Milder, J. Katz, R. Boni, V. N. Goncharov, E. M. Campbell, P. Michel, D. Strozzi, M. Glensky, K. Peterson, J. W. Bates, A. Schmitt, J. L. Weaver, and J. F. Myatt, "Laser–Plasma Instabilities and R&D Plans for Fourth-Generation ICF Lasers."

M. Wei, "LaserNetUS Facility Readiness—Omega Laser Facility," presented at the LaserNetUS PI Meeting, Rockville, MD, 16 January 2019.

The following presentations were made at the Japan–U.S. Symposium, Washington, DC, 23–24 January 2019:

G. W. Collins, "Forging a New Frontier of HED Science Through Japan–U.S. Collaborations."

D. H. Froula, "Japan–U.S. Collaborations—Future Collaborations and the Direction of LLE Laser Science and Plasma Physics Research."

E. M. Campbell, "Fusion: Making a Star on Earth and the Quest for the Ultimate Energy Source to Power the Planet," presented at the Cornell University Seminar, Ithaca, NY, 31 January 2019.

The following presentations were made at LASE 2019, San Francisco, CA, 2–7 February 2019:

K. A. Bauer, M. Heimbueger, S. Sampat, L. J. Waxer, E. C. Cost, J. H. Kelly, V. Kobilansky, J. Kwiatkowski, S. F. B. Morse, D. Nelson, D. Weiner, G. Weselak, and J. Zou, "Comparison of On-Shot, In-Tank, and Equivalent-Target-Plane Measurements of the OMEGA Laser System Focal Spot."

W. R. Donaldson and A. Consentino, "Co-Timing UV and IR Laser Pulses on the OMEGA EP Laser System."

B. E. Kruschwitz, J. Kwiatkowski, C. Dorrer, M. Barczys, A. Consentino, D. H. Froula, M. J. Guardalben, E. M. Hill, D. Nelson, M. J. Shoup III, D. Turnbull, L. J. Waxer, and D. Weiner, "Tunable UV Upgrade on OMEGA EP."

S. Sampat, T. Z. Kosc, K. A. Bauer, R. D. Dean, W. R. Donaldson, J. Kwiatkowski, R. Moshier, A. L. Rigatti, M. H. Romanofsky, L. J. Waxer, and J. H. Kelly, "Power Balancing a Multibeam Laser."

L. J. Waxer, K. A. Bauer, E. C. Cost, M. Heimbueger, J. H. Kelly, V. Kobilansky, S. F. B. Morse, D. Nelson, R. Peck, R. Rinefierd, S. Sampat, M. J. Shoup III, D. Weiner, G. Weselak, and J. Zou, "In-Tank, On-Shot Characterization of the OMEGA Laser System Focal Spot."

The following presentations were made at Photonics West, San Francisco, CA, 2–7 February 2019:

I. A. Begishev, M. H. Romanofsky, S. Carey, R. Chapman, G. Brent, M. J. Shoup III, J. D. Zuegel, and J. Bromage, "High-Efficiency, Large-Aperture Fifth-Harmonic–Generation of

211-nm Pulses in Ammonium Dihydrogen Phosphate Crystals for Fusion Diagnostics."

K. Kopp and S. G. Demos, "Microscopy with Ultraviolet Surface Excitation (MUSE) Enables Translation of Optical Biopsy Principles to Enhance Life Science Education."

T. Z. Kosc, T. J. Kessler, H. Huang, R. A. Negres, and S. G. Demos, "Raman Scattering Cross-Section Measurements Using KDP Polished Crystal Spheres to Understand Transverse Stimulated Raman Scattering."

S. P. Regan, R. Epstein, M. Bedzek, R. Betti, T. R. Boehly, M. Bonino, N. Chartier, G. W. Collins, J. A. Delettrez, D. H. Froula, V. Yu. Glebov, V. N. Goncharov, S. X. Hu, I. V. Igumenshchev, D. R. Harding, J. P. Knauer, M. Lawrie, F. J. Marshall, D. T. Michel, P. B. Radha, M. J. Rosenberg, J. R. Rygg, R. Saha, R. C. Shah, M. J. Shoup III, C. Stoeckl, T. C. Sangster, W. Theobald, E. M. Campbell, H. Sawada, R. C. Mancini, K. Falk, E. Rowe, J. Topp-Mugglestone, P. Kozlowski, G. Gregori, J. Wark, J. A. Frenje, M. Gatu Johnson, N. Kabadi, C. K. Li, H. Sio, R. D. Petrasso, P. Keiter, P. X. Belancourt, R. P. Drake, N. Woolsey, I. E. Golovkin, J. J. MacFarlane, S. H. Glenzer, B. A. Hammel, L. J. Suter, S. Ayers, M. A. Barrios, P. M. Bell, D. K. Bradley, M. J. Edwards, K. B. Fournier, S. W. Haan, O. A. Hurricane, C. A. Iglesias, N. Izumi, O. L. Landen, D. Larson, A. Nikroo, M. Schneider, H. A. Scott, T. Ma, P. K. Patel, D. Thorn, B. G. Wilson, D. A. Haynes, D. D. Meyerhofer, H. Huang, J. Jaquez, J. D. Kilkenny, L. Gao, K. Hill, B. Kraus, P. Efthimion, Y. Lu, X. Huang, and P. Fan, "X-Ray Spectroscopy and Inertial Confinement Fusion," presented at the University of Nebraska, Lincoln, NE, 13 February 2019.

E. M. Campbell, "Fusion: Making a Star on Earth and the Quest for the Ultimate Energy Source to Power the Planet," presented at SUNY Geneseo Seminar, Geneseo, NY, 14 February 2019.

E. M. Campbell, "Fusion: Making a Star on Earth and the Quest for the Ultimate Energy Source to Power the Planet," presented at the ASME Student Banquet, Rochester, NY, 15 February 2019.

M. S. Wei, "LaserNetUS-OMEGA EP Laser System and Experimental Capability," presented at LaserNetUS, Virtual Meeting, 15 February 2019.

The following presentations were made at the 59th Sanibel Symposium, St. Simons Island GA, 17–22 February 2019:

J. Hinz, V. V. Karasiev, S. X. Hu, M. Zaghoo, and D. Mejia-Rodriguez, "Deorbitalized Meta-GGA with the Long-Range van der Waals Exchange-Correlation Functional Calculations of the Insulator–Metal Transition of Hydrogen."

V. V. Karasiev, S. X. Hu, M. Zaghoo, T. R. Boehly, S. B. Trickey, and J. W. Dufty, "Exchange-Correlation Thermal Effects: Softening the Deuterium Hugoniot and Thermophysical Properties."

R. Paul, V. V. Karasiev, and S. X. Hu, "High-Pressure Phases and Spectral Properties of Silicon."

J. L. Peebles, J. R. Davies, R. Moshier, M. Bradley, T. Nguyen, G. Weselak, G. Fiksel, R. Shapovalov, R. Spielman, G. Brent, D. W. Jacobs-Perkins, A. Bose, M. Gatu Johnson, C. K. Li, J. A. Frenje, R. D. Petrasso, and R. Betti, "Magnetizing 60-Beam Spherical Implosions on OMEGA," presented at the 2019 Stewardship Science Academic Programs Symposium, Albuquerque, NM, 19–20 February 2019.

E. M. Campbell, "LLE Priorities FY2020–FY2021," presented at the ICF Executives Meeting, Albuquerque, NM, 21–22 February 2019.

G. W. Collins, "Extreme Matters: A Laboratory Exploration of Planets, Stars, and Quantum Matter," presented at the Phelps Colloquium, Rochester, NY, 27 February 2019.

G. W. Collins, J. R. Rygg, T. R. Boehly, M. Zaghoo, D. N. Polsin, B. J. Henderson, X. Gong, L. Crandall, R. Saha, J. J. Ruby, G. Tabak, M. F. Huff, Z. K. Sprowal, D. A. Chin, M. K. Ginnane, P. M. Celliers, J. H. Eggert, A. Lazicki, R. F. Smith, R. Hemley,

F. Coppari, B. Bachmann, J. Gaffney, D. E. Fratanduono, D. G. Hicks, Y. Ping, D. Swift, D. G. Braun, S. Hamel, M. Millot, M. Gorman, R. Briggs, S. Ali, R. Kraus, P. Loubeyre, S. Brygoo, R. Jeanloz, R. Falcone, M. McMahon, F. N. Beg, C. Bolme, A. Gleason, S. Glenzer, H. Lee, T. Duffy, J. Wang, J. Wark, and G. Gregori, "Laser Focus on Planets: Exploring Planets and Stars Through High Energy Density Science," presented at the APS March Meeting, Boston, MA, 4–8 March 2019.

The following presentations were made at Matter in Extreme Conditions from Material Science to Planetary Physics, Montgenevre, France, 17–23 March 2019:

G. W. Collins, J. R. Rygg, T. R. Boehly, M. Zaghoo, D. N. Polsin, B. J. Henderson, X. Gong, L. E. Crandall, R. Saha, J. J. Ruby, G. Tabak, M. F. Huff, Z. K. Sprowal, D. A. Chin, M. K. Ginnane, P. M. Celliers, J. H. Eggert, A. Lazicki, R. F. Smith, R. Hemley, F. Coppari, B. Bachman, J. Gaffney, D. E. Fratanduono, D. G. Hicks, Y. Ping, D. Swift, D. G. Braun, S. Hamel, M. Millot, M. Gorman, R. Briggs, S. Ali, R. Kraus, P. Loubeyre, S. Brygoo, R. Jeanloz, R. Falcone, M. McMahon, F. N. Beg, C. Bolme, A. Gleason, S. H. Glenzer, H. Lee, T. Duffy, J. Wang, J. Wark, and G. Gregori, "Shock Physicists: Today's Explorers of the Universe."

B. J. Henderson, M. Zaghoo, X. Gong, D. N. Polsin, J. R. Rygg, T. R. Boehly, G. W. Collins, S. Ali, P. M. Celliers, A. E. Lazicki, M. Gorman, M. Millot, J. H. Eggert, and M. McMahon, "Broadband Reflectivity Diagnostic Development for Dynamic Compression Experiments on OMEGA EP."

J. R. Rygg, D. N. Polsin, X. Gong, T. R. Boehly, G. W. Collins, S. P. Regan, C. Sorce, J. H. Eggert, R. Smith, A. Lazicki, M. Ahmed, A. Arsenlis, M. A. Barrios, J. Bernier, K. Blobaum, D. G. Braun, R. Briggs, P. M. Celliers, A. Cook, F. Coppari, D. E. Fratanduono, M. Gorman, B. Heidl, M. Hohenberger, D. H. Kalantar, S. Khan, R. Kraus, J. McNaney, D. Swift, J. Ward, C. Wehrenberg, A. Higginbothom, M. Suggit, J. Wark, J. Wang, T. Duffy, J. Wicks, and M. McMahon, "X-Ray Diffraction in the Terapascal Regime."

W. T. Shmayda, C. Fagan, and R. C. Shmayda, "Reducing Releases from Tritium Facilities," presented at the First Tritium School, Ljubljana, Slovenia, 25–28 March 2019.

The following presentations were made at the International Conference on High Energy Density Science, Oxford, UK, 31 March–5 April 2019:

R. Betti, "Recent Advances in Direct-Drive Laser Fusion."

S. X. Hu, Y. H. Ding, V. V. Karasiev, R. Paul, M. Ghosh, J. Hinz, P. M. Nilson, T. R. Boehly, P. B. Radha, V. N. Goncharov, S. Skupsky, J. R. Rygg, G. W. Collins, S. P. Regan, E. M. Campbell, L. A. Collins, J. D. Kress, A. J. White, O. Certik, and B. Militzer, "Warming Up Density Functional Theory (DFT) for High-Energy-Density Plasmas."

D. N. Polsin, X. Gong, M. F. Huff, L. E. Crandall, G. W. Collins, T. R. Boehly, J. R. Rygg, A. Lazicki, M. Millot, P. M. Celliers, J. H. Eggert, and M. I. McMahon, "High-Pressure Structural and Electronic Properties of Ramp-Compressed Sodium."

J. Bromage, A. Agliata, S.-W. Bahk, M. Bedzyk, I. A. Begishev, W. A. Bittle, T. Buczek, J. Bunkenburg, D. Canning, A. Consentino, D. Coppenbarger, R. Cuffney, C. Dorrer, C. Feng, D. H. Froula, G. Gates, M. J. Guardalben, D. Haberberger, S. Hadrich, C. Hall, B. N. Hoffman, R. K. Jungquist, T. J. Kessler, E. Kowaluk, B. E. Kruschwitz, T. Lewis, J. Magoon, D. D. Meyerhofer, C. Mileham, M. Millecchia, S. F. B. Morse, P. M. Nilson, J. B. Oliver, R. G. Peck, A. L. Rigatti, H. Rinderknecht, R. G. Roides, M. H. Romanofsky, J. Rothhardt, E. M. Schiesser, K. Shaughnessy, M. J. Shoup III, C. Smith, M. Spilatro, C. Stoeckl, R. Taylor, B. Wager, L. J. Waxer, B. Webb, D. Weiner, and J. D. Zuegel, "Laser Technology Development for Ultra-Intense Optical Parametric Chirped-Pulse Amplification," presented at Optics and Optoelectronics 2019, Prague, Czech Republic, 1–4 April 2019.

G. W. Collins, J. R. Rygg, T. R. Boehly, M. Zaghoo, D. N. Polsin, B. J. Henderson, X. Gong, L. Crandall, R. Saha, J. J. Ruby, G. Tabak, M. Huff, Z. K. Sprowal, D. A. Chin, M. K. Ginnane, P. M. Celliers, J. H. Eggert, A. Lazicki, R. F. Smith, R. Hemley, F. Coppari, B. Bachmann, J. Gaffney, D. E. Fratanduono, D. G. Hicks, Y. Ping, D. Swift, D. G. Braun, S. Hamel, M. Millot, M. Gorman, R. Briggs, S. Ali, R. Kraus, M. McMahon, P. Loubeyre, S. Brygoo, R. Jeanloz, R. Falcone, F. N. Beg, C. Bolme, A. Gleason, S. H. Glenzer, H. Lee, T. Duffy, J. Wang, J. Wark, and G. Gregori, "Extreme Matters: Pressure to Explore New Worlds and Exotic Solids," presented at the 2019 Mach Conference, Annapolis, MD, 3–5 April 2019.

The following presentations were made at CEIS 2019, Rochester, NY, 4 April 2019:

W. R. Donaldson and Y. Zhao, "Picosecond UV Photodiodes."

A. Stenson, G. Chen, Y. Akbas, I. Komissarov, R. Sobolewski, A. Jafari-Salim, and O. Mukhanov, "Superconducting Single-Photon Detectors as Smart Sensors."

E. M. Campbell, "Laser-Direct-Drive Status and Future Plans," presented at MIT, Cambridge, MA, 5 April 2019.

The following presentations were made at the 15th Direct-Drive and Fast-Ignition Workshop, Rome, Italy, 8–10 April 2019:

R. Betti, V. Gopalaswamy, J. P. Knauer, N. Luciani, D. Patel, K. M. Woo, A. Bose, I. V. Igumenshchev, E. M. Campbell, K. S. Anderson, K. A. Bauer, M. J. Bonino, D. Cao, A. R. Christopherson, G. W. Collins, T. J. B. Collins, J. R. Davies, J. A. Delettrez, D. H. Edgell, R. Epstein, C. J. Forrest, D. H. Froula, V. Yu. Glebov, V. N. Goncharov, D. R. Harding, S. X. Hu, D. W. Jacobs-Perkins, R. T. Janezic, J. H. Kelly, O. M. Mannion, A. V. Maximov, F. J. Marshall, D. T. Michel, S. Miller, S. F. B. Morse, J. P. Palastro, J. L. Peebles, P. B. Radha, S. P. Regan, S. Sampat, T. C. Sangster, A. B. Sefkow, W. Seka, R. C. Shah, W. T. Shmayda, A. Shvydky, C. Stoeckl, A. A. Solodov, W. Theobald, and J. D. Zuegel, "Progress Toward Demonstrating Hydro-Equivalent Ignition with Direct-Drive Inertial Confinement Fusion."

V. N. Goncharov, "Acoustic Trapping and Perturbation Amplification in Nested Rarefaction Waves."

J. P. Palastro, R. K. Follett, D. Turnbull, C. Dorrer, E. M. Hill, L. Nguyen, A. S. Davies, A. M. Hansen, R. J. Henchen, A. Milder, A. A. Solodov, A. Shvydky, J. Bromage, V. N. Goncharov, D. H. Froula, J. Bates, J. L. Weaver, S. Obenschain, and A. Colaïtis, "Expanding the Inertial Confinement Fusion Design Space with Broadband Mitigation of Laser–Plasma Instabilities."

S. P. Regan, V. N. Goncharov, T. C. Sangster, R. Betti, E. M. Campbell, K. A. Bauer, T. R. Boehly, M. J. Bonino, D. Cao, A. R. Christopherson, G. W. Collins, T. J. B. Collins, R. S. Craxton, D. H. Edgell, R. Epstein, C. J. Forrest, R. K. Follett, J. A. Frenje, D. H. Froula, V. Yu. Glebov, V. Gopalaswamy, D. R. Harding, S. X. Hu, I. V. Igumenshchev, S. T. Ivancic, D. W. Jacobs-Perkins, R. T. Janezic, J. H. Kelly, M. Karasik, T. J. Kessler, J. P. Knauer, T. Z. Kosc, O. M. Mannion, J. A. Marozas, F. J. Marshall, P. W. McKenty, Z. Mohamed, S. F. B. Morse, P. M. Nilson, J. P. Palastro, R. D. Petrasso, D. Patel, J. L. Peebles, P. B. Radha, H. G. Rinderknecht, M. J. Rosenberg, S. Sampat, W. Seka, R. C. Shah, J. R. Rygg, J. G. Shaw, W. T. Shmayda, M. J. Shoup III, A. Shvydky, A. A. Solodov, C. Sorce, C. Stoeckl, W. Theobald, D. Turnbull, J. Ulreich, M. D. Wittman, K. M. Woo, J. D. Zuegel, J. A. Frenje, M. Gatu Johnson, R. D. Petrasso, M. Karasik, S. P. Obenschain, and A. J. Schmitt, "Multidimensional Effects on Hot-Spot Formation in OMEGA DT Cryogenic Implosions."

E. M. Campbell, "Fusion: Making a Star on Earth and the Quest for the Ultimate Energy Source to Power the Planet," presented at Torch Club, Rochester, NY, 9 April 2019.

E. M. Campbell, "Laser-Direct-Drive Status and Future Plans," presented at Washington State University, Pullman, WA, 11 April 2019.

The following presentations were made at the APS April Meeting 2019, Denver, CO, 13–16 April 2019:

C. J. Forrest, J. P. Knauer, E. M. Campbell, G. W. Collins, V. Yu. Glebov, O. M. Mannion, Z. Mohamed, P. B. Radha, S. P. Regan, T. C. Sangster, C. Stoeckl, A. Deltuva, and W. U. Schröder, "Neutron-Induced Breakup of Deuterium at 14 MeV."

A. Schwemmlein, W. U. Schröder, C. Stoeckl, C. J. Forrest, V. Yu. Glebov, S. P. Regan, T. C. Sangster, W. Theobald, "Using the OMEGA EP Laser for Nuclear Experiments at LLE."

G. W. Collins, "Extreme Matters: Pressure to Explore New Worlds and Exotic Solids," presented at the Materials Science and Engineering Colloquium, New York, NY, 19 April 2019.

The following presentations were made at the 12th International Conference on Tritium Science and Technology, Busan, Korea, 22–26 April 2019:

C. Fagan, M. Sharpe, W. T. Shmayda, and W. U. Schröder, "Thin-Alumina Film as a Tritium Adsorption Inhibitor for Stainless-Steel 316."

M. D. Sharpe, K. Glance, and W. T. Shmayda, "Measurement of Palladium Hydride and Palladium Deuteride Isotherms Between 130 and 393 K."

W. T. Shmayda, M. D. Sharpe, C. Fagan, M. D. Wittman, R. F. Earley, and N. P. Redden, "Tritium Activities at the University of Rochester's Laboratory for Laser Energetics."

The following presentations were made at the Target Fabrication Meeting 2019, Annapolis, MD, 23–26 April 2019:

M. J. Bonino, D. R. Harding, W. Sweet, M. Schoff, A. Greenwood, N. Satoh, M. Takagi, and A. Nikroo, "Properties of Vapor-Deposited and Solution-Processed Targets for Laser-Driven Inertial Confinement Fusion Experiments."

T. Cracium, M. J. Bonino, L. Crandall, B. J. Henderson, J. J. Ruby, J. R. Rygg, J. L. Peebles, M. Huff, X. Gong, D. N. Polsin, D. A. Chin, and M. K. Ginnane, "High-Energy-Density Target Production at LLE."

A. Lighty and D. R. Harding, "Using a Liquid–Liquid Extraction Technique to Reduce the Number and Size of Vacuoles in Polystyrene Films."

J. L. Shaw, D. Wasilewski, D. R. Harding, Z. Barfield, D. Haberberger, A. M. Hansen, J. Katz, D. Mastrosimone, D. H. Froula, P. Fan, Y. Lu, J. Campbell, J. P. Sauppe, and K. A. Flippo, "Targets for Underdense Plasma Studies at the Laboratory for Laser Energetics."

D. W. Turner, M. J. Bonino, T. Cracium, J. L. Peebles, J. Streit, and J. Hund, "Manufacture of Targets for Magnetized Liner Inertial Fusion Campaigns on the OMEGA-60 Laser System."

D. Wasilewski, D. R. Harding, J. L. Shaw, Y. Lu, P. Fan, and J. Campbell, "Methods for Removing Fragile Printed-Foam Structures from Their Substrates."

M. D. Wittman, D. R. Harding, N. P. Redden, J. Ulreich, R. Chapman, and L. Carlson, "Progress on Filling and Layering DT-Filled Fill-Tube Capsules for OMEGA Experiments."

S.-W. Bahk, "Programmable Beam-Shaping System for High Power Laser Systems," presented at the RIT Center for Imaging Science Seminar, Rochester, NY, 24 April 2019.

The following presentations were made at the Omega Laser Facility Users Group Workshop, Rochester, NY, 24–26 April 2019:

M. Barczys, R. Brown, D. Canning, A. Consentino, D. Coppenbarger, M. J. Guardalben, E. M. Hill, T. Z. Kosc, B. E. Kruschwitz, R. Russo, M. Spilatro, A. Szydlowski, and L. J. Waxer, "Advancements in Pulse Shaping on OMEGA EP."

K. A. Bauer, L. J. Waxer, M. Heimbueger, J. H. Kelly, J. Kwiatkowski, S. F. B. Morse, D. Nelson, S. Sampat, and D. Weiner, "Comparison of On-Shot, In-Tank, and Equivalent-Target-Plane Measurements of the OMEGA Laser System Focal Spot."

J. Bromage, "Capabilities and Future Prospects for the Multi-Terawatt (MTW) Laser Facility at LLE."

K. M. Glance, W. T. Shmayda, and M. D. Sharpe, "Using Paladium Hydride to Fill Inertial Confinement Fusion Targets."

Z. L. Mohamed, J. P. Knauer, C. J. Forrest, and M. Gatu Johnson, "Wave-Function Amplitude Analysis of the ^{5}He Resonance in the TT Neutron Spectrum."

S. F. B. Morse, "Omega Facility OLUG 2019 Update: Progress on Recommendations and Items of General Interest."

H. G. Rinderknecht, "Summary of the EP OPAL Workshop."

A. Sharma and R. S. Craxton, "Optimization of Cone-In-Shell Targets for an X-Ray Backlighter at the National Ignition Facility."

A. Sorce, J. Kendrick, D. Weiner, T. R. Boehly, J. R. Rygg, M. K. Ginnane, J. Zou, A. Liu, and M. Couch, "Recent Upgrades to the Omega Laser Facility's VISAR and SOP Diagnostics."

C. Sorce, "Gas-Jet System on OMEGA and OMEGA EP."

A. J. Howard, D. Turnbull, A. S. Davies, P. Franke, D. H. Froula, and J. P. Palastro, "Photon Acceleration in a Flying Focus," presented at Design Day, Rochester, NY, 2 May 2019.

V. V. Karasiev and S. X. Hu, "Development of Finite-T Exchange-Correlation Functionals: Improving Reliability for WDM Applications," presented at the 10th International Workshop on Warm Dense Matter, Travemünde, Germany, 5–9 May 2019 (invited).

The following presentations were made at CLEO 2019, San Jose, CA, 5–10 May 2019:

S. Bucht, D. Haberberger, J. Bromage, and D. H. Froula, "Designing Grism Stretchers for Idler-Based Optical Parametric Chirped-Pulse–Amplification Systems."

Y. Zhao and W. R. Donaldson, "Ultrafast AlGaN UV Photodetectors with Picoseconds Response."

J. L. Shaw, J. P. Palastro, D. Turnbull, T. J. Kessler, A. Davies, P. Franke, A. Howard, L. Nguyen, D. Ramsey, G. W. Jenkins, S.-W. Bahk, I. A. Begishev, R. Boni, J. Bromage, S. Bucht, R. K. Follett, D. Haberberger, J. Katz, F. A. Hegmann, D. Purshchke, N. Vafaei-Najafabadi, J. Vieira, and F. Quere, "Flying Focus and Its Application to Laser-Plasma Accelerators," presented at the Laser-Plasma Accelerator Workshop, Split, Croatia, 5–10 May 2019 (invited).

The following presentations were made at the UBUR Superconductivity Workshop, Buffalo, 10 May 2019:

W. R. Donaldson, "Measuring Optically Activated Transient Superconductivity Events at LLE."

J. R. Rygg, "Tutorial: High Pressure Physics."

M. Zaghoo, "Capabilities and Techniques for Diamond Anvil Cells."

H. G. Rinderknecht, "Frontiers in Ultrahigh Intensity and Relativistic Physics Enabled by an Optical Parametric Amplifier Laser (EP OPAL) Facility," presented at Plasma Physics Town Hall Meeting, Rochester, NY, 16 May 2019.

R. Epstein, "Laser Fusion at the University of Rochester's Laboratory for Laser Energetics," presented at Science Exploration Day, Rochester, NY, 17 May 2019.

M. S. Wei, "National Laser Users' Facility and Basic Science Programs at the Omega Laser Facility," presented at Workshop on Opportunities, Challenges, and Best Practices for Basic Plasma Science User Facilities, College Park, MD, 20–21 May 2019.

The following presentations were made at CEA–NNSA Joint Diagnostic Meeting, Washington, DC, 21–22 May 2019:

R. Boni, "Update on Streak Tube Simulations."

S. T. Ivancic, W. Theobald, C. Sorce, M. Bedzyck, F. J. Marshall, C. Stoeckl, R. C. Shah, M. Lawrie, S. P. Regan, T. C. Sangster, E. M. Campbell, T. J. Hilsabeck, K. Englehorn, J. D. Kilkenny, T. M. Chung, J. D. Hares, A. K. L. Dymoke-Bradhshaw, P. Bell, J. Celeste, A. C. Carpenter, M. Dayton, D. K. Bradley, M. C. Jackson, E. Hurd, L. Pickworth, S. R. Nagel, G. Rochau, J. Porter, M. Sanchez, L. Claus, G. Robertson, and Q. Looker, "The Single Line-of-Sight Time-Resolved X-Ray Imager on OMEGA."

S. P. Regan, "Neutron Imaging Systems on OMEGA."

The following presentations were made at the Laser Imprint Workshop, Rochester, NY, 22–24 May 2019:

T. J. B. Collins, C. Stoeckl, R. Epstein, S. Miller, O. M. Mannion, R. Betti, J. A. Delettrez, W. A. Bittle, C. J. Forrest,

V. Yu. Glebov, V. N. Goncharov, D. R. Harding, I. V. Igumenshchev, D. W. Jacobs-Perkins, R. J. Janezic, J. H. Kelly, T. Z. Kosc, C. Mileham, D. T. Michel, R. L. McCrory, P. W. McKenty, F. J. Marshall, S. F. B. Morse, P. B. Radha, S. P. Regan, B. Rice, T. C. Sangster, M. J. Shoup III, W. T. Shmayda, C. Sorce, W. Theobald, J. Ulreich, M. D. Wittman, J. A. Frenje, M. Gatu Johnson, and R. D. Petrasso, "Mixing at the Fuel–Ablator Interface in Backlit OMEGA Cryogenic Implosions."

C. Dorrer, "The FLUX Project."

S. X. Hu, J. L. Peebles, W. Theobald, S. P. Regan, P. B. Radha, A. Shvydky, V. N. Goncharov, M. Karasik, J. Oh, A. Velikovich, S. Obenschain, A. Casner, G. Duchateau, B. Chimier, H. Huang, M. Farrell, A. Nikroo, M. Hohenberger, V. A. Smalyuk, M. J. Bonino, D. R. Harding, T. R. Boehly, D. T. Michel, T. J. Kessler, J. P. Knauer, R. Epstein, I. V. Igumenshchev, M. J. Rosenberg, V. T. Tikhonchuk, A. Kar, C. Cao, C. Stoeckl, T. J. B. Collins, J. A. Marozas, K. S. Anderson, T. C. Sangster, R. Betti, D. H. Froula, J. P. Palastro, D. Turnbull, F. J. Marshall, M. Wei, T. Mehlhorn, and E. M. Campbell, "Review of Imprint Effects on Direct-Drive Inertial Confinement Fusion."

J. P. Knauer, "The Effect of Imprint on OMEGA Cryogenic Target Implosions."

J. L. Peebles, "OHRV Measurements in Direct-Drive Experiments."

A. Shvydky, P. B. Radha, M. J. Rosenberg, K. S. Anderson, V. N. Goncharov, J. A. Marozas, F. J. Marshall, P. W. McKenty, S. P. Regan, T. C. Sangster, M. Hohenberger, J. M. Di Nicola, J. M. Koning, M. M. Marinak, L. Masse, and M. Karasik, "Hydrodynamic Instability Growth and Imprint Experiments at the National Ignition Facility."

G. Chen, R. Adam, D. E. Burgler, I. Komissarov, S. Heidtfeld, H. Hardtdegen, M. Mikulics, C. M. Schneider, and R. Sobolewski, "Ultrabroadband THz Radiation Transients Emitted from Ta/NiFe/Pt Nanolayers upon Excitation by Femtosecond Laser Pulses," presented at Frontiers in Materials Science for the 21st Century Symposium, Rochester, NY, 23 May 2019.

C. Thomas, "Laser-Direct-Drive Status and Future Plans," presented at the 28th IEEE Symposium on Fusion Engineering, Ponte Vedra Beach, FL, 2–6 June 2019.

The following presentations were made at Optical Interference Coatings, Santa Ana Pueblo, NM, 2–7 June 2019:

S. MacNally, C. Smith, J. Spaulding, J. Foster, and J. B. Oliver, "Glancing-Angle-Deposited Silica Films for Ultraviolet Wave Plates."

J. B. Oliver, "Precision Coatings for Large Optics."

J. B. Oliver, A. L. Rigatti, T. Noll, J. Spaulding, J. Hettrick, V. Gruschow, G. Mitchell, D. Sadowski, C. Smith, and B. Charles, "Large-Aperture Coatings for Fusion-Class Laser Systems."

J. B. Oliver, J. Spaulding, and B. Charles, "Stress Compensation by Deposition of a Nonuniform Corrective Coating."

C. Smith, S. MacNally, and J. B. Oliver, "Ellipsometric Modeling of Serially Bi-Deposited Glancing-Angle–Deposition Coatings."

The following presentations were made at the 49th Anomalous Absorption Conference, Telluride, CO, 9–14 June 2019:

D. H. Edgell, R. Bahr, J. Katz, and D. H. Froula, "Anomalous Asymmetry of Unabsorbed Light in OMEGA Implosions."

R. K. Follett, J. G. Shaw, D. H. Edgell, D. H. Froula, C. Dorrer, J. Bromage, E. M. Hill, T. J. Kessler, A. V. Maximov, A. A. Solodov, E. M. Campbell, J. P. Palastro, J. F. Myatt, J. W. Bates, and J. L. Weaver, "Mitigation of Laser–Plasma Instabilities Using Bandwidth," (invited).

P. Franke, D. Turnbull, J. P. Palastro, J. Katz, I. A. Begishev, R. Boni, J. Bromage, J. L. Shaw, A. Howard, A. L. Milder, A. Davies, S. Bucht, D. Haberberger, A. M. Hansen, and D. H. Froula, "Measurement and Control of Ionization Waves of Arbitrary Velocity" (invited).

A. M. Hansen, D. Turnbull, J. Katz, A. L. Milder, J. P. Palastro, D. Mastrosimone, and D. H. Froula, "Phase Plates in Thomson-Scattering Experiments."

A. Howard, D. Turnbull, A. S. Davies, P. Franke, D. H. Froula, and J. P. Palastro, "Photon Acceleration in a Flying Focus."

A. Kar, S. X. Hu, P. B. Radha, and G. Duchateau, "A Microphysics Model to Understand the Solid-to-Plasma Transition of Dielectric Ablator Materials for Direct-Drive Implosions."

A. V. Maximov, J. G. Shaw, and J. P. Palastro, "Modeling Stimulated Raman Scattering and Cross-Beam Energy Transfer in Direct-Drive National Ignition Facility Plasmas."

A. L. Milder, R. Boni, J. Katz, P. Franke, S. T. Ivancic, J. L. Shaw, J. P. Palastro, A. Davies, A. M. Hansen, D. Turnbull, I. A. Begishev, D. H. Froula, M. Sherlock, H. Le, and W. Rozmus, "Measuring Electron Distribution Functions Driven by Inverse Bremsstrahlung Heating with Collective Thomson Scattering" (invited).

J. P. Palastro, T. M. Antonsen Jr., L. Nguyen, A. Howard, D. W. Ramsey, T. T. Simpson, R. K. Follett, D. Turnbull, J. Vieira, and D. H. Froula, "Cherenkov Radiation from a Plasma."

H. G. Rinderknecht, H. S. Park, J. S. Ross, P. A. Amendt, D. P. Higginson, S. C. Wilks, R. K. Follett, D. Haberberger, J. Katz, D. H. Froula, N. M. Hoffman, G. Kagan, B. Keenan, A. Simakov, L. Chacon, and E. Vold, "Ion-Velocity Structure in Strong Collisional Plasma Shocks" (invited).

M. J. Rosenberg, A. A. Solodov, W. Seka, R. K. Follett, S. P. Regan, C Ren, R. Epstein, A. R. Christopherson, R. Betti, A. V. Maximov, T. J. B. Collins, V. N. Goncharov, R. W. Short, D. H. Froula, P. B. Radha, J. F. Myatt, P. Michel, M. Hohenberger, L. Masse, G. Swadling, J. S. Ross, T. Chapman, J. D. Moody, J. W. Bates, and A. J. Schmitt, "Planar Laser–Plasma Interaction Experiments at Direct-Drive Ignition-Relevant Scale Lengths at the National Ignition Facility."

A. Ruocco, A. V. Maximov, J. P. Palastro, R. K. Follett, W. Theobald, A. Casner, D. Batani, J. Trela, A. Colaïtis, G. Duchateau, and V. T. Tikhonchuk, "Modeling of Laser–Plasma Interaction in the Shock-Ignition Regime with *LPSE*: Comparison with Particle-in-Cell Simulations and Experiments."

A. A. Solodov, M. J. Rosenberg, A. R. Christopherson, R. Betti, M. Stoeckl, W. Seka, R. Epstein, R. K. Follett, P. B. Radha, S. P. Regan, D. H. Froula, V. N. Goncharov, J. F. Myatt, M. Hohenberger, B. Bachmann, and P. Michel, "Hot-Electron Preheat and Energy Deposition in Direct-Drive Implosion Experiments at the National Ignition Facility."

D. Turnbull, C. Dorrer, D. Edgell, R. K. Follett, D. H. Froula, A. M. Hansen, J. Katz, B. Kruschwitz, A. L. Milder, J. P. Palastro, A. Colaïtis, T. Chapman, L. Divol, C. Goyon, G. E. Kemp, D. Mariscal, P. Michel, J. D. Moody, B. B. Pollock, J. S. Ross, D. J. Strozzi, E. R. Tubman, and N. C. Woolsey, "Crossed-Beam Energy Transfer Model Validation for Increased Confidence in Proposed Laser Upgrades and Implosion Scaling."

C. J. Forrest, V. Yu. Glebov, J. P. Knauer, P. B. Radha, J. R. Rygg, U. Schroeder, O. M. Mannion, Z. L. Mohamed, S. P. Regan, T. C. Sangster, A. Schwemmlein, C. Stoeckl, J. A. Frenje, M. Gatu Johnson, F. H. Seguin, R. D. Petrasso, D. T. Casey, C. Cerjan, D. Dearborn, M. J. Edwards, R. Hatarik, O. S. Jones, O. L. Landen, A. J. Mackinnon, S. Quaglioni, S. Sepke, P. Springer, I. Thomson, R. E. Tipton, A. B. Zylstra, G. Grim, C. Brune, A. Voinov, J. D. Kilkenny, B. Appelbe, A. Crilly, G. Hale, H. W. Herrmann, Y. H. Kim, M. Paris, W. Martin, and B. Augierre, "Nuclear Science at the University of Rochester's Omega Laser Facility," presented at Texas A & M University, College Station, TX, 13 June 2019.

The following presentations were made at the 21st Biennial Conference of the APS Topical Group on Shock Compression of Condensed Matter, Portland OR, 16–21 June 2019:

D. A. Chin, P. M. Nilson, J. J. Ruby, X. Gong, D. N. Polsin, T. R. Boehly, D. Mastrosimone, D. Guy, J. R. Rygg, G. W. Collins, I. Szumila, J. Buettner, D. Trail, M. Harmand, Y. Ping, F. Coppari, U. Feldman, and J. Seely, "An Extended X-Ray Absorption Fine Structure Spectroscopy Study of Iron Oxides."

L. Crandall, G. Tabak, Z. K. Sprowal, D. N. Polsin, J. R. Rygg, G. W. Collins, D. E. Fratanduono, R. F. Smith, and J. H. Eggert, "Dynamic Precompression: Secondary Hugoniot of MgO."

M. Ghosh and S. X. Hu, "Diamond Formation from Hydrocarbons in Planetary Conditions: An *ab initio* Study."

M. K. Ginnane, D. N. Polsin, X. Gong, T. R. Boehly, J. R. Rygg, G. W. Collins, A. Lazicki, R. Kraus, J. H. Eggert, M. Marshall, D. E. Fratanduono, J. P. Davis, C. A. McCoy, and C. Seagle, "X-Ray Diffraction of Shock-Ramped and Shock-Released Platinum."

X. Gong, D. N. Polsin, R. Paul, R. Saha, J. R. Rygg, and G. W. Collins, "Structure and Optical Properties of Ramp Compressed Silicon Up to 550 GPa."

B. J. Henderson, T. R. Boehly, M. Zaghoo, J. R. Rygg, D. N. Polsin, X. Gong, L. Crandall, M. F. Huff, M. K. Ginnane, G. W. Collins, S. Ali, P. M. Celliers, R. Briggs, M. Gorman, M. Marshall, and J. H. Eggert, "A Broadband Reflectance Diagnostic for Matter at Extreme Conditions."

M. Huff, J. R. Rygg, G. W. Collins, T. R. Boehly, M. Zaghoo, D. N. Polsin, B. J. Henderson, L. Crandall, D. E. Fratanduono, M. Millot, R. F. Smith, J. H. Eggert, P. M. Celliers, M. C. Gregor, and C. A. McCoy, "Sound Velocity in Shocked Iron and Beryllium to ~1500 GPa."

D. N. Polsin, X. Gong, M. F. Huff, L. E. Crandall, G. W. Collins, T. R. Boehly, J. R. Rygg, A. Lazicki, M. Millot, P. M. Celliers, J. H. Eggert, and M. I. McMahon, "High-Pressure Structural and Electronic Properties of Ramp-Compressed Sodium."

J. J. Ruby, J. R. Rygg, C. J. Forrest, V. Yu. Glebov, D. A. Chin, G. W. Collins, B. Bachmann, J. A. Gaffney, Y. Ping, H. Sio, and N. V. Kabadi, "Measurement of Spherically Converging Shock Waves on OMEGA."

J. R. Rygg, A. B. Zylstra, P. Grabowski, M. Millot, M. Gatu Johnson, B. Lahmann, R. D. Petrasso, F. H. Seguin, H. Sio, Y. H. Ding, and S. X. Hu, "Precision Measurements of Stopping Power in Shock-Compressed Carbon."

R. Saha, J. Topp-Mugglestone, G. Gregori, T. R. Boehly, G. W. Collins, S. P. Regan, T. G. White, and J. R. Rygg, "Atomic and Electronic Structure of Warm Dense Silicon."

Z. K. Sprowal, D. N. Polsin, T. R. Boehly, D. G. Hicks, J. R. Rygg, G. W. Collins, and M. F. Huff, "Double Shock in Polystyrene."

G. Tabak, M. A. Millot, S. Hamel, T. Ogawa, P. M. Celliers, D. E. Fratanduono, A. Lazicki, D. C. Swift, S. Brygoo, P. Loubeyre, T. R. Boehly, L. Crandall, B. J. Henderson, M. Zaghoo, S. Ali, R. Kodama, K. Miyanishi, N. Ozaki, T. Sano, R. Jeanloz, D. G. Hicks, G. W. Collins, J. H. Eggert, and J. R. Rygg, "Equation of State and Metallization of Methane Shock-Compressed to 400 GPa."

The following presentations were made at the 12th International Laser Operations Workshop 2019, Aldermaston, UK, 17–20 June 2019:

K. A. Bauer, M. Heimbueger, S. Sampat, L. J. Waxer, E. C. Cost, J. H. Kelly, V. Kobilansky, J. Kwiatkowski, S. F. B. Morse, D. Nelson, D. Weiner, G. Weselak, and J. Zou, "On-Shot, In-Tank Measurements of the OMEGA Laser System Focal Spot."

D. Canning, "Formalized Incident Investigation, Reporting, and Recurrence Mitigation."

S. Householder, G. Brent, J. Coon, M. Labuzeta, M. Barczys, J. H. Kelly, B. Kruschwitz, T. Smith, and S. F. B. Morse, "Improvements to Omega Disk Amplifier Performance Through Analysis of High-Resolution Flash-Lamp Waveforms."

J. Kwiatkowski, S. Sampat, K. A. Bauer, B. Ehrich, V. Guiliano, J. H. Kelly, T. Z. Kosc, R. G. Peck, and L. J. Waxer, "Characterization of Mid-Chain Transmission and Losses on OMEGA."

M. Labuzeta, J. Armstrong, M. Bonino, D. Canning, A. Consentino, S. Householder, M. Krieger, G. Pien, and C. Sorce, "Qualification Process for Experimental Users at the Omega Laser Facility."

L. J. Waxer, "Omega Facility Overview."

B. Rice, J. Ulreich, and M. J. Shoup III, "Prediction of Deuterium–Tritium Ice Layer Uniformity in Direct-Drive Confinement Fusion Target Capsules," presented NAFEMS World Congress 2019, Quebec City, Canada, 17–20 June 2019.

S.-W. Bahk, "Phase Retrieval Using Gaussian Basis Functions," presented at Computational Optical Sensing and Imaging, Munich, Germany, 24–27 June 2019.

V. N. Goncharov, "High-Energy-Density Physics Research at the Laboratory for Laser Energetics," presented at JOWOG 37, Aldermaston, UK, 8–11 July 2019.

A. S. Davies, J. Katz, S. Bucht, D. Haberberger, J. P. Palastro, J. L. Shaw, D. Turnbull, R. Boni, I. A. Begishev, S.-W. Bahk, J. Bromage, A. Sorce, J. Konzel, B. Cuffney, J. D. Zuegel, D. H. Froula, W. Rozmus, J. D. Sadler, R. Trines, R. Bingham, and P. A. Norreys, "Investigation of Electron Plasma Waves and Picosecond Thermodynamics in a Laser-Produced Plasma Using Thomson Scattering," presented at the 46th European Physical Society Conference on Plasma Physics, Milan, Italy, 8–12 July 2019.

D. H. Froula, "Lessons from Glenzer: Measuring Electron Distribution Functions with Thomson Scattering," presented at the Workshop on High-Energy-Density Physics, Rostock, Germany, 12 July 2019.

M. S. Wei, H. G. Rinderknecht, J. D. Zuegel, J. Bromage, P. M. Nilson, S. X. Hu, D. H. Froula, F. Albert, B. M. Hegelich, M. Roth, and E. M. Campbell, "Frontiers in High-Energy-Density and Relativistic Plasma Physics Enabled by EP-OPAL: A Multibeam Ultrahigh-Intensity Laser User Facility," presented at the First Community Workshop for High Energy, College Park, MD, 16–17 July 2019.

H. G. Rinderknecht, J. D. Zuegel, J. Bromage, M. S. Wei, P. M. Nilson, S. X. Hu, D. H. Froula, F. Albert, B. M. Hegelich, M. Roth, and E. M. Campbell, "Frontiers in High-Energy-Density and Relativistic Plasma Physics Enabled by EP-OPAL: A Multibeam Ultrahigh-Intensity Laser User Facility," presented at the Discovery Plasma Science Community Planning Workshop, Madison, WI, 23–25 July 2019.

The following presentations were made at High-Energy-Density Science Summer School, La Jolla, CA, 28 July–10 August 2019:

A. Kish and A. B. Sefkow, "Preliminary Work Toward an Investigation of Burn-Wave Propagation in Magnetized Cylindrical Targets."

T. T. Simpson, D. H. Froula, J. Vieira, and J. P. Palastro, "Nonlinear Self-Focusing of Flying Focus Pulses."

J. Wilson, V. N. Goncharov, C. Dorrer, A. Shvydky, and J. P. Palastro, "Broadband Smoothing of Laser Pulses for Imprint Reduction in Direct-Drive Inertial Confinement Fusion."

M. S. Wei, "LaserNetUS–OMEGA EP Laser System and Experimental Capability," presented at LaserNetUS, Virtual Meeting, 29 July 2019.

G. W. Collins, "Extreme Matters: Pressure to Explore Planets and Revolutionary Materials," presented at the 27th International Conference on High Pressure Science and Technology (AIRAPT27), Rio de Janeiro, Brazil, 4–9 August 2019.

L. S. Leal, A. V. Maximov, R. Betti, A. B. Sefkow, and V. Ivanov, "*HYDRA* Modeling of Laser-Ablated Plasma in Megagauss Magnetic Fields," presented at the Tenth Workshop on Fundamental Science with Pulsed Power and User Meeting, Albuquerque, NM, 11–14 August 2019.

R. B. Spielman and E. M. Campbell, "OMEGA-Z: A 15-TW Pulsed-Power Facility for High-Energy-Density Physics," presented at the Z Fundamental Science Program Workshop, Albuquerque, NM, 11–14 August 2019.

T. Filkins, J. Katz, and S. T. Ivancic, "Design of an Image-Relay Optical Time-Domain Reflectometer to Measure Fiber-Optic Time Delays at Inertial Confinement Fusion Relevant Wavelengths," presented at SPIE Optical Engineering and Applications, San Diego, CA, 11–15 August 2019.

K. L. Marshall, D. J. Batesky, J. U. Wallace, L. Garrett, T. Z. Kosc, S. Papernov, B. N. Hoffman, and J. Shojaie, "UV-Transmissive Glassy Liquid Crystals Employing Chiral Synthons Based on Natural Products," presented at SPIE Optics and Photonics, Liquid Crystals XXIII, San Diego, CA, 11–15 August 2019 (invited).

The following presentations were made at the International Workshop on Optical Thomson Scattering, Rochester, NY, 13–14 August 2019:

A. S. Davies, J. Katz, S. Bucht, D. Haberberger, J. P. Palastro, J. L. Shaw, D. Turnbull, R. Boni, I. A. Begishev, S.-W. Bahk, J. Bromage, A. Sorce, J. Konzel, R. Cuffney, J. D. Zuegel, D. H. Froula, and W. Rozmus, "Investigation of Electron Plasma Waves and Picosecond Thermodynamics in a Laser-Produced Plasma Using Thomson Scattering."

R. K. Follett, J. A. Delettrez, D. H. Edgell, R. J. Henchen, J. Katz, J. F. Myatt, and D. H. Froula, "Subtleties to Fitting Thomson-Scattering Spectra."

A. M. Hansen, D. Turnbull, J. Katz, A. L. Milder, J. P. Palastro, D. Mastrosimone, and D. H. Froula, "Phase Plates in Thomson-Scattering Experiments."

J. Katz, "Lessons Learned from the Implementation and Operation of the OMEGA Thomson Scattering System."

A. L. Milder, J. Katz, R. Boni, D. Nelson, J. P. Palastro, K. Daub, R. K. Follett, and D. H. Froula, "Measurements of Arbitrary Distribution Functions Using Angularly Resolved Thomson Scattering."

H. G. Rinderknecht, H. S. Park, J. S. Ross, P. A. Amendt, D. P. Higginson, S. C. Wilks, R. K. Follett, D. Haberberger, J. Katz, D. H. Froula, N. M. Hoffman, G. Kagan, B. Keenan, A. Simakov, L. Chacon, and E. Vold, "Imaging Thomson Scattering: Measuring Plasma Conditions in a Strong Shock."

H. G. Rinderknecht, D. H. Froula, S. X. Hu, P. M. Nilson, and J. D. Zuegel, "Frontiers in Physics Enabled by EP-OPAL: A Multibeam Ultra-Intense Laser User Facility," presented at ExHILP 2019, Stanford, CA, 3–6 September 2019.

J. D. Zuegel, "The Brightest Light Initiative (BLI): A Path Forward for Ultra-Intense Ultrafast Lasers in the U.S.," presented at Frontiers in Optics, Washington, DC, 15–19 September 2019.

The following presentations were made at the 41st Tritium Focus Group Meeting, Augusta, GA, 17–19 September 2019:

D. Bassler, "Making an Optimal Hafnium Oxide Film as a Hydrogen Diffusion Barrier."

C. Fagan, M. Sharpe, W. T. Shmayda, and W. U. Schröder, "Distribution of Tritium in the Near Surface of 316 Stainless Steel."

M. Sharpe and W. T. Shmayda, "Measurement of Palladium Hydride Isotherms Between 130 K and 393 K Using Pure H_2, Pure D_2, and HD Mixtures."

The following presentations were made at the U.S.–Japan Workshop on Theory and Simulations of High Energy Density Physics with Extreme Fields, Osaka, Japan, 21–22 September 2019:

D. H. Froula, S.-W. Bahk, I. A. Begishev, R. Boni, J. Bromage, A. Davies, R. K. Follett, D. Haberberger, A. Howard, G. Jenkins, J. Katz, T. J. Kessler, L. Nguyen, J. P. Palastro, D. Ramsey, J. L. Shaw, D. Turnbull, N. Vafaei-Najafabadi, J. Vieira, and F. Quéré, "Flying Focus: Spatiotemporal Control of Intensity for Laser-Based Applications."

H. G. Rinderknecht, M. S. Wei, J. P. Palastro, G. Bruhaug, A. Arefiev, T. Wang, T. Toncian, H. J. Quevedo, T. Ditmire, and J. Williams, "Megatesla Magnetic Fields and Efficient Gamma-Ray Generation Using Microstructured Targets: Preparations for Experiments at TPW."

The following presentations were made at Laser Damage 2019, Boulder, CO, 22–25 September 2019:

B. N. Hoffman, A. A. Kozlov, J. B. Oliver, T. J. Kessler, A. L. Rigatti, S. G. Demos, A. Shestopalov, and N. Liu, "Damage Morphology and Damage-Initiation Mechanisms in Multilayer Dielectric Gratings at Different Pulse Durations."

K. R. P. Kafka, S. G. Demos, and B. N. Hoffman, "Short-Pulse Laser Irradiation of Microparticle Contamination on Reflective Optics."

A. A. Kozlov, D. Canning, B. N. Hoffman, B. E. Kruschwitz, A. L. Rigatti, and L. J. Waxer, "Review of Decade-Long Monitoring Damage Resistance of Multilayer Dielectric Gratings Inside the Vacuum Compressor Chamber on OMEGA EP."

L. Lamaignère, A. Ollé, M. Chorel, N. Roquin, A. A. Kozlov, B. N. Hoffman, J. B. Oliver, L. Gallais, and S. G. Demos, A. Melninkaitis, "Round-Robin Measurements of Optical Monolayer Laser-Induced–Damage Threshold in the Subpicosecond Range."

J. B. Oliver, "Coatings for Large-Aperture Laser Systems."

A. A. Shestopalov, N. Liu, B. N. Hoffman, A. A. Kozlov, and S. G. Demos, "Chemical Composition, Structure Morphology, Contaminant Cleaning and Laser-Induced–Damage Threshold in Coarse Fused-Silica Gratings."

J. U. Wallace, K. L. Marshall, T. Z. Kosc, D. J. Batesky, B. N. Hoffman, S. Papernov, L. Garrett, J. Shojaie, and S. G. Demos, "Laser-Induced–Damage Behavior of Novel Glassy Liquid Crystal Materials at 1 ns and Multiple Wavelengths."

A. Milder, J. Katz, R. Boni, D. Nelson, J. P. Palastro, A. M. Hansen, D. Turnbull, P. Franke, S. T. Ivancic, J. L. Shaw, K. Daub, R. K. Follett, D. H. Froula, H. Le, M. Sherlock, and W. Rozmus, "Novel Techniques and Uses of Collective Thomson Scattering," presented at Laser Aided Plasma Diagnostics 2019, Whitefish, MT, 22–26 September 2019.

The following presentations were made at 11th International Conference on Inertial Fusion Science and Applications, Osaka, Japan, 22–27 September 2019:

A. R. Christopherson, R. Betti, S. Miller, V. Gopalaswamy, D. Cao, and O. M. Mannion, "Theory of Ignition and Burn Propagation in Inertially Confined Plasmas."

D. H. Froula, C. Dorrer, E. M. Hill, J. Bromage, T. J. Kessler, J. D. Zuegel, R. K. Follett, L. Nguyen, A. A. Solodov, J. P. Palastro, D. Turnbull, D. H. Edgell, J. G. Shaw, A. M. Hansen, A. L. Milder, J. Katz, R. Boni, V. N. Goncharov, M. Sherlock, H. Le, D. J. Strozzi, P. Michel, L. Divol, J. F. Myatt, W. Rozmus, J. Bates, A. Schmitt, J. Weaver, A. Colaïtis, L. Yin, and B. Albright, "A Path to an Expanded Inertial Confinement Fusion Design Space Through a Better Understanding and Mitigation of Laser–Plasma Instabilities."

F. García Rubio, R. Betti, and H. Aluie, "The Effect of Self-Generated Magnetic Fields on the Ablative Rayleigh–Taylor Instability Dynamics."

V. N. Goncharov, "Progress Toward the Demonstration of Burning Plasma in the U.S. Inertial Confinement Fusion Program."

V. Gopalaswamy, R. Betti, J. P. Knauer, A. Lees, D. Patel, A. R. Christopherson, K. M. Woo, O. M. Mannion, Z. L. Mohammed, F. J. Marshall, C. Stoeckl, V. Yu. Glebov, S. P. Regan, R. C. Shah, D. H. Edgell, D. Cao, V. N. Goncharov, I. V. Igumenshchev, P. B. Radha, T. J. B. Collins, T. C. Sangster, E. M. Campbell, M. Gatu Johnson, R. D. Petrasso, C. K. Li, and J. A. Frenje, "Statistically Guided Design of Direct-Drive Inertial Confinement Fusion Experiments."

S. X. Hu, R. Epstein, W. Theobald, V. N. Goncharov, S. P. Regan, P. W. McKenty, R. Betti, E. M. Campbell, H. Xu, H. Huang, and D. S. Montgomery, "Direct-Drive Double-Shell (D^3S) Implosion: A Platform for Burning-Plasma Studies."

P. B. Radha, M. J. Rosenberg, A. Shvydky, A. A. Solodov, R. Betti, E. M. Campbell, T. J. B. Collins, R. S. Craxton, V. N. Goncharov, J. A. Marozas, F. J. Marshall, S. P. Regan, T. C. Sangster, and D. Turnbull, "Direct-Drive Physics at the National Ignition Facility."

S. P. Regan, V. N. Goncharov, T. C. Sangster, R. Betti, E. M. Campbell, K. A. Bauer, T. R. Boehly, M. J. Bonino, D. Cao, A. R. Christopherson, G. W. Collins, T. J. B. Collins, R. S. Craxton, D. H. Edgell, R. Epstein, C. J. Forrest, R. K. Follett, D. H. Froula, V. Yu. Glebov, V. Gopalaswamy, D. R. Harding, S. X. Hu, I. V. Igumenshchev, S. T. Ivancic, D. W. Jacobs-Perkins, R. T. Janezic, J. H. Kelly, T. J. Kessler, J. P. Knauer, T. Z. Kosc, O. M. Mannion, J. A. Marozas, F. J. Marshall, P. W.

McKenty, Z. L. Mohamed, S. F. B. Morse, P. M. Nilson, J. P. Palastro, D. Patel, J. L. Peebles, P. B. Radha, H. G. Rinderknecht, M. J. Rosenberg, S. Sampat, W. Seka, R. C. Shah, J. R. Rygg, J. G. Shaw, W. T. Shmayda, M. J. Shoup III, A. Shvydky, A. A. Solodov, C. Sorce, C. Stoeckl, W. Theobald, D. Turnbull, J. Ulreich, M. D. Wittman, K. M. Woo, J. D. Zuegel, J. A. Frenje, M. Gatu Johnson, R. D. Petrasso, M. Karasik, S. P. Obenschain, A. J. Schmitt, T. J. Hilsabeck, K. Englehorn, J. D. Kilkenny, J. D. Hares, A. K. L. Dymoke-Bradshaw, P. Bell, A. Carpenter, D. K. Bradley, S. Nagel, G. Rochau, and L. Claus, "Multidimensional Effects on Hot-Spot Formation in OMEGA DT Cryogenic Implosions."

H. Rinderknecht, C. J. Forrest, J. P. Knauer, W. Theobald, S. P. Regan, R. Simpson, and J. A. Frenje, "Knock-On Deuteron Imaging to Diagnose Hot-Spot Fuel and ρR Symmetry in Directly Driven Inertial Confinement Fusion Implosions."

M. Zaghoo, T. R. Boehly, J. R. Rygg, P. M. Celliers, S. X. Hu, and G. W. Collins, "Breakdown of Fermi Degeneracy in Shocked Deuterium."

J. D. Zuegel, "Laboratory for Laser Energetics," presented at the Visit of the Honorable Carl Heastie, Speaker of the NYS Assembly, Rochester, NY, 23 September 2019.

M. S. Wei, "Opportunities for U.S.–ELI Collaborations: Laboratory for Laser Energetics Perspective," presented at the U.S.–ELI Joint Workshop, Washington, DC, 25 September 2019.

R. Betti, "Status and Prospects for Nuclear Fusion with Lasers," presented at FisMat 2019, Catania, Italy, 30 September–4 October 2019 (invited).

UNIVERSITY *of* ROCHESTER